Vol. 282, No. 3, October 29, 1993
Completing Volume 282

ISSN 0003-2670

ANALYTICA CHIMICA ACTA

An international journal devoted to all branches of analytical chemistry

ELSEVIER

ANALYTICA CHIMICA ACTA

Scope. *Analytica Chimica Acta* publishes original papers, preliminary communications and reviews dealing with every aspect of modern analytical chemistry. Reviews are normally written by invitation of the editors, who welcome suggestions for subjects. Preliminary communications of important urgent work can be printed within four months of submission, if the authors are prepared to forego proofs.

Submission of Papers

Americas

Prof. Harry L. Pardue
Department of Chemistry
1393 BRWN Bldg, Purdue University
West Lafayette, IN 47907-1393
USA

Tel:(+1-317) 494 5320
Fax:(+1-317) 496 1200

Computer Techniques

Prof. J.T. Clerc
Universität Bern
Pharmazeutisches Institut
Baltzerstrasse 5, CH-3012 Bern
Switzerland

Tel:(+41-31) 654171
Fax:(+41-31) 654198

Prof. Sarah C. Rutan
Department of Chemistry
Virginia Commonwealth University
P.O. Box 2006
Richmond, VA 23284-2006
USA
Tel:(+1-804) 367 1298
Fax:(+1-804) 367 8599

Other Papers

Prof. Alan Townshend
Department of Chemistry
The University
Hull HU6 7RX
Great Britain

Tel:(+44-482) 465027
Fax:(+44-482) 466410

Prof. Willem E. van der Linden
Laboratory for Chemical Analysis
Department of Chemical Technology
Twente University of Technology
P.O. Box 217, 7500 AE Enschede
The Netherlands
Tel:(+31-53) 892629
Fax:(+31-53) 356024

Prof. Paul Worsfold
Dept. of Environmental Sciences
University of Plymouth
Plymouth PL4 8AA
Great Britain

Tel:(+44-752) 233006
Fax:(+44-752) 233009

Submission of an article is understood to imply that the article is original and unpublished and is not being considered for publication elsewhere. *Anal. Chim. Acta* accepts papers in English only. There are no page charges. Manuscripts should conform in layout and style to the papers published in this issue. See inside back cover for "Information for Authors".

Publication. *Analytica Chimica Acta* appears in 16 volumes in 1994 (Vols. 281-296). *Vibrational Spectroscopy* appears in 2 volumes in 1994 (Vols. 6 and 7). Subscriptions are accepted on a prepaid basis only, unless different terms have been previously agreed upon. It is possible to order a combined subscription (*Anal. Chim. Acta* **and** *Vib. Spectrosc.*).
Our p.p.h. (postage, packing and handling) charge includes surface delivery of all issues, except to subscribers in the U.S.A., Canada, Australia, New Zealand, China, India, Israel, South Africa, Malaysia, Thailand, Singapore, South Korea, Taiwan, Pakistan, Hong Kong, Brazil, Argentina and Mexico, who receive all issues by air delivery (S.A.L.-Surface Air Lifted) at no extra cost. For Japan, air delivery requires 25% additional charge of the normal postage and handling charge; for all other countries airmail and S.A.L. charges are available upon request.

Subscription orders. Subscription prices are available upon request from the publisher. Subscription orders can be entered only by calendar year and should be sent to: Elsevier Science Publishers B.V., Journals Department, P.O. Box 211, 1000 AE Amsterdam, The Netherlands. Tel: (+31-20) 5803 642, Telex: 18582, Telefax: (+31-20) 5803598, to which requests for sample copies can also be sent. Claims for issues not received should be made within six months of publication of the issues. If not they cannot be honoured free of charge. Readers in the U.S.A. and Canada can contact the following address: Elsevier Science Publishing Co. Inc., Journal Information Center, 655 Avenue of the Americas, New York, NY 10010, U.S.A. Tel: (+1-212) 6333750, Telefax: (+1-212) 6333990, for further information, or a free sample copy of this or any other Elsevier Science Publishers journal.
Advertisements. Advertisement rates are available from the publisher on request.

US mailing notice - Analytica Chimica Acta (ISSN 0003-2670) is published biweekly by Elsevier Science Publishers (Molenwerf 1, Postbus 211, 1000 AE Amsterdam). Annual subscription price in the USA US$ 3035.75 (valid in North, Central and South America), including air speed delivery. Application to mail at second class postage rate is paid at Jamaica, NY 11431. *USA Postmasters*: Send address changes to Anal. Chim. Acta, Publications Expediting, Inc., 200 Meacham Av., Elmont, NY 11003. Airfreight and mailing in the USA by Publication Expediting.

CHEMOMETRICS TUTORIALS II

edited by **R.G. Brereton**, University of Bristol, Bristol, UK, **D.R. Scott**, U.S. Environmental Protection Agency, Research Triangle Park, NC, USA, **D.L. Massart**, Vrije Universiteit Brussel, Brussels, Belgium, **R.E. Dessy**, Virginia Polytechnic Institute, Blackburg, VA, USA, **P.K. Hopke**, Clarkson University, Potsdam, NY, USA, **C.H. Spiegelman**, Texas A&M University, College Station, TX, USA and **W. Wegscheider**, Universität Graz, Graz, Austria

The journal Chemometrics and Intelligent Laboratory Systems has a specific policy of publishing tutorial papers (i.e. articles aiming to discuss and illustrate the application of chemometric and other techniques) solicited from leading experts in the varied disciplines relating to this subject. This book comprises reprints of tutorials from Volumes 6-11 of this journal, covering the period from mid 1989 to late 1991. The authors of the papers include analytical, organic and environmental chemists, statisticians, pharmacologists, geologists, geochemists, computer scientists and biologists, which reflects the strong interdisciplinary communication. The papers have been reorganized into major themes, covering most of the main areas of chemometrics.

This book is intended both as a personal reference text and as a useful background for courses in chemometrics and laboratory computing.

Contents: Foreword.
Software. 1. Teaching and Learning Chemometrics with MatLab *(T.C. O'Haver)*. 2. Expert System Development Tools for Chemists *(F.A. Settle, Jr., M.A. Pleva)*. 3. Spectral Databases *(W.A. Warr)*.
Signal Processing. 4. Specification and Estimation of Noisy Analytical Signals. Part I. Characterization, Time Invariant Filtering and Signal Approximation *(H.C. Smit)*. 5. Specification and Estimation of Noisy Analytical Signals. Part II. Curve Fitting, Optimum Filtering and Uncertainty Determination *(H.C. Smit)*. 6. Fast On-Line Digital Filtering *(S.C. Rutan)*.
Multivariate Methods. 7. Cluster Analysis *(N. Bratchell)*. 8. Interpretation of Latent-Variable Regression Models *(O.M. Kvalheim, T.V. Karstang)*. 9. Quantitative Structure-Activity Relationships (QSAR) *(W.J. Dunn, III)*. 10. Analysis of Multi-Way (Multi-Mode) Data *(P. Geladi)*.
Factor Analysis. 11. Target Transformation Factor Analysis *(P.K. Hopke)*. 12. An Introduction to Receptor Modeling *(P.K. Hopke)*. 13. The Spectrum Reconstruction Problem. Use of Alternating Regression for Unexpected Spectral Components in Two-Dimensional Spectroscopies *(E.J. Karjalainen)*.
Statistics. 14. Analysis of Variance (ANOVA) *(L. Ståhle, S. Wold)*. 15. Multivariate Analysis of Variance (MANOVA) *(L. Ståhle, S. Wold)*. 16. The Validation of Measurement through Inter-laboratory Studies *(J. Mandel)*. 17. Regression and Calibration with Nonconstant Error Variance *(M. Davidian, P.D. Haaland)*. 18. Interpolation and Estimation with Spatially Located Data Sets *(D.E. Myers)*.
Optimization. 19. Optimization Using the Modified Simplex Method *(E. Morgan, K.W. Burton, G. Nickless)*. 20. Optimization Using the Super-Modified Simplex Method *(E. Morgan, K.W. Burton, G. Nickless)*.
Fractals. 21. Fractals in Chemistry *(D.B. Hibbert)*. Author Index. Subject Index.

1992 x + 314 pages
Paperback
Price: US $ 156.50 / Dfl. 250.00
ISBN 0-444-89858-1

ORDER INFORMATION

For USA and Canada
ELSEVIER SCIENCE PUBLISHERS
Judy Weislogel
P.O. Box 945
Madison Square Station,
New York, NY 10160-0757
Tel: (212) 989 5800
Fax: (212) 633 3880

In all other countries
ELSEVIER SCIENCE PUBLISHERS
P.O. Box 211
1000 AE Amsterdam
The Netherlands
Tel: (+31-20) 5803 753
Fax: (+31-20) 5803 705

US$ prices are valid only for the USA & Canada and are subject to exchange rate fluctuations; in all other countries the Dutch guilder price (Dfl.) is definitive. Books are sent postfree if prepaid.

ELSEVIER
SCIENCE PUBLISHERS

ANALYTICA CHIMICA ACTA

An international journal devoted to all branches of analytical chemistry

(Full texts are incorporated in CJELSEVIER, a file in the Chemical Journals Online database available on STN International; Abstracted, indexed in: Aluminum Abstracts; Anal. Abstr.; Biol. Abstr.; BIOSIS; Chem. Abstr.; Curr. Contents Phys. Chem. Earth Sci.; Engineered Materials Abstracts; Excerpta Medica; Index Med.; Life Sci.; Mass Spectrom. Bull.; Material Business Alerts; Metals Abstracts; Sci. Citation Index)

VOL. 282 NO. 3 CONTENTS OCTOBER 29, 1993

(Continued overleaf)

Contents (continued)

Analytica Chimica Acta, 282 (1993) 459–470
Elsevier Science Publishers B.V., Amsterdam

Determination of folic acid in sea water using adsorptive cathodic stripping voltammetry

Anne-Christine Le Gall and Constant M.G. van den Berg

Oceanography Laboratory, Department of Earth Sciences, University of Liverpool, Liverpool L69 3BX (UK)

(Received 12th May 1993; revised manuscript received 16th June 1993)

Abstract

Folic acid is of biological origin and occurs ubiquitously in the natural system. Very little is known about its likely occurrence and distribution in natural waters. A voltammetric method is proposed to determine folic acid in sea and estuarine waters. The method is based on cathodic stripping voltammetry (CSV) preceded by adsorptive collection on a hanging mercury drop electrode. Using cyclic voltammetry at two pH values it is confirmed that folic acid undergoes reduction in three steps. The first step is electrochemically reversible producing a two-electron reduction peak at −0.75 V at pH 8.5. Comparative experiments indicate that the benzene ring is responsible for the adsorptive behaviour of folic acid on the mercury drop electrode. The adsorbed layer of folic acid is rearranged when the adsorption density is increased above $\sim 5.10^{-11}$ mol cm^{-2} causing the appearance of a sharp capacitance peak. The best sensitivity for the determination of folic acid in sea water is obtained at pH 8.5 at a deposition potential of −0.25 V and using the square-wave modulation at frequencies between 25 and 100 Hz. The voltammetric response for 60 s adsorption was found to increase linearly with the folic acid concentration from the limit of detection (0.09 nM) to 500 nM. The method was applied successfully to the determination of dissolved folic acid in samples from the Mersey estuary. The folic acid concentration was found to lie between 0.1 and 3 nM increasing generally with decreasing salinity due to freshwater inputs.

Keywords: Stripping voltammetry; Folic acid; Sea water; Waters

Part of the vitamin B group, folic acid is a water soluble vitamin, initially identified as an antianaemia and growth factor. It is produced by plants (green leaves, algae) and micro-organisms (bacteria, yeast). In mammals, folic acid and its derivatives, the folates, serve as acceptors and donors of one carbon units and are involved in amino acid and nucleotide formation [1–2]. Because of its ubiquitous occurrence in biological systems it is likely that folic acid occurs also in natural waters as a result of algal exudations [3] or of involuntary releases as a result of cellular damage, but surprisingly little is known about its occurrence and distribution. The concentrations of other vitamins, especially vitamin B_{12}, biotin and thiamine, have been estimated in various water bodies such as lakes [4] coastal waters [5–8] and open sea [9–11]. The distribution of folic acid in natural waters has not been reported perhaps because no analytical techniques were available to detect the low levels occurring there.

Analytical methods for folic acid include bioassays, enzymatic methods, fluorimetry, colorimetry and chromatography [2]. The introduction of liquid chromatography (LC) and radioactive labelling have improved the specificity and sensitivity of folic acid measurements [1]. Electrochemical methods have been used to detect folic acid

Correspondence to: C.M.G. van den Berg, Oceanography Laboratory, Department of Earth Sciences, University of Liverpool, Liverpool L69 3BX (UK).

[12] and to investigate its redox properties [13]. Cathodic stripping voltammetry (CSV) has been used previously to detect low nanomolar levels of folic acid in weakly acidic solutions and synthetic electrolytes [14–16].

Adsorptive CSV is here optimised to determine folic acid in estuarine and sea water at a limit of detection of 0.02 nM using an adsorption time of 5 min (this limit of detection is similar to or better than that quoted by previous work [14–16] although the optimised conditions differ). The electrode mechanism is investigated by cyclic voltammetry and comparative experiments with constituents of folic acid. The method is applied to samples from the Mersey estuary (UK).

EXPERIMENTAL

Equipment and reagents

Voltammograms were recorded with a PAR 174A polarograph in conjunction with a PAR 303 HMDE (reference electrode: Ag/AgCl, saturated with KCl; counter electrode: platinum wire; drop size: 1.9 mm^2) or with a computerised Autolab polarograph (Ecochemie, Netherlands) with a 663 VA Metrohm electrode (reference electrode: Ag/AgCl, 3 M KCl; counter electrode: platinum wire; drop size: 0.38 mm^2). A Metrohm E 506 Polarorecord was used in conjunction with the 663 VA Metrohm electrode for experiments involving tensammetry.

Water was purified using a fused silica double distillation unit or a Millipore apparatus for reverse osmosis (Milli-RO 10 Plus) followed by ion-exchange (Milli-Q). This water was used for reagent preparation, rinsing and preliminary experiments. Reagents were supplied by BDH (AnalaR grade), except for humic acid which was from EGA-Chemie (FRG).

Sample bottles of high density polyethylene (HDPE) were cleaned by soaking with hot water and detergent. They were then rinsed with water, soaked in 50% HCl (GPR grade) for a week, rinsed again with water, and soaked in 2 M nitric acid for another week. Finally, the bottles were rinsed with water, filled with 0.01 M HCl (Aristar grade, BDH) and stored in resealable bags, ready for sample collection.

Reagents were Analar Grade (BDH) unless indicated differently. A borate pH buffer (1 M boric acid, 0.4 M NaOH) and a sodium acetate buffer [2 M sodium acetate, 0.5 M hydrochloric acid (Aristar grade)] were used to buffer sea water at pH 8.5 and 5.2 respectively. Folic acid solutions were prepared daily from a 0.1 M stock solution which was prepared weekly in 0.1 M sodium hydroxide and kept in the dark at 4°C.

Sea water from Menai Straits ($S = 32.5$ p.s.u.) was used for preliminary experiments; it was UV-irradiated in fused silica containers (100 ml) with a 1-kW mercury vapour lamp for 4 h prior to use.

Samples from the Mersey estuary were collected using a jet-foil vessel (NRA North West) on July 11, August 21 and September 20, 1990. The samples were collected at high tide forward of the slowly moving vessel using a polypropylene bucket which was deployed and recovered by hand using a nylon rope. The bucket was rinsed with freshly collected sea water prior to each sample collection. The samples were stored in HDPE bottles in the dark at 4°C and analysed within one week. The samples were not filtered but suspended matter was allowed to sediment to the bottom of the bottles prior to the taking of subsamples for voltammetric analysis. Sample analyses were carried out in a random order, and about half the samples were analysed twice, once in the beginning of the series and the second time at the end to test for sample degradation.

Procedure

A 10 ml aliquot of sea water was pipetted into a glass polarographic cell. Borate or acetate pH buffer (final concentrations 0.01 M and 0.02 M respectively) was added and the solution was purged (8 min) with O_2-free nitrogen. A 60 s preconcentration step was then completed on a new mercury drop at a potential of -0.2 V whilst stirring. Subsequently the stirrer was switched off for a 15 s quiescent period. Finally, a potential scan was carried out in a negative direction from -0.2 V. Unless specified differently the differential pulse modulation was used with a scan rate of

20 mV/s, a modulation amplitude of 25 mV and a pulse time of 0.1 s. The procedure was repeated after addition of folic acid standard to calibrate the sensitivity.

Tensammetry was used to evaluate variations in the double-layer capacitance upon adsorption on the electrode. An AC-waveform was thereto superimposed on the slowly scanning potential (20 mV s^{-1}) with an amplitude of 10 mV and a frequency of 75 Hz. The phase angle was 90°. Other conditions were as for differential pulse voltammetry.

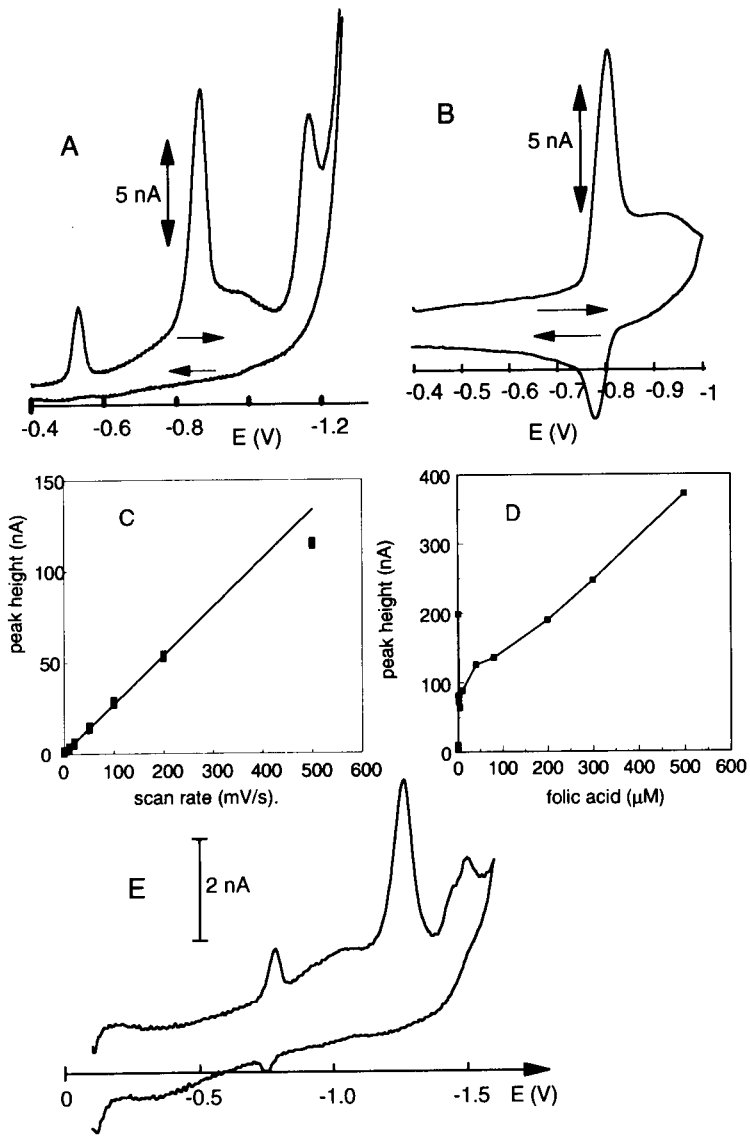

Fig. 1. Cyclic voltammetry of 100 nM folic acid (A and B) and 5,8-dihydrofolic acid (E) preceded by 60 s adsorption. (A) pH 5.2; (B) pH 8.5; (C) peak height of the reduction peak of 200 nM folic acid at pH 8.5 as a function of the scan-rate. (D) Peak height as a function of the folic acid concentration; note the high concentration range along the x-axis which causes the linear increase at low folic acid concentrations (< 1 μM) including the maximum in the peak height caused by the capacitance peak at ~ 1 μM folic acid to appear close to the vertical axis. (E) Cyclic voltammetry at pH 8.5.

RESULTS AND DISCUSSION

Cyclic voltammetry of folic acid

Cyclic voltammetry was used to investigate the reaction mechanism of folic acid. Three cathodic peaks were present at pH 5 at −0.5, −0.8 and −1.2 V whereas no anodic peaks were observed (Fig. 1A) indicating that the reduction steps were electrochemically irreversible. A single peak was obtained at −0.8 V at pH 8.5 (Fig. 1B) corre-

Reaction 1:

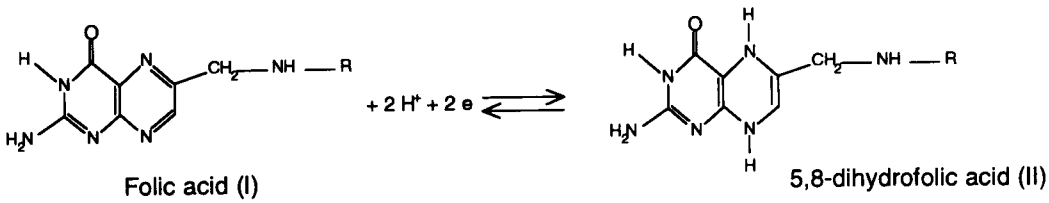

Reaction 2:

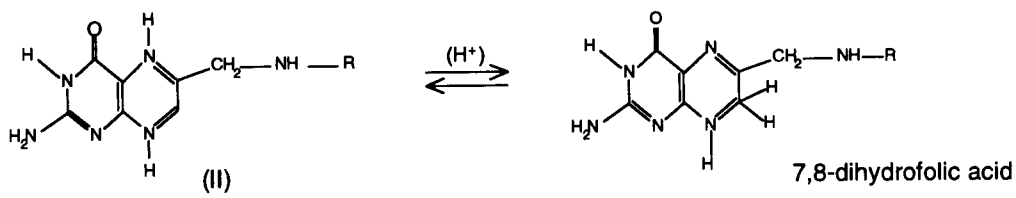

Reaction 3:

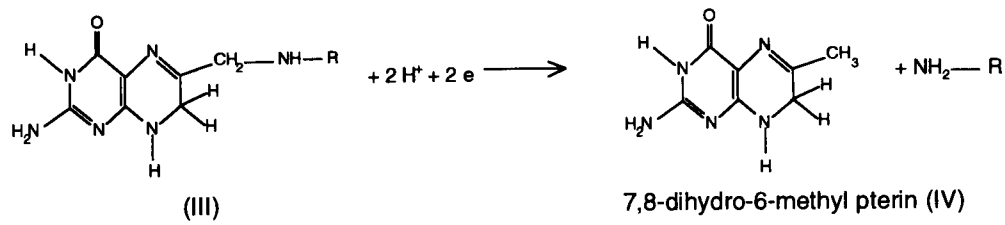

Reaction 4:

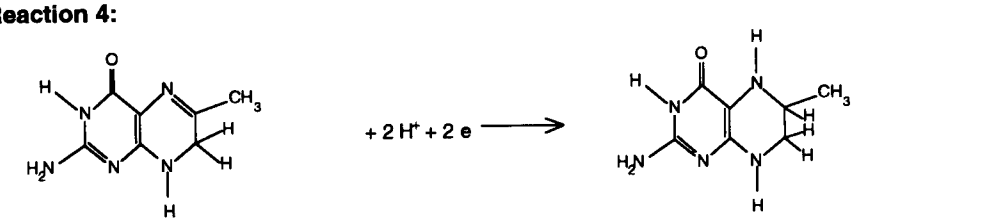

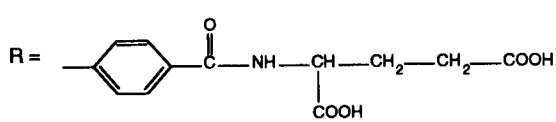

Fig. 2. Reduction mechanism of folic acid.

sponding with the peak at −0.5 V at pH 5 but shifted to a more negative potential as a result of the pH change. An anodic peak was apparent on the reverse scan indicating that this reduction step was reversible at pH 8.5.

The presence of three peaks at pH 5 and a single peak at pH 8.5 is in agreement with a reduction mechanism consisting of a two-electron reduction (reaction 1 in Fig. 2 at −0.5 V at pH 5, at −0.8 V at pH 8.5) followed by a tautomerisation (reaction 2) and two irreversible reduction steps (reactions 3 and 4 in Fig. 2, and peaks at −0.8 and −1.2 V at pH 5 in Fig. 1A) [13,17]. The tautomerisation is catalysed by protons which ex-

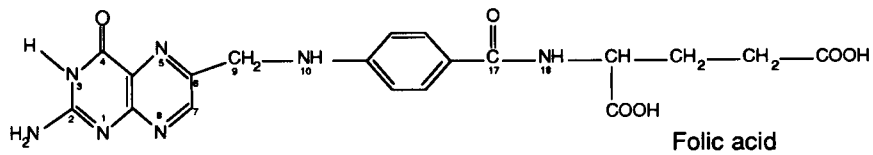

Folic acid

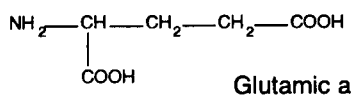

Glutamic acid

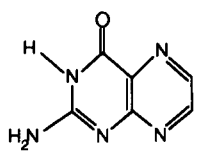

Pterin

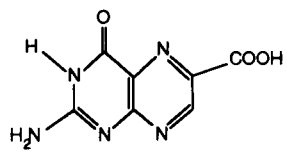

Pterin-6-carboxilic acid

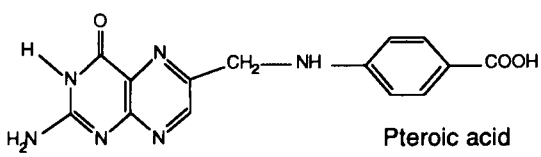

Pteroic acid

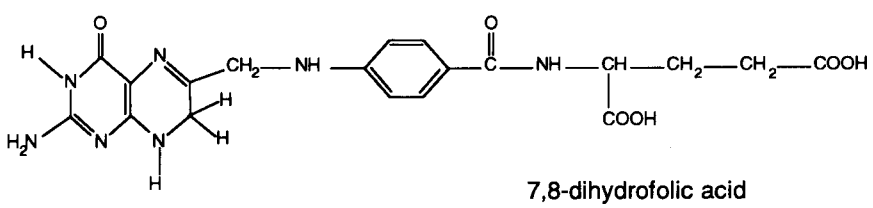

7,8-dihydrofolic acid

Fig. 3. Structural formulas for folic acid, precursors and reduction product.

plains the absence of a further reduction of the folic acid beyond the first reduction step at pH 8.5 as a result of stabilisation of the reaction product (5,8-dihydrofolic acid) as the tautomerisation was inhibited at this pH.

The scans in Fig. 1 were preceded by deposition at −0.4 V. In comparison with scans without adsorption (not shown) the peaks were much enhanced indicating that the folic acid was adsorbed on the electrode. The height of the folic acid reduction peak was much reduced (about 50%) when the cyclic scan was repeated on the same mercury drop without renewed adsorption indicating irreversibility either as a result of partial desorption of the reduction product [5,8-dihydrofolic acid (5,8-DHF)] or of partial irreversibility of the redox reaction. The adsorptive preconcentration greatly enhances the CSV sensitivity for folic acid.

Variation of the scan-rate between 10 and 500 mV s^{-1} showed that the CSV peak height (preceded by 60 s adsorption) for 200 nM folic acid increased linearly with the scan rate until 200 mV s^{-1} and non-linearly thereafter (Fig. 1C). The linear increase indicates that the reduction current is essentially independent of diffusion during the scan, in accordance with the proposed process in which an adsorbed compound (folic acid) is reduced. The non-linear increase at high scan-rates indicates that the reduction process becomes kinetically slow in this condition.

Cyclic voltammetry was used to investigate the electrochemical activity of compounds with a chemical composition similar to that of folic acid or to that of components of folic acid in an attempt to evaluate which part of the molecule is responsible for the adsorptive process. The chemical composition of precursors of folic acid selected for the comparative experiments [glutamic acid (R in folic acid, Fig. 2), pterin, pterin-6-carboxilic acid and pteroic acid] can be compared in Fig. 3 along with that of the reduction product of folic acid (5,8-DHF). Pterin, pterin-6-carboxilic acid, pteroic acid and 5,8-DHF were found to produce a reduction peak at between −0.7 and −0.8 V at pH 8.5 corresponding with the peak for reaction 1 of folic acid, whereas glutamic acid was electroinactive. However, only pteroic acid and dihydrofolic acid adsorbed on the HMDE (analogous with folic acid), indicating that the adsorption site (common to these compounds and folic acid but absent in pterin) is located between atoms N(10) and N(18) in the folic acid molecule (Fig. 3). It is therefore likely that the benzene ring is responsible for the folic acid adsorption, in accordance with the known importance of free p-orbital electrons to adsorption of organic compounds on the mercury electrode [18,19].

Cyclic voltammetry of 5,8-DHF at pH 8.5 (Fig. 1E) showed a comparatively small peak at the reduction potential corresponding with that for folic acid indicating that only part of the 5,8-DHF was oxidised and adsorbed during the deposition step at −0.2 V. A second peak was apparent at −1.25 V presumably corresponding with the reduction of 7,8-DHF (tautomerisation product of 5,8-DHF), and a smaller peak at −1.5 V corresponding with the third reduction step (reaction 4 in Fig. 2). Interestingly no reduction peak corresponding with that of folic acid was apparent upon cyclic voltammetry of 5,8-DHF at pH 5 (not shown) presumably because of the rapid tautomerisation of the 5,8-DHF at this pH which rendered the redox process irreversible. However, the two peaks corresponding with reactions 3 and 4 of folic acid (Fig. 2) were clearly apparent.

The reduction current was determined at increasing concentration of folic acid to evaluate the maximum adsorption density of folic acid on the mercury drop. Interestingly the reduction current continued to increase with the concentration of the folic acid concentration (at pH 8.5) and did not show the curvature characteristic of saturation of the mercury drop at high folic acid concentration. However, a sharp and narrow peak became superimposed on the folic acid peak at concentrations around 1 μM (adsorption time of 60 s). This superimposed peak disappeared at longer adsorption times and at higher concentrations of folic acid. Such narrow peaks are usually associated with capacitive phenomena and can be due to rearrangement of the adsorbed layer [19,20]. Folic acid is thought to form a metastable adsorbed layer which rearranges when a critical adsorption density of folic acid is reached [14]

presumably when the electrode is fully covered by the adsorbed molecules. The rearrangement then allows higher densities which are stable to high folic acid concentrations [14]. In accordance with this scenario the current increased linearly from low nanomolar folic acid concentrations to ~1 μM; the sensitivity then dropped to a lower value causing the current to increase further in a linear fashion from 5 to 500 μM (the experiment was not continued to higher concentrations) (Fig. 1D). No additional capacitive peaks were observed at folic acid concentrations above 1 μM indicating that no further rearrangements occurred in the adsorbed monolayer of folic acid despite the very high concentrations.

The adsorption density of folic acid was 3.1×10^{-11} mol cm^{-2} at 0.5 μM folic acid, just before the rearrangement of the adsorbed layer (calculated using Faraday's law, using two electrons per molecule of reduced folic acid). At this density the surface area available to each folic acid molecule was 570 $Å^2$, much greater than that (approximately 71 $Å^2$; less if only the benzene ring adsorbs) occupied by the adsorbed part of folic acid between the N(10) and the N(18) atoms. It is therefore likely that the reorganisation of the adsorbed layer is due to interactions between the non-adsorbed components of the folic acid molecule rather than due to interactions between the adsorbed fractions. Apparently the reorganised molecules could be compacted to much higher densities on the electrode surface since no capacitive effect or curvature of the response was apparent at concentrations up to 500 μM, albeit at a reduced ($10^{-3} \times$) sensitivity compared to the CSV response prior to the collapse of the adsorbed film.

Tensammetry of folic acid

The mechanism of adsorption was further investigated using tensammetry utilising an AC-waveform superimposed on a DC scan with 90° out-of-phase sampling of the capacitance current; the frequency was 75 Hz. A large suppression of the capacitive signal at the HMDE was caused by folic acid in the region between −0.2 and −0.78

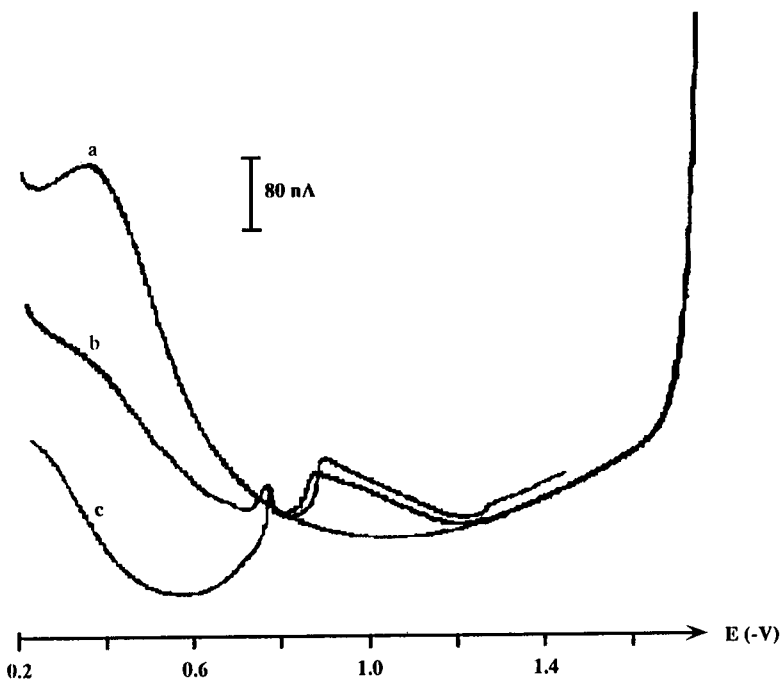

Fig. 4. Tensammetry of folic acid in sea water of pH 8.5. (a) no folic acid; (b) 0.5 μM folic acid; (c) 1 μM folic acid. Each scan was preceded by 60 s adsorption at −0.2 V.

V at pH 8.5. This suppression increased with the folic acid concentration until 1 μM folic acid (Fig. 4). The suppression was cancelled by a peak at −0.78 V, coinciding with the Faradaic peak, and was followed by an increase in the capacitance between −0.8 and −1.2 V. The region of increased capacitance extended from −0.8 V to −1.2 V and may be a result of either a reorientation of the adsorbed molecules or to their desorption. The capacitance current at potentials more negative than −1.3 V was not affected by variation in the concentration of folic acid suggesting that the folic acid was desorbed at this potential region.

Effect of varying the pH and adsorption potential on the CSV response of folic acid

Variation of the pH between 3 and 9 showed that the peak height for folic acid in sea water increased from 0 nA at pH 3 to 38 nA at pH 9.2 (Fig. 5A). Maximum sensitivity was obtained at pH values between 8 and 9.5. A pH of 8.5 was selected to carry out folic acid analyses as it is close to the natural pH of sea water and is buffered conveniently using borate pH buffer. The peak potential increased with the pH at a rate of 0.07 V/pH unit, rather greater than that (0.03 V/pH unit) predicted from the involvement of 2 protons in the reduction of folic acid (Fig. 2) suggesting that the folic acid is stabilised more by the increased pH than its reduction product (dihydrofolic acid).

The peak height of folic acid decreased slightly and gradually when the deposition potential was varied from −0.1 V to −0.8 V, whilst it decreased strongly at deposition potentials more negative than the reduction potential because the reduction product did not adsorb on the HMDE (Fig. 5B). Adsorption potentials between −0.2 and −0.4 V give greatest sensitivity but a more negative potential can be selected to eliminate possible adsorption of interfering compounds at little loss in sensitivity.

Linear range and limit of detection

CSV of increasing concentrations of folic acid in sea water using an adsorption time of 60 s indicated that the peak height increased in a linear fashion until ~ 500 nM folic acid (Fig. 6A). At this concentration a capacitive peak became superimposed on the shoulder of the Faradaic peak interfering with its measurement. This observation is in accordance with the results obtained with cyclic voltammetry. The capacitance peak disappeared at higher folic acid concentrations where the faradaic peak increased again linearly with the folic acid concentration but at a lower sensitivity.

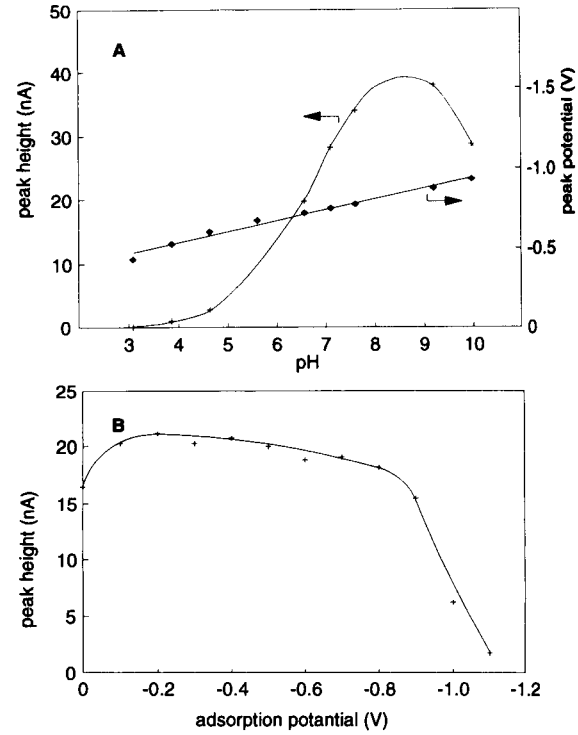

Fig. 5. A. Effect of varying the pH (A) and the deposition potential (B) on the CSV response for folic acid in UV-irradiated sea water containing 5 nM folic acid; the adsorption time was 60 s.

The limit of detection was calculated from repeated determinations of a low concentration of folic acid in sea water using two different instruments. The Autolab polarograph/Metrohm electrode combination gave a standard deviation of 6% ($n = 10$) for 0.5 nM folic acid (using an adsorption time of 60 s) from which a limit of detection of 0.09 nM is calculated from 3σ. The sensitivity was 0.8 nA/nM. The same experiment using the PAR polarograph/PAR 303 electrode

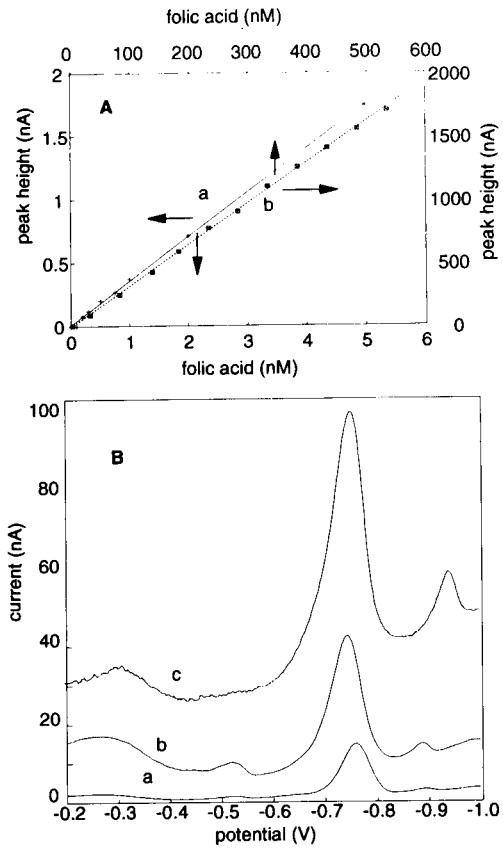

Fig. 6. CSV of folic acid in sea water. (A) The peak height as a function of the folic acid concentration after 60 s adsorption. (a) Low concentrations (using Autolab polarograph with Metrohm electrode); (b) high concentrations (PAR polarographic system). (B) Comparison of differential-pulse (scan a) and square-wave (scans b and c) CSV of 15 nM folic acid using 60 s deposition; modulation amplitude 25 mV, step height 2.4 mV. The scans have not been smoothed. scan a: differential-pulse, 5 pulses s^{-1}; scans b and c: square-wave, frequencies: 50 Hz (b) and 200 Hz (c).

combination had a greater standard deviation (11%) giving a calculated limit of detection of 0.3 nM. The lower standard deviation of the computerised Autolab polarographic system may be due to a lower level of electronic noise and (or) full automation of the measuring parameters. Scans for low levels of folic acid in sea water are shown in Fig. 6B (discussed below).

Variation of the adsorption time showed that the peak height for 5 nM of folic acid increased linearly with the adsorption time between 15 s and 10 min. The limit of detection for folic acid can therefore be lowered to 0.02 nM by extending the adsorption time to 5 min. This limit of detection is similar to that quoted for an electrolyte solution of sodium perchlorate at pH 4 [14] but better than that (0.1 nM) quoted for 0.1 M sulphuric acid [15] using the same adsorption time. However, it may not be possible to increase the sensitivity to this extent with adsorption time from natural water samples due to interference by organic surface-active compounds (see below).

Square-wave voltammetry

Comparative measurements of folic acid in sea water using the square-wave (50 and 200 Hz) and the differential-pulse (5 Hz) modulations showed that higher currents were obtained for the reduction of folic acid as a result of the greater frequency and faster scanning rate of the square-wave modulation (Fig. 6B). However, the difference of the peak height between the two modulations was small considering the large increase in the scan rate. Increasing the square-wave frequency from 50 to 200 Hz caused only little change (40%) in the sensitivity whereas the peak became broadened indicating that the reduction of the folic acid was irreversible at these high frequencies as a result of slow reduction kinetics. Greater electronic noise in the scans at the greater frequencies cancelled out any analytical advantage of the greater peak heights, so the sensitivity for folic acid could not be improved significantly by selecting a greater scanning frequency.

Interferences

Potential interferences in adsorptive CSV include organic compounds occurring in natural waters which adsorb with or without production of reduction peaks, and diffusion currents of other reducible elements present at high concentrations. Such interferences were tested by CSV of UV-irradiated sea water containing 5 nM of folic acid to which various organic compounds and metals were added which were known or suspected to adsorb or produce a voltammetric peak under the conditions used for folic acid.

Glutathione [22] and various purines [23] are known to produce peaks by CSV under condi-

tions similar to those used here. Addition of up to 1 μM glutathione and uric acid, and 160 nM guanine did not significantly affect the folic acid determination, as their reduction peaks appeared at potentials more positive than that of folic acid. The height of the folic acid peak decreased by 30% when 0.5 μM of adenine was added, and by 20% when 1 μM of guanine was added, presumably as a result of competitive adsorption of these compounds. However, the reduction peak of folic acid is located at a more negative potential than that for these compounds, so its concentration can still be evaluated by calibration of the CSV sensitivity by standard additions of folic acid to the sample. The folic acid peak decreased by 20% when 1 μM of EDTA was added; this effect was either caused by impurities as EDTA does not form a reduction peak, or it indicates that EDTA adsorbs on the HMDE.

Although several of the precursors and reduction products of folic acid produced peaks in the potential range of folic acid only DHF and pteroic acid adsorbed; the other compounds do not interfere unless present at much higher concentration than folic acid. The peak potentials of the DHF and pteroic acid (and of the other compounds) did not coincide with that of folic acid although they were near it (within 100 mV), and furthermore the sensitivity for DHF was quite poor. Verification of the analyte (folic acid) in natural water samples can therefore be achieved successfully from the peak potential and by inspection of the peak shape using standard additions of folic acid.

Surface active matter with an adsorptive effect comparable to 0.1–3 mg l^{-1} Triton X-100 (a non-ionic surfactant) is known to be present in coastal sea water [24]. An interference test indicated that the peak of 5 nM folic acid was masked completely by addition of 2 mg l^{-1} Triton X-100 to sea water. Such compounds could therefore potentially interfere with the determination of folic acid in sea water.

Interestingly the reduction current of folic acid was enhanced by addition of humic acid (HA) up to a concentration of 0.8 mg C l^{-1}. This effect may have been caused by an enhancement of the adsorption due to either molecular or ionic interactions between the HA and the folic acid. the folic acid peak height was diminished sharply by higher concentrations of HA possibly because of competitive adsorption of the HA or because of binding of the folic acid by the HA.

Additions were made of several elements to investigate their potential interference with the folic acid determination. The elements were selected on basis of their known ability to produce a voltammetric peak in conditions similar to those for the determination of folic acid, and the added concentrations were much higher than those occurring naturally. The folic acid peak was not affected by additions of 300 nM selenium, 1 μM copper or 150 nM cadmium to the sea water. Higher concentrations of cadmium caused the folic acid peak to decrease. These elemental concentrations are 100–1000-fold greater than normally encountered in clean sea water so it is unlikely that they will interfere with the determination of folic acid in this environment.

Sample storage

Sample stability upon storage was investigated using UV-irradiated sea water containing 1 nM folic acid in glass (salinity) and HDPE 250-ml bottles. The bottles were kept in the dark at 4°C. CSV determinations indicated that the folic acid concentration decreased with storage time presumably as a result of adsorption on the bottle walls: 10% in 4 h, 25% in 5 days, and 45% in 25 days. The decrease was generally larger and poorly reproducible in the HDPE bottles. Glass bottles are therefore advisable and were used in this work for sample storage. Storage in unfiltered and un-irradiated sample aliquots was not tested but this was expected to be subject to biological activity.

Determination of folic acid in the Mersey estuary

Situated in the North West of England, the Mersey estuary is surrounded by a large industrial area and is heavily polluted with untreated sewage. Folic acid was measured in samples collected in August and September 1990 using differential pulse CSV. The samples were not filtered but the suspended material was allowed to sediment to the bottom of the sample bottles for

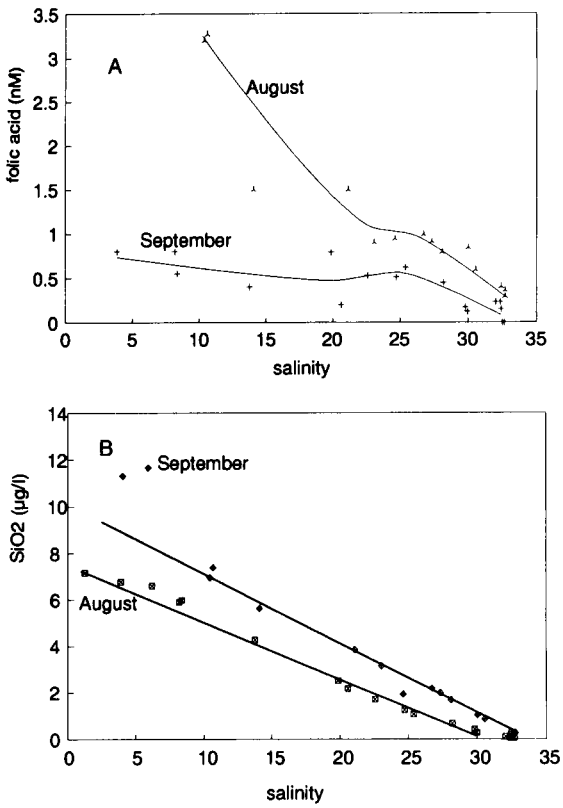

Fig. 7. The distribution of folic acid (detected by CSV) (A) and silicate (B) in the estuary of the Mersey in August and September.

several hours prior to the analyses. The analyses were carried out in a random order to prevent possible imposition of systematic errors. Repeated analyses (a week later) of samples which had been analysed early on unexpectedly showed no significant differences in the detected folic acid concentrations indicating that the folic acid concentrations in these samples were quite stable.

The folic acid concentration in the Mersey estuary was found to decrease generally with increasing salinity (Fig. 7A), ranging between below the limit of detection (estimated at about 0.1 nM in the presence of surfactants in these samples) to 3.2 nM. The folic acid concentration increased at intermediate salinity presumably as a result of local inputs (presumably from sewage) or local production by bacteria. The folic acid concentration was higher in August than in September probably due to a higher folic acid concentration in the freshwater end-member, but the general behaviour in the Mersey estuary was similar during both sampling periods.

Comparisons of the folic acid concentration with that of other variables (nutrients, suspended solids, dissolved oxygen and temperature) showed that folic acid was inversely correlated with dissolved oxygen ($r^2 = 0.87$) in September, the folic acid concentration decreasing with increasing salinity whereas the dissolved oxygen concentration increased. This could be explained by the consumption of oxygen by bacteria while they are decomposing organic matter including folic acid; the sea water endmember acting as a source of oxygen whereas the freshwater endmember acted as a source of dissolved organic carbon and folic acid. However, this relationship was not confirmed by the data collected in August. Data for silicate in the Mersey estuary are shown in Fig. 7B to illustrate the distribution of a compound which behaves generally conservatively in this estuary: comparison shows an almost linear dilution pattern for the silicate (variations at the freshwater end are due to variable freshwater input whilst an intercept with the salinity axis at a salinity below 35 (average sea water) indicates biological uptake at the high salinity end during August) whereas the folic acid has a more varied pattern due to local inputs, breakdown and/or production.

The oceanic distribution of folic acid is to be investigated using this method in future work.

Assistance with the sample collection from the Mersey estuary by Peter Jones (NRA North West) is gratefully acknowledged. The research of ACLG was partially supported by a student award from the NERC.

REFERENCES

1 T. Brody, B. Shane and E.L.R. Stokstad, in L.J. Machlin (Ed.), Handbook of Vitamins. Nutritional, Biochemical, and Clinical Aspects, Marcel Dekker, New York 1984, pp. 459–496.

2 P.A. Mayes, In R.K. Murray, D.K. Granner, P.A. Mayes and V.W. Rodwell (Eds.), Harper's Biochemistry. 22nd edn., Appleton and Lange, Norwalk, CN, 1990, pp. 547–560.
3 S. Aaronson, S.W. Dhawale, N.J. Patni, B. DeAngelis, O. Frank and H. Baker, Arch. Microbiol., 112 (1977) 57.
4 K.W. Daisley, Limnol. Oceanogr., 14 (1969) 224.
5 S.F. Bruno, R.D. Staker and L.L. Curtis, J. Mar. Res., 39 (1981) 335.
6 D.G. Swift, J. Mar. Res., 39 (1981) 375.
7 C. D'Silva and A. Rajendran, Mahasagar, 16 (1983) 153.
8 T. Nishijima and Y. Hata, In T. Tokaichi, D.M. Anderson, T. Nemoto (Eds.), Red Tides: Biology, Environmental Science and Toxicology, Elsevier, Amsterdam, 1989, pp. 257–260.
9 M. Fiala, Oceanol. Acta, 5 (1982) 339.
10 D.W. Menzel and J.P. Spaeth, Limnol. Oceanogr., 7 (1962) 151.
11 M. Fiala and L. Oriol, Mar. Biol., 79 (1984) 325.
12 E. Jacobsen and M.W. Bjørnsen, Anal. Chim. Acta, 96 (1978) 345.
13 S. Kwee, Bioelectrochem. Bioenerg., 11 (1983) 467.
14 A.N. El-Maali, J.C. Vire, G.J. Patriarche and M.A. Ghandour, Analusis, 17 (1989) 213.
15 D.B., Luo, Anal. Chim. Acta, 189 (1986) 277.
16 J.M. Fernandez-Alvarez, A. Costa-Garcia, A.J.M. Ordieres and P. Tunon-Blanco, J. Electroanal. Chem., 225 (1987) 241.
17 K. Kretzschmar and W. Jaenicke, Z. Naturforsch., 26 B (1971) 225.
18 B.E. Conway, R.G. Barrados, Electrochim. Acta, 5 (1961) 319.
19 P. Valenta, H.W. Nürnberg and D. Krznaric, Bioelectrochem. Bioenerg., 3 (1976) 418.
20 P.T. Kissinger, C.R. Preddy, R.E. Shoup and W.R. Heineman, In P.T. Kissinger and W.R. Heineman (Eds.), Laboratory Techniques in Electroanalytical Chemistry, Marcel Dekker, Amsterdam, 1984, pp. 9–49.
21 M.T., Stankovich, and A.J., Bard, J. Electroanal. Chem., 75 (1977) 487.
22 A.-C. Le Gall and C.M.G. van den Berg, Analyst, (1993) in press.
23 B.C. Househam, C.M.G. van den Berg and J.P. Riley, Anal. Chim. Acta, 200 (1987) 291.
24 B. Cosovic, V. Zutic, V. Vojvodic and T. Plese, Mar. Chem., 17 (1985) 127.

Analytica Chimica Acta, 282 (1993) 471–484
Elsevier Science Publishers B.V., Amsterdam

Fully automated potentiometric determination of the free ligand concentration in complexation titrations: the system Ag(I) with *N*-methylethylenediamine

R. Garner, J. Yperman, J. Mullens and L.C. Van Poucke

Laboratory of Inorganic and Physical Chemistry, Limburgs Universitair Centrum, B-3590 Diepenbeek (Belgium)

(Received 8th March 1993; revised manuscript received 24th May 1993)

Abstract

A fully automated potentiometric procedure is presented for the determination of free ligand concentrations of ternary systems in aqueous solutions. A primary model selection and an estimation of the stability constants of the ternary system can be obtained from the same data. The automated technique is demonstrated on the complexation of Ag(I) with *N*-methylethylenediamine in 1 M NO_3^- medium and the results are compared with the standard ratio procedure.

Keywords: Potentiometry; Aliphatic diamines; Complexometry; Methylethylenediamine; Silver

A polyfunctional open-chain ligand like ethylenediamine usually forms several species during complexation with a metal ion in aqueous solution. The normal procedure to determine the formation constants of such a ternary system is to perform pH and if possible pM measurements over a sufficiently large concentration range of metal (M), ligand (L) and proton (H), in as many as possible different metal to ligand ratios, obtaining hundreds of points in order to solve the mass balances for a proposed model. For most organic molecules no suitable potentiometric sensors exist so that pL values can only be determined if the model is successfully refined by non-linear optimization programs. The importance of the knowledge of pL values is obvious, e.g., most auxiliary functions such as Leden's F_n functions and Bjerrum's $\bar{n}$ function need [L] to be calculated.

One can obtain pL and pM values without any prior knowledge of the complexating model with the free ion concentration in solution or FICS strategy [1,2], using only pH measurements. More reliability is obtained when both pH and pM measurements are performed. In that case the so-called "dilution technique" [3] can be used. This technique was developed theoretically by some of the authors [3,4] and has been tested manually on the complexation of *N*-methyl substituted 4-H- and 4-methyldiethylenetriamines with Ag(I) in nitrate medium [5,6]. These kinds of experiments are very tedious and time consuming. A procedure for a complete automation of the dilution technique seemed desirable.

In the continuing study of the complexation of Ag(I) with aliphatic amines [7,8] this automated titration technique is tested by a complexation study of Ag(I) with *N*-methyl substituted eth-

Correspondence to: L.C. Van Poucke, Laboratory of Inorganic and Physical Chemistry, Limburgs Universitair Centrum, B-3590 Diepenbeek (Belgium).

ylenediamines. In order to illustrate the procedure and its possibilities of this type of titrations, the complexation of the ligand *N*-methylethylenediamine with Ag(I) is described in some detail.

The validity of these results is tested by performing a second series of experiments where the standard ratio technique is used. The obtained potentiometric data are analysed using the least squares program SUPERQUAD [9–11].

THEORY

The general equilibrium of a metal ion, a proton and a ligand is usually expressed as:

$$pM + qL + rH \leftrightharpoons M_pL_qH_r$$

$$\beta_{pqr} = \frac{[M_pL_qH_r]}{[M]^p[L]^q[H]^r}$$

The ligand is often a polyprotic acid with j dissociable protons:

$$L + jH \leftrightharpoons LH_j$$

$$\beta_{01j} = \frac{[LH_j]}{[L][H]^j}$$

Metal hydrolysis might also occur during complexation and should be taken into account:

$$pM + kOH \leftrightharpoons M_p(OH)_k$$

$$\beta_{p0-k} = \frac{[M_pH_{-k}]}{[M]^p[H]^{-k}}$$

β_{pqr} is the global stability constant of the complex $M_pL_qH_r$. β_{01j} is the formation constant of the acid LH_j and β_{p0-k} are the possible metal hydrolysis constants. The charges are omited for clarity.

The dilution technique is based on several equations derived from differentiating the Gibbs function and using the Duhem–Margules relation in aqueous solution for a ternary system [3]. The complexity sum C_S (or Sillen sum) [12] can be determined by solving the following equations using the appropriate experimental data:

$$C_S = \sum_i [M_pL_qH_r]_i \quad (1)$$

$$C_S = C - [M] - [L] - [H] - [OH] - \sum_j (LH_j) \quad (2)$$

$$C - C_0 = -2.303\left[\int_{h_0}^{h}\left(\frac{\partial \log[H]}{\partial v}\right)_{m,l,h} dh\right]_{m,l,v} \quad (3)$$

$$C - C_0 = C_M \ln\frac{[M]}{[M]_0} + C_L \ln\frac{[L]}{[L]_0} + \int_{\ln[H]_0}^{\ln[H]} C_H \, d\ln[H] \quad (4)$$

where m, l and h are the total number of moles of metal, ligand and proton, v is the total volume, C and C_0 represent the total concentration of all solutes for two different titration points, C_M, C_L and C_H are the total concentrations of metal, ligand and proton and [M], [L] and [H] are the free concentrations of metal, ligand and proton, respectively.

The indexes i, j and k denote all possible metal–ligand–hydrogen complexes, all protonated ligand species without metal, and the metal hydrolysis products without ligand, respectively.

The subscript 0 denotes a titration point where no complexation occurs. These points can also be used for internal calibration of the electrodes.

If [M], [H], C_L, C_M, C_H, the $pK_W(=\beta_{00-1})$, the pK_A values of the ligand and the possible metal hydrolysis constants are known one can determine C_0, C, C_S and [L] for each titration point.

Some idea of the composition of the complexes in solution can be obtained by calculating the average stoichiometric coefficients: $\bar{p}$ (average bound metalions per complex), $\bar{q}$ (average bound ligands per complex) and $\bar{r}$ (average bound protons per complex) using the following equations [3]:

$$\bar{p} = \left[C_M - [M] - \sum_k p\beta_{p0-r}[M]^p[H]^{-r}\right]/C_S \quad (5)$$

$$\bar{q} = \left[C_L - [L] - \sum_j q\beta_{0qr}[L]^q[H]^r\right]/C_S \quad (6)$$

$$\bar{r} = \Big[C_H - [H] + [OH] - \sum_k r\beta_{p0-r}[M]^p[H]^{-r} - \sum_j r\beta_{0qr}[L]^q[H]^r \Big] / C_S \quad (7)$$

As a consequence of obtaining this kind of potentiometric data, the mass balances become a set of linear equations of the form $A \cdot X = B$, because each titration point yields 3 sets of linear equations.

$$C_M - [M] - \sum_k p\beta_{p0-r}[M]^p[H]^{-r} = \sum_i \beta_{pqr}[M]^p[L]^q[H]^r \quad (8)$$

$$C_L - [L] - \sum_j q\beta_{0qr}[L]^q[H]^r = \sum_i \beta_{pqr}[M]^p[L]^q[H]^r \quad (9)$$

$$C_H - [H] + [OH] - \sum_j r\beta_{0qr}[L]^q[H]^r - \sum_k r\beta_{p0-r}[M]^q[H]^{-r} = \sum_i \beta_{pqr}[M]^p[L]^q[H]^r \quad (10)$$

No estimates of the values of the stability constants are needed anymore to calculate a given model.

EXPERIMENTAL

Reagents

$AgNO_3$ (Merck p.a.), KNO_3 (Merck p.a.) are used without further purification. KOH and HNO_3 solutions are prepared from Titrisol ampoules (Merck p.a.). KOH solutions are prepared under a N_2 atmosphere with freshly boiled doubly distilled, deionized water and are kept under

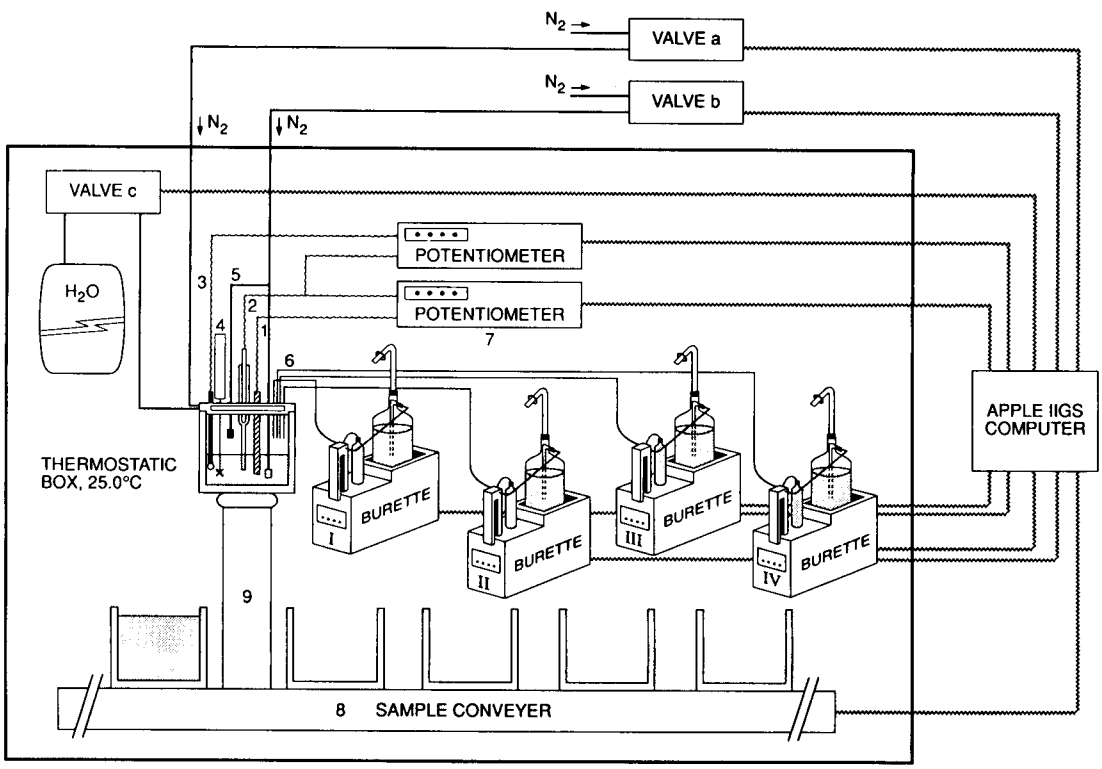

Fig. 1. Experimental set-up for the dilution method. (1) Ag/Ag_2S electrode, (2) reference electrode in a salt bridge, (3) glass electrode, (4) automatic stirrer, (5) gas bubbler, (6) anti-diffusion burettetip from (I) automatic burette with strong base, (II) automatic burette with metal solution, (III) automatic burette with ligand solution, (IV) automatic burette with indifferent electrolyte solution, (7) precision potentiometers, (8) automatic sample changer, (9) lift from the sampler changer.

a CO_2-free atmosphere in a polyethylene bottle and are used within two weeks of preparation.

The ionic strength of all solutions is kept constant at 1 M NO_3^- with KNO_3.

N-Methylethylenediamine (Aldrich Chem. 99%) is purchased under the amine form and is neutralized with 2 equivalents HNO_3. The corresponding dinitrate salt is purified by repeated crystallization in ethanol and dry dimethyl ether and is dried on P_4O_{10} in a vacuum desiccator until colourless white crystals are obtained.

Calibration

The following electrodes are used: a glass electrode (Ingold pH 0-14 U262-S7), a reference electrode (Ingold Argental 363-S7) in a saltbridge (Schott-Geräte B511 with ceramic plug) filled with 1.5 M KNO_3 and a Ag/Ag_2S electrode (Orion 94-16). The emf values are registered through 2 Radiometers PHM-64 or -84 with a resolution of 0.1 mV. The "dilution method" and the standard ratio technique are performed with the same electrodes.

The calibration of the glass electrode and the Ag/Ag_2S electrode, the determination of their characteristics, the determination of the pK_w (13.775 ± 0.003) and the pK_A values of the *N*-methylethylenediamine (7.44 ± 0.01 and 10.30 ± 0.01) are described in a set of previous papers [8,13,14].

Dilution technique

Setup. The experimental design is shown in Fig. 1. An Apple II GS microcomputer controls the Metrohm 637 sample changer, the 4 automatic Schott T 100 piston burettes and the automated stirrer, reads the 2 precision digital Radiometers, controls the valves for bubbling inert gas through and above the solution and the valves for blowing the electrodes dry and washing then off with doubly distilled water. The entire setup is placed in a thermostated box at 25°C in a thermostated room. The microcomputer is interfaced with the burettes, potentiometers and the sample changer through two I/O 32 cards.

With some slight modifications in the users program the setup is also used for the sodium determination in bread [15], for the iodometric determination of Cu^+, Cu^{2+} and Cu^{3+} in the superconductor $YBa_2Cu_3O_x$ [16] and for the determination of sulfur functionalities in fossil fuels [17].

The sample changer mainly consists of 3 parts: a conveyer belt, a carroussel, and a lift. Bekers are placed on the conveyer belt in sets of 3. The first 2 are for rinsing and drying the electrodes and the third one for internal calibration and the actual measurements. There is a specially adapted double wall holder on the top of the lift which contains 4 antidiffusion burettetips, the reference electrode in a saltbridge, the glass electrode and the Ag/Ag_2S electrode. In the double wall holder are some small concentric openings around the electrodes for rinsing and blowdrying. The control program is written in UCSD-Pascal with incorporated Assembler subroutines.

Measurements. The C_{Ag}/C_L ratio is kept constant and set equal to 1/2 as being the most interesting ratio. The stock solutions for the respective burettes are: Burette I, 5 ml, 0.1 M KOH in 1.0 M KNO_3; Burette II, 20 ml, 0.01 M $AgNO_3$ in 0.99 M KNO_3; Burette III, 20 ml, 0.01 M $LH_2(NO_3)_2$ + 0.002 M HNO_3 in 0.978 M KNO_3; Burette IV, 50 ml, 1.0 M KNO_3.

The starting solutions consist of 10 ml from burette II, 20 ml from burette III, 10 ml from burette IV, x ml from burette I and $(5-x)$ ml from burette IV. x is a value between 0 and 5 ml.

The x values are choosen in such a way that the difference in potential of both the glass electrode and the Ag/Ag_2S electrode is less then 15 mV for two successive starting solutions. Simulations have shown that the deviations of the calculated pL value are less than 0.002 units if the dh values (see Eqn. 3) are choosen so that the ΔpH between two successive curves is less than 0.2–0.3 pH units [3]. The extra 10 ml from burette IV is added to make sure that all electrodes can make contact with the mixture. Before adding the strong base, an internal calibration of both the glass electrode and the Ag/Ag_2S electrode is possible due to the excess of HNO_3. At such a low pH no complexation is expected.

The obtained solution is then diluted with 1 M KNO_3 (burette IV) in steps of 5 ml until a total volume of 165 ml is reached, therefore the name

"dilution technique". About a dozen dilution titrations, each lasting approximately 40 min, can be performed in a day before the electrodes show signs of a sluggish response. The carry over of silver from one dilution series to another was tested potentiometrically and is less than the experimental error (< 0.1%). We expect that this is the same for ligand and proton.

Ratio technique

Setup. Details of the experimental setup, equilibrium criteria and estimation of the standard errors of the burettes and the electrodes are discussed in a previous paper [8].

Measurements. Because we expect a large diversity of complexes, mononuclear, polynuclear and protonated complexes, several different C_{Ag}/C_L ratios are employed: 2/1, 1/1, 1/2, 1/4, 1/8.

Two main stock solutions are used. Ligand solution: 0.01 M $LH_2(NO_3)_2$ in 0.98 M KNO_3; silver solution: 0.01 M $AgNO_3$ in 0.99 M KNO_3.

The ratios 1/1–1/2–1/4–1/8 are obtained by keeping the number of mmoles ligand constant and varying the volume of the silver solution added to the mixture. The initial volume of the mixture is kept constant by adding 1 M KNO_3: e.g., 1/2 ratio: 20 ml ligand solution + 10 ml silver solution + 10 ml KNO_3, 1/8 ratio: 20 ml ligand solution + 2.5 ml silver solution + 17.5 ml KNO_3.

The 2/1 ratio is prepared using 20 ml ligand solution and 40 ml silver solution. The titration is continued until both protons are liberated from the ligand or until precipitation from Ag_2O becomes visible. All titrations are performed at least in duplicate. The calibration of the glass electrode and the Ag/Ag_2S electrode are performed externally before and after each complexation titration. All solutions are added using precise burettes instead of pipets.

Calculations

A program written in Fortran 77, "ANAL_DILUT", solves Eqns. 1–4 in order to calculate the Sillen sum and the free ligand concentration [L]. Subsequently $\bar{p}$, $\bar{q}$ and $\bar{r}$ are calculated from these values using Eqns. 5–7. Several subroutines for calculating derivatives of discrete numerical data are tested, but the smoothing and differentiation subroutine from Gorry [18] based on the Savitzky–Golay [19] algorithm for equidistant data seems to obtain the best results. The integrals were calculated using an algorithm based on the trapezoidal rule. Standard input files for SUPERQUAD can also be generated by this program.

Values of the stability constants from data of the dilution technique are calculated with the linear regression program STACAL3. The advantage of linear regression in comparison with non-linear regression is the absence of any arbitrary convergence criterium. Hence it is possible to list a considerable number of probable models. Another advantage is the fact that in linear regression well-defined statistics are obtained. Further, no initial guesses about the values of the stability constants are needed, and the danger that bad guesses lead to a local minimum is excluded. STACAL3 solves Eqns. 8–10 using a modified version of Bevington's subroutine REGRES [20]. The program systematically covers all possible combinations of species for a maximum number of possible species. As input parameters are needed: the free concentrations and total concentrations for all titration points, the acidity constants of the complexating ligand, the pK_w of the solvent, the possible metal hydrolysis constants and the stoichiometric coefficients of the possible complexes. The best models are selected on the basis of the following tests as defined by Bevington [20]: the reduced chisquare =

$$\text{Chisqr.} = \frac{\sum_i \frac{1}{\sigma_i^2}(y_i - y_{\text{fit}})^2}{\text{number of degrees of freedom}}$$

R_{fac} = the crystallographic R factor:

$$R_{\text{fac}} = \sqrt{\frac{\sum_i \frac{1}{\sigma_i^2}(y_i - y_{\text{fit}})^2}{\sum_i \frac{y_i^2}{\sigma_i^2}}}$$

R_{mul} = multiple linear correlation coefficient:

$$R_{\text{mul}} = \sum_{j=1}^{n} b_j \frac{S_{jy}^2}{S_y^2}$$

where b_j is defined by the linear equation

$$y = a + \sum_{j=1}^{n} b_j x_j$$

and

$$S_{jy}^2 = \frac{1}{(N-1)}\left[\sum_i x_i^j y_i - \frac{1}{N}\sum_i x_i^j \sum_i y_i\right]$$

(sample covariance) and

$$S_y^2 = \frac{1}{(N-1)}\left[\sum_i y_i^2 - \frac{1}{N}\left(\sum_i y_i\right)^2\right]$$

(sample variance)

y_{fit} = fitted y value and $y_i = y$ value. Unit weights are applied to all data points, i.e., $\sigma_i = 1$ mol dm^{-3}, and on the basis of the species distribution, where we assume that a meaningful species should be above the arbitrary value of 3%.

The data from the ratio technique are analysed using SUPERQUAD. As a starting model, estimates from the complexation model of Ag(I) with ethylenediamine [7,21] are used as we expected *N*-methylethylenediamine to behave analogously.

Superquad minimizes the error square sum $U = \Sigma w_i (E_i^{\text{exp}} - E_i^{\text{calc}})^2$ with weight

$$w_i = 1/\left[\sigma_E^2 + \left(\frac{\partial E}{\partial V}\right)^2 \sigma_V^2\right]$$

The goodness-of-fit is judged by the overal fit statistics

$$S = \left(\frac{\epsilon^T w \epsilon}{m-n}\right)^{1/2}$$

where ϵ is a vector of residuals in the potential, ϵ^T its transpose, w is the weight matrix, m is the number of data points and n is the number of parameters to be refined. The model selection criteria used for SUPERQUAD are:

a good overall fit: an S value between 1 and 3 is generally accepted as a good fit [10];

a low standard deviation of the constant;

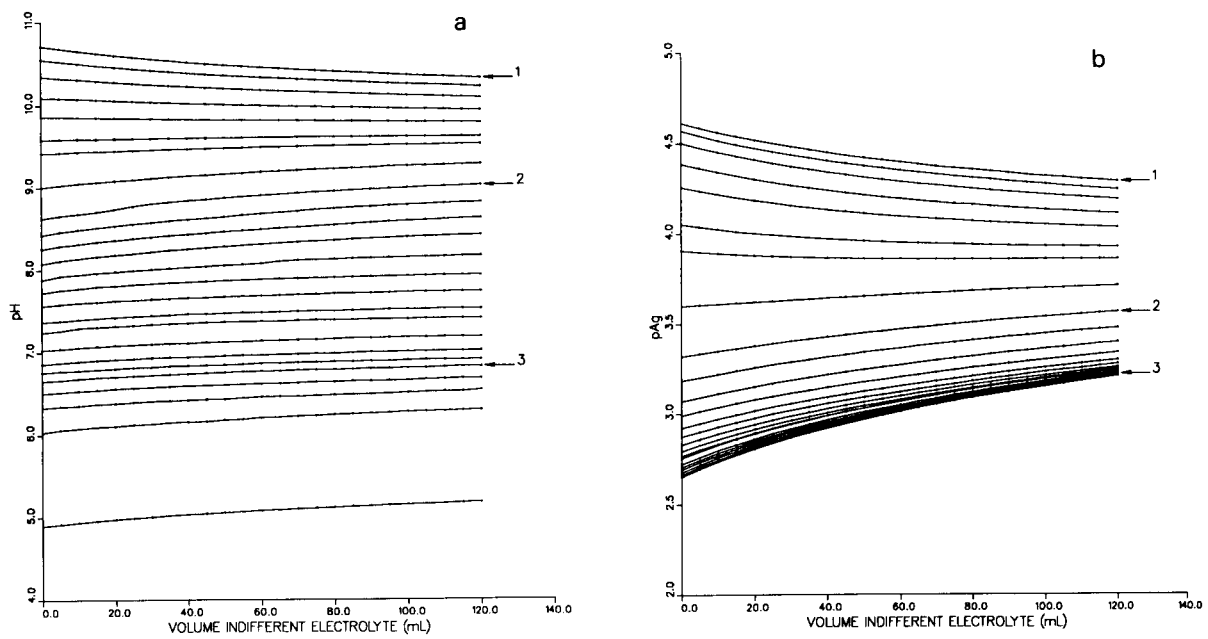

Fig. 2. (a) pH data from the dilution method vs. volume of added indifferent electrolyte. $C_{Ag} = 0.09979$ mmol, $C_L = 0.2000$ mmol, C_H varies from 0.41998 to 0.000 mmol. Full lines are drawn according to the way the data are collected. Three individual titrations are marked as reference points: (1) $C_H = -0.02$ mmol, (2) $C_H = 0.14$ mmol, (3) $C_H = 0.36$ mmol. (b) pAg data from the dilution method (mass balances same as mentioned above). Full lines are drawn analogously to Fig. 2a. The three individual titrations are also marked.

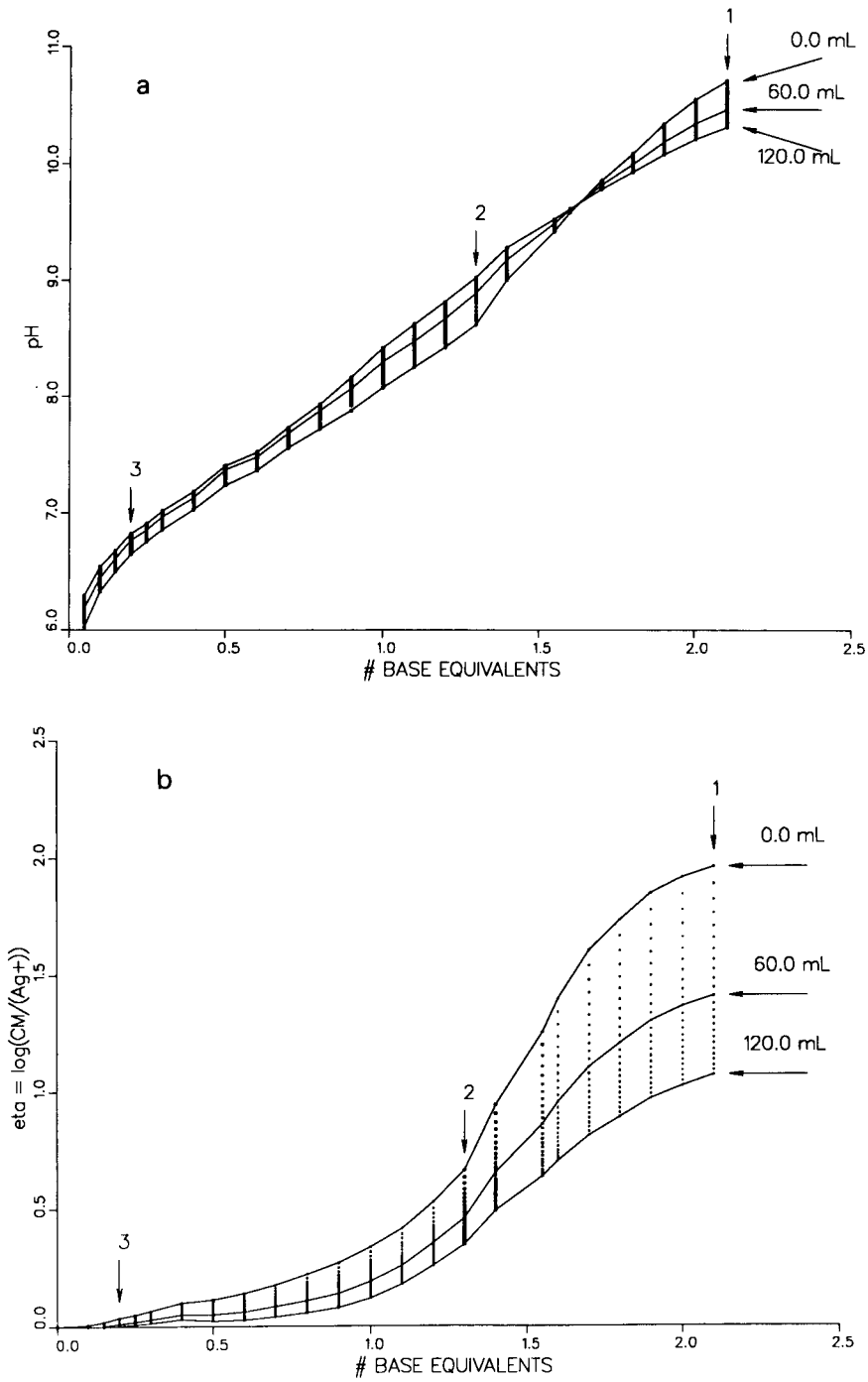

Fig. 3. (a) pH data from the dilution method vs. number of base-equivalents. The three individual titrations are marked. Three full lines connect the data points with the same amount of added volume indifferent electrolyte at respectively 0.0, 60.0 and 120.0 ml. (b) Relative complexation function $\eta = \log(C_M/[Ag^+])$ vs. number of base-equivalents. The three individual titrations are marked. The full lines have the same meaning as in Fig. 3a.

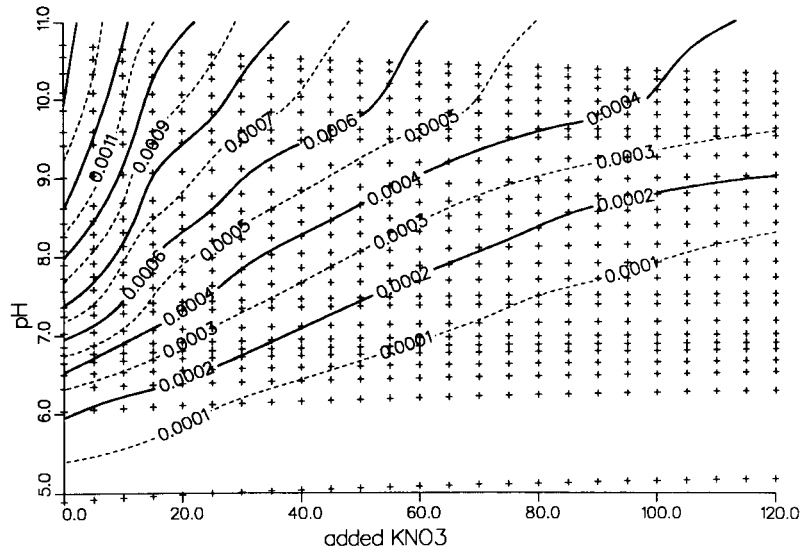

Fig. 4. Contour values are the Sillen sum of the data points in the dilution method.

a significant % species presence (an arbitrary minimum value of 3%);

a minimum number of species.

The acidity constants, the pK_w, the mass balances and the electrode parameters are kept constant during model refinement.

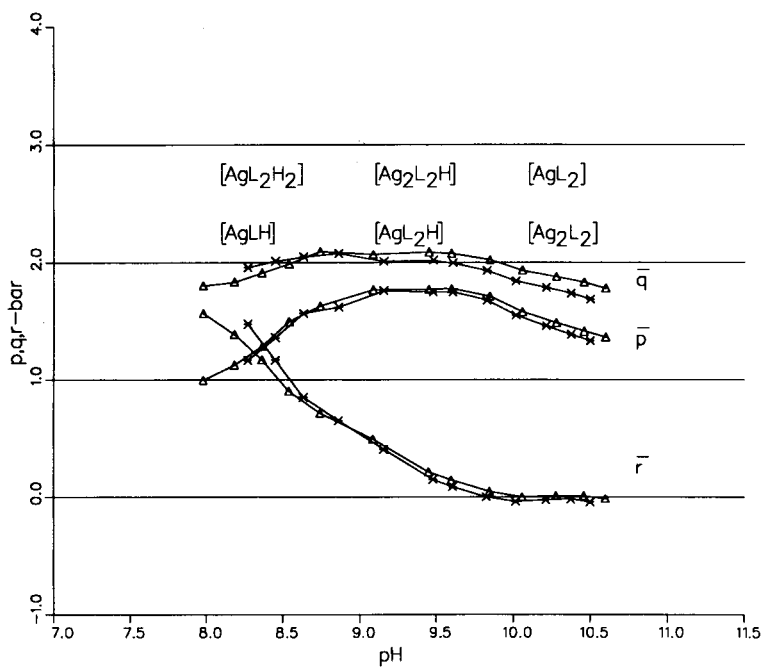

Fig. 5. Average stoichiometric coefficients $\bar{p}$, $\bar{q}$ and $\bar{r}$ vs. pH. (Δ) $C_{Ag} = 0.001426$ M, $C_L = 0.002857$ M. (∗) $C_{Ag} = 0.001050$ M, $C_L = 0.002105$ M.

All calculations are done in double precision. The drawings are made using the Disspla drawing subroutine library. Listings of all programs, including those used for the graphical analysis, are available from the authors.

RESULTS AND DISCUSSION

Dilution technique

The experimental data resulting from the dilution procedure are shown in Fig. 2a and b. The full lines in Fig. 2a and b connect the data points that are obtained in a single dilution titration. Three individual titrations are referenced: (1) $h = -0.02$ mmol (2) $h = 0.14$ mmol, (3) $h = 0.36$ mmol. A different, but more conventional way of visualizing the same data, are presented in Fig. 3a and b. Three full lines connect all data points with the same amount of added volume indifferent electrolyte at respectively 0.0, 60.0 and 120.0 ml resulting in the more familiar titration curves. The isohydric point occurring in the neighbourhood of pH 9.5 is probably due to an equilibrium between a minimum of two non-protonated species. The same individual tirations referenced in Fig. 2a and b become vertical lines of dots in Fig. 3a and b. As can be seen from Fig. 3b the smaller the spread of data for a given equivalent the less complexation has occurred. The corresponding pH values also lie very close to each other. The complexation really starts when the first proton of the biprotic ligand is neutralized. The Sillen sum (Fig. 4) decreases as the volume increases, but increases as the pH rises. The $\bar{p}$, $\bar{q}$ and $\bar{r}$ curves vs. pH for two different total concentrations of metal and ligand are presented in Fig. 5 so that some idea about the predominant species can be made. The region where the complexation is the lowest gives unreliable results on $\bar{p}$, $\bar{q}$ and $\bar{r}$. Large errors are also found in the beginning and at the end of each titration curve. We can see from Eqn. 2, if the complexation is low, the Sillen sum will have a large error due to the additivity of the errors of the individual terms. Furthermore, calculating accurate numerical derivatives is known to be difficult at the begin- and endpoints of curves.

We therefore use two cutoff values when calculating the average stoichiometric coefficients. If the Sillen sum was less than 2.0×10^{-4} mol dm^{-3} or the relative complexation function η [$= \log(C_M/[Ag^+])$] was less than 0.2 the respective experimental value is not included in the calculation.

Using Fig. 5 in the pH range 9.5–10.5, $\bar{p} = 1.5$, $\bar{q} = 1.7$ and $\bar{r} = 0$ suggest a polynuclear species Ag_2L_2 and a mononuclear species AgL_2. Around pH = 8.5, $\bar{p} = 1.2$, $\bar{q} = 1.8$ and $\bar{r} = 1$ suggesting the formation of AgL_2H, Ag_2L_2H and AgLH and at even lower pH (< 8.0) AgL_2H_2 and AgLH are expected to be formed. Polynuclear complex formation starts around pH = 8.0. $\bar{r}$ does not go below 0 indicating that there is no evidence that hydroxy ligand complexes exist in solution in this ratio. Nevertheless, two hydroxy ligand species are added to the possible species list because other investigators [22,23] have detected mixed ligand hydroxy complexes (AgLOH) of ethylenediamine with Ag(I) pH-metrically.

All possible models containing the following 11 species: AgLH, AgL_2H_2, AgL_2, AgL, AgL_2H, Ag_2L_2, Ag_2L, Ag_2L_3, Ag_2L_2H, AgL(OH) and $AgL_2(OH)$ were tested using STACAL3.

The number of all theoretically possible models thus tested runs up to 2047 ($= 2^{11} - 1$). Using STACAL3 this only takes 3 h runtime on our CDC mainframe. With SUPERQUAD, this would have taken days to do. No successful models consisted of any of the mixed ligand hydroxy complexes, confirming the $\bar{r} > 0$ values.

The formation constants, standard deviations and respective goodness-of-fit values (R_{mul} and R_{fac}) of the best model are listed in Table 1. Unit weights are applied to all data points. A list of the 4 best models is given in Table 2. Table 2 shows that, despite the fact that models 2, 3 and 4 have more species, no better minimum is found, contrary to what is generally predicted by non-linear least squares. The significant difference of reduced chi-square between model 1 and the other models makes the choise obvious so that the best description for complexation in this C_{Ag}/C_L ratio and concentration area can be attributed to model 1.

There is an alternative way of calculating the

TABLE 1

Best model obtained from the dilution technique [a]

Species	log (β)	S.D.	Max % species
AgLH	12.69	0.07	25
AgL_2H_2	25.47	0.07	16
AgL_2	7.30	0.03	27
AgL_2H	16.83	0.07	8
Ag_2L_2	12.05	0.01	79

[a] Chisqr. = 6.79×10^{-9}, $R_{mul} = 0.991$, $R_{fac} = 3.01 \times 10^{-3}$. Number of titration points = 278. Number of data points = 834.

stability constants from these data using SUPERQUAD. The pH and pAg data can be analysed with this program in two ways:

as a collection of constant volume titrations (coulometric option in SUPERQUAD); or

as a collection of dilution titrations at a constant mass balance of proton.

In both ways, one has the option to weight the data or not. Since the weights are calculated from the derivatives of the titration curves one chooses towards the independent variable, the weights on the respective titration points will be different. When no weights are used, both ways give identical results. The independent variable depends on the way the data are analysed: at constant volume σ_v is dependant on the burette adding the KOH and at constant mass balance of proton, σ_v is dependant on the burette adding the KNO_3.

The results of the best models, i.e., the models with the lowest S value analysed in both ways are shown in Table 3. A few aspects of Table 3 immediately draw our attention. Weighting the data according to the dilution titration at constant mass balance of the proton (the way the data are obtained experimentally) or using unit weights render the same formation constants and standard deviations. With hindsight, this is to be expected as we can see from Fig. 2a and b the pH and pAg values hardly vary during a dilution titration (maximum 0.5 log units) so that all points practically recieve the same weight from SUPERQUAD. This is not the case when the data are analysed at constant volume. The high X values obtained when the weighted option in SUPERQUAD is used, indicate systematic errors in the data, which is not very surprising considering the large amount of manipulations needed to perform the dilution technique. Also, one must not forget that SUPERQUAD was not originally designed to cope with this kind of titrations. Either way the data are analysed SUPERQUAD ignores one aspect of the titration curves. If the data are analysed at constant mass balance of proton the buffer area of the titration curves are not taken into account and at constant volume the concentration or dilution aspects will be neglected. Both aspects are taken implicitly into account when the pL values are calculated with "ANAL_DILUT" through Eqns. 3 and 4.

TABLE 2

Survey of the four most successful models found using STACAL3 (The formation constants are tabulated for each model with the standard deviations on the last digit between brackets, followed by its % species presence)

Species	Model 1	%	Model 2	%	Model 3	%	Model 4	%
AgLH	12.68 (7)	25					12.62 (9)	22
AgL_2H_2	25.48 (7)	16	25.77 (3)	28	25.73 (2)	29	25.50 (7)	17
AgL_2	7.30 (3)	27	7.32 (3)	29	7.33 (3)	29	7.33 (3)	29
AgL_2H	16.83 (7)	8	16.83 (9)	20	16.89 (7)	9	16.91 (7)	10
Ag_2L_2	12.05 (1)	79	11.94 (4)	64	11.94 (1)	64	11.95 (4)	65
Ag_2L_2H			19.72 (2)	7				
AgL			4.0 (1)	8	4.0 (1)	22	4.0 (1)	20
Ag_2L					6.548	4		
Chisqr.	6.69×10^{-9}		7.30×10^{-9}		7.45×10^{-9}		7.49×10^{-9}	
R_{mul}	0.991		0.990		0.0990		0.992	
R_{fac}	0.0856		0.0887		0.0896		0.0898	

TABLE 3

List of the best models obtained from the possible ways of analysing pH and pAg data obtained from the dilution technique using SUPERQUAD

Same pH and pAg data as STACAL3				All pH and pAg data			
Species	log β	S.D.	%	Species	log β	S.D.	%
Constant mass balance proton (weighted option): $\sigma_v = 0.01$ ml, $\sigma_{pAg} = 0.004$, $\sigma_{pH} = 0.004$							
				AgLH	11.8	0.1	3
AgL_2H_2	25.75	0.02	29	AgL_2H_2	25.80	0.02	32
AgL_2	7.52	0.01	38	AgL_2	7.525	0.009	38
Ag_2L_2H	20.12	0.04	16	Ag_2L_2H	19.77	0.07	8
Ag_2L_2	12.029	0.005	78	Ag_2L_2	12.041	0.004	80
$S = 5.81$				$S = 6.14$			
Constant volume (weighted option): $\sigma_v = 0.002$ ml, $\sigma_{pAg} = 0.004$, $\sigma_{pH} = 0.004$							
				AgLH	11.97	0.06	5
AgL_2H_2	25.77	0.02	30	AgL_2H_2	25.75	0.02	30
AgL_2	7.532	0.009	38	AgL_2	7.536	0.008	38
Ag_2L_2H	20.05	0.04	14	Ag_2L_2H	19.70	0.07	7
Ag_2L_2	12.034	0.004	79	Ag_2L_2	12.042	0.004	80
$S = 4.91$				$S = 4.86$			
Constant mass balance proton = constant volume (unit weights option)							
				AgLH	11.8	0.1	3
AgL_2H_2	25.75	0.02	29	AgL_2H_2	25.80	0.02	32
AgL_2	7.52	0.01	38	AgL_2	7.525	0.009	38
Ag_2L_2H	20.11	0.04	16	Ag_2L_2H	19.77	0.07	8
Ag_2L_2	12.029	0.005	79	Ag_2L_2	12.041	0.004	80
$S = 1.38$				$S = 1.45$			

The four different methods of calculation for a given data set using SUPERQUAD yield the same model and practically the same formation constants. In comparison with the results of STACAL3 when the limited pH and pAg data set is used (with cutoff values) the species [AgLH] is removed from the model by SUPERQUAD due to an excessive standard deviation of the constant. This is not surprising if one considers the fact that the pH and pAg area where this species is predominant is almost completely removed by the cutoff values.

It is interesting to note that SUPERQUAD (with or without cutoff values) prefers the minor species [Ag_2L_2H] above the other minor species [AgL_2H]; the latter was prefered by STACAL3.

Ratio technique

The data obtained from this procedure are shown in Fig. 6a and b. As no pL values are available STACAL3 cannot be used so that the data can only be analysed using SUPERQUAD. Several models are tested using the weighted option in SUPERQUAD ($\sigma_{E\ glass} = 0.2$ mV, $\sigma_{E\ Ag/Ag_2S} = 0.1$ mV and $\sigma_V = 0.002$ ml). The most successful model is presented in Table 4 together with its final fit statistic S and the maximum % species presence for all ratios. The maximuim % species

TABLE 4

Best model obtained from the ratio technique [a]

Species	log β	S.D.	Max % species (all ratios)	Max % species (1/2 ratio)
AgLH	12.600	0.003	28	24
AgL_2H_2	25.277	0.007	21	13
AgL_2	7.265	0.005	71	25
AgL_2H	16.741	0.009	20	7
Ag_2L_2	11.986	0.001	84	79
Ag_2L_2H	19.42	0.02	5	4

[a] Final fit statistic $S = 3.15$, Number of titration points = 746, number of data points = 1492.

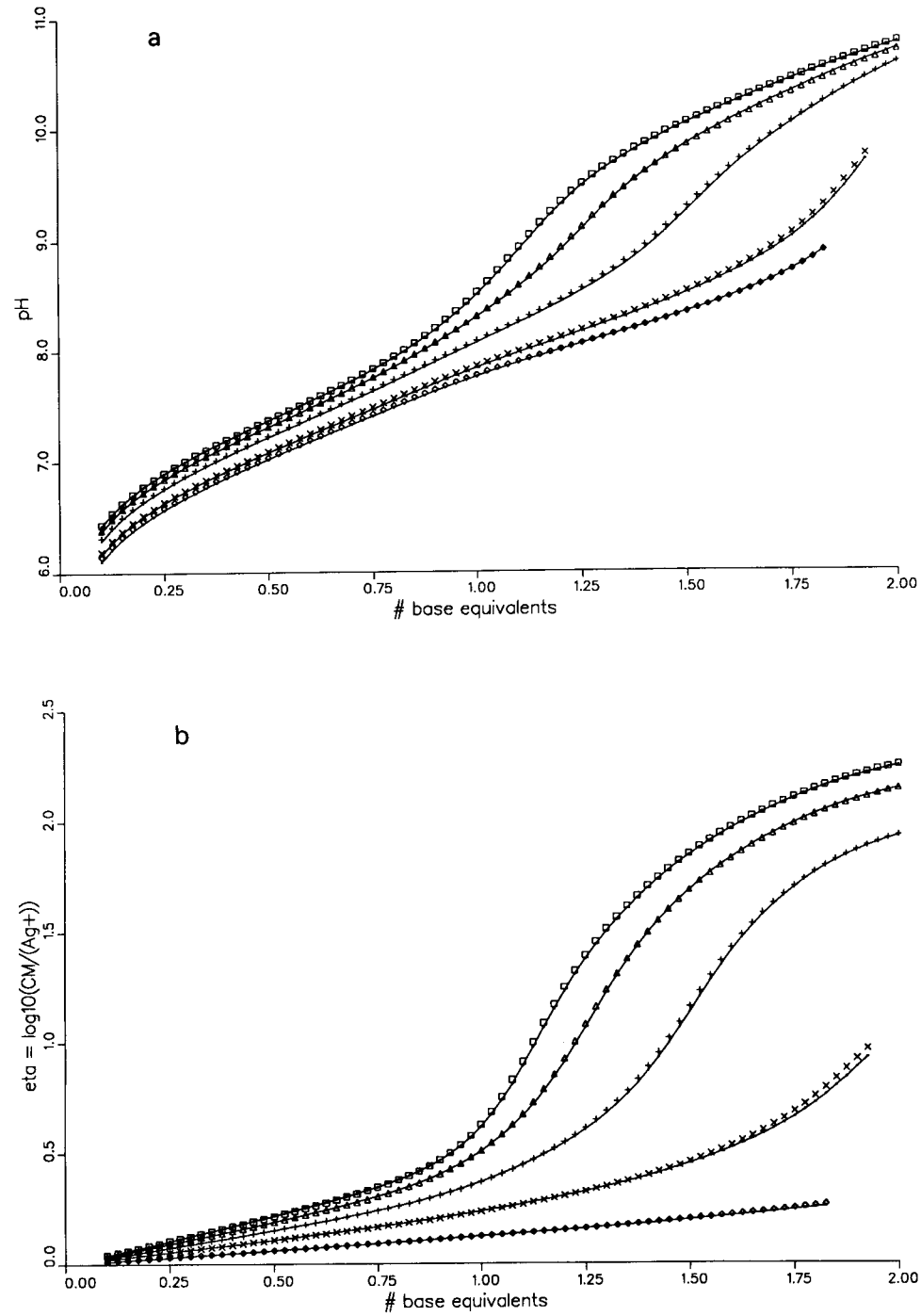

Fig. 6. (a) pH data from the ratio technique vs. number of base-equivalents. The ratios 1/8 (□), 1/4 (△), 1/2 (+), 1/1 (×), 2/1 (◇) are shown. The full lines are the theoretical values using model 2 from Table 5. (b) pAg data from the ratio technique vs. number of base-equivalents. The ratios 1/8 (□), 1/4 (△), 1/2 (+), 1/1 (×), 2/1 (◇) are shown. The full lines have the same meaning as in Fig. 6a.

TABLE 5

Survey of the most successful models found using SUPERQUAD

[The formation constants are tabulated for each model with the standard deviations on the last digit between brackets, followed by its % species presence. [a] denotes that the standard deviation is less than 0.01 log units. The % species presence is the maximum % occurrence of the respective species over all ratios and over the entire pH area. The *S* statistic (goodness-of-fit) is also given for each model]

Species	Model 1	%	Model 2	%	Model 3	%	Model 4	%	Model 5	%
AgLH	12.63 [a]	29	12.60 [a]	28	12.62 [a]	29	12.60 [a]	28	12.60 [a]	27
AgL_2H_2	25.27 [a]	21	25.28 [a]	21	25.20 (1)	18	25.30 [a]	22	25.28 [a]	21
AgL_2	7.26 [a]	71	7.26 [a]	71	7.15 [a]	58	7.26 [a]	71	7.24 [a]	69
AgL_2H	16.75 (1)	21	16.74 [a]	20	16.0 (1)	4	16.79 [a]	23	16.74 [a]	21
Ag_2L_2	11.99 [a]	85	11.99 [a]	84	11.84 (1)	71	11.98 [a]	84	11.98 [a]	84
Ag_2L_2H			19.42 (2)	5					19.44 (2)	5
AgL					4.15 (3)	31				
Ag_2L							5.98 (2)	4		
Ag_2L_3									13.6 (1)	3
S	3.79		3.15		3.54		3.32		3.13	

	Model 6	%	Model 7	%
AgLH	12.60 [a]	27	12.56 [a]	25
AgL_2H_2	25.39 [a]	28	25.39 [a]	28
AgL_2	7.29 [a]	74	7.30 [a]	75
AgL_2H				
Ag_2L_2	12.02 [a]	86	12.02 [a]	86
Ag_2L_2H			19.46 (3)	5
S	5.60		5.14	

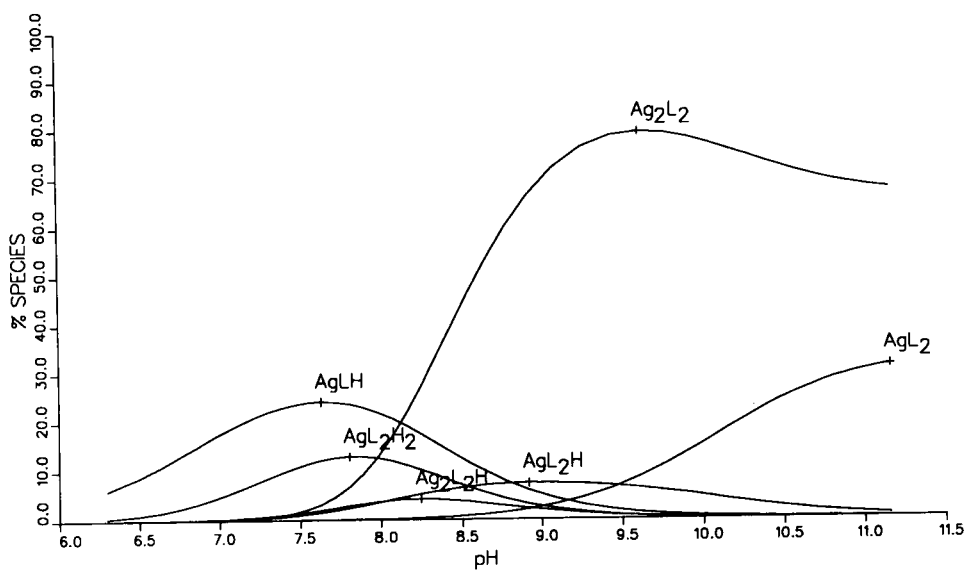

Fig. 7. Species distribution of the model shown in Table 4 in function of pH calculated sing $C_{Ag} = 0.1$ mmol, $C_L = 0.2$ mmol, $C_H = 0.4$ mmol. Initial volume: 40 ml.

presence of the 1/2 ratio is also given in order to make a comparison between the dilution method and ratio technique possible. The arbitrary criterium of minimum 3% species presence is used in the model selection. A list of the most successful models is shown in Table 5. Model 2 is prefered above model 5 due to the large standard deviation of the formation constant of $[Ag_2L_3]$ and is low per cent species presence.

As can be seen from table 4, both AgL_2H and Ag_2L_2H are accepted. Using the dilution method, both calculation procedures prefered only these two species. From the percentage of appearance, it is clear that both species are of minor importance.

Conclusion

The best models of both techniques agree fairly well, although the dilution method covers a large concentration area but only uses one C_{Ag}/C_L ratio whereas the ratio technique covers a limited concentration area but uses a broad C_{Ag}/C_L ratio.

The species $[Ag_2L_2H]$ is not identified in the dilution technique using STACAL3. This is understandable if the percentage of species presence is checked for a 1/2 C_{Ag}/C_L ratio using the model obtained from the ratio technique (Table 4 and Fig. 7).

The best model found in the dilution technique agrees with the prediction based on the average stoichiometric coefficients. We feel confident that the rigorous model testing in the dilution technique through the $\bar{p}$, $\bar{q}$ are $\bar{r}$ curves and STACAL3 forms a sound basis and identifies the predominant species for further model testing. The standard deviations on the constants obtained from the dilution technique and STACAL3 are of a more realistic magnitude (± 0.05) than obtained from SUPERQUAD. If the experimental conditions in the dilution technique can be improved, both pathways will be comparable. In view of the results and the more definite model selection possible with STACAL3, it should be worthwhile to optimize the dilution technique. Nevertheless if pL values are not known STACAL3 can not be used. In that case, a program like SUPERQUAD remains the only alternative.

REFERENCES

1 R. Guevremont and D.L. Rabenstein, Can. J. Chem., 57 (1979) 466.
2 A. Avdeef and K.N. Raymond, Inorg. Chem., 18 (1979) 1605.
3 L.C. Van Poucke, J. Yperman and J.P. François, Inorg. Chem., 19 (1980) 3078.
4 L.C. Van Poucke, Inorg. Nucl. Chem. Lett., 8 (1972) 801.
5 J. Yperman, J. Mullens, J.P. François and L.C. Van Poucke, Inorg. Chem., 22 (1983) 1361.
6 J. Yperman, J. Mullens, J.P. François and L.C. Van Poucke, Talanta, 31 (1984) 735.
7 L.C. Van Poucke, Talanta, 23 (1976) 161.
8 R. Garner, J. Yperman, J. Mullens and L.C. Van Poucke, J. Coord. Chem., in press.
9 P. Gans and A. Sabatini, Inorg. Chim. Acta, 79 (1983) 219.
10 P. Gans and A. Sabatini, J. Chem. Soc. Dalton Trans, (1985) 1195.
11 P. Gans, Data Fitting in the Chemical Sciences, Wiley, Chichester, 1992, Chapt. 10.
12 L.G. Sillen, Acta Chem. Scand., 15 (1961) 1981.
13 R. Garner, J. Yperman, J. Mullens and L.C. Van Poucke, Fresenius' J. Anal. Chem., in press.
14 R. Garner, J. Yperman, J. Mullens and L.C. Van Poucke, Bull. Soc. Chim. Belg., 102 (1993) 3.
15 J. Yperman, R. Carleer, G. Reggers, J. Mullens and L.C. Van Poucke, J. AOAC. Int., in press.
16 J. Yperman, A. De Backer, A. Vos, D. Franco, J. Mullens and L.C. Van Poucke, Anal. Chim. Acta, 273 (1993) 511.
17 B.B. Majchrowicz, J. Yperman, J. Mullens and L.C. Van Poucke, Anal. Chem., 63 (1991) 760.
18 P.A. Gorry, Anal. Chem., 62 (1990) 570.
19 A. Savitzky and M. Golay, Anal. Chem., 36 (1964) 1627.
20 P.R. Bevington, Data Reduction and Error Analysis for the Physical Sciences, McGraw-Hill, New York, 1969, Chap. 6–9.
21 R.M. Smith and A.E. Martell, Critical Stability Constants, 1975, Volume 2, Amines, 1982, Volume 5, First Supplement, 1989, Volume 6, Second Supplement, Plenum Press, New York.
22 H. Ohtaki and Y. Ito, J. Coord. Chem., 3 (1973) 131.
23 H. Ohtaki and K. Cho, Bull. Chem. Soc. Jpn., 50 (1977) 2674.

Analytica Chimica Acta, 282 (1993) 485–488
Elsevier Science Publishers B.V., Amsterdam

Determination of stability constants of metal complexes with potentiometric pH titrations

G. Anderegg

Laboratorium für Anorganische Chemie, ETH-Zentrum, Universitätstrasse 6, CH-8092 Zürich (Switzerland)

(Received 17th March 1993; revised manuscript received 17th June 1993)

Abstract

The use of different cells for pH measurements for the determination of equilibrium constants of metal complexes is discussed in relation to the liquid junction potential connected with them. The effects of H^+_{aq} and OH^-_{aq} on this quantity are also considered. The literature values for the conversion factor A, representing the difference in pH value based on the calibration with NBS buffers and that defined in terms of H^+ concentration, are discussed.

Keywords: Potentiometry; Titrimetry; Metal complexes; Stability constants

A paper [1] concerned with some aspects of potentiometric pH titrations related to the determination of equilibrium constants of metal complexes recently appeared in this journal. This problem is, in general, complex but can be approached in a reasonable way if the measurements are carried out using solutions that contain an inert salt in order to maintain a constant ionic strength. Under these conditions the activity coefficients of all species present remain virtually constant and, therefore, concentrations instead of activities can be used in the calculations of the equilibrium constants. In this way the use of more or less exactly known activity coefficients can be avoided. As in practice the equilibria often occur in the presence of a known concentration of inert salt(s), the quantitative data obtained in this way are very valuable. These pH measurements demand the use of galvanic cells with a liquid junction, as the reference electrode (RE) has to be separated from the investigated solution. This results in cells with one or two regions in which two solutions with different composition are separated by porous glass allowing the ion transport. Each of these junctions is responsible for an electrical potential which is added to the required potential difference of the two electrodes giving the experimental E or pH values. These junction potentials, E_j, are generally not known and cannot be calculated exactly. Therefore, one has to choose cells and solution compositions for which the pH values being measured are not altered by junction potentials.

CELLS FOR pH MEASUREMENTS

In the case under discussion, commercially available combined glass electrodes were used for such measurements. These electrodes have often been employed for the measurement of pH values in the activity scale (pH_{NBS}), also using the commercially available NBS (National Bureau of Standards) buffer solutions for their calibration. In the above-mentioned paper [1], only in one case were two separate electrodes used and, as the results obtained were very similar to those with the combined electrodes, the same conclusions were drawn for all cells when taken together. This agreement is due to the fact that

both RE have identical KCl solutions. These electrodes are made primarily for pH measurements in the activity scale following IUPAC recommendations [2], but not always with the claimed KCl concentration ($\geqslant$ 3.5 m, Metrohm 3 M KCl, Beckmann 4 m KCl and Orion 3 m KCl). This accounts for the claim "that companies selling combined glass electrodes have a tendency to state that their electrodes measure the 'hydrogen ion activity'" [1]. As the junction potential depends mainly on the concentrations of the two solutions coming into contact, the use of a saturated KCl solution in the calomel electrode (= saturated calomel electrode: 4.16 M or 4.8 m KCl at 25°C) is considered to be the best way for its minimization, its value being equivalent to 0.02–0.10 pH units. The choice of this particular salt is further due to the fact that a factor appearing in the expression of the junction potential given by Henderson [3] is the difference in the limiting ionic conductivity [3] and its value is in this instance fairly low for KCl (2.85 $cm^2\ \Omega^{-1}\ mol^{-1}$ [4]). [1] Further errors in E_j are expected if the solutions for the calibration and measurement have other inert salt compositions, because they give different E_j values and the measured pH value deviates from its true value by an amount that corresponds to the difference in E_j between the two solutions. This quantity is called the residual liquid junction, ΔE_j. For this, the use of solutions of the same inert salt and at the same concentrations for all solutions being measured is the best solution for more exact measurements.

Instead of a saturated calomel electrode one can use a 0.1 M (KCl) calomel electrode, which, as mentioned by Bates [5], has some advantages. If the measurements are carried out in 0.1 M NaCl one then has a liquid junction between the two solutions. Also in this instance one could insert between the two solutions a saturated KCl bridge. If one considers the junction potential E_j:

RE, 0.1 M KCl | 0.1 M NaCl $\quad E_j = 6.4$ mV

RE, 0.1 M KCl | 3.5 M KCl | 0.1 M NaCl $\quad E_j = 0.4$ mV

On the basis of the limiting ionic conductivities, smaller differences are obtained for NH_4NO_3 (2.39), CsCl (0.91) and CsI (0.31 $cm^2\ \Omega^{-1}\ mol^{-1}$). Among these three salts only the first has previously been used for salt bridges.

on the basis of the data of Milazzo [6], one notes the effectiveness of the concentrated KCl solution. For routine measurements this advantage can be nullified through contamination by chloride ions of the solution under study. The flow of KCl in the test solution has only been mentioned in one paper [7] and was found to be of 0.004 M h^{-1}. It should depend on the dimensions of the pores of the sintered glass of the RE and on the volume of the test solution. This effect can be much larger if in the test solution chloride ions are absent and, instead of NaCl, $NaNO_3$ is used as an inert salt. As the reference electrode solution contains chloride to stabilize Hg_2Cl_2(s) and the potential of the electrode, the connection with the test solution can then be made as follows:

$$\mathrm{Hg, Hg_2Cl_2, 0.1\ M\ NaCl} \quad |0.1\ \mathrm{M\ NaNO_3}|^{\text{solution with } I = 0.1(\mathrm{NaNO_3})} \qquad \text{(I)}$$

$$\mathrm{Hg, Hg_2Cl_2,} \begin{matrix} \text{0.09 M NaNO}_3 \\ \text{0.01 M NaCl} \end{matrix} \Big| 0.1\ \mathrm{M\ NaNO_3} |^{\text{Solution with } I = 0.1(\mathrm{NaNO_3})} \qquad \text{(II)}$$

or similar half-cells with other alkali metal ions. The 0.1 M $NaNO_3$ solution of the bridge can be changed in order to exclude the chloride ions. If this solution is combined with the test solution in 0.1 M $NaNO_3$ then the quantity ΔE_j is negligible if the molar concentrations of the components investigated and of the buffer used for calibration amount to a few per cent (1–5%) of that of the inert salt. The calibration is made with solutions with known values of $[H^+]$, giving another scale for these measurements, $pH_c = -\log[H^+]$. In order to avoid large changes in the ionic strength, one has to calculate this quantity for all ionic species present with $I = 1/2(\Sigma_i c_i z_i^2)$ (c_i = ion concentration and z_i = ion charge) during the titration and show that its value is correct in the volume range in which constants are calculated. Otherwise, a change in the concentration of the inert salt is necessary. This last condition is not always respected and even an exact description of the experimental conditions cannot increase the reliability of equilibrium constants, especially if the ionic strength during the measurements goes outside the limit $I \pm 0.1I$. This is because changes

in the junction potential and in the activity coefficients of the species present are then expected. Particularly the statement of the constancy of the concentration of the inert salt instead of that of the ionic strength cannot always ensure reliable results.

If for the calibration alkalimetric titrations of a strong acid with a strong base are used, it is very important to show the influence of H^+_{aq} and OH^-_{aq} on E_j, because of their large ionic mobilities with respect to those of the other ions, owing to the different mechanisms of ionic transport [8].

EFFECTS OF H^+ AND OH^- ON E_j

An examination of the values of E_j reported by Milazzo [6] for solutions in contact with 3.5 M KCl show clearly that with solutions of strong acids higher E_j values are found with respect to salt solutions. A similar effect, with E_j values of opposite sign, is found for solutions of strong bases. This effect can be followed with accuracy for solutions at constant ionic strengths, for which a mathematical relationship was obtained more than 80 years ago [3]. For two solutions in contact, having the same ionic strength (cells I and II), one containing the electrolyte MX and in the other this electrolyte is being successively replaced with the corresponding strong acid HX, the junction potential E_j can be calculated with the equation of Henderson:

$$E_j = -59.16 \log(1 + d[H^+]/I) \quad (1)$$

where $d = (\Lambda_{MX} - \Lambda_{HX})/\Lambda_{MX}$. Biedermann and Sillén [9], using different metal and glass electrodes, obtained for the junction 3 M $NaClO_4$ | (3 $-x$) M $NaClO_4$, xM $HClO_4$ $d = 1.95$ instead of 3.3 calculated from the molar conductivities Λ_{MX} and Λ_{HX}. For $I = 0.1$ ($NaNO_3$), with further use of a mercury electrode, it was found [10] that Na^+ can be completely replaced with H^+ in one solution involving E_j values that can be obtained within the errors of the glass and mercury electrodes used (1 mV) from the above expression using the limiting molar conductivities. The value of d is 2.55 at 21.7°C. Similar equations are obtained in strongly basic solutions with $d = 0.93$ for $I = 3$ M $Na(ClO_4, OH)$ and $d = 1.057$ for $I = 0.1$ m $Na(ClO_4, OH)$. For low E_j values, the linear expression $E_j = -a[H^+] + b[OH^-]$, with $a = 17$ and $b = 8$ at $I = 3$ [11] and $a = 647$ and $b = 272$ at $I = 0.1$ can be used [12].

THE CONVERSION FACTOR A

For cells with RE of type I and II no problems are expected in the exact determination of stability constants of metal complexes because the residual junction potential is negligible and corrections for H^+_{aq} and OH^-_{aq} can be made exactly. The calibration was done normally with solutions of weak acids with known pK values or with strong acids.

If a commercial combined glass electrode is used for measurements of stability constants at constant ionic strength I, one needs a calibration under the same conditions which gives the pH_c in addition to the pH_{NBS} scale discussed earlier for the same cell. If within both scales the junction potential of each calibration solution is the same, the difference $A = pH_{NBS} - pH_c$ represents $-\log \gamma$ (γ = activity coefficient of H^+) corrected by ΔE_j. Sigel et al. [1] investigated solutions in the presence of $NaNO_3$ ($I = 0.1$ M) and KNO_3 ($I = 0.1$ and 0.5 M) against a concentrated (KCl) calomel electrode and found in each instance the same value of A. They considered that this value is independent of the ionic strength at $I = 0.1$–0.5 and of the inert salt used, although the two nitrates were used only at $I = 0.1$. They recommended the same value of A also for the range $I = 1$–2 M. The data on E_j in pH units for HCl solutions in KCl, NaCl and LiCl against saturated. KCl obtained by Harned [13] and discussed by Feldmann [14] conflict with the above generalization, but in the range 0.1–0.5 M MCl (M = K^+ or Na^+) differ by only 0.02. This difference increases to 0.05 at $I = 3$. For LiCl, the E_j value is larger and reaches 0.11 at $I = 3$. The value of A of ca. 0.02 obtained at an ionic strength of 0.1, practically within the error of the pH measurements (± 0.02), is unexpected considering that under this condition the liquid junction potential of the solutions investigated should be virtually

identical [5], within 0.02. Therefore, the expected value of A should be almost identical with $-\log \gamma \approx 0.10$, where γ is the activity coefficient of H^+ at $I = 0.1$. In this context, one should remember that the residual liquid junction potentials of the NBS buffer solutions used are never larger than 0.01 pH unit [15].

Values of A close to $-\log \gamma$ have been reported for solutions at $I = 0.04$–0.2 [7], at $I = 0.05$–0.5 (KCl or $NaClO_4$ or KNO_3) [16] and at $I = 0.1$ (KNO_3) [17], obtaining values around 0.1 and only at $I = 0.5$ did the A value deviate substantially. A comparison of A values is more adequate at $I = 0.1$, as the NBS buffers also have a similar ionic strength and therefore a match of the liquid junction potential is possible, γ being very similar. In the solutions investigated the ionic strength has not always been maintained at the given value because of high concentrations of other components and sometimes the strong acid present [7] contributes to E_j. Nevertheless, it seems improbable that the A values obtained previously [7,16,17] are a consequence of some small inadequacies. As mentioned by Covington [18], the value of E_j seems to depend on the geometry of the liquid junction and only if that is sufficiently defined is its E_j value reproducible. This is generally achieved by the use for a capillary tube. "Most commercial designs for the formation of liquid junctions are of ill-defined geometry and hence poor reproducibility" [18]. By correct and repeated calibration this effect can also be excluded!

Conclusions

For practical reasons and in order to avoid contamination, the use of cells containing only solutions at the same ionic strength is considered to be the most effective way to obtain reliable potential measurements. Under this condition, in the presence of H^+_{aq} and OH^-_{aq} at high concentrations, a correction is necessary, which can be determined exactly experimentally.

The variability of the conversion factor A from 0.1 to 0.02, assuming no changes or contamination of all solutions involved, can be explained by errors in ΔE_j due to the use of "commercial combined" glass electrodes with variable KCl concentration (3–4.18 m KCl) and calibration of the cell without checking the junction potentials for H^+_{aq} and OH^-_{aq} [19]. The above assumption and these two points can be controlled by the use of further measurements by those who prefer the different commercial combined glass electrodes for equilibrium studies.

REFERENCES

1 H. Sigel, A.D. Zuberbühler and O. Yamauchi, Anal. Chim. Acta, 63 (1991) 255.
2 M.L. McGlashan, IUPAC Manual of Symbols and Terminology for Physicochemical Quantities and Units, Butterworths, London, 1970.
3 P. Henderson, Z. Phys. Chem., 59 (1907) 118.
4 R.A. Robinson and R.H. Stokes, Electrolyte Solutions, 2nd edn., Butterworths, London, 1959.
5 R. Bates, Determination of pH; Theory and Practice, Wiley, New York, 1973.
6 G. Milazzo, Elektrochemie I, Birkhäuser, Basle, 1980, p. 176, Table III, 3.
7 G.R. Hedwig and H.K. Powell, Anal. Chem., 43 (1971) 1206.
8 J.O'M. Bockris and A.K.N. Reddy, Modern Electrochemistry, Vol. 1, Plenum, New York, 1970, p. 481.
9 G. Biedermann and L.G. Sillén, Ark. Kemi., 5 (1952) 425.
10 G. Schwarzenbach and G. Anderegg, Helv. Chim. Acta, 40 (1957) 1773.
11 N. Ingri, G. Lagerström, M. Frydman and L.G. Sillén, Acta Chem. Scand., 11 (1957) 1034.
12 G. Anderegg, Program for the Calculation of Calibration Titrations, Lab. für Anorganische Chemie, ETH, Zürich, 4th edn., 1982.
13 H.S. Harned, J. Phys. Chem., 30 (1926) 433.
14 I. Feldmann, Anal. Chem., 28 (1956) 1859.
15 A.K. Covington, R.G. Bates and R.A. Durst, Pure Appl. Chem., 57 (1985) 53.
16 W.A.E. McBryde, Analyst, 94 (1969) 337.
17 H.M. Irving, M.G. Miles and L.D. Pettit, Anal. Chim. Acta, 38 (1967) 475.
18 A.K. Covington Anal. Chim. Acta, 127 (1981) 1.
19 A. Braibanti, G. Ostacoli, P. Paoletti, L.D. Pettit and S. Sammartano, Pure Appl. Chem., 59 (1987) 1721.

Analytica Chimica Acta, 282 (1993) 489–495
Elsevier Science Publishers B.V., Amsterdam

Protonation constants of some substituted salicylideneanilines in dioxan–water mixtures

Turgut Gündüz, Esma Kılıç and Esin Canel

Department of Chemistry, Faculty of Science, University of Ankara, Ankara (Turkey)

Fitnat Köseoğlu

Department of Sciences, Faculty of Gazi Education, University of Gazi, Ankara (Turkey)

(Received 23rd February 1993; revised manuscript received 22nd June 1993)

Abstract

Sixteen Schiff's bases have been prepared from salicylaldehyde and substituted anilines and their stoichiometric protonation constants have been determined in dioxan–water mixtures of 30, 40, 50 and 60% dioxan (v/v) using a combined pH electrode at 25°C, under nitrogen atmosphere. The calculation of the constants has been carried out using a PKAS computer programme. The effects of the substituents on the protonation constants and the additivities of these effects are discussed. Furthermore, it was found that the log K_{OH} value increases but the log K_{NH} value decreases for all Schiff's bases if the percentage of dioxan is increased.

Keywords: Potentiometry; Titrimetry; Protonation constants; Schiff's bases

Schiff's bases are becoming increasingly important as analytical, biochemical and antimicrobial reagents, and in addition they have received much attention due to their use as liquid crystals and dyes [1–5]. Because of their diverse uses in science, the protonation constants of such compounds are of interest. Although there is a number of publications on the determination of the protonation constants of the various Schiff's bases in solvent mixtures [6–12], a literature survey reveals that the protonation constants of Schiff's bases prepared from substituted anilines and salicylaldehyde have not been determined systematically in dioxan–water mixtures. This article, therefore, deals with the determination of the stoichiometric protonation constants of salicylideneaniline, salicylidene-2-methylaniline, salicylidene-3-methylaniline, salicylidene-4-methylaniline, salicylidene-2-ethylaniline, salicylidene-3-ethylaniline, salicylidene-4-ethylaniline, salicylidene-2-methoxyaniline, salicylidene-3-methoxyaniline, salicylidene-4-methoxyaniline, salicylidene-2,3-dimethylaniline, salicylidene-2,4-dimethylaniline, salicylidene-2,5-dimethylaniline, salicylidene-3,4-dimethylaniline, salicylidene-2,4-dimethoxyaniline and salicylidene-3,5-dimethoxyaniline. Moreover, this work reports an investigation aimed at gaining information about the specific effects of the substituents and the effect of the solvent composition on the protonation constants of the Schiff's bases.

Correspondence to: T. Gündüz, Department of Chemistry, Faculty of Science, University of Ankara, Ankara (Turkey).

EXPERIMENTAL

The measurements in this study were carried out at 25.0 ± 0.1°C in aqueous–dioxan media

containing 30, 40, 50 and 60% dioxan (v/v). Ionic strength of media were adjusted to 0.1 M with sodium perchlorate.

Materials

All Schiff's bases were prepared by condensing salicylaldehyde with aniline and substituted anilines. The Schiff's bases were purified by recrystallisation from ethanol. Stock solutions were prepared in dioxan. Salicylaldehyde and all substituted anilines were purchased from Merck (reagent grade) and were used as received.

The concentrations of stock solutions of perchloric acid (Merck, 70%) and sodium hydroxide (Merck) were 0.1 M. Acid solutions were standardised against primary standard sodium carbonate (Merck). Alkali solutions were potentiometrically standardised against $HClO_4$ by use of Gran's plot techniques, allowing determination of dissolved carbonate impurity [13,14].

Chemically pure sodium perchlorate (Merck) was used to keep the ionic strength constant.

Dioxan was purchased from Merck and purified by the method given in Ref. 15.

Potentiometric apparatus and procedure

Potentiometric titrations were carried out in jacketed glass reaction vessels as described in Ref. 16. The cell e.m.f. was measured using an Orion 720 A Model pH-ionmeter equipped with combined pH electrode (Ingold). The electrode was modified by replacing its aqueous KCl solution with 0.01 M NaCl + 0.09 M $NaClO_4$ saturated with AgCl.

Titrations were performed in an atmosphere of nitrogen with carbonate free standard 0.1 M NaOH on 50 ml solutions containing 0.1 M $NaClO_4$ and (i) 2.5×10^{-3} M $HClO_4$ (for cell calibration) plus (ii) 2.5×10^{-3} M $HClO_4 + 1.5 \times 10^{-3}$ M Schiff's base.

Cell calibration

The potentiometric cell was calibrated for use of the combined pH electrode as a hydrogen ion concentration probe rather than as an activity probe. The ionic strength of the test solutions used in this study is kept constant; therefore the e.m.f. of the cell can be written in the form

$$E_{cell} = E^{o\prime}_{cell} + E_j + k \log[H^+] \quad (1)$$

where $E^{o\prime}_{cell}$ represents a quantity independent of $[H^+]$ but dependent on the activity of Cl^- in the filling solution of the electrode and the activity coefficient of H^+ in the test solution [17]. The activity coefficient of H^+ can be considered to be constant throughout the titration because the ionic strength of the solution is almost constant. E_j is the liquid junction potential and the constant k, denoted as electrode calibration slope, represents the Nernstian factor.

The calibration constants $E^{o\prime}_{cell}$ and k were determined by titration of a 2.5×10^{-3} M solution of perchloric acid with 0.1 M sodium hydroxide solution for each medium studied. All solutions for the calibration titrations were made up to an ionic strength of 0.1 M with $NaClO_4$. In all

TABLE 1

Stoichiometric protonation constants of Schiff's bases derived from salicylaldehyde and methyl-substituted anilines at 25.0 ± 0.1°C, for different dioxan–water mixtures (μ = 0.1 M $NaClO_4$) [a]

	log K_{NH}	log K_{OH}	log β_2 [b]	Δ log k [c]
30% Dioxan				
Reference [d]	4.35	9.14	13.49	0
2-CH_3	4.30	9.05	13.35	−0.05
3-CH_3	4.56	9.08	13.64	0.21
4-CH_3	4.87	9.15	14.02	0.52
40% Dioxan				
Reference [d]	4.10	9.00	13.10	0
2-CH_3	3.95	9.00	12.95	−0.15
3-CH_3	4.30	9.20	13.51	0.20
4-CH_3	4.60	9.25	13.85	0.50
50% Dioxan				
Reference [d]	3.85	9.49	13.34	0
2-CH_3	3.70	9.29	12.99	−0.15
3-CH_3	4.10	9.40	13.52	0.25
4-CH_3	4.45	9.50	13.95	0.60
60% Dioxan				
Reference [d]	3.60	9.85	13.45	0
2-CH_3	3.30	9.55	12.85	−0.30
3-CH_3	3.90	9.70	13.60	0.30
4-CH_3	4.20	9.85	14.05	0.60

[a] All errors are 0.03 or lower. [b] log β_2 = log K_{OH} + log K_{NH}. [c] Δ log k = log K_{NH} (ref.) − log K_{NH}. [d] Salicylideneaniline.

titrations, experimental points obtained in the region $2.2 < pH < 3.0$ were used for calibrations, where pH, represents $-\log[H^+]$. Within this range of pH, the E_j is effectively constant [18]. Eqn. 1 in the form $E_{cell} = E^\circ_{cell} + k \log[H^+]$ (where $E^\circ_{cell} = E^{o\prime}_{cell} + E_j$) was found to reproduce the calibration data to a precision typically of the order of ± 1.0 mV.

The standardization of the combined pH electrode was checked in the alkali range too, by the addition of an excess of NaOH. By assuming the E°_{cell} value determined in the acidic range to be reliable and $[OH^-]$ = concentration of base added in excess, we calculated reproducible values of pK_w, for all the solvent mixtures examined [19,20].

Calculation techniques

The computer programme PKAS was used for the calculation of the protonation constants of Schiff's bases from potentiometric titration data [17].

RESULTS AND DISCUSSION

The stoichiometric protonation constants of Schiff's bases are presented in Tables 1–4. The $\log K_{OH}$ and $\log K_{NH}$ values are related to the protonation of phenolate and imine nitrogen, respectively, as follows:

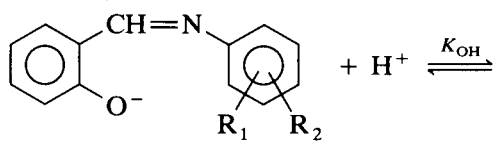

(L^-)

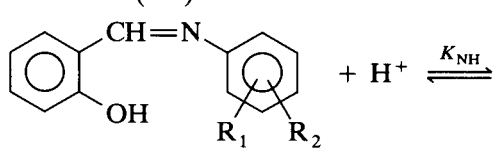

(HL)

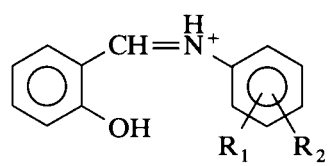

(H_2L^+)

where R_1 and R_2 = H, methyl, ethyl and methoxy. As can be seen from Tables 1 and 2, the protonation constants, $\log K_{NH}$, of salicylideneaniline (as reference) and its alkylderivatives vary in all the media investigated like 2-R < reference < 3-R < 4-R. This order can be used as an indication to the extend of the contributions of the alkyl groups to the basicity of the azomethine nitrogen. Furthermore electronic and steric effects of the alkyl groups can also be inferred. Methyl and ethyl groups are capable of releasing electrons by a resonance mechanism and are best able to stabilize a positive center when positioned *ortho* or *para* to it. This effect is known as hyperconjugation [21]. If the hyperconjugation was the only effect on the basicity of the azomethine nitrogen, the 2-R derivatives would also be more basic than the reference. The fact that the reference is more basic than the 2-R derivatives indicates that the steric effect is dominant to the resonance effect

TABLE 2

Stoichiometric protonation constants of Schiff's bases derived from salicylaldehyde and ethyl-substituted anilines at 25.0± 0.1°C, for different dioxan–water mixtures (μ = 0.1 M $NaClO_4$) [a]

	$\log K_{NH}$	$\log K_{OH}$	$\log \beta_2$ [b]	$\Delta \log k$ [c]
30% Dioxan				
Reference [d]	4.35	9.14	13.49	0
2-C_2H_5	4.15	9.24	13.39	−0.20
3-C_2H_5	4.40	9.40	13.80	0.05
4-C_2H_5	4.77	9.12	13.89	0.42
40% Dioxan				
Reference [d]	4.10	9.00	13.10	0
2-C_2H_5	3.90	9.05	12.95	−0.20
3-C_2H_5	4.15	9.30	13.45	0.05
4-C_2H_5	4.55	9.21	13.76	0.45
50% Dioxan				
Reference [d]	3.85	9.49	13.34	0
2-C_2H_5	3.60	9.41	13.01	−0.25
3-C_2H_5	3.94	9.34	13.28	0.09
4-C_2H_5	4.32	9.53	13.85	0.47
60% Dioxan				
Reference [d]	3.60	9.85	13.45	0
2-C_2H_5	3.30	9.72	13.02	−0.30
3-C_2H_5	3.70	9.70	13.40	0.10
4-C_2H_5	4.07	9.80	13.87	0.47

[a] All errors are 0.03 or lower. [b] $\log \beta_2 = \log K_{OH} + \log K_{NH}$. [c] $\Delta \log k = \log K_{NH}$ (ref.) − $\log K_{NH}$. [d] Salicylideneaniline.

in the case of *o*-substitution. The 4-R derivative is more basic than the 3-R derivative. This is in agreement with the prediction that the *p*-alkyl will contribute more to the electron density of the azomethine group than the *m*-alkyl.

A comparison of the basicities of methyl and ethyl derivatives with the same pattern of substitution shows that the methyl group is a more powerful electron-releasing group than the ethyl group. With any pattern of substitution, the order $-CH_3 > -C_2H_5$ always holds in all the media investigated.

An inspection of the log K_{NH} values (Table 3) for the methoxy derivatives of differing pattern of substitution reveals that the order is 3-OCH_3 < references < 2-OCH_3 < 4-OCH_3, regardless of medium. The order 3-OCH_3 < ref. indicates that the effect of OCH_3 is predominantly inductive in the *meta* position. On the other hand, the same group appears to be acting through resonance and steric mechanisms when it is in the *ortho* position and resonance mechanism in the case of the *para* position. The reason why the 2-methoxy, derivative is less basic than the 4-methoxy isomer can best be explained on the grounds that inductive electron depletion by oxygen is more pronounced in the *o*-derivative [21].

TABLE 3

Stoichiometric protonation constants of Schiff's bases derived from salicylaldehyde and methyl-substituted anilines at 25.0 ± 0.1°C, for different dioxan–water mixtures (μ = 0.1 M $NaClO_4$) [a]

	log K_{NH}	log K_{OH}	log β_2 [b]	Δ log k [c]
30% Dioxan				
Reference [d]	4.35	9.14	13.49	0
2-OCH_3	4.40	8.99	13.39	0.05
3-OCH_3	4.20	9.10	12.30	−0.15
4-OCH_3	4.96	9.20	14.16	0.61
40% Dioxan				
Reference [d]	4.10	9.00	13.10	0
2-OCH_3	4.15	9.17	13.32	0.05
3-OCH_3	3.80	9.20	13.00	−0.30
4-OCH_3	4.80	9.40	14.20	0.70
50% Dioxan				
Reference [d]	3.85	9.49	13.34	0
2-OCH_3	4.00	9.17	13.17	0.15
3-OCH_3	3.65	9.33	12.98	−0.20
4-OCH_3	4.65	9.58	14.23	0.80
60% Dioxan				
Reference [d]	3.60	9.85	13.45	0
2-OCH_3	3.65	9.75	13.40	0.05
3-OCH_3	3.28	9.65	12.73	−0.32
4-OCH_3	4.50	10.22	14.72	0.90

[a] All errors are 0.03 or lower. [b] log β_2 = log K_{OH} + log K_{NH}. [c] Δ log k = log K_{NH} (ref.) − log K_{NH}. [d] Salicylideneaniline.

TABLE 4

Stoichiometric protonation constants of Schiff's bases derived from salicylaldehyde and substituted anilines at 25.0 ± 0.1°C, for different dioxan–water mixtures (μ = 0.1 M $NaClO_4$) [a]

	log K_{NH} (exp.)	log K_{NH} (calc.)	log K_{OH}	log β_2 [b]
30% Dioxan				
Reference [c]	4.35	4.35	9.14	13.49
2,3-diCH_3	4.50	4.51	9.03	13.53
2,4-diCH_3	4.70	4.82	9.15	13.85
2,5-diCH_3	4.27	4.51	8.96	13.23
3,4-diCH_3	4.90	5.08	9.20	14.10
2,4-diOCH_3	4.90	5.01	9.25	14.15
3,5-diOCH_3	3.86	4.05	9.18	13.04
40% Dioxan				
Reference [c]	4.10	4.10	9.00	13.10
2,3-diCH_3	4.26	4.15	9.05	13.31
2,4-diCH_3	4.40	4.45	9.10	13.50
2,5-diCH_3	3.95	4.15	8.95	12.90
3,4-diCH_3	4.80	4.80	9.40	14.20
2,4-diOCH_3	4.80	4.85	9.25	14.05
3,5-diOCH_3	3.55	3.50	9.15	12.70
50% Dioxan				
Reference [c]	3.85	3.85	9.49	13.34
2,3-diCH_3	4.15	3.95	9.49	13.64
2,4-diCH_3	4.29	4.30	9.20	13.49
2,5-diCH_3	3.85	3.95	9.46	13.31
3,4-diCH_3	4.55	4.70	9.64	14.19
2,4-diOCH_3	4.65	4.80	9.49	14.14
3,5-diOCH_3	3.45	3.45	9.29	12.74
60% Dioxan				
Reference [c]	3.60	3.60	9.85	13.45
2,3-diCH_3	3.91	3.60	9.64	13.55
2,4-diCH_3	4.03	3.90	9.87	13.90
2,5-diCH_3	3.55	3.60	9.50	13.05
3,4-diCH_3	4.40	4.50	10.05	14.45
2,4-diOCH_3	4.41	4.55	9.87	14.28
3,5-diOCH_3	3.14	2.96	9.50	12.64

[a] All errors are 0.03 or lower. [b] log β_2 = log K_{OH} + log K_{NH}. [c] Salicylideneaniline.

When the basicities of methyl, ethyl and methoxy derivatives of the same substitution pattern are compared, the following orders can be seen:

$2\text{-}C_2H_5 < 2\text{-}CH_3 < 2\text{-}OCH_3$

$4\text{-}C_2H_5 < 4\text{-}CH_3 < 4\text{-}OCH_3$

$3\text{-}OCH_3 < 3\text{-}C_2H_5 < 3\text{-}CH_3$

These orders are valid in all the media investigated and on the basis of electronic and steric effects, these are exactly the predicted orders.

Using the same media, the protonation constants of the Schiff's bases derived from the condensation of disubstituted anilines with salicylaldehyde have been found and the relevant data are given in Table 4. These data can be of use in judging the additivities of the numeric contributions of various groups on the protonation constant, log K_{NH}, of the parent Schiff's base. For this purpose, the differences (Δ log k) between the protonation constants of the reference and of methyl and methoxy derivatives are listed in Tables 1 and 3. Using these differences, predictions have been made for the log K_{NH} of the disubstituted derivatives. The calculated and experimental log K_{NH} values are listed in Table 4. An inspection of these values leads to the conclusions that the basicity contributions of individual groups are roughly additive and the protonation constants of these Schiff's bases can be approximated to some extend.

As to the log K_{OH} values of the phenolic moiety of these Schiff's bases, we have not observed any regularity between the log K_{OH} values and the type and position of the substituents. This lack of regularity can probably be attributed to the fact that the substituents are far from the OH group.

The effects of the solvent itself on the protonation constants of various compounds have been studied by several authors [22–26]. For a discussion of the effect of solvent composition on the protonation constants of Schiff's bases, the variation of log K_{NH} values with the percentage of dioxan is plotted in Figs. 1–4. These figures show that the linear relationships exist between log K_{NH} and the percentage of dioxan for methyl, ethyl, methoxy and disubstituted derivatives. The

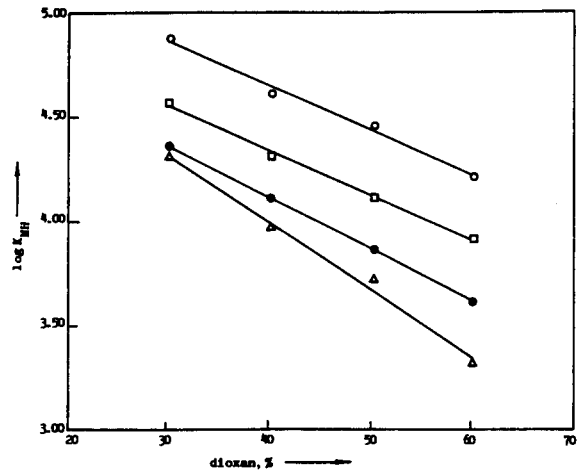

Fig. 1. The variation of log K_{NH} values of methyl substituted Schiff's bases against the percent of dioxan. Key: ● = reference; △ = 2-CH_3; □ = 3-CH_3; ○ = 4-CH_3.

inverse relation between the dioxan percentage and log K_{NH} values may be related to the variation of the medium dielectric constant. Log K_{NH} values are the formation constants of the ionic species H_2L^+ from the molecular species HL. Since the dielectric constant of the medium decreases with the increase of dioxan percentage, solvents of higher percentage of dioxan would

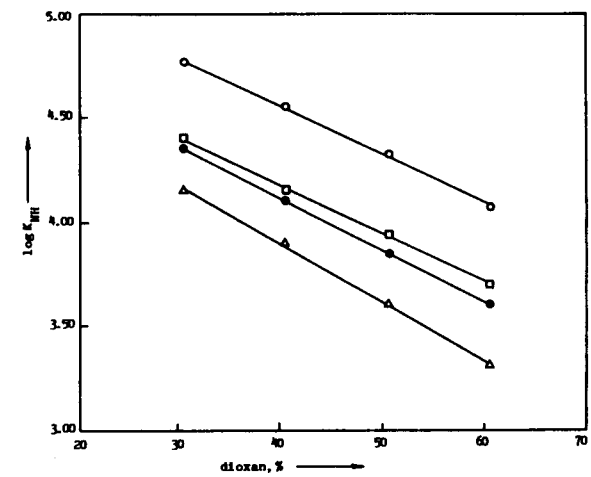

Fig. 2. The variation of log K_{NH} values of ethyl substituted Schiff's bases against the percent of dioxan. Key: ● = reference; △ = 2-C_2H_5; □ = 3-C_2H_5; ○ = 4-C_2H_5.

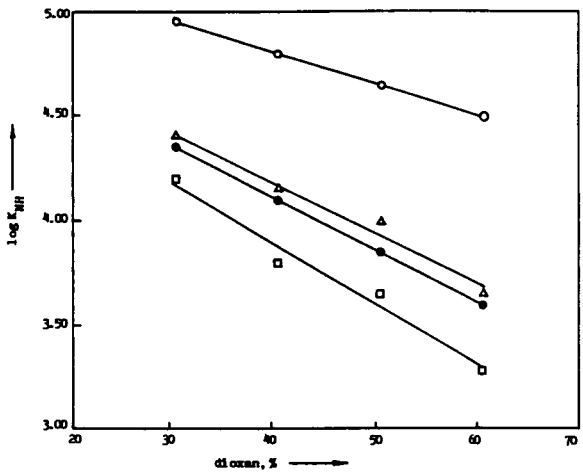

Fig. 3. The variation of log K_{NH} values of methoxy substituted Schiff's bases against the percent of dioxan. Key: ● = reference; △ = 2-OCH_3; □ = 3-OCH_3; ○ = 4-OCH_3.

solvate HL better than H_2L^+ whereas the opposite would be true for solvent rich in water. As to the variation of the log K_{OH} values of Schiff's bases with the solvent composition, we have observed that these protonation constants increase with the dioxan percentage except for 30% dioxan (Tables 1–4). The increase of the log K_{OH} values

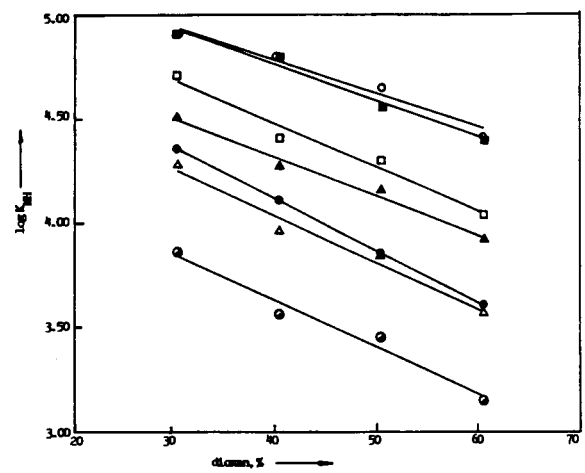

Fig. 4. The variation of log K_{NH} values of disubstituted Schiff's bases against the percent of dioxan. Key: ● = reference; ▲ = 2,3-diCH_3; □ = 2,4-diCH_3; △ = 2,5-diCH_3; ■ = 3,4-diCH_3; ○ = 2,4-diOCH_3; ◒ = 3,5-diOCH_3.

with the percentage of dioxan can also be explained on the same grounds. Of course, changes in the effective solvation of the charged and uncharged species involved in going from 30 to 60% dioxan would affect the protonation constants also.

We gratefully acknowledge the financial support of Ankara University Research Fund (Project No. 92-05-04-04).

REFERENCES

1 B.L. Kaul, Fr. Demande FR 2,586,421 (Cl. CO9K19/22), C.A., 104 (1986) 150788t.
2 M. Butez, L. Rabas and F. Vinet, Ger. Offen DE 3,413,603 (Cl. CO9B55/00), C.A., 107 (1987) 124755x.
3 C. Monticelli, G. Brunora, A. Fignani and A. Marchi, Korroz. Figy, 28 (1988) 118.
4 B. Dash, P.K. Mahapotra, D. Panda and J.M. Pattnaik, J. Indian Chem. Soc., 61 (1984) 1061.
5 J. Casaszar, J. Morvay and O. Herczeg, Acta Phys. Chem., 31 (1985) 717.
6 R.K. Mehta and R.K. Gupta, Indian J. Chem., 9 (1971) 1150.
7 M.S. Masoud and F.M. Eizawawy, Indian J. Chem., 23A (1984) 149.
8 N. Shori, Y. Dutt and R.P. Singh, J. Inorg. Nucl. Chem., 34 (1972) 2007.
9 V.G. Ratolikor, D.V. Jahagirdar and D.D. Khanolkar, Indian J. Chem., 16A (1978) 510.
10 M.S. Mayadeo and D.N. Patel, Indian J. Chem., 22A (1983) 542.
11 M.S. Mayadeo and R.K. Banavali, Indian J. Chem., 25A (1986) 396.
12 E.S. Jayadevappa and S.C. Galgali, J. Indian Chem. Soc., LX (1983) 1098.
13 G. Gran, Acta Chem. Scand., 4 (1950) 559.
14 G. Gran, Analyst, 77 (1952) 661.
15 D.D. Perrin and W.L.F. Armarega, Purification of Laboratory Chemicals, Pergamon Press, Oxford, 1st edn., 1966, p. 148.
16 A.E. Martell and R.J. Motekaitis, The Determination and Use of Stability Constants, VCH, 1988.
17 H. Rossotti, The Study of Ionic Equilibria, An Introduction, Longman, London, 1978.
18 P. May, D.R. Williams, P.W. Linder and R.G. Torrington, Talanta, 29 (1982) 249.
19 E.P. Serjeant, Potentiometry and Potentiometric Titrations, Wiley, New York, 1984.
20 E.M. Woolley, D.G. Hurkot and L.G. Hepler, J. Phys. Chem., 74 (1970) 3908.

21 N.S. Isaacs, Physical Organic Chemistry, Longman, New York, 1986.
22 Kwan-Kit Mui, W.A.E. McBryde and E. Neiboer, Can. J. Chem., 52 (1974) 1821.
23 G. Faraglia, F.J.C. Rossotti and H.S. Rossotti, Inorg. Chim. Acta, 4 (1970) 488.
24 L.G. Van Uitert and C.G. Haas, J. Am. Chem. Soc., 75 (1953) 451.
25 C.L. Norman, J.M. White and R.L. Yoest, J. Am. Chem. Soc., 78 (1956) 5218.
26 T. Gündüz, N. Gündüz, E. Kılıç and A. Kenar, Analyst, 111 (1986) 1345.

Analytica Chimica Acta, 282 (1993) 497–503
Elsevier Science Publishers B.V., Amsterdam

Polyaniline-dispersed mercury electrode for the detection of monochloramine and dichloramine

Anhua Liu and Erkang Wang

Laboratory of Electroanalytical Chemistry, Changchun Institute of Applied Chemistry, Chinese Academy of Sciences, Changchun, Jilin 130022 (China)

(Received 11th December 1992; revised manuscript received 21st May 1993)

Abstract

A novel type of electrochemical detector based on a polyaniline-dispersed mercury-coated glassy carbon chemically modified electrode was investigated for the detection of monochloramine and dichloramine. A polyaniline dispersed-mercury modified electrode, which was prepared by coating polyaniline on a thin mercury film electrode using fast-sweep voltammetry, was developed. The selectivity could be altered using various counter ions incorporated into the polymer. The results indicated that the use of a conducting polymer-based electrochemical sensor for the selective determination of chloramine is a feasible approach.

Keywords: Amperometry; Voltammetry; Chloramine; Electrochemical detection; Polyaniline-dispersed mercury electrode

It has been demonstrated that the use of conducting polymer coatings for modified surfaces provides advantages in chemical analysis [1–3]. Electrochemistry provides a simple, clean, and efficient route to polymer synthesis. The use of conducting polymers to modify the selectivity of electrochemical sensors has been explored [4–6]. The most extensively employed conducting polymer for this purpose is that based on polypyrrole [1]. Different counter ions (C^-) are readily incorporated during the polymer synthesis and therefore the chemical selectivity (activity) of the polymer is readily adjusted. The incorporation of metallic centres into the polymer coating results in enhanced electrochemical properties. In the case of a conductive electroactive polymer, it can be achieved by incorporating the metal species electrochemically to form metallic centres [7–9].

Correspondence to: E. Wang, Laboratory of Electroanalytical Chemistry, Changchun Institute of Applied Chemistry, Chinese Academy of Sciences, Changchun, Jilin 130022 (China)

Alternatively, the metal can be predeposited on the substrate to be used for electropolymerization, using a transient (pulsed, fast cycle) waveform, metal nucleation and polymer formation can be initiated according to the following reaction [10]:

$$M^0 \xrightarrow{+E_{app}} M^{n+} \xrightarrow{-E_{app}} M^0$$

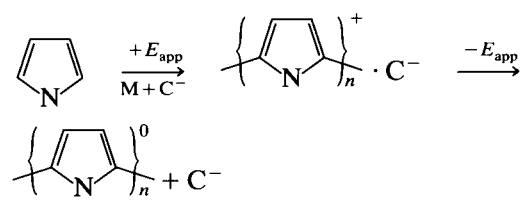

Wallace and co-workers [4–6,10,11] have studied polypyrrole-dispersed mercury-coated glassy carbon electrodes systematically. The most recent work was to investigate the use of polypyrrole coatings to modify the selectivity of the amperometric response to chloramines for developing a specific dichloramine sensor [11].

TABLE 1

Conditions employed for synthesis of polyaniline

Type of polyaniline	Solution (aqueous)	Potential scan range (V)	Scan rate ($mV\ s^{-1}$)	No. of potential cycles
PAn/Cl	0.1 M PAn + 1.0 M HCl	−0.2 to +1.1	100	10
PAn/SO_4	0.1 M PAn + 1.0 M H_2SO_4	−0.2 to +1.1	100	10
PAn/NO_3	0.1 M PAn + 1.0 M HNO_3	−0.2 to +1.1	100	10

It is well known that water chlorination proceeds according to the following reactions [12]:

$$NH_3 + HOCl \rightarrow NH_2Cl + H_2O$$

$$NH_2Cl + HOCl \rightarrow NHCl_2 + H_2O$$

$$NHCl_2 + HOCl \rightarrow NCl_3 + H_2O$$

The relative amount of each chloramine formed depends on the pH. As phosphate buffer (pH 5.0) is employed, NH_2Cl and $NHCl_2$ are formed at this pH [13]. It has been recognized that the specific form of the chloramines, in particular the presence of dichloramine, has a dramatic effect on taste and odour problems in drinking water. Chloramines have been determined using amperometric and UV detection [14]. All of chloramines respond indicating no selectivity for their individual detection.

In this work, a novel approach to the preparation of a polyaniline polymer and a polyaniline dispersed-mercury modified electrode was investigated. Electropolymerization of a conducting polymer proceeds according to

The direct incorporation of species into polyaniline-based polymers is not so easily achieved. Polyaniline must usually be grown from acidic media to ensure the formation of a conductive polymer. The insoluble layers produced are conductive and electroactive, and this process involves the incorporation of counter ions into the polymer matrix during synthesis, where X^- is an anion in the monomer solution. When this process is induced at a mercury film substrate, the mercury is predeposited on the substrate to be used for electropolymerization, by fast-sweep voltammetry, and then the mercury can be oxidized at potentials required for the polymerization. However, if the potential is switched rapidly to a negative potential to reduce the mercury before all of it has diffused away from the electrode surface, then the mercury will be redeposited. Simultaneously, a layer of polyaniline polymer is formed on the electrode surface. The procedure is such that a series of counter ions X^-, such as Cl^-, SO_4^{2-} and NO_3^-, may be incorporated during the polymerization process. The

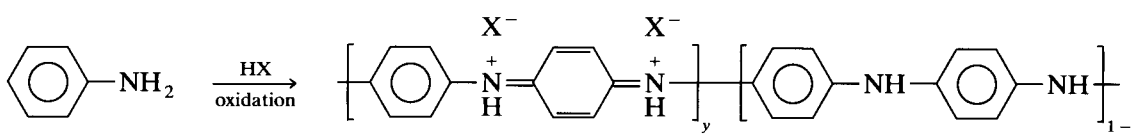

TABLE 2

Conditions employed for coating polyaniline on the mercury film electrode

Electrode	Solution	Potential scan range (V)	Scan rate ($V\ s^{-1}$)	No. of potential cycles [a]
PAn/Cl	0.1 M PAn + 1.0 M HCl	−0.2 to +0.8	1.0	15
PAn/SO_4	0.1 M PAn + 1.0 M H_2SO_4	−0.2 to +0.8	1.0	15
PAn/NO_3	0.1 M PAn + 1.0 M HNO_3	−0.2 to +0.8	1.0	15

[a] 15 cycles fast-sweep scan of 1.0 $V\ s^{-1}$ between −0.2 and +0.8 V on the mercury film electrode.

purpose of this work was to investigate the selectivity effect for chloramine detection by incorporating different ions on the polyaniline-dispersed mercury electrode.

EXPERIMENTAL

Reagent and solutions

All reagents were of analytical-reagent grade, unless stated otherwise, and distilled water was employed throughout. Analytical-reagent grade aniline was obtained from Beijing Chemicals. The solutions used for polymer synthesis were freshly prepared by mixing the monomer solutions with a suitable acid solution before polymerization. Ammonium sulphate and sodium hypochlorite (Beijing Chemicals) were dissolved in distilled water to obtain 0.1 mol l^{-1} stock solutions. Phosphate buffer were prepared from 0.01 mol l^{-1} K_2HPO_4 and 0.01 mol l^{-1} KH_2PO_4, adjusting the pH to 5.0. This buffer solution was also used as the eluent. Chloramine solutions were prepared as described [13].

Apparatus

Cyclic voltammetry (CV) was performed with a laboratory-built potentiostat [15] with a three-electrode cell containing a silver/silver chloride (saturated with potassium chloride) and a platinum-wire reference and counter electrode, respectively. A glassy carbon electrode (area 0.12 cm^2) was employed as the substrate for the polyaniline-modified electrode.

All liquid chromatographic (LC) experiments were done using a Model 510 pump, a U6K injection valve (Waters) and a 7-μm particle size Nucleosil C_{18} column (200 mm × 4.0 mm i.d.) as an analytical column. A glassy carbon electrode (area 0.071 cm^2) was employed as the substrate for the polyaniline-modified electrode. A UV–visible spectrophotometer (Model 481, BAS) was also used for the detection of chloramines.

Preparation of polyaniline-modified electrode. Polyaniline (PAN) electrodes incorporating various anions were prepared by cylic voltammetric (CV) electropolymerization on to the glassy carbon electrode from an acidic solution containing aniline monomer and the anion chosen. The experimental conditions are summarized in Table 1.

A polyaniline-cated mercury film electrode was prepared as follows. First, a prepared thin mercury film was plated at an applied potential of −0.5 V on a glassy carbon electrode from a stirred 100 μg ml^{-1} $Hg(NO_3)_2$ solution for 60 s. Second, polyaniline was coated on to the mercury film electrode by potential scanning at a scan rate of 1.0 V s^{-1} between −0.2 and 0.8 V for 10–20 cycles in the solution. The conditions for each counter ion are summarized in Table 2.

RESULTS AND DISCUSSION

Electrochemistry

Cyclic voltammograms were recorded in 0.01 M KH_2PO_4–0.01 M K_2HPO_4 (pH 5.0) base electrolyte. From CV experiments, we observed that chloramine had different responses on the glassy carbon (GC) and polymer-based electrodes. Chloramine showed a feeble oxidation reaction at the GC electrode within potential window (Fig. 1A) and an oxidation peak on the GC–Hg electrode at a potential of ca. −0.6 V (vs. Ag/AgCl) (Fig. 1B). Cyclic voltammograms of polyaniline in base electrolyte are shown in Fig. 1C; a poor oxidation–reduction response was observed owing to the base electrolyte of intermediate acidity.

The presence of chloramine increased the polyaniline background current and gave a varied peak shape because of the Cl^- doping and undoping from the polyaniline film (Fig. 1C). Finally, a clear oxidation peak appeared with the polyaniline-dispersed mercury electrode at a potential of ca. −0.5 V (vs. Ag/AgCl) and the peak height was directly proportional to the sample concentration (Fig. 1D). This was due to the oxidation–reduction process of the polyaniline film at ca. −0.5 V, the transition making the conducting polymer favourable for chloramine oxidation on the GC–Hg–PAn electrode. This result provided information for chloramine liquid chromatographic–electrochemical (LC–EC) separation and detection.

The effect of the mercury film thickness was studied. The responses observed for chloramine at the GC–Hg electrode were constant with mercury plating times of 60, 120 and 180 s in 100 μg ml^{-1} $Hg(NO_3)_2$ solution at an applied potential of −0.5 V. However, the background current increased with increasing plating times of mercury and consequently a plating time of 60 s was adopted.

The effect of the thickness of the conducting polymer layer on the deposited mercury film was then investigated. With thick polymers, the ratio

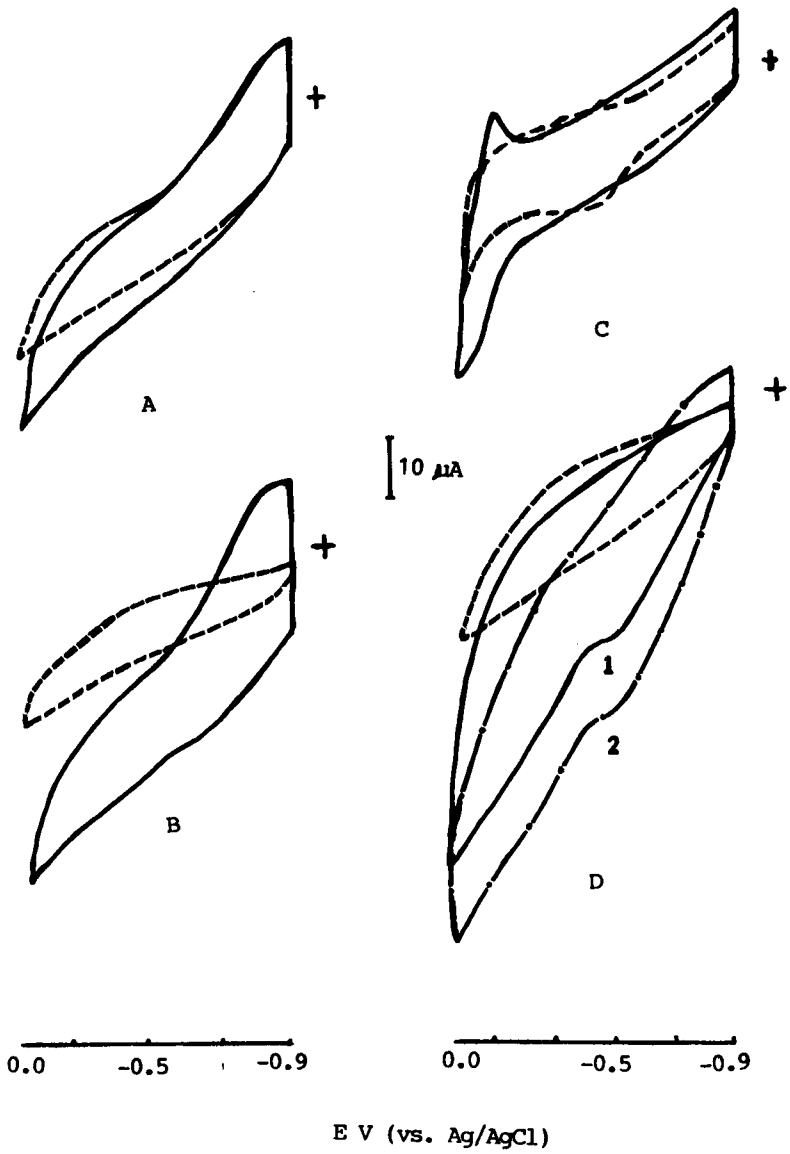

Fig. 1. Cyclic voltammograms for the chloramine sample at GC and polymer-dispersed GC electrodes. Base electrolyte, 0.01 M K_2HPO_4–0.01 M KH_2PO_4 (pH 5.0); scan rate, 100 mV s^{-1}, potential range, −0.9 to −0.0 V (vs. Ag/AgCl); chloramine sample, 0.01 M NaClO + 0.01 M $(NH_4)_2SO_4$. Dashed lines, CVs of blank solution (base electrolyte); solid lines, CVs of chloramine sample in base electrolyte. (A) At GC electrode; (B) at GC–HG electrode; (C) at GC–PAn/SO_4 electrode; (D) at GC–HG–PAn/SO_4 electrode. (1) 0.01 mol l^{-1} chloramine sample; (2) 0.03 mol l^{-1} chloramine sample.

of mercury to polymer on the electrode surface decreased and thus the metal ions had less chance to access the substrate, particularly at more negative potentials, where the polyaniline coating were inherently less conductive. A detailed discussion is given in the next section.

LC with electrochemical detection

The selectivity factor is defined as the ratio of the responses of di- and monochloramine. All experimental conditions in this instance were constant except for the applied potential and the coating on the working electrode.

GC and GC–Hg electrode. The effect of applied potential on the response factor obtained using glassy carbon was studied and it was found that the selectivity factor decreased at more negative potentials. Figure 2A shows the mono- and dichloramine responses at the GC electrode. The mercury film electrode was found to increase the chloramine response considerably compared with the bare glassy carbon electrode. Figure 2B shows the increase in the responses at the GC–Hg electrode.

Polyaniline-coated electrode. The use of a polyaniline-coated electrode was considered. The polyaniline-coated glassy carbon electrode was found to be more sensitive for dichloramine. At −0.7 V, the dichloramine response was higher than that at 0.0 V (Table 3), because polyaniline is more hydrophobic when it is reduced at negative potentials. This is favourable for the detection of dichloramine, as it is more hydrophobic than monochloramine.

At 0.0 V the polymer is in the oxidized state and is more polar. At −0.5 V the polymer is in the transition stage between the oxidized and reduced states, and at −0.7 V the polymer is in the reduced (neutral charge) state. Table 3 indicates that dichloramine has the best response at −0.5 V; probably in this instance polyaniline is in the transition stage between the oxidized and reduced states, and it is favourable for deintercalation of the counter anions to the film at this negative applied potential. The response decreased at a more negative potential (−0.7 V) because at this potential the polyaniline was in

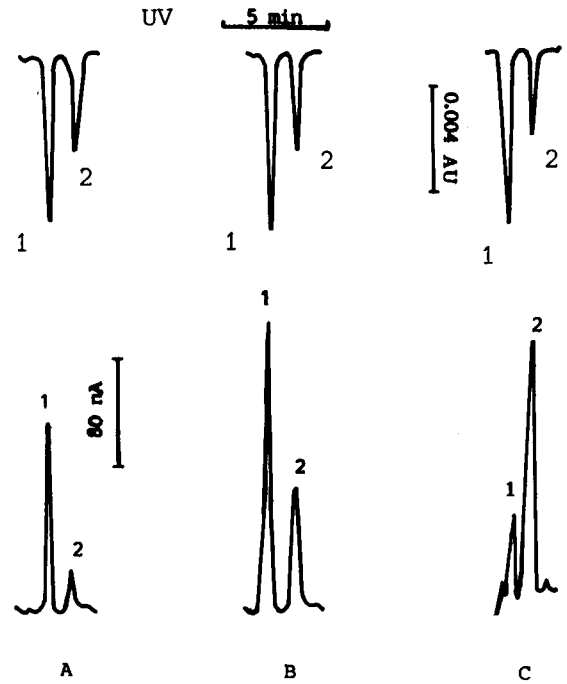

Fig. 2. Chloramine separation. Eluent, 0.01 M K_2HPO_4–0.01 M KH_2PO_4 (pH 5.0); flow-rate, 1.0 ml min^{-1}; UV detection at 221 nm; electrochemical detection, $E_{app} = -0.50$ V (vs. SCE); sample injection, 20 μl of 1×10^{-3} M NaClO + 1×10^{-3} M $(NH_4)_2SO_4$ in eluent. Response: (1) NH_2Cl; (2) $NHCl_2$. (A) At GC electrode; (B) at GC–Hg electrode; (C) at GC–Hg–PAn/NO_3 electrode.

TABLE 3

Effect of incorporated counter ions on chloramine electrochemical response (nA) at polyaniline electrodes [a]

Electrode	Chloramine	E_{app} (V)		
		0.0	−0.5	−0.7
GC–PAn/Cl	$NHCl_2$	44	148	82
	NH_2Cl	0.0	110	0.0
	$NHCl_2/NH_2Cl$	–	1.3	–
GC–PAn/SO_4	$NHCl_2$	28	132	54
	NH_2Cl	0.0	73	0.0
	$NHCl_2/NH_2Cl$	–	1.8	–
GC–PAn/NO_3	$NHCl_2$	88	188	125
	NH_2Cl	0.0	65	0.0
	$NHCl_2/NH_2Cl$	–	2.9	–

[a] Eluent, 0.01 M KH_2PO_4 − 0.01 M K_2HPO_4; flow-rate, 1.0 ml min^{-1}; sample injection, 20 μl of 1×10^{-3} M NaClO + 1×10^{-3} M $(NH_4)_2SO_4$ in eluent; polymer deposition, 0.01 M polyaniline + 1.0 M counter ion; polymer coating, 10 cycles; scan rate of 100 mV s^{-1} between 0.0 and +1.1 V on GC electrode.

TABLE 4

Comparison of chloramine detection with GC, GC–Hg and GC–Hg–PAn electrodes [a]

Electrode	Detector response (nA)		$NHCl_2/NH_2Cl$ selectivity factor
	$NHCl_2$	NH_2Cl	
GC–Hg	88	220	0.4
GC–Hg–PAn/Cl	132	380	0.3
GC–Hg–PAn/SO_4	130	320	0.4
GC–Hg–PAn/NO_3	280	116	2.4

[a] $E_{app} = -0.50$ V for amperometric detection; polymer coating, 15 cycles fast scan of 1.0 V s^{-1} between −0.2 and +0.8 V for polyaniline-dispersed mercury electrode; other conditions as Table 3.

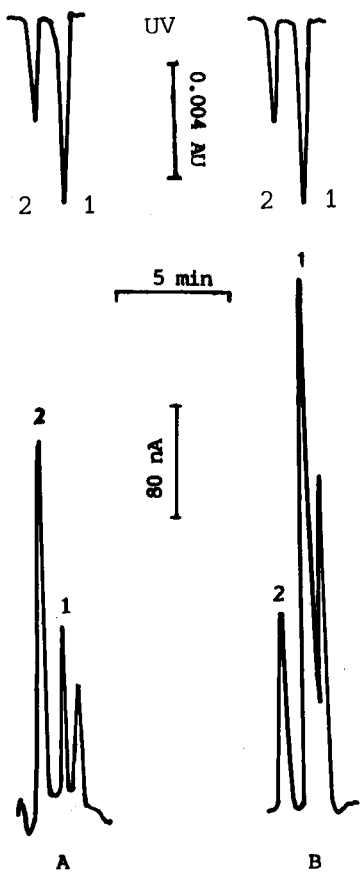

Fig. 3. Selective chloramine detection at polyaniline-dispersed mercury film electrode. Other conditions as in Fig. 2. (A) At GC–Hg–PAn/NO_3 electrode; (B) at GC–Hg–PAn/Cl electrode.

TABLE 5

Detection limits and linear range for NH_2Cl and $NHCl_2$ at the polyaniline-dispersed mercury film electrode

Electrode	Linear range (μM)		Detection limit (μM)	
	NH_2Cl	$NHCl_2$	NH_2Cl	$NHCl_2$
GC–Hg–PAn/Cl	0.2–100	50–100	0.1	32
GC–Hg–PAn/NO_3	10–100	1–25	8.0	0.8

the neutral state and no counter anion intercalation was possible.

As expected, the counter ion that was incorporated into the polymer influenced the chloramine responses (Table 3); of the three polyaniline electrodes investigated, the PAn/NO_3-coated glassy carbon electrode showed the highest selectivity for dichloramine (Fig. 2C).

Polyaniline-coated mercury film electrode. The ability of a polyaniline-coated mercury film to alter the chloramine selectivity was investigated with three polyaniline-coated mercury film electrodes (Table 4). The highest dichloramine response was observed with the GC–Hg–Pan/NO_3 and the highest monochloramine response with the GC–Hg–PAn/Cl electrode (Fig. 3). All results reported were obtained at an applied potential of −0.5 V; the response was not improved at more negative potentials.

The effect of the polymer thickness on the deposited mercury film for detection of dichloramine was investigated. The procedure involved 3–30 potential scan cycles for preparing a GC–Hg–PAn electrode. It was found that 10–15 scan cycles at a scan rate of 1.0 V s^{-1} gave adequate sensitivity and improved mechanical stability. Thin polymers showed unstable responses owing to the poor reproducibility and thicker polymers showed increased background current and decreased responses owing to the increased resistance of the polymer.

The linear range for determination and the detection limit of mono- and dichloramine using both GC–Hg–PAn/Cl and GC–Hg–PAn/NO_3 electrodes are summarized in Table 5.

Conclusion

A polyaniline-modified electrode was developed that gave improved selectivity and adequate sensitivity and chemical stability for the detection of chloramines. The polyaniline film electrode increases the response factors for dichloramine in all instances. A mercury film on the polymer electrode increases the monochloramine response in all instances studied except with the GC–Hg–PAn/NO_3 electrode. The highest response for monochloramine was obtained with the GC–Hg–PAn/Cl and that for dichloramine with the GC–Hg–PAn/NO_3 electrode.

Perhaps the most interesting aspect is that the selectivity could be altered by incorporating various counter ions in the polyaniline. Incorporating various counter ions during the polymerization process is responsible for the chemical selectivity of the polyaniline. In particular, the selectivity of the polyaniline is associated with the passage of the anion sample plugs through the polymer to the electrode surface as a major factor in the signals obtained. The loose polyaniline film, obtained by incorporating NO_3^- during the polymerization process, is favourable for dichloramine determination. The PAn/Cl polymer is more compact than the PAn/NO_3 polymer, so the GC–Hg–PAn/Cl electrode is beneficial for monochloramine determination.

Comparing polyaniline and polypyrrole polymer electrodes, it seems that the modes of action of both electrode systems are similar. The polyaniline electrode appears to have distinct advantages for use in analytical applications. In particular, the polyaniline film is chemically very stable. In this work, the electrodes were found to be extremely durable. Usually the same electrode surface could be used for CV and LC studies for periods of 2 weeks and longer with no evidence of chemical or mechanical deterioration. In addition, the oxidation of the polyaniline occurs at a lower potential than does that of polypyrrole, and the incorporation of anionic samples into the polyaniline film is very rapid.

The lower sensitivity of these new electrodes is an important problem for polymer-dispersed electrode that needs to be improved. This problem also occurs with polypyrrole film electrodes. To increase the sensitivity of these new electrodes attention is currently being paid to speeding up the electrode transfer rate to increase the percentage of species involved in the electrochemical analysis step.

This project was supported by the National Natural Science Foundation of China.

REFERENCES

1 M.W. Espencheid, A.R. Ghatak-Roy, R.B. Moore, R.M. Penner, M.N. Szentirmay and C.R. Martin, J. Chem. Soc., Faraday Trans., 82 (1986) 1051.
2 A.R. Guadalupe, L.M. Wier and H.O. Abruna, Am. Lab., 18 (1986) 102.
3 A.R. Hillman, in R.G. Linford (Ed.), Electrochemical Science and Technology of Polymers, Elsevier, London, 1987, p. 241.
4 M.D. Imisides, P.J. Riley, R. John and G.G. Wallace, Electroanalysis, 3 (1991) 879.
5 Y.-P. Lin and G.G. Wallace, J. Electroanal. Chem., 247 (1988) 145.
6 H.-L. Ge, H.-J. Zhao and G.G. Wallace, Anal. Chim. Acta, 238 (1990) 345.
7 K.M. Kost, D.E. Bartak, B. Kazee and T. Kuwana, Anal. Chem., 60 (1988) 2379.
8 S. Holdcroft and B.L. Funt, J. Electroanal. Chem., 240 (1988) 89.
9 F. Vork and E. Barandrecht, Synth. Met., 28 (1989) C121.
10 H.L. Ge, G.G. Wallace and H. Zhao, Anal. Chim. Acta, 238 (1990) 451.
11 Y.-P. Lin and G.G. Wallace, Anal. Chim. Acta, 263 (1992) 71.
12 H.-L. Ge, G.G. Wallace and R.A.J. O'Halloran, Anal. Chim. Acta, 237 (1990) 149.
13 J.C. Morris, Modern Methods in Water and Waste Water Treatment, Vol. 1, Int. Course in Sanitary Engineering, Int. Inst. for Hydraulic and Environmental Engineering, Delft, 1978.
14 M. Brunetto, C. Colin and R. Rosset, Analusis, 15 (1987) 393.
15 H. Ji, G. Zhu and E. Wang, SEPU, 15 (1987) 897.

Analytica Chimica Acta, 282 (1993) 505–515
Elsevier Science Publishers B.V., Amsterdam

Acoustic network analysis and equivalent circuit simulation of the thickness-shear mode acoustic wave sensor in the liquid phase

Mengsu Yang and Michael Thompson

Department of Chemistry, University of Toronto, 80 St. George Street, Toronto, Ontario M5S 1A1 (Canada)

(Received 20th April 1993)

Abstract

Network analysis of the behavior of the thickness-shear mode (TSM) acoustic wave sensor is validated and the ability of the Butterworth–Van Dyke (BVD) equivalent circuit to describe the electrical characteristics of the sensor was examined under various conditions. The results demonstrate that the impedance of the quartz crystal can be measured when one or both sides of the device are immersed in a viscous liquid or a conductive solution. The equivalent circuit is satisfactory in simulating the impedance characteristics of the TSM sensor in the liquid phase under most conditions except for total immersion of the sensor in highly viscous or conductive liquids. It is shown that the frequency response of the TSM device depends on individual crystals and experimental configurations.

Keywords: Sensors; Piezoelectric sensors; Acoustic wave sensors; Equivalent circuit; Network analysis;

The piezoelectric quartz crystal is an electromechanical transducer which converts electrical energy to mechanical energy, and vice versa. The electromechanical coupling and stresses resulting from an applied electric field depend on the crystal symmetry, angle of cut of the crystal substrate, and configuration of the excitation electrodes used to apply the electric field across the crystal. The various modes of electromechanical coupling result in different types of acoustic waves, modes of propagation, and particle displacements. AT-cut quartz is obtained by cutting wafers of quartz at an angle of 35°15′ to the z-axis. Application of an alternating field across the thickness of an AT-cut quartz crystal by two excitation electrodes on opposite sides of the crystal results in shear vibration in the x-axis direction parallel to the electric field and propagation of a transverse wave through the crystal in the thickness direction. The thickness-shear mode (TSM) acoustic wave sensor has been used in a number of studies involving the liquid phase, including the development of chemical and biosensors [1] and the investigation of electrochemical processes [2–4].

The most common method employed to study the TSM sensor is the oscillator method [5–7], in which the series resonant frequency of the quartz crystal is measured. This method suffers from some serious limitations due to the active role of the quartz device in the oscillating circuit [1,6]. More recently, the network analysis method has been developed to more completely characterize the TSM sensor in the liquid phase [8–11]. The responses of the TSM sensor, including the resonant frequencies, the impedance characteristics, and the equivalent circuit elements, have been related to the bulk properties of the contacting

Correspondence to: M. Thompson, Department of Chemistry, University of Toronto, 80 St. George Street, Toronto, Ontario M5S 1A1 (Canada).

liquid as well as the interfacial properties of the sensor–liquid interface [10–13].

Physically, the impedance of a quartz crystal can be measured from the ratio of the applied voltage across the crystal and the current flowing through the crystal for a large number of frequencies in the resonant frequency region. The experimental values of the magnitude and phase of impedance can be calculated at each frequency and plotted against the frequency to give the impedance–frequency curves. The prominent characteristics from the impedance (magnitude and phase) measurements are the frequencies at the minimum and maximum magnitudes of impedance and the corresponding values of the magnitude of impedance, the frequencies at zero phase, and the value of maximum phase. The piezoelectric resonator can be represented by the Butterworth–Van Dyke (BVD) circuit of the series combination of a capacitor (C_m), an inductor (L_m), and a resistor (R_m) in parallel with a capacitor (C_0) (Fig. 1) [14,15]. The subscript m is used to denote the fact that the RLC series is associated with the motion of the quartz plate. The equivalent circuit responds to an applied voltage in the same way as the quartz crystal itself. The impedance of each circuit element is also given in Fig. 1, where ω is the angular frequency (in rad s^{-1}). The values of the equivalent circuit parameters can be calculated from the impedance–frequency curves by circuit analysis. However, the BVD circuit is typically used to describe a lossless resonator (without mass or liquid loading). In this study, a series of experiments was performed in order to examine the validity of the network analysis method in characterizing the TSM sensor and to verify the ability of the BVD equivalent circuit to describe the electrical behavior of a liquid-loaded TSM sensor.

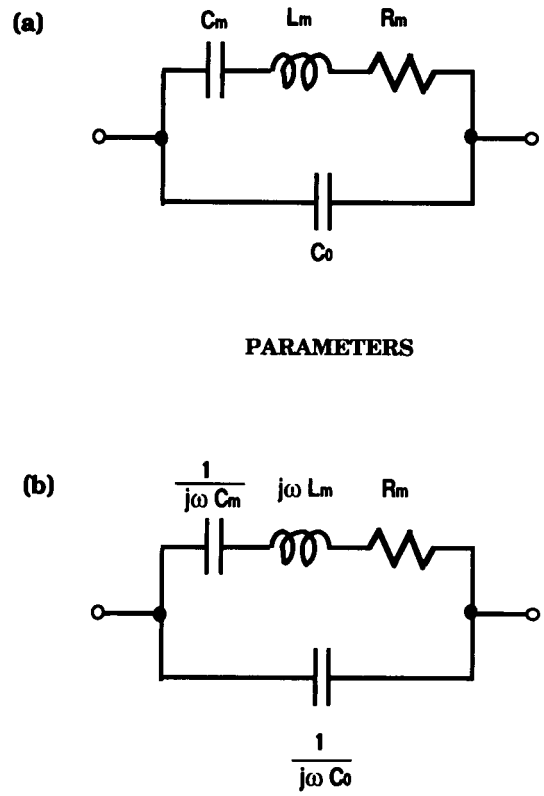

Fig. 1. Butterworth–Van Dyke (BVD) equivalent electrical circuit of the thickness-shear mode acoustic wave sensor: (a) circuit parameters; (b) impedance of circuit elements.

EXPERIMENTAL

Reagents

All liquids were of analytical-reagent grade and used as received. Potassium chloride (BDH, Toronto) was dissolved in doubly distilled water to prepare standard KCl solutions.

Apparatus

AT-cut quartz piezoelectric crystals coated with gold electrodes were supplied by International Crystal Manufacturing, Oklahoma City. The instrument used to characterize the TSM devices was an HP 4195A Network/Spectrum Analyzer (Hewlett-Packard). An HP 41951A impedance test kit and HP 16092A spring clip fixture were used to make impedance measurements directly. The values of the equivalent circuit elements of the quartz crystal are calculated internally by the HP 4195A from the measured data.

Procedures

Prior to the impedance measurements, the crystals were rinsed with acetone, ethanol, and

water and subjected to high rf in a PD-3XG plasma cleaner (Harrick). Advancing contact angles were measured to ensure the surfaces were completely wetted by water. The TSM device was clamped in a cell with O-rings on both sides. One side of the crystal was immersed in about 50 μl liquid. The cell was connected to the network analyzer and allowed to stabilize until reaching a constant frequency reading. The network analyzer scanned 401 points at a centre frequency of 9 MHz (with 120 KHz bandwidth).

RESULTS AND DISCUSSION

Impedance measurement and equivalent circuit simulation

Ideally, the equivalent circuit should simulate the electrical characteristics of the TSM sensor over a range of frequencies near resonance. A comparison between the experimental impedance measurement and the equivalent circuit simulation will determine if the circuit model can be employed to describe the impedance behavior of the TSM sensor under various conditions.

One side immersed in liquid. The magnitude and phase of the impedance of a 9-MHz TSM device were measured with one side of the crystal immersed in a series of organic liquids and water. Figure 2 shows the impedance measurements (points) and the equivalent circuit simulations (lines) for methanol, water, and cyclohexanol. As the viscosity of the liquid increases, the impedance curves become diminished and broadened while moving towards lower frequency. The results of this are that the maximum magnitude, Z_{max}, and the maximum phase angle, θ_{max}, of the impedance decrease while the minimum magnitude of the impedance, Z_{min}, increases as the viscosity of the liquid increases. The maximum phase of the impedance becomes negative when cyclohexanol is being studied. Therefore, the series and parallel resonant frequencies (frequencies at zero phase) cease to exist. The most important feature of Fig. 2 is that very good agreement is obtained between the impedance measurements and the equivalent circuit simulations for a wide range of liquids within the frequency span.

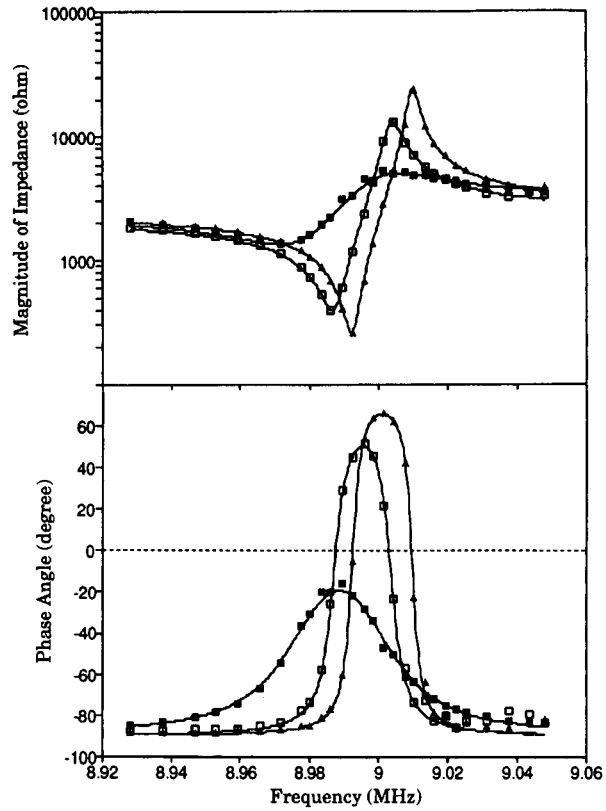

Fig. 2. Impedance measurements (points) and equivalent circuit simulations (lines) of the magnitude ($|Z|$) and phase angle (θ) of impedance for a 9-MHz uncoated gold electrode TSM device. One side of the crystal was in contact with methanol (▲), water (□), and cyclohexanol (■) while the other side was under nitrogen.

When one side of the TSM sensor is immersed in a highly viscous liquid, such as glycerol, viscous loading causes damping and broadening of the resonant peaks (Fig. 3). Under this condition, the equivalent circuit model becomes less satisfactory in describing the impedance behavior of the quartz crystal. As depicted in Fig. 3, the circuit simulations do not fit exactly to the impedance curves, although the shapes of the simulation curves still resemble those of the experimental peaks.

In conductive liquids, the damping of the impedance peaks is caused by the energy dissipation due to acoustoelectrical coupling between the surface potential associated with the quartz

crystal and the ionic and dipolar species, and by the energy transfer from the quartz dielectric to the electrical double layer. The impedance curves and the equivalent circuit simulations for a 9-MHz TSM sensor with one side under a KCl (0.01 M) solution are shown in Fig. 4. It is apparent that the equivalent circuit provides a reasonable description of the impedance measurements, although the value of the maximum impedance is overestimated because of additional capacitive effects from field fringing and cell mounting. The impedance curves show a small peak at higher frequency (but not at a harmonic frequency), indicating the generation of a different mode of acoustic wave.

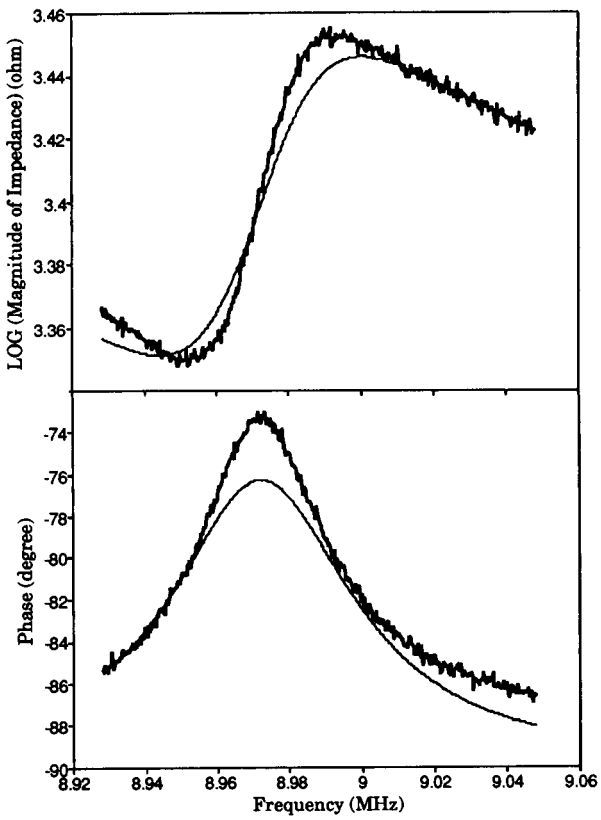

Fig. 3. Impedance measurements (heavy solid) and equivalent circuit simulations (solid) of the magnitude ($|Z|$) and phase angle (θ) of impedance for a 9-MHz uncoated gold electrode TSM device. One side of the crystal was in contact with glycerol.

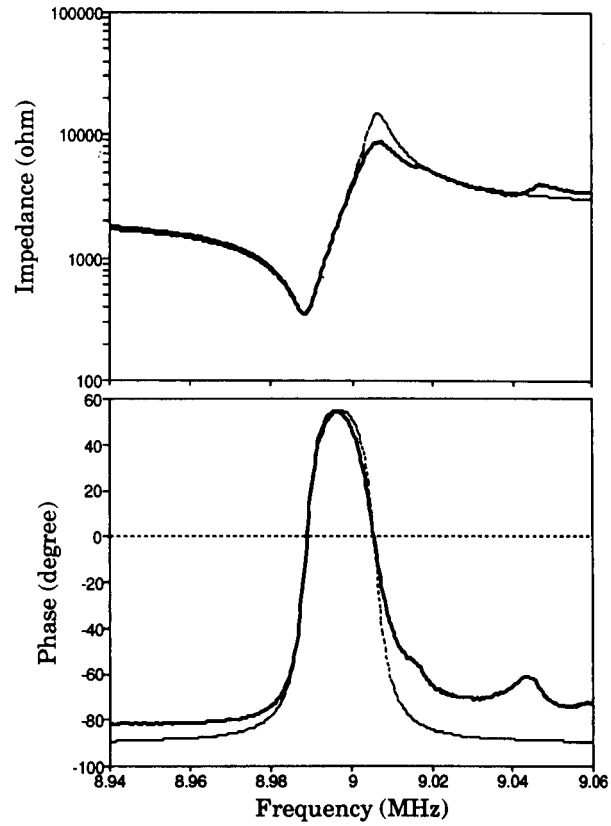

Fig. 4. Impedance measurements (heavy solid) and equivalent circuit simulations (dotted) of the magnitude ($|Z|$) and phase angle (θ) of impedance for a 9-MHz uncoated gold electrode TSM device. One side of the crystal was in contact with 0.01 M KCl.

Two sides immersed in liquid. The magnitude and phase of the impedance of a 9-MHz TSM device were measured with both sides of the crystal immersed in a series of organic liquids and water. Figure 5 illustrates the impedance measurements (solid lines) and the equivalent circuit simulations (dotted lines) for methanol and water. It can be seen that the circuit simulations are in good agreement with the experimental values. The maximum phase angle of the impedance is less than zero under water, which prevents the measurement of the frequencies at zero phase for liquids with similar or higher viscosity.

The deviation between the circuit simulation and the experimental measurement becomes more obvious when the TSM sensor is totally

immersed in viscous liquids. As shown in Fig. 6, the simulation does not fit the measurements when the crystal is totally immersed in cyclohexanol. The inconsistency is most severe with the total immersion of the crystal in glycerol (Fig. 7). In addition, the highly viscous loading of glycerol results in the broadening of the impedance peaks beyond the frequency span so that a part of the impedance curves is not measured. This can be avoided by increasing the scanning frequency span.

When both sides of the TSM device are immersed in a conductive solution, the result is the complete damping of the resonant peaks due to onset of the conduction current in the solution. Nevertheless, the impedance curves of the system

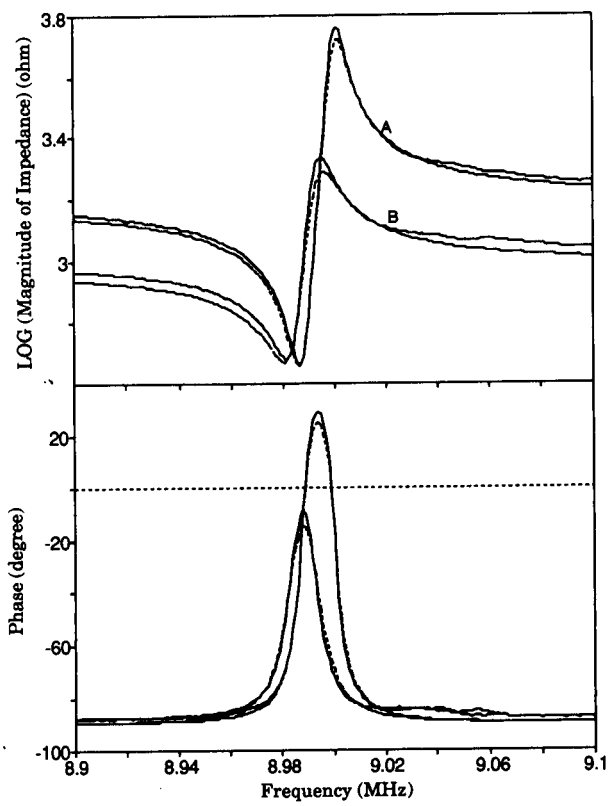

Fig. 5. Impedance measurements (solid) and equivalent circuit simulations (dotted) of the magnitude ($|Z|$) and phase angle (θ) of impedance for a 9-MHz uncoated gold electrode TSM device. Both sides of the crystal were immersed in methanol (A, $\theta_{max} > 0$) and water (B, $\theta_{max} < 0$).

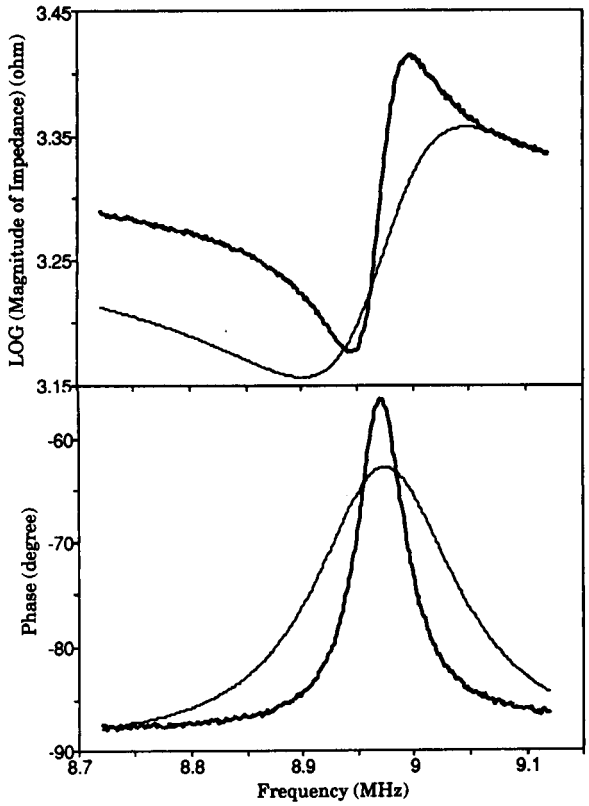

Fig. 6. Impedance measurements (heavy solid) and equivalent circuit simulations (solid) of the magnitude ($|Z|$) and phase angle (θ) of impedance for a 9-MHz uncoated gold electrode TSM device. Both sides of the crystal were immersed in cyclohexanol.

can still be measured (Fig. 8), although the characteristics of the magnitude and phase of the impedance are totally different from those under non-conductive liquids. The existence of such behavior likely arises from the resistance component (ion–ion and ion–dipole interactions) and the reactance component (ion mobility and relaxation) of the conductive solution. Note that the scales of the impedance measurements are much smaller compared to those under non-conductive conditions. In addition, the BVD circuit completely fails to simulate the impedance curves in these conditions.

TSM devices and experimental configuration

The ability of the network analysis method to describe the behavior of the TSM sensor in the

liquid phase has been verified by the impedance–frequency measurements. The BVD equivalent circuit provides a good representation of the TSM device when one side of the device is immersed in liquids with viscosities less than 100 cP. In order to establish the relationship between the TSM sensor response and the properties of the contacting liquid, characteristic parameters will have to be extracted from the impedance measurements and the equivalent circuit. The performance of the TSM sensor also depends on the individual devices and the experimental configurations. The TSM sensor response was examined by comparing the behavior of crystals with the same fundamental frequency, crystals with different fundamental frequencies, and crystals with

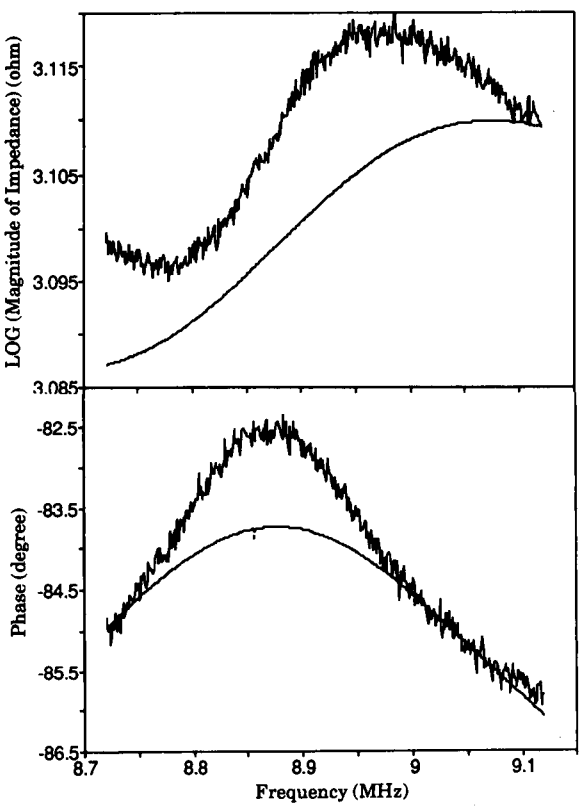

Fig. 7. Impedance measurements (heavy solid) and equivalent circuit simulations (solid) of the magnitude ($|Z|$) and phase angle (θ) of impedance for a 9-MHz uncoated gold electrode TSM device. Both sides of the crystal were immersed in glycerol.

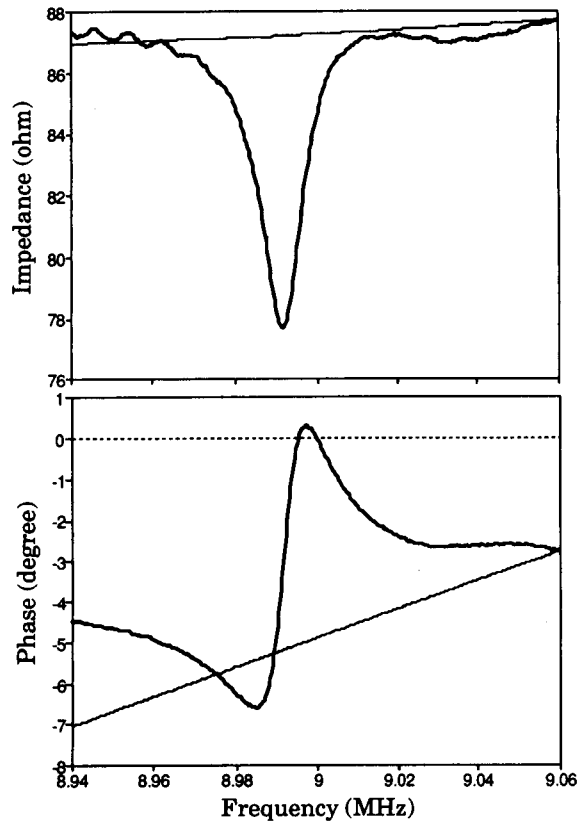

Fig. 8. Impedance measurements (heavy solid) and equivalent circuit simulations (solid) of the magnitude ($|Z|$) and phase angle (θ) of impedance for a 9-MHz uncoated gold electrode TSM device. Both sides of the crystal were immersed in 0.01 M KCl.

one side or both sides immersed in liquid. For this purpose, three parameters were chosen as probes to study the TSM sensor response due to their different properties. These are the series resonant frequency, f_s, the maximum phase angle of the impedance, θ_{max}, and the motional resistance of the equivalent circuit, R_m. The frequency shift reflects the velocity change of the acoustic wave; a change in the motional resistance represents the power attenuation of the quartz device; and the phase angle depicts the overall shape of the impedance peaks. Furthermore, the viscosity–density product of the bulk liquid is used as the variable since it is considered to be the dominant factor affecting the sensor response for non-conducting liquids [16,17].

TSM sensors with the same fundamental frequency. The impedance curves and the equivalent circuit parameters were measured for several clean, 9-MHz gold electrode TSM devices with one side immersed in a series of alcohols and water. The shifts in the series resonant frequency, Δf_s, were calculated based on the decrease of f_s *relative to air*. Under identical conditions, it is expected that the TSM sensors with the same fundamental frequency will give similar responses within experimental error. However, the results show that although similar Δf_s values were obtained for some crystals, there are obvious differences for others. As shown in Fig. 9, two 9-MHz gold electrode TSM devices exhibit different Δf_s under the same conditions. The Δf_s to $\rho_L \eta_L$ plots for both crystals show a similar slope. The proportional increase of Δf_s with increasing viscosity–density product, $(\rho_L \eta_L)$, of the liquid is consistent with the theoretical predictions [16]

$$\Delta f = -\frac{f_0^{3/2}}{2\pi}\sqrt{\frac{\rho_L \eta_L}{\rho_Q \mu_Q}} \quad (1)$$

On the other hand, the values of Δf_s are displaced by several hundreds of Hertz. This clearly demonstrates the dependence of the frequency response on individual crystals. The difference in Δf_s may arise from different mechanical stress applied to the TSM sensor when it was mounted into the cell fixture. Differences in morphology between the electrode surfaces may also result in a change in Δf_s. One way to circumvent this problem is to calculate Δf_s based on the changes in f_s *relative to a particular liquid*, which may reduce the difference resulting from the different intercepts. It should be pointed out that Δf_s for water deviates from the alcohols in both plots. This could be due to the presence of trace amounts of ionic species in distilled water and/or the different interfacial structure of water molecules.

As shown in Fig. 2, the maximum phase angle becomes negative when the viscosity of a liquid reaches a certain value. Thus, the series resonant frequency does not exist. However, the impedance of the TSM sensor and its equivalent circuit parameters can still be measured. Figure 10 shows the responses of the maximum phase of the impedance and the motional resistance of the equivalent circuit under the same conditions as in Fig. 9. The shifts in both θ_{max} and R_m are calcu-

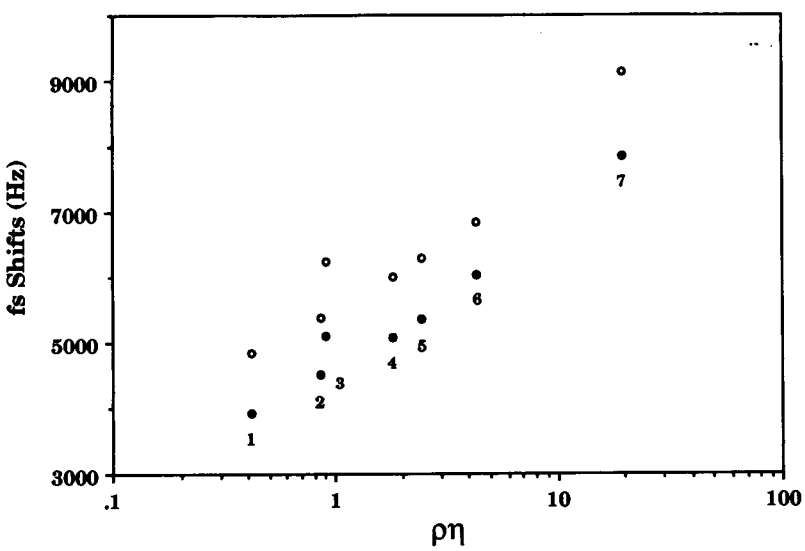

Fig. 9. Responses of the series resonant frequency, f_s, of two 9-MHz bare gold electrode TSM devices with one side immersed in liquid. Δf_s is plotted against the viscosity–density product of the bulk liquid. The testing liquids are: (1) methanol; (2) ethanol; (3) water; (4) *n*-propanol; (5) *n*-butanol; (6) *n*-hexanol; and (7) ethylene glycol.

lated *relative to air*. It is clear that θ_{max} and R_m cover a greater $\rho_L\eta_L$ range than f_s. The most important feature of Fig. 10 is that the shifts in θ_{max} and R_m for the two TSM devices are identical under the same conditions. In addition, the shifts in θ_{max} and R_m for other 9-MHz devices with either gold or silver electrodes are in agreement with the plotted values. This seems to indicate that even though f_s may be sensitive to other factors, the responses of the impedance characteristics of the TSM device are dominated by the properties of the contacting liquids.

Similar behavior is observed when comparing several 5-MHz gold electrode TSM devices and 9-MHz silver electrode TSM devices. Provided that the electrode surfaces are sufficiently clean, Δf_s may differ under the same conditions for crystals with the same fundamental frequency, but the values of θ_{max} and R_m are always the same within experimental error.

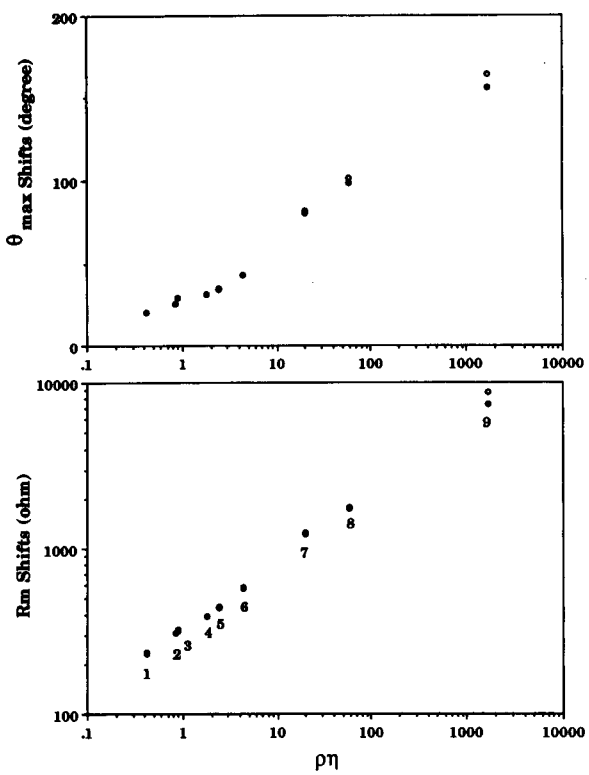

Fig. 10. Responses of (top) the maximum phase angle of the impedance and (bottom) the motional resistance of the equivalent circuit of two 9-MHz bare gold-electrode TSM devices upon liquid loadings. One side of each crystals is immersed in: labels 1–7, same as in Fig. 9; label 8, cyclohexanol; and label 9, glycerol.

TSM sensors with different fundamental frequencies. The shifts in f_s for a 5-MHz silver electrode TSM sensor with one side immersed in various liquids are illustrated in Fig. 11. For comparison, the values of Δf_s for a 9-MHz silver electrode device under the same conditions are also plotted in Fig. 11. In general, the trends in Δf_s for both 5- and 9-MHz devices are in agreement with the prediction that Δf_s increases with increasing $\rho_L\eta_L$. The ratio of the slopes of the plots between 9- and 5-MHz devices is about 2.5, similar to that predicted by Eqn. 1, $(f_{9MHz}/f_{5MHz})^{3/2} = (9/5)^{3/2} = 2.4$.

The changes in θ_{max} and R_m for both devices are shown in Fig. 12. The shifts in θ_{max} are almost identical for both 9- and 5-MHz devices. This is expected since the phase of the impedance is determined by the ratio of the reactance (imaginary part) and the resistance (real part) of the impedance rather than the absolute values of each device. On the other hand, the shifts in R_m for the 5-MHz device are about twice of those for the 9-MHz device. This is similar to the ratio of the geometric areas of the electrodes between 5-MHz TSM devices (0.38 cm^2) and 9-MHz devices (0.20 cm^2). (In reality, the actual surface areas of the electrodes are larger than the geometric areas because of the surface roughness factor.) Since R_m is related to the energy dissipation of the TSM sensor in the liquid phase, there is greater energy loss for the 5-MHz crystal than for the 9-MHz crystal due to the different electrode areas.

Total immersion of the TSM sensor in a liquid. When both sides of the crystal were immersed in a liquid, f_s ceases to exist under most conditions. However, impedance characteristics and the equivalent circuit parameters are still available. The changes in θ_{max} and R_m are depicted in Fig. 13 for a 9-MHz gold electrode TSM sensor totally immersed in different liquids. For comparison, the shifts in θ_{max} and R_m for the same crystal with only one side immersed in the same liquids are also shown in Fig. 13. As demonstrated in Figs. 6 and 7, total immersion of the TSM sensor

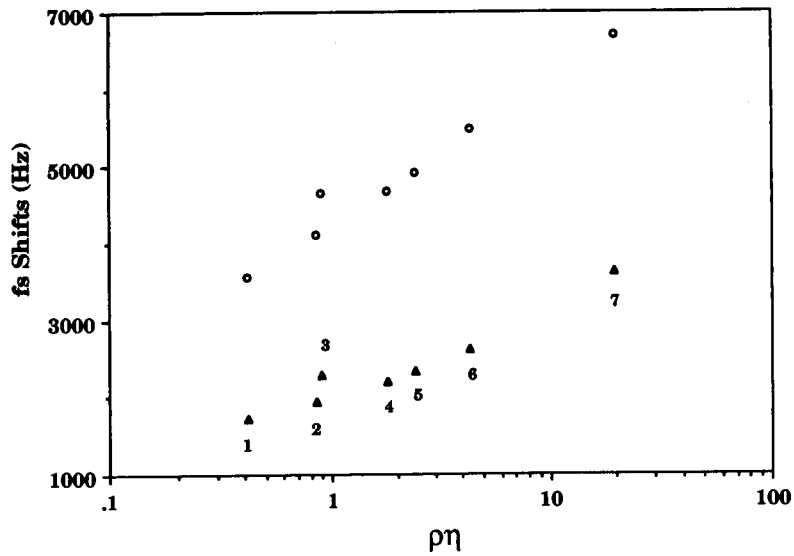

Fig. 11. Responses of the series resonant frequency, f_s, of a 9-MHz (circles) and a 5-MHz (triangles) bare gold electrode TSM device with one side immersed in liquid. Δf_s is plotted against the viscosity–density product of the bulk liquid. Same conditions as in Fig. 9.

in viscous liquids results in severe damping of the impedance peaks. This can be seen from the shifts in θ_{max}, in which the maximum phase angle of the impedance ($\theta_{max} \approx 90°$ in air) decreases rapidly and reaches a minimum at a much lower $\rho_L\eta_L$ value when both sides were immersed than when only one side was immersed. However, it is interesting to note that the changes in R_m under total immersion show a proportional increase with increasing $\rho_L\eta_L$ values. Even though the equivalent circuit is not suitable for describing the impedance behavior of the TSM sensor under these conditions (Figs. 6 and 7), it seems the R_m values still reflect the energy dissipation processes of the system.

Conclusions

The network analysis method is employed in the study of the performance of the TSM sensor in the liquid phase. This method can be applied to characterize the behavior of the TSM sensor under virtually all conditions. The impedance of the quartz crystal can be measured when one or both sides of the device is immersed in a liquid. For the latter experiments a large frequency span is required to cover the broadened impedance peaks.

The BVD equivalent circuit can be used to describe the electrical characteristics of the impedance of the TSM sensor when one side of the device is immersed in the liquid phase, although some deviation is observed under extremely viscous liquid loading. The circuit model can also simulate the impedance behavior of the crystal when both sides of the device are immersed in a less viscous liquid such as methanol and water. However, the equivalent circuit model is inadequate in describing the electrical characteristics of the impedance with total immersion in viscous liquids and conductive solutions. The breakdown of the BVD model when the energy losses are high suggests that equivalent circuits with more than four parameters are required to deal with the complex acoustic coupling at the solid–liquid interface.

The series resonant frequency of the TSM sensor is affected by a number of factors such as the surface stress and surface roughness. Different responses may be observed under similar conditions for crystals with the same fundamental

frequency. Thus, caution should be taken when comparing the results obtained from different devices and experimental configurations. On the other hand, the sensitivity of f_s towards changing surface conditions may be exploited as a probe to study the interfacial processes. The series resonant frequency can not be measured with the network analyzer when one side of the TSM sensor is immersed in highly viscous liquids and when both sides of the sensor are immersed in viscous liquids and conductive solutions.

Other parameters obtained from the impedance analysis, such as the maximum phase angle of the impedance, and the equivalent circuit elements, such as the motional resistance, are less sensitive towards the factors arising from different TSM devices and cell fixtures. Thus, these parameters may provide unequivocal information

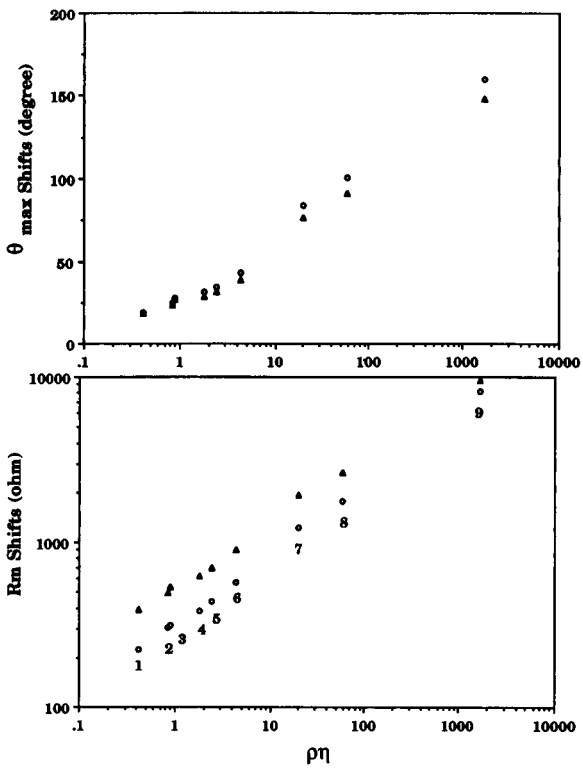

Fig. 12. Responses of (top) the maximum phase angle of the impedance, θ_{max}, and (bottom) the motional resistance of the equivalent circuit, R_m, of a 9-MHz (circles) and a 5-MHz (triangles) bare gold-electrode TSM device upon liquid loading. Same conditions as in Fig. 10.

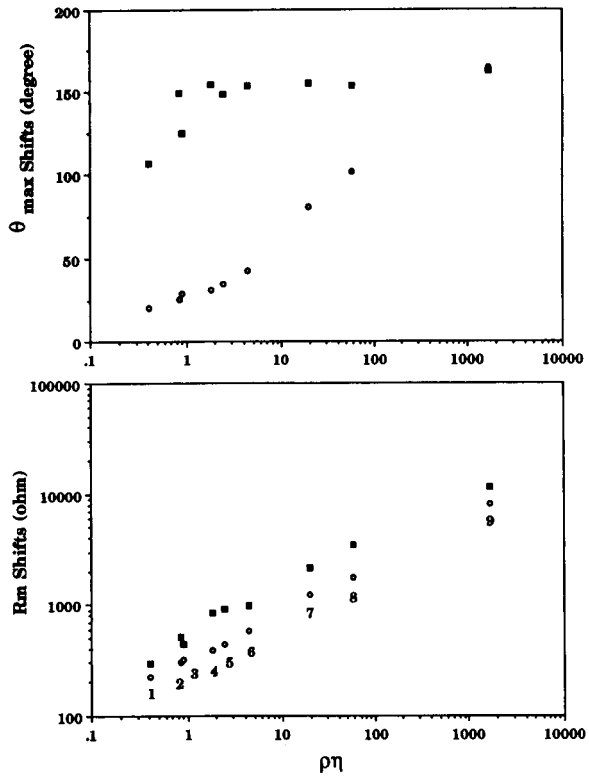

Fig. 13. Responses of (top) the maximum phase angle of the impedance, θ_{max}, and (bottom) the motional resistance of the equivalent circuit, R_m, of a 9-MHz bare gold electrode TSM device with one side (circles) and both sides (squares) of the crystal immersed in liquid. Same conditions as in Fig. 10.

regarding the sensor-liquid interactions. In addition, these parameters are available for liquids with a much greater range of $\rho_L\eta_L$ than f_s.

We are grateful to The Natural Sciences and Engineering Research Council of Canada for support of this work. We also thank D.C. Stone of the University of Toronto for much helpful discussion.

REFERENCES

1 M. Thompson, A.L. Kipling, W.C. Duncan-Hewitt, Lj.V. Rajaković and B.A. Čavić-Vlasak, Analyst, 116 (1991) 881.
2 M.R. Deakin and D.A. Buttry, Anal. Chem., 61 (1989) 1147A.
3 R. Schumacher, Angew. Chem. Int. Ed. Engl., 29 (1990) 329.

4 D.A. Buttry and M.D. Ward, Chem. Rev., 92 (1992) 1335.
5 S.-Z. Yao and Z.-H. Mo, Anal. Chim. Acta, 193 (1987) 97.
6 Lj.V. Rajaković, B.A. Čavić-Vlasak, V. Ghaemmaghami, K.M.R. Kallury, A.L. Kipling and M. Thompson, Anal. Chem., 63 (1991) 615.
7 C. Barnes, Sensors Actuators, A30 (1992) 197.
8 R. Beck, U. Pittermann and K.G. Weil, Ber. Bunsenges. Phys. Chem., 92 (1988) 1363.
9 A.L. Kipling and M. Thompson, Anal. Chem., 62 (1990) 1514.
10 S.J. Martin, V.E. Granstaff and G.L. Frye, Anal. Chem., 63 (1991) 2272.
11 M. Yang and M. Thompson, Anal. Chim. Acta, 269 (1992) 167.
12 M. Yang and M. Thompson, Anal. Chem., 65 (1993) 1158.
13 M. Yang, M. Thompson and W.C. Duncan-Hewitt, Langmuir, 9 (1993) 802.
14 W.G. Cady, Piezoelectricity, Dover, New York, 1964.
15 V.E. Bottom, Introduction to Quartz Crystal Unit Design, Van Nostrand Reinhold, New York, 1982.
16 K.K. Kanazawa and J.O. Gordon, Anal. Chim. Acta, 175 (1985) 99.
17 S. Bruckenstein and M. Shay, Electrochim. Acta, 30 (1985) 1295.

Analytica Chimica Acta, 282 (1993) 517–525
Elsevier Science Publishers B.V., Amsterdam

Biosensor based on direct detection of membrane potential induced by immobilized hydrolytic enzymes

D.M. Ivnitskii and J. Rishpon

Department of Molecular Microbiology and Biotechnology, Faculty of Life Sciences, Tel-Aviv University, Ramat-Aviv 69978 (Israel)

(Received 16th November 1992; revised manuscript received 9th June 1993)

Abstract

A potentiometric investigation of solid-state enzyme electrodes prepared by electropolymerization of hydrolytic enzymes (acetylcholinesterase, urease and arginase) on the surface of inert electrodes is reported. The theoretical description of the membrane potential is based on the Donnan effect and diffusion potential. It is shown that the ionic strength, pH and nature of the electrolyte influence the magnitude and sign of the membrane potential. At high pH and at high ionic strength the membrane potential is mainly a function of the diffusion potential. The mechanism of direct transformation of enzymatic reactions into an electric signal is considered in detail with the example of an acetylcholinesterase sensor. The solid-state enzyme electrode was tested in the determination of acetylcholine, urea and arginine. Typical calibration graphs for these substrates showed a linear response over the range 10^{-4}–10^{-3} M. The solid-state enzyme electrodes presented here do not require the specific introduction of an internal reference system.

Keywords: Biosensors; Enzymatic methods; Potentiometry; Enzyme electrodes; Membranes

Electrochemical biosensors have attracted much attention over the past two decades owing to their potential for high sensitivity and selectivity, low cost and ease of use [1–6]. These devices are based, in principle, on the conjugation of biomolecules, such as enzymes, and an electrochemical detector. A biocatalyst recognizes the corresponding substrate and specifically converts it into the product by an enzymatic reaction.

Two general types of detectors can be recognized in potentiometric biosensors: ion-selective and redox sensors. The potential signal is given by the expressions

$$E = \text{constant} + (RT/zF) \ln a_{M^+} \quad (1)$$

$$E = \text{constant} + (RT/nF) \ln([\text{ox}]/[\text{red}]) \quad (2)$$

Correspondence to: D.M. Ivnitskii, Microbiology and Biotechnology, Faculty of Life Sciences, Tel-Aviv University, Ramat-Aviv 69978 (Israel)

where z is the charge on the detected ionic species, n the electron exchanges by the redox couple, a_{M^+} the activity of the species involved and the other symbols have their usual meanings.

As natural electroactive substrates and products of different enzyme systems are different, e.g., oxygen, hydrogen, peroxide, ammonium and phenol, each enzyme system requires the development of individual electrochemical biosensors. The ideal situation, when using potentiometric biosensors, would be to adopt a universal (generic) approach of direct (unmediated) transformation of the enzymatic reactions into an electric signal. This makes attractive the idea of constructing solid-state biosensors which are based on the transmembrane ion-current modulation caused by enzyme–substrate, antigen–antibody or ligand–receptor selective interactions. In such electrodes, a relationship exists between the electrostatic effect at a membrane surface and the elec-

trochemical description of the transmembrane potential which can be considered to be based on the Donnan effect. The resulting change of the membrane potential could be specifically monitored by the transducing element without the use of other reagents.

The concept used in solid-state potentiometric biosensors, i.e., the complexation of an enzymatic reaction with transmembrane ion current modulation, has the following potential advantages. This approach provided the direct transformation of the biochemical reaction into an electric signal for different biosystems. It may be the general approach for designing sensors for other biologically active substances, including non-electroactive species, e.g., selectivity of the enzyme membrane for one substance over others can be altered simply by changing the kind of enzyme in the membrane. The potentiometric response does not depend on the size of the active area of the sensor. This has the advantage of the possibility of proving measurements in extremely small volumes and in vivo. The procedure and apparatus are very simple. Such devices can offer the advantages of miniaturization and the capability of including multiple sensors on a single chip.

Electrostatic effects at the membrane/solution interface of solid-state sensors can be well described by the surface diffusion potential theory [7,8]. This model connects the electrostatic and electrochemical values at a membrane surface and can be applied to establish the mechanism of the generation of transmembrane potential.

There are a number of papers related to these subjects [9–15], and many of the investigations concern the detection of immunoreactions. Collins and Janata [9] gave a critical evaluation of the mechanism of potential response with PVC membranes containing a mixture of cardiolipin, lecithin and cholesterol. These membranes appeared to respond to some specific proteins by changing the surface potential. Lee et al. [10] demonstrated a model system based on the use of a protein A–IgG complex. Binding of IgG to protein A will create an additional electric field around protein A. Recently the requirements for the construction of an immunological field-effect transistor, based on the direct potentiometric sensing of protein charges, were discussed [11–13]. A theoretical approach was given based on the Donnan equilibrium description. The basic underlying electrical effects are the protein-modulated dielectric constant, conductivity, electrical potential, ion permeability and ion mobility. Generation of a membrane potential by the enzyme–substrate complex was recently reported [14,15].

The purpose of this paper is to consider some basic factors that modulate membrane potential in solid-state potentiometric biosensors based on hydrolytic enzymes.

Enzyme electrodes were prepared by electropolymerization of hydrolytic enzymes on inert electrodes, which has a number of advantages [16–18]. First, the spatial distribution of the immobilization of proteins can be readily controlled. Second, the thickness of the protein films can be varied and is easily controlled. Third, it should be simple to build up multi-layer structures using different proteins. Finally, it should be possible to modulate the properties and structure of electrogenerated polymers by controlling the electrolysis conditions.

The process of electrodeposition of enzymes on the surface of electrodes in the presence of glutaraldehyde may be written as follows [19]:

$$\text{Prot-NH}_2 + \cdots -\underset{\displaystyle \underset{\displaystyle \text{HC=N-Prot}}{|}}{\overset{\displaystyle \overset{\displaystyle \text{CHO}}{|}}{\text{CH=C}}}-(\text{CH}_2)_2-\text{CH}=\cdots \longrightarrow \cdots -\underset{\displaystyle \underset{\displaystyle \text{HC=N-Prot}}{|}}{\text{CH=C}}-(\text{CH}_2)_2-\text{CH}=\cdots \quad (3)$$

followed by an electrochemical process in which ethylenic double bonds are involved:

$$\text{R-CH=CH}_2 + e^- \longrightarrow \text{R-}\overline{\text{C}}\text{H} - \text{CH}_2^{\cdot} \xrightarrow{+H^+}$$

$$\text{R-CH}_2\text{-CH}_2^{\cdot} + n\text{R-CH=CH}_2 \longrightarrow$$

protein membrane (4)

EXPERIMENTAL

Purified acetylcholinesterase (AChE) (EC 3.1.1.7, 1000 U mg^{-1}, from electric eel), urease (EC 3.5.1.5, 12000 U mg^{-1}, from jack beans), arginase (EC 3.5.3.1, 150 U mg^{-1}, from bovine

liver), acetylcholine chloride (ACh), urea, arginine and chicken egg albumin were obtained from Sigma and glutaraldehyde (50%) from Aldrich. Dialysis membranes were obtained from Spectra/por (Houston, TX). All other chemicals were of analytical-reagent grade.

Preparation of the enzyme membrane electrode

A PAR Model 273 potentiostat–galvanostat was employed for the electrochemical deposition of the enzymes. Enzyme-modified electrodes were obtained galvanostatically at a stationary platinum and glassy carbon disc electrode at a current density of 0.50 mA cm^{-2} for 45 s without stirring of the electrolyte. Working electrodes were cleaned by hand polishing with 0.3-μm alumina slurry and washed copiously.

The solution for electrodeposition of the enzyme membrane contained 0.4 ml of enzyme (4 mg ml^{-1}), 0.02 ml of glutaraldehyde (25%), 0.02 ml of ethanol and 0.02 ml of HCl (0.01 M). The enzyme solution was dialysed against a large volume of distilled water (pH 7.0) for 12 h to remove salts in the enzyme sample.

The deposition of the enzyme membrane on the electrodes was followed by washing in 5 mM 4-(2-hydroxyethyl)-1-piperazineethanesulphonic acid (HEPES) buffer solution (pH 6.79) for 15 min to remove any weakly bound enzyme.

The enzyme membranes produced under these conditions were physically stable, did not crack, completely covered the electrode and were adherent to the electrode surface under both wet and dry conditions. The thickness of the enzyme membrane was controlled by the time of the electrodeposition and was estimated to be 0.1 μm [20].

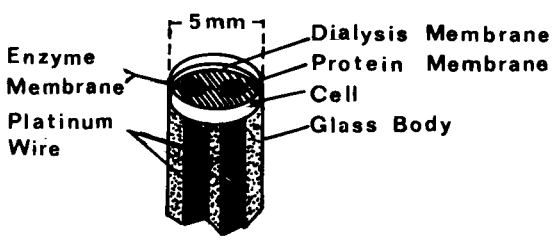

Fig. 1. Layout of the enzymatic biosensor.

Scanning electron microscopy

Electron microscopy was performed with a JEOL-840a scanning electron microscope with an accelerating voltage of 25 kV, a magnification of 5000 and an objective aperture of 1 μm. Negatively stained AChE membranes were prepared according to the procedure of Karnovsky and Roots [21].

Measurement of potential

All the potential measurements were made in a cell with a working volume of 3 ml, equipped with a magnetic stirrer and thermostated at 25°C. The potential was recorded with a Radiometer PHM 64 pH connected to a Sefran SRD 429 recorder. The reference electrode was a Radiometer saturated calomel electrode (SCE). The potential measurements were carried out in a solution of 5 mM HEPES buffer (pH 6.8) containing 0.2 mM NaCl. The enzyme and reference electrodes were placed in the reaction cell containing 3 ml of the buffer solution and the baseline potential was recorded. Following the establishment of a steady baseline potential (several minutes), various concentrations of the substrate were added and the potential change was recorded.

A series of measurements were also made as differential measurements with the biosensor supported vertically (Fig. 1). In this set of experiments the working and reference electrodes were made by electrodeposition of enzyme and albumin on two platinum wires (diameter 0.5 mm). The analysis involved injection of 20 μl of ACh solution into the cell of the AChE sensor with a working volume of HEPES buffer of 0.2 ml, without stirring.

RESULTS AND DISCUSSION

Figure 2 shows a scanning electron micrograph of the AChE membrane surface. The thiocholine–hexacyanoferrate(III) method was used for the investigative localization of active acetylcholinesterase [21]. Thiocholine reduces the hexacyanoferrate(III) and copper(II) ions of this medium competitively, giving simultaneously cop-

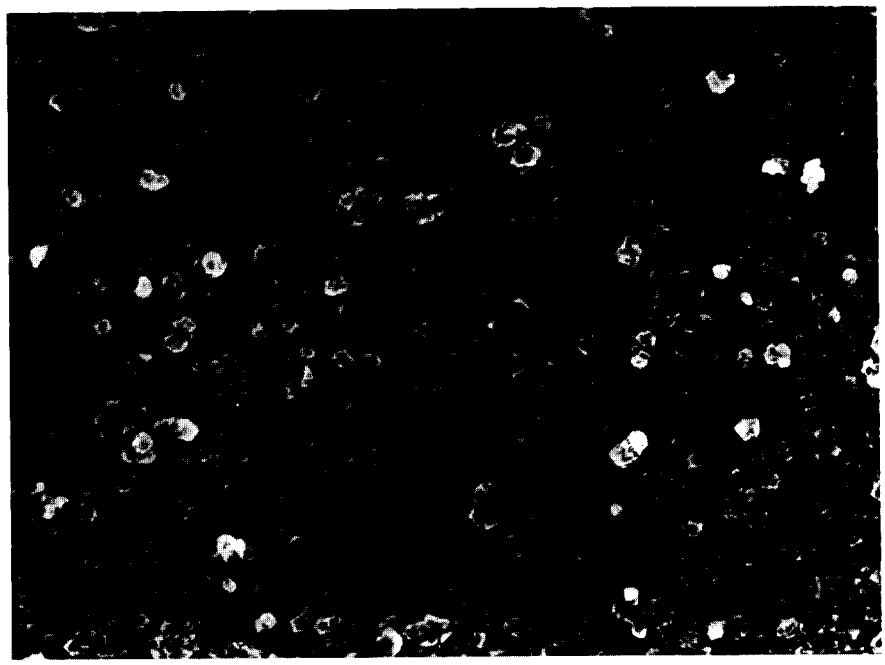

Fig. 2. Scanning electron micrograph of AChE membrane.

per(II) hexacyanoferrate(III) and copper(I) thiocholine iodide. The present results were obtained when the enzyme membrane was treated with an incubation medium consisting of 9.15 ml of 0.1 M citrate buffer (pH 5.0), 0.25 ml of 0.1 M $CuCl_2$ (2.5 mM), 0.5 ml of 0.1 M potassium hexacyanoferrate(III) (5 mM), and 0.1 ml of 0.1 M acetylthiocholine iodide (1 mM). A heterogeneous dense microstructure of the AChE membrane, with aggregates of protein microparticles (ca. 0.3–0.6 μm in diameter) was observed. Strong evidence has accumulated that molecules of acetylcholinesterase in the process of electrodeposition are fixed in orientation respect to the electrode surface. Measurements of the electric resistance of the AChE membranes showed that it is ca. 2.5×10^6 Ω. This means that on the surface of the platinum electrode the AChE membrane may act partially as a dielectric layer between the metal surface and the electrolyte. In aqueous solutions AChE molecules have dissociable groups which either release positive or negative ions, and these disassociated groups themselves become ionized forms depending on the H_3O^+ concentration and on the concentrations of the ions dissociable from the molecular groups. The properties at the membrane surface are intimately related to the electrical potential originating from the fixed charge or electrical polarization of the membrane constituents.

Figure 3 shows response curves of the ACh sensor as a function of ACh concentration. The ACh sensor was formed on the platinum electrode as described under Experimental. Solutions of ACh with different concentrations in 5 mM HEPES buffer (pH 6.79) were stirred at 25°C and the potential change was measured continuously. After injection of acetylcholine the potential shifted in the positive direction and constant values were reached within 8–10 min. Potentiometric responses within the 0.01–1 mM ACh concentration range were found to be completely reversible. Enough enzyme was immobilized on the ACh sensor that the amount of substrate could be rate limiting. The maximum response was obtained in 5 mM HEPES buffer (pH 6.79) contain-

ing 0.2 mM NaCl. The higher the concentration of buffer, the lower was the potential change observed.

To investigate non-specific phenomena, the response of the electrodes modified by albumin membranes in place of the AChE membrane were examined in the acetylcholine solution. The sensor surface with immobilized albumin produced a change in membrane potential of 2%, as compared with the AChE electrode, owing to non-specific binding of ACh. Hence the potentiometric response results only from the enzymatic reaction in the enzymatic membrane. The potentiometric change is coupled with a disturbance of the Donnan equilibrium and redistribution of ions in the protein membrane and at the membrane/solution interface.

The ionic strength and pH of the solution influence the magnitude of the membrane potential of the ACh sensor [7]. The effect of ionic strength was examined in the presence of 0.1 mM ACh with 5 mM HEPES buffer at 25°C. Figure 4 shows the relationship between the potential change of the ACh sensor and salt concentration.

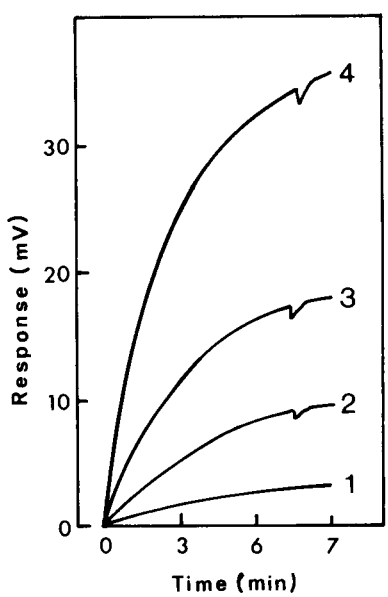

Fig. 3. Response curves of the AChE sensor. ACh was measured in 5 mM HEPES buffer (pH 6.79) containing 0.2 mM NaCl at 25°C. Final concentration of ACh: (1) 0.02; (2) 0.10; (3) 0.26; (4) 1.30 mM.

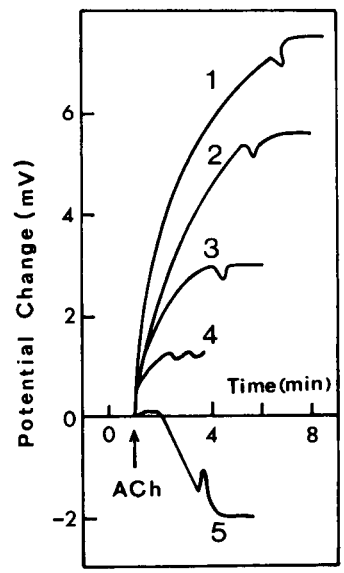

Fig. 4. Effect of ionic strength on the response of the AChE sensor in 5 mM HEPES buffer (pH 6.79) containing 0.1 mM acetylcholine at 25°C. Concentration of NaCl: (1) 0.1; (2) 0.6; (3) 3.0; (4) 6.0; (5) 100 mM.

The potentiometric curves obtained indicated two effects. As can be seen from Fig. 4, curves 1–4, at low concentrations of NaCl (< 6 mM) in 5 mM HEPES buffer, the ACh addition changes the membrane potential momentarily. Under these conditions it is assumed that the main factor contributing to the membrane potential is the Donnan potential and not the diffusion potential. The response of the ACh sensor decreases with increasing concentration of electrolyte, NaCl or KCl. At high electrolyte concentrations it is probable that ions of both signs enter the enzyme membrane and the Donnan ratio is smaller. Figure 4, curve 5, shows that the ACh-induced electric response in 5 mM HEPES buffer containing 100 mM NaCl changes both the size and the sign of the membrane potential. These potential changes are associated with the diffusion potential. Unlike the first effect, here the initial rate of the change in membrane potential is slow. In this instance the membrane potential depends mainly on the relative permeabilities of ions and products of enzymatic reaction, and also on the degree of binding of ions with the charged groups of

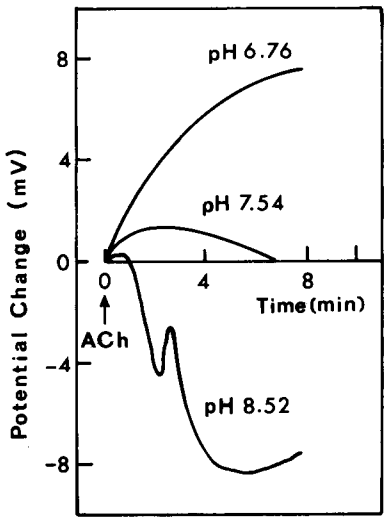

Fig. 5. Effect of pH on the response of a glassy carbon AChE sensor in 5 mM HEPES buffer containing 0.2 mM NaCl and 0.1 mM acetylcholine at 25°C.

the AChE membrane. The effect of solution pH on the membrane potential of the ACh sensor was examined in the presence of 0.1 mM ACh with 5 mM HEPES buffer, containing 0.2 mM NaCl (Fig. 5).

As the protein charges in the AChE membrane are a function of pH, it is necessary to consider the ionic product of the AChE reaction, acetic acid, because it may generate local pH changes in the inner and surface regions of the membrane. Such a pH change in the membrane was measured with a glass pH electrode [22]. The rate of change of pH depends on the concentration of ACh in the reaction cell. Hence the fixed charge density of the AChE membrane is expected to be affected by the acetic acid.

The results of investigations using the differential mode (Fig. 1) with an acetylcholinesterase sensor at higher ionic strength (0.1 M NaCl) and at pH 8.5 are shown in Fig. 6. It was observed that the potential difference between AchE- and albumin-modified electrodes after 10–12 min begins to shift towards the negative direction. As at high pH and ionic strength of the solution the Donnan potential decreases, this potential shift is associated with the diffusion potential. In this instance the selectivity of the enzyme membrane is dependent mainly on the mobility of the charged complexes in the membrane, their partition coefficients and the equilibrium binding constants of the ions with the carriers in the membrane phase. This may be the reason for the change not only in the direction but also in the shape of the responses of the potentiometric sensor (Fig. 6).

Analogous effects were also observed with solid-state enzyme sensors based on urease and arginase. Urease and arginase electrodes were prepared by electrodeposition on the glassy carbon electrodes, as described under Experimental. The investigation showed that urease and arginase electrodes in the process of the enzymatic reaction produce significant changes in the membrane potential during a time scale of several minutes. The ionic strength, pH of the solution and nature of the electrolyte influence the magnitude of the membrane potential similarly to when ACh was used. Typical calibration graphs for the urea, acetylcholine and arginine electrodes are shown

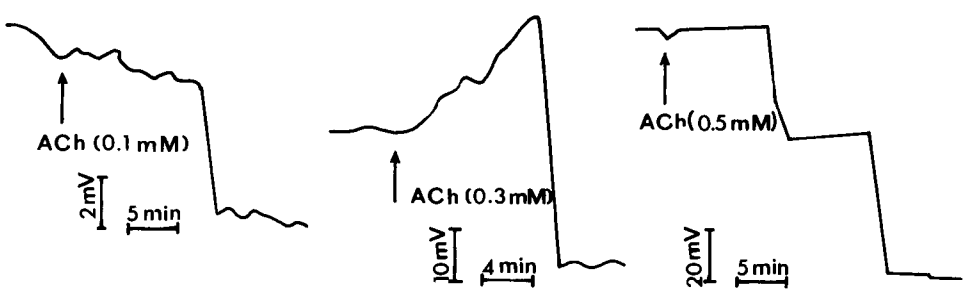

Fig. 6. Shift of the membrane potential of the AChE sensor caused by the addition of acetylcholine to 5 mM HEPES buffer (pH 8.5) containing 0.1 M NaCl at 25°C.

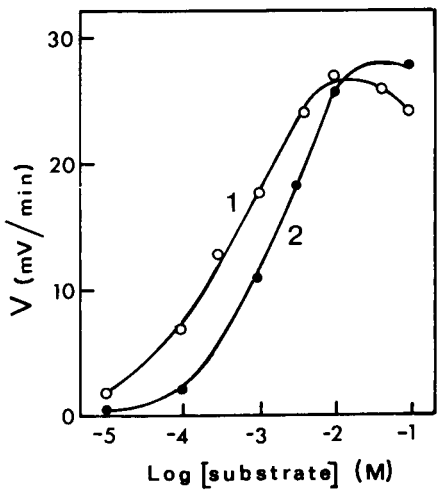

Fig. 7. Calibration graph for the (1) urea and (2) acetylcholine sensors. Urea was measured in 1 mM Tris–HCl buffer (pH 7.3) and ACh in 5 mM HEPES buffer (pH 6.79) containing 0.2 mM NaCl at 25°C.

in Figs. 7 and 8. The urea electrode displayed a linear response with a slope of 11 mV min^{-1} per decade in the range 5×10^{-5}–5×10^{-3} M. Figure 8 shows the dependence of the response of the arginase electrode on the concentration of arginine in the (1) presence and (2) absence of Mn^{2+}.

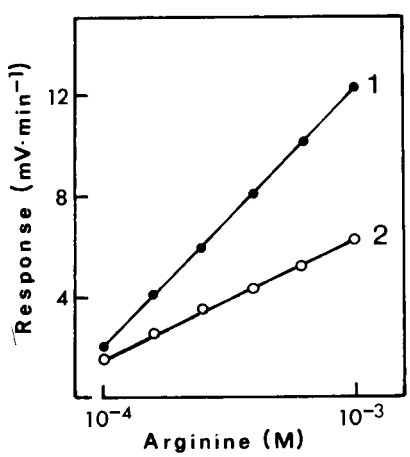

Fig. 8. Calibration graph for the arginine sensor. Measurements were made in 0.01 M glycine–NaOH buffer (pH 9.5) at 25°C, (1) in the presence of 1×10^{-8} M Mn^{2+}; and (2) in the absence of Mn^{2+}.

The stability of the enzyme electrodes was investigated by measuring the effect of time on the calibration graphs. In a typical experiment, the operational stability of AChE electrode was tested over a 24-h period under the optimum conditions defined above. After 8 h of continuous use the decrease in the electrode sensitivity was no more than 5%; after storage for 1 week in 5 mM HEPES buffer (pH 7.5), or in air under refrigeration at 4°C, the tensor still retained 68% of its initial sensitivity and 55% activity remained after 1 month. The storage stability of the urease electrode showed a decline of about 20% of the slope obtained for calibration graphs obtained with the urease electrode during a period of 1 month. The stability of the arginase electrode was not investigated.

The reproducibility of the AChE electrode was studied in 5 mM HEPES buffer (pH 6.8). The relative standard deviations of six repetitive measurements were 5.3%, 5.0% and 4.8% for solutions of 0.1, 0.5 and 1.0 mM ACh, respectively.

The all-solid-state enzyme electrodes presented here do not require the specific introduction of an internal reference. The source of the potential response is a change in the proton potential gradient in the membrane (and other ions) and not a change in the Nernst equilibrium of an electroactive reference. Experiments conducted in the presence of a low concentration (< 1 mM) of a redox couple that is pH dependent, such as quinone–hydroquinone, showed that the potential changes observed are considerably higher. The presence of the quinone–hydroquinone also changes the shape of the response curves. On the other hand, the presence of a redox couple such as $Fe(CN)_6^{3-}$–$Fe(CN)_6^{4-}$ did not affect the response of the enzyme electrode at low concentrations (< 1 mM). In the absence of these mediators, the only redox system that might be present and affect the measured potential is the O_2–H_2O couple. However, experiments under an argon atmosphere showed similar responses (within 2–3 mV) to those under an oxygen atmosphere.

An AChE membrane on a platinum electrode at a pH higher than the isoelectric point of AChE (p*I* 4.0–4.5) may be regarded as a cation exchanger with fixed negative charges. It is pre-

sumed that part of the fixed charges in the membrane are inside the active centre of the enzyme. According to Nolte et al. [23], there are about six negatively charged carboxylic groups in the active centre of AChE which bind electrostatically with cation groups of ACh^+. Therefore, the active centres of AChE are complexing agents of ACh^+. The process of enzymatic hydrolysis of acetylcholine (ACh^+) to choline (Ch^+) and acetic acid (Ac) is given in the following scheme [24]:

$$E + ACh^+ \underset{K_{-1}}{\overset{K_1}{\rightleftharpoons}} EACh^+ \xrightarrow{K_2, Ch^+} E\text{–}Ac \xrightarrow[H_2O]{K_3}$$

$$E + Ac^- + H^+$$

where E = free enzyme, $EACh^+$ = enzyme–acetylcholine complex, E–Ac = acetylated enzyme and the constants K_1, K_{-1}, K_2 and K_3 have their usual meanings.

Assuming that the process of enzyme–substrate complexation is accompanied by the conformational perturbation of membrane-embedded acetylcholinesterase and orientation changes of dipolar molecules, a modification of transmembrane ion transfer is expected. The reorganization of chemical species and charge in the interfacial regions leads to the depolarization of the AChE membrane and the modulation of the membrane potential. A scheme illustrating the mechanism of the generation of membrane potential by membrane-embedded AChE is given in Fig. 9. It involves the formation of a proton electrochemical potential gradient ($\delta\mu H$) between the internal compartment of the AChE membrane and the external solution. The concentration gradient of H^+ in the membrane may be the driving force for the exit of protons to the solution and entry of Na^+ ions into the AChE membrane. The pH gradient in the membrane is of the order of 1–2 units [12] and it is also assumed that the basic form of Ch^+ remains in the acidic compartment of the AChE membrane, while the protonated form of the acetic acid moves across the AChE membrane into the bulk solution.

It is concluded that ion exchange of H^+ and Na^+ (or K^+) across the membrane/aqueous interfaces and diffusion of Ac and Ch^+ across the AChE membrane are the origins of the changes

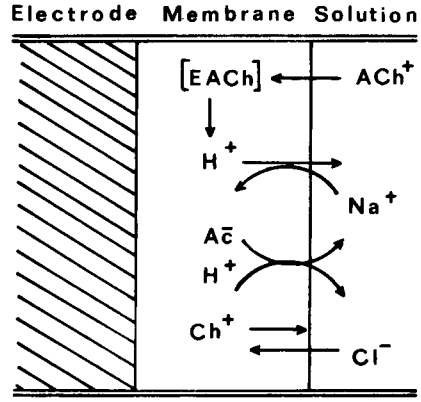

Fig. 9. Scheme illustrating the generation of membrane potential in AChE membrane. ACh^+ = acetylcholine; Ch^+ = choline; [EACh] = acetylcholinesterase–acetylcholine complex; AC = acetate acid.

in the membrane potential. Ion-exchange processes and mobility of ions in the enzyme membrane can also be associated with conformation perturbation of the AChE in the membrane. The response of the ACh sensor is interrelated to the interfacial charge, the ionic strength and pH of the solution. At high pH and ionic strength of the solution the Donnan potential decreases and the membrane potential in the sensor is mainly a function of the diffusion potential. As the enzymatic reaction takes place on the surface of the AChE sensor there is certain directionality. The vectorial characteristic of the membrane transport also contributes to the electrical signal of the biosensors.

In summary, preliminary considerations of some basic factors that modulate the membrane potential in solid-state potentiometric biosensors indicate that a direct transformation of enzymatic reactions into an electrical signal based on the transmembrane ion current modulation is possible. It is believed that this could be a general approach for designing potentiometric biosensors capable of detecting different enzyme reactions and substances. Moreover, a detailed understanding of the induced changes in membrane potential during an enzymatic reaction will contribute to the resolution of fundamental questions, such as the charge transport mechanism in protein membranes and at the membrane/solution interfaces.

Finally, sensors based on thin-film enzyme membranes should be easy to miniaturize and there is a prospect of using a single sensor body to make multiple biosensors.

REFERENCES

1 J. Janata and R.J. Huber (Eds.), Solid State Chemical Sensors, Academic, Orlando, 1985.
2 R.P. Buck, W.E. Hatfield, M. Umana and E.F. Bowden (Eds.), Biosensor Technology—Fundamentals and Applications, Dekker, New York, 1990.
3 M. Aizawa, Anal. Chim. Acta, 250 (1991) 249.
4 J. Janata, Anal. Chem., 64 (1992) 196R.
5 J. Rishpon and I. Rosen, Biosensors, 4 (1989) 61.
6 J. Rishpon and S. Gottesfeld, Biosensors Bioelectron., 6 (1991) 143.
7 S. Ohki, Compr. Treatise Electrochem., 10 (1985) 1.
8 A.L. Hodgkin and B. Katz, J. Physiol., 108 (1949) 37.
9 S. Collins and J. Janata, Anal. Chim. Acta, 136 (1982) 93.
10 C.S. Lee, P.Y. Huang and D.M. Ayres, Anal. Chem., 63 (1991) 464.
11 J. Janata, Chem. Rev., 90 (1990) 691.
12 R.B.M. Schasfoort, P. Bergveld, R.P.H. Kooyman and J. Greve, Anal. Chim. Acta, 238 (1990) 323.
13 P. Bergveld, Biosensors Bioelectron., 6 (1991) 55.
14 D.M. Ivnitskii, M.F. Yulaev and A.P. Kashkin, Z. Anal. Khim., 44 (1989) 2248.
15 M. Demura, T. Komura and T. Asakura, Bioelectrochem. Bioenerg., 26 (1991) 167.
16 R. Lal, Bioelectrochem. Bioenerg., 27 (1992) 121.
17 P.N. Bartlett and R.G. Whitaker, J. Electroanal. Chem., 224 (1987) 37.
18 P.N. Bartlett, P. Tebbutt and C.H. Tyrrell, Anal. Chem., 64 (1992) 138.
19 P. Monsan, J. Mol. Catal., 3 (1978) 371.
20 A.F. Diaz, J.I. Castillo, J.A. Logan and W.Y. Lee, J. Electroanal. Chem. Interfacial Electrochem., 129 (1981) 115.
21 M.J. Karnovsky and L. Roots, J. Histochem. Cytochem., 12 (1964) 219.
22 C. Tran-Minh, P.C. Pandey and S. Kumaran, Biosensors Bioelectron., 5 (1990) 461.
23 H.J. Nolte, T.L. Rosenberry and E. Neumann, Biochemistry, 19 (1980) 3705.
24 P. Hofer, V.P. Fringeli and W.H. Hopff, Biochemistry, 23 (1984) 2730.

Analytica Chimica Acta, 282 (1993) 527–534
Elsevier Science Publishers B.V., Amsterdam

Direct electrochemical transduction of an immunological reaction by bilayer lipid membranes

Dimitrios P. Nikolelis and Manolis G. Tzanelis

Laboratory of Analytical Chemistry, Chemistry Department, University of Athens, Panepistimiopolis-Kouponia, 15771 Athens (Greece)

Ulrich J. Krull

Chemical Sensors Group, Department of Chemistry, Erindale Campus, University of Toronto, 3359 Mississauga Road North, Mississauga, Ontario L5L 1C6 (Canada)

(Received 3rd March 1993; revised manuscript received 17th May 1993)

Abstract

This work reports the electrochemical transduction of an immunological interaction by use of bilayer lipid membranes (BLMs) which were prepared from mixtures of egg phosphatidylcholine (PC) and dipalmitoyl phosphatidic acid (DPPA). Thyroxin (T4)/anti-rabbit T4 was used as a representative immunological reaction for these studies. Antibody–antigen complexation caused transient ion current signals due to dynamic changes of the electrostatic fields at the surface of such membranes. The mechanism of signal generation is based on the perturbation of the electrical double layer and surface structure of the BLMs. The transient charging signals occurred as singular or multiple events which lasted for a period on the order of seconds. The magnitude of these transient ion current signals was directly related to the concentration of the antigen in bulk solution, which could be determined over a range of nM to mM levels in a period of seconds to minutes. Investigation of the effects of lipid composition of BLMs, pH and the presence of Ca^{2+} in bulk electrolyte solution indicated that the response could be optimized for sensitivity and speed.

Keywords: Biosensors; Antibody–antigen; Bilayer lipid membranes; Immunological reaction

An imaginative array of analytical methods has been developed to create and amplify analytical signals from antibody–antigen interactions, viz. sandwich assays, competitive binding assays and enzyme labelling [1]. Generally, these methods are sensitive and selective, but often have serious deficiencies in terms of biosensor development on the basis of speed, the need for separation steps, the requirement of secondary labelling and the introduction of secondary reactants. Recently a number of investigations have reported direct electrical monitoring of an immunological reaction [2–7]. The direct monitoring of antibody–antigen binding and the construction of an immunological biosensor based on the determination of an intrinsic property of the protein (charge density, molecular mass, dielectric constant, refractive index, etc.) is an attractive alternative to enzyme-linked or radiometric immunoassays if comparable sensitivity and speed can be achieved.

Bilayer lipid membranes (BLMs) can provide the basis for the development of immunological biosensors for the direct monitoring of antibody

Correspondence to: U.J. Krull, Chemical Sensors Group, Department of Chemistry, Erindale Campus, University of Toronto, 3359 Mississauga Road North, Mississauga, Ontario L5L 1C6 (Canada).

–antigen binding [8]. The use of BLMs to directly monitor immunological reactions was first demonstrated years ago by Del Castillo, and transient electrical phenomena involving changes in membrane conductance were observed [9,10]. Further studies of the use of ion current through BLMs as a basis for transduction of antibody–antigen and lectin–saccharide interactions indicated that signals appeared as multiple transients with ion current alterations of variable magnitude and frequency [11,12]. Of significance was that signal frequency and magnitude data accumulated for any one BLM over a period of an hour could be correlated semi-quantitatively with analyte concentration, and that the multiple transient events were due to electrostatic alterations at the membrane surface. Such a transduction method for concentration determinations is inherently limited by the length of time required for analysis, and by the use of statistical probabilities to identify concentrations by analyzing frequency of response. The goal of the present work was to identify whether the structure of BLMs could be designed so that transduction of antibody–antigen interactions was based on the magnitude of a single signal.

The interactions of hydronium and calcium ions with BLMs composed of egg PC and DPPA have recently been studied by an electrochemical method [13,14]. The results have shown that the surface charge density and phase structure of these membranes depends on the composition of BLMs, the hydronium activity and the presence of calcium ions in the electrolyte solution. Enzyme–substrate interactions which modify the charge density at the surface of these BLMs can generate analytically useful signals by perturbation of the electrostatic fields and phase structure of membranes [15]. Alteration of an electrical double layer which can be made to exist at a BLM–solution interface is a process which has been observed to provide rapid response characteristics for acetylcholine-acetylcholinesterase reaction (seconds for μM detection).

In the present work the analytical utility of BLMs as electrochemical transducers for immunoreactions which modulate the electrostatic charge at the membrane surface is presented. The thyroxin (T4)/anti-rabbit T4 interaction was chosen as the immunoreaction, owing to the clinical significance of T4 [16]. The BLMs provided transduction by alterations of the charging of the double layer which was modified by the immunoreaction. By appropriate selection of lipid composition and solution conditions it was possible to transduce the selective antibody–antigen interaction as a single transient charging current signal, which phenomenologically had an appearance similar to a gated process but without a quantized magnitude (i.e., an electrochemical switch).

EXPERIMENTAL

Materials and apparatus

The materials and equipment used throughout this study were essentially identical to those described previously [13,17]. The lipids that were used were lyophilized egg phosphatidylcholine (PC; Avanti Polar Lipids, Birmingham, AL) and dipalmitoyl phosphatidic acid (DPPA; Sigma, St. Louis, MO). HEPES (*N*-2-hydroxyethylpiperazine-*N'*-2-ethanosulfonic acid) which was used for the pH adjustment and thyroxin were also purchased from Sigma. Rabbit antiserum to T4 was supplied from UCB Bioproducts (Braine-l'Alleud, Belgium). Water was purified by passage through a Milli-Q cartridge filtering system (Milli-Q, Millipore, El Passo, TX) and had a minimum resistivity of 18 Mohm cm. All other chemicals were of analytical-reagent grade.

Solventless BLMs were formed in a circular aperture of 0.32 mm diameter, which was located in a Saran-Wrap™ partition (10 μm thickness) that was used to separate two identical solution cell compartments. Each plexiglass solution chamber had a volume of ca. 10 ml and an air/electrolyte interface area of 3 cm^2. An external voltage of 25 mV d.c. was applied across the membrane between two Ag/AgCl reference electrodes. A digital electrometer (Model 614, Keithley Instruments, Cleveland, OH) was used as a current-to-voltage converter. The electrochemical cell and the electronic equipment were isolated in a grounded Faraday cage.

Procedures

The dilute lipid solution used for the formation of the solventless BLMs contained 0.2 mg ml^{-1} total lipid and was composed of 0, 15 and 35% (w/w) DPPA; these solutions were prepared daily from stock solutions of PC (2.5 mg ml^{-1}) and DPPA (2.5 mg ml^{-1}) in *n*-hexane–absolute ethanol (80 + 20). The stock lipid solutions were stored in the dark in a nitrogen atmosphere at −4°C. The BLMs were supported in a 0.1 M KCl electrolyte solution which contained HEPES as a buffer.

The antiserum had a volume of 1.6 ml (protein concentration 17.5 mg ml^{-1}) and was diluted to 10.0 ml with a 0.02 M phosphate buffer pH 7.4. Samples of 100 μl volume were removed on a daily basis and were used for the deposition of the protein onto the air/electrolyte interface in the electrochemical cell. The stock solution of thyroxin (0.1 mg ml^{-1}) was prepared daily just before use.

The process of membrane formation by a modified "monolayer folding" technique was described previously [13,17]. Lipid solution (10 μl) was added dropwise from a microliter syringe to the water surface in one cell compartment near the partition. A volume of 3 μl of the protein solution was applied to the same air/water interface subsequent to the deposition of lipid. The level of the electrolyte was dropped below the aperture and then raised again within a few seconds. The formation of a membrane was verified by the magnitude of the ion current, and by the electrical properties of the membranes. When the ion current stabilized (over a period of 20 min) and no more transient ion current changes occured, the antigen was injected in bulk solution. All solutions were gently stirred and all experiments were done at 25 ± 1°C.

RESULTS AND DISCUSSION

The antibody was deposited directly onto egg PC–DPPA mixtures at the air/water interface of one solution cell compartment. This promoted incorporation of the protein into the lipid layer and maximized the loading of the protein when BLMs were formed. Data on immunoglobulin interactions with lipids have been reported [18,19], but specific data for anti-rabbit T4 has not been given. Therefore experiments were done to determine the maximum loading of protein that can be inserted in the BLM structure without inducing permanent permeability changes, and to estimate the time required for association of the IgG with

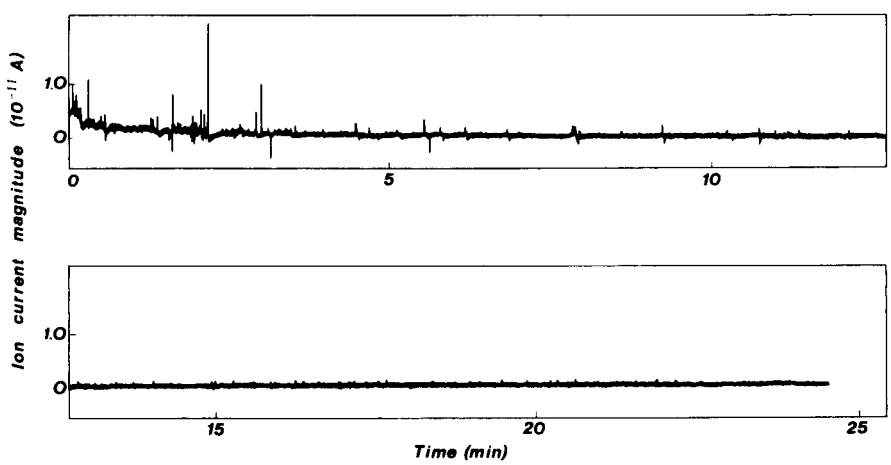

Fig. 1. Recording obtained at pH 6.0 (0.1 M KCl, 10 mM HEPES and in the absence of Ca^{2+}) with membranes composed of 15% (w/w) DPPA with anti-rabbit T4 in the BLM structure and without antigen present in the bulk solution. A volume of 3 μl of antibody solution was deposited onto the air/water interface subsequent to the lipid deposition. The recording begins after BLM has thinned to a bilayer structure and stabilization of the baseline has occurred (e.g., 3 min after membrane formation).

the PC/DPPA BLMs. Various volumes of the solution containing antibody were deposited onto the air/water interface after the deposition of lipid (15% DPPA, pH 6.0). Volumes of anti-rabbit T4 solution less than or equal to 3 μl did not alter the residual ion current (background signal) associated with conductivity through these BLMs. Such additions did result in the appearance of random transient signals as the BLMs stabilized (Fig. 1) reminiscent of ion-channel gating events [20]. Similar results were obtained with BLMs composed of only PC or 35% DPPA, and when the electrolyte solution contained 1.0 mM Ca^{2+}. The time for stabilization of the BLMs which contained antibody was less than 20 min and injection of antigen in bulk solution was done after this time. An instability of ion current with time was noticed for volumes of antibody solution that were larger than 3 μl; e.g., the ion current was initially as observed in Fig. 1 when a volume of 5 μl of antibody solution was deposited onto the air/water interface, but it increased over a period of 7 min to 100 pA and after a total of 10 min to 1 nA.

Some models of the association of antibodies with BLMs have been proposed [19,21]. The results presented herein indicate that it is unlikely that the protein spans the membrane to form a conductive pore since permanent alterations of ion current were not observed when using significant but lower concentrations of antibody (i.e., 3 μl volumes or less). The destabilizing effect of larger quantities of protein is likely due to concurrent protein–lipid and protein–protein interactions which tend to disrupt the continuum of lipid interactions on one side of a BLM. A pertinent analogy can be drawn here to the function of a detergent, and the electrochemical results do indicate that a critical concentration of protein exists beyond which BLM destabilization and failure occurs. The IgG likely exists at the membrane–solution interface [19] with a substantial protrusion of the functional F_{ab} and F_c groups into the electrochemical double layer. Aggregative events associated with increasing concentrations of the protein in a BLM could readily cause disruption of a double layer, and the rapid reorganization of the double layer would be observed

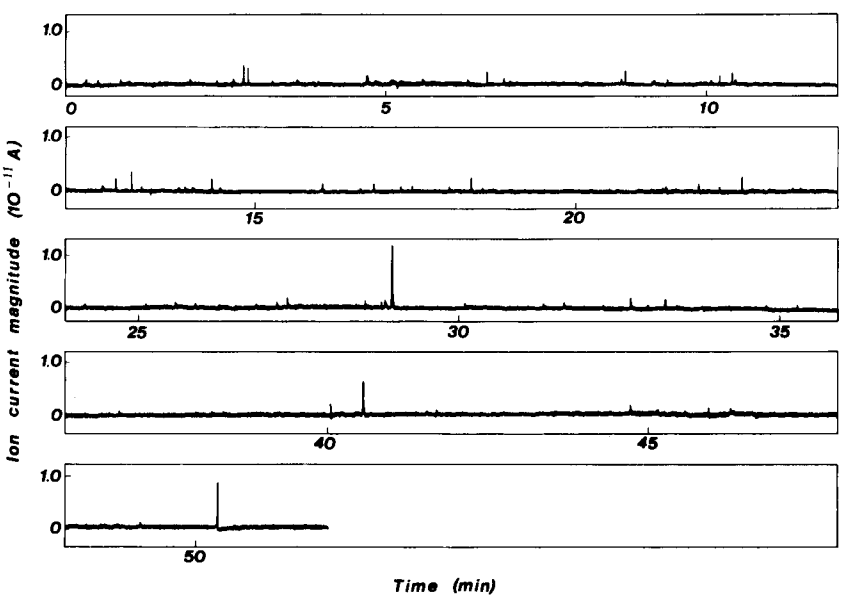

Fig. 2. Experimental results obtained at pH 6.0 (0.1 M KCl, 10 mM HEPES and 1.0 mM Ca^{2+}) with membranes consisting of 35% (w/w) DPPA when a volume of 3 μl of antibody solution were co-deposited onto the air/water interface and the concentration of T4 in bulk solution was 1.12×10^{-7} M.

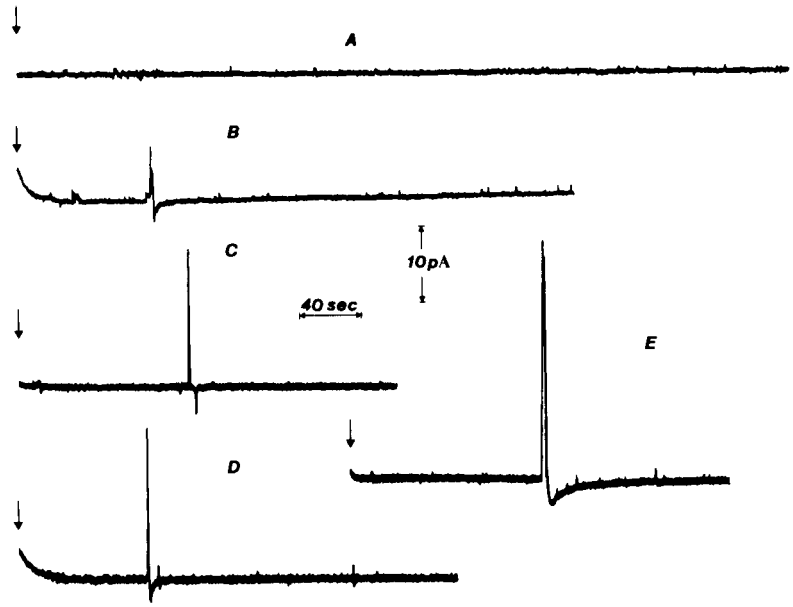

Fig. 3. Experimental results obtained at pH 6.0 (0.1 M KCl, 10 mM HEPES and in the absence of Ca^{2+}) with BLMs composed of 15% (w/w) DPPA when 3 μl of antibody stock solution was co-deposited onto the air/water interface. Thyroxine concentrations; (A) 1.12×10^{-9} M; (B) 1.12×10^{-8} M; (C) 3.36×10^{-8} M; (D) 1.12×10^{-7} M; (E) 1.12×10^{-6} M. Arrow indicates injection of antigen.

as a transient current signal. In addition the aggregation of charged protein molecules, and interactions with the charged lipid component of the BLMs (protein binding to hydrogen bond accepting sites of DPPA [22]) can induce electrostatic field gradients at a BLM surface [23]. These processes should reduce in frequency and then terminate as an equilibrium concentration of protein and subsequent equilibrium of aggregation at the membrane–solution interface was reached, and occurred in a period of up to 20 min in our experiments.

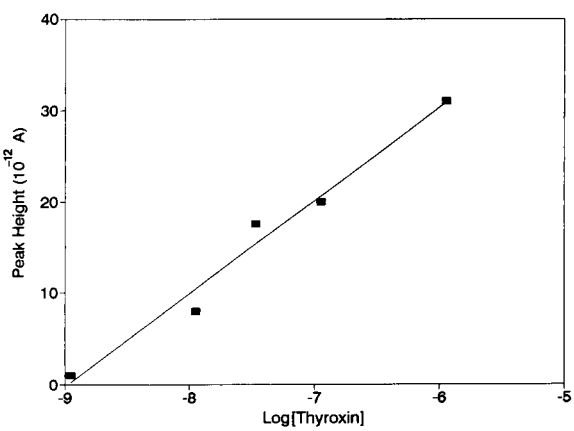

Fig. 4. Calibration of the analytical signal from the experimental results that are shown in Fig. 3.

Figure 2 shows recordings of the signals obtained at pH 6.0 (in the presence of calcium ions) with BLMs composed of 35% DPPA. It can be seen that the immunological interactions that occur at the membrane surface produce multiple transient events of the form that has previously been shown to relate frequency to concentration [11,12]. Similar results were obtained at different experimental conditions, such as in the absence of calcium ions in the bulk electrolyte solution and with BLMs consisting of 0% (w/w) DPPA. Figure 3 shows recordings of the signals obtained at pH 6.0 (in the absence of Ca^{2+}) for different concentrations of thyroxin with membranes composed of 15% DPPA. This lipid composition and electrolyte composition was the only one (using the stated lipids and salts) which was found to provide single current transients. The magnitude of the transient responses is in direct proportion

to the concentration of antigen in bulk solution as can be seen in Fig. 4. Control experiments involving the use of antigen alone and non-selective protein interactions were completed to demonstrate that the transient ion current signals were due to selective interactions.

Previous studies have shown that ion conduction through BLMs depends on the phase structure and/or the surface potential, which directly depend on the concentration and the degree of ionization of DPPA [13], and on the presence of Ca^{2+} in bulk electrolyte solution [14]. The most significant difference between these previous experiments and those reported in the present work is that the former experiments report permanent alterations of ion conductivity by concurrently adjusting the electrostatic charge on both sides of BLMs, while the latter provides surface charge alterations only at the one membrane interface (exposed to the antibody). The results indicate that it is possible to control the structure and/or electrostatic fields of one leaflet of a BLM without disturbing the opposite surface (over relatively short periods), as recently shown by the generation of transient signals based on pH variations caused by hydrolytic enzyme–substrate reactions at BLMs prepared from PC/DPPA [15].

The transient signals shown in Fig. 3 are intriguing due to the reproducibility and speed of signal development at even low concentrations of antigen. The transient currents have a duration of seconds or less and are indicative of a rapid reorganization of charge at the surface of membranes. Rabbit antithyroxin antiserum is polyclonal and is composed of a mixture of antibodies with isoelectric points (pI) in the range 6.3 to 9.0 [24,25]. The antigen T4 has a pI of 5.0 [25]. Electrostatic forces are important in the mechanism of formation of the antibody–antigen complex [25]. At pH 6.0 the formation of the complex would result in partial neutralization of the net positive charge of the antibody by the net negative charge of the antigen.

Electrostatic changes induced by the antibody–antigen interaction on one side of a BLM would be expected to cause a slow (many minutes) non-linear double layer reorganization to occur, which would provide a slow transient change of signal (it is unknown whether the kinetics of the antibody–antigen reaction, or associations of the immunocomplexes, or diffusion of the antigen to the membrane surface is rate limiting). The appearance of a rapid transient current after a substantial time delay (i.e., much longer than mixing or diffusion times) therefore suggests that a capacitive charging current develops when some critical magnitude of surface charge is achieved, which results in a transition of membrane structure from one form to another. This was the case for hydrolytic enzyme–substrate reactions, and related the time required for the appearance of a transient current of constant magnitude to different concentrations of substrate [15]. However, the results for the antibody–antigen experiments of Figs. 3 and 4 indicate the evolution of a transient signal with a relatively constant time correlation, and varying magnitudes which are directly related to antigen concentration. The relatively constant delay times for transient current evolution for widely varying concentrations of antigen indicate that the mechanism responsible for the transient is not directly related to the charge associated with varying quantities of antigen at the BLM surface.

The process of formation of BLMs requires variable times, and antigen additions have been done at different times after membrane formation and stabilization. Only after addition of T4 were the transient currents of Fig. 3 observed, confirming that the transients were not associated with a spontaneous structural relaxation of the BLMs. This undefined singular structural transition is furthermore unique in that it only has been observed to occur for the experimental conditions listed for Fig. 3. The magnitude of the transient currents are consistent with the proposed capacitive charging events and are related to the concentration changes of ions of the double layer as follows; the concentration of univalent ions at the membrane-solution interface, $C_i(x)$, is given by the Boltzmann relation:

$$C_i(x) = C_i \exp[-ze\Psi_0/kT] \quad (1)$$

where C_i is the electrolyte concentration in bulk solution, z, e, k and T have their usual meanings and Ψ_0 is the surface potential. The magnitude of

TABLE 1

Summary of responses for different compositions of BLMs and electrolyte solution

% (w/w) DPPA in BLMs	$[Ca^{2+}]$ (mM)	pH	Signal appearance (average)	Max. signal (pA)	Effect of [antigen] increase	Average delay to first signal (min)
35	1	6	Multiple spikes, 3–4 pA	10	Increased spike freq. and magnitude	3
35	none	6	Multiple spikes, 2–3 pA	4	Increased spike freq. and magnitude	1.5
15	1	6	Multiple spikes, 2–3 pA	4	Increased spike freq. and magnitude	10
15	none	6	Single transient	dep. [antigen] (e.g., 21 pA for 1.12×10^{-7} M)	Increased spike mag.	1.5
15	none	8	Single transient	dep. [antigen] (e.g., 10 pA for 1.12×10^{-7} M)	Increased spike mag.	1.5

the transient charging signals is observed to approximately follow a logarithmic dependence of T4 concentration.

The signal profile of Figs. 3 and 4 indicates an interesting opportunity for development of a sensor that can act as a modulator or switching device. More generally, Table 1 summarizes the results from experiments which provide current transients based on the chemical composition and environment of BLMs. The magnitudes of the multiple signals and therefore the sensitivity for antigen calibration depends on the quantity and extent of ionization of DPPA. The signal magnitude is increased when the quantity of the acidic lipid in the membrane decreases. A continuation of this trend is not evident for membranes consisting only of PC. The results indicate that the phase structure of the lipid membrane is a predominant factor that sets the magnitude of the current alterations. The time for appearance of the first of a series of multiple transient signals does not substantially alter as the concentration of DPPA is changed. An increase of the pH of bulk electrolyte solution (e.g., pH 8.0) which increases the degree of ionization of DPPA and reduces the net charge of the antibody results in a decrease of the signal magnitude. This may be due to the properties of the membrane, but the binding activity and attractive electrostatic interactions between antibody and antigen are also reduced [25,26]. The presence of Ca^{2+} in bulk solution generally delays the time of appearance of the multiple transients. BLMs can therefore be designed to provide fast, sensitive transduction of interactions of charged antibodies with antigens; the example shown here having a detection limit for determination of T4 near 10^{-9} M of thyroxin (for $S/N = 2$ when based on the experimental noise level of 0.5 to 0.7 pA, and using a time window based on the full range of experimentally observed times of responses from 50 to 120 s).

REFERENCES

1 C. Blake and B.J. Gould, Analyst, 109 (1984) 533.
2 M. Aizawa, S. Kato and S. Suzuki, J. Membrane Sci., 2 (1977) 125.
3 P. Bataillard, F. Gardies, N. Jaffrezic-Renault, C. Martelet, B. Colin and B. Mandrand, Anal. Chem., 60 (1988) 2374.
4 R.B.M. Schasfoort, R.P.H. Kooyman, P. Bergveld and J. Greve, Biosensors Bioelectronics, 5 (1990) 103.
5 P. Bergveld, Biosensors Bioelectronics, 6 (1991) 55.
6 R.F. Taylor, I.G. Marenchic and R.H. Spencer, Anal. Chim. Acta, 249 (1991) 67.
7 V. Billard, C. Martelet, P. Binder and J. Therasse, Anal. Chim. Acta, 249 (1991) 367.
8 O.S. Wolfbeis, Anal. Chim. Acta, 250 (1991) 181.
9 J. Del Castillo, A. Rodriguez, C.A. Romero and V. Sanchez, Science, 153 (1966) 185.
10 E. Toro-Goyco, A. Rodriguez and J. Del Castillo, Biochem. Biophys. Res. Commun., 23 (1966) 341.

11 M. Thompson, U.J. Krull and L.I. Bendell-Young, Bioelectrochem. Bioenerg., 13 (1984) 255.
12 U.J. Krull, R.S. Brown, R.N. Koilpillai, R.S. Nespolo, A. Safarzadeh-Amiri and E.T. Vandenberg, Analyst, 114 (1989) 33.
13 D.P. Nikolelis, J.D. Brennan, R.S. Brown and U.J. Krull, Anal. Chim. Acta, 257 (1992) 49.
14 D.P. Nikolelis and U.J. Krull, Anal. Chim. Acta, 257 (1992) 239.
15 D.P. Nikolelis, M.G. Tzanelis and U.J. Krull, Anal. Chim. Acta, 281 (1993) 569.
16 M. Fernandez-Ulloa and H.R. Maxon III, in L.A. Kaplan and A.J. Pesce (Eds.), Clinical Chemistry, Theory, Analysis, and Correlation, Mosby, St. Louis, 2nd edn., 1989, Chap. 41, pp. 620–638.
17 D.P. Nikolelis and U.J. Krull, Talanta, 39 (1992) 1045.
18 M. Thompson, H.E. Wong and A.W. Dorn, Anal. Chim. Acta, 200 (1987) 319.
19 M. Vandenbranden, G. Kayser, S. Banerjee and J.M. Ruysschaert, Biochim. Biophys. Acta, 685 (1982) 177.
20 B. Hille, Ionic Channels of Excitable Membranes, Sinauer, Sunderland, MA, 2nd edn., 1992, p. 4.
21 M.K. Jain and D. Zakim, Biochim. Biophys. Acta, 906 (1987) 33.
22 J.M. Boggs, Biochem. Cell Biol., 64 (1986) 50.
23 I. Lundstrom, FEBS Lett., 83 (1977) 7.
24 Y. Endo, K. Miyai, N. Hata and K. Ichihara, Anal. Biochem., 144 (1985) 41.
25 Y. Endo, K. Miyai, N. Hata and Y. Iijima, Biotechnol. Appl. Biochem., 9 (1987) 74.
26 P. Nuutila, P. Koskinen, K. Irjala, L. Linko, H.-L. Kaihola, J.U. Eskola, R. Erkkola, P. Seppala and J. Vilkari, Clin. Chem., 36 (1990) 1355.

Analytica Chimica Acta, 282 (1993) 535–541
Elsevier Science Publishers B.V., Amsterdam

Piezoelectric quartz crystal with separated electrode for the simultaneous determination of atropine sulphate and sodium chloride

Wenhong Zhu, Wanzhi Wei, Lihua Nie and Shouzhuo Yao

Department of Chemistry and Chemical Engineering, Hunan University, Changsha 410082 (China)

(Received 29th September 1992; revised manuscript received 26th April 1993)

Abstract

A piezoelectric quartz crystal with one separated electrode that could be immersed in liquid was applied to the simultaneous determination of atropine sulphate and sodium chloride in atropine sulphate eye drops. The average relative errors were 4.0% for atropine sulphate and 2.7% for sodium chloride.

Keywords: Piezoelectric sensors; Atropine sulphate; Pharmaceuticals; Sodium chloride

The piezoelectric quartz crystal (PQC) sensor has attracted increasing interest and applications since it was introduced in 1964. For multi-component analysis in gaseous phases, the use of piezoelectric crystal arrays has also been proposed. Carey et al. [1] used a piezoelectric crystal array modified by different coating films. Chang et al. [2] identified odorants with a piezoelectric crystal array through neural-network pattern recognition. For the analysis of liquid samples, a multicalibration technique has been established for the simultaneous determination of micro amounts of *o*- and *m*-cresol using a liquid piezoelectric array [3] and a method for the simultaneous determination of aspirin and salicylic acid using an unmodified piezoelectric sensor has also been suggested [4].

Recently, a new type of piezoelectric sensor for gases and liquids, the electrode-separated piezoelectric quartz crystal, has been reported [5–8]. These sensors have been investigated with regard to solution properties, density, viscosity, specific conductance, permittivity, and mass, and applied to chromatographic detection. In this work, a piezoelectric quartz crystal sensor with one separated electrode (PCSE) was designed that can be inserted in liquids like the normal piezoelectric quartz crystal (PQC). The sensor was constructed with a piezoelectric crystal and a silver rod. It was found that this PCSE sensor shows a high response sensitivity to changes in the specific conductance of solutions under certain conditions. Using this device, we carried out the simultaneous determination of atropine sulfate and sodium chloride in guttae atropini sulphatis (atropine sulphate eye drops) with the help of a calibration technique. The results showed that the PCSE is more sensitive than the conventional PQC detector; in addition, it is simple to operate and has a rapid response owing to the lack of a need for an inconvenient flowing system, and can be applied to determine the traces of several components in pharmaceutical systems simultaneously and rapidly.

Correspondence to: Shouzhuo Yao, Department of Chemistry and Chemical Engineering, Hunan University, Changsha 410082 (China).

EXPERIMENTAL

Apparatus and reagents

An AT-cut, 9-MHz piezoelectric quartz crystal (12.5 mm diameter, having two coated silver electrodes) was obtained commercially (Peking). One electrode of the piezoelectric crystal was dissolved away with aqua regia, and then the crystal was washed with water and acetone and dried. A silver rod of diameter 0.5 mm was ground with sand paper, washed with water and acetone before drying and then fixed to the crystal. Lead wires were soldered on the silver rod.

The PCSE designed here is shown in Fig. 1. The silver rod electrode faced the electrodeless surface of the crystal. The PCSE can be immersed in liquid like a normal PQC. The PCSE, holder and detection cell were placed in a thermostated water-bath. In contrast with a device reported by Nomura et al. [6], the surrounding of the piezoelectric quartz crystal and the separated electrode were entirely filled with a same kind of solution. Both sides of the crystal were in contact with liquid. The distance between the silver rod and the crystal was about 0.5 mm and the volume of the detection cell was about 10 ml.

The lead wires soldered to electrodes were connected to a TTL oscillator made in this laboratory. The frequency change was monitored by an SS3320 frequency counter (Shijiazhuang Electronic 4th Factory) and the power was supplied by a JY-30B d.c. voltage regulator (Shijiazhuang Electronic 4th Factory). A Model 78-1 magnetic stirrer (Shanghai Nanhui Telecommunications Equipment Factory) was used to mix the solution. The temperature was controlled by a Model CS501 thermostat (Chongqin Trial Equipment Factory). A microsyringe and a medical injector (Shanghai Medical Injector Factory) were used to add sample solution and remove waste solution.

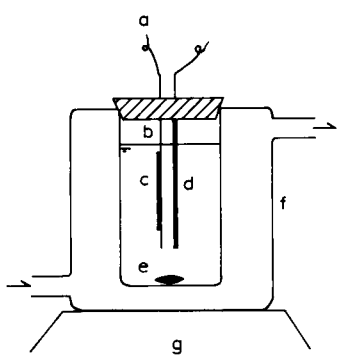

Fig. 1. Configuration of the PCSE. (a) Lead wire; (b) quartz crystal disc; (c) coated silver electrode; (d) silver rod electrode; (e) solution; (f) water-jacket; (g) magnetic stirrer.

All solutions were prepared from analytical-reagent grade chemicals. Atropine sulphate was of pharmaceutical purity. Doubly distilled water was used throughout.

Measurements

First, the PCSE device was immersed in 10 ml of water which was thermostated at 25 ± 0.2°C and stirred at a constant rate. The stable oscillation frequency, f_0, was recorded. After adding electrolyte solution, the stable frequency, f, was again recorded, giving the frequency shift, $\Delta f = f - f_0$. In order to ensure reproducility of the measurements, the detection system was kept in place throughout the determinations. The waste solution was removed with medical injector. The detection cell was then blown dry after washing with water and acetone.

Suitable amounts of atropine sulphate and sodium chloride were weighed accurately and dissolved in water to give standard solutions.

The sensor was immersed in the detection cell containing 10 ml of freshly prepared 1.5 mM NaOH solution (25 ± 0.2°C; constant stirring rate). To avoid the possibility of the dilute sodium hydroxide reacting with atmospheric CO_2, leading to frequency drift, the detection cell was sealed with a cover in which a small hole was left to insert a microsyringe. The stable frequency response, f_1, was measured. After injecting a certain amount of atropine sulphate and NaCl, the initial reaction time was registered immediately and the frequency values at different times, $f_2(t)$, were recorded. The frequency shift, $\Delta f(t) = f_2(t) - f_1$, was measured twice and the average was used as the response of the PCSE.

Data analysis

Multiple linear regression (MLR) was used to predict concentrations:

$$[C]_{b\times n} = [P]_{b\times m}[R]_{m\times n} \quad (1)$$

where [C] is a concentration matrix, [P] is a coefficient matrix, [R] is a response matrix and b, m and n are the numbers of components, time windows and samples, respectively. The [P] matrix can be estimated via a calibration set with known concentrations and measured frequency responses.

The program was written in BASIC and the computer used was an AST 286.

RESULTS AND DISCUSSION

Characteristics of PCSE

It was found that this type of PCSE sensor could oscillate stably in gas and liquid environments in the same way as a normal PQC. For the PCSE in air, the two separated electrodes have the function of a capacitor, so an alternating electric field can be exerted in the piezoelectric quartz crystal and make it oscillate. The oscillation frequency is higher than that for a normal PQC in air. With the PCSE in a liquid, it can bring about stable oscillation with the help of the properties of solutions. In contrast to the results of Nomura et al. [6], this PCSE resonator can oscillate stably in non-electrolyte-containing liquids such as water and ethanol.

The equivalent circuit of the proposed PCSE is shown in Fig. 2. R_1, L_1, C_1 and C_0 are the dynamic resistance, dynamic inductance, dynamic capacitance and static capacitance of the piezoelectric quartz crystal in a liquid, respectively. R_s and C_s are the solution resistance and solution capacitance. R_s' and C_s' are also solution resistance and capacitance, but different to R_s and C_s. It can be seen that the circuit becomes more complicated than that of a normal PQC [9] because of the separated electrode and the two sides of the crystal in contact with solution.

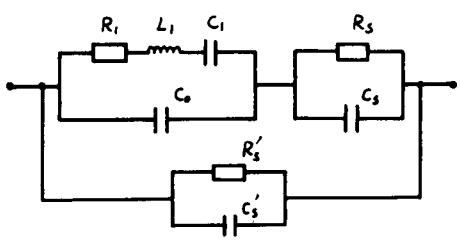

Fig. 2. Equivalent circuit of PCSE.

With the present system the specific conductance changes were investigated, but the influence of permittivity, density and viscosity of solution can be ignored. As shown in Fig. 3, when the concentration of the electrolyte solution increases, i.e., the specific conductance increases, the resonant frequency becomes more negative. The frequency shift is proportional approximately to the concentration of electrolyte within a certain range. The slope of the frequency change increases gradually. If the electrolyte concentration is too high, e.g. more than 5×10^{-3} M sodium chloride, the PCSE resonator will stop oscillating owing to the too large frequency shift (the frequency is too low to oscillate stably). If the electrolyte is added continuously, the frequency will increase slowly and the resonator will restore oscillation gradually in concentrated electrolyte solution (about 2×10^{-2} M), and when the concentration is up to certain value the frequency will not change with variation of the electrolyte concentration. In the range of experimental concentrations used, the frequency shift of the PCSE resonator is several time larger than that of the normal PQC [10,11].

A suitable volume of water was transferred to the PCSE detection cell so that the level of the water reached the centre of the coated silver electrode of the piezoelectric quartz crystal. The stable frequency (f') was recorded. Other stable frequencies (f'') were monitored after adding 50-μl aliquots of water. The relationship between the oscillation frequency shift and the volume of water is shown in Fig. 4. It can be seen that with the addition of water the frequency decreases and the influence of the depth of solution gradually weakens. When the surface of the liquid is above the top of coated silver electrode, despite the separated electrode of the quartz crystal, the influence of the depth of liquid on the frequency change is restricted to a few Hz, which corresponds to the flat part of the curve. This result is similar to that with a normal PQC. As the area of the unseparated silver electrode is much larger than that of the separated electrode, the effect on the silver rod electrode frequency is slight com-

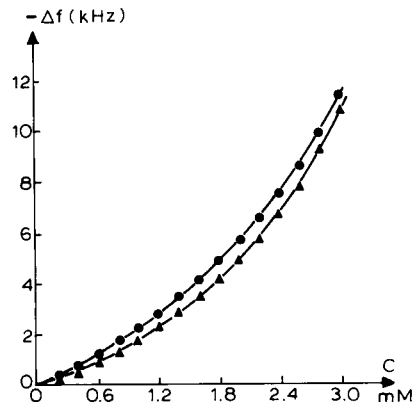

Fig. 3. Correlation of frequency shift and concentration for PCSE in (▲) NaCl and (●) $MgSO_4$.

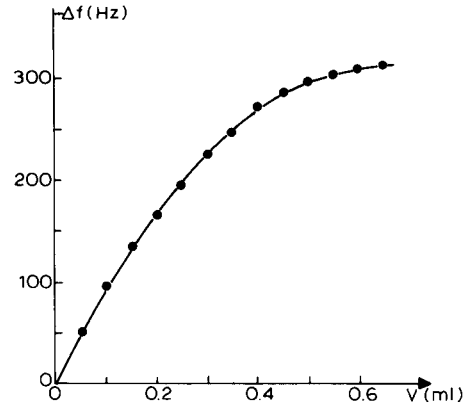

Fig. 4. Influence of depth, i.e., volume of liquid added.

pared with the coated silver electrode. Hence the influence of depth can be neglected provided that the coated silver electrode of the crystal is fully immersed in solution. In this work, the distance between the surface of the liquid and the top of coated silver electrode was kept at about 1 mm. Additionally, the size and shape of the detector cell and the stirring rate were kept constant.

As shown in Figs. 3 and 5, if the water is regarded as the reference solution, then the relationship between frequency shift and concentration of the electrolyte over a large range is not strictly linear. However, under certain conditions, for example, relative to the most dilute electrolyte solution (e.g., 2×10^{-4} M), the frequency change is proportional to the electrolyte concentration, i.e., the specific conductance. It was found that the background electrolyte had a large influence on the determination. The presence of a large amount of background electrolyte makes the sensitivity of the frequency response increase considerably and improves the linear relationship between the frequency shift and concentration. In this work, the analyses of the calibration set and the unknown sample set were carried out in a certain background electrolyte (1.5 mM NaOH) and, moreover, the frequency shift was relatively small (a few hundred Hz), in order to ensure that the frequency shift response was restricted strictly to the linear range.

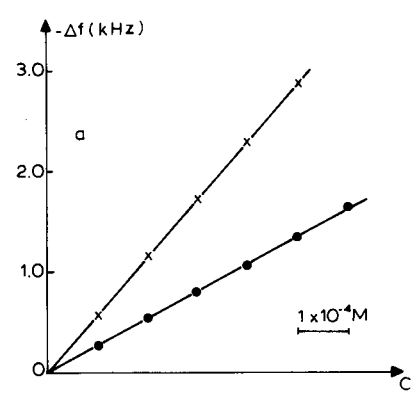

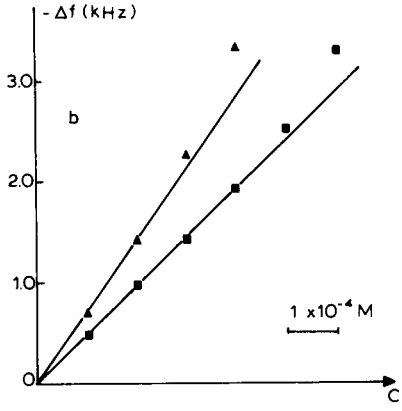

Fig. 5. Linear relationships between frequency shift and concentration. (a) NaCl. ● = 2×10^{-4} M sodium chloride background; × = 1.5×10^{-3} M sodium hydroxide background. (b) NaOH. ■ = 2×10^{-4} M sodium hydroxide background; ▲ = 2×10^{-3} M sodium chloride background.

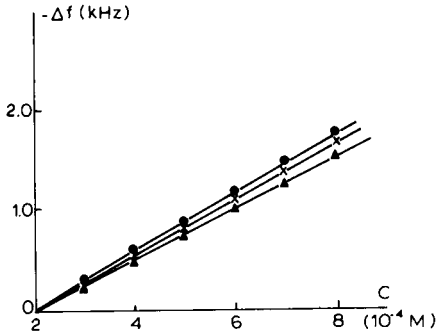

Fig. 6. Influence of distance, d, on NaCl (calibration). ▲ = < 0.5 mm; × = 0.5 mm; ● = 1.5 mm. 2×10^{-4} M NaCl background.

It was found that the greater the distance between the rod electrode and the silver-coated electrode of the crystal, the higher is the oscillating frequency. Figure 6 indicates that an increase in the distance, d, is slightly advantageous for improving the response sensitivity. However, the effect is small, i.e., the cell constant does not influence the slope of the frequency shift significantly. Hence the measurement shows little dependence on the distance, d, if the change is not too large (0.5–1.5 mm). An increase in this distance, however, eventually makes the resonant frequency unstable, and may even cause the resonator not to oscillate (e.g., more than 3 mm in water). The suitable distance between the piezoelectric crystal and the separated electrode was selected as 0.5 mm and was maintained in all subsequent experiments.

Simultaneous determination of atropine sulphate and sodium chloride

Similarly to the normal PQC resonator, the frequency shift (Δf) of PCSE varies linearly with the change in specific conductance ($\Delta\kappa$) over a limited concentration range, as has been discussed:

$$\Delta f = S_c \Delta\kappa \tag{2}$$

where S_c is the sensor sensitivity for the specific conductance. Denoting the equivalent concentration as C_i and equivalent conductance as λ_i, Eqn. 2 becomes

$$\Delta f = \frac{S_c}{1000} \sum_i \Delta C_i \lambda_i \tag{3}$$

In the general experimental case, the value of S_c is about 2×10^5 Hz Ω m, greater than the slope of a normal PQC.

If an acid, HA, whose dissociation constant is not very small is added to a large amount of base (BOH), the frequency shift resulting from the change of conductance is

$$\Delta f = S(l_{A^-} - l_{OH^-})C_{HA} \tag{4}$$

l is the equivalent ionic conductance. For n acids, then

$$\Delta f = S \sum_{i=1}^{n} (l_{A_i^-} - l_{OH^-})C_{HA_i} \tag{5}$$

Atropine sulphate $[(C_{17}H_{23}NO_3)_2 \cdot H_2SO_4 \cdot H_2O]$ is a belladonna alkaloid. As an antispasmodic anticholine drug, it is widely used in clinical treatment. There are many methods for its determination, including non-aqueous titrimetry [12].

Guttae atropini sulphatis is a hospital preparation in common use, sodium chloride being added to obtain an isotonic solution. The stability of atropine sulphate is dependent on the solution pH. In alkaline solution, the atropine will dissociate:

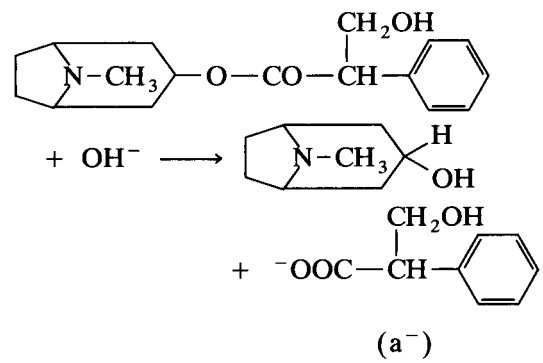

This is a second-order reaction. For simplification, a large excess of base is used, making the reaction quasi-first order. Also, the large amount of base in solution acts as a background electrolyte. This is advantageous for the PCSE sensor because it makes the response of the frequency shift of the sensor more sensitive and linear.

At a certain temperature, the kinetic equation of the quasi-first-order reaction is

$$C(t) = C_0\, e^{-kt}$$

Hence, for atropine sulphate, the frequency shift that changes with time in basic solution is

$$\Delta f_1(t) = S[(l_{OH^-} - l_{a^-})C_0 \, e^{-kt} + l_{a^-}C_0 - l_{OH^-}C_0] = S_1(t)C_0 \quad (6)$$

where C_0 is the initial concentration of atropine sulphate and k is the rate constant (independent on the concentration).

For sodium chloride, the frequency shift is

$$\Delta f_2 = S[(l_{Na^+} + l_{Cl^-})C_{NaCl}] = S_2C_{NaCl} \quad (7)$$

Hence the total frequency change Δf is

$$\Delta f = \Delta f_1(t) + \Delta f_2 = S\{[(l_{OH^-} - l_{a^-})\, e^{-kt} + l_{a^-} - l_{OH^-}]C_0 + (l_{Na^+} + l_{Cl^-})C_{NaCl}\} = S_1(t)C_0 + S_2C_{NaCl} \quad (8)$$

With progress of the reaction, $\Delta f_1(t)$ changes with time, but Δf_2 does not. Therefore, quantitative difference information on atropine sulphate and sodium chloride can be obtained through recording the frequency shift response at different times, then carry out the simultaneous determination of the two components by a suitable calibration technique.

The relationship between the response of the frequency shift and the reaction time when various concentrations of atropine sulphate were added to excess of sodium hydroxide is shown in Fig. 7. On account of the consumption of OH^- by the scopolic acid produced in the hydrolysis, the osillation frequency of PCSE increases with reaction time. The shapes of the curves at different concentrations all approximate to first-order decay graphs. Also, the frequency shifts at different times are proportional to initial concentration. Hence the selective determination of atropine sulphate in the mixture could be carried out conveniently by linear calibration. This method can remove the interference of non-hydrolysable substances. Figure 8 shows the plots of frequency shift against reaction time for atropine sulphate and sodium chloride. The two linear response models are obviously different. Moreover, the curve for the frequency shift of the mixed solution is the sum of the frequency shifts of two components, indicating that the response of the sensor to the specific conductance of the solution possesses linear additability.

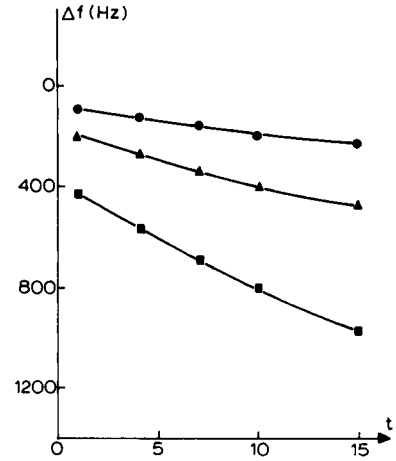

Fig. 7. Frequency shift of PCSE for different concentrations of atropine sulphate at different times (min). ● = 0.01 mM; ▲ = 0.02 mM; ■ = 0.04 mM.

Sample analysis

Nine mixed solutions of atropine sulphate and sodium chloride of various concentration were

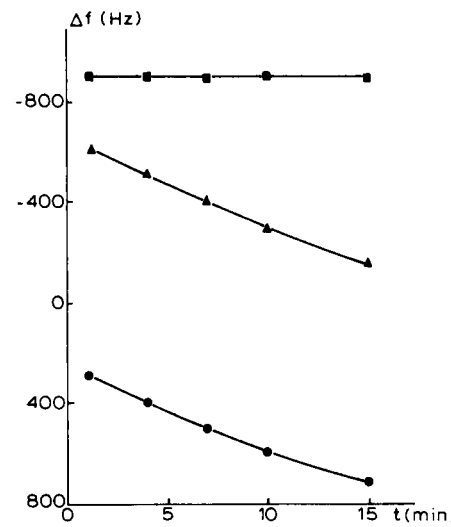

Fig. 8. Frequency shift patterns for atropine sulphate and sodium chloride. ● = 0.03 mM atropine sulphate; ■ = 0.15 mM sodium chloride; ▲ = sum of 0.03 mM atropine sulphate and 0.15 mM sodium chloride.

TABLE 1

Regression coefficients of [P] matrix

t (min)	1	4	7	10	15
A [a]	−1.148	−0.572	+0.158	+0.825	+1.364
B [a]	−2.001	+0.152	−2.447	+3.755	−0.089

[a] A = atropine sulphate; B = sodium chloride.

TABLE 2

Multivariate determination of atropine sulphate and sodium chloride [a]

Sample No.	Actual concentration (10^{-5} M)		Found concentration (10^{-5} M)		Relative error (%)	
	A	B	A	B	A	B
1	1.00	10.00	0.97	10.05	−3.01	0.50
2	1.50	6.00	1.52	6.28	0.97	4.72
3	2.50	5.00	2.63	4.90	5.12	−1.99
4	3.00	4.00	2.81	4.14	−6.33	3.43
5	2.00	5.00	1.91	4.86	−4.47	−2.72
Average					3.98	2.67

[a] A = atropine sulphate; B = sodium chloride.

prepared as a calibration set. The frequency shift responses were determined according to the measurement procedure. The coefficients of the matrix which was evaluated based on Eqn. 1 are listed in Table 1. Five other mixed solutions containing 1×10^{-5}–3×10^{-5} M atropine sulphate and 4×10^{-5}–10×10^{-5} M sodium chloride were prepared as unknown samples and measured under the same experimental conditions.

The predicted concentration results are given in Table 2. The average relative errors are 4.0% for atropine sulphate and 2.7% for sodium chloride. The lowest concentration that can be determined with the PCSE device is 1×10^{-5} M, which is much lower than is possible with the normal PQC [4].

Conclusion

The simultaneous determination of atropine sulphate and sodium chloride can be carried out with the proposed piezoelectric sensor (PCSE) using an MLR calibration method. It shows a higher sensitivity to specific conductance than the normal PQC. This type of PCSE does not need complex flowing devices, in contrast to others that have been reported [5,6,8], so it is much simpler to operate. This PCSE, immersed in solution like a normal unmodified PQC, can also be used in frequency titrations, for example, and should have wider applications.

This work was supported by the Natural Science Foundation and the Education Commission Foundation of China.

REFERENCES

1 W.P. Carey, K.R. Beebe and B.R. Kowalski, Anal. Chem., 59 (1987) 1529.
2 S.M. Chang, Y. Iwasaki, M. Suzuki, I. Karube and H. Muramatsu, Anal. Chim. Acta, 249 (1991) 323.
3 W.Z. Wei, Z.H. Mo and S.Z. Yao, Anal. Chim. Acta, 251 (1991) 143.
4 W.Z. Wei, L.H. Nie and S.Z. Yao, Anal. Chim. Acta, 263 (1992) 77.
5 T. Nomura and F. Tanaka, Bunseki Kagaku, 39 (1990) 773.
6 T. Nomura, F. Tanaka, T. Yamada and H. Itoh, Anal. Chim. Acta, 243 (1991) 273.
7 T. Nomura and K. Takada, Bunseki Kagaku, 40 (1991) 567.
8 T. Nomura, T. Yanagihara and T. Mitsui, Anal. Chim. Acta, 248 (1991) 329.
9 T.A. Zhou, L.H. Nie and S.Z. Yao, J. Electroanal. Chem., 293 (1990) 1.
10 T. Nomura and T. Nagamune, Anal. Chim. Acta, 155 (1983) 231.
11 S.Z. Yao and Z.H. Mo, Anal. Chim. Acta, 193 (1987) 97.
12 Pharmaceutical Analysis, Pharmaceutical Institute of Nanjin, Nanjin, 1981.

Analytica Chimica Acta, 282 (1993) 543–550
Elsevier Science Publishers B.V., Amsterdam

Flow-injection derivative Fourier transform infrared determination of methyl *tert*-butyl ether in gasolines

Miguel de la Guardia, Máximo Gallignani and Salvador Garrigues

Department of Analytical Chemistry, University of Valencia, 50 Dr. Moliner Street, 46100 Burjassot, Valencia (Spain)

(Received 1st April 1993; revised manuscript received 2nd June 1993)

Abstract

A procedure was developed for the flow-injection Fourier transform (FT) infrared spectrometric determination of methyl *tert*-butyl ether (MTBE) in unleaded gasolines. The method is based on the use of first-order derivative measurements in a flow system. The experimental procedure requires only the dilution of samples with hexane and the injection of a 320-μl volume into a carrier flow of hexane. The FT-IR spectra are continuously recorded and the first-order derivative obtained. The flow-injection peaks are established from the variation with time of the $dA/d\bar{\nu}$ values found between 1209 and 1201 cm^{-1}. Using a micro flow cell with a 0.117 mm path length and a carrier flow-rate of 0.45 ml min^{-1}, the limit of detection of the method corresponds to 0.035% (v/v). The recovery of MTBE varies from 98.2 to 102% and the relative standard deviation is 0.6% for samples containing 0.8% (v/v) MTBE. Results obtained in the analysis of real unleaded gasoline samples compare well with those found by gas chromatography.

Keywords: Infrared spectrometry; Flow injection; Derivative spectroscopy; Gasoline; Methyl *tert*-butyl ether

The development of flow-injection (FI) procedures for the analysis by infrared (IR) spectrometry, and especially Fourier transform (FT) IR spectrometry, has helped to solve some of the main problems [1–3] of quantitative determinations by FT-IR methods. The use of FI–FT-IR decreases the consumption of reagents, provides rapid sampling and easy cleaning of the flow cell, permits the continuous monitoring of the baseline of spectra and enhances the simultaneous determination of several components in the same sample [4–13].

However, the determination of organic compounds in complex matrices suffers from serious limitations owing to the overlapping of absorbance bands, which prevents the direct determination of a series of compounds and causes strong matrix interferences.

The use of derivative techniques in spectrometry has opened up new possibilities for the resolution of mixtures and compensation for matrix interferences [14–17]. Several methods have been developed in derivative IR spectrometry [18,19].

Methyl *tert*-butyl ether (MTBE) is an anti-knock agent commonly employed in unleaded gasolines. The additive is frequently determined by gas chromatography (GC) in gasolines [20–25], in synthetic products [26] and in estuarine waters and sediments [27]. Spectrometric techniques have also been employed for the determination of MTBE in gasolines. A nuclear magnetic resonance spectrometric method, which provides a detection limit of 0.1% (v/v), has been developed [28], and a near-infrared method has been applied to the direct measurement of MTBE in gasolines with an associated standard error of

Correspondence to: M. de la Guardia, Department of Analytical Chemistry, University of Valencia, 50 Dr. Moliner Street, 46100 Burjassot, Valencia (Spain).

0.1% (v/v) by using the second overtone near-IR region [29].

Only one reference was found to the FI-IR determination of MTBE, namely a batch method for determination of MTBE in gasolines based on direct absorbance measurement at 851 cm^{-1} by using attenuated total reflectance, which provides poor sensitivity and a relative standard deviation between 1 and 1.6% for the analysis of samples containing 7% (v/v) of MTBE [30].

The aim of this work was to develop a procedure for the direct determination of MTBE in gasolines by FI–derivative FT-IR spectrometry.

EXPERIMENTAL

Apparatus and reagents

A Perkin-Elmer Model 1750 Fourier transform infrared spectrometer, with an FR-DTGS temperature-stabilized coated detector and equipped with a Series 7700 data station, was employed for absorbance measurements, with a nominal resolution of 4 cm^{-1}, using a Specac (Orpington, UK) micro flow cell with KBr windows and a path length of 0.117 mm.

The manifold employed for FI measurements and for stopped-flow experiments was essentially the same described previously for the determination of carbaryl in pesticide formulations [13] and benzene [11] in gasolines.

Analytical-reagent grade MTBE supplied by Repsol (Cartagena, Spain) and hexane from Panreac (Barcelona, Spain) were used as received.

Software

A series of computer programs were developed in order to carry out FI measurements and the software package developed for the continuous monitoring of the absorbance spectra, as a function of time, has been described previously [9,12]. This previous software was modified in order to obtain and store the peak-height absorbance values, taking into account the selected baseline and the exact position of the absorbance maxima, and to determine the derivative spectra and establish the corresponding FI peaks in the derivative mode.

The second part of the software was developed for this study and from the program CALCULAR.oy (written in OBEY). It combines the possibilities of the data station to carry out the mathematical treatment of the IR spectra and those of the developed software to select and store the IR data. The data obtained by this modified program (at present called PROCESS.oy) are employed in the program FIAGRAMA.bas (written in BASIC) to record, as a function of time, the derivative values of the absorbance spectra, in a similar way to that described previously [9] for zero-order spectra.

General procedure

To develop the FI–FT-IR procedure, the IR spectra of real gasoline samples and standard solutions of MTBE in hexane were studied in the range 1350–800 cm^{-1}, carrying out direct absorbance measurements in the zero-order and different derivative order modes to obtain the most appropriate conditions for the determination of MTBE in gasolines without any sample pretreatment. Subsequently effect of flow-injection parameters was studied in order to determine the analytical figures of merit under the most convenient conditions. Several experiments were also carried out in the stopped-flow mode in order to improve the limit of detection by means of the accumulation of a series of spectra.

FI derivative FT-IR analysis

Dilute 10 ml of gasoline to 25 ml with hexane and inject 320 μl of this solution into a 0.45 ml min^{-1} carrier stream of pure hexane. Solutions of MTBE in hexane, in a concentration range from 0.035 to 1.5% (v/v) and containing also 40% (v/v) of a leaded gasoline without MTBE, were employed as standards. Record the FT-IR spectra of samples and standards, using a nominal resolution of 4 cm^{-1} between 1350 and 800 cm^{-1}, calculate the first-order derivative and determine the derivative values between 1209 and 1201 cm^{-1}. From these data construct the FI peaks for each solution. Determine the peak heights and, from the measurement obtained for standards, adjust the corresponding calibration line by the

least-squares method. Interpolate the peak-height values of samples in the above regression line.

MTBE standards in pure hexane provide, in the derivative mode, a calibration line similar than that obtained in the presence of a leaded gasoline matrix, so this kind of standard can also be employed.

Alternatively, gasoline samples were analysed by using the zero-order absorbance spectra, working at 1088 cm^{-1} with a baseline established between 1154 and 985 cm^{-1}, both directly and by the standard addition method. In the latter instance, known volumes of a stock solution of 5% (v/v) MTBE in hexane were added to 5-ml volumes of gasoline and the volume was completed to 25 ml with hexane.

Gas chromatographic analysis

Using the ASTM procedure [20], commercial samples of gasoline were analyzed by an independent laboratory (British Petroleum, Castellón, Spain).

The standard test method consists of in adding *tert*-amyl alcohol, as an internal standard, to the gasoline samples, which are then injected (3 μl) into a gas chromatograph equipped with a polar 1,2,3-tris-2-cyanoethoxypropane (TCEP) liquid-phase column, a non-polar wall-coated open tubular methylsilicone capillary column and a column-switching valve.

RESULTS AND DISCUSSION

FT-IR spectra of MTBE

Figure 1 shows the transmittance spectrum of a film of pure MTBE compared with the spectrum of hexane. The additive shows a series of well defined bands in the wavenumber range 1350–800 cm^{-1}, so these bands could be employed for the determination of MTBE in paraffinic solutions. However, when the spectra of different types of gasolines are recordered in the above-mentioned wavenumber range (see Fig. 2), strong matrix interferences can be seen.

Figure 3 demonstrates that the absorbance spectra of hexane solutions containing MTBE, measured in a micro flow cell with a spacer of

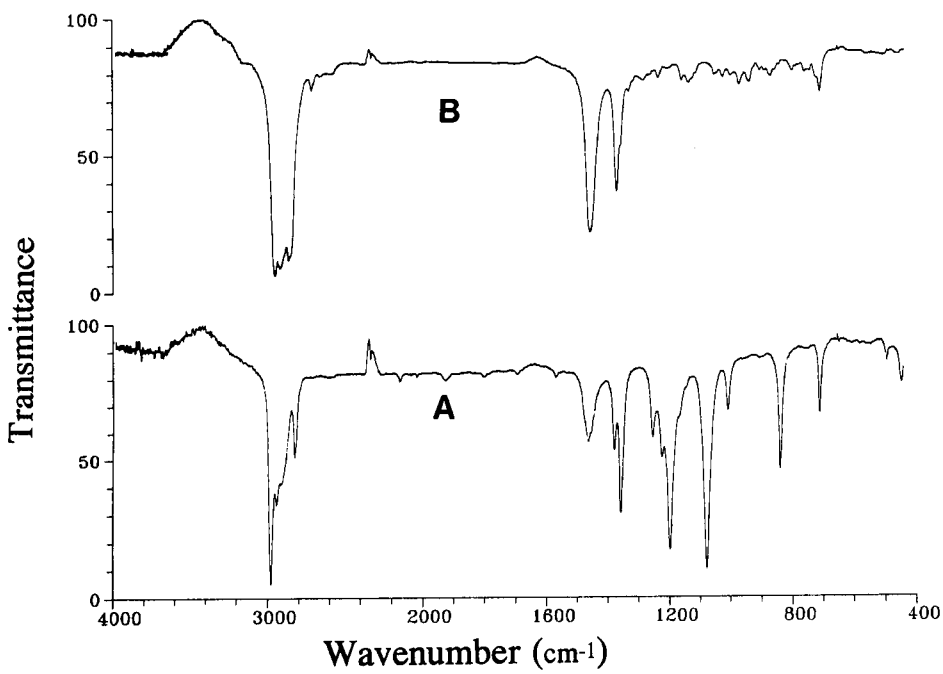

Fig. 1. Transmittance spectra, obtained in film for (A) pure MTBE and (B) hexane.

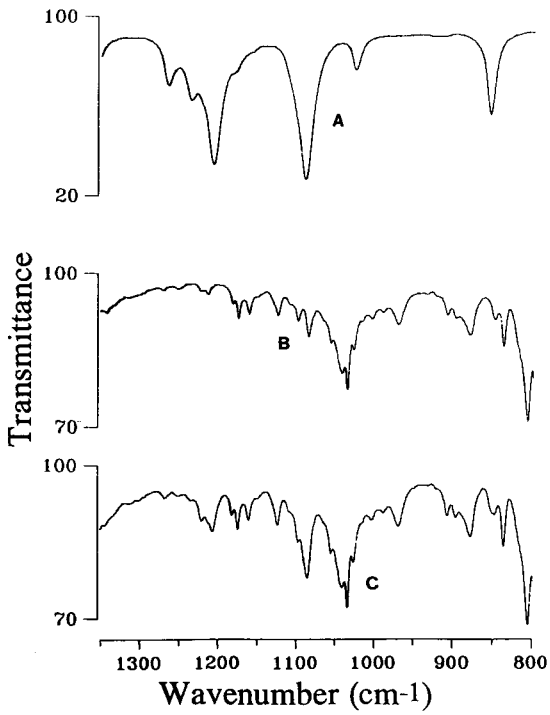

Fig. 2. Transmittance spectra of (A) MTBE, (C) a gasoline sample containing MTBE and (B) a gasoline without MTBE. All the spectra were obtained in film.

0.117 mm, provides two strong bands at 1205 and 1088 cm^{-1} and a less intense band at 853 cm^{-1}. These bands overlap the matrix bands (see the spectrum of a leaded gasoline without MTBE), but could be employed to determine the additive in real gasoline samples, as can be seen in Fig. 4. Figure 4 shows the spectra of a 1% (v/v) MTBE in hexane solution, a hexane solution of a real gasoline sample containing MTBE and the same sample fortified with an additional concentration of MTBE, and it can be seen that probably an appropriate selection of the spectral baseline and the use of the standard addition technique could provide good results in the analysis of real gasolines.

Direct determination of MTBE in gasolines

Attempts were made to determine MTBE in real gasoline samples by using the highest sensitivity band, at 1088 cm^{-1}. Volumes of 320 μl of different standards of pure MTBE in hexane (from 0.035 to 1.5%, v/v) were injected into a hexane carrier flow of 0.45 ml min^{-1} and the absorbance at 1088 cm^{-1} was recordered as a

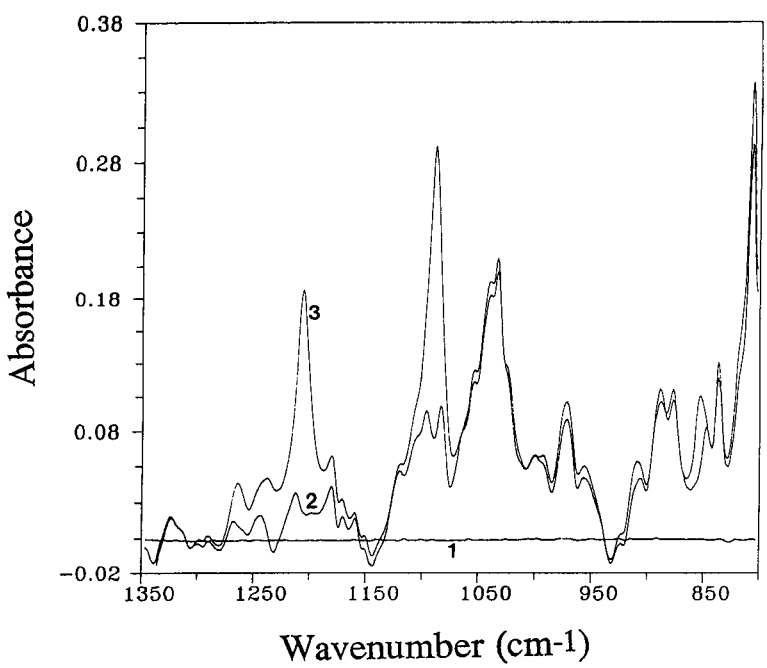

Fig. 3. Absorbance spectra, obtained in a micro flow cell with a 0.117-mm spacer, of: (1) hexane and 40% (v/v) gasoline in hexane solutions both (2) without and (3) with MTBE.

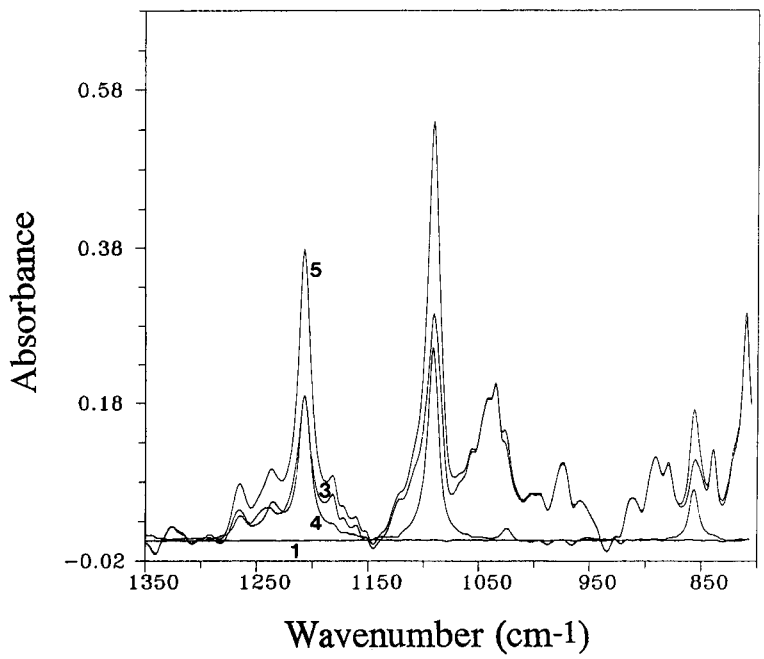

Fig. 4. Absorbance spectra of (4) a 1% (v/v) MTBE solution in hexane, (3) a 40% (v/v) gasoline solution and (5) the same solution of gasoline fortified with an additional 1% (v/v) of MTBE. Reference: hexane (1).

function of time. A baseline between 1154 and 985 cm^{-1} was employed.

The least-squares fitting of the absorbance values (A) versus MTBE concentration [C (%, v/v)] provides the following regression line:

$$A = 0.0018 + 0.2510C$$

with a regression coefficient $R = 0.99989$ ($n = 7$), which is similar to that obtained by the standard addition method for the analysis of an unleaded sample:

$$A = 0.300 + 0.2536C$$

However, analysis of a sample containing 1.78% (v/v) MTBE gave a result of 2.94% (v/v) by the direct procedure and 2.90% (v/v) by the standard addition method, indicating that the band at 1088 cm^{-1} is strongly affected by spectral interferences from the matrix. Similar results were obtained when the same study was carried out at 1205 cm^{-1} using different baselines. On the other hand, low values of MTBE in leaded gasolines (which do not contain the additive) were obtained by direct FT-IR measurements at 1088 and 1205 cm^{-1}, also indicating the presence of spectral interferences from the matrix.

For the band at 853 cm^{-1}, the following calibration line could be established:

$$A = 0.000_5 + 0.0645C$$

which shows a considerably decreased sensitivity and makes it necessary to prepare standard solutions of MTBE in a leaded gasoline matrix (not containing MTBE) in order to define an appropriate baseline between 865 and 840 cm^{-1}.

By using the above-mentioned calibration line, values of the same order as the real values ones could be obtained for unleaded gasolines. A concentration of 0.38% (v/v) was obtained for a gasoline sample actually containing 0.46% (v/v) of MTBE.

Derivative spectra of MTBE

Figure 5 shows the zeroth-, first-, second-, third- and fourth-order derivative absorbance spectra of a 40% (v/v) solution in hexane of a gasoline without additive, a 1% MTBE solution

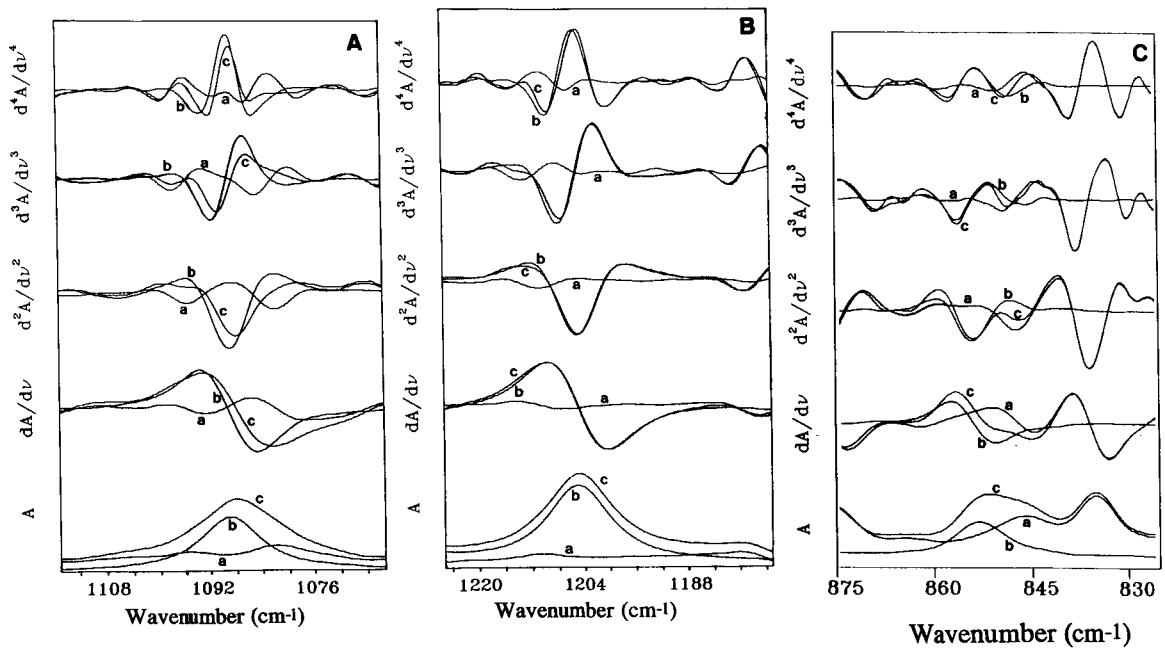

Fig. 5. Zeroth-, first-, second-, third- and fourth-order derivative spectra of MTBE at (A) 1088, (B) 1205 and (C) 853 cm^{-1}. Spectra (a) correspond to a real matrix of leaded gasoline diluted 40% (v/v) in hexane, spectra (b) were obtained for 1% (v/v) MTBE in hexane solutions and spectra (c) for the same solutions in the presence of 40% (v/v) of a real gasoline not containing the additive.

in hexane and the same solution in the presence of a 40% (v/v) real gasoline matrix and it can be seen that the matrix strongly affects the most important bands of MTBE (1088 and 1205 cm^{-1}). However, the use of derivatives provides greater similarity between MTBE signals both in the presence and absence of the matrix, especially at the 1205 cm^{-1}. Therefore, for the direct determination of MTBE in real gasolines, the use of the first-order derivative spectra at 1205 cm^{-1} can be recommended. For the band at 853 cm^{-1} poorer results were found (see Fig. 5C) owing to the low sensitivity of the MTBE determination at this wavenumber.

All the spectra in Fig. 5 correspond to the same concentration of MTBE and the sequence of the different order derivative spectra indicates that the spectrometer changes the ordinate scale, in order to compensate for the loss of sensitivity caused by the use of derivatives. However, there is an increase in noise, as evidenced by the signals obtained for blank solutions. Hence, it is preferable to use low derivative orders for the determination of MTBE by FT-IR spectrometry.

In this study, peak-to-peak measurement between 1209 and 1201 cm^{-1} in the first-order derivative spectra was selected, which permits an analytical sensitivity comparable to that obtained by using zero-order absorbance values to be obtained.

Effect of the derivative window on the FT-IR determination of MTBE

To work in the derivative mode it is necessary to select the derivative window of the spectrometer. As can be see in Fig. 6, the increase in the size of the window provides a decrease of sensitivity and this parameter must be optimized. A sensitivity value (expressed as the slope of the calibration line) of 0.3518 "derivative units" per % (v/v) of MTBE was found for a derivative window of five points. Under the same conditions a limit of detection of 0.035% (v/v) for MTBE and a relative standard deviation of 0.6%, for five independent measurements of a sample containing 0.8% (v/v) of MTBE, were found.

The above figures of merit compare well with those obtained by direct measurement of the

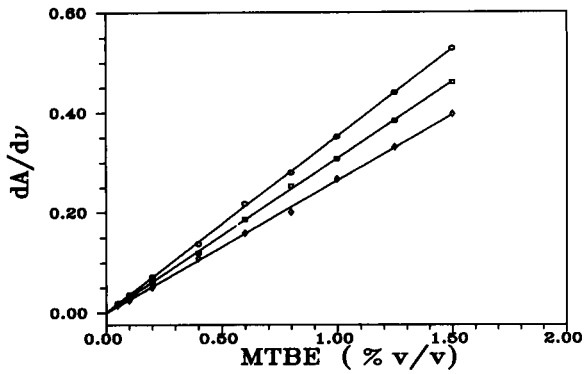

Fig. 6. Effect of the derivative window on the calibration lines obtained for the derivative spectra of MTBE solutions. Windows values of (○) 5, (□) 9 and (◇) 13 data points were assayed for a reading interval of 1 cm^{-1} and a resolution of 4 cm^{-1}.

absorbance at 1205 cm^{-1}, because in this instance a sensitivity of 0.1881 absorbance per % (v/v) and a limit of detection of 0.025% were found.

To check the accuracy of the derivative FT-IR determination of MTBE, the recovery of MTBE added to leaded gasolines not containing the additive was measured. The results in Table 1 indicate that the method provides a recovery between 98.2 and 101.2%.

FI–derivative FT-IR determination of MTBE in real gasoline samples

Based on the above, the first-order derivative FT-IR spectra measured between 1209 and 1201 cm^{-1} can be selected for the determination of MTBE in gasoline using hexane as the carrier and diluent of samples. The FI parameters were chosen in the same way as in previous studies [9–13] in order to obtain a good sensitivity and a high sample throughput.

TABLE 1

Recoveries of MTBE obtained by the derivative FT-IR analysis of gasoline samples

MTBE added (%, v/v)	MTBE found (%, v/v)	Recovery (%)
0.400	0.395	98.8
0.800	0.810	101.2
1.200	1.180	98.3

TABLE 2

Results obtained for the GC and FI–derivative FT-IR analyses of commercial gasoline samples for MTBE

Sample No.	MTBE found (%, v/v)	
	GC	FT–derivative FT-IR [a]
1	0.38	0.39 ± 0.02
2	1.78	1.77 ± 0.03
3	0	Below detection limit
4	0.82	0.83 ± 0.01
5	0	Below detection limit
6	4.4	4.6 ± 0.1

[a] Mean ± S.D. ($n = 5$).

An injection volume of 320 μl assumes only an 8% decrease in the sensitivity obtained when working in the batch mode. The use of a carrier flow-rate of 0.45 ml min^{-1} provides a 45 injections per hour sample throughput. Under these conditions each FI peak can be defined from three FT-IR spectra (taking into account that the instrument employed permits only one spectrum to be obtained and stored every 19 s).

Under the above conditions, and using the procedure described under Experimental, a series of real gasolines samples were analysed. Table 2 summarizes the results obtained by the proposed FI–derivative FT-IR method and also those obtained for the GC determination of MTBE, carried out by a control laboratory in the petroleum industry. As can be seen, the developed procedure provides the same results as the ASTM GC procedure [20].

A typical equation of the calibration line obtained by FI–FT-IR is

$$dA/d\bar{r} = 0.000_1 + 0.3524C$$

with a regression coefficient $R = 0.9998$ ($n = 7$) when standards were prepared in hexane and

$$dA/d\bar{r} = 0.000_2 + 0.3518C$$

with a regression coefficient $R = 0.9998$ ($n = 7$) when standards were prepared in leaded gasoline not containing MTBE.

In order to improve the limit of detection of the FI–derivative FT-Ir determination of MTBE, a series of experiments were carried out in the stopped-flow mode. Under these conditions good

calibration lines were obtained with a typical equation

$$dA/d\bar{r} = 0.000_4 + 0.3830C$$

with a regression coefficient $R = 0.9998$ ($n = 7$), which provides a small increase in sensitivity and a limit of detection of 0.025% (v/v), which is lower than that obtained in the FI mode. Under these conditions the relative standard deviation for five measurements of a sample containing 0.8% (v/v) of MTBE was 0.2%.

Máximo Gallignani acknowledges a grant from the Agencia Española de Cooperación Internacional for carrying out PhD studies in Spain and financial support from Los Andes University and CONICIT (Venezuela). Salvador Garrigues acknowledges a grant from the Conselleria de Cultura, Educació i Ciència de la generalitat Valenciana for carrying out PhD studies.

REFERENCES

1 J.R. Ferraro and J.R. Barrle (Eds.), Fourier Transform Infrared Spectroscopy, Academic, New York, 1982.
2 P.R. Griffiths and J.A. De Haseth, Fourier Transform Infrared Spectrometry (Chemical Analysis, Vol 83), Wiley, New York, 1986.
3 R.A. Nyquist, M.A. Leugers, M.L. Mc Kelvy, R.R. Papenfuss, C.L. Putzig and L. Yurga, Anal. Chem., 62 (1990) 223R.
4 D.J. Curran and W.G. Collier, Anal. Chim. Acta, 177 (1985) 259.
5 S.V. Olesick, S.B. French and M. Novotny, Anal. Chem., 58 (1986) 2256.
6 D.K. Morgan, N.D. Danielson and J.E. Katon, Anal. Lett., 8 (1988) 1979.
7 B.E. Miller, N.D. Danielson and J.E. Katon, Appl. Spectrosc., 42 (1988) 401.
8 M. Guzmán, J. Ruzicka, G.D. Christian and P. Shelley, Vibr. Spectrosc., 2 (1991) 1.
9 M. de la Guardia, S. Garrigues, M. Gallignani, J.L. Burguera and M. Burguera, Anal. Chim. Acta, 261 (1992) 53.
10 S. Garrigues, M. Gallignani and M. de la Guardia, Analyst, 117 (1992) 1849.
11 M. Gallignani, S. Garrigues and M. de la Guardia, Anal. Chim. Acta, 274 (1993) 267.
12 S. Garrigues, M. Gallignani and M. de la Guardia, Talanta, 40 (1992) 89.
13 M. Gallignani, S. Garrigues, A. Martínez-Vado and M. de la Guardia, Analyst, (1993) in press.
14 R.N. Hager, Anal. Chem., 45 (1973) 1131A.
15 A.F. Fell, Anal. Proc., 15 (1978) 260.
16 J.N. Miller, T.A. Ahmad and A.F. Fell, Anal. Proc., 19 (1982) 37.
17 F. Sánchez Rojas, C. Bosch Ojeda and J.M. Cano Pavón, Talanta, 35 (1989) 753.
18 J.G. McWilliams, Anal. Chem., 41 (1969) 674.
19 P. Paseiro Losada, J. Simal Lozano and J. Simal Gandara, J. Assoc. Off. Anal. Chem., 73 (1990) 632.
20 ASTM Standards, D-4815-89, American Society for Testing and Materials, Philadelphia, 1989.
21 G.R. Verga, A. Sironi, W. Schneider and F.C. Frohne, J. High Resolut. Chromatogr. Chromatogr. Commun., 11 (1988) 248.
22 E.A. McNamara, S.A. Montzka, R.M. Barkley and R.E. Sievers, J. Chromatogr., 452 (1988) 75.
23 D. Steinmueller, Am. Lab., 21 (1989) 120.
24 F.P. Di Sanzo, J. Chromatogr. Sci., 28 (1990) 73.
25 N. Orlowska, Przem. Chem., 70 (1991) 270.
26 H. Gu and B. Wang, Sepu, 6 (1988) 226.
27 A. Bianchi, M.S. Varney, J. High Resolut. Chromatogr., 12 (1989) 184.
28 A. Galtieri and C. Vecchi, Riv. Combust., 43 (1989) 171.
29 B. De Simas and L. Lane, Adv. Instrum. Control. 45 (1990) 451.
30 E.F. Daton, F.P. Fuller, F.T. White and R.D. Battiste, Anal. Chem., 55 (1983) 408.

Analytica Chimica Acta, 282 (1993) 551–557
Elsevier Science Publishers B.V., Amsterdam

Determination of morphine in process streams using flow-injection analysis with chemiluminescence detection

Neil W. Barnett and Douglas G. Rolfe

School of Biological and Chemical Sciences, Deakin University, Geelong, Victoria 3217 (Australia)

Tim A. Bowser and T. Walter Paton

Process Development Department, Glaxo Australia-Chemicals Division, Port Fairy, Victoria 3284 (Australia)

(Received 24th May 1993)

Abstract

Flow analysis methodology is presented for the determination of morphine in process streams. Detection is achieved by monitoring the resultant chemiluminescence (CL) emission from the reaction of morphine and acidic potassium permanganate in the presence of tetraphosphoric acid. Calibration graphs are linear over two orders of magnitude of concentration with a detection limit (3:1 signal-to-noise ratio) of 5×10^{-8} M and relative standard deviation of 0.4% at 1.4×10^{-4} M. Interferences from other alkaloids in the extract are negligible due either to lack of CL response or to low concentrations of the concomitants. Some discussion regarding the nature of the emitting species is presented based on CL spectra from morphine and other structurally related alkaloids. The analytical results obtained on process samples compared most favourably with results from a validated liquid chromatographic method.

Keywords: Chemiluminescence; Flow injection; Morphine

Analytical interest in chemiluminescence (CL) has increased considerably in the last few years as shown in the review of CL by Townshend [1] which indicated the selectivity and sensitivity possible with this mode of detection. It has been assumed that the oxidation of morphine to its dimer (pseudomorphine) directly produces CL, with the use of acidic permanganate and tetraphosphoric acid giving the greatest intensity [1,2]. Abbott et al. [2] employed this reaction with flow-injection analysis (FIA) to produce a screening method for forensic purposes.

Morphine is extracted from *Papaver somniferum* (opium poppies) by a proprietary process involving a series of alkaline, acidic and solvent extraction procedures. Two aqueous process streams were studied and are designated here as extract A and extract B. Control of the concentration of morphine in these process streams influences directly manufacturing capacity and efficiency. Therefore rapid measurement of the morphine concentration allows adjustment of process control parameters (e.g., extraction ratios, flow-rates) to allow continual system optimisation. Historically the analysis of these streams has been performed using variants of colorimetric techniques [3], radioimmunoassay [4] and liquid chromatography (LC) [5]. On-line analysis has been performed on the above process with segmented flow analysis (SFA) [6] using oxidation of morphine to pseudomorphine followed by fluorescence detection. The disadvantages of this ap-

Correspondence to: N.W. Barnett, School of Biological and Chemical Sciences, Deakin University, Geelong, Victoria 3217 (Australia).

proach are the need for the removal of fluorescent interferences by solvent extraction, long analysis times (20 min per determination), high cost of reagents and the intrinsic limitations of process SFA. The typical aqueous process stream from morphine manufacture presents a number of challenges to the design of a system for on-line analysis. The process liquors are characterised by a pH between 9.0 to 12.6 and a large organic content containing a mixture of organic acids, sugars, as well as complex aromatic and aliphatic species including the presence of other alkaloids related structurally to morphine. The major alkaloids present in extracts of Australian *P. somniferum* are morphine, codeine, thebaine, papaverine, pseudomorphine and oripavine [7] with morphine concentrations typically 100 times greater than the other alkaloids [8].

This paper describes the modification and utilisation of a FIA–CL method [2] for the determination of morphine in aqueous solutions obtained during the full-scale process extraction of alkaloids from *P. somniferum*. Quantitative data are compared with results using established reversed-phase LC methodology [9]. CL emission spectra were recorded for morphine, pseudomorphine and oripavine with a view to elucidating the possible nature of the emitting species.

EXPERIMENTAL

Instrumentation

A simple two-line FIA manifold was employed with no reaction coil required, reagent and carrier solutions were pumped at flow-rates between 1–4 ml min^{-1} by a peristaltic pump (Technicon AA2). Samples and standards were injected into the carrier stream via a six port valve (Waters) with a 100-μl sample loop. PTFE tubing (0.8 mm i.d.) was used to connect the reagent streams to a T-piece with 0.9 mm i.d. The CL emission was detected with a modified Millipore (Waters) Model 420 fluorescence detector with the flow cell and lamp removed and a replacement flow cell consisting of a coil of PTFE tubing placed directly in front of the PMT, as described previously [1,2]. The cell housing was covered to prevent entry of stray light to the PMT. The detector response was recorded on a Millipore (Waters) Model 745 computing integrator. The CL intensity time profile was measured on a modified Beckman DB-G spectrophotometer. The light source was removed, the reference beam blocked and a microswitch added to permit synchronisation of injection time. CL spectra were obtained by continuously pumping solutions of alkaloids (0.1%) and potassium permanganate (1.2×10^{-3} M) in sodium hexametaphosphate solution at pH 1.2 into a mixing T-piece positioned immediately prior to the flow cell of a spectrofluorimeter (Perkin Elmer Model 204A). The respective flow-rates of the two streams were 2.5 ml min^{-1} and 0.7 ml min^{-1}. The spectrofluorimeter was operated with the excitation source shutter closed and in scanning made from 220 nm to 780 nm at 60 nm min^{-1}. The resultant spectra were recorded on a computing integrator (Perkin Elmer 740). ^{31}P NMR measurements were made on a Jeol Model JNM-GX270 FT-NMR spectrometer.

Reagents

Analytical-reagent grade chemicals were used throughout with the exception of sodium hexametaphosphate technical grade (Albright and Wilson, Melbourne). Solutions were prepared in high purity deionised water (Millipore, MilliQ Water System, Bedford, MA). Morphine and other alkaloid standards were obtained from Glaxo Australia and solutions were prepared by dissolving the free base in dilute sulfuric acid and diluting as required. The potassium permanganate solution was kept in a light-tight bottle at a concentration of 6×10^{-4} M and the sulfuric acid carrier solution was maintained at 0.1 M except for the experiments with sodium hexametaphosphate at varying pH values.

RESULT AND DISCUSSION

Preliminary experiments

Approximately 2 ml of various alkaloid solutions (5×10^{-4} M) in tetraphosphoric acid (0.1 M) were injected into test tubes containing 2 ml of potassium permanganate solution (6×10^{-4} M

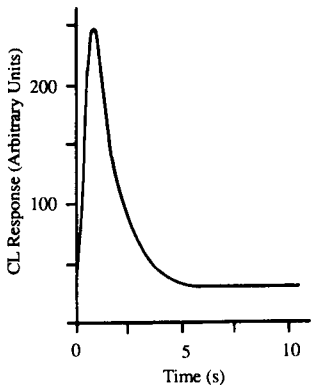

Fig. 1. A typical CL intensity–time profile resulting from the mixing of morphine (5×10^{-4} M) in tetraphosphoric acid (0.1 M) with potassium permanganate (6×10^{-4} M, pH 1.2).

at pH 1.2). This was carried out in a darkened room in order to visually observe any resultant CL emission. A rapid flash of bright red-orange light was observed for morphine, pseudomorphine and oripavine, however no light was seen upon introduction of either codeine or thebaine solutions. These qualitative tests were transferred to the modified Beckman DB-G spectrophotometer so as to investigate the intensity versus time profiles of the CL reactions. Figure 1 shows a typical response for morphine with the maximum occurring around 0.9 s after injection. While less intense, response profiles for the other alkaloids which exhibited CL were similar. To complement the visual observations, CL emission spectra were obtained for morphine, pseudomorphine and oripavine (Fig. 2). The poor signal-to-noise ratio (SNR) characteristics of these spectra result from insufficient damping of the LC pump pulsations. However, within the limits of the SNR the three spectra are essentially the same with respect to wavelength, all exhibiting emission maxima in the range 608 to 611 nm. The magnitude of the change in CL intensities from morphine to oripavine to pseudomorphine is quantified in the following section. The high degree of coincidence of the three spectra shown in Fig. 2 together with the observed kinetic similarity implies that the emitting species in each case is the same or closely related. Tsaplev [10] has shown that acidic potassium permanganate solutions will generate red-orange CL from compounds including ascorbic acid, hydroquinone and *p*-phenylenediamine as well as morphine. Both in this study [10] and in the work of Abbott et al. [2] the presence of Mn^{2+} was shown to enhance the CL resulting from the reaction of morphine with acidic $KMnO_4$ in orthophosphate solution. Tsaplev [10] uses this observation to propose a mechanism for the gen-

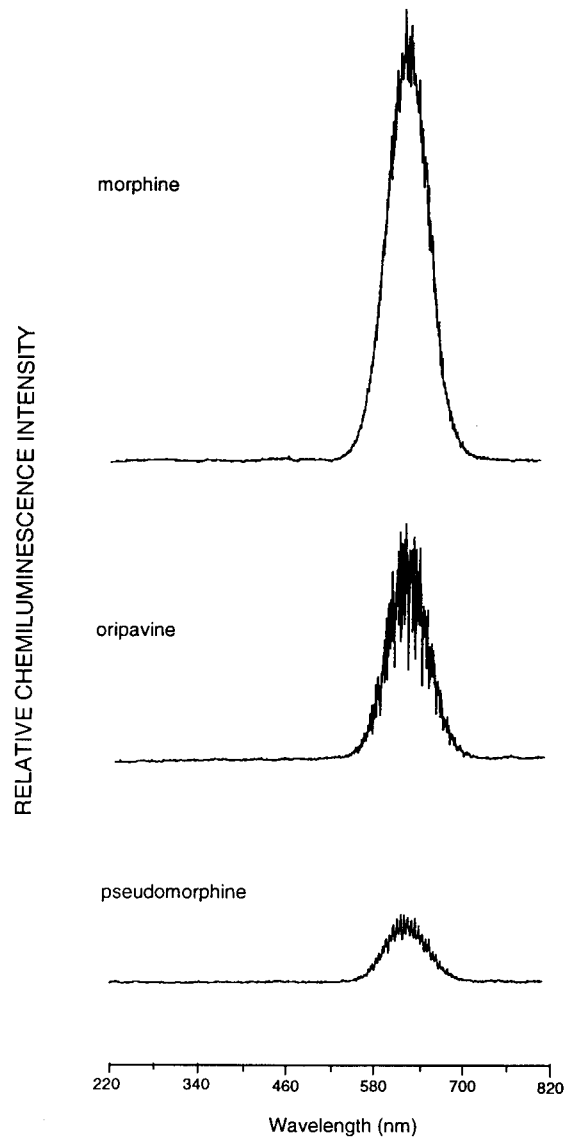

Fig. 2. CL emission spectra of the three alkaloids which gave a positive visual response. All three alkaloid solutions were 0.1% and the spectra were recorded at the same attenuation.

eration of CL that involves the reduction of manganese(III) ions to electronically excited manganese(II) ions which subsequently emit orange photons to return to the ground state. This pathway is not unreasonable since Mn(III) is relatively stable in acidic solution and can be obtained by either oxidation of Mn(II) or reduction of Mn(VII) [11].

We should like to extend this proposed mechanism [10] by considering some common structural features of the molecules studied here and by others [2,10]. Many of the compounds investigated by ourselves and Abbott et al. [2] are structurally related as illustrated below by the six major alkaloids from *P. somniferum* [7] with paparavine being the obvious exception.

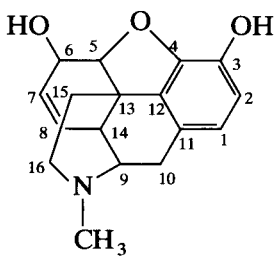

Morphine

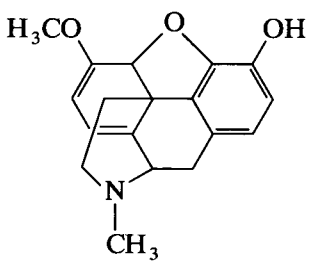

Oripavine

Pseudomorphine is the dimer of morphine joined at carbon-2.

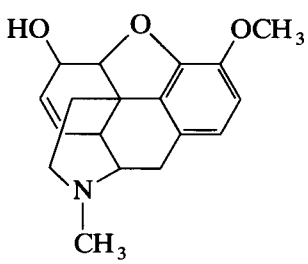

Codeine

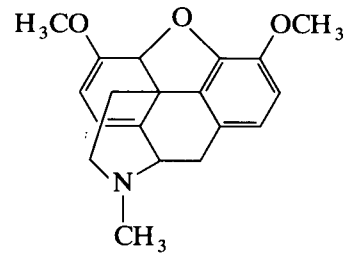

Thebaine

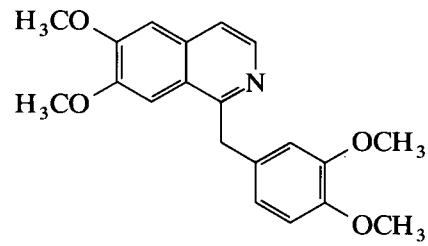

Papaverine

The only molecules which gave analytically useful CL in either the present study or that of Abbott et al. [2] were those possessing the phenolic-OH group at carbon-3 and the furan bridge between carbons-4 and -5.

It is feasible that the manganese(II) may be complexed via the furan and phenolic oxygens; two or three suitable molecules may form the complex. It is known [11] that manganese(II) complexes can be oxidised to manganese(III) species using acidic potassium permanganate. It is our postulate that the manganese(III)–alkaloid complex is subsequently reduced (possibly via the tertiary amine between carbon-9 and -16) to an electronically excited manganese(II) complex which then emits a photon. The proposed pathway is analogous to the generation of CL from the reduction of ruthenium(III) chelates [12]. The computer generated structure of morphine shown in Fig. 3 is instructive for visualising how the Mn^{2+} ion might coordinate with the oxygen atoms thus forming a rigid complex, which is most desirable for all types of luminescence [13]. The variation in CL intensity between compounds (see Fig. 2) probably reflects the relative ease of forming the manganese(II) complex. Given the size of pseudomorphine it is reasonable to expect that it may be sterically hindered in forming a chelate with Mn^{2+} relative to morphine and/or oripavine and this is reflected in the relative FIA

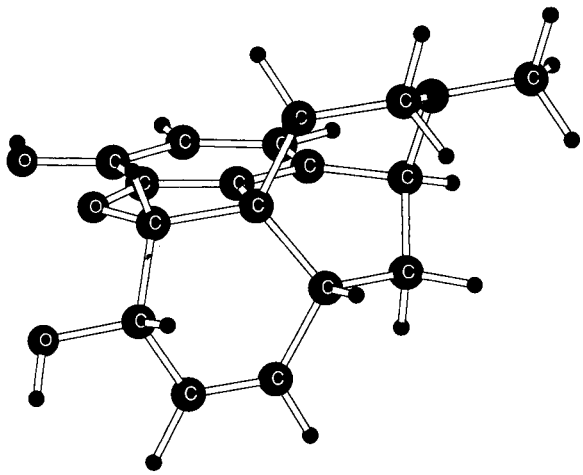

Fig. 3. A computer generated structure of morphine showing the positions of the chelating oxygens and the rigid nature of benzene and furan rings.

responses observed. It is also clear from our study and the work of others [2] that the large "polyphosphate" anions play a role in the generation of CL. However what is not understood is their actual function which may be either as a complexing ligand or as a media organiser (similar to a micelle).

Method development

The geometry of the modified fluorescence detector restricted the positioning of the mixing T-piece (which joined the reagent and carrier tubes) to a minimum distance of 15 mm from the flow cell. CL response for a 3.5×10^{-4} M morphine standard was monitored with the T-piece at various distances up to 100 mm from the flow cell. The maximum response was achieved with the T-piece as close as possible (15 mm) to the flow cell. This was to be expected on the basis of the kinetic profile shown in Fig. 1. In order to ensure that the maximum amount of CL emission was seen by the PMT, the coiled flow cell was 150 mm in length. The CL response from the PTFE flow cell was compared with that from a similar device fabricated from a glass capillary. The resultant CL intensities were the same within instrumental precision. Therefore, PFTE was chosen for all further work providing adequate sensitivity and the robustness required in process analysis. In a purpose built process instrument the T-piece would be placed inside the detector housing.

The total flow-rate (with equal carrier and reagent flow-rates) was varied from 2.2 ml min^{-1} up to 6.3 ml min^{-1} with the maximum response being achieved at 6.3 ml min^{-1}. The measured response at 2.2 ml min^{-1} was about 40% of that at 6.3 ml min^{-1}, which is consistent with the rate of the CL reaction and the respective linear flow velocities. A total flow-rate of 5.0 ml min^{-1} was chosen for the system as we had experienced some back pressure problems at the higher flow-rates. The slight drop in response ($\sim$ 10%) at the lower flow-rate was considered an acceptable exchange for the increase in instrumental reliability. Reagent consumption at these flow-rate was appropriate for continuous process monitoring.

It has been shown [2] that the presence of tetraphoshoric acid greatly enhances the CL signal. However, the CL response when using tetraphosphoric acid decreases significantly overnight. As the sample throughput of the present system is better than 100 h^{-1} periodic recalibration will compensate for the changing response. The loss in response was postulated to be caused by the acid hydrolysis of the tetraphosphoric acid to orthophosphoric acid thereby creating a significantly different molecular environment. To test this hypothesis a fresh solution of 0.1 M tetraphosphoric acid was used to examine morphine response in the system and a second sample of the acid was placed simultaneously in a ^{31}P NMR sample tube. Tri-*n*-butylphosphine oxide (0.1 M) was used as an internal standard. The peak integrals for the major peaks observed in the tetraphosphoric acid spectra were processed relative to the internal standard (see Fig. 4). The conversion of the phosphorus chemical environment was represented by the chemical shift of -23.4 ppm into another environment at $+0.74$ ppm. While the ^{31}P NMR results do not definitively support the hypothesis it is clear that there is a change in the phosphorus species present which parallels the decrease in CL intensity. Sodium hexametaphosphate was thought to be a possible alternative to tetraphosphoric acid as it has a slower hydrolysis. Instrumental response

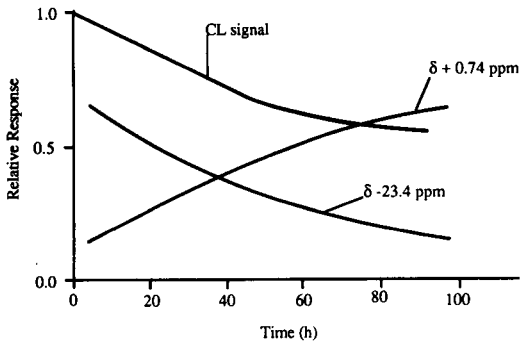

Fig. 4. A comparison of relative responses (with time) between the morphine CL response (5×10^{-4} M) and two ^{31}P NMR signals at +0.74 ppm and −23.4 ppm.

and temporal stability was monitored for a morphine standard (3.5×10^{-4} M) in solutions of sodium hexametaphosphate (0.1 M) at various pH values. These results were compared with the response from a morphine standard (3.5×10^{-4} M) prepared in tetraphosphoric acid (0.1 M) at pH 1.2. The initial responses at pH 1.2 with both tetraphosphoric acid and sodium hexametaphosphate were identical. After 24 h the decreases in the responses were 40% and 20%, respectively. This improved temporal stability was observed as the pH of the sodium hexametaphosphate was increased to pH 6.6 (unadjusted) at which point the percentage change in response after 24 h was zero. However, the sensitivity was degraded by about an order of magnitude. Depending upon the dilution factors chosen for the process extracts A and B the sodium hexametaphosphate matrix at its unadjusted pH of 6.6 may provide adequate sensitivity coupled with the reagent stability necessary for continuous on-line monitoring.

To ascertain the magnitude of concomitant interferences, solutions of five major alkaloids from *P. somniferum* (3.5×10^{-4} M) were monitored with the FIA–CL system. Relative to the 3.5×10^{-4} M morphine signal the codeine, thebaine and papaverine standards gave no measurable response, however, the relative responses of pseudomorphine and oripavine were 29% and 71% of the morphine signal. Thus, the latter two alkaloids could interfere with the determination of morphine at this concentration. Fortunately these species are present in the process extracts at concentrations considerably less than 100 times that of the morphine [8] and thus they do not constitute a significant interference problem.

Calibration graphs were obtained with the tetraphosphoric acid at pH 1.2 and the sodium hexametaphosphate at pH 6.6. Five aqueous morphine standards ranging in concentration from 3.5×10^{-6} M to 3.5×10^{-4} M were injected five times and the mean area plotted. Both graphs were linear up to the highest standard with equations to the lines of $y = 2.4x - 6.8$ and $y = 0.25x + 2.4$ respectively, where y is the CL signal in area counts and x is the morphine concentration ($\times 10^{-6}$ M), the correlation coefficients were 0.9999 and 0.9989, respectively. Detection limits were determined (signal to noise ratio of 3 : 1) as 5×10^{-8} M using tetraphosphoric acid and 1×10^{-6} M with sodium hexametaphosphate. The respective relative standard deviations were calculated from ten replicate injections as 0.4% (at 1.4×10^{-4} M) and 1.4% (at 3.5×10^{-4} M). These two morphine concentrations were chosen for the precision determinations as they represent the approximate concentrations of the diluted process extract A used for analysis.

Analysis of process streams

In order to alleviate sample matrix effects arising from the pH and dissolved solids content the extracts were manually diluted prior to analysis. Dilution was routinely carried out with 0.1 M sulfuric acid to increase compatibility with the carrier and reagent streams. As the morphine concentration range of extract A was 0.3% to 0.5% w/v (1.1×10^{-2} M to 1.8×10^{-2} M) a dilution factor of 100 was required to ensure good sensitivity in the linear region of the calibration graph obtained with tetraphosphoric acid. The relatively high dilution of extract A samples also facilitated the elimination of any possible interferences from either pseudomorphine or oripavine. The morphine concentration in extract B was generally 100 times less than that of extract A, therefore a dilution factor of 5 only was employed. While the dissolved solids contents of extracts A and B are essentially the same, the concentrations of pseudomorphine and oripavine

TABLE 1

Comparative results for the determination of morphine in process liquors by LC and FIA–CL

Extract	LC (%) (w/v, morphine)	FIA–CL [a] (%, w/v, morphine)
A	0.31	0.31
	0.28	0.28
	0.41	0.41
	0.48	0.48
	0.50	0.50
B	0.002	0.003
	0.003	0.003
	0.004	0.004
	0.002	0.002
	0.004	0.004
	0.004	0.004
	0.003	0.006
	0.003	0.007
	0.004	0.004
	0.003	0.002

[a] The FIA–CL results are the means of triplicate determinations.

are proportionally lower and as such do not interfere with the morphine determinations.

Five samples of extract A and ten samples of extract B were taken randomly from the process and the morphine concentrations were determined using both FIA–CL and LC. The reversed-phase LC methodology [9] was based on an ion-pair technique using a C_{18} column with an acetonitrile–water (80:20) mobile phase containing octanesulfonic acid and adjusted to pH 3.5. Detection was achieved by UV absorption at 230 nm. The resultant sample throughput is 2 h^{-1}. A high degree of confidence exists in the validity of this methodology [9] for the analysis of samples of extract A, however, in the analysis of extract B there are potential concomitant interferences arising from the complex organic matrix. The results obtained from the two procedures are listed in Table 1. An excellent correlation exists for the more concentrated extract samples. This demonstrates the utility of the FIA–CL for monitoring this particular stream in the morphine extraction process. The generally good agreement for the extract B samples is acceptable given the lower analyte concentrations and the LC uncertainties. Following the work of Abbott et al. [14] we are investigating coupling the CL detection chemistry to the present LC separation [9] so as to eliminate interferences by increasing detector selectivity and sensitivity. With improved LC data for extract B samples a more valid comparison with the FIA–CL results could be made. The FIA–CL methodology also exhibited greater instrumental stability and reliability than that shown by the current on-line SFA system. Together with the demonstrated analytical performance the FIA–CL system offers lower capital and consumable costs plus the facility for automated on-line instrumentation.

Future studies will be concerned with the design, construction and evaluation of an automated on-line instrument. The process instrumentation will incorporate a zone sampler and a robust purpose built CL detector. A proposed mechanism for the generation of CL from morphine and other species has been also outlined based upon our experiments and the investigations of others [2,10].

REFERENCES

1 A. Townshend, Analyst, 115 (1990) 495.
2 R.W. Abbott, A. Townshend and R. Gill, Analyst, 111 (1986) 635.
3 R.R.A. Pride and E.S. Stern, J. Pharm. Pharmacol., 6 (1954) 590.
4 U. Wieczorek, N. Nagakura, S. Curd, S. Jendrejewski and M.H. Zenk, Phytochemistry, 25 (1986) 2639.
5 J.O. de Beer, J. Corthout and A.J. Vlientinck, Pharmeuropa, 3 (1991) 274.
6 D.J. Blackmore, A.S. Curry, T.S. Hayes and E.R. Rutter, Clin. Chem., 17 (1971) 896.
7 I. Dannis and M. Ronis, Australian Government Analytical Laboratories Report of Investigations, No. S20, 1983.
8 Idem Ibid No. S22, 1984.
9 Glaxo Australia Chemicals Division Internal Analytical Methods, AM010, AM024, 1987.
10 Yu.B. Tsaplev, Zh. Fiz. Khim., 65 (1991) 799.
11 F.A. Cotton and G. Wilkinson, Advanced Inorganic Chemistry, Wiley, New York, 5th edn., 1988.
12 F.E. Lytle and D.M. Hercules, Photochem. Photobiol., 13 (1971) 123.
13 D.M. Hercules (Ed.), Fluorescence and Phosphorescence Analysis, Principles and Applications, Interscience, New York, 1966.
14 R.W. Abbott, A. Townshend and R. Gill, Analyst, 112 (1987) 397.

Analytica Chimica Acta, 282 (1993) 559–564
Elsevier Science Publishers B.V., Amsterdam

Liquid chromatographic assay of pyronaridine in plasma and blood

M.I. Saleh and H.K. Loh

School of Chemical Sciences, Universiti Sains Malaysia, 11800 Penang (Malaysia)

(Received 22nd March 1993; revised manuscript received 21st May 1993)

Abstract

A reversed-phase liquid chromatographic method for the determination of the anti-malarial drug pyronaridine in plasma was developed. The optimum conditions for the determination of pyronaridine in spiked human plasma were also used to assay the drug in animal plasma and blood. Diethyl ether used for liquid–liquid extraction was found to give the highest recovery (85%) among several solvents tested. A column packed with 10-μm octadecyl (C_{18}) particles was used with isocratic elution with 0.08 M potassium dihydrogenphosphate buffer–acetonitrile (85:15, v/v) containing 1% triethylamine. The detection limit with a UV detector measuring at 278 nm was 5 and 70 ng on-column for the pure compound and plasma, respectively.

Keywords: Liquid chromatography; Blood; Pharmaceuticals; Plasma; Pyronaridine

The development of resistance by *Plasmodium falciparum* to chloroquine has led to the synthesis of new anti-malarial drugs with high activity and low toxicity. Zheng et al. [1] synthesized pyronaridine at the Institute of Parasitic Disease, Chinese Academy of Medical Sciences, Shanghai. Pyronaridine is a Mannich base, 2-methoxy-7-chloro-10[3′,5′-bis(pyrolidiyl-1-methyl)-4′-hydroxyanilinol]benzo[*b*]-1,5-naphthyridines, with the structure shown in Fig. 1. This drug was reported to be effective against the disease caused by *P. falciparum* (which is resistant to chloroquine) and to have no major side effects [2]. Minor side-effects such as mild abdominal pain, vomiting and diarrhoea were observed, however, in a chemical trial by oral administration; the drug is not yet endorsed by the WHO for human testing.

Pharmacokinetic studies have utilized a fluorimetric method for quantification [3–5], and the

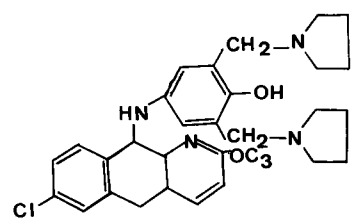

(I)

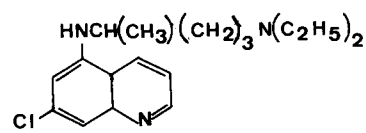

(II)

Fig. 1. Structures of pyronaridine (I) and the internal standard chloroquine (II).

Correspondence to: M.I. Saleh, School of Chemical Sciences, Universiti Sains Malaysia, 11800 Penang (Malaysia).

assay methods involved laborious separation before measurement. In order to shorten the analysis time and achieve reliable detection, studies on some chemical properties for the liquid chromatographic (LC) assay of pyronaridine have been reported previously [6]. As pyronaridine is very basic in nature, very soluble in water and easily ionized, reversed-phase LC is a suitable method for separation [7,8]. This paper is concerned with the isolation of pyronaridine from plasma and blood samples by liquid–liquid extraction followed by LC separation and determination.

EXPERIMENTAL

Chemicals

Solvents of analytical-reagent grade, namely hexane, ethyl acetate and chloroform, were obtained from Merck (Darmstadt); dichloromethane was obtained from Ajax (Auburn, Australia) and diethyl ether and ethanol from May and Baker (Dagenham).

Components of the buffer solution were of analytical-reagent grade; acetic acid was obtained from Merck, citric acid, phosphoric acid and hydrochloric acid from BDH (Poole), potassium dihydrogenphosphate and trisodium phosphate from Merck and TRIZMA base from Sigma. Sodium hydroxide and triethylamine of analytical reagent grade and methanol and acetonitrile of HPLC grade were obtained from Merck. Pyronaridine tetraphosphate was supplied by the WHO. Chloroquine diphosphate was purchased from Sigma. Stock standard solutions and internal standard solutions were prepared in methanol (0.1 mg ml^{-1}). An appropriate volume of stock solution was pipetted into a screw-capped test-tube followed by 10 μl of chloroquine (Fig. 1) as internal standard. Plasma or whole blood (200 μl) was added to make a standard solution. Whole blood samples were preserved with sodium heparinate and stored at −20°C until required.

Instrumentation

pH values were measured with a Hanna Model 8417 pH meter. Plasma and blood were extracted with a Thermolyne Maximix MI6710-12 vortex mixer followed by centrifugation using a Hettich EBA 3S centrifuge (2500 rpm). LC with an HP 1090 diode-array detector was used for peak identification. For method development a Gilson Model 303 LC system with dual pumps and a Rheodyne Model 7125 injector, a Waters Lamda-Max Model 481 detector, an HP 3392 integrator and an Apple microcomputer were used.

Sample preparation

A plasma or blood sample of 200 μl was spiked with 250 ng of chloroquine in a screw-capped test-tube. Buffer solution (500 μl) was added followed by 3 ml of organic solution. The mixture was homogenized with a vortex mixer for 2 min, followed by centrifugation for 10 min (2500 rpm). The organic layer was transferred into a new test-tube and 100 μl of ethanol were added before drying under a flow of nitrogen. The dried sample was dissolved in 100 μl of mobile phase and a 50-μl aliquot was injected.

Stability and validity tests

The stability of pyronaridine in human plasma was investigated. Spiked samples were prepared with drug-free plasma and were stored at −20°C, thawed and analysed every day using a standard calibration with freshly prepared solution.

The recoveries of pyronaridine and the internal standard from plasma and blood were assessed by comparison of the peak heights obtained by direct injection of stock standard solutions of the compounds with those found by isolation of the spiked samples. The precision and accuracy of the method in within-day analyses of plasma were evaluated by assaying replicate spiked samples ($n = 4$ for each concentration of pyronaridine used). For blood six different concentrations were evaluated. For evaluation of the day-to-day precision and accuracy replicate samples ($n = 5$) were measured on five consecutive days. The observed concentrations were calculated using calibration graphs prepared daily. The limit of detection was defined as the amount of pyronaridine per 200 μl of plasma and blood that can be detected with a relative standard deviation (R.S.D.) of less than 10%.

RESULTS AND DISCUSSION

As pyronaridine is a basic compound and easily ionized, the mobile phase has to be buffered for rapid equilibration and to avoid unsymmetric peaks due to slow kinetic processes. In order to improve the peak shape or eliminate tailing, in addition to the pH of the mobile phase, several other parameters such as the concentrations of triethylamine and phosphate, ion pairing with perchlorate and mobile phase composition were studied. Table 1 gives a summary of the conditions and peak symmetries. From the observation of zone broadening due to slow kinetic processes, the optimum conditions were achieved at a mobile phase composition of 15% acetonitrile and 85% phosphate buffer (pH 2.8) containing 1% of triethylamine. At this low pH, the cationic form of the drug is easily paired with perchlorate, as can be seen from the increase in retention time with the decrease in peak symmetry on increasing the concentration of perchlorate. Even phosphate ion is capable of pairing with pyronaridine, as observed from the increase in retention time with increase in phosphate concentration. The buffer solution therefore not only maintains a constant pH of the solution, but can also affect the peak shape. Melander and Horvath [9] suggested that maintaining a high concentration of buffer will speed up the protonic equilibration, hence peak splitting or asymmetric peaks are due to the slow kinetic processes. With a bulky molecule such as pyronaridine, surface silanol adsorption (silanophilic) can still be observed, as by the addition of triethylamine lowered the retention time, even though the manufacturer claimed that the column was end-capped.

Figure 2 shows the chromatograms of blank human plasma and plasma spiked with 100 ng of pyronaridine and 250 ng of internal standard in 200 μl of plasma. Chloroquine was found to be suitable as an internal standard owing to its structure (see Fig. 1) and its recovery was 94.47% and 79.46% from plasma and whole blood, respectively. Even though the blank extract was rather "dirty", the pyronaridine and chloroquine peaks were clearly distinct and can be used for quantification. Peak height was used instead of peak area for quantification. A good straight line (r = 0.9999) with a negligible intercept on the ordinate was obtained for the calibration graph. The lowest amount detected was 5 ng or 5.5×10^{-12} mol

TABLE 1

Peak symmetry as a measure of peak width at 10% height for several mobile phase compositions and conditions

Mobile phase condition			Peak width at 10% peak height (min)
Fixed parameter	Variable parameter		
Aqueous 0.02 M KH_2PO_4 (pH 3) and 1% TEA	Solvent	35% methanol	1.2
		25% acetonitrile	0.5
Aqueous 75% 0.02 M KH_2PO_4, 1% TEA and 25% acetonitrile	Buffer pH	2.50	0.4
		3.50	0.5
		4.00	4.0
Aqueous 75% 0.02 M KH_2PO_4, (pH 3) and 25% acetonitrile	TEA	0.5%	1.2
		1.0%	0.5
		1.5%	0.4
Aqueous 80% KH_2PO_4, 1% TEA and 20% acetonitrile	KH_2PO_4	0.02 M	0.7
		0.05 M	0.6
		0.08 M	0.5
Aqueous 75% 0.02 M KH_2PO_4, 1% TEA and 25% acetonitrile	$HClO_4$	None	0.5
		0.03 M	1.0
		0.01 M	2.0

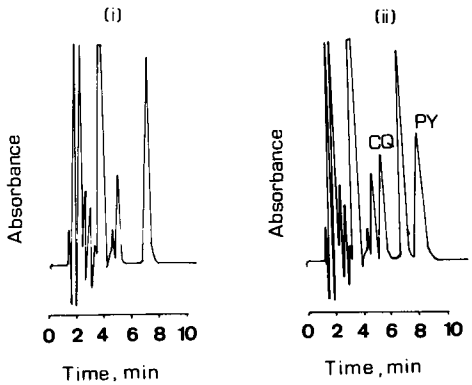

Fig. 2. Chromatograms of (i) blank human plasma and (ii) plasma spiked with 100 ng of pyronaridine (PY) and 250 ng of chloroquine (CQ) (internal standard).

of pure pyronaridine tetraphosphate on-column with R.S.D. 5.3% ($n = 5$) at a signal-to-noise ratio at 4. The detection limit of pyronaridine in plasma samples was 70 ng or 7.7×10^{-11} mol.

Extraction with several solvents did not reduce the unwanted peaks. The recovery of pyronaridine from plasma by different solvents is shown in Fig. 3; only diethyl ether gives recoveries > 80%. With respect to the recovery and easy reconstitution to the desired volume, diethyl ether was the best choice. Maximum recovery for all solvents studied did not occur at the same pH, as shown in Fig. 3; the highest recovery was obtained at pH 9–11 for diethyl ether and hexane whereas dichloromethane and ethyl acetate gave maximum extraction at pH 5–8. The highest recovery (85%) attained with diethyl ether is due to its moderate polarity and ability to accept protons according to the solvent selectivity classification of Snyder and Kirkland [7]. Pyronaridine, with its phenol groups, can donate its proton for hydrogen bonding with diethyl ether. The volume of the extraction solvent did not have any effect on the recovery of pyronaridine, no significant difference being observed on changing the volume from 1 to 7 ml. These was also no significant difference between single and double extraction with 3 ml of diethyl ether.

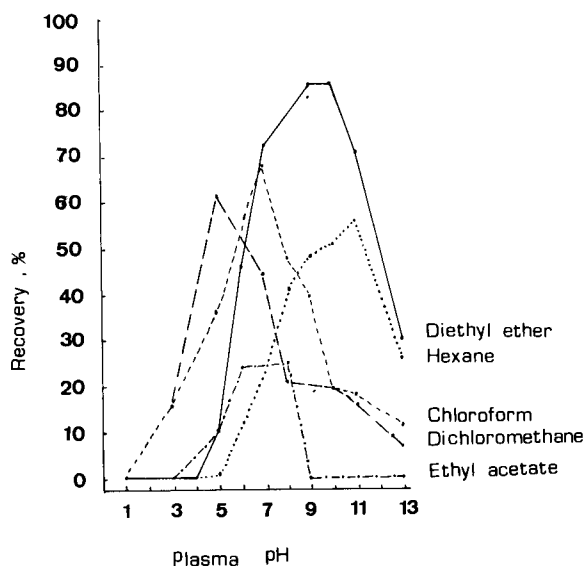

Fig. 3. Recovery of pyronaridine from plasma buffered at different pHs extracted with various solvents ($n = 3$ for every point).

The recovery of pyronaridine from plasma and whole blood extracted with diethyl ether is shown in Table 2. The separation and determination procedure developed is very effective, with an R.S.D. for 50 ng on-column of 1.3% ($n = 8$). Table 3 gives the within-day precision for plasma and whole blood and Table 4 gives the day-to-day variation. A high R.S.D. of ca. 10% was only observed at the low concentrations of pyronaridine. At high concentrations (above 10 ng) R.S.D.s of less than 5% were observed.

The method developed for human plasma and blood was applied to the determination of py-

TABLE 2

Recovery of pyronaridine from 20 μl of plasma and blood ($n = 4$)

Amount added to plasma or blood (ng)	Recovery			
	From plasma		From blood	
	ng	%	ng	%
14.00	12.80	91.43	12.13	86.64
25.00	21.21	84.84	22.24	88.96
50.00	41.56	83.12	–	–
100.00	89.80	85.80	86.24	86.84
200.00	170.92	85.55	167.50	83.75
400.00	336.19	84.05	337.90	84.47
800.00	705.32	88.16	659.27	82.41
1000.00	859.00	85.90	–	–

TABLE 3

Within-day precision for the determination of pyronaridine added to 200 μl of plasma or blood ($n = 4$)

Amount added to plasma or blood (ng)	Found			
	Plasma		Blood	
	ng	R.S.D. (%)	ng	R.S.D. (%)
14.00	12.97	8.27	13.12	8.76
25.00	27.12	9.47	23.50	9.73
50.00	50.70	9.71	–	–
100.00	96.00	2.76	97.00	3.24
200.00	200.00	3.84	185.63	4.87
400.00	392.54	4.68	395.81	1.57
800.00	803.90	1.55	780.00	2.54

TABLE 4

Day-to-day-precision for the determination of pyronaridine added to 200 μl of plasma or blood ($n = 5$)

Amount added (ng)	Found			
	Plasma		Blood	
	ng	R.S.D. (%)	ng	R.S.D. (%)
25.00	24.87	5.35	26.37	9.60
100.00	102.04	4.72	98.57	2.06
400.00	401.29	1.42	400.54	1.65

ronaridine in rat and monkey samples. Figure 4 shows the chromatogram of blank rat plasma extract and for samples taken 1 and 6 h after drug administration. The interference of an unknown peak between the internal standard and

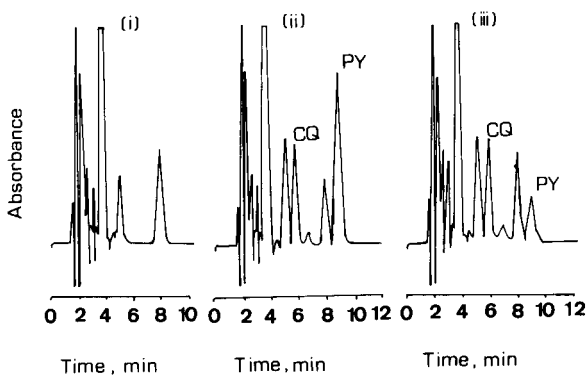

Fig. 4. Representative chromatograms of extracts from (i) drug-free plasma, (ii) plasma 1 h after and (iii) plasma 6 h after drug administration to rat.

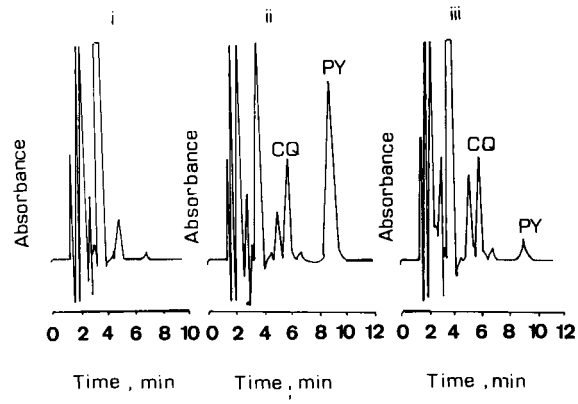

Fig. 5. Representative chromatograms of extract from (i) drug-free plasma, (ii) plasma 15 min after and (iii) plasma 1 h after drug administration to monkey.

pyronaridine (see Fig. 2) was not observed here. Figure 5 shows the chromatogram of blank monkey plasma extract and for samples taken 15 min and 1 h after drug administration.

Conclusion

A method for isolation prior to separation of pyronaridine from plasma and blood sample was developed. Pyronaridine, which is basic, was shown to be very dependent on the hydrogen ion concentration for extraction or separation by reversed-phase LC. The use of triethylamine for elution is important, as elution is impractical without the addition of a masking agent even though the column is claimed to be end-capped. The use of volatile diethyl ether for extraction decreases the total analysis time. Sample preparation requires about 2 h and the analysis time by LC was 10 min. By using a guard column, the analytical column did not show any deterioration after several hundred injections. The method developed is suitable for the analysis of human, rat and monkey plasma and whole blood samples.

This project was financed by a UNDP/World Bank/WHO Institutional Strengthening Grant for Tropical Disease Research. The Director of Drug Research Centre, Universiti Sains Malaysia, is thanked for the facilities provided for this project.

REFERENCES

1 X.Y. Zheng, X.Y. Gao, F.H. Gao, H.Z. Gua and C. Chem, Yao Hsueh Pao, 14 (1979) 736.
2 New Drug Group of the Former Department of Malaria, Acta Pharm. Sin., 15 (1980) 630.
3 Z. Feng, N.X. Jiang, C.Y. Wang and W. Zheng, Acta Pharmacol. Sin., 21 (1986) 801.
4 Z. Feng, N.X. Jiang, C.Y. Wang and W. Zheng, Acta Pharmacol. Sin., 21 (1986) 801.
5 Z. Feng, Z.F. Wu and C.Y. Wang and W. Zheng, Acta Pharmacol. Sin., 8 (1987) 543.
6 M.I. Saleh and H.K. Loh, J. Phys. Sci. 2 (1991) 1.
7 L.R. Snyder and J.J. Kirkland, Introduction to Modern Liquid Chromatography, Wiley, New York, 2nd edn., 1979.
8 C.F. Poole and S.A. Schuette, Contemporary Practice of Chromatography, Elsevier, Amsterdam, 1984.
9 W.R. Melander and C. Horvath, in C. Horvath (Ed.), High Performance Liquid Chromatography, Advances and Perspectives, Vol. 2, Academic, New York, 1980, p. 114.

Analytica Chimica Acta, 282 (1993) 565–570
Elsevier Science Publishers B.V., Amsterdam

Determination of the specific surface area of silica gel by on-column titration with hydrochloric acid

Toyohide Takeuchi and Tomoo Miwa

Faculty of Engineering, Gifu University, 1-1 Yanagido, Gifu 501-11 (Japan)

(Received 6th April 1993; revised manuscript received 8th June 1993)

Abstract

Specific surface areas of silica gel packings could be determined by an on-column acid–base titration method. Silica gel materials packed in microcolumns were equilibrated with sodium hydrogencarbonate, followed by titration with hydrochloric acid. The effluents from the columns were monitored by an electrical conductivity detector and the end-points were determined from the breakthrough curves. The breakthrough volume was linearly dependent on the surface area per unit volume of the packings or on the total surface area of the column.

Keywords: Liquid chromatography; Titrimetry; Silanol groups; Silica gel packings; Specific surface area

Among packing materials developed for liquid chromatography (LC), silica-based materials are the most widely employed [1]. The chromatographic characteristics of silica-based materials are affected by their size, shape and surface properties such as particle diameter, specific surface area, pore diameter, pore volume, residual silanol groups, metal impurities and type of bonded groups.

It is generally accepted that the surface silanol concentration for most forms of silica is about 8 μmol m^{-2} (or 4.8 silanol groups per square nm^2). Amounts of silanol groups of silica gel and residual silanol groups of bonded-phase materials have been quantitatively measured by isotope exchange methods [2–4], methyl red adsorption [5], complexation with metal species [6], titration [7,8] and gas chromatographic retention of cyclohexane and benzene [9]. Another approach for the evaluation of residual silanol groups of bonded-phase materials involves spectroscopic methods such as infrared, photoacoustic and nuclear magnetic resonance spectrometry.

The specific surface area of silica-based materials has been commonly determined by a nitrogen adsorption method. In addition, some of the above methods which give quantitative information on silanol groups can also provide the specific surface area. Among the methods reported, the titration methods described by Sears [7] and Cheng and McCown [8], in which silica gel materials were titrated with sodium hydroxide in a batch operation, achieve a rapid and accurate determination of the specific surface area of silica-based materials.

Sears' method [7] involves the titration of the silica surface with 0.1 M sodium hydroxide in a medium of 20% aqueous sodium chloride between pH 4.0 and 9.0 This is based on the fact that 1.26 hydroxyl ions are adsorbed per nm^2 of surface at pH 9.0 and the titration volume can be related to the surface area. Cheng and McCown [8] modified Sears' method for the determination of the silanol concentration of alkyl-bonded silica gel packings, in which 1-propanol was added to

Correspondence to: T. Takeuchi, Faculty of Engineering, Gifu University, 1-1 Yanagido, Gifu 501-11 (Japan).

the solution in order to disperse such hydrophobic packings. In our experience, alkyl-bonded silica packings became coagulated during the titration even if 1-propanol was added to the solution, which caused difficulty in the accurate determination of the surface silanol concentration.

This paper describes an on-column acid–base titration method for the determination of the specific surface area of silica gel packings.

EXPERIMENTAL

Apparatus

The microcolumn liquid chromatograph was assembled from an MF-2 microfeeder (Azumadenki Kogyo, Tokyo) equipped with a 0.5-ml MS-GAN050 gas-tight syringe (Ito, Fuji) as a pump, an ML-522 microvalve injector with an injection volume of 0.02 μl (Jasco, Tokyo), a 150 mm × 0.35 mm i.d. microcolumn, an LIC-10-EI electrical conductivity detector (DKK, Tokyo) with a laboratory-made flow cell and a Chromatopac C-R4AX data processor (Shimadzu, Kyoto). The flow cell was composed of four electrodes made of stainless-steel tubes of 0.13 mm i.d. × 0.31 mm o.d. [10]. The time constant of the conductivity detector was kept at 1 s. The microcolumn was prepared from fused-silica tubing as reported previously [11] and 5-μm silica gel and octadecyl-bonded silica gel (Develosil; Nomura Chemical, Seto) were employed as packings. The packings employed and their surface properties are listed in Table 1. The pore volumes (*PV*) (defined as the pore volume per unit weight) and weight-specific surface areas (*WSA*) (defined as the surface area per unit weight) were given by the manufacturer. The flow-rate of the eluent was 2.8 μl min^{-1}. When the column was exchanged, the ML-522 microvalve injector was used as a stop valve to maintain the pressure applied between the injector and the pump.

The separation of ions was also performed with the above chromatograph, and they were determined by ion chromatography with indirect photometric detection. For this purpose, a Uvidec-100V UV detector (Jasco) with a laboratory-made flow cell was used.

Reagents

Guaranteed-reagent grade solvents and reagents were obtained from Nacalai Tesque (Kyoto), unless indicated otherwise. These reagents were used as received. Purified water was prepared from distilled water by using a Milli-Q Plus system (Millipore, Molsheim, France). All standard solutions and eluents were prepared with this purified water.

TABLE 1

Surface properties of the packing materials used

Packing	*PV* [a] (ml g^{-1})	*WSA* [b] (m^2 g^{-1})	*VSA* [c] (m^2 ml^{-1})	Packing amount [d] (mg)	*TSA* [e] (m^2)	EC [f]	Carbon content (%)
Develosil:							
300-5	1.03	156	106	4.9	0.76		
100-5	1.06	324	215	4.8	1.6		
100-5	1.04	360	242	5.6	2.0		
60-5	0.84	437	339	6.0	2.6		
30-5	0.62	704	659	7.9	5.6		
ODS-5	0.38	157	–	7.1	1.1	Y	20.2 [g]
ODS-T-5	0.42	150	–	7.7	1.1	Y	19.7 [g]
ODS-A-5	0.42	152	–	7.6	1.1	N	19.4

[a] Pore volume per unit weight. [b] Weight-specific surface area (surface area per unit weight). [c] Volume-specific surface area (surface areas per unit volume). [d] Amounts per 15-cm column. [e] Total surface area per 15 cm column. [f] Y = trimethylsilylated for end-capping; N = no end-capping. [g] Carbon content after end-capping.

Titration method

A 80–250-μl volume of 0.1 M sodium hydrogencarbonate (pH 9.9, adjusted with sodium hydroxide) was passed through 150 mm × 0.35 mm i.d. columns packed with the silica gel materials listed in Table 1, followed by titration with 0.1 M hydrochloric acid at a flow-rate of 2.8 μl min^{-1}. The effluent was monitored with an electrical conductivity detector. Titration was carried out at room temperature (ca. 20°C).

RESULTS AND DISCUSSION

On-column titration with hydrochloric acid

When silica gel is treated with sodium hydrogencarbonate, it is considered that sodium ions are introduced into silanol groups by ion exchange:

$$\underset{\text{(silica)}}{\equiv SiOH} + NaHCO_3 \longrightarrow \underset{\text{(silica)}}{\equiv SiONa} + H_2CO_3 \quad (1)$$

The sodium ions introduced can in turn be removed by treatment with hydrochloric acid:

$$\underset{\text{(silica)}}{\equiv SiONa} + HCl \longrightarrow \underset{\text{(silica)}}{\equiv SiOH} + NaCl \quad (2)$$

Excess of hydrochloric acid elutes from the column when the reaction shown in Eqn. 2 is completed. The replaced sodium ions, therefore, can be calculated from the breakthrough volume and the hydrochloric acid concentration. The amount of sodium ions introduced into silica gel are then related to the surface area of the packing.

Figure 1 shows a titration curve for a Develosil 30-5 silica gel column, in which two jumps are observed in ca. 3 and 16 min. The column was previously equilibrated with 0.1 M sodium hydrogencarbonate (pH 9.9) and was titrated with 0.1 M hydrochloric acid. The latter solution gave an electrical conductivity of ca. 1 mS cm^{-1}. The distance from the electrodes of the flow cell was adjusted so that the signal remained within the full scale [10]. When used a silica gel column equilibrated with 0.1 M hydrochloric acid was titrated with 0.1 M sodium hydrogencarbonate (pH 9.9) in the absence of sodium chloride, broad

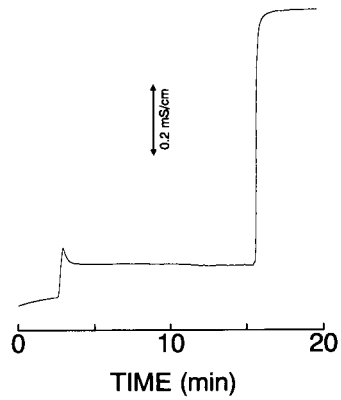

Fig. 1. On-column titration curve for Develosil 30-5 column. Column, 150 mm × 0.35 mm i.d., packed with Develosil 30-5; titration eluent, 0.1 M hydrochloric acid; flow-rate, 2.8 μl min^{-1}; detector, electrical conductivity.

breakthrough curves were observed, which did not allow the accurate determination of the titration volume. This is because the number of hydroxyl ions adsorbed per unit area depends on the pH, e.g., 1.26 hydroxyl ions per nm^2 at pH 9.0, 2.2 at pH 10.0, 3.3 at pH 11.0, etc. [7]. In contrast, when silica gel columns equilibrated with 0.1 M sodium hydrogencarbonate (pH 9.9) were titrated with hydrochloric acid, sharp breakthrough curves were observed, as shown in Fig. 1.

It is presumed that the first jump is due to elution of sodium chloride and the second to elution of hydrochloric acid. In order to confirm this assumption, the concentration of ions contained in the effluent between the two jumps was determined by ion chromatography.

Ion chromatography of effluents

For the determination of anions, octadecyl-bonded silica gel (ODS) coated with cetyltrimethylammonium bromide (Cetrimide) was employed as the anion-exchange column and 1 mM sodium salicylate dissolved in 5% acetonitrile aqueous solution was employed as the eluent [12]. Anions were detected indirectly at 230 nm as demonstrated in Fig. 2. In Fig. 2A the separation of a reference mixture of 2 mM hydrogencarbonate and 2 mM chloride is demonstrated, and Fig. 2B shows the separation of ions contained in the effluent eluting between the two jumps appearing

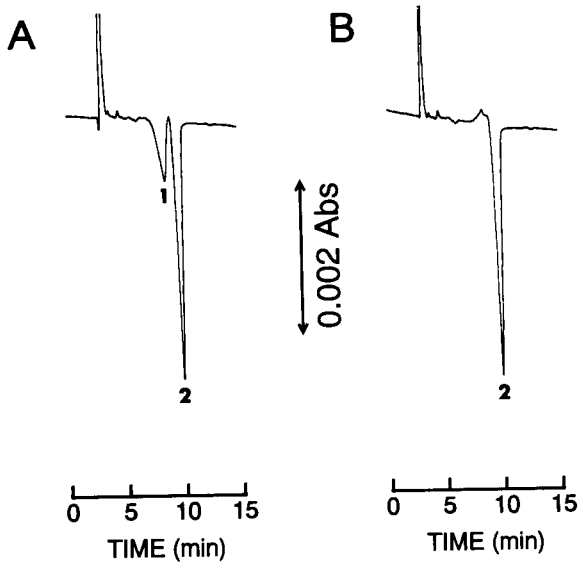

Fig. 2. Separation of anions by ion chromatography with indirect photometric detection. Column, 150 mm×0.35 mm i.d., packed with Cetrimide-coated Develosil ODS-5; eluent, 1 mM sodium salicylate in 5% aqueous acetonitrile; flow-rate, 2.8 μl min^{-1}; injection volume, 0.02 μl. Samples: (A) 2 mM hydrogencarbonate (1) and 2 mM chloride (2); (B) 50-fold diluted effluent eluting between the two jumps appearing in Fig. 1.

in the titration curve. The effluent was diluted 50-fold with the eluent before injection. It was found that 2 mM chloride ion only appeared in Fig. 2B, which led to the conclusion that 0.1 M chloride ion was contained in the effluent.

On the other hand, cations contained in the same effluent were also determined by ion chromatography with indirect photometric detection as reported previously [13], in which aqueous copper sulphate was employed as the eluent. It was found that 0.1 M sodium ion was contained in the effluent.

From these results, it was concluded that the effluent eluting between the two jumps appearing in Fig. 1 contained 0.1 M sodium chloride. This confirmed that the reaction shown in Eqn. 2 takes place during such a titration.

Amount of sodium ions replaced

The amounts of sodium ions replaced for the Develosil 30-5 column, as demonstrated in Fig. 1, can be calculated to be 3.6 μmol from the breakthrough time (12.81 min), flow-rate (2.8 μl min^{-1}) and the hydrochloric acid concentration (0.1 M). This column has a total surface area of 5.6 m^2, as shown in Table 1. If it is assumed that the surface silanol concentration of silica gel is 8 μmol m^{-2}, the Develosil 30-5 column has 45 μmol of total silanol groups. These results indicate that not all forms of silanol groups of silica gel can be replaced by sodium ions when treated with sodium hydrogencarbonate, and only 8% of silanol groups were subjected to replacement with sodium ions. This may be because there are various types of silanol groups existing on silica gel, such as free hydroxyl groups, vicinal hydroxyl groups and hydroxyl groups bound to water by hydrogen bonding [2], and because some types of silanol groups cannot be replaced with sodium ions.

The reproducibility of the breakthrough volume for five successive measurements was determined by using a single column packed with Develosil 60-5. The breakthrough volume gradually increased during the successive experiments, and the relative standard deviation of the breakthrough volume was 4.9%. This result suggests that the properties of the silica surface change during the titration. Therefore, the breakthrough volume obtained in the first measurement was adopted as the value for each material.

Relationship between breakthrough volume and surface area

Figure 3 shows the relationship between the breakthrough volume and *WSA* for the 150 mm ×

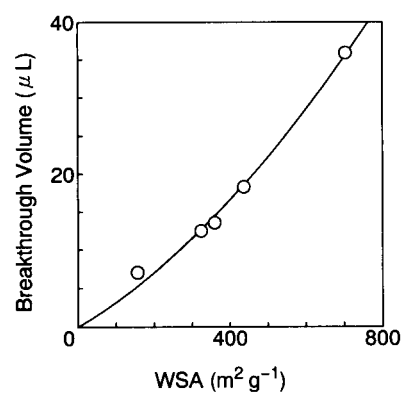

Fig. 3. Breakthrough volume as a function of the weight-specific surface area (*WSA*). Columns, 150 mm×0.35 mm i.d.; titration eluent, 0.1 M hydrochloric acid; flow-rate, 2.8 μl min^{-1}; detector, electrical conductivity.

0.35 mm i.d. columns packed with various silica gels. The relationship is not linear, because the density of each packing is different and different amounts of silica gel materials are therefore packed in the column.

As the column volume is constant, it is reasonable to plot the breakthrough volume versus the volume-specific surface area [defined as the surface area per unit volume (*VSA*)]. When the pore volume (*PV*) and the density of the core of silica gel (2.23 g ml^{-1}) are known, *VSA* can be calculated from

$$VSA = WSA/(2.23^{-1} + PV) \quad (3)$$

Figure 4 shows a plot of the breakthrough volume versus *VSA*, which is linear. This result indicates that if *WSA* is known, *PV* can be calculated from the breakthrough volume using Eqn. 3, and vice versa.

When the amounts of silica gel packed in the column are measured, the total surface area (*TSA*) can be calculated from its *WSA*. In Fig. 5 the breakthrough volume is plotted as a function of the *TSA* of the, column, showing the linear relationship between the two parameters. Therefore, the *WSA* of silica packings can be calculated using such a calibration graph from their breakthrough volumes and the amounts packed in the column. Then, *PV* can be calculated using the calibration graph shown in Fig. 4 and Eqn. 3.

As the column tubing employed in this work was narrow (0.35 mm i.d.), the precision is slightly

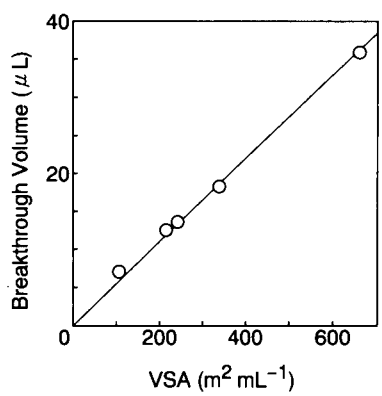

Fig. 4. Breakthrough volume as a function of volume-specific surface area (*VSA*). Operating conditions as in Fig. 3.

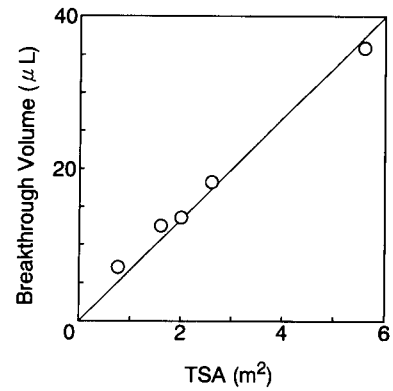

Fig. 5. Breakthrough volume as a function of total surface area (*TSA*). Operating conditions as in Fig. 3.

poor. There are two reasons why microcolumns were employed in this work: microcolumns could easily be disposed of when the column efficiency was lost after titration, and the electrical conductivity of 0.1 M hydrochloric acid was much higher than the full-scale signal of the detector when the flow cell commercially available for conventional LC was employed. The magnitude of the output signal could be easily altered with micro flow cell employed in this work by changing the distance of the electrodes [10]. It should be noted that the precision will be improved by using large-bore columns and an appropriate detector such as a refractive index detector.

Determination of residual silanol groups on ODS materials

The method was applied to the determination of residual silanol groups for the ODS materials Develosil ODS-5, ODS-T-5 and ODS-A-5, as shown in Table 1. Develosil ODS-5 was prepared with dimethyloctadecylchlorosilane, whereas ODS-T-5 and ODS-A-5 were prepared with octadecyltrichlorosilane in the absence of water. ODS-5 and ODS-T-5 were further subjected to trimethylsilylation for end-capping. These materials were packed into fused-silica tubing of 150 mm × 0.35 mm i.d.. The breakthrough volumes achieved with these columns under the same conditions as in Fig. 5 were 0.39, 1.3 and 2.2 μl, respectively. The breakthrough volumes then al-

low the determination of the percentage of residual silanol groups by using the calibration graph shown in Fig. 5. Unfortunately, the breakthrough volumes observed for the ODS column were so small that residual silanol groups cannot be determined accurately. In order to improve this, additional experiments should be carried out for silica gel with much smaller *WSA* values.

Conclusion

The present on-column titration method can rapidly determine the specific surface area or pore volume of silica gel materials and also allows the determination of the residual silanol groups of bonded-phase materials. As the method does not involve ion exchange of all types of silanol groups of silica gel materials with sodium ions, a calibration graph will be required for each brand (or type) of silica gel material.

The authors thank Nomura Chemical for the kind gift of the packing materials employed in this work.

REFERENCES

1 L.C. Sander and S.A. Wise, CRC Crit. Rev. Anal. Chem., 18 (1987) 299.
2 K.K. Unger, Porous Silica—Its Properties and Use as Support in Column Liquid Chromatography, Elsevier, Amsterdam, 1977.
3 P. Roumeliofis and K.K. Unger, J. Chromatogr., 149 (1978) 211.
4 J. Goworek, F. Nooitgedacht, M. Rijkhof and H. Poppe, J. Chromatogr., 352 (1986) 399.
5 I. Shapiro and I.M. Kolthoff, J. Am. Chem. Soc., 72 (1950) 776.
6 E.C. Jennings, Jr., and R.G. Brownlee, Anal. Chem., 58 (1986) 2895.
7 G.W. Sears, Jr., Anal. Chem., 28 (1956) 1981.
8 W. Cheng and M. McCown, J. Chromatogr., 318 (1985) 173.
9 T. Takeuchi, T. Miwa and N. Nagae, Chromatographia, 35 (1993) 375.
10 T. Takeuchi, T. Miwa, A. Hemmi and T. Maeda, Chromatographia, 37 (1993) in press.
11 T. Takeuchi and D. Ishii, J. Chromatogr., 213 (1981) 25.
12 T. Takeuchi, E. Suzuki and D. Ishii, J. Chromatogr., 447 (1988) 221.
13 T. Takeuchi and T. Miwa, Chromatographia, 34 (1992) 386.

Analytica Chimica Acta, 282 (1993) 571–580
Elsevier Science Publishers B.V., Amsterdam

Nickel–chromium alloy electrode as a carbohydrate detector for liquid chromatography

Juan M. Marioli [1], Peifang F. Luo and Theodore Kuwana

Department of Chemistry and the Center for Bioanalytical Research, The University of Kansas, 2095 Constant Avenue, Lawrence, KS 66045 (USA)

(Received 3rd November 1992; revised manuscript received 17th May 1993)

Abstract

A nickel–chromium alloy electrode was applied as an electrochemical detector for the analysis of carbohydrates by high performance anion-exchange liquid chromatography. This alloy electrode exhibited excellent sensitivity, reproducibility and stability. The carbohydrates are oxidatively detected by a surface catalyzed process, proposed to involve nickel(III) oxyhydroxides, which are formed in the range of ca. 0.45 to 0.5 V vs. a Ag/AgCl reference electrode. The cyclic voltammograms of the Ni–Cr electrode are compared to pure Ni in order to understand the basic mechanism of the oxidation. The effects of the temperature, the sodium hydroxide concentration, the mobile phase flow-rate, and the working potential on the electrode response were analyzed to optimize the detection conditions. The reproducibility of the electrode response to the injection of 100 pmol of glucose was studied continuously for a period of 21 days. A limit-of-detection (LOD) of approximately 500 fmol of glucose (signal-to-noise ratio of 3) makes this alloy electrode well suited for the high sensitive detection of carbohydrates.

Keywords: Liquid chromatography; Chromium; Nickel; Ni–Cr alloy electrode

The electrochemical detection (EC) of carbohydrates following liquid chromatographic (LC) separations has several advantages over other methods of detection. For example, refractive index and conductivity based detection methods exhibit relatively low sensitivity [1]. High sensitivity optical detection in the ultraviolet region of the spectrum for carbohydrates on the other hand, requires extreme precaution in controlling the purity of the mobile phase. Also, it is necessary to derivatize the carbohydrates in order to use UV–visible detection methods, which have sensitivities similar to their EC counterpart [2,3]. However, the need for derivatization adds complexity to the analysis. Only fluorescence based detection methods give higher sensitivity compared to EC methods [4]. But derivatization is also required for fluorescence.

The electrochemical detection of carbohydrates can be performed using different electroanalytical techniques with a variety of electrode materials. Pulsed amperometry at gold or platinum electrodes in alkaline solution [5,6], potentiometry at copper electrodes in solution containing cupric ions and weakly complexing compounds [7], and constant potential amperometry at metallic and modified electrodes [8–11] are among the various EC detection schemes. With constant potential amperometry it is possible to achieve sensitivities in the femtomole range [12,13] with certain metal electrodes. Such sensi-

Correspondence to: T. Kuwana, Department of Chemistry and the Center for Bioanalytical Research, The University of Kansas, 2095 Constant Avenue, Lawrence, KS 66045 (USA).
[1] Present address: Departamento de Quimica y Fisica, Universidad Nacional de Rio Cuarto (UNRC), Estafeta Postal No. 9, 5800 Rio Cuarto (Argentina).

tivity can be attained because the background current can be very low at constant potential, after the initial charging of the electrochemical double layer and the formation of surface oxides. On the other hand, constant potential amperometry has the problem of electrode contamination, or slow surface changes that lead to decreases in the sensitivity and reproducibility of the response [6,8].

Metal and metal oxide electrodes have shown high catalytic activity to the oxidation of carbohydrates [8,10,14,15]. However, the corrosion of the electrode surface or the formation of inactive oxide layers are problems that need to be overcome in order to improve their analytical performance.

Nickel electrodes exhibit catalytic activity to the oxidation of a wide variety of organic compounds in alkaline solutions [16–18]. The Ni(III) species is generated on the electrode surface at potentials in the region of 0.45 to 0.5 V vs. Ag/AgCl reference electrodes. The Ni(III) surface acts as an effective catalyst to oxidize the carbohydrates [16]. The general pathway proposed is illustrated by reactions 1–4:

$$Ni + 2OH^- \longleftrightarrow Ni(OH)_2 + 2e \quad (1)$$

$$Ni(OH)_2 + OH^- \longleftrightarrow NiOOH + e \quad (2)$$

$$NiOOH + \text{organic molecule} \longrightarrow Ni(OH)_2 + \text{intermediate} \quad (3)$$

$$\text{intermediate} \longrightarrow \text{product} + e \quad (4)$$

Several research groups have applied the catalytic activity of the nickel-nickel oxide electrode for the electrochemical detection of various organic compounds [8,10,17,18]. However, the response of the electrode decayed after a short time [8].

It is our goal to find an electrode that possesses high sensitivity, reproducibility and long-term stability for the amperometric LC-EC detection of carbohydrates. To that end, we have explored the addition of chromium or other metals to stabilize nickel and have found that in addition to increased stability, the nickel alloys retain the electrochemical characteristics of the base metal, nickel [19]. It is the combination of these properties that have led us to undertake a study of various alloys, as being reported herein for Ni–Cr.

Cyclic voltammetric (CV) results show that the oxidation of the carbohydrates is associated with the Ni(III)/Ni(II) redox couple. This oxidation is clearly seen by the current increase on the anodic Ni(III)/Ni(II) current-voltage (i–E) wave, when a carbohydrates such as glucose is added to the solution. This increase followed by a decrease in the cathodic current for the reduction of Ni(III) on CV scan reversal is consistent with a catalytic mechanism in which a chemical reaction (reaction 3) follows the electron transfer step (reaction 2).

Liquid chromatographic experiments were performed to assess various analytical properties (e.g., the linearity of the response with concentration, the reproducibility, etc.) of the Ni–Cr electrode. Hydrodynamic voltammograms of various carbohydrates, performed in a flowing solution, showed a current plateau in the potential range between 0.48 and 0.52 V, prior to the region for oxygen evolution. However, the signal-to-noise (S/N) ratio for the amperometric LC-EC detection with the Ni–Cr electrode was found to be optimal at 0.48 V vs. a Ag/AgCl reference electrode in 0.10 M NaOH solution.

EXPERIMENTAL

Reagents

Solutions of sorbitol, glucose, xylitol, maltose, ribose and sucrose (Aldrich, Milwaukee, WI), rhamnose, and lactose (Sigma, St. Louis, MO) were prepared daily. The water used in the experiments were purified by the NANOpure System (Barnstead, Boston, MA). Sodium hydroxide solutions of the desired concentrations were prepared from electrolytic grade sodium hydroxide (Aldrich) and NANOpure water.

Equipment

Cyclic voltammetric (CV) experiments were performed with a laboratory built potentiostat or a Cypress Model CS1090 computerized potentiostat (Cypress Systems, Lawrence, KS). A BAS Model MF-1052 (Bioanalytical Systems, West Lafayette, IN) electrochemical cell was used for the voltammetric experiments. A Ag/AgCl, 3 M

KCl reference electrode (BAS Model RE-1), and a platinum wire auxiliary electrode were used throughout the voltammetric experiments.

The chromatographic system (Shimadzu, Columbia, MD) consisted of pumps (LC-600), a column oven (CTO-6A), an electrochemical detector (L-ECD-6A), an auto sampler (SIL-6B), a system controller (SCL-6B), and a recorder (CR-4A). Either a CarboPac PA-1, 250 × 4 mm (Dionex, Sunnyvale, CA), or a Wescan Anion-R, 250 × 4 mm (Hamilton, Santa Clara, CA) anion exchange columns were used for the liquid chromatographic (LC) separations. The electrochemical cell for the flow experiments consisted of a home made working electrode, a stainless steel auxiliary electrode and a Ag/AgCl (3 M KCl) reference electrode.

The working electrodes for the CV experiments were made of Ni, or Ni–Cr (80:20) wires of 1.0 mm diameter (Goodfellow, Malvern, PA) embedded in PTFE shrinkable tubes. The working electrodes for the LC experiments were made of Ni–Cr (80:20) wires of 1.0 mm diameter embedded in Kel-F blocks of 0.5 × 1.0 × 1.0 in. The electrodes were polished successively with emery paper of 400, 600, and 0000 grit, and finished to a mirror surface with 1, 0.3, and 0.05 μm alumina particles suspended in water on a microcloth pad (Buehler, Lake Bluff, IL), sonicated, and then thoroughly washed with NANOpure water.

RESULTS AND DISCUSSION

Electrochemical properties of Ni and Ni–Cr electrodes

CV studies were conducted with both the Ni and Ni–Cr electrodes to compare their behavior in the absence and presence of a carbohydrate such as glucose in 0.1 M NaOH solution. In the potential region of ca. −1.0 to −0.34 V, as seen in Fig. 1 (solid line), a quasi-reversible oxidative and reductive CV wave is observed for pure Ni with an anodic peak potential (E_{pa}) of −0.60 V (Fig. 1, peak A) and cathodic peak (E_{pc}) of −0.96 V (Fig. 1, peak B). This CV wave has been attributed to the redox couple involving Ni^0 and Ni(II) [20,21]. It has been postulated [21] that the

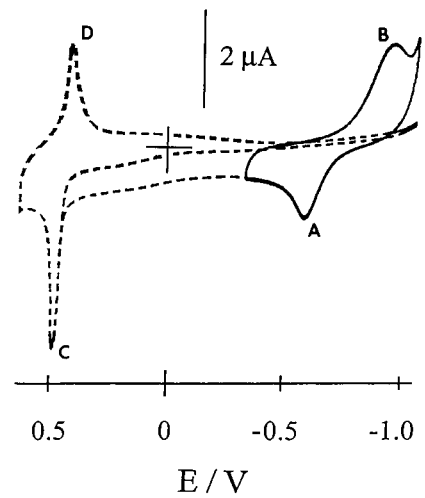

Fig. 1. Cyclic voltammetric response of a Ni electrode in 0.10 N NaOH. Scan rate = 0.05 V/s. T = 25°C. CV potential limits: −1.07 V to −0.34 V (solid line); −1.07 V to 0.65 V (dashed line).

initial oxidation of Ni^0 produces $\alpha(Ni(OH)_2$, as a solid, on the electrode surface. This alpha-form apparently converts with time to beta-$Ni(OH)_2$. If the CV scanning is continued, the height of the peak currents for both the anodic and cathodic waves decreases.

When the anodic limit for the potential is increased to +0.65 V, a second nearly reversible CV wave is observed with an E_{pa} of +0.47 V (Fig. 1, peak C) and an E_{pc} of +0.42 V (Fig. 1, peak D). The symmetric peak shapes of both the anodic and cathodic waves are indicative of a surface confined redox process. These waves have been attributed to the oxidation of $Ni(OH)_2$ to Ni(III) as the nickel oxyhydroxide (i.e., NiOOH) and its reduction back to Ni(II). The current plateau between the first and second anodic waves, has been attributed [21] to an increase in the beta-form of the nickel hydroxide. This plateau is observed only in the first CV cycle, decreasing dramatically thereafter to nearly background. Since both the alpha- and beta-forms of nickel hydroxide may be present, the one electron oxidation of the Ni(II) to Ni(III) may involve the formation of two forms of nickel oxyhydroxide. This assumption, may partially explain the presence of a broad shoulder appearing at less posi-

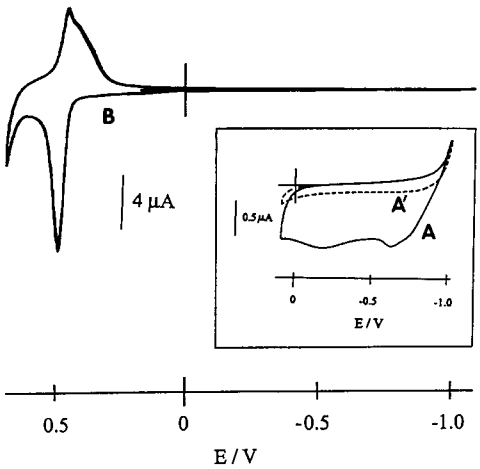

Fig. 2. Cyclic voltammograms shown for Ni–Cr electrode in 0.1 M NaOH solution. Inset shows a CV scan of a freshly prepared Ni–Cr electrode scanned from −1.0 to +0.05 V (trace A, solid line); trace A′ (dotted line) is for the second CV scan. Trace B is the CV scan for subsequent scan between the potential of −1.0 to +0.65 V (note change in current scale from 0.5 μA for inset to 4 μA for CV curve B). Cyclic voltammograms taken at a scan rate of 50 mV/s and T = 25°C.

tive potentials on both the anodic and cathodic Ni(III)/Ni(II) waves. If the CV scanning is continued between the potential limits of 0.0 and +0.65 V, the peak height of the anodic wave increases with the shoulder becoming less pronounced. However, the cathodic wave reaches a steady state and the wave at less positive potentials becomes more prominent in size. The appearance of more than one reversible wave for the Ni(III)/Ni(II) couple has been ascribed [22] to the presence of more than one crystalline form of both $Ni(OH)_2$ and NiOOH. Intercalation of ions also plays a role in the properties of the hydrated nickel hydroxide/oxide layer [23,24].

The presence of chromium in the nickel changes the CV waves in the potential range of −1.05 V to 0.09 V (inset of Fig. 2, solid line A). The CV wave for the first scan varies somewhat depending on the previous history (or pretreatment) of the electrode. A broad anodic wave is observed in the region of ca. −0.63 V. A second broad anodic wave is seen at approximately −0.17 V. The −0.63 V wave may be due to the oxidation of Ni^0 to Ni(II), similar to the results for a pure nickel electrode. The peak at −0.17 V is most likely due to the oxidation of chromium, although further experiments are needed to confirm this assumption. No cathodic waves are observed during the reverse scan. The current remains close to zero until the potential reaches a value of −0.90 V, where the current increases due to hydrogen evolution. Another interesting characteristic of the i–E trace at Ni–Cr alloy electrodes is that neither the anodic nor cathodic waves are observed after the first CV cycle (inset of Fig. 2, dashed line A′). Thus, the i–E curves are featureless thereafter in the potential region of −1.05 V to 0.09 V.

The CV i–E pattern for a Ni–Cr electrode, after a few scans, is similar to that obtained for pure Ni in the potential region of −1.06 V to 0.65 V (Fig. 2, curve B). The i–E curve is flat and featureless in the potential interval of −1.06 V to +0.05 V. As the potential is scanned toward more positive potentials, a well-defined oxidative wave develops with an E_{pa} value of ca. 0.48 V. On reverse scan, a reductive wave is observed with an E_{pc} of 0.40 V. These oxidative and reductive waves, as in the case of pure nickel, are attributed to the Ni(II)/Ni(III) redox couple. Any increase in the potential limit beyond +0.65 V does not alter the featureless i–E response in the potential region of −1.06 V to 0.05 V.

The changes to the CV waves in the potential region of 0.0 V to 0.60 V for the Ni–Cr electrode as a function of successive CV scans are essentially similar to those of pure Ni. These changes are shown in Fig. 3 as the potential is continuously scanned between the limits of 0.0 V and 0.60 V in 0.1 M NaOH solution. The values of the anodic and cathodic peak potentials, E_{pa} and E_{pc}, for the 50th (Fig. 3, curve c) and 400th (Fig. 3, curve f) CV scans at a pure Ni and a Ni–Cr electrode are summarized in Table 1. The data were obtained at a scan rate of 50 mV/s. There are very small differences between the E_{pa} and E_{pc} values, particularly as both the Ni and Ni–Cr electrodes are continually cycled between the anodic and cathodic limits of 0.0 and 0.60 V. For both electrodes the wave at less positive potential on the reverse cathodic scan becomes more

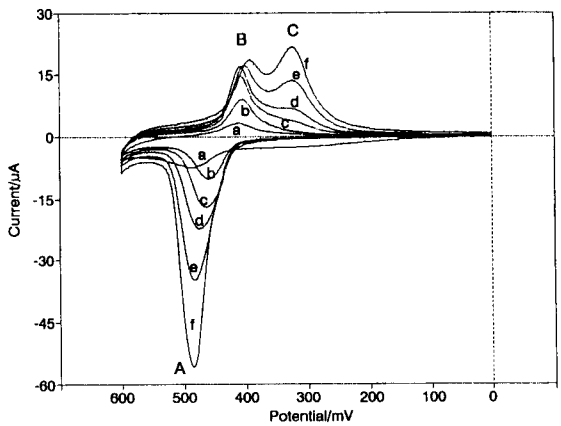

Fig. 3. Cyclic voltammograms shown for multiple scans of Ni–Cr electrode in 0.1 M NaOH solution. Scan numbers: a = 1, b = 10, c = 50, d = 100, e = 200 and f = 400. Scan rate 100 mV/s and T = 25°C. (See text for discussion of peaks A, B and C.)

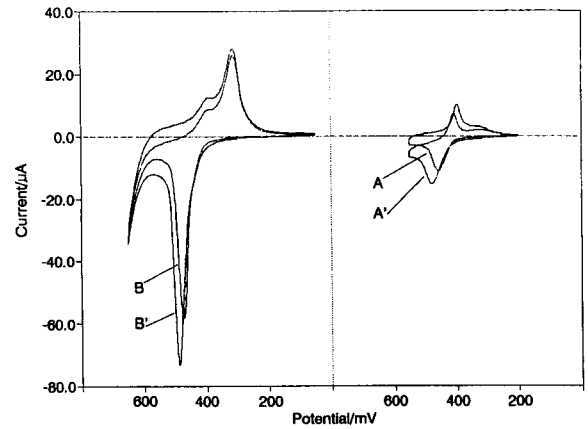

Fig. 4. Cyclic voltammetric traces for Ni–Cr electrode with and without added glucose in 0.1 M NaOH solution. Right side: Voltammograms of 100th CV cycle without (A) and with added 0.0010 M glucose (A'). Left side: voltammograms of 600th CV cycle without (B) and with added 0.0010 M glucose (B'). Scan rate 50 mV/s. T = 25°C.

prominent as the number of scan cycles increases. That is, the wave with an E_{pc} of 0.31 V (Fig. 3, peak C) increases with respect to the wave with a peak at 0.39 V (Fig. 3, peak B). The ratio of the electrochemical charge under the anodic and cathodic waves, when the cathodic charge is determined by taking the charge under both reductive waves, remains essentially constant and close to unity. The ratio being close to unity indicates that the anodically formed NiOOH on the surface of the electrode is totally retained and not lost to solution. The development of two reductive peaks means that there is an interconversion occuring in the type of nickel hydroxide/oxide on the surface. This conversion may be the transformation of the beta-NIOOH to the gamma-NiOOH form, as proposed by other authors [22]. The electrochemical behavior of Ni–Cr electrodes, and the possible influence of this crystallographic inter-conversion to the catalytic rate for glucose electrooxidation, has yet to be studied.

TABLE 1

Cyclic voltammetric peak potentials for nickel and nickel–chromium electrodes [a]

	Electrodes			
	Ni		Ni–Cr	
	E_{pa}	E_{pc}	E_{pa}	E_{pc}
A	0.48	0.40	0.45	0.40
B	0.49	0.39, 0.30	0.49	0.39, 0.31

[a] Data taken at a scan rate of 50 mV/s in 0.1 M NaOH solution. Peak potentials reported with respect to a Ag/AgCl (3 M KCl) reference electrode. (A) after completion of 50 CV cycles. (B) after 400 CV cycles. Temperature is 25°C.

Electrocatalytic oxidation of glucose

The addition of glucose to the background solution produced an increase in the charge and peak current under the wave assigned to the oxidation of Ni(II) to Ni(III) while the reverse cathodic peak height decreased. This effect of glucose is typical of an EC catalytic mechanism (Fig. 4, traces A and A', and B and B') where the electrogenerated catalyst, Ni(III), oxidizes the glucose diffusing to the electrode surface from the bulk solution. Although the background current under the Ni(III)/Ni(II) oxidation–reduction wave increases and the predominant oxide form changes with the number of cycles, the electrode still remains active toward glucose oxidation. Since the background current is considerably higher as the electrode is cycled, the increase in current in the presence of glucose is proportionally larger at a freshly produced NiOOH electrode rather than at the one having been cycled

for prolonged lengths of time. This proportional enhancement is seen by comparing the ratio of catalytic current for glucose oxidation to background at the Ni–Cr electrode. The charge and current ratios are 1.66 and 1.39, respectively, for the CVs obtained at the electrode which had been cycled for 100 times (Fig. 4, curves A and A′); while these ratios drop to 1.36 and 1.25, respectively, after the electrode had been cycled for 600 times (Fig. 4, curves B and B′).

The catalytic current is higher at a Ni–Cr electrode than at pure Ni for the same oxidative preparation. Thus, one finds that the slope of the calibration curve for carbohydrates at the Ni–Cr electrode is higher than that obtained with nickel. Although the reason for this higher sensitivity is currently unexplained, it does mean that the Ni–Cr should yield correspondingly higher sensitivity when it is used as an LC detector.

Liquid chromatography

Liquid chromatographic experiments were performed with the Ni–Cr electrode in order to evaluate various analytical parameters. Thus, the hydrodynamic voltammograms (HDVs) with various carbohydrates present, the signal-to-noise ratio, the effect of the mobile phase flow rate and of the temperature on the electrode response, and the long term reproducibility of the response were analyzed in order to determine the optimal conditions for carbohydrates detection. Also, the results obtained with the Ni–Cr electrode were compared with those reported in the literature using Ni electrodes.

Typical hydrodynamic voltammetric responses for five common sugars are shown in Fig. 5. The initial working potential was 0.32 V. After obtaining a stable, drift free baseline at each set potential, ten separate injections of the carbohydrate mixture were analyzed. The working potential was then increased by increments of 0.020 V, and the chromatographic analyses repeated. In the region between 0.32 and 0.44 V, there is essentially no evidence for carbohydrate oxidation. At potentials greater than 0.44 V the current increases and then plateaus at values above ca. 0.48 V. At potentials above 0.52 V, oxygen evolution commences as characterized by an increase in the

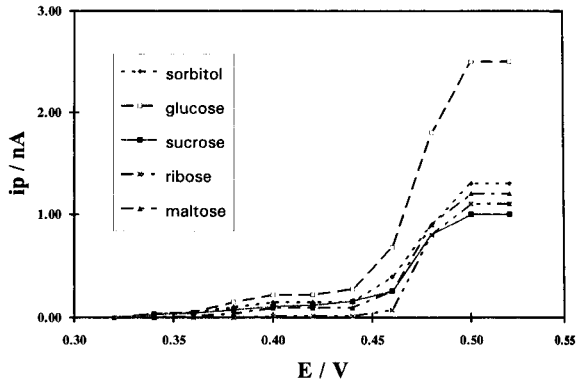

Fig. 5. Hydrodynamic voltammogram of various carbohydrates at Ni–Cr electrodes in 0.10 M NaOH. Flow-rate 0.50 ml/min. T = 25°C. LC column = Wescan anion-R. 100 pmol of each carbohydrate injected onto column.

background noise level. Both mono and disaccharides are readily oxidized at the Ni–Cr electrode, although glucose gave the highest response (Fig. 5).

The signal-to-noise ratio was analyzed in the potential region of 0.32 V to 0.52 V (Fig. 6) to determine the potential giving the highest S/N ratio. This potential should be taken as the "optimum" working potential [25] for the LC analysis of carbohydrates. In the potential region of 0.32 V to 0.42 V there is little change to the S/N ratio. Above ca. 0.42 V the S/N increases with

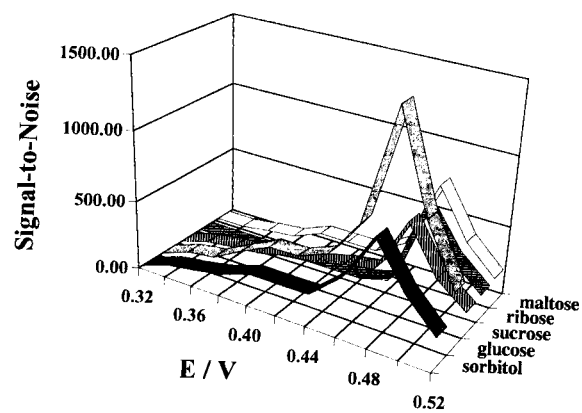

Fig. 6. Analysis of signal-to-noise ratio for various carbohydrates with Ni–Cr electrodes at different working potentials in 0.10 M NaOH solution. Flow-rate = 0.50 ml/min. T = 25°C. LC column Wescan anion-R. 100 pmol of each carbohydrate injected onto column.

the maximum value in the region of 0.44 to 0.48 V, depending on the particular carbohydrate. At higher potentials, the S/N ratio decreases. Maxima in the S/N ratio occur because in the potential region of 0.42 V to 0.48 V, the signal levels increase while the background noise remains nearly constant. On the other hand, the signal remains almost constant while the noise increases in the potential region above 0.48 V. The observed increase in the noise at high potentials, as explained earlier, is due to the proximity of the potential to oxygen evolution.

The S/N ratio for the detection of glucose was also studied at the Ni–Cr electrode as a function of the working potential and of the concentration of sodium hydroxide (Fig. 7). This analysis is important not only to assess the "best" pH for carbohydrate analysis, but also to determine if this pH is within the recommended range for use with the anion exchange column.

The S/N ratio for glucose detection increases with increasing NaOH concentration. This increase is noticeable (close to three times) when the concentration of the sodium hydroxide is increased from 0.05 M to 0.10 M. However, only a small increase was observed when the NaOH concentration in the mobile phase was increased from 0.10 M to 0.20 M (Fig. 7). Moreover, the S/N ratio at these two concentrations may be considered as being approximately the same if the errors in the S/N ratio determination are taken into account. Thus, a concentration of 0.10 M NaOH is essentially the optimum pH value (at an applied potential of 0.46 V), consistent with the compatibility of the LC column to pH.

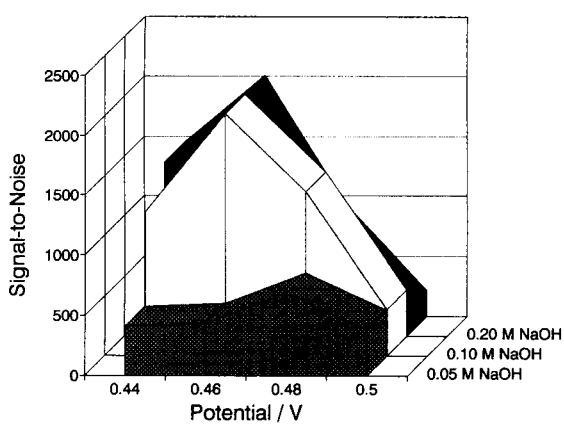

Fig. 7. Signal-to-noise ratio analysis for glucose at various working potentials and at different sodium hydroxide concentrations. Flow-rate = 0.50 ml/min. T = 25°C. LC column = Wescan anion-R. 100 pmol of glucose injected.

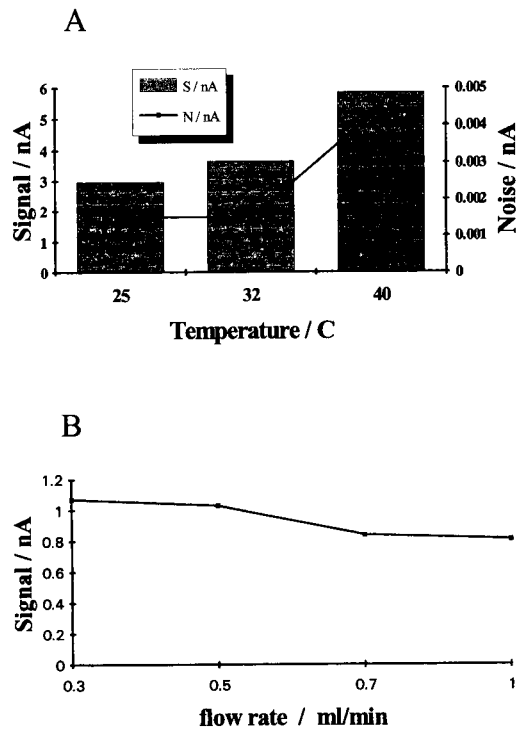

Fig. 8. Effect of temperature (A) and flow-rate (B) on the response of the Ni–Cr electrode for the injection of 100 pmol of glucose in 0.10 M NaOH solution. (A) Flow-rate = 0.5 ml/min; (B) T = 25°C.

The effects of the mobile phase flow rate and the temperature on the electrode response for glucose are plotted in Fig. 8. An increase of approximately 20% is observed to the electrode response when the temperature is increased from 25°C to 32°C (Fig. 8A). As a consequence of the background noise remaining nearly constant, the S/N ratio increases within this temperature increment.

An increase of approximately 65% is obtained when the temperature is increased from 32°C to 40°C (Fig. 8A). However, the background noise concomittantly increases by nearly a factor of

three so that the S/N ratio decreases. The reason for the increase in the signal with temperature may be explained by the following: (a) At higher temperatures, the peak potential for the oxidation of Ni(II) to Ni(III) may be shifting in the cathodic direction by -2 mV/°C [22]. With such a shift, the electrocatalytic activity may be higher even though the working potential is maintained at the same value; and (b) the temperature increment may increase the velocity constant of reaction 3. This reaction has been proposed [16] as the rate limiting step in the electrocatalytic mechanism.

A small decrease in the LC-EC current is observed for glucose when the mobile phase flow rate is increased from 0.3 to 1.0 ml/min (Fig. 8B). The reason for this decrease is believed to arise from the fact that the potential is set at 0.46 V rather than at 0.52 V, where the oxidation of glucose would be mass transfer controlled. At 0.46 V the rate of glucose oxidation is governed by reaction 3.

The reproducibility of the response for the long term use of the Ni–Cr electrode was tested during 21 days of continuous chromatographic analysis. Thirty injections were made every half an hour each day (an average of 15 hours of use per day). The results are shown in Fig. 9. The relative response is defined as the peak current for the injection of 100 pmol of glucose, relative to the response obtained during the first four hours of analysis. As such, the electrode response at any time can be easily compared to that obtained at the beginning of the analysis (taken as 100%). The average relative response for daily injections of thirty samples, once every 0.5 h, is then plotted as a function of the number of days.

There is a decrease of approximately 30% in the relative response during the first seven days of analysis (Fig. 9). However, the signal remains nearly constant after that time, decreasing only by ca. 20% during the next two weeks. This is a marked improvement to the reproducibility reported in the literature for a nickel electrode [8]. Stitz and Buchberger [10] reported a high stability for the detection of carbohydrates at a nickel electrode for periods of time up to three weeks. They pretreated the electrode by applying 2–3 V

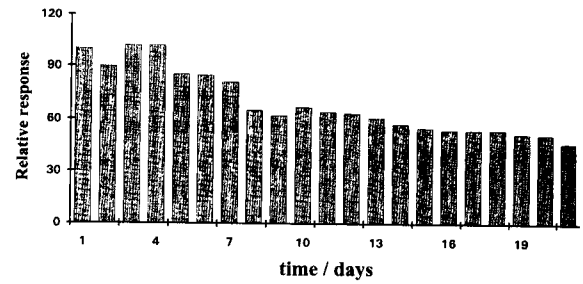

Fig. 9. Reproducibility of Ni–Cr electrodes for the injection of 100 pmol of glucose in 0.10 M NaOH solution. Flow-rate 0.50 ml/min. $T = 25$°C. Potential of the working electrode set at 0.47 V. LC column Wescan anion-R, relative response $r_r = i_p(t)/i_p(0) \times 100$. Peak height, i_p (t), at any time of analysis. $i_p(0)$ = average peak height during the first four hours of analysis. Electrode "on" for 15 h per day.

for 5 min in 0.2 M or 0.3 M NaOH at 70°C. However, the limit of detection for glucose at an S/N ratio of three was approximately 150 pmol, which is markedly higher than that obtained at the Ni–Cr electrode.

It should be mentioned that the relative percentage of error for the thirty daily injections is at or below 5% for the 21 days of analysis. Errors were below this value during the sixth and seventh days of the analyses.

A chromatographic calibration curve was made for several carbohydrates at the Ni–Cr electrode. The results are summarized in Table 2. A wide linear concentration range was obtained for all the carbohydrates analyzed, including sugar alcohols, mono- and disaccharides. Excellent correlation coefficients were obtained over the range of

TABLE 2

Data for liquid chromatographic analysis of carbohydrates at Ni–Cr electrode

Compound	Concentration range	Correlation data [a]
Sorbitol	1×10^{-6}–1×10^{-3}	1.000 (10)
Glucose	1×10^{-7}–1×10^{-3}	1.000 (13)
Ribose	3×10^{-7}–1×10^{-3}	1.000 (10)
Maltose	6×10^{-7}–1×10^{-3}	0.999 (12)

[a] Correlation coefficient; (in parenthesis) number of points for the linear regression calculation. Each point is the average of ten injections. Experimental conditions: mobile phase, 0.10 M NaOH; flow-rate = 0.5 ml/min; applied potential = 0.47 V; and temperature = 25°C.

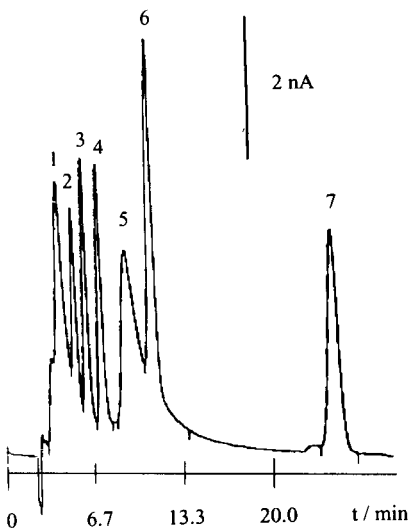

Fig. 10. Chromatogram of various carbohydrates detected with the Ni–Cr electrode in 0.10 M NaOH solution. Flow-rate 0.50 ml/min. Potential of working electrode set at 0.47 V. T = 25°C. LC column CarboPac PA-1. Injection volume 10 μl. Injected amount: 100 pmol each of xylitol, glucose, and rhamnose (1, 3 and 4), 200 pmol of lactose and maltose (6 and 7), and 400 pmol of sorbitol and ribose (2 and 5).

concentrations determined. The linearity at the Ni–Cr alloy electrode is better than those obtained at the Ni–Cr–Fe and the Ni–Cu alloy [26]. Based on a S/N ratio of 3, the limit of detection for glucose was 500 fmol, as calculated from the extrapolated S/N ratio obtained with an injection of 100 pmol. To confirm this sensitivity, a 3 pmol sample of glucose in 0.1 M NaOH was injected into the anion exchange LC column. A peak current of 100 pA was obtained. The S/N ratio was approximately 15 at this current sensitivity so that the calculated limit of detection is 600 fmol, close to the extrapolated value of 500 fmol. This sensitivity with the Ni–Cr electrode is considerably better than that found with pure nickel electrodes [8,10,12].

Various sugar alcohols, mono- and disaccharides can be separated and detected with the Ni–Cr electrode, as seen in Fig. 10. The electrode responds quickly so that the column resolution is maintained.

The time required to obtain a stable baseline is another parameter of considerable importance. A background baseline was considered "stable" when the baseline changed less or equal to 5% at a sensitivity setting of 1 nA full scale during a 20 min period. Four hours were required to obtain a stable baseline with the Ni–Cr electrode, similar to the time required with a Ni–Cr–Fe alloy [26], and markedly less than that necessary with Ni–Cu and Cu electrodes (24 and 36 h, respectively). Moreover, the magnitude of the background current at the Ni–Cr electrode was ca. 2–6 nA when the applied potential was 0.47 V and the mobile phase flow rate was 0.5 ml/min. The background is considerably less than those obtained at the Ni–Cr–Fe and Ni–Cu electrodes. A low background current usually exhibits less noise and thus, gives an enhanced S/N ratio. The Ni–Cr electrode appears viable as an amperometric LC-EC detector for carbohydrate analysis in high-performance anion exchange separations.

Conclusions

The Ni–Cr alloy can be used for the constant potential amperometric detection of carbohydrates in high-performance anion exchange chromatography. This alloy is quite resistant to corrosion. As such, its electrochemical response is improved in comparison to that of pure nickel. Cyclic voltammetric experiments suggest that the sugars are oxidized in the region of potential between 0.4 and 0.5 V by nickel oxyhydroxides that are formed on the electrode surface in the strong alkaline solution. Additional studies are needed to fully resolve the mechanistic details of oxidative EC catalysis of the carbohydrates. With optimization of the experimental parameters, a limit of detection for glucose in the range of 500–600 fmol was achieved at a S/N ratio of three. The electrode reaches a stable background current after a relatively short period of 4 h. Continuous operation for over 21 days was achieved without serious degredation in the signal response. The electrode can be reactivated easily by manually polishing the Ni–Cr surface, if needed.

This work was supported by the Shimadzu Co., Kyoto, Japan, and the Kansas Technology Enterprise Corporation under their Applied Research

Matching Grants Program. JMM acknowledges support of a fellowship grant from the National Research Council of Argentina (CONICET).

REFERENCES

1 L.R. Snyder and J.J. Kirkland, Introduction to Modern Liquid Chromatography, Wiley, New York, 2nd edn., 1979, p. 162.
2 S. Honda, E. Akao, S. Suzuki, M. Okuda, K. Kakehi and J. Nakamura, Anal. Biochem., 180 (1989) 351.
3 F. Natchman and K.W. Budna, J. Chromatogr., 136 (1977) 279.
4 S. Honda, M. Takahashi, K. Kakehi and S. Ganno, Anal. Biochem., 113 (1981) 130.
5 G.G. Neuburger and D.C. Johnson, Anal. Chem., 59 (1987) 150.
6 S. Hughes and D.C. Johnson, Anal. Chim. Acta, 149 (1983) 1.
7 C.E. Cowie, P.R. Haddad and P.W. Alexander, Chromatographia, 21 (1986) 417.
8 P. Luo, F. Zhang and R.P. Baldwin, Anal. Chim. Acta, 244 (1991) 169.
9 L.M. Santos and R.P. Baldwin, Anal. Chem., 59 (1987) 1766.
10 A. Stitz and W. Buchberger, Fresenius' J. Anal. Chem., 339 (1991) 55.
11 J.M. Zadeii, J.M. Marioli and T. Kuwana, Anal. Chem., 63 (1991) 649.
12 T. Ueda, R. Mitchell, T. Metcalf, T. Kuwana and A. Nakamoto, J. Chromatogr., 593 (1992) 265.
13 J. Marioli and T. Kuwana, PittCon 92, paper No. 1301, New Orleans, 1992.
14 S.V. Prabhu and R.P. Baldwin, J. Chromatogr., 503 (1990) 227.
15 N.A. Hampson, J.B. Lee, J.R. Morley and B. Scanton, Can. J. Chem., 47 (1989) 3729.
16 M. Fleischmann, K. Korinek and D. Pletcher, J. Electroanal. Chem., 31 (1971) 39.
17 B.S. Hui and C.O. Huber, Anal. Chim. Acta, 134 (1982) 211.
18 I.G. Casella, E. Desimoni and T.R.I. Cataldi, Anal. Chim. Acta, 248 (1991) 117.
19 R.A. Pacey, Chromium Rev., 5 (1985) 32.
20 R.S. Schrebler-Guzman, J.R. Vilche and A.J. Arvia, J. Electrochem. Soc., 125 (1978) 1578.
21 F. Hahn, B. Beden, M.J. Croissant and C. Lamy, Electrochim. Acta, 31 (1986) 335.
22 H. Gomez Meier, J.R. Vilche and A.J. Arvia, J. Appl. Electrochem., 10 (1980) 611.
23 J. Desilvestro, D.A. Corrigan and M.J. Weaver, J. Electrochem. Soc., 135 (1988) 885.
24 D. Fan and R.E. White, J. Electrochem. Soc., 138 (1991) 2952.
25 K. Stulik and V. Pacakova, Electroanalytical Measurements in Flowing Liquids, Ellis Horwood, Chichester, 1987, p. 29.
26 J.M. Marioli and T. Kuwana, Electroanalysis, 5 (1993) 11.

Analytica Chimica Acta, 282 (1993) 581–588
Elsevier Science Publishers B.V., Amsterdam

Automatic method for on-line preparation of fatty acid methyl esters from olive oil and other types of oil prior to their gas chromatographic determination

E. Ballesteros, M. Gallego and M. Valcárcel

Department of Analytical Chemistry, Faculty of Sciences, University of Córdoba, 14004 Córdoba (Spain)

(Received 27th February 1993; revised manuscript received 3rd June 1993)

Abstract

Fatty acids in oils were on-line methylated with acetyl chloride in methanol by dissolving 10–120 mg of oil in 100 ml of *n*-hexane, followed by continuous transesterification of the triglycerides, and flushing of residual reaction products by circulating a water stream through the derivatization manifold, after which the *n*-hexane phase from a membrane separator containing the fatty acid methyl esters was injected (5 μl) via a valve into the injection port of a gas chromatograph. Comparison of this transesterification method with the manual method involving saponification with methanolic sodium hydroxide and esterification with boron trifluoride in methanol (Official Method of Analysis) revealed good agreement between the results provided by both for olive and other vegetable oils as well as codfish oil.

Keywords: Gas chromatography; Continuous derivatization; Fatty acid methyl esters; Oils

The fatty acid composition of olive oil and other vegetable oils is still used by lipid analysts to determination of adulteration [1,2]. The direct gas chromatographic analysis of triglycerides is exceedingly difficult because of the low volatility of these compounds [3]; thus, liquid chromatography has been proposed for the direct determination of triglycerides using a refractive index detector [4]; however, the analysis of samples having triglycerides with a broad molecular weight distribution is rather difficult. Accordingly, liquid chromatographic analysis of oils and fats is not yet practical, so gas–liquid chromatography (GLC) continuous to be the most usual choice. Derivatization of fatty acids is more frequently accomplished by converting carboxyl groups into trimethylsilyl esters or methyl esters [5]. Trimethylsylation is usually achieved with bis(trimethylsilyl)trifluoracetamide [6,7] or *N*-(*tert*-butyldimethylsilyl)-*N*-methyltrifluoro-acetamide [8], while methylation of fatty acids is more commonly performed with diazomethane [9,10], methyl iodide in *N*,*N*-dimethylacetamide [11] or tetramethyl-ammonium [12] in ethyl ether, or boron trifluoride [13–15], hydrochloric acid [16], sulphuric acid [17] or acetyl chloride [18,19] in methanol. As regards application, GLC has been used to determine fatty acids in various types of oil and fats, namely: olive oil [16,20], sunflower oil [21], soybean oil [22,23], fish oil [24], milk [25–27] and cheese [26,28], and various other products. Other chromatographic techniques frequently used for the determination of fatty acids include thin layer chromatography [29] and liquid chromatography [30–33]. Two GC methods for the determination of a variety of phenols in water

Correspondence to: M. Valcárcel, Department of Analytical Chemistry, Faculty of Sciences, University of Córdoba, 14004 Córdoba (Spain).

samples by use of a continuous liquid–liquid extraction–derivatization system were also recently developed by our group [34,35].

Procedures for preparation of fatty acid methyl esters for subsequent GLC analysis usually employ anhydrous methanol containing an acid or basic catalyst and involve refluxing for a few minutes to a few hours. In addition, the boiled mixture must be washed, filtered and evaporated several times, and most derivatizing reagents are toxic, explosive and expensive. Therefore, the aim of this paper was to develop a new automatic method for the direct determination of the fatty acid composition of olive oil and other vegetable oils with none of the lengthy steps of the conventional procedure. In addition, it should minimize contamination/losses of fatty acids typically involved in the manual steps, as well as toxic hazards (the reaction would take place in a closed flow system) and reagent consumption. This paper thus reports on the use of a continuous derivatization system to preparate fatty acid methyl esters and determine them by on-line GLC.

EXPERIMENTAL

Chemicals

Fatty acids (palmitic, palmitoleic, stearic, oleic, linoleic and linolenic) and acetyl chloride were purchased from Aldrich. Heptadecanoic acid (internal standard) was obtained from Sigma, and the remaining reagents (sodium sulphate, sodium hydroxide, potassium methylate, sulphuric acid, boron trifluoride reagent in methanol, *n*-hexane, *n*-heptane, methanol, ethyl acetate and ethyl ether) were supplied by Merck. The oils were purchased from local suppliers.

Fatty acids were identified by using reference standards of 4 g l^{-1} in *n*-hexane that were stored in PTFE bottles at 4°C. The optimal conditions for GLC were established by using a mixture of fatty acids based on the composition of olive oil in *n*-hexane. A solution containing 5% (v/v) acetyl chloride in methanol was used as derivatizing reagent.

Apparatus

A Hewlett-Packard 5890 gas–liquid chromatograph equipped with a Hewlett-Packard 3392-A integrator was used. The chromatograph was provided with a flame ionization detector (FID) and a 30 m × 0.53 mm i.d. Supelcowax-10 glass column packed with polyethylene glycol (1 μm film thickness). Nitrogen was used as carrier gas at a flow-rate of 16.2 ml min^{-1}. The injector and detector temperatures were kept at 250°C. The column temperature was raised from 165°C (2 min) to 180°C at 4°C min^{-1} (3 min), then to 200°C at 5°C min^{-1}, and finally to 260°C at 15°C min^{-1}, this last temperature being held for 2 min.

The flow derivatization system consisted of a Gilson Minipuls-2 peristaltic pump, a Tecator A-10 T solvent segmenter and a custom-made phase separator [36] furnished with a fluoropore membrane (1.0 μm pore size, FALP, Millipore). Poly(vinyl chloride) and Solvaflex pumping tubes for water and organic solutions, respectively, and PTFE tubing (0.5 mm i.d.) for coils were also used. A six-port Knauer 6332000 injection valve whose original volume was reduced to 5 μl was mounted over the injection port of the gas chromatograph. A thermostated water bath was also used.

Procedure

The manifold used is depicted in Fig. 1. It was operated as follows: a liquid fat sample solution containing 10–120 mg of oil plus 10 mg heptadecanoic acid as internal standard in 100 ml of *n*-hexane was continuously introduced into the flow system and mixed with a stream of 5% (v/v) acetyl chloride in methanol (derivatizing reagent). Transesterification of triglycerides (i.e., formation of fatty acid methyl esters) took places in a 500-cm long reaction tube (0.5 mm i.d.) which was heated at 80°C. Exactly 2 min after continuous introduction of sample reagent (the time required to load the derivatization reactor with sample), the flow was halted for 15 min to allow the derivatization reaction to complete in the reaction coil. A water stream was then inserted into the system to effect separation of excess of acetyl chloride in methanol and residual reaction products prior to the determination of the esters in the *n*-hexane phase. For

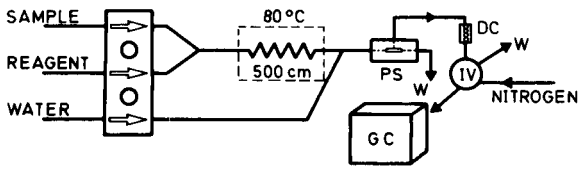

Fig. 1. Schematic diagram of the system used for continuous derivatization of triglycerides and determination of fatty acid methyl esters. PS, phase separator; DC, desiccating column; IV, injection valve; W, waste; GC, gas chromatograph. Sample and reagent flow-rate, 0.28 ml min^{-1}; water flow-rate, 1 ml min^{-1}; injected volume, 5 μl.

this purpose, 5-μl fraction of fatty acid methyl esters was injected into the nitrogen carrier gas and transferred to the chromatograph port. To prevent any water trace from entering the column, the derivatization system included a desiccating column (50 × 3 mm i.d.) located before the injection valve that was filled with sodium aluminosilicate pellets (pore diameter, 4 Å).

RESULTS AND DISCUSSION

Selection of the derivatizing reagent and organic solvent

The manifold used was similar to that depicted in Fig. 1. Selection of reagents and optimization of chemical variables were done by collecting the extracts of fatty acid methyl esters in *n*-hexane from the membrane separator in 4-ml glass vials containing anhydrous sodium sulphate and injecting 2-μl fractions manually into the chromatograph by means of a syringe.

The derivatizing reagent (potassium methylate, boron trifluoride, acetyl chloride and sulphuric acid, all in methanol) was prepared by dissolving 1.25 ml of each in 25 ml of methanol and the sample containing 40 mg olive oil was diluted in 100 ml of *n*-hexane; for comparison, a reference standard mixture of fatty acids (40 mg) with the same composition as olive oil reported in the literature [1] was also prepared in 100 ml of *n*-hexane and assayed in parallel. The results obtained are listed in Table 1; the esterification yield relative to the reference standard mixture of fatty acids was calculated and a mean was obtained by using the normalization method [14]. When sulphuric acid or boron trifluoride in methanol were used, the derivatization efficiency ranged between 4.5 and 27.0% for triglycerides in olive oil relative to the reference standard mixture of fatty acids because the derivatization reaction was favoured when the fatty acids were in free form. With acetyl chloride, the transesterification efficiency of triglycerides of olive oil and the esterification of fatty acids in the reference standard were similar and close to 94% in both instances. Potassium methylate only derivatized the olive oil sample (the peak area of each fatty acid was similar to that obtained with acetyl chloride), but none of the fatty acids in the reference standard under the assayed conditions; therefore, Table 1 does not give the reaction yield, but only

TABLE 1

Comparison of different esterification methods for the obtainment of methyl esters from olive oil

Fatty acid	Method								Mean [c] (%)
	H_2SO_4–MeOH		BF_3–MeOH		CH_3COK–MeOH		CH_3COCl–MeOH		
	Yield [a] (%)	Mean [b] (%)	Yield [a] (%)	Mean [b] (%)	Yield [a] (%)	Mean [b] (%)	Yield [a] (%)	Mean [b] (%)	
Palmitic	8.2	11.7	15.9	12.6	–	10.6	100.0	11.5	11
Palmitoleic	5.5	0.7	27.0	1.9	–	0.5	87.6	1.3	3
Stearic	6.3	2.5	11.5	2.5	–	1.7	88.3	1.8	1
Oleic	7.4	76.3	13.5	76.8	–	83.0	95.5	79.3	79
Linoleic	12.7	8.2	16.2	5.8	–	3.7	100.5	5.4	5
Linolenic	4.5	0.6	5.5	0.4	–	0.5	91.4	0.7	1

[a] Yield of the reaction of each fatty acid from olive oil relative to the corresponding fatty acid free of a reference standard of olive oil prepared as described elsewhere [1]. [b] Mean obtained by the normalization method [14]. [c] Reported mean for olive oil [1].

the mean for each fatty acid. In was thus concluded that neither sulphuric acid nor boron trifluoride were efficient transestrification agents for the triglycerides (both provided a reaction yield of only 25%). Acetyl chloride was thus chosen as derivatizing reagent because it provided roughly the same reaction efficiency as potassium methylate, but it also derivatized free fatty acids. Also, as it can be seen in Table 1, the mean obtained for individual fatty acids (%) derivatized with acetyl chloride was closen to reported values [1] than was that obtained with potassium methylate.

Four organic solvents (ethyl acetate, ethyl ether, heptane and *n*-hexane) were assayed to recove the esters. *n*-Hexane and *n*-heptane were found to be the most efficient for transesterifiying fatty acids in olive oil with acetyl chloride and recovering the esters (recoveries were roughly 4 times higher than those afforded by ethyl acetate and ethyl ether). *n*-Hexane was finally chosen as solvent because Solvaflex pumping tubes are more resistant to it than they are to *n*-heptane.

For optimization of variables, heptadecanoic acid was used as internal standard on account of its ready derivatization and virtual constancy of its peak area throughout the experiments. The concentration of acetyl chloride in methanol was varied between 0 and 7% (v/v) and a sample containing 40 mg olive oil and 10 mg of internal standard in 100 ml *n*-hexane was used. Experiments were done by stopping the flow 2 min after continuous introduction of sample-reagent for 15 min and heating the mixture at 80°C to allow complete transesterification. The analytical signal thus obtained increased with increase in the concentration of acetyl chloride up to 4% (v/v). A concentration of 5% (v/v) in methanol was thus chosen for further experiments.

The effect of temperatures in the automatic procedure was studied in the range 25–90°C. Increasing temperatures of the reaction coil resulted in sharply increasing peak areas, as can be seen in Fig. 2; the signal corresponding to oleic acid was the tallest (its content in olive oil is ca. 79%). The analytical signal remained virtually constant between 75 and 85°C, above which it decreased lightly, probably through decomposition of the derivatizing reagent (b.p. 52°C). The derivatization coil (500 cm long) was heated at 80°C in a thermostated water bath.

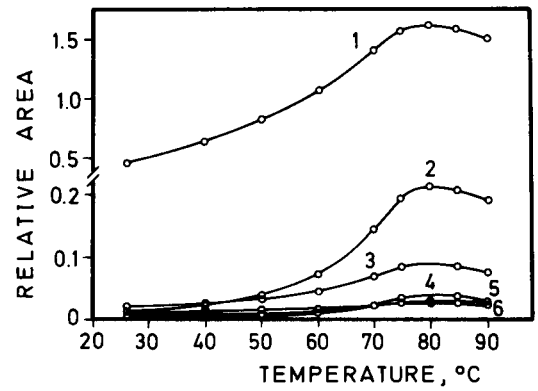

Fig. 2. Influence of temperature on the derivatization reaction of fatty acids present in an olive oil sample. (1) Oleic acid; (2) palmitic acid; (3) linoleic acid; (4) stearic acid; (5) palmitoleic acid; (6) linolenic acid. Sample, 40 mg olive oil in 100 ml *n*-hexane. Relative area (analyte peak area/internal standard peak area ratio).

Optimization of the flow derivatization system

The flow variables studied were flow-rates, length of the derivatization coil and flow halting interval (residence time of the sample-derivatizing reagent mixture).

The flow-rates of sample, derivatizing reagent and water (for removal of excess of derivatizing reagent and residual products of the derivatization reaction) were optimized. The chromatographic signals increased with decreasing flow-rate of sample and reagents because the reaction was quite slow. The water flow-rate had no effect over the assayed range (0.3 to 1.5 ml min^{-1}) as the stream was only required to remove residual products, which must not reach the chromatographic column. A compromise was thus made and identical sample and reagent flow-rates of 0.28 ml min^{-1} (overall flow-rate in the derivatization coil, 0.56 ml min^{-1}) and a water stream flow-rate of 1 ml min^{-1} were chosen.

The influence of the derivatization coil length was investigated between 10 and 700 cm (0.5 mm. i.d.). Short reactor coils (less than 450 cm long) resulted in too short residence times of the sam-

ple-reagent mixture for the reaction to complete, so a coil length of 500 cm was chosen. The residence time was thus crucial in order to ensure completion of the derivatization reaction. As can be seen in Fig. 3, not stopping the mixing flow of sample-reagent in the derivatization coil resulted in short residence times (1.75 min) and hence in inefficient mixing and incomplete reaction (some fatty acids remained unesterified and the signals were quite low). For a minimum residence time of 10 min, transesterification was virtually complete. Halting the flow for 15 min exactly 2 min after continuous introduction of sample-reagent was sufficient for the derivatization reaction to complete (Fig. 3); this time was thus chosen as optimal.

Coupling of the continuous derivatization system to a gas chromatograph

The interface unit between the derivatization system and gas chromatograph was an injection valve similar to that previously used to couple an extraction unit with a gas chromatograph [35], but was slightly modified for the present purpose. The first modification involved the injected volume. Owing to the large volume of the valve loop (10 μl), a new loop of 2.5 μl was constructed from PTFE tubing (35 × 0.3 mm i.d.). The new injected sample volume was 5 μl (2.5 μl of inner volume of valve plus 2.5 μl of loop). A second alteration to the valve involved fitting a 4 cm

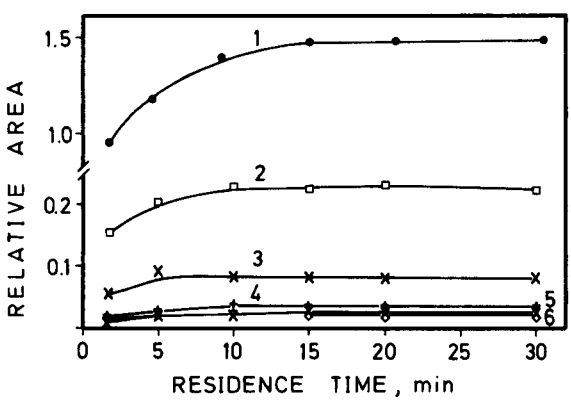

Fig. 3. Effect of the residence time on the derivatization reaction of fatty acids present in an olive oil sample. Numbers corresponds to the same fatty acids as in Fig. 2.

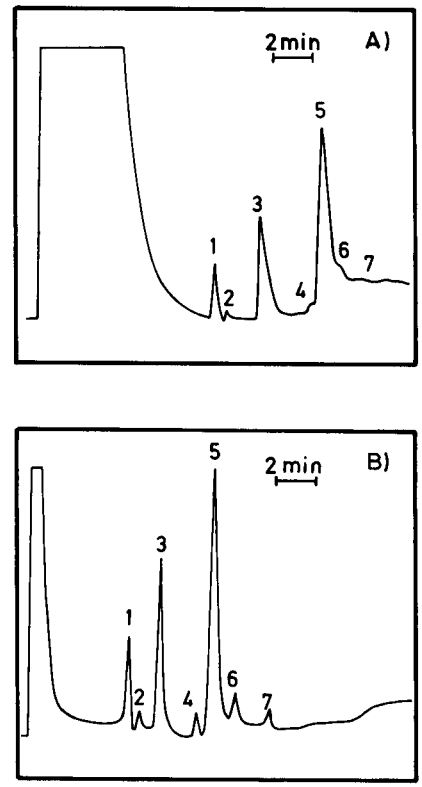

Fig. 4. Gas chromatograms of the fatty acid methyl esters in olive oil (400 mg l^{-1}) obtained by automatic injection at different carrier flow-rates: (A) 6.5 ml min^{-1} and (B) 16.2 ml min^{-1}. Peaks: (1) palmitic acid; (2) palmitoleic acid; (3) heptadecanoic acid (internal standard, 100 mg l^{-1}); (4) stearic acid; (5) oleic acid; (6) linoleic acid; (7) linolenic acid.

PTFE tubing (0.3 mm i.d.) to the carrier outlet. At the end of this tube was introduced a stainless steel needle which was finally inserted into the injection port of the instrument. The carrier gas (nitrogen) inlet was split into two which were directly connected to one of the ports of the valve and the chromatograph injection port. The inlet was shut by a stopcock so that the instrument could be used for manual injections by allowing the nitrogen stream to follow its normal route through the instrument. Optimizing the flow-rate gas carrier was necessary in order to reduce adsorption of the derivatized sample in *n*-hexane by the loop and tube valve port, as well as to improve chromatographic resolution of the peaks. Figure 4 shows the chromatograms obtained by

TABLE 2

Features of the calibration graphs and determination of fatty acid methyl esters

Fatty acid	Regression equation [a]	Correlation coefficient	Linear range (mg l^{-1})	Detection limit (mg l^{-1})	Relative standard deviation (%)
Palmitic	$A = 5.10 \times 10^{-3}X + 1.28 \times 10^{-3}$	0.998	1 –1000	0.8	2.10
Palmitoleic	$A = 6.25 \times 10^{-3}X + 2.50 \times 10^{-4}$	0.997	0.9–1000	0.7	2.58
Stearic	$A = 3.79 \times 10^{-3}X + 2.57 \times 10^{-4}$	0.997	2 –1000	0.9	3.40
Oleic	$A = 4.60 \times 10^{-3}X + 8.80 \times 10^{-3}$	0.998	3 –1000	0.9	2.92
Linoleic	$A = 3.68 \times 10^{-3}X + 4.82 \times 10^{-3}$	0.999	2 –1000	0.8	3.11
Linolenic	$A = 7.29 \times 10^{-3}X + 1.30 \times 10^{-4}$	0.997	0.7–1000	0.5	2.78

[a] A = Analyte peak area/internal standard peak area ratio; X = concentration (mg l^{-1}).

injecting extracts of the fatty acid methyl esters of olive oil in *n*-hexane at various nitrogen flow-rates. As can be seen, low nitrogen flow-rates (Fig. 4A) resulted in broad peaks (increased retention times) and prevented the methyl esters of stearic, linoleic and linolenic acids from being identified. An overall gas flow-rate of 16.2 ml min^{-1} (flow-rate through the valve and injection port 11.6 and 4.6 ml min^{-1}, respectively) was found to be optimal.

Figures of merit of the proposed method

The analytical figures of merit of the proposed method were shown in Table 2. The standard

TABLE 3

Fatty acid contents in oil samples obtained by the proposed continuous method [a] and the Official Method [b]

Oil samples	Fatty acids						
	Palmitic	Palmitoleic	Stearic	Oleic	Linoleic	Linolenic	Others [c]
Virgin olive	11.3 ± 0.3 [a]	1.4 ± 0.1	1.8 ± 0.1	79.3 ± 0.5	5.5 ± 0.3	0.7 ± 0.05	–
	10.9 ± 0.1 [b]	1.5 ± 0.1	1.9 ± 0.1	79.4 ± 0.6	5.4 ± 0.4	0.9 ± 0.08	–
Refined olive	9.6 ± 0.4 [a]	1.0 ± 0.1	–	76.8 ± 0.5	12.3 ± 0.2	0.3 ± 0.03	–
	9.6 ± 0.5 [b]	1.1 ± 0.2	–	76.9 ± 0.6	12.1 ± 0.5	0.3 ± 0.02	–
Raw olive	12.0 ± 0.2 [a]	1.6 ± 0.2	–	73.1 ± 0.6	13.3 ± 0.3	–	–
	11.6 ± 0.1 [b]	1.5 ± 0.1	–	74.1 ± 0.4	12.8 ± 0.3	–	–
Sunflower-seed	7.9 ± 0.2 [a]	–	1.7 ± 0.2	29.6 ± 0.5	60.8 ± 0.6	–	–
	7.7 ± 0.1 [b]	–	1.8 ± 0.2	29.8 ± 0.4	60.7 ± 0.5	–	–
Maize	9.5 ± 0.5 [a]	–	2.3 ± 0.2	24.1 ± 0.7	64.1 ± 0.7	–	–
	9.9 ± 0.6 [b]	–	1.9 ± 0.1	25.5 ± 0.7	62.7 ± 0.7	–	–
Grape-seed	6.5 ± 0.2 [a]	0.6 ± 0.1	4.4 ± 0.3	19.5 ± 0.9	68.6 ± 0.9	0.4 ± 0.08	–
	6.8 ± 0.1 [b]	0.6 ± 0.1	3.6 ± 0.1	20.2 ± 0.4	68.6 ± 0.5	0.2 ± 0.02	–
Wheat-germ	10.7 ± 0.4 [a]	–	2.9 ± 0.2	24.7 ± 0.5	58.9 ± 0.8	2.8 ± 0.1	–
	11.1 ± 0.5 [b]	–	2.8 ± 0.2	24.5 ± 0.6	58.7 ± 0.9	2.9 ± 0.2	–
Avocado pear	10.8 ± 0.5 [a]	3.6 ± 0.2	1.2 ± 0.07	61.8 ± 0.7	22.6 ± 0.3	–	–
	10.9 ± 0.3 [b]	3.8 ± 0.4	1.2 ± 0.04	62.3 ± 0.5	21.8 ± 0.4	–	–
Peanut	7.9 ± 0.3 [a]	–	2.9 ± 0.1	49.1 ± 0.7	30.6 ± 0.6	2.2 ± 0.1	7.3 ± 0.5
	8.9 ± 0.9 [b]	–	3.0 ± 0.1	48.1 ± 1.1	30.5 ± 0.3	2.3 ± 0.2	7.2 ± 0.3
Carrot	5.5 ± 0.4 [a]	0.3 ± 0.02	2.2 ± 0.2	26.5 ± 0.8	60.8 ± 1.0	3.4 ± 0.2	1.3 ± 0.1
	5.4 ± 0.2 [b]	0.3 ± 0.03	2.2 ± 0.2	26.5 ± 0.8	60.9 ± 0.7	3.5 ± 0.1	1.2 ± 0.1
Linseed	5.6 ± 0.3 [a]	–	3.5 ± 0.2	19.0 ± 0.3	27.8 ± 0.7	43.3 ± 0.6	0.8 ± 0.05
	6.0 ± 0.2 [b]	–	3.5 ± 0.2	20.3 ± 0.8	25.0 ± 0.4	44.1 ± 1.1	1.1 ± 0.09
Codfish-liver	14.2 ± 0.5 [a]	13.6 ± 0.3	3.4 ± 0.2	35.1 ± 0.9	1.2 ± 0.05	4.6 ± 0.2	27.9 ± 0.9
	15.5 ± 0.6 [b]	13.5 ± 0.3	3.0 ± 0.2	35.2 ± 0.7	1.0 ± 0.03	4.3 ± 0.3	27.5 ± 0.8

[c] This column includes overall fatty acids not included in the above columns.

curves obtained by plotting the analyte-to-internal standard peak area ratio against the analyte concentrations in *n*-hexane were linear over the tested range (0.7–1000 mg l^{-1}). The detection limit was calculated as the concentration yielding the minimum detectable signal in the chromatogram. The relative standard deviation was checked on 11 samples containing 100 mg l^{-1} of each free fatty acid. The proposed method can be applied to olive oil samples by diluting between 10 and 120 mg of sample in 100 ml of *n*-hexane. The repeatability obtained in 11 injections of the same sample containing 40 mg of olive oil in 100 ml of *n*-hexane ranged between 0.6 and 3.8% for oleic and palmitoleic acid, respectively, expressed as the relative standard deviation.

Application to oil samples

The proposed method was applied to the determination of fatty acids in different types of oil: virgin olive, refined olive, raw olive, maize, sunflower-seed, carrot, grape-seed, wheat-germ, peanut, avocado pear, codfish-liver and linseed. The results found were compared with those provided by the Official Method [14]. Saponification of triglycerides in the lattes was performed with methanolic sodium hydroxide and refluxing until fat globules disappeared, while esterification was carried out in the presence of BF_3 (catalyst) in methanol. *n*-Heptane was added, as was saturated NaCl several times in order to float the *n*-heptane solution; then, the water was removed by adding Na_2SO_4 to the upper *n*-heptane solution for GC analysis. For continuous analysis of oils, 5 individual solutions containing 40 mg of each plus 10 mg of internal standard were diluted in *n*-hexane and introduced into the flow system for analysis. The results obtained for 12 oils are listed in Table 3. The composition was calculated by using the normalization method (all sample components are represented in the chromatogram, so the sum of peak areas represents 100% of constituents) and the peak area for each fatty acid was divided into that of the internal standard. Oils containing fatty acids other than those indentified by the proposed method, are grouped fatty acids of right-most Table 3. As can be seen, proportions of fatty acids provided by the conventional Official Method and the proposed automatic method are quite consistent.

Conclusions

In this work we assayed various classical derivatizing reagents and selected acetyl chloride because it converts fatty acids to their methyl esters in a single step in only a few minutes. the proposed automatic method permits fatty acids to be derivatized in a closed system without the need to handle toxic derivatizing reagents (as in recent commercialized pretreatment modules) and with minimal costs since of organic solvents and reagents are consumed very sparingly. Finally, the results obtained in the analysis of oils show the advantageous features of the automatic proposed method againts the official method [14] that involves two derivatization steps (saponification of triglycerides and esterification of fatty acids with BF_3 for further analysis), a great deal of manipulation and a long sampling time.

The Spanish CICYT is acknowledged for financial support awarded (Grant No. PB90-0925).

REFERENCES

1 T.P. Coultate (Ed.), Food, the chemistry of its components, The Royal Society of Chemistry, London, 1984.
2 H.D. Belitz and W. Grosch (Eds.), Food Chemistry, Springer Verlag, Berlin, 1986.
3 A. Stolyhwo, H. Colin and G. Guiochon, Anal. Chem., 57 (1985) 1342.
4 G.W. Jensen, J. Chromatogr., 204 (1981) 407.
5 H.M. Liebich, Anal. Chim. Acta, 236 (1990) 121.
6 M.F. Lefevere, B.J. Verhaeghe, D.M. Declerk and A.P. De Leenheer, Biomed. Environ. Mass Spectrom., 15 (1988) 311.
7 R.P. Evershed, C. Heron and L.J. Goad, Analyst, 115 (1990) 1339.
8 K.R. Kim, M.K. Hahn, A. Zlatkis, E.C. Horning and B.S. Middleditch, J. Chromatogr., 468 (1989) 289.
9 H. Schlenk and J.L. Gellerman, Anal. Chem., 32 (1960) 1412.
10 R.H. Voss and A. Rapsomatiotis, J. Chromatogr., 346 (1985) 205.
11 K.G. Allen, J. MacGee, M.E. Fellows, P.A. Tornheim and K.R. Wagner, J. Chromatogr., 309 (1984) 33.
12 P.C. Fourie and D.S. Basson, J. Am. Oil Chem. Soc., 67 (1990) 18.

13 Y.L. Ha, N.K. Grimm and M.W. Pariza, J. Agric. Food Chem., 37 (1989) 75.
14 H. Kenneth (Ed.), Official Methods of Analysis of the Association of Official Analytical Chemists, Association of Official Analytical Chemists, Virginia, 15th edn., 1990.
15 H. Rotzsche, J. Chromatogr., 552 (1991) 281.
16 B.N. Kyriakidis and G. Dianysopoulos, Analyst, 108 (1983) 738.
17 D.R. Osborne and P. Voogt (Eds.), The Analysis of Nutrients in Foods, Academic Press, London, 1978.
18 R. Misir, B. Laarveld and R. Blair, J. Chromatogr., 331 (1985) 141.
19 W. Welz, W. Sattler, H.J. Leis and E. Malle, J. Chromatogr., 526 (1990) 319.
20 R. Barragán-Ruiz, L. Coll-Hellin and A. Rueda-Clausell, Ann. Bromatol., 42 (1990) 41.
21 F. Pérez and J.J. Permanyer, Riv. Ital. Sostanze Grasse, 62 (1985) 605.
22 B. Freedman, W.F. Kwolek and E.H. Pryde, J. Am. Oil Chem. Soc., 63 (1986) 1370.
23 M.M. Mossoba, R.E. McDonald, J.Y.T. Chen, D.J. Armstrong and S.W. Page, J. Agric. Food Chem., 38 (1990) 86.
24 N.C. Shantha and R.G. Ackman, J. Chromatogr., 533 (1990) 1.
25 I. Martínez-Castro, L. Alonso and M. Juarez, Chromatographia, 21 (1986) 37.
26 C. De Jong and H.T. Badings, J. High Resolut. Chromatogr., 13 (1990) 94.
27 F. Ulberth and E. Achs, J. Chromatogr., 504 (1990) 202.
28 G.P. McNeill and J.F. Connolly, Ir. J. Food Sci. Technol., 13 (1989) 119.
29 J.I. Sebedio, Analusis, 18 (1990) 14.
30 M.G. Fatica, J. Am. Oil Chem. Soc., 66 (1989) 572.
31 G. Márquez-Ruiz, M.C. Pérez-Camino and M.C. Dobarganes, J. Chromatogr., 514 (1990) 37.
32 H. Kaneda, Y. Kano, M. Kamimura, T. Osawa and S. Kawakishi, J. Agric. Food Chem., 38 (1990) 1363.
33 G. Gutnikov and J.R. Streng, J. Chromatogr., 587 (1991) 292.
34 E. Ballesteros, M. Gallego and M. Valcárcel, J. Chromatogr., 518 (1990) 59.
35 E. Ballesteros, M. Gallego and M. Valcárcel, Anal. Chem., 62 (1990) 1587.
36 M. Gallego, M. Silva and M. Valcárcel, Anal. Chem., 58 (1986) 2269.

Analytica Chimica Acta, 282 (1993) 589–601
Elsevier Science Publishers B.V., Amsterdam

Evaluation of ashing procedures for the gas chromatographic determination of fluoride in biological material

M. Haldimann and B. Zimmerli

Federal Office of Public Health, Section of Food Chemistry, CH-3000 Bern 14 (Switzerland)

(Received 15th March 1993, revised manuscript received 18th June 1993)

Abstract

Fluoride in acidic aqueous solution was extracted with chlorodimethylphenylsilane in cyclohexane and converted to fluorodimethylphenylsilane, which was quantified by gas-liquid chromatography (GC) with flame ionization detection. The potential of GC, combined with different ashing procedures, including high pressure closed vessel acid digestion, to determine trace amounts of fluoride was evaluated with different biological standard reference materials. Major constituent elements such as Ca, Mg, Al and Si were also measured, but no correlation was apparent as to their effect on fluoride yields. Cluster analysis of fluoride yields with the various ashing methods revealed a difference between plant- and non-plant materials. Using alkaline fusion (KOH) for plant materials and a retaining agent (CaO) for non-plant materials good agreement with either certified or published values was obtained. The combination of both ashing aids gave satisfactory results regardless of the sample type. Application of this ashing method to Swiss total diet samples from the year 1983 and comparison with an ion-selective procedure in another laboratory yielded consistent results and identical mean values of 1.9 μg F g^{-1} (dry matter), corresponding to a daily dietary intake of 0.9 mg F per adult.

Keywords: Gas chromatography; Ashing; Fluoride in biological material

Fluoride is a natural trace constituent of foodstuffs and drinking water. Although sufficient evidence to qualify fluoride as an essential trace element is lacking, the determination of fluoride in biological samples is of interest. The majority of effects ascribed to fluoride supplement are probably pharmacological, including the prevention of dental caries in children and osteoporosis in elderly women [1]. On the other hand fluoride may also be of some concern as an environmental contaminant. Airborne fluoride in the vicinity of urbanized areas is generated through human activities (e.g. the aluminium industry). The fluoride content of topsoil may also be increased by fluoride-containing phosphate fertilisers. It has been estimated that the mean annual fluoride input to Swiss agricultural soils through fertilizer amounts to nearly 120 mg m^{-2}, e.g. about 1000 times more than cadmium [2].

There is a need to document the reliability of analytical procedures for the determination of fluoride, especially since no data on the daily intake of fluoride through foodstuffs have been published to date in Switzerland. The present investigation was undertaken to develop an alternative method in order to measure fluoride in total diet samples, to validate the results previously obtained by an ion-selective electrode (ISE)

Correspondence to: M. Haldimann, Federal Office of Public Health, Section of Food Chemistry, CH-3000 Bern 14 (Switzerland).

procedure carried out in another laboratory [3] as well as to study the effect of different ashing procedures on the "measurable" fluoride content in biological samples. The determination of electroactive species such as fluoride with ISE is widely used. However, the precise measurement of low concentrations is difficult owing to deviation from linearity of the electrode response. Complexation of fluoride in the presence of various ions (e.g. aluminium, iron, calcium, magnesium) may result in an additional problem. To overcome such potential difficulties, an extraction procedure followed by gas chromatographic determination was employed, paying special attention to sample preparation.

While numerous reference materials with certified element concentrations, mainly metals, are available for testing the accuracy of analytical methods, values for fluoride are normally lacking. The National Institute of Technology (NIST) standard reference material (SRM) 2695, fluoride in vegetation, is an exception. However, there are a number of reference materials for which either an indicative value or a fluorine concentration has been published.

Ashing procedures

Sample preparation is crucial owing to the different forms of fluoride found in biological samples (for a review see [4]). They can be classified as: ionic fluoride, complexed fluoride and covalent fluoride. Among the various published pretreatment steps, the most important ones are open ashing, fusion, oxygen combustion and digestion. These procedures can be followed by separation or concentration steps such as distillation, diffusion, pyrolysis and solvent extraction. In this work open ashing and nitric acid digestion in closed vessels were investigated in more detail, the latter method is not commonly recommended for fluoride.

Open ashing is normally carried out in platinum crucibles, often in combination with fluoride retaining agents. The residual ash can be fused with alkali hydroxide to release fluoride from a complex matrix. The crucibles used in this work were made from glassy carbon, which is a carbon modification [5]. Exposed to air they can be used up to 550°C. In contrast to platinum, this material is resistant to acids, alkali hydroxides and corrosive ions such as fluoride, which reduces the susceptibility to memory effects.

Nitric acid digestion is rarely used because in an open system the method is limited to moderate temperatures [6] to avoid losses of volatile fluoride compounds (e.g. HF). Being a rather mild decomposition procedure it can yield low results through incomplete liberation of fluoride from its matrix or insolubility of its compounds. In this work a closed vessel sample decomposition method was developed using a high pressure asher and vessels made from glassy carbon as well.

Absorption of diffusing hydrogen fluoride is normally applied to ashes, in order to separate fluoride from interferents (e.g. Al, Si). It is an established procedure and was used in this work for purposes of comparison [7–10].

Gas chromatographic determination

The technique, according to the original idea of Bock and Semmler [11], is based on the principle that appropriate chloroalkyl- or chloroarylsilanes are converted by water into the corresponding silanol. The silanol reacts selectively to form the fluorosilane, which can be extracted from the acidified solution by an organic solvent and determined by GC. In contrast to the ion-selective electrode (ISE), which directly measures fluoride activity, dissolved metal ions with a tendency to form fluorocomplexes do not interfere in this procedure.

Bock and Semmler made a comparative study of various compounds capable of forming fluorosilanes useful for GC [11]. Chlorotrimethylsilane is commonly used [12–16] because it appears in the chromatogram before the solvent and has a favourable reaction rate. On the other hand the resulting fluorotrimethylsilane has a boiling point below room temperature (16.4°C) and therefore evaporation may be a source of losses [14]. Chlorotriethylsilane is of some importance as well, but separation from interfering peaks seems to be more difficult [17,18]. Most authors used packed GC columns instead of the newer wide-bore capillary column used in this work, and measured the

silanes with flame ionization detectors which give a signal proportional to the number of carbon atoms in the derivative [17].

In this work chlorodimethylphenylsilane was successfully used. It is comparable to chlorotrimethylsilane in reaction rate and was among the reagents Bock and Semmler recommended for analytical use [11].

EXPERIMENTAL

Reagents and reference materials

Chlorodimethylphenylsilane (Fluka, No. 78390, Buchs, Switzerland) was distilled; the collected portion showed no contaminating GC peak in the range of interest. Cyclohexane (Merck, No. 2822, Darmstadt) was used without further purification. Filtered, deionized water was obtained using a Nanopure™ cartridge system (Skan, Basel). Nitric acid (65%, Merck No. 456) was distilled in a sub-boiling point quartz apparatus (Trabold, Bern). Potassium hydroxide (Merck No. 5033) was used without further purification. Calcium oxide low in fluoride was prepared by extracting a calcium chloride solution (10%, Merck No. 2382), adjusted to 1 M HCl with 20% hydrochloric acid (Merck, Suprapur®), with a solution of 1% chlorotrimethylsilane (Fluka No. 92361) in cyclohexane, followed by precipitation of $Ca(OH)_2$ with saturated sodium carbonate solution (Merck No. 6392). The precipitate was heated in a platinum crucible over a flame, first at moderate heat to dry the precipitate and then glowing for 30 min, to yield calcium oxide. For fluoride standard solutions a stock solution of 1000 mg l^{-1} (Merck No. 19814) was used.

Instrumentation

The high temperature/pressure asher-system (HPA, Kürner, Rosenheim) consists of an autoclave and a microprocessor control unit. The autoclave holds six 20 ml glassy carbon vessels for acid digestion at up to 320°C. The autoclave pressure is restricted to 130 bar by a release valve. The following heating program was used for acid digestion: initial temperature 80°C, a temperature gradient of 1°C min^{-1} for 30 min, a gradient of 13°C min^{-1} for 10 min, followed by 80 min at 240°C. The initial pressure was set to 100 bar.

A gas chromatograph (Fractovap series 2161, Carlo Erba, Milan) equipped with a Grob-type on-column injection system, a flame ionization detector, a wide-bore capillary column (30 m × 0.53 mm i.d., film thickness 1 μm, DB-17, J and W, Folsom, CA), and an integrator (3390^A, Hewlett Packard, Palo Alto, CA) was operated under the following conditions: detector temperature 200°C, helium pressure 0.5 bar (carrier gas), hydrogen pressure 0.7 bar and air pressure 1.3 bar. Temperature program: 75°C (5 min), gradient of 30°C min^{-1}, 170°C (5 min). The injection volume was 2.5 μl. Under these conditions the retention time of the fluorodimethylphenylsilane was 4.5 min, allowing easy detection of 20 pg fluoride (signal to noise ratio > 3).

A gas chromatograph–mass spectrometer (ion trap system, ITS 40, Finnigan MAT, San Jose, CA) equipped with a capillary column (30 m × 0.25 mm i.d., film thickness 0.25 μm, DB-5, J and W) was operated under the following conditions: 0.8 μl split injection (ratio 1:25), injection temperature 230°C, helium pressure 0.8 bar (carrier gas) and transfer line temperature 265°C. Temperature program: 70°C (6 min), gradient of 20°C min^{-1}, 260°C (2 min). MS parameters: ionization by electron impact, mass range (m/e) 50–300, manifold temperature 220°C, automatic ionization control. Under these conditions the retention time of the fluorodimethylphenylsilane was 6.7 min.

An inductively coupled plasma-mass spectrometer (ICP-MS, Elan 5000, Perkin Elmer, Norwalk, CT and Sciex, Thornhill, Ontario) with a cross-flow nebulizer was operated under the following argon flow conditions: plasma 15 l min^{-1}, nebulizer 0.9 l min^{-1} and auxiliary 0.8 l min^{-1}. Forward power was 1 kW and the dwell time per element was 25 ms with 50 sweeps. Major constituent elements were measured by external calibration using the masses ^{44}Ca, ^{24}Mg, ^{28}Si and ^{27}Al in the range of 0.1 to 0.2 μg l^{-1}. Yttrium was used as internal standard.

Statistics were performed on a microcomputer (IBM PS/2 70) with Systat software (Evanston, IL).

Methods 1–3: open ashing on a hot plate

A mass of 400–500 mg dried sample was weighed into a glassy carbon crucible (10 ml volume, Sigradur®, Sigri Elektrographit, Meitingen) and ashed as outlined in Table 2. Methods 2 and 3 require calcium oxide; 40–60 mg of finely ground CaO was added and blended thoroughly with the dried sample using a vortex mixer. Ten crucibles were placed together in a specially constructed nickel-plated copper box (18 cm × 18 cm × 10 cm) that reflects heat. The box was fixed upon a glass-ceramic heating element ($\phi = 25$ cm, 1.2 kW, Müller and Krempel, Bülach). In a first step the samples were kept for one hour at moderate temperature (200–300°C) to avoid frothing. Afterwards the lid of the box was closed and the heat was increased to crucible surface temperatures of about 550°C. The temperature was measured with a nickel/chrome–nickel thermoelement (D 1000, Huber, Offenburg). After two hours the crucibles were allowed to cool down.

In methods 1 and 2 where the residues were fused, 2–3 pellets (500–600 mg) potassium hydroxide were added and the temperature was again raised to 400°C for 30 min. In method 1, with no calcium oxide, a clear melt resulted, with the other methods a white crust ensued. Shortly before extraction, the residues were dissolved in 3 ml water (with methods 2 and 3 a suspension resulted) and 2 ml of concentrated nitric acid was added dropwise. Care is essential at this stage as the reaction is very vigorous. The subsequent extraction of the solution (or an aliquot) is described below.

Method 4: direct diffusion (unashed)

A mass of 100 mg dried sample was placed into a polypropylene beaker ($\phi = 3.5$ cm, height = 3.5 cm, Semadeni No. 2026) and about 5 mg silver sulphate was added to precipitate halogens other than fluoride. A filter-paper was wetted with 180 μl of 6.5% potassium hydroxide dissolved in a water propylene glycol (50% v/v) mixture (Siegfried, Zofingen). This solvent mixture absorbs the diffusing hydrofluoric acid and delays drying out of the impregnated filter-papers. 2 ml perchloric acid was added to the sample and the beaker was immediately closed with a lid holding the prepared filter-paper and allowed to stand for 48 h at 60°C in a drying cupboard. The filter-papers were removed and soaked in 5 ml nitric acid (6.5%) for one hour prior to extraction with cyclohexane.

Method 5: closed vessel acid digestion

A mass of 100–200 mg dried sample was weighed directly into glassy carbon vessels (20 ml, Kürner, Rosenheim) and 2 ml concentrated nitric acid added. Immediately, each vessel was sealed with an analytical grade strip of Teflon® tape and closed with a lid fastened firmly with a tungsten spring. The vessels were put into the autoclave. After closing, the autoclave was filled with nitrogen to a pressure of 100 bar. As the vessels were heated the counter pressure still exceeded the reaction pressure, thus keeping the lids closed. Once the temperature program was finished the autoclave cooled down to below 30°C, leaving a residual pressure in the vessels. After the nitrogen was released slowly from the autoclave and vessels they were removed and opened. Immediately, the contents were diluted with 5 ml water and the solutions extracted without further treatment.

Derivatisation of fluoride and extraction

The acidic, fluoride-containing solution (or an aliquot thereof, depending on the fluoride content) was transferred into a 10-ml fluoroethylene-propylene (FEP) test-tube (Semadeni No. 3436, Ostermundigen). A 0.1% chlorodimethylphenylsilane solution in cyclohexane (2.0 ml) was added using a dispenser (Tamm, Salem). The tubes were closed and shaken for one hour in a shaker (Infors, Bottmingen). 2.5 μl of the organic layer was injected directly into the gas chromatograph. Although FEP is a fluorine polymer it did not contribute fluoride measurably to blank solutions under experimental conditions. Its advantage is the absence of easily soluble additives that could migrate into organic solvents and result in potentially interfering peaks in the GC. In contrast to findings by other authors [17], contamination by low molecular products was observed when polypropylene tubes were used (Semadeni No.

3199). In FEP tubes the solutions were stable for several days.

Calibration

Standard solutions were prepared by extracting 5 ml nitric acid (6.5%) containing 0, 0.3, 0.6, 0.9, 1.2, and 1.5 μg fluoride as described above. With four independent replicates for each level, a linear graph was obtained. Using least-squares regression the calibration curve, including standard errors for slope and intercept was: $Y_F = (0.0108 \pm 0.0001)X - (0.008 \pm 0.006)$. Y_F is the amount of fluoride in μg, corresponding to sample weight or aliquot, X is the GC peak area in arbitrary units. The correlation coefficient was 0.999. The slope did not change significantly over a period of some weeks.

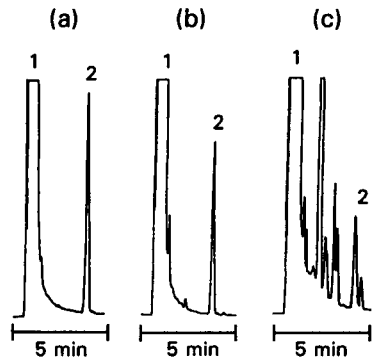

Fig. 1. Chromatograms of fluoride determinations (FID). (a) Standard containing 0.75 ng fluoride, corresponding to 0.12 μg ml^{-1} in the aqueous extraction solution. (b) Total diet sample (level 1.2 μg g^{-1}, dry ashing). (c) IAEA A-11 sample (milk powder, 0.26 μg g^{-1}, closed vessel acid digestion). Peaks: 1 = solvent (cyclohexane), 2 = fluorodimethylphenylsilane.

RESULTS AND DISCUSSION

Identification with GC–MS

The mass spectrum of the analyte gave the molecular ion $[M]^+$ (*m/e* 154) and the most abundant ion $[M - CH_3]^+$ (*m/e* 139) with relative abundances of 9% and 100%, respectively. The latter is characteristic for dimethylphenylsilyl derivates [22]. Other major fragment ions were (*m/e*): 50(9%), 51(17%), 77(15%), 79(9%) and 91(21%), 140(11%) and 141(4%). Calculated isotopic abundances of the $[M - CH_3]^+$ ion fit the pattern found in the spectrum. As there were no contradictions the analyte peak was identified as fluorodimethylphenylsilane. The quantitative measurements were based on the most abundant $[M - CH_3]^+$ ion. To verify the flame-ionization detector response, identical extracts of a four-value calibration series in the range of 0–0.4 μg fluoride and a standard reference material were measured jointly in flame-ionization (FID) and ion-trap (ITD) systems. The reference material used was milk powder ashed according to method 5 (closed vessel acid digestion). Although inlet systems and columns were different, the FID peak (Fig. 1) could be matched with the ITD

TABLE 1

Standard reference materials containing trace amounts of fluoride

Biological material	Code/origin	Certified values (μg g^{-1})	Indicative values (μg g^{-1})	Values from publications [a] (μg g^{-1})
Vegetation (grass)	NIST SRM 2695	64.0 ± 8.4	–	–
Oyster tissue	NIST SRM 1566	–	5.2	–
Tomato leaves	NIST SRM 1573	–	–	5.0 [19]
Pine needles	NIST SRM 1575	–	–	3.7 [19]
Bowen's kale	Reading University	–	5.87 ± 0.97	–
Milk powder	AEA A-11	–	0.27	0.26 ± 0.07 [10]
Aquatic moss	BCR CRM 061	–	60.0	60.5 ± 3.3 [20]
Single cell protein	BCR CRM 27	–	17.6 ± 2.2	17.5 ± 0.3 [21]; 16.0 ± 1.6 [10]

[a] Reference literature in brackets.

TABLE 2

Overview of the ashing methods used

Method code	Procedure	Temperature (°C)	Oxidant	Ashing aid	Fusion
1	Hot plate, open (fusion)	550	Air	–	KOH
2	Hot plate, open (CaO/Fusion)	550	Air	CaO	KOH
3	Hot plate, open (CaO)	550	Air	CaO	–
4	Diffusion [a]	60	$HClO_4$	–	–
5	Pressure (closed vessel)	240	HNO_3	–	–

[a] Sample not ashed, proposed procedure for determining "acid-labile fluoride" [4].

peak, because under these conditions the analyte peak appeared well separated in calibration standards. The values for two independent replicates detected with FID and ITD were 0.24/0.24 $\mu g\ g^{-1}$ and 0.28/0.31 $\mu g\ g^{-1}$, respectively. The figures are in good agreement with the values given in Table 1, thus indicate the absence of impurities masked in FID chromatograms due to peak overlapping. Such impurities could result from incomplete degradation of organic compounds (Fig. 1c). As method 5 did not yield higher results than the methods 1–3 (Table 3) with total degradation of organic matter, the chromatograms were considered to be free from interfering peaks for the remaining samples too.

Equilibration time

The time profile of the extraction procedure was carried out by extracting a 1 $\mu g\ ml^{-1}$ fluoride standard solution as described and injecting aliquots of the organic layer at the time intervals shown in Fig. 2. A maximum response was obtained after only 10 min; thus the one hour extraction time includes a safety margin to allow for possible matrix-dependent delays. The diagram obtained is very similar to the one reported by Bock and Semmler [11] at higher fluoride concentrations. Under slightly different conditions they found only a minor increase in the signal after 10 min.

Limit of quantification

The limit of quantification (LOQ) can be defined as mean fluoride concentration in the blank (X_m) and 10 times the standard deviation (s) of its measurement: $LOQ = X_m + 10s$ [23]. For the methods 2 and 3 the measurable amount of fluoride depends on the standard deviation (s_b) associated with the measurements of the blank levels of calcium oxide rather than on instrumental

TABLE 3

Comparison of major elemental concentrations found (ICP-MS) with reference values quoted by the manufacturer or published by other authors

	Element							
	Ca ($mg\ g^{-1}$)		Mg ($mg\ g^{-1}$)		Al ($mg\ g^{-1}$)		Si ($mg\ g^{-1}$)	
	Sample [a]							
	Found	Ref.	Found	Ref.	Found	Ref.	Found	Ref.
Vegetation (grass)	8.1	–	2.6	–	0.35	–	12	–
Oyster tissue	4.5	1.5	1.4	1.3	0.23	–	1.2	1.3 [c]
Tomato leaves	24	30	6.7	7.1 [b]	1.0	1.2	10	10 [c]
Pine needles	3.7	4.1	1.1	1.4 [b]	0.53	0.55	1.5	1.4 [c]
Bowen's kale	50	41	1.6	1.6	0.055	0.040	1.2	0.25
Aquatic moss	32	17	4.2	3.9	7.8	11	61	75
Single cell protein	25	–	2.4	–	0.090	–	1.6	–

[a] See Table 1. [b] [19]. [c] [26].

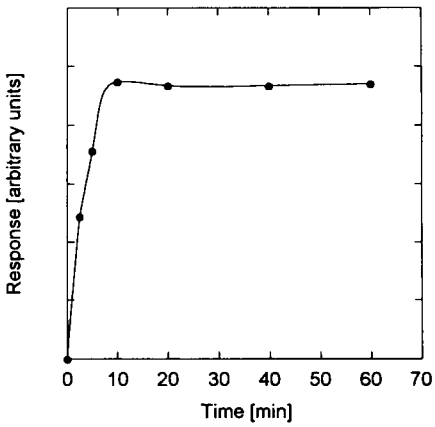

Fig. 2. Overall rate of formation of fluorodimethylphenylsilane during the extraction of 1 μg fluoride in 5 ml aqueous solution.

noise. The mean fluoride concentration of the prepared calcium oxide was estimated by direct extraction of its nitric acid solutions as described above: $X_m = 0.85\ \mu g\ g^{-1}$, $s_b = 0.21\ \mu g\ g^{-1}$, $n = 6$. We were not successful in preparing calcium oxide containing less fluoride because the sodium carbonate used itself had a low fluoride concentration (0.1–0.2 $\mu g\ g^{-1}$) and also possibly some recontamination by air occurred during the preparation of CaO. Even though this level is much lower than that of commercially available calcium oxide (e.g. 10–20 $\mu g\ g^{-1}$), it cannot be neglected. The corresponding limit of quantification using our batch of CaO results in LOQ = 0.3 $\mu g\ g^{-1}$, for a sample-to-calcium oxide mass ratio of 10 to 1. This is not critical for most of the samples used in this work except milk powder (0.27 $\mu g\ g^{-1}$).

The potassium hydroxide did not contribute significantly to the blank value and consequently the LOQ is lower for method 1. Method 5 shows no peaks in blanks under experimental conditions. However, if the temperature was raised to over 260°C, blank peaks were observed, probably due to partial degradation of the teflon strip seal of the reaction vessel. Moreover, the fact that residual decomposition products might cause interfering GC peaks has to be considered when method 5 is used.

Effect of major constituent elements

Ashing process. Constituent elements such as Ca, Mg, Al and Si in the sample can have a dominant influence on the determination of fluoride. Especially the major elements present in large excess compared to fluoride can affect its extractability for final determination. Although not precisely known, it has been suggested that fluorine in plant tissues is present in combination with calcium, magnesium, or in a complex matrix with aluminium [24] and silicates [8].

To make a complete estimate of the concentrations of these most abundant elements, the reference samples were ashed according to method 1, which is also recommended for silicon determinations [25], and elemental concentrations were determined by ICP-MS after further dilution. The results are summarized in Table 3 and compared with certified or indicative reference values as far as available. Although we were only interested in approximate levels, the concentrations determined are in fairly good agreement with the reference values.

Extraction process. Bock and Semmler [11] have demonstrated that zirconium and thorium, as coexisting cations, lower the extraction yield of fluoride in acidic solution. Thorium is present in the plant samples, but only in sub-microgram per gram levels, too low to influence the extraction. The elements listed in Table 3 are less critical with respect to fluoride extraction, thus at concentrations of up to 10 mg l^{-1} should not influence fluoride yields [11]. Hence the extraction itself was not considered to be a possible source of fluoride deficiencies.

Analysis of biological reference materials and ashing methods

Standard solutions. Determinations of ionic fluoride from stock solutions (1 μg fluoride) subjected to the five preparation procedures were made. These results gave no information about the actual ashing processes but indicated whether severe losses could occur under practical working conditions. In all determinations the recoveries were higher than 98%, except, as expected, for method 1 (6%). This demonstrated the importance of having a retaining agent or residual ash,

which may serve the same purpose, in the ashed mixture.

Survey of fluoride yields. The results of the different ashing procedures are summarized in Table 4, the values fluctuating according to the method used. The results compared reasonably well with the certified and indicative values (see Table 1), provided an appropriate sample preparation method such as method 2 was used. It seems that the results in Table 4 given some information, but not apparently, about the chemical form (ionic, metal-complexed and covalent) of the fluoride that is normally not known for a certain type of sample. The results obtained with method 2 consist obviously of total inorganic fluoride, whereas method 4 theoretically yields the contents of ionic fluoride. However, there could be a chemical equilibrium between free ionic and complexed fluoride, hence it may to some extent appear in the diffusate as well. On the other hand the powdered materials used in our study formed gelatinous residues that may have inhibited the diffusion of hydrogen fluoride. The method 5 conditions are more favourable to establish chemical equilibria, this may explain the considerably high results obtained in comparison to method 4. The results obtained with method 5 are a better measure for the content of ionic fluoride than method 4.

Natural organic fluorine compounds (i.e. fluoro-oleic acid) are very rare in plant and food samples, this is in contrast to human and animal blood or serum [4,8,24]. The possibility, however, remote, should not be overlooked. Whether the differences in the results really reflect covalent organic fluoride cannot be deduced from Table 4, as this type of fluoride is probably not responsive to the ashing methods tested in this work. Several authors reported low recoveries for selected organic compounds with open ashing methods [4]. This is possibly due to evaporation during the procedure. Moreover, simple mono or perfluoro compounds cannot be degraded completely by nitric acid as utilized in the closed vessel method 5. A suggested procedure for the selective determination of such organic fluoride is extraction with a solvent followed by reaction with sodium biphenyl or combustion in an oxygen bomb [4].

Cluster analysis. The multivariate data-set (Table 4, without milk powder), was analysed with the aim of classifying the samples into groups with broadly similar fluoride result profiles, i.e. groups that respond in a similar fashion to the various ashing procedures. As a measure of association, correlation coefficients (r) were used, calculated for each possible combination of samples. A high correlation of the values with methods 1–5 for two samples formulates similarity. A

TABLE 4

Effect of the different ashing procedures on fluoride yields
(The values represent a mean of duplicate measurements with the difference in brackets)

	Method [a]				
	1	2	3	4	5
	Sample [c]				
	Fusion ($\mu g\,g^{-1}$)	CaO/Fusion ($\mu g\,g^{-1}$)	CaO ($\mu g\,g^{-1}$)	Diffusion [b] ($\mu g\,g^{-1}$)	Closed vessel ($\mu g\,g^{-1}$)
Vegetation (grass)	66.2 (0.7)	65.5 (1.2)	63.3 (0.1)	17.4 (3.1)	18.5 (1.5)
Oyster tissue	2.4 (0.3)	7.9 (0.7)	6.4 (0.2)	2.9 (0.3)	6.8 (0.8)
Tomato leaves	8.0 (0.2)	8.2 (0.7)	5.4 (0.5)	2.1 (0.2)	7.2 (0.3)
Pine needles	2.6 (0.1)	2.6 (0.2)	2.1 (0.3)	1.1 (0)	2.7 (0.2)
Bowen's kale	5.2 (0.5)	5.4 (0.1)	5.2 (0)	2.9 (0.3)	5.7 (0)
Milk powder [d]	0.24 (0.1)	–	–	–	0.24 (0)
Aquatic moss	63.5 (2.0)	62.7 (5.1)	29.6 (0.3)	18.8 (1.7)	42.2 (0.4)
Single cell protein	1.6 (0.2)	17.4 (2.8)	18.7 (0.8)	11.9 (0.3)	16.0 (1.7)

[a] See Table 2. [b] Not a real ashing method. [c] See Table 1 for reference values. [d] Not determined with the methods 2, 3 and 4.

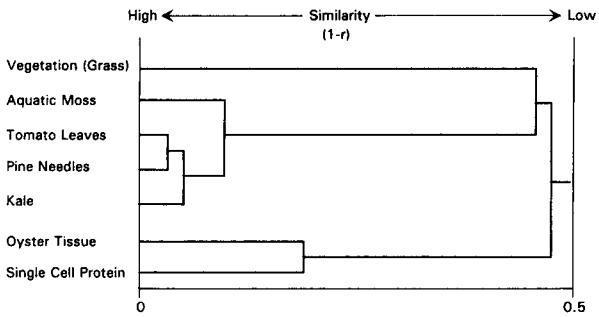

Fig. 3. Dendrogram visualizing the hierarchical clustering of reference samples. Metric distance is 1 − correlation coefficient, and the single linkage method (nearest neighbour) is employed.

tree (Fig. 3) was printed with a unique hierarchical ordering in which every branch is lined up in such a manner that the most similar samples (high values of r) are closest to each other and hence dissimilar to distant groups. The linkage shows clustering and the distance is a similarity index displayed as $1 - r$. The method with correlation coefficients was used because the measurements were not affected by the broad differences of fluoride levels in the reference samples. Figure 3 reveals two main groups: plant, and non-plant materials. Within the plant-group the vegetation sample (grass) shows little similarity to the remaining samples even though it is of plant origin. It is noteworthy that the different ashing characteristics of plant and non-plant materials were reported by Oelschläger as well [27,28].

Plant materials. This group showed no significant difference in results whether calcium oxide was used or not, as demonstrated by the comparison of methods 1 and 2, hence it seems that fluoride was fixed by a matrix. However, if one compares methods 2 and 3, it is clear that potassium hydroxide fusion was necessary for this type of sample. The efficiency of fusion was very pronounced for aquatic moss. Moss contains substantial amounts of silicon and aluminium in comparison to kale (Table 3), which showed the most constant results in all instances. It can be concluded that for samples with high concentrations of silicon part of the fluoride is released only by potassium hydroxide fusion, which degrades refractory fluorine compounds. This fact was further corroborated by the poor results seen for aquatic moss with method 5. With the latter method total decomposition of the matrix was not achieved, hence there is some analogy to method 3.

In contrast, to the above, the grass sample, which also had a high silicon content, although showing low values for method 5 gave reasonable values with method 2. This effect is likely to be attributed to the elevated fluoride level, above the baseline of natural plant materials. This sample was prepared by the NIST to simulate contaminated material possibly by the addition of a fluoride-containing salt and accordingly it showed a different response in comparison to aquatic moss, which has a high natural fluoride level.

Non-plant materials. Generally, the complete decomposition and dissolution of biological samples requires complete oxidation of the organic matter. Although fusion had little influence on the samples in this group, it was observed that in methods where it was applied, hardly any residual carbon remained, probably due to the oxidizing effect of KO_2 formed under these conditions [29]. The retaining agent (CaO) may assist the oxidation process, but its main function is to retain fluoride. Absence of CaO significantly lowered results (method 1 vs. 2, Table 4). It is interesting to note that although calcium and magnesium are already present in the protein sample to a considerable extent (Table 3), they are obviously not in a form capable of retaining fluoride!

Methods. Low values for moss and grass were obtained with method 5, probably because of incomplete dissolution of concomitant inorganic compounds, in particular siliceous material, which remained as a visible fine residue. In order not to attribute this to random losses, additional measurements were carried out on the grass sample and a mean value of 18.5 $\mu g\ g^{-1}$ (S.D. = 1.5 $\mu g\ g^{-1}$, $n = 6$) was obtained. Method 5 theoretically provides a good alternative to open ashing because the sealed system prevents both the introduction of airborne fluoride as well as losses of volatile compounds such as HF and SiF_4 during decomposition. However, it can be applied only if the samples are readily dissolved, without resid-

ual inorganic material. This excludes aquatic moss and grass samples. Repeatability of this method was tested using the kale sample; a mean fluoride concentration of 5.4 $\mu g\ g^{-1}$ (S.D. = 0.3 $\mu g\ g^{-1}$, $n = 6$) was obtained.

Only method 2 seems to be applicable to every type of biological sample. This is in accordance with the proposal of an analytical working group of the Comité Technique Européen du Fluor [30]. It recommended a similar method, consisting of alkaline fusion and the use of a retaining agent. However, the method may be plagued by two general problems: a higher blank level and the possibility of contamination with variable amounts of extraneous fluoride that make blank correction more difficult in the cases of low-level concentrations. The mean fluoride concentration of repeated Bowen's kale determinations with method 2 was 5.9 $\mu g\ g^{-1}$ (S.D. = 0.5 $\mu g\ g^{-1}$, $n = 7$). The good agreement between kale results obtained with methods 2 and 5 (see above) indicates that both methods are valid for this type of sample.

It was not unexpected that the direct diffusion (method 4) produced comparatively low results for all samples. The perchloric acid at 60°C is unable to completely digest the samples, hence some fluoride was apparently trapped in gelatinous residues. This is in accordance with the results of other authors [7,31], where direct diffusion gave lower values in comparison to an open ashing procedure. This method may be useful to give some information about acid-diffusible (biologically available) ionic fluoride. However, a clear distinction between ionic and total fluoride cannot be made, as the results of the more vigorous acid procedure (method 5) demonstrate (Table 4).

In summary, the most important reasons for lower results are: losses during open ashing, and the inaccessibility of fluoride in complex matrices due either to the stability of the matrices or simply to poor solubility. Referring to the data in Table 3 (in comparison to Table 4) no general rule for the ashing characteristics of fluoride in relation to major constituent elements can be derived, except that it seems that for samples with a silicon content of > 10 mg g^{-1} acidic digestion is inappropriate and a fusion method has to be used. Apparently it is the structure incorporating the fluoride which determines the most appropriate type of preparation method, and not simply the excess of aggregates of interfering elements present in the sample.

Application to total diet samples and comparison to an ion-selective procedure

Complete daily menus for adults including breakfast, were sampled in 1983 at four different food service kitchens in the city of Bern; the fluoride concentration of drinking water in July 1991 was 0.06 to 0.08 $\mu g\ ml^{-1}$. The specific locations were: a company cafeteria, a hospital, a vegetarian restaurant and military canteen. Details on sampling and composition of the samples are described elsewhere [32]. Each sample was homogenized, the pH values (normally 4.4–6.0) adjusted to 7.1–7.5 by addition of sodium hydroxide solution and then dried [3].

As in the total diet samples consist of plant and non-plant materials the specimens were ashed with method 2, which seems to be the most universal method for biological samples. Using identical batches, our results were compared with those previously obtained by another laboratory [3], which followed a standard procedure for determination of fluoride in biological samples [33]. This procedure consists of a sample preparation very similar to method 1. Fluoride was quantified by ISE measurements.

Both procedures resulted in identical mean values of the fluoride level of 39 samples: 1.9 $\mu g\ g^{-1}$. This corresponds to a mean daily intake of about 0.9 mg fluoride per adult on the basis of a mean daily intake of 460 g dried matter. However, other sources such as fluoride containing dentifrices may significantly increase the daily intake. A detailed discussion of the results (including nitrate, nitrite and sulphur dioxide), will be published elsewhere [34].

These data were used to further investigate the reliability of method 2 combined with gas chromatographic measurement. Figure 4 shows a scatter plot of the mean GC values (duplicates) versus ISE values. The position of the linear regression line theoretically should reveal any analytical bias; however, when comparing analyti-

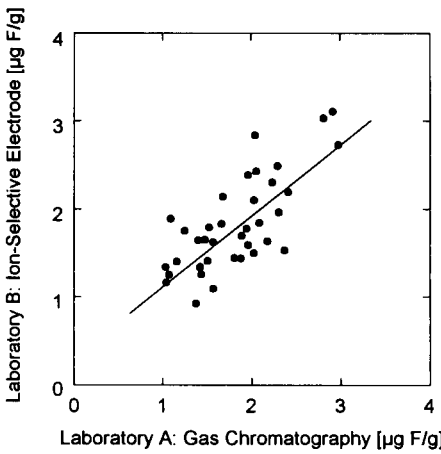

Fig. 4. Comparison (with the linear regression line) of fluoride results of total diet samples determined in different laboratories by an ion-selective electrode method and a gas chromatographic method, respectively.

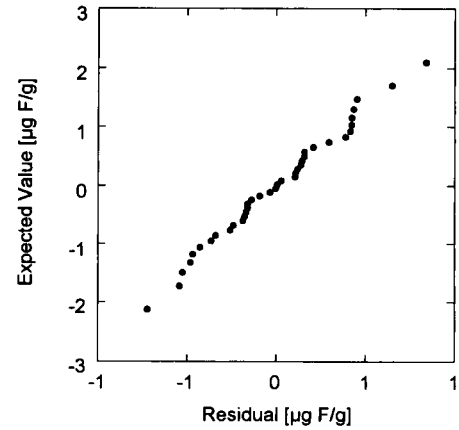

Fig. 5. Probability plot: residuals of the regression data in Fig. 4 vs. expected values of the normal distribution.

cal methods this is not strictly valid because it must be assumed that the independent variable (x-value) is free from error. But fairly accurate estimates of bias can be obtained if the method giving the least variation is used as x-value [35]. Precision data for each of the ISE values were not provided, so a more rigorous statistical comparison was not possible, but standard deviations vary from 0.2 to 0.6 μg g^{-1} [3]. For the proposed GC procedure in this work an estimate of the standard deviation (s_e) of 0.2 μg g^{-1} ($n = 38$) was estimated from the ranges (R) of the independent duplicate determinations according to: $s_e = (\Sigma R^2/2n)^{1/2}$ [35]. Therefore, the GC procedure was chosen as independent variable. An additional requirement when comparing methods is that the analyte levels should cover the measured range uniformly [36], therefore the highest measured value, (above 6 μg g^{-1}) was not taken into account. If no bias exists, an intercept (a) of zero and a slope (b) of one should result. Whether the likely range of "a" includes zero or that of "b" includes one was tested as shown in Table 5. The values of t_a and t_b are less than the critical value ($t_{0.95}$) at the 95% level with $n - 2$ degrees of freedom (ν), thus no significant bias was detected. Although different methods were used in different laboratories and the fluoride concentrations were relatively low (1–3 μg g^{-1} dry matter) the data compare acceptably well.

Whether our data fit the regression model is demonstrated by the probability plot in Fig. 5. The differences between the observed and predicted ISE values (residuals) are plotted against the corresponding percentage points of the normal distribution: a normal distribution of the residuals exists if the plotted residuals fall approximately on a straight line.

TABLE 5

Statistical calculations of the method comparison ISE vs. GC for total diet samples (see Fig. 4) [a]

	Estimate	Standard error	Hypothesis	t-Value calculation	$t_{0.95}$ ($\nu = 36$)
Intercept a: (μg F/g)	0.38	0.22 (s_a)	$a = 0$	$t_a = \lvert a \rvert / s_a = 1.73$	2.03
Slope b: (−)	0.80	0.12 (s_b)	$b = 1$	$t_b = \lvert (b - 1) \rvert / s_b = 1.74$	2.03

[a] Linear regression model: $y_{ISE} = a + bx_{GC}$ (correlation coefficient = 0.749).

Conclusions

Gas chromatographic determination of fluoride with the newly introduced dimethyl-phenylsilane derivative is suitable for biological samples. The combination with the ashing method 2, involving the use of CaO as a retaining agent and subsequent fusion with KOH, has been shown effectively to yield results that compare reasonably well with either certified or indicative values. However, the limit of quantification is relatively high (0.3 $\mu g\ g^{-1}$), owing to the concentration of fluoride in the CaO. The glassy carbon crucibles have proven to be advantageous in comparison to platinum ones because of their inertness, hence no fluoride contribution attributed to the material was observed.

In general, GC measurement of fluoride via organosilane is accurate and specific and it is applicable over a wide range because the extraction step can also be used to concentrate the analyte. However, the dynamic range that GC provides may not be fully exploited if in the course of sample preparation retaining agents are employed that contribute considerable amounts of fluoride to the blank.

The results of total diet determinations with the proposed GC procedure and with a standard ISE procedure, that was carried out in another laboratory, compare acceptably well. This suggests that the use of CaO was unnecessary because the latter procedure did not include the use of a retaining agent. The repeatability for the total diet samples and for Bowen's kale was about 10% (concentration range 1–6 $\mu g\ g^{-1}$ in dry matter).

It is a well-known fact that constituent elements such as Ca, Mg, Al and Si may interfere with the determination of fluoride. However, as the measurements of these elements indicated there is no simple relationship between the concentration of the constituent elements and the fluoride yields of the different ashing procedures. The survey made of the different ashing methods gives some information on the properties of the fluoride or its matrix, respectively. The use of a retaining agent (CaO) is particularly suitable for non-plant samples, whereas the fusion (KOH) of residual ash seems to be necessary for plant samples. Used in combination CaO and KOH have been shown effectively to yield satisfactory results for both types of samples.

The high temperature/pressure asher (HPA) is a good means for preparing difficult sample material for elemental analysis by ICP-MS. To measure fluoride it is favourable for samples that show no inorganic residues after the ashing process and furthermore, as some concomitant organic products are not completely decomposed a good chromatographic separation of interfering peaks is needed. Losses due to diffusing hydrogen fluoride have not been observed. Complementary studies are necessary to clarify whether the HPA procedure can provide useful information on the dietary bioavailability of fluoride.

The authors thank Ms. Tanja Venner for her help with the experimental work, Dr. Martin Schüpbach for his helpful suggestions and Dr. Sarah Shephard for her kind interest and very valuable advice on the manuscript. These studies were supported by Dr. H.R. Strauss and Dr. H. Schwab, Federal Office of Public Health, Switzerland.

REFERENCES

1 H.H. Messer, in E. Frieden (Ed.), Biochemistry of the Essential Ultratrace Elements, Plenum Press, New York, London, 1984, pp. 55–87.
2 Anonymous, Schwermetalle und Fluor in Mineralduenger. Schriftenreihe Umwelt Nr. 162, Bundesamt fuer Umwelt, Wald und Landschaft, Bern, November, 1991.
3 P. Hegersweiler, Kantonales Laboratorium Basel-Stadt, personal communication, 1988.
4 P. Venkateswarlu, J. Dent. Res., 69 (1990) 514.
5 R. Dübgen and G. Popp, Z. Werkstofftech., 15 (1984) 331.
6 M.A. Van Den Heede, A.M. Heyndrickx, C.H. Van Peteghem and W.A. Van Zele, JAOAC, 58 (1975) 1135.
7 L. Gustafsson and L.W. Njenga, Anal. Chim. Acta, 212 (1988) 133.
8 R.J. Hall, Analyst, 93 (1968) 461.
9 M. Nedeljkovic, B. Antonijevic and V. Matovic, Analyst, 116 (1991) 477.
10 M. Gomez, I. Rodriguez, C. Camara and M.A. Palacios, Analyst, 115 (1990) 553.
11 R. Bock and H. Semmler, Z. Anal. Chem., 230 (1967) 161.
12 K. Chiba, K. Kazuo, K. Tanabe, M. Ozaki, H. Haraguchi, J D. Wineforder and K. Fuwa, Anal. Chem., 54 (1982) 761.

13 J.A. Fresen, F.H. Cox and M.J. Witter, Pharm. Weekblad, 103 (1968) 909.
14 J.H. Glerum, A. van Dijk and S.W. Klein, Pharmaceutisch Weekblad Sci. Ed., 6 (1984) 75.
15 R. Ikenishi and T. Kitagawa, Chem. Pharm. Bull., 36 (1988) 810.
16 G. Yamamoto, K. Yoshitake, T. Sato, T. Kimura and T. Ando, Anal. Biochem., 182 (1989) 371.
17 G. Yamamoto and K. Yoshitake, Anal. Chim. Acta, 222 (1989) 121.
18 J. Belisle and D.F. Hagen, Anal. Biochem., 87 (1978) 545.
19 E.S. Gladney, Anal. Chim. Acta, 118 (1989) 385.
20 U. Bartels, Fresenius, Z. Anal. Chem. 330 (1988) 158.
21 J.R.W. Woittiez and G.V. Iyengar, Fresenius Z. Anal. Chem., 332 (1988) 657.
22 D.J. Harvey, J. Chromatogr., 147 (1978) 291.
23 ACS Committee on Environmental Improvement, Anal. Chem., 52 (1980) 2242.
24 Anonymous, WHO, Fluorine and Fluorides, Env. Health Criteria Series 36, Geneva, 1984.
25 K.E. Jarvis, A.L. Gray and R.S. Houk, Handbook of Inductively Coupled Mass Spectrometry, Blackie, Glasgow and London, 1992, p. 172.
26 E.S. Gladney, P.E. Neifert and N.W. Bower, Anal. Chem., 61 (1989) 1834.
27 W. Oelschläger, Z. Anal. Chem., 228 (1967) 361.
28 W. Oelschläger, Staub-Reinhalt. Luft, 42 (1982) 383.
29 R. Bock, Aufschlussmethoden der anorganischen und organischen Chemie, Verlag Chemie, 1972, p. 77.
30 Anonymous, Anal. Chim. Acta, 182 (1986) 1.
31 L. Singer, R.H. Ophaug and B.F. Harland, Am. J. Clin. Nutr., 33 (1980) 328.
32 B. Zimmerli and R. Knutti, Mitt. Gebiete Lebensm. Hyg., 76 (1985) 168.
33 Verein Deutscher Ingenieure, VDI-Handbuch zur Reinhaltung der Luft, Band 1, Beuth Verlag, Berlin and Köln, 1981, VDI 3795, Blatt 2.
34 B. Zimmerli, U. Buxtorf, P. Hegersweiler and M. Haldimann, Mitt. Gebiete Lebensm. Hyg., 84 (1994) in preparation.
35 L. Sachs, Applied Statistics, Springer, New York, 1984, p. 97.
36 M. Thompson, Analyst, 107 (1982) 1169.

Analytica Chimica Acta, 282 (1993) 603–612
Elsevier Science Publishers B.V., Amsterdam

Application of UV absorbance and second-derivative spectrophotometry for analysing casein hydrolysates

Marialice P.C. Silvestre

Departamento de Alimentos, Faculdade de Farmacia da UFMG, Belo Horizonte (Brazil)

Chantal Dauphin and Michel Hamon

Laboratoire de Chimie Analytique, Faculté de Pharmacie, Châtenay-Malabry (France)

(Received 15th March 1993; revised manuscript received 5th June 1993)

Abstract

UV absorbance and second-derivative spectrophotometry were used to analyse some tryptic and pancreatic casein hydrolysates. The decrease in absorptivities detected at the initial stage of protein hydrolysis indicated some similarities with the denaturation process, probably owing to the rupture of hydrophobic bonds. This technique was used to determine the degree of hydrolysis and the homogeneity of such preparations and was shown to be useful as a complementary method in characterizing casein hydrolysates. Tryptophan addition, used to compensate for the losses during the fabrication of protein hydrolysates, could also be detected by this technique.

Keywords: UV–Visible spectrophotometry; Casein hydrolysates; Derivative spectroscopy

Knowledge of protein hydrolysate composition is difficult to obtain because of the large number of possible constituents. This is due to the multiple degrees of polymerization of the peptides, characterized by twenty natural amino acids. Official methods used total nitrogen and α-amino nitrogen assays are unsuitable for assessing the nutritional quality of these products. Recent work has demonstrated the interest in small peptides for which prehydrolysis is not needed [1–5]. These findings show that a better estimation of the extent of hydrolysis is required. Gel permeation chromatography allows a first estimation. However, considering the great complexity of protein hydrolysates, it is desirable to use rapid and simple techniques.

Correspondence to: M. Hamon, Laboratoire de Chimie Analytique, Faculté de Pharmacie, Châtenay-Malabry (France).

A cuprimetric assay for analysing casein hydrolysates was described recently [6]. Another possibility would be UV spectrophotometry. Analytical methods using visible and UV spectrophotometry have attracted increasing interest in recent years owing to the introduction of commercial devices allowing the rapid calculation of absorbance derivatives with respect to wavelength. Notably, second-derivative spectra, highlighting inflection points and shoulders of the absorbance spectrum, allow an easier identification of a component [7–12].

In the field of protein analysis, this technique has allowed the titration of isolated or mixed proteins [13–15], determination of their aromatic amino acid content [16–20] and assessment of their positions within a protein molecule [17,21–23]. Coupled with liquid chromatography, derivative spectrophotometry has been used to identify

aromatic amino acids [24–26] and protein oligomers [27] in the chromatograms.

This paper describes a comparative spectrophotometric study of casein hydrolysates with regard to native casein and its constituent amino acids.

EXPERIMENTAL

Equipment

All spectra were recorded with a Shimadzu (Kyoto) Model 2100 UV–visible spectrophotometer.

Chemicals and reagents

Commercial casein hydrolysates were provided by Nutripharm-Gallia (Steevoorde, France): H1 (2% free amino acids), H2 (5% free amino acids) and H3 (25% amino acids). Amino acids and peptides were purchased from Sigma (St. Louis, MO) and other reagents from Prolabo (Paris).

Preparation of casein hydrolysates

Bovine whole casein was precipitated from fresh skimmed milk by the addition of 1 M HCl until the solution reached pH 4.6. Four successive precipitations were carried out, between each of which the precipitate was washed and dissolved in water by slow addition of 1 M NaOH until the solution reached pH 7. After the fourth precipitation, the solution of casein of pH 7 was dialysed against distilled water and then lyophilized.

A 1% solution of whole casein in 0.01 M phosphate buffer (pH 7.5) was submitted to proteolysis by pancreatin and trypsin, at 37°C, using the following enzyme-to-substrate ratios (E/S) and hydrolysis times: with pancreatin, E/S = 1:25, 6 h (P1), E/S = 1:200, 6 h (P2), and E/S = 1:200, 2 h (P3); and with trypsin, E/S = 1:25, 15 h (T1) and E/S = 1:200, 2 h (T2). The reactions were stopped by decreasing the pH to 2.0 with formic acid and these preparations, named standard hydrolysates, were lyophilized.

Tryptophan addition

Three products were prepared, P1W1, P1W2 and P1W3, by adding 50, 100 and 150 mmol kg^{-1} of tryptophan, respectively, to the hydrolysate P1.

UV absorbance and second-derivative spectrophotometry

Spectra were recorded between 250 and 300 nm directly on solutions of the components to be analysed in 0.1 M phosphate buffer (pH 7). For the second-derivative spectra, the wavelength difference ($\Delta\lambda$) used was 2 nm. For each product studied, we recorded five spectra, except for peptides containing three or more amino acid residues, for which we recorded a single spectrum.

The concentrations of the studied solutions were as follows: tryptophan (W), 9.79×10^{-6} M; tryptophanylglycine (W-G), 7.65×10^{-6} M; glycyl tryptophan (G-W), 7.65×10^{-6} M; lysyltryptophanyllysine (K-W-K), 8.68×10^{-6} M; leukokinin I (D-P-A-F-N-S-W-G), 7.42×10^{-6} M; tyrosine (Y) 3.67×10^{-4} M; glycyltyrosine (G-Y), 5.88×10^{-5} M; tyrosylglycine (Y-G), 5.88×10^{-5} M; α-bag cell peptide 1–9 (A-P-R-L-R-F-Y-S-L), 1.1×10^{-4} M; and whole casein, sodium caseinate, standard, commercial and tryptophan-added casein hydrolysates, protein–hydrolysate and protein–amino acid mixtures, 1 g l^{-1}.

Calculations of peak-to-peak distances in second-derivative spectra were made by the peak–trough method, using both pairs of spectra (Figs. 1 and 4), labelled *a* (peak around 288 nm, through around 284 nm) and *b* (peak around 294 nm, trough around 291 nm), with *r* representing the *a*/*b* ratio.

RESULTS AND DISCUSSION

Study of absorbance spectra

First, it is important to note that, owing to the development of the chromatographic method, it was possible to separate and determine the different components of the standard hydrolysates and, consequently, to classify them in relation to their degree of hydrolysis, expressed as the ratio between the number of free amino acid moles contained in 1 g of hydrolysate and the number of moles of amino acid achieved after total hydrolysis of the same mass of product. This classification, according to the degree of hydrolysis, is as follows: P1 > P2 > P3 > T1 > T2 [29].

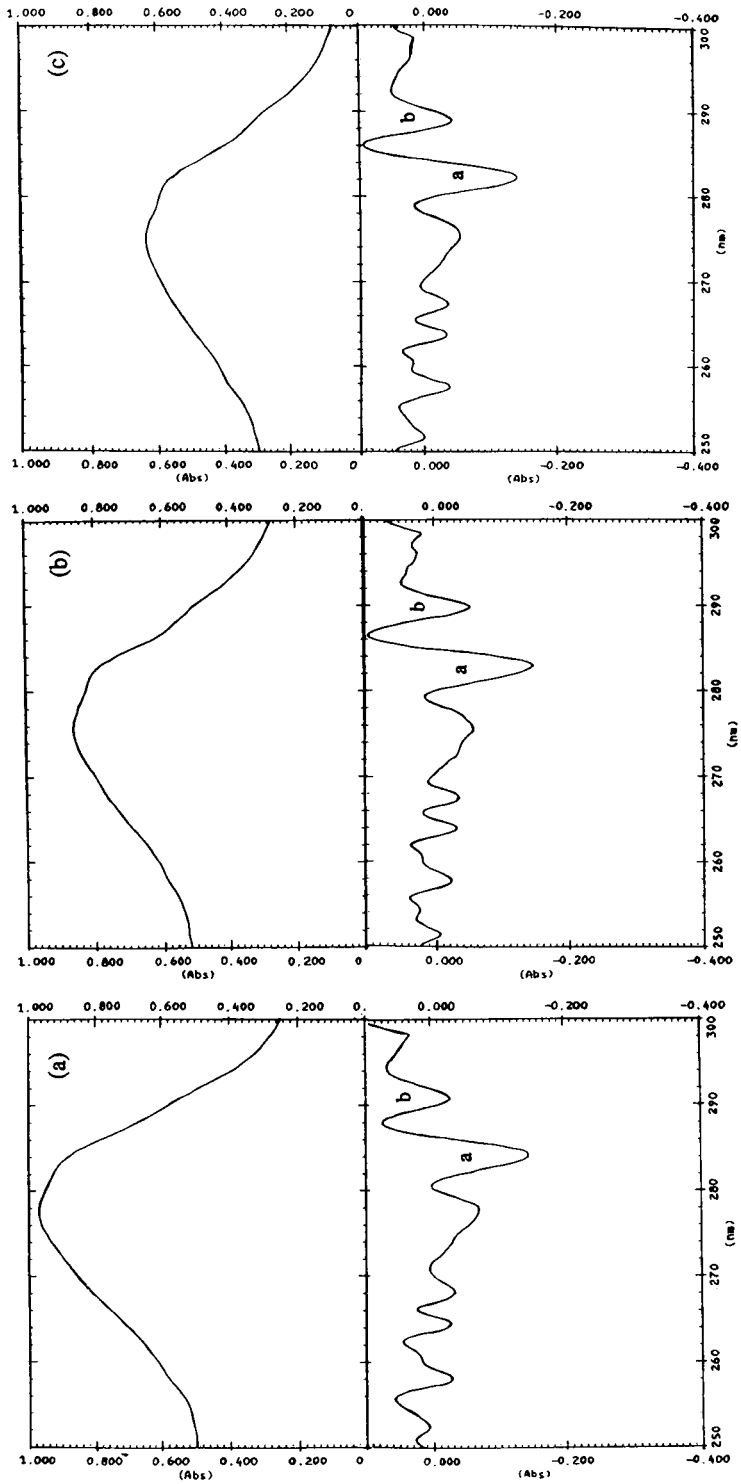

Fig. 1. Absorbance and second-derivative spectra of (a) casein, (b) T2 hydrolysate and (c) P1 hydrolysate, in 0.1 M phosphate buffer (pH 7.0).

TABLE 1

Wavelengths and absorptivities (1%/cm, on a molar basis), at the maximum of absorption, on absorbance spectra of casein and pure and tryptophan added casein hydrolysates [a]

Product	λ (max) (nm)	Absorptivity
Casein	277.5	9.7
P3 hydrolysate	275.5	5.5
P2 hydrolysate	274.9	5.9
P1 hydrolysate	274.6	6.4
T2 hydrolysate	275.7	8.6
T1 hydrolysate	275.4	6.4
H1 hydrolysate	274.9	9.2
H2 hydrolysate	275.0	8.3
H3 hydrolysate	273.6	7.7
P1W1	274.5	9.3
P1W2	274.1	12.7
P1W3	276.4	15.2

Wavelength (λ) and absorptivity (A) values at the absorption maximum (Table 1) show the difference between casein and its pancreatic and tryptic hydrolysates. As an example, the weaker (T2) and the stronger (P1) casein hydrolysate spectra are shown in Fig. 1. A low tryptic and pancreatic hydrolysis (T2 and P3 hydrolysates) produced hypsochromic and hypochromic effects with respect to the casein spectrum.

The presence of hydrophobic bonds, mainly due to aromatic nuclei, leads to a poorly polar environment around the aromatic amino acid residues. It is well known that a difference in spectral behaviour exists for oxygen and nitrogen-containing molecules, depending on the solvent used, and that the use of a polar solvent produces a hypsochromic and a hypochromic effect with respect to a non-polar solvent, owing to the formation of dipole–dipole interactions or hydrogen bonds.

It is possible to consider, at the beginning of the protein hydrolysis, the occurrence of similar phenomena to those described during protein denaturation [30]. In the latter instance, rupture of hydrophobic bonds, involved in the formation of tertiary and quaternary structures, produces an unfolding of the molecule, increasing the solvation, particularly near the aromatic amino acids. At the beginning of enzymatic action, attack of some peptidic bonds leads to cleavage of the protein into several independent chains and thereby prompts the disappearance of hydrophobic bonds. As hydrolysis continues, successive protein cleavages lead to the production of shorter and shorter peptides, in which tryptophan is necessarily situated closer to the ends of the peptides. This leads to an "exposure" [23] of this amino acid and thus an increase in absorptivity (Table 1). This evolution is shown for some examples of peptides (Table 2).

For tryptic hydrolysis, this evolution is logically less clear than in pancreatic hydrolysis, as trypsin does not cleave peptidic chains near the aromatic amino acids. In contrast, for the pancreatic hydrolysis, chymotrypsin activity leads to a cleavage of the chains beside the aromatic amino acids, notably tryptophan. This results in an earlier increase in absorptivity than in the case of tryptic hydrolysis. These observations could explain, at least in part, the hypsochromic and hypochromic followed by hyperchromic effects observed in absorbance spectra, during protein enzymic hydrolysis. Both stages of hypochromic followed by hyperchromic variation of absorptivity with respect to the extent of hydrolysis can be better observed in Fig. 2.

The solvation of tryptophan, more important at the beginning of hydrolysis, is shown in ab-

TABLE 2

Wavelengths and absorptivities (1%/cm, on molar basis), at the absorption maximum, on a absorbance spectra of tryptophan- (W), tyrosine- (Y) and tryptophanyl tyrosine-containing peptides [a]

Product	λ (max) (nm)	Absorptivity	Molar absorptivity, ε ($l\ mol^{-1}\ cm^{-1}$)
W	278.4	2555	52200
W-G	278.1	1840	48100
G-W	278.9	1610	42100
K-W-K*	279.7	865	39800
D-P-A-F-N-S-W-G*	279.5	171	15200
Y	274.5	74	1300
Y-G	274.0	519	12500
G-Y	274.5	508	12000
A-P-R-L-R-F-Y-S-L*	274.4	17	1900

[a] Values are the means for five spectra (one spectrum for the products marked with asterisks), recorded between 250 and 300 nm in 0.1 M phosphate buffer (pH 7.0).

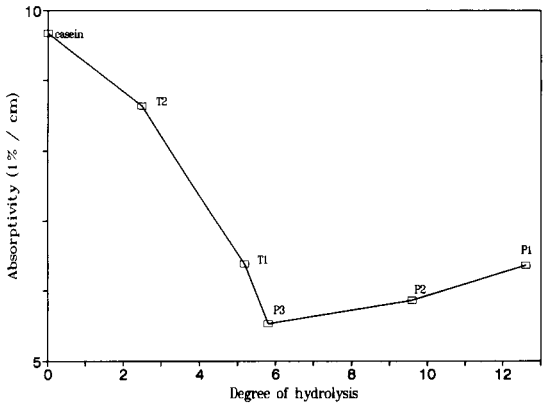

Fig. 2. Plots of absorptivities (1%/cm), at the absorption maximum, as a function of the degree of hydrolysis, for casein, pancreatic (P) and tryptic (T) casein hydrolysates.

sorbance spectra by the evolution of the shoulder situated around 287 nm (Fig. 1). Although not very clear in the casein spectrum, it becomes more pronounced in the weaker hydrolysate spectrum (T2). Nevertheless, no noteworthy alteration appears in relation to the degree of hydrolysis. Hence the increasing terminal "exposure" of tryptophan in the peptides formed does not alter the spectrum at that level.

Study of second-derivative spectra

The results described above are corroborated, even more clearly, by second-derivative spectrophotometry. The spectra of tyrosine and tryptophan containing proteins display two important peak-to-peak systems, *a* and *b*, the former corresponding to both tryptophan and tyrosine and the latter to tryptophan only. Hence measurement of the peak-to-peak distances for both systems and calculation of their ratio *r* allowed the spectrophotometric study of casein hydrolysates to be improved (Table 3).

An increase in solvation of aromatic amino acid residues, corresponding to the descending part of the curve in Fig. 2, occurred here in three different stages (Fig. 3). In the first (transformation of native casein into the weaker hydrolysate T2), the *a* and *b* distances increased, the former more than the latter, leading to a small increase in *r*. This could be due, at least in part, to "exposure" of tyrosine to a more polar medium.

TABLE 3

a and *b* peak-to-peak distances and their ratio *r* on second-derivative spectra of casein and pure and tryptophan-supplemented casein hydrolysates [a]

Product	*a*	*b*	*r*
Casein	215	91	2.36
P3 hydrolysate	218	80	2.73
P2 hydrolysate	223	81	2.74
P1 hydrolysate	232	91	2.54
T2 hydrolysate	245	101	2.43
T1 hydrolysate	248	86	2.89
H1 hydrolysate	311	178	1.75
H2 hydrolysate	289	175	1.66
H3 hydrolysate	281	274	1.02
P1W1	265	173	1.53
P1W2	320	264	1.21
P1W3	509	545	0.93

[a] The *a* and *b* values, calculated by the peak–trough method, correspond to 1 g l^{-1} concentrations and represent the means for five spectra (one spectrum for the products marked with asterisks), recorded between 250 and 300 nm in 0.1 M phosphate buffer (pH 7.0). The *a* (in absorbance $nm^{-2} \times 10^{-4}$) distance corresponds to *a* peak around 285 nm and a trough around 281 nm, and the *b* distance (in absorbance $nm^{-2} \times 10^{-4}$) to a peak around 292 nm and a trough around 288 nm.

Indeed, according to Ragone et al. [23], the influence of solvent polarity on the ratio *r*, absent in the case of tryptophan, becomes important for tyrosine, causing a hypsochromic effect. This phenomenon leads to two effects: at wavelengths near 284 nm *a*, the minimum on the tyrosine

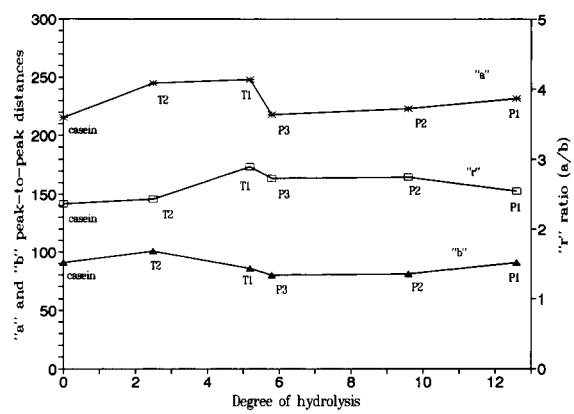

Fig. 3. Plots of *a* and *b* peak-to-peak distances and their ratio *r* as a function of the degree of hydrolysis, for casein, tryptic (T) and pancreatic (P) casein hydrolysates.

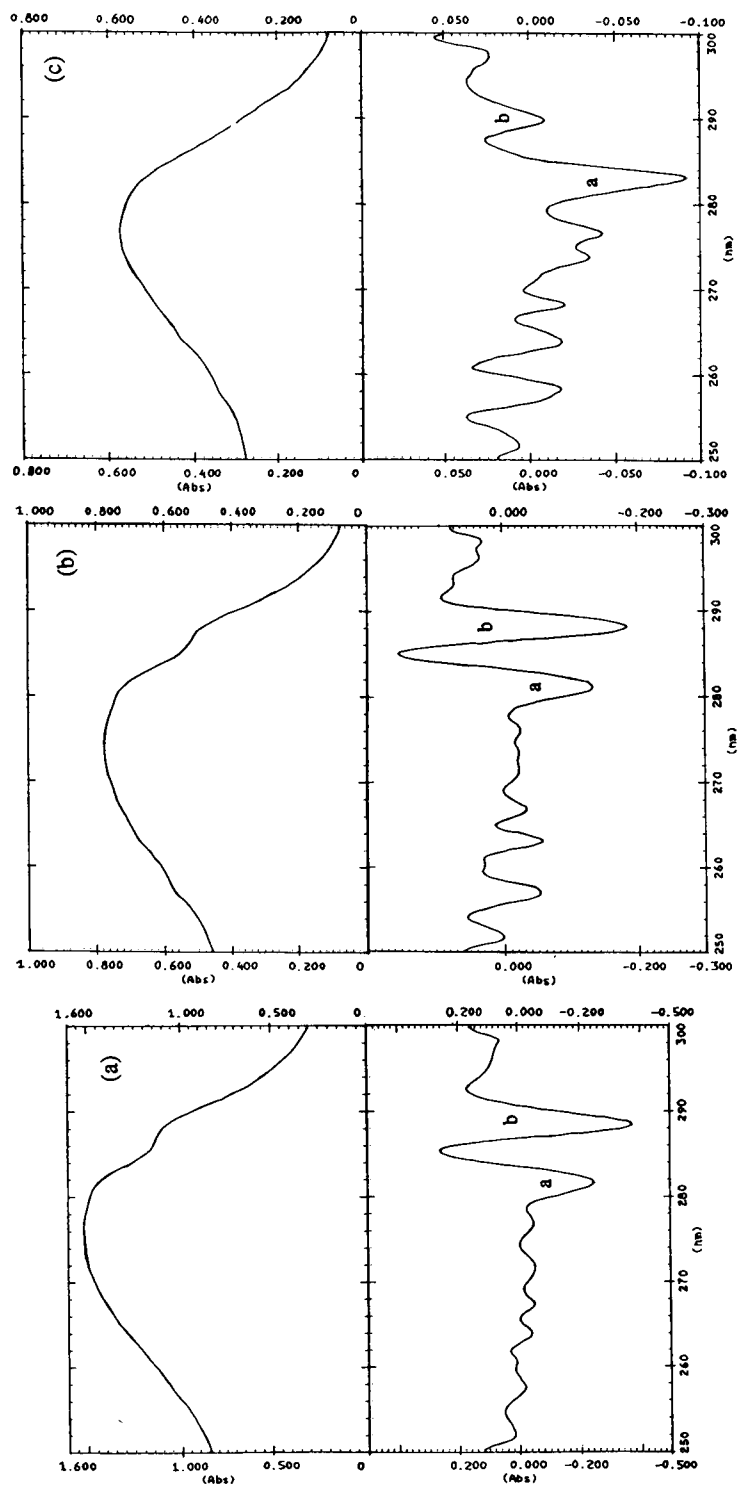

Fig. 4. Absorbance and second-derivative spectra of (a) P1W3 hydrolysate (150 mmol kg^{-1} added tryptophan), (b) H3 commercial hydrolysate and (c) sodium caseinate–amino acid mixture, in 0.1 M phosphate buffer (pH 7.0).

spectrum comes closer to that on the tryptophan spectrum. In contrast, at wavelengths near 291 nm *b*, the maximum on the tyrosine spectrum tends towards low values, so decreasing its negative influence on the importance of the minimum on the tryptophan spectrum. The overall result was an increase in *a* and *b* distances but, quantitatively, the change in *a* was larger than that in *b*, resulting in an increase in *r*.

For the other stages, corresponding to an increase in solvation of aromatic amino acid residues (between T2 and T1, then T1 and P3), variations in the *a* and *b* distances allows the existence of numerous and opposing influences to be anticipated. The results obtained with some peptides are insufficient to explain these modifications (Table 4).

The increase in absorptivity, covered by the ascending portion of the curve in Fig. 2, also corresponds to an increase in the *a* and *b* distances. As *b* increased more than *a*, it caused a decrease in *r* (Fig. 3). This is probably due to a release of peptides containing tryptophan closer to the ends of the peptides. This evolution is shown for some peptides in Table 4.

TABLE 4

a and *b* peak-to-peak distances and their ratio *r* on second-derivative spectra of tryptophan-, tyrosine- and tryptophanyl tyrosine-containing peptides [a]

Product	*a*	*b*	*r*
W	223	325	0.69
W-G	224	323	0.69
G-W	161	207	0.78
K-W-K*	153	217	0.71
D-P-A-F-N-S-W-G*	67	70	0.96
Y	7	–	–
Y-G	70	–	–
G-Y	64	–	–
A-P-R-L-R-F-Y-S-L*	7	–	–

[a] The *a* and *b* values, calculated by the peak–trough method, correspond to 10 μM concentrations and represent the means for five spectra (one spectrum for the products marked with asterisks), recorded between 250 and 300 nm, in 0.1 M phosphate buffer (pH 7.0). The *a* (in absorbance $nm^{-2} \times 10^{-4}$) distance corresponds to *a* peak around 285 nm and a trough around 281 nm, and the *b* distance (in absorbance $nm^{-2} \times 10^{-4}$) to a peak around 292 nm and a trough around 288 nm.

Although it is difficult to explain accurately all these spectral modifications, it is important to emphasize that at any stage of the studied enzymatic hydrolysis, the ratio *r* for hydrolysed caseins was greater, even if the variation was sometimes very small compared with that of native casein. This confirms the analogy with protein denaturation suggested previously. In fact, Ragone et al. [23] observed an increase in *r*, also sometimes very small, after guanidine hydrochloride treatement for denaturating proteins.

Moreover, according to Ragone et al. [23], as *r* for tryptophan is not influenced by the nature of the solvent, the increase induced by protein denaturation should be associated with the changes that occur around the tyrosine residues. However, the results for some tryptophan-containing peptides (Table 4) showed that other elements could influence *r*, such as the nature of the linking amino acids, the mode of tryptophan linkage (by the carboxylic or by the amino function) and the peptide size. Hence, in the case of protein hydrolysis, in addition to tyrosine-associated alterations, an influence of these tryptophan-related factors on *r* ratio could be observed. This observation, different from that stated by Ragone et al. [23], seems to be due to the fact that, in contrast to denaturation, the enzymatic action leads to cleavage of the protein molecule.

Effect of adding tryptophan to hydrolysates

Commercially available casein hydrolysates are often supplemented with tryptophan to compensate for losses during their preparation. We therefore studied the influence of this addition on the absorbance and second-derivative spectra. Increasing amounts of this amino acid were added to the P1 hydrolysate and spectra of the three prepared products, P1W1, P1W2 and P1W3, were recorded. As an example, absorbance and second-derivative spectra of P1W3 are shown in Fig. 4.

It can be seen in Table 1 that absorptivity increased on tryptophan addition and that even the smallest amount added (50 mmol kg^{-1}) produced an increase of about 50%. Moreover, the shoulder situated around 287 nm became more visible as tryptophan was added. It should be

noted that this small amount added corresponds to an increase of about 60% in the tryptophan fraction, as the tryptophan content of bovine casein is about 1.7% [31]. However, it is not possible to determine a quantitative relationship between the absorptivity of a nontryptophan supplemented hydrolysate and that of tryptophan-supplemented products. In fact, a 275 nm, tyrosine, whose fraction in the casein molecule is much higher than that of tryptophan, absorbs significantly. In addition, the tryptophan absorptivity was different depending on whether it was in the free form or within a peptide molecule (Table 2).

These differences were even more obvious in the derivative spectra. There was a greater increase in *b* than *a* and, consequently, a decrease in *r* parallel to tryptophan addition.

On the other hand, the shifts of the peaks and troughs in the second-derivative spectra were negligible when small amounts of tryptophan were added (Table 4). Nevertheless, adding an larger amount (150 mmol kg^{-1}) led to a marked bathochromic shift in the absorbance spectrum, bringing the absorption wavelength nearer to that of free tryptophan (Table 1).

Analysis of commercial casein hydrolysates

After studying the spectra of the standard casein hydrolysates, this technique was applied to the analysis of three commercial casein hydrolysates. As an example, the absorbance and second-derivative spectra of the H3 hydrolysate are shown in Fig. 4.

It can be seen that the absorption maxima (Table 1) on the absorbance spectra are situated in the same wavelength region as those of standard hydrolysates, except for H3, for which a slightly lower value can be observed. The same applies to the wavelengths of *a* and *b* on the derivative spectra (Table 5).

It should be noted that the H1 and H2 absorbance spectra look similar to those of standard hydrolysates, whereas that of H3, the richest in free amino acids, displays a more pronounced shoulder around 287 nm. This might indicate that H3 contains more "exposed" tryptophan.

Also, it seemed of particular interest to compare the experimental results on the degree of hydrolysis with those which can be obtained from the curve in Fig. 2. In fact, transferring the measured absorptivities on this curve demonstrated that for H1 and H2 hydrolysates, the calculated degrees of hydrolysis were 1.3 and 3.0, respectively. Regarding H3, from the determination of the P3–P1 and P2–P1 straight-line slopes and their interests on the ordinate in Fig. 2, the degrees of hydrolysis could be obtained by extrapolating the two straight lines and were 19.8 and 18.2, respectively. The latter in particular is very near to the experimental value of 18.4.

The analysis of the second-derivative spectra showed a discrepancy between the results obtained with these commercial hydrolysates and those described above for the standard hydrolysates. In fact, the values found for *a*, *b* and *r* do not agree with those expected, considering the degree of hydrolysis (Table 3). Thus, the peak-to-peak distances were much larger than expected and their ratio definitely smaller. Comparing these results with those obtained with tryptophan-supplemented hydrolysates led to the hypothesis that supplementation with this amino acid might explain these discrepancies. The current work mentioned above should allow this hypothesis to be confirmed.

TABLE 5

Wavelengths of *a* and *b* systems on second-derivative spectra of casein and pure and tryptophan supplemented casein hydrolysates [a]

Product	*a* system, peak–trough (nm)	*b* system, peak–trough (nm)
Casein	288.0–284.1	294.3–290.8
P3 hydrolysate	286.2–282.4	292.8–289.1
P2 hydrolysate	286.1–282.3	292.7–289.1
P1 hydrolysate	285.9–282.1	292.3–288.8
T2 hydrolysate	286.4–282.9	292.6–289.8
T1 hydrolysate	286.5–282.6	293.8–289.6
H1 hydrolysate	285.5–281.7	292.3–288.6
H2 hydrolysate	285.5–281.6	292.4–288.5
H3 hydrolysate	284.9–281.1	291.6–288.2
P1W1	285.6–282.0	292.7–288.6
P1W2	285.5–281.8	292.4–288.6
P1W3	285.3–281.6	292.5–288.4

[a] Values are the means for five spectra recorded between 250 and 300 nm, in 0.1 M phosphate buffer (pH 7.0).

Determination of casein hydrolysate homogeneity

In a previous study [32], we showed the usefulness of a cuprimetric titration for checking the homogeneity of casein hydrolysates. Some commercial products whose labels indicated α-amino nitrogen and total nitrogen contents, which should logically be used to estimate the average size of peptides, were, in fact, heterogeneous. They may be composed of proteolysates of different degrees of hydrolysis with the addition of native proteins or amino acids. Some examples are given in Table 6.

For this study, three preparations were analysed, exhibiting a similar free amino acid content (2%): a homogenous casein hydrolysate (H1), a mixture of sodium caseinate and 2% of free amino acids in the proportions existing in casein and a mixture of 92% of sodium caseinate and 8% of a casein hydrolysate containing 25% of amino acids (H3). As an example, absorbance and second-derivative spectra of the caseinate–amino acid mixture are shown in Fig. 4.

It can be seen that the absorptivity is higher in the homogeneous hydrolysate than in mixtures of casein and either amino acids or hydrolysate having the same free amino acid content (Table 6). On the other hand, the shoulder situated at 287 nm is more pronounced on the spectrum of the mixtures containing the H3 hydrolysate. This is probably due to its higher "exposed to solvation" tryptophan content with respect to other preparations studied.

TABLE 6

Wavelengths and absorptivities (1%/cm), at the absorption maximum, on absorbance spectra of sodium caseinate, a homogeneous casein hydrolysate and 2% free amino acid-containing mixture [a]

Product	λ (max) (nm)	Absorptivity
Sodium caseinate	276.6	4.2
H1 hydrolysate (2% of free amino acids)	274.9	9.2
92% sodium caseinate + 8% H3 hydrolysate	275.0	7.7
98% sodium caseinate + 2% amino acid mixture (in casein proportions)	276.2	5.8

[a] Values are the means for five spectra recorded between 250 and 300 nm, in 0.1 M phosphate buffer (pH 7.0).

TABLE 7

a and *b* peak-to-peak distances and their ratio *r* on second-derivative spectra of sodium caseinate, a homogeneous casein hydrolysate and a 2% free amino acid-containing mixture [a]

Product	*a*	*b*	*r*
Sodium caseinate	97	48	2.02
H1 hydrolysate (2% of free amino acids)	311	178	1.75
92% sodium caseinate + 8% H3 hydrolysate	213	199	1.08
98% sodium caseinate + 2% amino acid mixture (in casein proportions)	117	42	2.52

[a] The *a* and *b* values, calculated by the peak–trough method, correspond to 1 g l^{-1} concentrations and represent the means for five spectra (one spectrum for the products marked with asterisks), recorded between 250 and 300 nm, in 0.1 M phosphate buffer (pH 7.0). The *a* (in absorbance $nm^{-2} \times 10^{-4}$) distance corresponds to a peak around 285 nm and a trough around 281 nm, and the *b* distance (in absorbance $nm^{-2} \times 10^{-4}$) to a peak around 292 nm and a trough around 288 nm.

Measurement of the *a* and *b* peak-to-peak distances and determination of *r* highlight even more the spectral differences between the three preparations studied (Table 7). Thus, for the casein–hydrolysate mixture, *a* decreased while *b* increased and as a result, *r* decreased with respect to the homogeneous hydrolysate. For the casein–amino acid mixture, both *a* and *b* decreased but, as *b* decreased more than *a*, *r* was greater than that for the homogenous hydrolysate.

On the other hand, shifts in the absorption maximum on the absorbance spectra and in the peaks and troughs on the derivative spectra (Tables 6 and 8), can be used to differentiate only a homogeneous hydrolysate from a casein–amino acid mixture. In fact, as the protein content in this mixture is high (98%), the *a* and *b* wavelengths are virtually identical with those observed for sodium caseinate. Conversely, when the protein is mixed with a hydrolysate, in the above-mentioned proportions, the positions of the absorption maximum and of peaks and troughs are those of the hydrolysate.

TABLE 8

Wavelengths of *a* and *b* systems on second-derivative spectra of sodium caseinate, a homogeneous casein hydrolysate and 2% free amino acid-containing mixtures [a]

Product	*a* system peak–trough (nm)	*b* system peak–trough (nm)
Sodium caseinate	287.2–283.3	294.1–290.3
H1 hydroplysate (2% of free amino acids)	285.5–281.7	292.3–288.6
92% sodium caseinate +8% H3 hydrolysate	285.4–281.6	292.2–288.5
98% sodium hydrolysate +2% amino acids (in casein proportions)	287.4–283.2	294.3–289.8

[a] These values are the means for five spectra recorded between 250 and 300 nm, in 0.1 M phosphate buffer (pH 7.0).

As UV absorbance and second-derivative spectrophotometry are simple and a rapid methods, they could be used to check the homogeneity of casein hydrolysates, in parallel with the cuprimetric technique developed previously [32].

REFERENCES

1 H. Hara, R. Funabiki, M. Iwata and K. Yamazaki, J. Nutr., 114 (1984) 1122.
2 R.G. Rees, G.K. Grimble, P.P. Keohane, B.E. Higgins, M. West, R.C. Spiller and D.B.A. Silk, Gut, 25 (1984) A547.
3 P.P. Keohane, G.K. Grimble, B. Brown, R.C. Spiller and D.B.A. Silk, Gut, 26 (1985) 907.
4 G.K. Grimble, P.P. Keohane, B.E. Higgins, M.V. Kaminski, Jr., and D.B.A. Silk, Clin. Sci., 71 (1986) 65.
5 K.E. Webb, Jr., J. Anim. Sci., 68 (1990) 3011.
6 E. Lati, M. Silvestre, C. Dauphin and M. Hamon, Anal. Chim. Acta, 268 (1992) 163.
7 T.C. O'Haver, Clin. Chem., 25 (1979) 1548.
8 J.E. Cahill and F.G. Padera, Am. Lab., 12 (1980) 101.
9 P. Levillain and D. Fompeydie, Analusis, 14 (1986) 1.
10 F.S. Rojas, C.B. Ojeda and J.M. Cano Pavon, Talanta, 35 (1988) 753.
11 D. Fompeydie and P. Levillain, Analusis, 17 (1989) 17.
12 H. Gotz, Biochromatography, 3 (1989) 156.
13 F.J.C. Rodrigue, F. James, P. Levillain and A. Lemonier, Acta Pharm. Biol. Clin., 3 (1984) 235.
14 G.-J.C.M. Sanderink and H.J.M. van Rijn, Clin. Chim. Acta, 146 (1985) 65.
15 H. Mach, J.A. Thomson and C.R. Middaugh, Anal. Biochem., 181 (1989) 79.
16 C. Balestieri, G. Colonna, A. Giovane, G. Irace and L. Sevillo, Eur. J. Biochem., 90 (1978) 433.
17 T. Ichikawa and H. Terada, Biochim. Biophys. Acta, 580 (1979) 120.
18 T. Ichikawa and H. Terada, Chem. Pharm. Bull., 29 (1981) 438.
19 L. Servillo, G. Colonna, C. Balestrieri, R. Ragone and G. Irace, Anal. Biochem., 126 (1982) 251.
20 Y. Nozaki, Arch. Biochem. Biophys., 277 (1990) 324.
21 T. Ichikawa and H. Terada, Biochim. Biophys. Acta, 494 (1977) 267.
22 T. Ichikawa and H. Terada, Biochim. Biophys. Acta, 671 (1981) 33.
23 R. Ragone, G. Colonna, C. Balestrieri, L. Servillo and G. Irace, 23 (1984) 1871.
24 B. Greco, E.C. Nice and R.J. Simson, J. Chromatogr., 352 (1986) 359.
25 D.E.H. Palladino and K.A. Cohen, J. Chromatogr., 29 (1991) 91.
26 C.W. Turck, Pept. Res., 5 (1992) 156.
27 G. Talsky and J. Dostal, J. Chromatogr., 282 (1983) 487.
28 H. Ficheux, Spectrophotométrie Dérivée et Spectrofluorimétrie Synchrone Dérivée: Application au Dosage des Uro et Coproporphyrines, Laboratoire de Biochimie, Hôpital de Bicêtre, 1988.
29 M.P.C. Silvestre, M. Hamon and M. Yvon, J. Agric. Food Chem., submitted for publication.
30 T.E. Creighton, Protein Structure–a Practical Approach, IRL, Oxford, 1989.
31 C. Alais, Science du Lait–Principe des Techniques Laitières, Sepaic, Paris, 1984.
32 M.P.C. Silvestre, E. Lati, C. Dauphin and M. Hamon, J. Assoc. Off. Anal. Chem., in press.

Analytica Chimica Acta, 282 (1993) 613–623
Elsevier Science Publishers B.V., Amsterdam

Dual-laser crossed-beam thermal lens spectrophotometer pumped with a semiconductor diode-array laser

Andreu Cladera Forteza, Consuelo Tomás Más, José M. Estela Ripoll and Víctor Cerdá Martín

Departament de Química, Universitat de les Illes Balears, 07071 Palma de Mallorca (Spain)

Guillermo Ramis-Ramos

Departament de Química Analítica, Universitat de València, 46100 Burjassot, València (Spain)

(Received 15th February 1993; revised manuscript received 18th May 1993)

Abstract

A simple and compact dual-laser crossed-beam thermal lens spectrophotometer pumped with a semiconductor diode-array laser, emitting up to 100 mW of power at 818 nm, is described. The pump laser aperture was located at a very small distance from the cell wall and was not focused. The He–Ne probe beam was made to pass near the cell wall, almost grazing the wall inner surface, crossing the pump beam at right-angles with respect to the beam propagation direction, but parallel to the major axes of the narrow elliptical lobes emitted by the array. Owing the particular spatial characteristics of the pump beam, a thermal lens signal with a complex spatial distribution was obtained. Univariant and simplex optimization of the set-up were performed using $CuSO_4$ and phosphomolybdenum blue solutions. Limits of detection of absorbance were 3.9×10^{-4} in CCl_4, 3.4×10^{-4} in 2-butanol, 1.1×10^{-3} in ethyl acetate and 3.0×10^{-3} in water.

Keywords: Diode lasers; Semiconductor lasers; Thermal lens; UV–Visible spectrophotometry

Very small absorbance values can be accurately measured using thermal lens spectrophotometry (TLS) [1–7]. In TLS, absorption of a pump laser beam generates a thermal gradient associated with a refractive index gradient. The intensity of the gradient is proportional to the concentration of the absorbing species and is measured with a probe laser beam. Coaxial pump–probe configurations are most frequently used in thermal lens spectrophotometry [8]. The thermal lens effect causes a change of divergence of the probe beam which is measured in the far-field with an intensity-sensitive detector.

Correspondence to: G. Ramis-Ramos, Departament de Química Analítica, Universitat de València, 46100 Burjassot, València (Spain).

In the last decade, the application of TLS to the field of trace analysis has been investigated [7–20]. In many instances, very low limits of detection have been obtained; however, the development of commercial TLS instruments is still prevented by the high prices, physical complexity and performance limitations of powerful lasers in the UV and visible regions.

Pulsed lasers have been used to pump TLS instruments [7,9]; however, continuous-wave (cw) lasers give much better limits of detection [7]. Ideally, the characteristics of a cw laser to be used as the pump beam source in TLS would be the following: one or several lines should be provided within the UV and visible regions, particularly within the 220–550-nm range, where most chromophores of analytical interest absorb;

line or band widths can be large, e.g., pumping with a band as wide as 10 nm would not be detrimental to most TLS applications; more than 500 mW of cw pump power are rarely used, but at least 50 mW of cw power per line or band should be available, otherwise the sensitivity would be low; the spatial characteristics of the beam should be adequate for a tight focus to be easily formed, which would maximize the thermal gradient and the sensitivity; the power should be easily and accurately reproduced from one working session to another; and long-term power drift and low-frequency variations of the power (e.g., below 1 kHz) should be as small as possible, preferably less than 1%, to reduce systematic errors associated with sensitivity variations and random noise. The latter condition also implies that the warming up period should not be too long.

The development of cw lasers approaching these characteristics is probably necessary for compact and practical TLS instruments, well adapted to the needs of routine analytical applications, to be made commercially available. Ion gas lasers approach some of these characteristics, and are most frequently used in TLS studies. Semiconductor or diode lasers are less convenient, but the cost is low, they are compact and rough and, when properly operated, they offer a long life and a high energy yield which makes the energy supply and cooling requirements low. In addition, they can be easily driven with a voltage source or a function generator, which facilitates pump modulation and power stabilization.

Unfortunately, diode lasers emit highly divergent beams of too long wavelength radiation to be of much interest in TLS applications. However, new diode lasers, emitting at decreasing wavelengths with increasing power, can be expected to be available in a near future. Further, diode laser systems with several linear (single-stripe arrays) and matrix (multi-stripe and stacked arrays) geometries are commercially available. The facet of a single diode laser is damaged by a high optical intensity (typically above 30–50 mW), which limits the available power [19]. Diode laser arrays produce much higher total output powers operating at a low power per emitter. Some manufacturers offer the possibility of producing special customer-designed products [18]. To take advantage of this possibility makes the design of TLS instruments pumped with diode lasers of new types a challenging and promising task.

A thermal lens instrument pumped by a diode laser emitting 10 mW at 824 nm was described by Nakanishi et al. [20]. They used two convergent lenses to form a beam waist at the sample location. The irregular profile and the aberrations led to a loss of sensitivity with respect to the expected theoretical value. The limit of detection (LOD) was 0.2 ng ml^{-1} phosphorus using the phosphomolybdenum blue method after extraction into 2-butanol. A low-cost coaxial beam-deflection TLS instrument, pumped by a GaAlAs diode laser emitting 10 mW at 790 nm, was also described by Bicanic et al. [21]; the LOD was 1.5 ng ml^{-1} phosphorus (5×10^{-8} M), again using the phosphomolybdenum blue method.

In this paper, a low-cost, simple and compact TLS instrument pumped with a linear-array diode laser, is described. The spatial characteristics of the beam are indicated in Fig. 1: the divergence was large and the energy was equally split in two lobes, each with the same narrow elliptical profile. A He–Ne laser was used to probe the thermal lens effects in a crossed-beam configuration. The pump laser was not focused; instead, the laser emission window was located at a very small

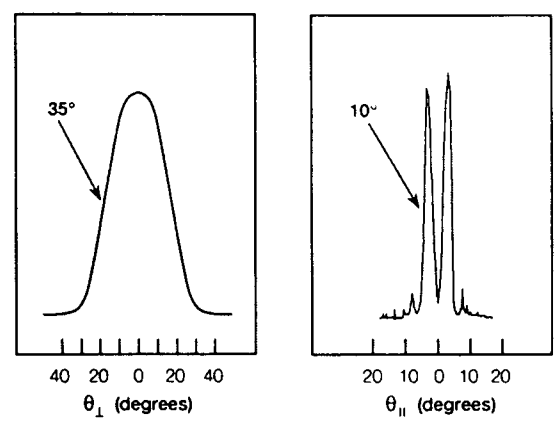

Fig. 1. Far-field energy distribution of the SDL-2410-H1 diode-array laser (reproduced from [18] with permission of Spectra Diode Labs., San Jose, CA).

distance from the cell wall, and the probe beam was made to pass near the cell wall, almost grazing the wall inner surface, crossing the pump beam at right-angles with respect to the propagation direction, but parallel to the major axes of the lobe profiles. In this way, maximum overlap between the probe and pump beams was achieved.

In this design, crossing of the beams at a short distance from the diode window prevented the use of any optical component to focus the pump beam, but at the crossing region, the section area of the pump beam was not excessively large, the instrument was simple and compact and optical alignment was very easy. Owing to the particular spatial characteristics of the pump beam, a thermal lens signal with a complex spatial distribution was obtained. Univariant and simplex optimization of the set-up were performed using both $CuSO_4$ and phosphomolybdenum blue solutions in several solvents.

EXPERIMENTAL

Apparatus and software

A schematic diagram of the set-up is shown in Fig. 2. The diode-array laser was a Model SDL-2410-H1 provided with a Model SDL 800 laser diode driver (Spectra Diode Labs., San Jose, CA), emitting a maximum power of 100 mW at 818 nm. The nominal dimensions of the linear array of emitters were 100×1 μm [18]. The probe beam, provided by a Model 102P He–Ne laser (Spectra-Physics, Mountain View, CA), was focused with a 200-mm biconvex lens (Pedret, Barcelona). The probe and pump beams crossed at right-angles. As shown in Fig. 3 (right), the probe beam propagated along the major axes of pump beam lobes.

The detector system was constructed using a 15-cm long aluminium tube which was blackened inside. A 1-mm pinhole mask was glued at one end and a 100 mm^2 silicon photodiode (Model OSD-100-5T; Centronic, Croydon, UK) was fixed at the other end of the tube. The signal was conditioned with a laboratory-made amplifier provided with offset correction, and fed to an analog input of a DAS-8 board (MetraByte, Taunton, MA). The board was installed in a PC-compatible computer (μP 386SX). The pump beam power was modulated with a Model 171 function generator (Wavetek, San Diego, CA). To synchronize pump modulation, data acquisition and analytical signal demodulation, the TTL reference output of the function generator was connected to a digital input of the DAS-8 board.

A fluorescence-type $1 \times 1 \times 4.5$ cm^3 standard quartz cell was used. A lateral wall of the cell holder (Shimadzu, Kyoto) was drilled to make it possible to mount the diode laser with the window aperture almost touching the cell wall. The diode laser was fixed to the cell holder using a laboratory-made aluminium mount. Thus, the cell–diode laser distance was not modified throughout this study. All the elements of the set-up were fixed on a 100×50 cm^2 12-mm thick aluminium plate using mounting elements from Ealing Electro-Optics (Watford, UK).

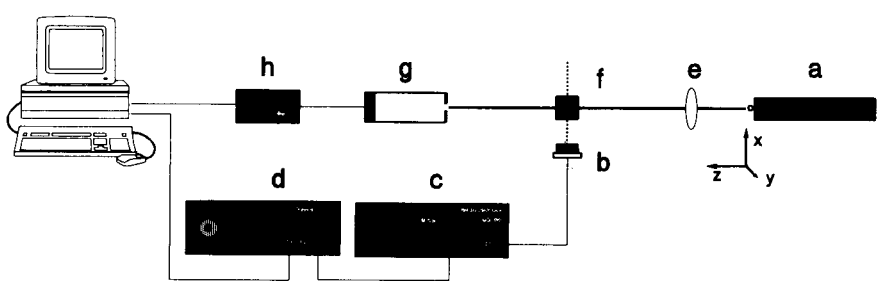

Fig. 2. Schematic diagram of the set-up. (a) He–Ne laser; (b) diode-array laser; (c) diode laser driver; (d) function generator connected to a digital input of the DAS-8 interface; (e) 200-mm biconvex lens; (f) cell; (g) detector; (h) signal conditioning circuit connected to an analog input of the DAS-8 interface. The *y*-axis is normal to the paper. The distances between optical elements are not reproduced to scale.

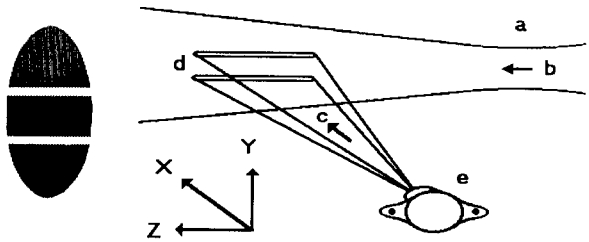

Fig. 3. Left: sketch of the spot observed at the detector mask when pumping is on; the grey level indicates the illuminated regions which are surrounded by dark regions. Right: schematic diagram showing a section of the probe beam at the crossed-beam region. (a) Probe beam waist; (b) probe beam propagation direction following the z-axis; (c) pump beam propagation direction following the x-axis (backwards normal to the paper); (d) pump beam profile at the crossed-beam region; (e) laser diode.

The program TLS4.EXE, written in Microsoft BASIC 7.1 and linked with the DAS-8 subroutines (MetraByte), was used to acquire and treat the data. The program continuously transferred data to an intermediate buffer where up to ten series of formation–dissipation thermal lens cycles could be optionally stored. Data transfer to the buffer was synchronized with pump modulation, hence an integer number of cycles with a constant dephase was stored.

To obtain a TLS measurement, the program transferred the contents of the buffer to the treatment subroutine. The difference between the maximum and minimum of the signal within each cycle was obtained and the mean and standard deviation of all the differences was calculated. Finally, the thermal lens signal was calculated as

$$S = [I(0) - I(\infty)]/I(\infty) \quad (1)$$

where $I(0) - I(\infty)$ is the mean of the differences and $I(0)$ is the mean of the maxima, which was not significantly different from the intensity given by the unperturbed probe beam. Other options of the program included monitoring of the TLS signal with time and simplex optimization.

Absorbance measurements were performed with a Model HP-8452A spectrophotometer (Hewlett-Packard). For all the TLS measurements the pump power was adjusted to 60 mW and was electronically chopped at 1 Hz.

Reagents and procedures

Analytical-reagent grade reagents from Probus (Barcelona) were used; the organic solvents were obtained from Solvent Doc. Synt. (Paris, France). Water was deionized and distilled. Optimization and characterization of the set-up were performed using a 1.5×10^{-3} M $CuSO_4 \cdot 5H_2O$ solution in a water–dimethyl sulphoxide (DMSO) (50 + 50, v/v) and a 50 μg ml^{-1} aqueous phosphorus standard solution prepared with H_2KPO_4.

To develop the chromogenic reaction, 10 ml of 0.1 M $Na_2MoO_4 \cdot 2H_2O$ solution in 5 M H_2SO_4, 4 ml of 0.01 M hydrazine sulphate in water and an aliquot of the phosphorus solution were introduced into a 100-ml volumetric flask and diluted to volume with water and the mixture was heated at 85°C in a water-bath for 10 min. After cooling, liquid–liquid extraction was performed when necessary and the absorbance and the TLS signal were measured. All results were calculated as averages of ten measurements, each being obtained from eight thermal lens formation–dissipation cycles.

Extraction was performed by shaking 10 ml of the aqueous phosphomolybdenum blue solution with 10 ml of 2-butanol or ethyl acetate and by drying the organic phase with anhydrous Na_2SO_4. The same procedure was followed for carbon tetrachloride, but 0.05% Adogen 464 was added before shaking.

RESULTS AND DISCUSSION

Nature of the signal and univariant optimization

$CuSO_4$ solution was used to study the nature and spatial distribution of the signal obtained and to optimize the geometric variables. The positive z- and x-axes were assumed to follow the orthogonal probe and pump beam propagation directions, respectively, and the y-axis was assumed to follow the positive vertical direction. The origin of the x- and y-axes was located at the centre of the probe beam section (see Fig. 2).

Within each pump cycle, the probe beam swung from a circularly symmetrical to an elliptical profile. Further, the elliptical profile of the perturbed probe beam showed two dark regions lo-

cated immediately above and below the beam centre, and crossing across the beam profile horizontally (Fig. 3, left). From Figs. 1 and 3, it is deduced that the formation of the dark regions is due to the increase in divergence produced by the thermal lens effect in those regions of the probe beam crossing the pump beam lobes. This was confirmed by the next experiment, in which the 1-Hz modulated signal was measured all along the probe beam profile.

The variations in sensitivity obtained by modifying the location of the detector along the x- and y-axes are shown in Fig. 4. The signal presented two elongated maxima of similar intensity at two y values, symmetrically located above and below the horizontal symmetry plane of the probe beam, and separated by an elongated minimum at $y = 0$.

The variation of sensitivity obtained by modifying the cell–pump laser assembly–detector distance and the detector vertical position is shown in Fig. 5. The two maxima increased and became more separated from each other when the cell–detector distance increased. A few secondary maxima were also observed. These can be attributed to diffraction, but also to the secondary maxima of the far-field energy distribution of the diode (see Fig. 1).

In the following experiments, the pinhole was always located at the centre of the probe beam section, so only thermal lens rather than thermal deflection effects could be detected. The variation of the signal with the position of the cell–diode laser assembly respecting the x- and y-axes is shown in Fig. 6. Each of the two maxima along the y-axis was resolved into a pair of maxima. This could be due to the formation of four regions with a maximum value of the thermal gradient along the y-axis.

Maximum sensitivity was obtained when the cell was located at the largest x-coordinate value, which corresponded to the probe beam crossing the pump beam at a minimum distance from the

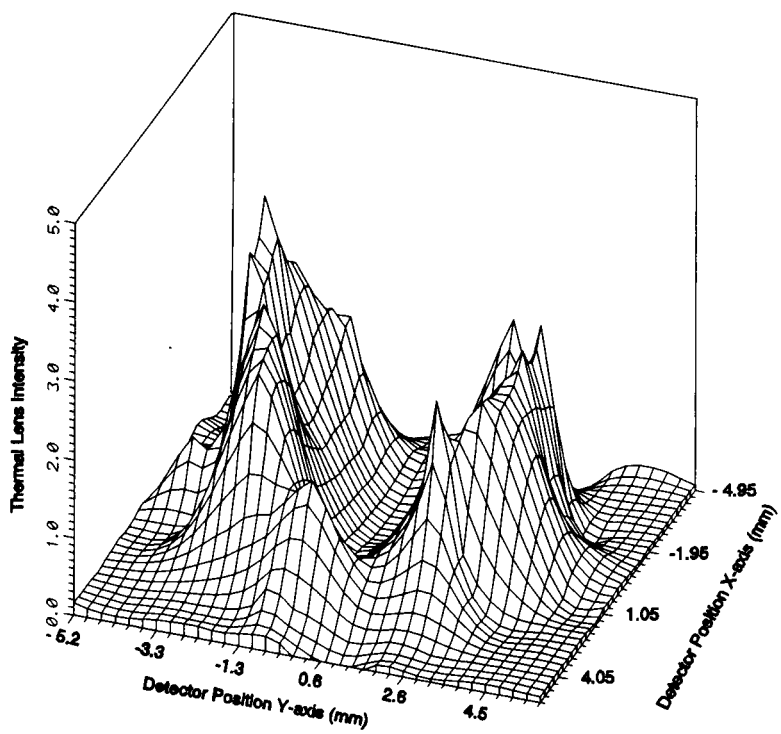

Fig. 4. Sensitivity (arbitrary units) as a function of the detector location along the x- and y-axes.

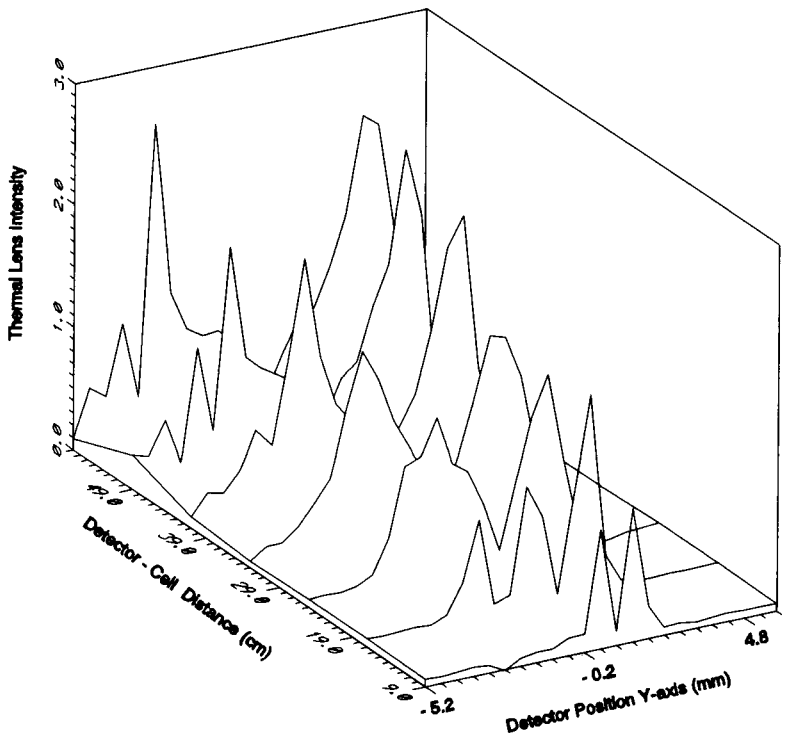

Fig. 5. Sensitivity (arbitrary units) as a function of the detector location along the y-axis and the cell–pump laser assembly–detector distance.

diode surface. At this position of the cell on the x-axis, the region of the four maxima extended over ca. 2 mm along the y-axis.

Experiments performed by turning the diode array round by 90° were also performed. In this instance, the probe beam crossed the pump beam perpendicularly to the major axes of the elliptical profiles of the lobes. Overlap between the probe and pump beams was very small, pumping did not produce a thermal gradient across the probe beam profile, and consequently an almost zero sensitivity was obtained.

Next, a vertical scan of the cell–diode laser assembly was performed, and data showing the form and sign (phase angle) of the signal at several points were obtained. In this scan the cell–diode laser assembly position along the x-axis was kept fixed at 3.9 mm. The results are shown in Figs. 7 and 8.

Figure 7 shows that the sensitivity was positive only along two broad regions surrounded by negative sensitivity regions. At the regions of a maximum positive value of the sensitivity, the shape of the time-resolved signal (Fig. 8, curves 1 and 8) indicated a typical thermal lens effect, with an exponential decrease in irradiation intensity during the pumping half-cycle. In contrast, the negative sensitivity regions showed an increase in intensity during pumping (Fig. 8, curve 5) or a mixed behaviour (Fig. 8, curves 3 and 4).

It is concluded that pumping caused the typical thermal lens increase of the divergence of the pump beam at the two regions of the probe beam profile where the pump and probe beams overlapped. In these regions the sensitivity was considered to be positive. Concentration of the energy of the probe beam in the vicinity of the two pumping regions, where deflected and unperturbed parts of the beam coincided, should cause negative sensitivity.

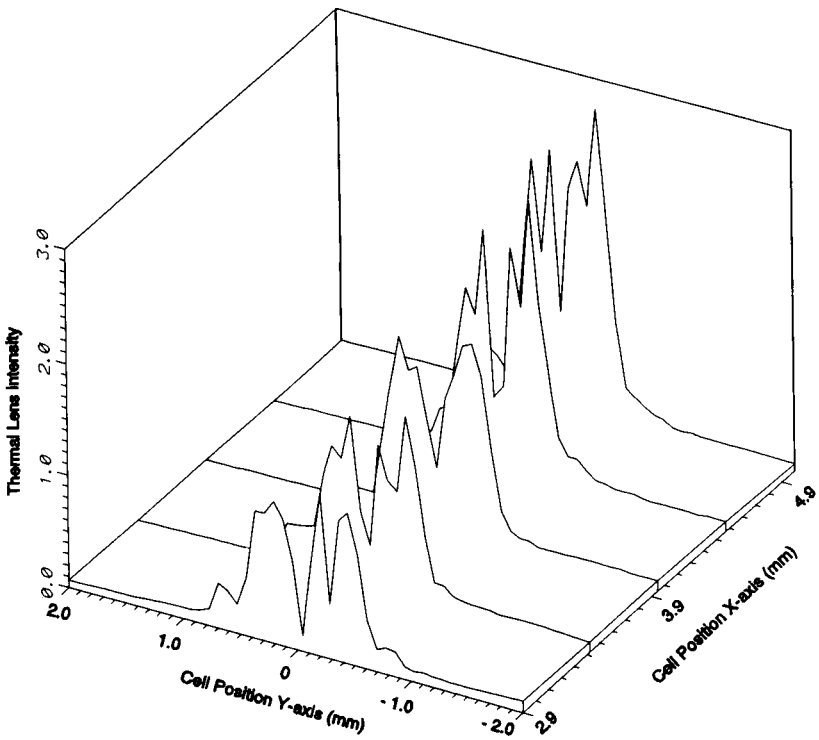

Fig. 6. Sensitivity (arbitrary units) as a function of the cell–pump laser assembly location along the x- and y-axes. The detector was maintained at the centre of the probe beam profile.

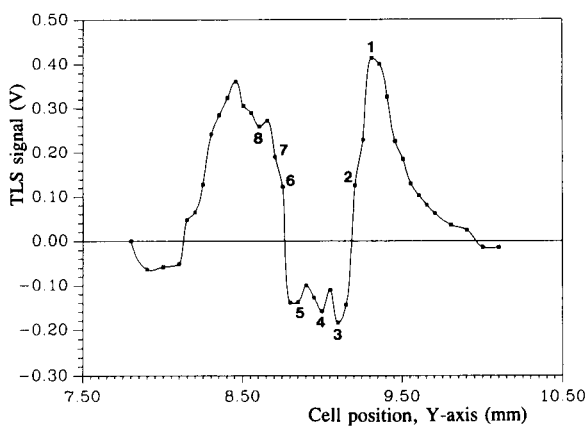

Fig. 7. Vertical scan of the cell–diode laser assembly showing the sign (positive or negative phase angle) and intensity of the signal. The numbers on the curve correspond to the modulated time-resolved thermal lens signal shown in Fig. 8. The detector was maintained at the centre of the probe beam profile.

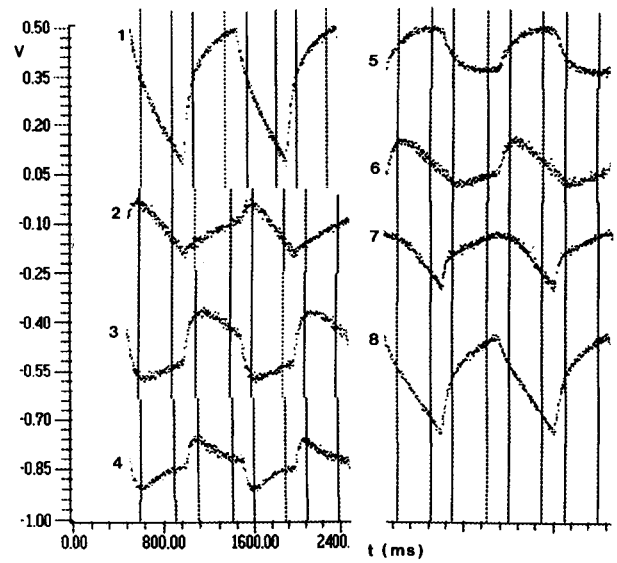

Fig. 8. Shape of the modulated time-resolved thermal lens signal at some selected points along the vertical scan of Fig. 7. The y-axis of the plot is arbitrarily offset.

Finally, Fig. 9 shows the results obtained by varying the cell–pump laser assembly–lens distance. At each position of the lens ($f = 200$ mm), the cell–pump laser assembly location with respect to the x- and y-axes was adjusted to maintain the maximum value of the signal within one of the two positive sensitivity regions. As expected, the sensitivity increased with increasing cell–lens distance, a maximum being obtained at 16.5 cm.

In most TLS set-ups, the thermal lens effect cannot be detected when the cell is located at the probe beam waist, the signal undergoing a 180° change of phase. However, Fig. 9 showed a minimum rather than a zero-crossing point (a 180° change of phase) at 21 cm from the lens, where the cell was located at the probe beam waist. This can be attributed to the large overlapping region of the beams, which should reach probe beam regions outside the waist. Further, the divergence of the probe beam should be continuously changed by the thermal lens effect all along the overlapping region. This made the interpretation and modelling of the thermal lens effect difficult.

Simplex optimization

The modified simplex algorithm, provided with unidirectional translation, contraction and interpolation operations, was used [22,23]. In the univariant optimization studies, sensitivity was found to depend mainly on the cell–detector and cell–lens distances and on the detector and cell positions along the y-axis. Therefore, these parameters were simultaneously optimized, while maintaining the locations of the detector and the cell along the x-axis at constant optimum values.

In addition, owing to the critical values of the cell y-coordinate, this parameter was not introduced in the optimization process, but it was manually adjusted within each iteration. The cell was always relocated along the y-axis, sensitivity being optimized at the positive maximum located at the lower position. As shown in Table 1, when the $CuSO_4$ solution was used the univariant and the simplex optimization procedures led to very similar values of the parameters.

The simplex optimization procedure was applied again using an aqueous phosphomolybdenum blue solution, in addition to phosphomolyb-

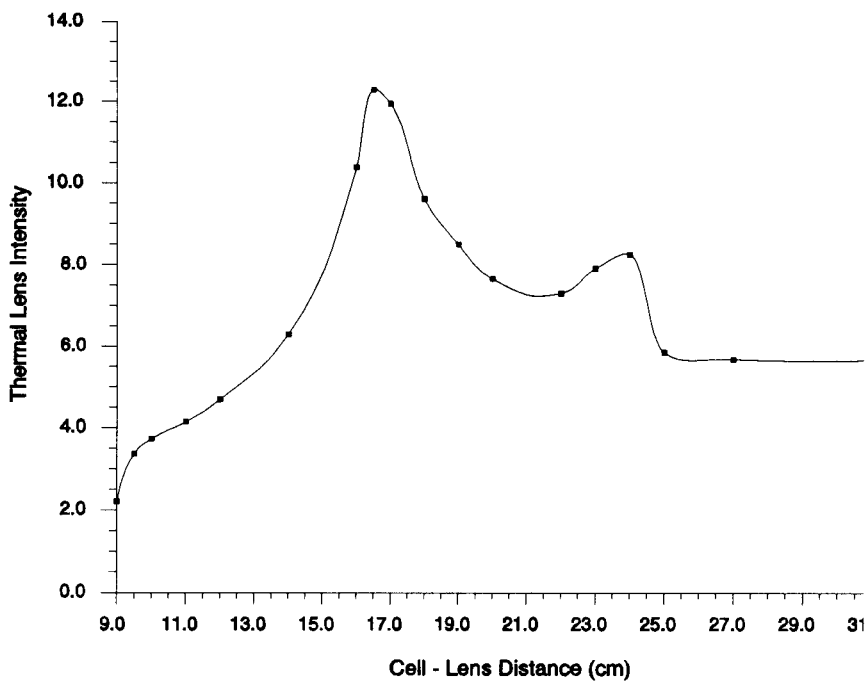

Fig. 9. Sensitivity (arbitrary units) as a function of the cell–pump laser assembly–lens distance.

TABLE 1

Optimum values of the parameters obtained by the univariant and simplex methods using 1.5×10^{-8} $CuSO_4$ solution in a water–DMSO (50+50)

Parameter	Univariant	Simplex
Lens–cell distance (cm)	16.5	15.0
Detector–cell distance (cm)	53.0	51.5
Detector location, *y*-axis (mm)	−1.5	−1.3
Cell location, *y*-axis (mm)	−0.2	−0.2
Signal ± standard deviation [a]	5.06 ± 0.03	5.126 ± 0.02

[a] Arbitrary units ($n = 10$).

denum blue extracts obtained with four organic solvents. The advance of the simplex is represented in Fig. 10 and the optimized parameters are given in Table 2. The differences between the values of the parameters were small, but not negligible. In some instances (e.g., water with respect to the other solvents), the differences were large enough to make optimization advisable.

Enhancement factors and figures of merit

In TLS, the enhancement factor, E, indicates how much the sensitivity is enhanced in relation to conventional spectrophotometry. The enhancement factors depend strongly on the nature of the media used, and can be theoretically calculated as

$$E_t = 0.52P(dn/dT)/\lambda\kappa \quad (2)$$

where P is the pump power, dn/dT is the temperature coefficient of the refractive index, λ is the wavelength of the probe laser and κ is the

TABLE 2

Optimum values of the parameters obtained by the simplex method using phosphomolybdenum blue solutions in different solvents

Parameter	Water	Ethyl acetate	Carbon tetrachloride	2-Butanol
Phosphorus concentration ($\mu g\,l^{-1}$)	500	100	50	100
Lens–cell distance (cm)	14.1	15.8	15.8	16.3
Detector–cell distance (cm)	47.0	52.4	53.7	53.6
Detector location, *y*-axis (mm)	−1.3	−2.2	−2.5	−2.4
Cell location, *y*-axis (mm)	−0.2	−0.4	−0.4	−0.3

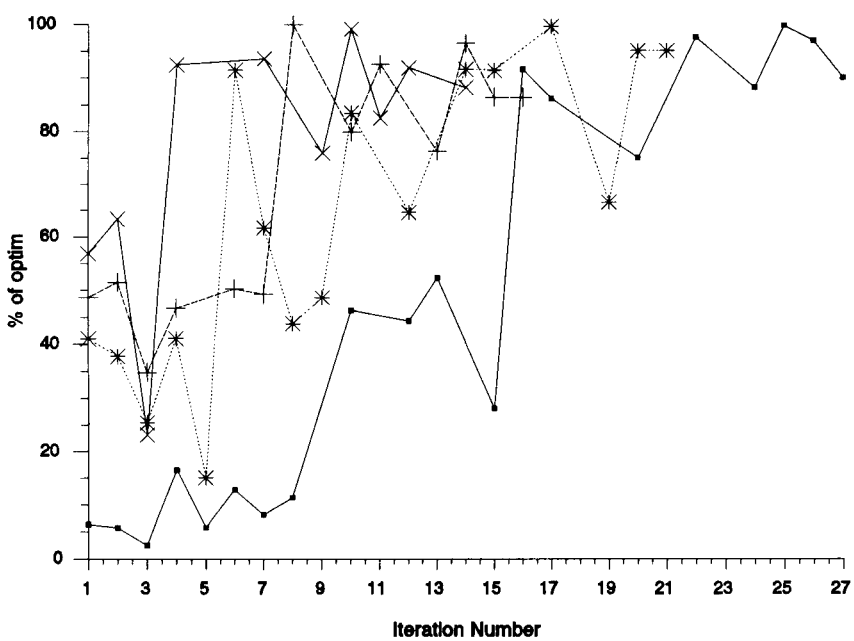

Fig. 10. Advance of the simplex optimization processes. Sample used: (■) 500 $\mu g\,l^{-1}$ P in water; (+) 100 $\mu g\,l^{-1}$ P in ethyl acetate; (*) 50 $\mu g\,l^{-1}$ P in CCl_4; (×) 100 $\mu g\,l^{-1}$ P in 2-butanol.

thermal conductivity. The enhancement factors can be also obtained experimentally using

$$E_e = S/2.3\ A \qquad (3)$$

where S and A are the TLS signal and the absorbance, respectively [7,24]. The differences between theoretical and experimental enhancement factors are a measure of the performance of the set-up. Phosphorus solutions of increasing concentrations were used to obtain the spectrophotometric and TLS sensitivities in the different media and to calculate the corresponding E_e factors. The values found were as follows: carbon tetrachloride, 76; 2-butanol, 37; ethyl acetate, 6.7; and water, 1.2. The results are compared in Fig. 11.

To compare these factors with those obtained under other working conditions, normalization is necessary. Some workers have referred the E factors to $P = 1$ mW and $\lambda = 632.8$ nm [2]. In this work, less than half the pump power was used in generating each of the two broad maxima. Therefore, it seems reasonable to use $P = 30$ mW instead of using 60 mW to normalize the E_e values. Theoretical and experimental normalized E values are given and compared in Table 3. The E_e/E_t ratios found were not much lower than those obtained by Nakanishi et al. [20], also using a diode laser to pump a TLS experiment. Larger differences were observed in water, with 38% in this work compared with 60% by Nakanishi et al. [20] and 100% obtained by Dovichi and Harris [2] using a He–Ne laser to pump the TLS set-up.

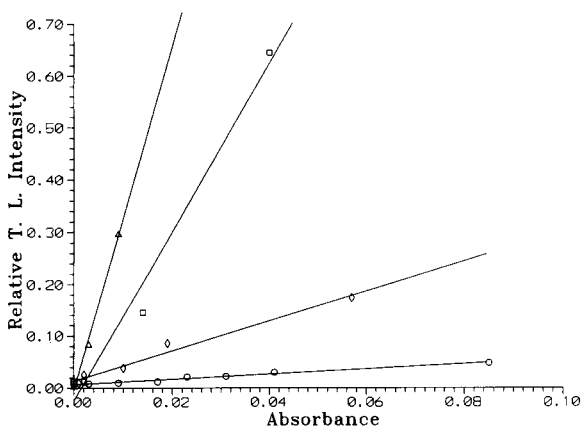

Fig. 11. TLS signal and absorbance values obtained using phosphomolybdenum blue solutions in several solvents: (△) CCl_4; (□) 2-butanol; (◇) ethyl acetate; (○) H_2O.

TABLE 3

Theoretical and experimental normalized enhancement factors, E_t and E_e [a]

Solvent	E_t	E_e (E_e/E_t, %)	
		This work	Other workers
CCl_4	4.9	2.5 (51)	–
$CHCl_3$	4.2	–	(38)
Ethyl acetate	2.7	0.23 (9)	–
2-Butanol	2.0	1.24 (62)	(25–33)
Water	0.11	0.042 (38)	(60)

[a] Theoretical calculations were made using data from [7]. Experimental values obtained by other workers pumping with a diode laser were adapted from [20].

Limits of detection (3σ, $n = 10$) given as absorbance were as follows: carbon tetrachloride, 3.9×10^{-4}; 2-butanol, 3.4×10^{-4}; ethyl acetate, 1.1×10^{-3}; and water, 3.0×10^{-3}. A value of 2×10^{-4} was obtained by Nakanishi et al. [20] using a 10-mW diode laser-pumped set-up and the same chromophore in 2-butanol.

Conclusions

The TLS instrument described here is compact and simple, and the normalized enhancement factors and limits of detection obtained were similar to those obtained by other workers also using a TLS set-up pumped with a diode laser. The results also indicated that diode lasers are less efficient than other lasers for pumping TLS instruments. This is a consequence of the difficulty found in concentrating the energy in a tight focus, the excessive dispersion of the pump energy leading to weaker thermal gradients than expected.

In the approach used in this work, the regions where the beams overlaped were large, in fact much larger than the usual values found in crossed-beam designs. At the optimum location of the cell–pump probe system, the overlapping region along the probe beam propagation direction could be estimated to be ca. 2.3 mm. This was probably very important in increasing the

sensitivity, but was not enough to compensate for the sensitivity decrease caused by the dispersion of the energy in two non-focused beams.

The difficulty in concentrating the energy produced by a diode laser in a tight focus should not to be considered as a serious drawback of diode TLS pumping, owing the large energetic yield of these devices, together with the possibility of reaching high powers. Diode pumping is not efficient in terms of sensitivity per mW, but it could be competitive in terms of sensitivity per cost of 1 mW. Further, it should be possible to increase the pumping efficiency of diode lasers by using very large and powerful matrix multi-stripe diode lasers provided with adequate masks and convergent optics in pump–probe coaxial configurations.

Finally, it has been shown that the geometric parameters of a TLS set-up can be adequately and conveniently optimized using the simplex method, which is of interest in automating optimization. However, a previous study of the significance of the variables to be included in the optimization process would always be required.

Thanks are due to the DGICyT of Spain for financial support (Projects PB90-0359 and PB90-0425).

REFERENCES

1 J.P. Gordon, R.C.C. Leite, R.S. Moore, S.P. Porto and J.R. Whinnery, J. Appl. Phys., 36 (1965) 3.
2 N.J. Dovichi and J.M. Harris, Anal. Chem., 51 (1979) 728.
3 N.J. Dovichi and J.M. Harris, Anal. Chem., 52 (1980) 2338.
4 N.J. Dovichi and J.M. Harris, Anal. Chem., 53 (1981) 106.
5 C.A. Carter and J.M. Harris, Appl. Opt., 23 (1984) 476.
6 N.J. Dovichi, T.G. Nolan and W.A. Weimer, Anal. Chem., 56 (1984) 1700.
7 N.J. Dovichi, CRC Crit. Rev. Anal. Chem., 17 (1987) 357.
8 J. Sen, R.D. Lowe and R.D. Snook, Chem. Phys., 165 (1992) 385.
9 N. Omenetto, P. Cavalli, G. Rossi, G. Bidoglio and G.C. Turk, J. Anal. At. Spectrom., 2 (1987) 579.
10 J.P. Haushalter and M.D. Morris, Appl. Spectrosc., 34 (1980) 445.
11 K. Fujiwara, H. Uchiki, F. Shimokoshi, K. Tsunoda, K. Fuwa and T. Kobayashi, Appl. Spectrosc., 36 (1982) 157.
12 C.A. Carter, J.M. Brady and J.M. Harris, Appl. Spectrosc., 36 (1982) 309.
13 K. Miyaishi, T. Imasaka and N. Ishibashi, Anal. Chem., 54 (1982) 2039.
14 J.A. Alfheim and C.H. Langford, Anal. Chem., 57 (1985) 861.
15 K.L. Jansen and J.M. Harris, Anal. Chem., 57 (1985) 1698.
16 K.L. Jansen and J.M. Harris, Anal. Chem., 57 (1985) 2434.
17 K. Fujiwara, W. Lei, H. Uchiki, F. Shimokoshi, K. Fuwa and T. Kobayashi, Anal. Chem., 54 (1982) 2026.
18 Laser Diode Product Catalog, Spectra Diode Labs., San Jose, CA, 1991.
19 O. Svelto and D.C. Hanna, Principles of Lasers, Plenum, New York, 3rd edn., 1989, p. 355.
20 K. Nakanishi, T. Imasaka and N. Ishibashi, Anal. Chem., 57 (1985) 1219.
21 D. Bicanic, J.P. Favier, E. Strauss, M. Lubbers and G. Fleuren, Int. J. Environ. Anal, Chem, 38 (1990) 623.
22 J.A. Nelder and R. Mead, Comput. J., 7 (1965) 308.
23 R.R. Ernst, Rev. Sci. Instrum., 39 (1968) 998.
24 G. Ramis-Ramos, Quím. Anal., 8 (1989) 299.

Analytica Chimica Acta, 282 (1993) 625–631
Elsevier Science Publishers B.V., Amsterdam

2-Aminothiophenols as fluorogenic reagents for aromatic aldehydes

Hitoshi Nohta, Fumie Sakai, Masaaki Kai and Yosuke Ohkura

Faculty of Pharmaceutical Sciences, Kyushu University 62, Maidashi, Higashi-ku, Fukuoka 812 (Japan)

Shuuji Hara and Masatoshia Yamaguchi

Faculty of Pharmaceutical Sciences, Fukuoka University, Nanakuma, Jonan-ku, Fukuoka 814-01 (Japan)

(Received 13th April 1993; revised manuscript received 18th June 1993)

Abstract

Substituted 2-aminothiophenols (7 species) were evaluated for fluorescence derivatization reagents of aromatic aldehydes in spectrofluorimetry and liquid chromatography. Of the compounds, 2-amino-5-methoxythiophenol was the most favourable in practical use. The reagent reacts selectively with aromatic aldehydes in acidic media within 70 min at 50°C. The fluorescent products from benzaldehyde and 4-hydroxybenzaldehyde are shown to be 2-phenyl-6-methoxybenzothiazole and 2-(4-hydroxyphenyl)-6-methoxybenzothiazole, respectively. The detection limits for aromatic aldehydes in the spectrofluorometric method were 7–80 pmol ml^{-1} depending on the aldehydes. The fluorescent derivatives of aromatic aldehydes can be separated by reversed-phase chromatography and their detection limits ($S/N = 3$) are 0.1–0.4 pmol on column.

Keywords: Fluorimetry; Aminothiophenols; Aromatic aldehydes; Fluorogenic reagents

Several aromatic 1,2-diamino compounds, i.e. 1,2-diaminonaphthalene [1], 1,2-diamino-4,5-dimethoxybenzene [2], 1,2-diamino-4,5-dimethylbenzene [3], 1,2-diamino-4,5-ethylenedioxybenzene [4] and 1,2-diamino-4,5-methylenedioxybenzene [4], have been developed as fluorogenic reagents for the determination of aromatic aldehydes. They are based on the cyclization reaction between the diamino moiety in the reagents and formyl moiety in the aldehydes, to form fluorescent imidazole derivatives. Through these studies, alkoxyl groups in the reagents were demonstrated to provide higher detection sensitivity [5]. On the other hand, aromatic 1-amino-2-sulfhydryl compounds, i.e. 2-aminothiophenol (AT) [6] and 2,2′-dithiobis(1-aminonaphthalene) (DTAN) which is derived to 1-amino-2-sulfhydrylnaphthalene when required for use [7], were also reported to be selective fluorogenic reagents for aromatic aldehydes. They react with the aldehydes in a similar manner, to form fluorescent thiazole compounds. DTAN afforded fairly intense fluorescence with a wide variety of aromatic aldehydes, and the reaction was applied to the assay for dopamine β-hydroxylase [8], monoamine oxidase [9] and catechol-*O*-methyltransferase [10] in biological samples. However, DTAN caused an intense blank peak in the liquid chromatographic (LC) determination of the derivatization reaction mixtures [8,10], and its derivatives of aromatic aldehydes are too hydrophobic to be completely

Correspondence to: Y. Ohkura, Faculty of Pharmaceutical Sciences, Kyushu University 62, Maidashi, Higashi-ku, Fukuoka 812 (Japan).

separated on a reversed-phase column. The purpose of this study was to find more favourable reagents for the manual spectrofluorometric and LC determination of aromatic aldehydes; 2-aminothiophenols substituted with alkoxyl, methyl or fluoro group(s) [2-amino-5-methoxythiophenol (MAT), 2-amino-5-ethoxythiophenol (EAT), 2-amino-4,5-methylenedioxythiophenol (MDAT), 2-amino-4,5-ethylenedioxythiophenol (EDAT), 2-amino-4,5-dimethoxythiophenol (DMOAT), 2-amino-4,5-dimethylthiophenol (DMAT) and 2-amino-5-fluorothiophenol (FAT)] (7 species) were examined together with AT. MAT selected as the most favourable reagent in practice was further investigated to establish the optimum conditions of spectrofluorometric and LC methods. The chemical structures of the fluorescent products of benzaldehyde and 4-hydroxybenzaldehyde with MAT were also investigated.

EXPERIMENTAL

Chemicals and solutions

The seven substituted aminothiophenols were synthesized according to the procedure in the literature [11] and their hydrochlorides were prepared in the usual manner. The hydrochlorides were stable at 4°C for at least three months. Other chemicals were of reagent grade. Each substituted aminothiophenol hydrochloride (0.2 mmol) was dissolved in 100 ml of a mixture of methanol and 20 mM perchloric acid (9:1, v/v) containing 2 mM tri-*n*-butylphosphine as an antioxidant. This solution could be used for at least 1 month when stored at 4°C. Stock solutions (10 mM) of aromatic aldehydes were prepared in water (or aqueous 50% (v/v) ethanol for hardly water-soluble aldehydes), and diluted with water before use. The stock solutions were stable for at least 1 month when stored at −20°C.

Apparatus

Uncorrected fluorescence excitation and emission spectra were measured with an MPF-4 spectrofluorimeter (Hitachi, Tokyo) in 10 × 10 mm quartz cells; spectral bandwidths of 5 nm were used for both the excitation and emission monochromators. Electron impact mass (MS) spectra were measured with a Jeol JMS-01-SG mass spectrometer. ^{1}H Nuclear magnetic resonance (NMR) spectra were taken on a Jeol JMN-PS-110 spectrometer at 100 MHz using approximately 5% (w/v) solution in chloroform-d_1 or dimethylsulfoxide-d_6 containing tetramethylsilane as an internal standard.

LC system and its operation conditions

A CCPM chromatograph (Tosoh, Tokyo) equipped with a Rheodyne 7125 syringe-loading sample injection valve (20-μl loop) and a Hitachi F1000 fluorescence spectrometer fitted with a 12-μl flow-cell was used. The fluorescence spectrometer was operated at the following excitation and emission wavelengths; 335 and 385 nm for MAT and EAT, 345 and 410 nm for MDAT, 340 and 410 nm for DMOAT, 340 and 400 nm for EDAT, 325 and 395 nm for DMAT and FAT, and 325 and 380 nm for AT, respectively. A TSKgel ODS-80T$_M$ (150 mm × 4.6 mm i.d.; particle size, 5 μm; Tosoh) column was used. The column temperature was ambient (25 ± 2°C). The mobile phase was an aqueous 70% (v/v) methanol, which was delivered at a flow rate of 0.8 ml min^{-1}.

Isolation of the reaction products of benzaldehyde and 4-hydroxybenzaldehyde with MAT

Benzaldehyde. To a methanolic solution of benzaldehyde (3 mmol in 10 ml) was added MAT solution (2.6 mmol MAT hydrochloride and 0.6 g of tri-*n*-butylphosphine in 10 ml of methanol), and 10 ml each of 3 M perchloric acid and 4 mM sodium sulphite – 0.35 M sodium hydrogen phosphite mixture. The mixture was allowed to stand at 45°C for 1 h with stirring, then followed by additional stirring for 12 h at room temperature (23–25°C). The precipitates were filtered, washed with aqueous 50% (v/v) methanol and dried in vacuo. The crude product was subjected to chromatography on a silica gel (30 g, Wako gel C-200; Wako Pure Chemicals) column (12 × 3 cm i.d.) with chloroform – *n*-hexane (1:1, v/v); the main fraction was collected and the solvent was removed in vacuo. The residue was recrystallized from methanol to give colorless needles, m.p.

118–120°C; yield 0.21 g (35% calculated from MAT). Elemental analysis (%), calculated for $C_{14}H_{11}NOS$, C 69.68, H 4.59, N 5.80; found C 69.65, H 4.61, N 5.79. MS spectrum, $m/z = 241$ (M^+, base peak), 226 ($M^+ - CH_3$), 198 ($M^+ - CH_3 - CO$). ^1H NMR spectrum (chloroform-d_1), (ppm) 3.8 (singlet, 3H, $-OCH_3$), 6.1–6.7 (multiplet, 3H, aromatic protons in benzothiazole moiety), 7.4–7.6 (multiplet, 4H, aromatic protons in phenyl moiety).

4-Hydroxybenzaldehyde. The precipitates produced from 4-hydroxybenzaldehyde under the same reaction conditions as those for benzaldehyde were recrystallized from methanol to give colorless needles, m.p. 232–234°C; yield 0.27 g (41%). Elemental analysis (%), calculated for $C_{14}H_{11}NO_2S$, C 65.35, H 4.31, N 5.44; found C 65.35, H 4.37, N 5.50. MS, $m/z = 257$ (M^+, base peak), 242 ($M^+ - CH_3$), 214 ($M^+ - CH_3 - CO$). ^1H NMR spectrum (dimethylsulfoxide-d_6), (ppm) 3.8 (singlet, 3H, $-OCH_3$), 6.9–7.1 (multiplet, 3H, aromatic protons in benzothiazole moiety), 7.7–7.9 (multiplet, 4H, aromatic protons in phenyl moiety), 10.3 (broad singlet, 1H, hydroxyl proton, exchangeable with deuterium).

Procedure for the spectrofluorometric and LC determinations with MAT

To 1.0 ml of aqueous test solution, 1.0 ml each of 3 M perchloric acid, 4 mM sodium sulfite–0.35 M disodium hydrogen phosphite mixture and 2.0 mM MAT solution were added. The mixture was allowed to stand at 50°C for 70 min, and the resulting fluorescence was measured at the excitation and emission maxima (see Table 2). To prepare the reagent blank, 1.0 ml of water in place of 1.0 ml of test solution was carried through the procedure.

For LC, the reaction mixture was neutralized to pH 6–7 with approximately 1 ml of 3 M sodium hydroxide, then an aliquot (20 μl) of the solution was used.

RESULTS AND DISCUSSION

Spectrofluorometric determination

All of the tested 2-aminothiophenols (8 species) gave fluorescence, but fluorescence intensities, and excitation and emission maxima differed depending on the reagents when examined in combination with benzaldehyde (Table 1). Alkoxyl groups introduced to the 4- and/or 5-position of the reagents provided the aldehyde with more intense fluorescence of which excitation and emission maxima were at longer wavelengths; MAT and EAT were further subjected to the investigations together with AT for comparison. All of the aromatic aldehydes tested fluoresced intensely with MAT and EAT (Table 2), though the intensities with AT strongly depended on the aldehydes used. The fluorescent derivatives of MAT and EAT showed close resemblance in their fluorescence properties: excitation and emission maxima (350–370 and 455–475 nm, respectively), and the intensities. From these results, MAT was selected as the most favourable reagent for aromatic aldehydes.

The fluorescent products of benzaldehyde and 4-hydroxybenzaldehyde were found to be 2-phenyl-6-methoxybenzothiazole and 2-(4-hydroxyphenyl)-6-methoxybenzothiazole, respectively, based on the spectral data. Further, the fluorescence excitation and emission spectra of the products dissolved in the reagent blank were identical with those of the reaction mixture of the corresponding aldehydes. The retention times of the products under the reversed-phase LC conditions also coincided with those for the corresponding reaction mixtures.

TABLE 1

Excitaton and emission maxima (λ_{ex}, λ_{em}) of the fluorescence from benzaldehyde with various aminothiophenols, and their relative fluorescence intensities (RFI) [a]

2-Aminothiophenol derivative	λ_{ex} (nm)	λ_{em} (nm)	RFI [b]
MAT	352	465	100
EAT	353	467	103
MDAT	371	485	54
EDAT	368	486	44
DMOAT	370	488	15
DMAT	344	420	13
FAT	328	400	15
AT	329	398	7

[a] Portions (1.0 ml) of 5 nmol ml^{-1} benzaldehyde were treated according to the procedure. [b] The intensity obtained with MAT was taken as 100.

The optimum conditions of the reaction was established using benzaldehyde because it reacted with MAT most slowly of the tested aldehydes (Table 2). Concentrations of MAT ranging from 1.7 to 2.2 mM gave almost maximum fluorescence intensity; 2.0 mM was recommended. MAT in a solution was slightly oxidized to the disulfide by molecular oxygen or other oxidants; 2 mM tri-*n*-butylphosphine was added to the MAT solution as an antioxidant; it did not affect the fluorescence reaction.

The reaction proceeded under strongly acidic conditions (perchloric acid or sulfuric acid). The maximum reaction rate was attained at concentrations of 2–6 M perchloric acid and 7–10 M sulfuric acid, but sulfuric acid could not give reproducible results with highly hydrophobic aldehydes such as benzaldehyde, naphthaldehyde and some alkoxybenzaldehydes probably due to the insolubility of the MAT-derivatives in the reaction mixture; 3 M perchloric acid was recommended in the procedure.

Sodium sulfite and disodium hydrogen phosphite accelerated the fluorescence reaction of aromatic aldehydes with DTAN [7]. They also accelerate the MAT reaction; 4.0 mM sodium sulfite and 0.35 M disodium hydrogen phosphite yielded the highest fluorescence intensity. Water-miscible organic solvents (methanol, ethanol, isopropanol, acetonitrile and 2-methoxyethanol) also accelerated the reaction; methanol, ethanol and isopropanol [20–30% (v/v) each in the reaction mixture] gave the best result. Methanol at concentration of 22.5% (v/v) was selected, which corresponded to 90% (v/v) methanol in the MAT solution.

The MAT reaction with the aldehydes (Table 2) occurred at a temperature above 0°C; higher temperature allowed the fluorescence to develop more rapidly. However, temperatures higher than 60°C caused reduction of the fluorescence, probably because of decomposition of the produced derivatives. The fluorescence intensities at 50°C reached maxima after standing for 30 min (vanillin and 4-hydroxybenzaldehyde) and for 45–60 min (the others), and the resulting fluorescence was stable at 50°C for at least 60 min. Warming at 50°C for 70 min was selected for reproducible results.

Aliphatic aldehydes (formaldehyde, acetaldehyde, propionaldehyde and *n*-butyraldehyde) and the following compounds of biological importance did not fluoresce under the conditions at a concentration of 100 nmol ml^{-1}; the compounds

TABLE 2

Excitation and emission maxima (λ_{ex}, λ_{em}) of the fluorescence from various aromatic aldehydes with MAT, EAT and AT and their relative fluorescence intensities (RFI) [a]

Aromatic aldehyde	MAT			EAT			AT		
	λ_{ex} (nm)	λ_{em} (nm)	RFI [b]	λ_{ex} (nm)	λ_{em} (nm)	RFI	λ_{ex} (nm)	λ_{em} (nm)	RFI
Benzaldehyde	352	465	100	352	465	103	329	398	7
Vanillin	375	452	23	376	455	24	369	440	4
4-Methoxybenzaldehyde	365	455	115	368	458	117	358	410	502
4-Methylbenzaldehyde	355	460	118	358	468	103	338	395	30
Piperonal	380	451	98	380	456	119	372	448	409
4-Chlorobenzaldehyde	357	470	148	357	470	137	331	400	98
2-Naphthaldehyde	370	468	130	370	473	99	348	465	192
4-Cyanobenzaldehyde	355	490	234	358	492	156	328	415	3
4-Phenylbenzaldehyde	370	468	429	370	470	307	359	440	580
4-Diethylaminobenzaldehyde	348	475	175	350	473	127	– [c]	–	< 0.1
Benzaldehyde-2-sulfonic acid, sodium salt	322	470	37	323	473	36	–	–	< 0.1
4-Hydroxybenzaldehyde	360	455	104	360	452	104	356	415	26

[a] Portions (1.0 ml) of 5 nmol ml^{-1} aromatic aldehyde solutions were treated according to the procedure using MAT, EAT and AT as fluorogenic reagents. [b] The fluorescence intensity of the MAT derivative of benzaldehyde was taken as 100. [c] Undiscernible.

tested were seventeen different L-α-amino acid, biogenic amines (dopamine, norepinephrine, epinephrine, serotonin and histamine), their metabolites (homovanillic acid, vanillylmandelic acid, 5-hydroxyindoleacetic acid and imidazoleacetic acid), α-keto acids (α-ketoglutaric acid and phenylpyruvic acid), oxalic acid, acetic acid, uric acid, L-ascorbic acid, creatine, creatinine, sugars (D-glucose, D-fructose, D-galactose, D-ribose, D-glucosamine, maltose and sucrose), nucleic acid bases (adenine, guanine, thymine, cytocine and uracil) and their nucleosides and nucleotides, and cholesterol. This suggests that the MAT reaction has sufficient selectivity for aromatic aldehydes.

The fluorescence developed from benzaldehyde under the recommended conditions did not change on irradiation for 30 min at its excitation maximum, and was stable for at least 5 h in daylight and for 48 h at 4°C in the dark.

The calibration graphs for the aldehydes listed in Table 2 were linear in the range 0.1–10 nmol ml^{-1}. The detection limits (defined as the concentration giving a fluorescence intensity corresponding to the blank value + three times the standard deviation) for the aldehydes varied from 7 to 80 pmol ml^{-1} depending on the aldehydes examined. This sensitivity was comparable to those with DTAN and 1,2-diamino-4,5-methylenedioxybenzene. The precision was established using 5 nmol ml^{-1} benzaldehyde; the relative standard deviation was 1.4% ($n = 10$).

LC determination with precolumn drivatization

Six aromatic aldehydes (3,4-dihydroxybenzaldehyde, isovanillin, vanillin, benzaldehyde, 4-methoxybenzaldehyde and 4-methylbenzaldehyde), were subjected to the reaction with the 2-aminothiophenols (8 species). Figure 1 shows typical chromatograms obtained with a standard mixture of the aldehydes using MAT, MDAT and DMOAT (recommendable in the procedure) as pre-column derivatization reagents. Table 3 shows the retention times, fluorescence excitation and emission maxima, and relative peak heights of the fluorescent derivatives under the LC conditions with the eight reagents. Under these conditions, all the reagents afforded the corresponding single

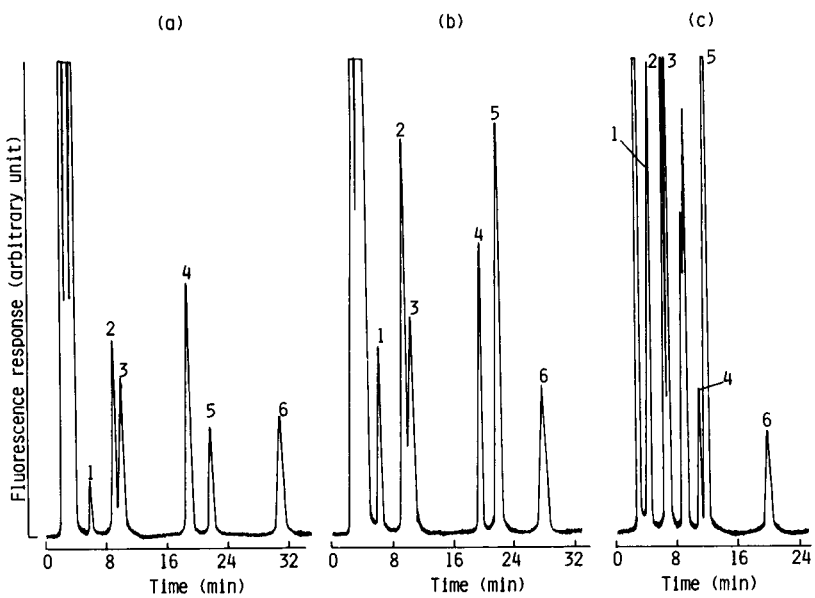

Fig. 1. Chromatograms of (a) MAT, (b) MDAT and (c) DMOAT derivatives of aromatic aldehydes. A portion (1.0 ml) of a standard mixture of six aldehydes (0.1 nmol ml^{-1} each) was treated according to the procedure with each reagent, and the resulting mixture was subjected to the LC. Peaks: 1 = 3,4-dihydroxybenzaldehyde; 2 = isovanillin; 3 = vanillin; 4 = benzaldehyde; 5 = 4-methoxybenzaldehyde; 6 = 4-methylbenzaldehyde; others = reagent blank.

TABLE 3

Retention times (t_R), excitation and emission maxima (λ_{ex}, λ_{em})[a] and relative peak heights (RPHs) of the fluorscent derivatives of aromatic aldehydes using various 2-aminothiophenols [b]

Aromatic aldehyde	MAT				EAT				MDAT				DMOAT			
	t_R (min)	λ_{ex} (nm)	λ_{em} (nm)	RPH [c]	t_R (min)	λ_{ex} (nm)	λ_{em} (nm)	RPH	t_R (min)	λ_{ex} (nm)	λ_{em} (nm)	RPH	t_R (min)	λ_{ex} (nm)	λ_{em} (nm)	RPH
Benzaldehyde	18.9	335	400	100	30.1	335	403	87	19.2	345	422	116	11.0	340	410	54
Isovanillin	9.0	335	380	74	14.6	350	400	70	9.4	350	410	150	6.4	340	415	142
Vanillin	10.0	340	385	53	15.7	350	400	44	10.3	350	410	73	6.7	350	400	141
4-Methoxybenzaldehyde	21.7	335	380	42	34.3	345	410	41	21.9	345	410	165	11.9	340	410	948
4-Methylbenzaldehyde	30.7	335	375	48	49.3	330	375	35	27.5	345	410	58	19.7	330	415	42
3,4-Dihydroxybenzaldehyde	6.0	330	390	22	9.4	355	400	18	6.3	348	410	73	4.5	345	405	189
	EDAT				DMAT				FAT				AT			
Benzaldehyde	21.0	315	380	5	39.2	325	385	5	18.6	320	385	4	18.6	320	370	4
Isovanillin	10.3	340	400	4	18.7	335	390	4	9.5	325	370	4	9.5	330	390	18
Vanillin	11.2	350	400	10	20.7	335	400	99	10.2	330	390	95	10.3	330	400	363
4-Methoxybenzaldehyde	23.6	345	405	129	45.8	330	380	118	21.6	325	375	542	22.5	326	375	79
4-Methylbenzaldehyde	33.3	340	380	1	63.1	325	380	1	29.4	320	360	2	30.0	318	366	11
3,4-Dihydroxybenzaldehyde	7.0	345	390	9	12.1	325	400	15	6.7	350	395	11	6.6	335	405	57

[a] The respective values of λ_{ex} and λ_{em} of the fluorescence from the aldehydes were different from those shown in Table 2 because of the solvent (mobile phase) effect. [b] Portions (1.0 ml) of a mixture of the six aldehydes (100 pmol ml^{-1} each) were treated according to the derivatization procedure using the eight 2-aminothiophenols, followed by the LC. [c] The peak height of the MAT derivative of benzaldehyde was taken as 100.

peaks to the aldehydes. However, the derivatives of vanillin and isovanillin were unsatisfactorily separated with any of the reagents: the resolution (*Rs*) values, calculated from retention times and peak widths of chromatograms of the pure compounds, were in the range of 0.5 (DMOAT) to 1.1 (MAT and EAT). The excitation and emission maxima of the fluorescence derivatives in the mobile phase shifted to shorter wavelengths (330–350 nm and 370–415 nm, respectively; Table 3), compared with those in strongly acidic media in the spectrofluorometric method (Table 2). MAT, EAT, MDAT and DMOAT gave greater peak heights to the aldehydes. MAT seems to be the best in practical use, because it did not show so great difference in fluorescent peak height among the aromatic aldehydes and its derivatives could be separated easily and rapidly by the reversed-phase LC. However, MDAT and DMOAT are also useful when higher sensitivity is required.

The calibration graphs for the aldehydes were linear in the range 0.05–10 nmol ml^{-1} with MAT, MDAT and DMOAT, and the detection limits (pmol on column, $S/N = 3$) were 0.1–0.4 for MAT, 0.1–0.2 for MDAT and 0.01–0.2 for DMOAT. The precision was established by repeated determination ($n = 10$) of a standard mixture of the eight aldehydes (5 nmol ml^{-1}) with MAT; the relative standard deviations did not exceed 3%.

MAT is easy to synthesize and stable in the reagent solution. Further, it is highly sensitive towards a wide variety of aromatic aldehydes, as well as highly selective.

REFERENCES

1 Y. Ohkura and K. Zaitsu, Talanta, 21 (1974) 547.
2 M. Nakamura, M. Toda, H. Saito and Y. Ohkura, Anal. Chim. Acta, 134 (1982) 39.
3 M. Katayama, Y. Mukai and H. Taniguchi, Anal. Sci., 3 (1987) 369.
4 W.-F. Chao, M. Kai, J. Ishida and Y. Ohkura, Anal. Chim. Acta, 215 (1988) 259.
5 Y. Ohkura, Anal. Sci., 5 (1989) 371.
6 T. Uno and H. Taniguchi, Bunseki Kagaku, 21 (1972) 76.
7 Y. Ohkura, K. Ohtsubo, K. Zaitsu and K. Kohashi, Anal. Chim. Acta, 99 (1978) 317.
8 H. Nohta, K. Ohtsubo, K. Zaitsu and Y. Ohkura, J. Chromatogr., 227 (1982) 415.
9 H. Nohta, K. Zaitsu, Y. Tsuruta and Y. Ohkura, Anal. Chim. Acta, 156 (1983) 253.
10 K. Zaitsu, Y. Okada, H. Nohta, K. Kohashi and Y. Ohkura, J. Chromatogr., 211 (1981) 129.
11 R.L. Mital and S.K. Jain, J. Chem. Soc., 2148 (1969).

Analytica Chimica Acta, 282 (1993) 633–641
Elsevier Science Publishers B.V., Amsterdam

Synthesis, spectral properties and photostabilities of symmetrical and unsymmetrical squaraines; a new class of fluorophores with long-wavelength excitation and emission

Ewald Terpetschnig, Henryk Szmacinski and Joseph R. Lakowicz

Center for Fluorescence Spectroscopy, University of Maryland at Baltimore, School of Medicine, Department of Biological Chemistry, 108 North Greene Street, Baltimore, MD 21201 (USA)

(Received 27th January 1993; revised manuscript received 7th June 1993)

Abstract

The absorption and fluorescence properties of squaraine derivatives in different organic solvents, and in water in presence of bovine serum albumin were investigated. The objective is to identify long-wavelength probes with reasonable quantum yields, reasonably long lifetimes and good photostabilities for use in fluorescence-based assays and/or imaging. Both symmetrical and unsymmetrical squaraines were studied and a correlation is made between the spectral properties and the electronic symmetry of the molecules. Like normal cyanines, squaraines show negative solvatochromy and band width broadening with increasing asymmetry. Based on this investigation the most suitable probes for use in a biological application were found to be the symmetrical indolenine derivatives of the squaraines, which display the highest photostability. Importantly, their quantum yields and lifetimes increase significantly upon binding to bovine serum albumin, suggesting that a conjugatable derivative of these indolenine squaraines will be suitable for use in labeling proteins. The squaraine absorbance maxima between 630 and 650-nm allows the use of the new commercially available 635- and 650-nm diode lasers.

Keywords: Fluorimetry; Phase-modulation fluorimetry; Squaraines

Fluorescence detection is widely used in immunoassays and fluorescence microscopy, and there is an increasing use of fluorescence in clinical chemistry. In such measurements it is advantageous to use long wavelength excitation and emission, which results in decreased autofluorescence from cells and tissues, and allows the use of simple laser light sources. However, the use of simple lasers, such as the 635- nm to 670-nm laser diodes, has been hindered by the lack of suitable fluorescent probes. The objective of the present work is to investigate the spectral properties of squaraines for use in fluorescence-based assays. For this purpose we synthesized ten squaraines with different combinations of their heterocyclic nuclei. These dyes have structures which are similar to those of cyanine dyes, but also contain a central squarate bridge. The squarate residue shifts the absorption and emission maxima to longer wavelengths, relative to the comparable cyanine dye, and is expected to increase the photostability of the dyes [1]. However, there is no information on the fluorescence properties of the

Correspondence to: J.R. Lakowicz, Center for Fluorescence Spectroscopy, Dept. Biological Chemistry, University of Maryland, School of Medicine, 108 N. Greene Street, Baltimore, MD 21201 (USA).

squaraines. In this paper we describe the absorption and emission spectral data, fluorescence lifetimes and quantum yields of ten squaraines, and attempt to correlate these properties with the heterocyclic moieties of the squaraines. Additionally, we studied the photostabilities of these squaraines in methylene chloride, isopropanol, and in water when bound to bovine serum albumin.

EXPERIMENTAL

^{1}H NMR spectra were recorded on a General Electric QE-300 spectrometer in $CDCl_3$ with TMS as internal standard unless otherwise stated. Absorption spectra were taken on a Perkin Elmer Lambda 6 UV–visible spectrometer. Emission spectra were taken with an SLM 8000 spectrofluorometer, and lifetimes were determined with

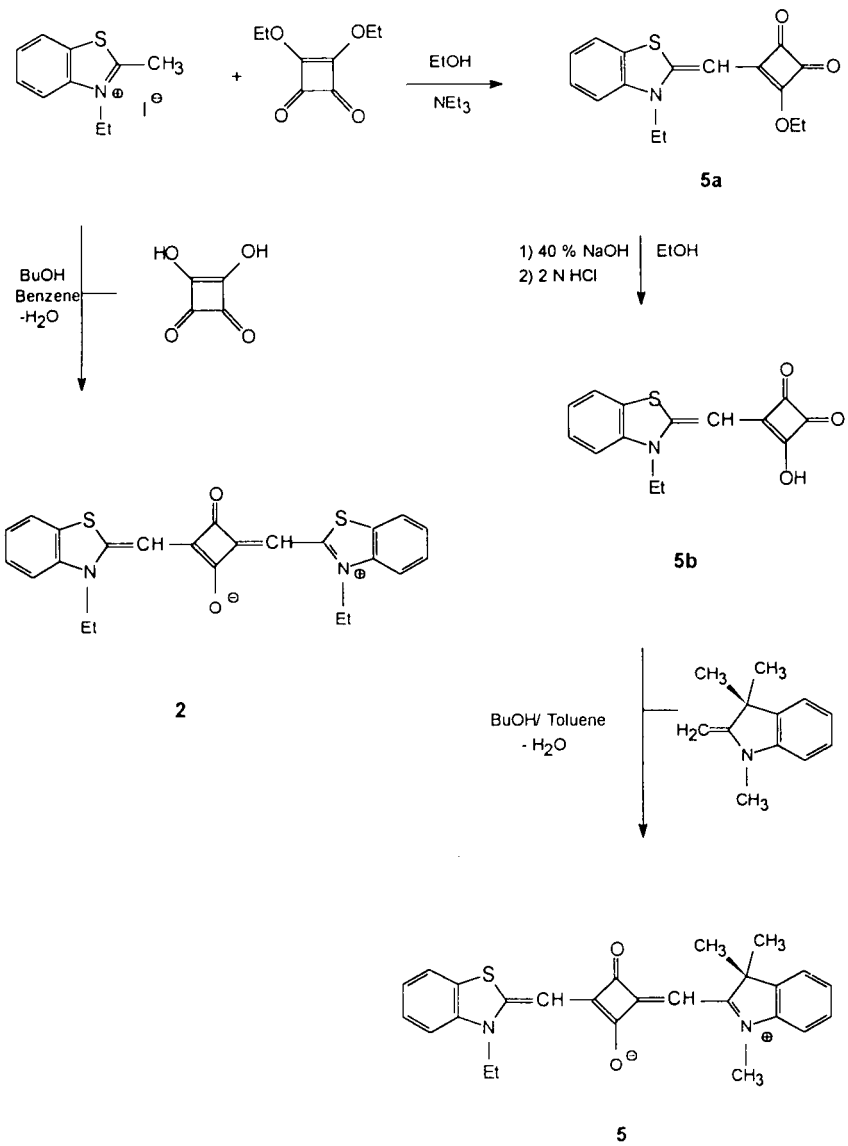

Scheme 1. Synthesis of a symmetrical and an unsymmetrical squaraine.

our frequency-domain instrument [2], using magic angle polarization conditions. The light source was the cavity-dumped output of rhodamine 6G dye laser at 600 nm. The emission was observed through 660 or 680 interference filters with a 10-nm bandpass.

The frequency-domain data were used to determine the lifetimes using the multi-exponential model,

$$I(t) = \sum_{i=1}^{n} \alpha_i \, e^{-t/\tau_i} \quad (1)$$

where α_i is the pre-exponential factor, τ_i the lifetime, and $n = 1$ or 2 for the single or double exponential fits, respectively. The fractional intensity of each component in the intensity decay $I(t)$ is given by

$$f_i = \alpha_i \tau_i / \sum_j \alpha_j \tau_j \quad (2)$$

The mean decay time is given by

$$\bar{\tau} = \sum_i \alpha_i \tau_i^2 = \sum_i f_i \tau_i \quad (3)$$

Prior to recording of spectra or lifetime the dyes **1–10** were purified with liquid chromatography (LC) using a C_{18} reversed-phase column with methanol as eluent. Quantum yields of the dyes were obtained using the method described in [3]. Quantum yields of the dyes in isopropanol were determined by comparison to a base form of carboxy-SNARF-6 at the excitation wavelength of 577 nm, which has a quantum yield 0.053 in potassium phosphate buffer [4]. The quantum yields of the squaraines **1–10** in water containing 5 mg ml^{-1} bovine serum albumin (BSA) were determined with CY-5.18-OH as the reference, which has a quantum yield of 0.27 in PBS [5]. The excitation wavelength was 600 nm, and the emission spectra were corrected for the different spectral response of the spectrofluorimeter at the appropriate emission.

Representative syntheses of the squaraines 2 and 5

The synthesis of dyes **1–10** was reported previously in more detail [6,7]. A representative synthesis of the symmetrical squaraine **2**, the unsymmetrical squaraine **5**, and its precursors **5a** and **5b** are given below (Scheme 1).

Symmetrical squaraine 2 [7]

3 mmole of *N*-ethyl-2-methylbenzothiazolium iodite, 1.5 mmole squaric acid, and 3 mmole of quinoline are suspended in 25 ml butanol–benzene (2:1) and the mixture is refluxed for 20 h using a Dean-Stark trap to separate the azeotropically removed water. After cooling the precipitate is collected and purified with column chromatography on silica gel using chloroform: isopropanol = 15:1 as eluent. Yield: 30 mg (25%), m.p. 300–301°C. δ 1.45 (t, 6H, CH_3), 4.16 (q, 4H, $N-CH_2$), 5.90 (s, 2H, =CH), 7.15 (t, 2H, H-6), 7.21 (d, 2H, H-4), 7.37 (t, 2H, H-5), 7.54 (d, 2H, H-7).

Unsymmetrical squaraine 5 [6–9]

This squaraine is synthesized in three steps (see Scheme 1).

1-[3'-Ethyl-2(3H)benzothiazolylidene-2'-methyl]3-ethoxycyclobuten-3,4-dione 5a

15 mmole of the *N*-ethyl-2-methylbenzothiazolium iodite are added to a stirred, hot solution of 10 mmole ethylsquarate and 2 ml of triethylamine in 15 ml ethanol. The solution is kept at 70–80°C for 5 min, cooled down to RT and the yellow to red colored precipitates are isolated, washed with diethyl ether and dried. The product was purified by column chromatography using $CHCl_3$–EtOAc = 9:1 as eluent. Yield: 41%, m.p. 185–187°C. δ 1.40 (t, 3H, CH_3), 1.52 (t, 3H, CH_3), 4.07 (q, 2H, $N-CH_2$), 4.85 (q, 2H, $O-CH_2$), 5.48(s, 1H, CH=), aromatic protons: 7.08 (d, 1H), 7.17 (t, 1H), 7.35 (t, 1H), 7.51 (d, 1H).

2-Hydroxy-1-[3'-ethyl-2(3H)benzothiazolylidene-2'-methyl]cyclobuten-3,4-dione 5b

5 mmole of **5a** are suspended in 20 ml boiling ethanol. On adding 0.6 ml of 40% NaOH the precipitate dissolves and the solution is kept at boiling for another 5 min and then cooled to RT. After addition of 6–7 ml 2 M HCl, the ethanol solution is concentrated by rotary evaporation, the resulting precipitate collected and used in the squaraine synthesis without further purification.

Yield: 89%, m.p. 246–248°C. δ (D_6-DMSO) 1.25 (t, 3H, CH_3), 4.12 (q, 2H, N–CH_2), 5.66 (s, 1H, CH=), aromatic protons: 7.18 (t, 1H), 7.39 (m, 2H), 7.77 (d, 1H).

Unsymmetrical squaraine 5

1 mmole of the squaric acid **5b** (see above) and 1 mmole of 2-methylene-1,3,3-trimethylindolenine were heated under reflux in a mixture of 20 ml toluene and 20 ml 1-butanol. The water was removed azeotropically using a Dean-Stark trap. After 16 h, the reaction mixture was cooled to room temperature and the solvents removed by rotary evaporation. The residue was treated with diethyl ether and the product was isolated by filtration. Further purification was achieved by column chromatography using chloroform–2-propanol mixtures as eluent or LC with methanol as solvent. Yield: 77%, m.p. 312 – 314°C. δ 1.45 (t, 3H, CH_2–CH_3), 1.71 (s, 3H, C-3–CH_3), 1.78 (s, 3H, C-3–CH_3), 3.46 (s, 3H, N–CH_3), 4.23 (q, 2H, N–CH_2) 5.77 (s, 1H, CH=), 6.03 (s, 1H, CH=), aromatic protons: 6.92 (d, 1H), 7.08 (t, 1H), 7.21–7.35 (m, 4H), 7.42 (t, 1H), 7.58 (d, 1H).

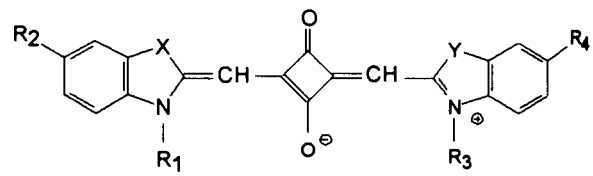

Compound	X	Y	R_1	R_2	R_3	R_4
1	$C(Me)_2$	$C(Me)_2$	Et	H	Et	H
2	S	S	Et	H	Et	H
3	Se	Se	Et	H	Et	H
4	$C(Me)_2$	$C(Me)_2$	Me	Cl	Me	Cl
5	$C(Me)_2$	S	Me	H	Et	H
6	$C(Me)_2$	Se	Me	H	Et	H
7	$C(Me)_2$	S	Me	Cl	Et	H
8	$C(Me)_2$	$C(Me)_2$	Me	Cl	Me	H
9	$C(Me)_2$	Se	Me	Cl	Et	H
10	S	Se	Et	H	Et	H

Fig. 1. Structure of the ten newly synthesized squaraines.

RESULTS AND DISCUSSION

The structures of the dyes synthesized are shown in Fig. 1. The absorption maxima (see Table 1) in methanol, chloroform, methylene chloride and water containing 5 mg ml^{-1} BSA range from 630 to 690 nm, which makes them perfectly suitable for excitation with a red He–Ne laser (633 nm) or laser diodes (635 and 670 nm). Their high extinction coefficients (ϵ = 200 000–250 000 l mol^{-1} cm^{-1}) [6] and their narrow ab-

TABLE 1

Absorption maxima (λ_{max}), solvatochromic shifts ($\Delta\lambda$) and bandwidths (σ) of the squaraine dyes in organic solvents

Dye	λ_{max} (nm) in				$\Delta\lambda$ (nm) ($\lambda_{CH_2Cl_2}$–λ_{MeOH})	σ (nm) in $CHCl_3$
	MeOH	$CHCl_3$	CH_2Cl_2	H_2O–BSA		
1	628	635	637	636	9	25
2	649	669	670	663	21	32
3	665	684	686	678	21	36
4	632	641	641	642	9	28
5	635 (638.5) [a]	649 (652)	650	647	15	35
6	643 (646.5)	657 (659.5)	658	659	15	33
7	634 (640.5)	649 (655)	650	651	16	40
8	629 (630)	637 (638)	638	643	9	27
9	644 (648.5)	655 (662.5)	659	663	14	39
10	658 (657)	677 (676.5)	678	671	20	32

[a] Values in parentheses are values calculated as the arithmetic mean of the absorption maxima values of related symmetrical dyes.

sorption band widths (see Table 1) are advantageous when used as sensing probes. This is because the energy of the laser light can be effectively coupled with the narrow absorption band of the probe, and the available emission occurs in a narrow region of the spectrum and can be readily isolated using an interference filter.

Absorption maxima of the unsymmetrical squaraines 5–10

In order to determine the effect of structural asymmetry on the spectral properties of dyes **5–10** we used the values of the absorption maxima of the symmetrical squaraines **1–4** to calculate λ_{max}calc for the unsymmetrical squaraines. The values of λ_{max}calc were obtained as the arithmetic means of the absorption maxima of the related symmetrical dyes (Table 1). The deviations (λ_{max}obs–λ_{max}calc) can be attributed to the different basicities of the heterocyclic nuclei in the squaraines and are a qualitative measure of the electronic asymmetry in cyanines [10]. Generally, the largest deviations are observed when heterocyclic bases with very different basicity are combined in a single dye, less sharply contrasting nuclei give smaller deviations. Our squaraines contain mostly three heterocyclic nuclei with basicity in the following order: (Se) benzoselenazolium- > (S) benzothiazolium- ≫ (CMe_2) dimethylindolenine nuclei. The largest deviations are observed for the squaraines **7** (−6.5 nm in methanol and −6.0 nm in $CHCl_3$) and **9** (−4.5 nm in MeOH and −7.5 nm in $CHCl_3$) with the combination of a 5-chloro-3,3-dimethylindolenine moiety and a benzothiazolium- (**7**) or benzoselenazolium base (**9**). The smallest deviations in electronic symmetry were calculated for the squaraines **8** (−1.0 nm in MeOH and −1.0 in $CHCl_3$) and **10** (+0.5 in $CHCl_3$). This is also revealed in their spectroscopic properties (lifetimes, solvatochromic shifts and photostabilities), which are similar to those of their symmetrical parent-squaraines (see Discussion).

Solvent effects on the absorption spectra of dyes 1–10

It is known that the ground state of ionic cyanine dyes has much more polar character than the excited state, and their absorption spectra generally display negative solvatochromism, that is a blue shift of the absorbance maximum with increasing solvent polarity [11]. Negative solvatochromic shifts are caused by interactions between the dye molecule and the solvent, which lowers the energy of the ground state relative to the excited state in the dye molecules. Compared to normal cyanines, the squaraines have two additional substituents (carbonyl and hydroxyl anion), which can interact with a polar solvent to stabilize the ground state. This produces a larger negative solvatochromic shift in the squaraines relative to the cyanines [1]. Due to their electronic asymmetry, squaraines **5–10** may be expected to show increased negative solvatochromy relative to the symmetrical dyes **1–4**. The effect of the solvent polarity on λ_{max} is illustrated by the $\Delta\lambda$ values, the difference of the absorption maxima values in CH_2Cl_2 and methanol (Table 1). The values for the solvatochromic shifts can be correlated with the basicity of the heterocyclic nuclei but do not show any dependence on the symmetry of the dyes. For both, symmetrical and unsymmetrical squaraines, these values are in the range of 9 to 21 nm, and do not show any evidence of larger blue shifts for the unsymmetrical squaraines **5–10**.

A comparison of the half bandwidth of the symmetrical and unsymmetrical squaraines shows that electronic asymmetry is correlated with a broadening of the absorption bands [12]. The highest values of peak broadening of the absorption bands in chloroform were measured for the spectra of the squaraines **7** and **9** (Table 1).

Fluorescence spectral properties of the squaraines

The emission maxima, Stokes' shifts, quantum yields and lifetimes of the squaraines **1–10** in different solvents are listed in Tables 2 and 3. The Stokes' shifts of compounds **1–10** are rather small and in the range of 14 to 21 nm in MeOH, 13 to 30 nm in $CHCl_3$ and 10 to 15 nm in water–BSA solutions (Table 2). The quantum yields as well as the lifetimes of dyes **1–10** vary with solvent, and are dependent on the nature of the heterocyclic bases (Table 3). In isopropanol the highest quantum yields are exhibited by sele-

TABLE 2

Emission maxima (λ_{max}) and Stokes' shifts (Δ) for squaraines in organic solvents and water–BSA

Dye	λ_{max} (nm)			Δ ($\lambda_{Em}-\lambda_{Abs}$)		
	MeOH	$CHCl_3$	BSA	MeOH	$CHCl_3$	BSA
1	644	645	669	16	10	13
2	663	687	677	14	18	14
3	688	714	688	23	30	10
4	653	654	652	21	13	10
5	651	666	662	16	17	15
6	661	675	672	18	18	13
7	653	664	661	19	15	10
8	648	653	655	19	16	12
9	662	677	676	18	22	13
10	674	699	684	16	22	13

nium and sulfur containing cyanines **2**, **3** and **10**, which also show the longest lifetimes in organic solvents. Importantly, on binding to BSA dyes **1**, **4** and **5** exhibit the highest quantum yields and the largest increase in lifetimes (15–20 fold) compared to methanol. The lifetimes of **2**, **3** and **10** are increased only 3–8 fold in this media. The increase in quantum yield of **1**, **4** and **5** in water–BSA solution is demonstrated in Fig. 2 with the representative plot of the absorption and emission spectra of dye **1** in methanol and water containing 5 mg ml^{-1} BSA. The non-polar dye binding site of BSA is revealed by the red shift of the absorption spectrum in relation to that in MeOH.

TABLE 3

Quantum yields (η) and mean fluorescence lifetime ($\bar{\tau}$) of the squaraine dyes [a]

Dye	Quantum yields (η) in		Mean lifetime $\bar{\tau}$ (ns) in		
	Isopropanol	BSA [b]	MeOH	$CHCl_3$	BSA [b]
1	0.09	0.70	0.20	1.52	3.25
2	0.13	0.26	0.56	4.05	4.03
3	0.14	0.30	1.19	4.15	3.42
4	0.10	0.68	0.21	1.42	2.80
5	0.10	0.78	0.24	1.95	3.53
6	0.11	0.38	0.41	2.44	3.56
7	0.08	0.34	0.26	1.65	3.01
8	0.07	0.34	0.20	1.05	2.29
9	0.10	0.20	0.43	2.14	2.27
10	0.17	0.38	0.83	4.41	3.93

[a] λ_{exc} = 600 nm, λ_{obs} = 660 or 680 nm (±10 nm), T = 25°C.
[b] In water with 5 mg ml^{-1} BSA.

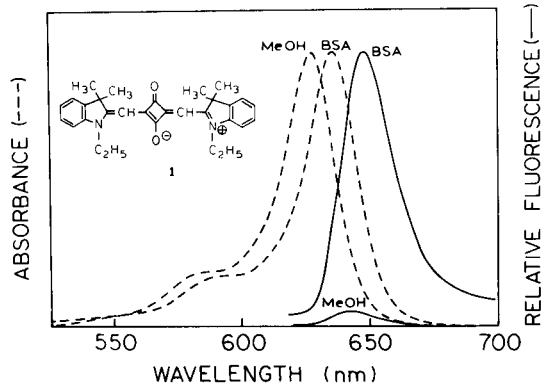

Fig. 2. Absorption and emission spectra of the photostable indolenine squaraine **1**, in methanol and in water with 5 mg ml^{-1} BSA. The emission spectra were recorded with an excitation wavelength of 600 nm with an excitation and emission bandpass of 16 and 8 nm, respectively.

As will be shown below, the symmetrical squaraines **1** and **4** are also the most photostable, and therefore the most suitable dyes for analytical use. For such uses we expect the squaraines to be covalently coupled to proteins, such as immunoglobins, to obtain the desired specificity. To mimic this use of the squaraines, without the need to synthesize conjugatable forms of all the dyes, we examined the absorption spectra, emission spectra, and the lifetimes of these dyes when non-covalently bound to BSA. Typical spectral data for representative squaraines **1–4**, as well as the emission spectrum of the cyanine dye CY5 are shown in Fig. 3. The fact that the squaraines display an increase in quantum yield upon binding to proteins can be an advantage, in that the emission may be dominantly due to the protein-bound species, with little emission from the free dye.

The use of fluorescence lifetimes offers many advantages in analytical and clinical chemistry applications, and lifetimes-based sensing is technologically simple at the present time [13–16]. In order to use moderately simple instrumentation it is desirable for the lifetime to be longer than 0.2 ns, as observed for the most photostable indolenine derivatives **1**, **4** and **8** in methanol. Fortu-

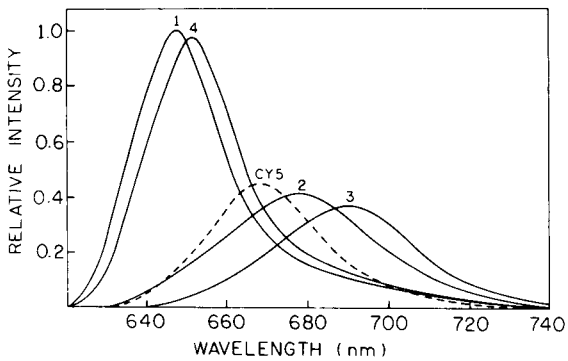

Fig. 3. Relative emission spectra of the symmetrical squaraines **1–4** in water–BSA (5 mg ml^{-1}) and CY-5.18-OH in PBS (— — —) with $\lambda_{exc} = 600$ nm and $T = 25°C$.

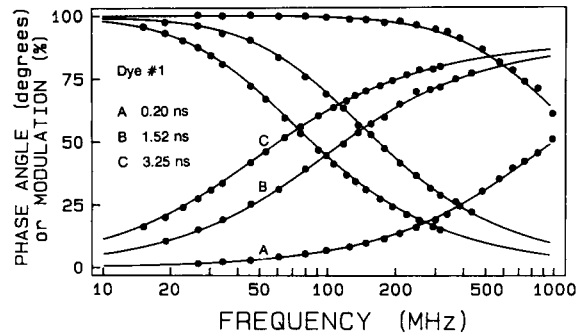

Fig. 4. Frequency responses and mean lifetimes of the symmetrical indolenine squaraine **1** in methanol (A), chloroform (B) and when bound to BSA (C) with $\lambda_{exc} = 600$ nm and $\lambda_{em} = 660$ nm, $T = 25°C$.

nately, the mean lifetimes increase substantially upon binding to BSA (Tables 3 and 4). The increase in lifetime when bound to BSA, relative to dissolved in methanol is demonstrated in Fig. 4, as seen by the dramatic shift to lower frequencies upon binding to BSA. It is important to note that there is already a substantial difference in phase shift of 35 to 55 degrees in the range from 100 to 200 MHz in the BSA-bound form of **1**. This is valuable for lifetime-based sensing, which will most likely be accomplished using standard dynode-type PMTs, which have a practical upper frequency limit near 200 MHz.

TABLE 4

Multiexponential intensity decays of squaraines in water with 5 mg ml^{-1} BSA, $\lambda_{exc} = 600$ nm, $T = 25°C$

Dye	τ_1 (ns)	τ_2 (ns)	α_1^a	f_1^a	χ_R^2
1	3.16	–	1.000	1.000	5.8 [b]
	3.38	1.52	0.862	0.933	2.1
2	3.95	–	1.000	1.000	4.2
	4.15	1.92	0.892	0.347	2.1
3	3.18	–	1.000	1.000	78.5
	3.56	0.50	0.748	0.955	2.7
4	2.66	–	1.000	1.000	16.8
	2.95	1.04	0.810	0.924	2.3
5	3.27	–	1.000	1.000	40.4
	3.73	0.98	0.769	0.927	2.5
6	3.36	–	1.000	1.000	11.5
	4.08	2.26	0.577	0.711	2.0
7	2.73	–	1.000	1.000	90.5
	3.21	0.63	0.705	0.924	3.5
8	1.95	–	1.000	1.000	153.7
	2.67	0.68	0.526	0.813	2.5
9	1.91	–	1.000	1.000	116.6
	2.78	0.89	0.466	0.731	2.7
10	3.79	–	1.000	1.000	5.4
	4.42	2.78	0.595	0.700	1.9

[a] $\alpha_2 = 1 - \alpha_1$, $f_2 = 1 - f_1$. [b] The value of χ_R^2 were calculated with uncertainties of 0.2° and 0.005, in phase angle and modulation, respectively.

The double exponential intensity decays parameters for the BSA-bound forms of **1–10** are summarized in Table 4. The intensity decays were found to be heterogeneous with a dominant contribution of the longer-lived component.

Photochemical stabilities of the squaraines

In order to be useful in a diagnostic assay, or for fluorescence microscopy, a fluorophore must display good photochemical stability. Therefore we tested the photostabilities of squaraines **1–10**. The fading tests were performed in methylene chloride, isopropanol and in water containing 5 mg ml^{-1} BSA. Two sets of dye solutions of **1–10** were made with known optical densities in the range of 0.2 to 0.4. One set was exposed to ambient light, which consisted of both fluorescent lighting and indirect light from nearby windows. The other set was kept in the dark. The absorption was measured after 40 and 120 h in case of methylene chloride, 120 h in water–BSA and 12 and 24 days in case of isopropanol. The absorptions were compared to those of the dye solutions in the dark. During this time the fading of the solutions which were kept in the dark was negligi-

TABLE 5

Remaining absorbance (%) of dyes **1–10** in methylene chloride, isopropanol and water–BSA, after exposure to ambient light

Dye	Absorbance remaining (%) in				
	CH_2Cl_2 after		isopropanol after		H_2O–BSA after
	40 h	120 h	12 d	24 days	120 h
1	92	85	100	100	90
2	27	0	53	3	0
3	14	0	45	1	0
4	98	92	100	98	100
5	88	68	96	92	45
6	83	52	88	79	18
7	93	76	97	94	55
8	95	90	100	98	98
9	86	55	100	99	21
10	13	0	46	1	0

ble. Time intervals of measurements were chosen in respect to the stabilities of dyes in different solvents.

After 24 days of exposure in isopropanol dyes **1**, **4**, **8** and **9** faded only 0–2%, whereas the extinction of **2**, **3** and **10** decreased 97–99%. In methylene chloride and water–BSA solutions the photobleaching occurred faster, but the stability patterns of the dyes remain similar (see Table 5). The data in Table 5 show that the lightfastness of the squaraines decreases in the order chloroindolenine > indolenine ≫ benzothiazole > benzoselenazole for these heterocyclic bases. Selenium and sulfur-containing squaraines fade rapidly, while the indolenine moiety seem to have a much higher photostability. The importance of the heterocyclic moiety as the determining factor for the photostabilities in cyanines is demonstrated in an earlier publication by Heilig and Luettke [17]. As reported in [17], the selenium-containing cyanines exhibited the lowest photostabilities. Compared to normal cyanines, the corresponding squaraine analogues appear to have better lightfastness [1].

DISCUSSION

Based on their spectral properties squaraines **1–10** can be divided into three subgroups. The first group containing the indolenine dyes **1**, **4** and **8** shows small solvatochromic shifts ($\Delta\lambda_{max}$ = 9 nm), high photostabilities and shorter lifetimes in organic solvents (τ = 1.1 to 1.5 ns in chloroform and 0.2 ns in methanol). The second subgroup with dyes **2**, **3** and **10** exhibits the largest solvatochromic shifts ($\Delta\lambda_{max}$ = 20–21 nm), low photostabilities and long lifetimes (τ = 4.1 to 4.4 ns in chloroform, and 0.6 to 1.2 ns in methanol). The remaining unsymmetrical squaraines **5**, **6**, **7** and **9** can be summarized in the last group. Their values for the solvatochromic shifts and lifetimes are in between those listed in the first two subclasses: ($\Delta\lambda_{max}$ = 14–16 nm), (τ = 1.7–2.4 ns in chloroform, and 0.2–0.4 ns in methanol).

Importantly, the most photostable indolenine squaraines also display the largest increase in lifetime and quantum yield upon binding to BSA (about 15 fold) compared to methanol. Based on our experience in lifetime-based sensing [13–16], the nanosecond lifetimes displayed by the indolenine derivatives when bound to BSA are adequately long to allow the use of simple phase-modulation instrumentation, which can be practical in a clinical environment. We conclude that the absorption and emission spectral properties, and the lifetime, of the indolenine derivatives of squaraines are suitable for their use as labels in immunoassays and other clinical applications. Synthesis of protein-conjugatable forms of the squaraines is now in progress. We are presently investigating the spectral properties of conjugatable forms of these dyes when they are covalently bound to proteins. Preliminary measurements on these protein conjugates also show evidence of significantly increased lifetimes [18] compared to unbound forms of these probes.

This work was supported by grants from the National Institutes of Health (RR 08119) with support for instrumentation from the NIH (RR-07510) and the National Science Foundation (DIR-8710401).

REFERENCES

1 S. Yasui, M. Matsuaka and T. Kitao, Dyes Pigments, 10 (1988) 13.

2 J.R. Lakowicz, G. Laczko and I. Gryczynski, Rev. Sci. Instrum., 57 (1986) 2499.
3 W.H. Melhuish, J. Phys. Chem., 65 (1961) 229.
4 J.E. Whitaker, R.P. Haughland and F.G. Prendergast, Anal. Biochem., 194 (1991) 330.
5 R.B. Mujumdar, L.A. Ernst, S.R. Mujumdar, C.J. Lewis and A.S. Waggoner, Bioconjugate Chem., 4 (1993) 105.
6 E. Terpetschnig and J.R. Lakowicz, Dyes and Pigments, 21 (1993) 227.
7 V.H.E. Sprenger and W. Ziegenbein, Angew. Chem., 78 (1967) 581.
8 K.Y. Law and B.C. Bailey, J. Chem. Soc. Chem. Commun., (1990) 864; K.Y. Law and B.C. Bailey, J. Org. Chem., 57 (1992) 3278.
9 A. Treibs and K. Jacob, Liebigs Ann. Chem., 712 (1968) 123.
10 L.G.S. Brooker, R.H. Sprague and H.W.J. Cressmann, J. Am. Chem. Soc., 67 (1945) 1889; L.G.S. Brooker, A.L. Sklar, H.W.J. Cressmann, G.H. Keyes, L.A. Smith, R.H. Sprague, E. Van Lare, G. Van Zandt, F.L. White and W.W. Williams, J. Am. Chem. Soc., 67 (1945) 1875.
11 J. Griffiths, Color and Constitution of Organic Molecules, Academic Press, London, 1976.
12 A.A. Ishchenko, V.M. Zubarovskii, G.A. Gromova and N.A. Derevyanko, Zh. Org. Khim., 23 (1967) 621 (Engl. Transl.).
13 J.R. Lakowicz, H. Szmacinski and M. Karakelle, Anal. Chim. Acta, 272 (1993) 179.
14 R.B. Thompson and J.R. Lakowicz, Anal. Chem., 65 (1993) 853.
15 H. Szmacinski and J.R. Lakowicz, Anal. Chem., 65 (1993) 1668.
16 J.R. Lakowicz, Laser Focus World, 28(5) (1992) 60.
17 G. Heilig and W. Luettke, Chem. Ber., 121 (1988) 407.
18 J.R. Lakowicz and E. Terpetschnig, unpublished results.

Analytica Chimica Acta, 282 (1993) 643–646
Elsevier Science Publishers B.V., Amsterdam

Flow-injection spectrofluorimetric determination of boron using Alizarin Red S in aqueous solution

N. Chimpalee, D. Chimpalee and B. Boonyanitchayakul

Department of Chemistry, Faculty of Science, Silpakorn University, Nakorn Pathom 73000 (Thailand)

D. Thorburn Burns

Department of Chemistry, The Queen's University of Belfast, Belfast BT9 5AG (UK)

(Received 26th April 1993)

Abstract

Boron can be determined spectrofluorimetrically based on the reaction of borate ion and Alizarin Red S in aqueous media using flow-injection analysis. The carrier stream was deionized water and the reagent streams were 1% (w/v) EDTA, phosphate buffer (pH 7.5) and 2×10^{-3} M Alizarin Red S solutions. The injection rate was 50 h^{-1}. The calibration graph was linear up to 40 $\mu g\ ml^{-1}$ boron and the relative standard deviation for the determination of 4.0 $\mu g\ ml^{-1}$ of boron was 0.83% ($n = 10$). The detection limit was 0.34 $\mu g\ ml^{-1}$ based on injection volumes of 250 μl. The system was applied to the determination of boron in electroplating solutions.

Keywords: Spectrophotometry; Fluorimetry; Flow System; Alizarin Red S; Boron

Boric acid is used as a buffer component when controlling the pH of the cathode film in electroplating, particularly for the deposition of nickel and cobalt [1]. Many spectrophotometric methods for the determination of boron utilise the reaction of boric acid with hydroxyl compounds, particularly those based on anthraquinone, in concentrated sulphuric acid media or after evaporation to dryness with the reagents [2,3]. Boron forms fluorescent compounds in concentrated sulphuric acid with dibenzoylmethane [4–6], 4′-chloro-2-hydroxy-4-methoxybenzophenone [7,10], Thoron I [11,12] resacetophenone [13,14], 2,4-dihydroxybenzophenone [15–17], salicylic acid [18,19], acetylsalicylic acid [20], carminic acid [21,22], quinizarin [23], quinizarin-2-sulfonic acid [24] and Alizarin Red S [25]. Milder conditions have been shown to apply for Alizarin Red S [26,27], chromotropic acid [28–30], Victoria Blue Violet [31] and for Phthalein Violet [32]. Of these only that based on chromotropic acid has been used in flow-injection analysis [33]. Herein we report the first flow injection application of the reaction of boric acid with Alizarin Red S under mild conditions for the spectrofluorimetric determination of boron.

Correspondence to: D.T. Burns, Department of Chemistry, The Queen's University of Belfast, Belfast BT9 5AG, UK.

EXPERIMENTAL

Apparatus

Emission intensities were measured at 575 nm (with excitation at 465 nm) using a Shimadzu

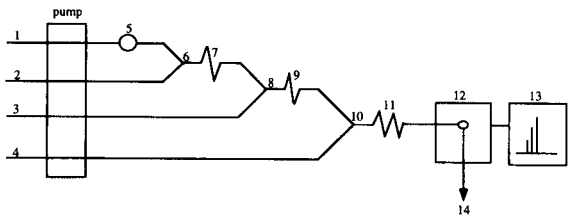

Fig. 1. Schematic diagram of the flow-injection system: (1) deionized water at 1.40 ml min^{-1}; (2) 1% (w/v) EDTA solution at 1.40 ml min^{-1}; (3) buffer solution pH 7.5 at 1.40 ml min^{-1}; (4) 2×10^{-3} M Alixarin Red S solution at 1.40 ml min^{-1}; (5) sample injector (250 μl); (6, 8, 10) mixing points (Omnifit three-way connector, "Hex"); (7,9) mixing coil (200 cm × 0.8 mm i.d.); (12) spectrofluorometer; (13) recorder; (14) waste.

RF-540 spectrofluorimeter fitted with a 25 μl, 1.5 mm Quartz Glass Suprasil I flow cell (Hellma) and recorded with a Shimadzu DR-3 data recorder. Solutions were pumped using a variable-speed peristaltic pump (MS-Reglo, Ismatec) fitted with Tygon pump tubes. Samples were injected using an Omnifit six-way valve fitted with a by-pass coil. Flow lines were PTFE tubing (0.8 mm i.d.). The flow system is shown in Fig. 1. Omnifit three-way connectors ("Hex") were used for mixing the solutions.

Reagents and solutions

All reagents were of analytical-reagent grade unless indicated otherwise. Deionized water was used throughout.

Boron standard solution 1000 $\mu g\ ml^{-1}$ B. 0.1429 g of boric acid (H_3BO_3) (AnalaR, BDH) was dissolved in 250 ml of water. The solution was stored in a polyethylene bottle. Working standard solutions were prepared by suitable dilution as required.

Alizarin Red S solution, 2×10^{-3} M. 0.68 g of Alizarin Red S (puriss, Fluka) was dissolved in 1000 ml of water.

Buffer solution, pH 7.5. 1.22 g of potassium dihydrogenphosphate and 4.25 g amount of disodium hydrogenphosphate were dissolved in 1000 ml of water.

EDTA solution, 1% (w/v). 5.0 g of EDTA (disodium salt) was dissolved in 500 ml of water.

General procedure

Samples and standards were examined using the flow system and conditions given in Fig. 1.

Examination of main experimental variables

The experimental variables were examined in a univariate manner.

Effect of reagent concentrations. When the concentration of EDTA solution was fixed at 1% (w/v), the peak heights were found to increase with Alizarin Red S concentration from 1.0×10^{-3} M to 2.0×10^{-3} M and only slightly increase thereafter, so an Alizarin Red S concentration of 2.0×10^{-3} M was used in the subsequent experiments.

With the concentration of Alizarin Red S fixed at 2.0×10^{-3} M, the peak heights were found to increase rapidly with increasing pH of the buffer solution up to 6.8 and very slightly increase up to pH 7.5 and then to decrease. A buffer solution of pH 7.5 was therefore adopted.

Effect of operating variables. The effect of flow-rate, reaction coil length, mixing coil length and sample injection volume were each studied under the above optimum concentrations of Alizarin Red S and pH. The total flow-rate was varied from 4.00 to 7.00 ml min^{-1}, keeping the flow-rate in each reagent line identical. The peak heights were found to decrease with increase in the total flow-rate and the peak widths became narrower. A total flow-rate of 5.50 ml min^{-1} was selected as a compromise between sampling rate and sensitivity.

When two mixing coils (7 and 9 in Fig. 1) were fixed at 200 cm, the peak heights were found to increase with increasing the reaction coil length from 100 to 300 cm and were slightly decreased and the peak widths also became broader above 300 cm. A 300 cm reaction coil (0.8 mm i.d.) was chosen from consideration of peak height and residence time. In the same way when the reaction coil was fixed, heights were slightly decreased with increase in the mixing coil length from 100 to 200 cm, but the baseline became more stable. A mixing coil of 200 cm was therefore adopted.

The volume of sample injected was varied from 100 to 500 μl by changing the length of the

sample loop in the injection valve. The peak heights increased non-linearly with increase in sample size as the peak widths became broader. A volume of 250 μl was a compromise between sensitivity and sample injection rate.

Effect of acid concentration of sample solution. The acid concentration in the sample solution was varied from 0 to 0.7% (v/v) hydrochloric acid. The peak heights were found to be constant up to 0.3% (v/v) and then increased with increasing acid concentration up to 0.5% (v/v) and decreased at higher concentrated ions. The acid concentration of sample solution was adjusted to be 0–0.3% (v/v) in subsequent work.

RESULTS AND DISCUSSION

A linear calibration graph was obtained up to 40 μg ml^{-1} B ($r = 0.999$, $n = 10$). The relative standard deviation for the determination of 4 μg ml^{-1} was 0.83% (10 replicates). The limit of detection (three times baseline noise) was 0.34 μg ml^{-1}. The possible interference of diverse ions on the determination of 6 μg ml^{-1} B was examined using the flow system and conditions given in Fig. 1. The tolerable (less than 2% change in peak height is considered free from interference) ratios, added ion to boron (w/w) were as follows: Mg^{2+}, Ca^{2+}, Co^{2+}, Cu^{2+}, Fe^{3+}, NO_3^-, SO_4^{2-}, PO_4^{3-} and tartaric acid, 50; F^-, 10; Ba^{2+}, 1.

TABLE 1

Determination of boric acid in plating solutions

Sample	Composition (g l^{-1})	Boric acid	
		Added (g l^{-1} H_3BO_3)	Found (g l^{-1} H_3BO_3)
A	$NiSO_4 \cdot H_2O = 240.0$ $NiCl_2 \cdot 6H_2O = 50.0$	32.21	32.27 ± 0.22
B	$CoSO_4 \cdot 7H_2O = 60.0$ $MgSO_4 \cdot 7H_2O = 140.0$ Tartaric acid = 120.0	29.72	30.16 ± 0.26
C	$CoSO_4 \cdot 7H_2O = 60.0$ $MgSO_4 \cdot 7H_2O = 140.0$ Tartaric acid = 120.0	34.73	36.37 ± 0.76
D	$CoSO_4 \cdot 7H_2O = 60.0$ $MgSO_4 \cdot 7H_2O = 140.0$ Tartaric acid = 120.0	39.50	40.72 ± 0.41

[a] Mean ± standard deviation for five replicates.

Analysis of plating solutions

The results for the determination of boric acid in plating solutions (Table 1) were in good agreement with the prepared values. Sample A was prepared according to Lowenheim [1]. B, C and D were working solutions obtained from industry (USAM Metals). The method is simple to operate and more rapid (50 injections h^{-1}) than the equivalent manual method.

REFERENCES

1 F.A. Lowenheim, Electroplating, McGraw-Hill, New York, 1978.
2 F.D. Snell, Photometric and Fluorometric Method of Analysis, Nonmetals, Wiley, New York, 1981.
3 W.J. Williams, Handbook of Anion Determination, Butterworths, London, 1979.
4 M. Marcantonatos, G. Gamba and D. Monnier, Helv. Chim. Acta, 52 (1969) 538.
5 Z. Skorko-Trybula and Z. Boguszewska, Mikrochim. Acta, Part II, 1976, 235.
6 J. Aznarez, A. Bonilla and J.C. Vidal, Analyst, 108 (1983) 368.
7 M. Marcantonatos, A. Marcantonatos and D. Monnier, Helv. Chim. Acta, 48 (1965) 194.
8 D. Monnier and M. Marcantonatos, Anal. Chim. Acta, 36 (1966) 360.
9 M. Marcantonatos, D. Monnier and J. Daniel, Anal. Chim. Acta, 35 (1966) 309.
10 B. Leibich, D. Monnier and M. Marcantonatos, Anal. Chim. Acta, 52 (1970) 305.
11 M. Marcantonatos, D. Monnier and A. Marcantonatos, Helv. Chim. Acta, 47 (1964) 705.
12 V.I. Rigin and N.N. Mel'nichenko, Zavod. Lab., 33 (1967) 3.
13 N.A. Raju and K. Neellakantum, Curr. Sci., 27 (1958) 432.
14 G.G. Rao and N.A. Raju, Z. Anal. Chem., 167 (1969) 325.
15 D. Monnier, A. Marcantonatos and M. Marcantonatos, Helv. Chim. Acta, 47 (1964) 1980.
16 P.V. Kristalev and Ya. F. Schevchenko, Sb. Nauchn. Tr. Permsk. Politekh. Inst., 71 (1970) 38.
17 P.V. Kristalev and M.N. Chelnokova, Zh. Anal. Khim., 29 (1974) 1650.
18 T. Shibazaki, Bunseki Kagaku, 12 (1963) 385.
19 T. Shibazaki, Yakugaku Zasshi, 88 (1968) 1393.
20 V.N. Podchainova, L.V. Skornyakova and B.L. Dvinyanivov, Izv. Vyssh. Uchebn. Zaved. Khim. Khim. Tekhnol., 11 (1968) 241.

21 T. Bruce and R.W. Ashley, Report of the Atomic Energy Commission of Canada, AECL-4446, 1973.
22 R. Gabriels and W. van Keirsbulck, Lab. Pract., 26 (1977) 620.
23 A. Holme, Acta Chem. Scan., 21 (1967) 1679.
24 F. Salinas, A. Muñoz de la Pena, J.A. Murillo and J.C. Jímenez Sånchez, Analyst, 112 (1987) 913.
25 L. Szebelledy and S. Tonay, Z. Anal. Chem., 107 (1936) 26.
26 K. Hiiro, Nippon Kagaku Zasshi, 83 (1962) 711.
27 A.M.C. Campana, F.A. Barrero and M.R. Ceba, Analyst, 117 (1992) 1189.
28 D.F. Kuemmel and M.G. Mellon, Anal. Chem., 29 (1957) 378.
29 H. Green, Br. Cast Iron Res. Assn. J., 10 (1962) 56.
30 J. Lapid, S. Farhi and Y. Koresh, Anal. Lett., 9 (1976) 355.
31 C.A. Reynolds, Anal. Chem., 31 (1959) 1102.
32 V. Patrovský, Talanta, 10 (1963) 175.
33 S. Motomizu, M. Oshima and K. Toei, Bunseki Kagaku, 32 (1983) 458.

Analytica Chimica Acta, 282 (1993) 647–669
Elsevier Science Publishers B.V., Amsterdam

On *k*-medoid clustering of large data sets with the aid of a genetic algorithm: background, feasibility and comparison

C.B. Lucasius, A.D. Dane and G. Kateman

Laboratory for Analytical Chemistry, Faculty of Science, Katholieke Universiteit Nijmegen, Toernooiveld 1, 6525 ED Nijmegen (Netherlands)

(Received 30th March 1993)

Abstract

A novel approach to the problem of *k*-medoid clustering of large data sets is presented, using a genetic algorithm. Genetic algorithms comprise a family of optimization methods based loosely upon principles of natural evolution. They have proven to be especially suited to tackle complex, large-scale optimization problems efficiently, including a rapidly growing variety of problems of practical utility. Our pilot study lays emphasis on the feasibility of GCA – our genetic algorithm for *k*-medoid clustering of large datasets – and provides some background information to elucidate differences with traditional approaches. The experimental part of this study is done on the basis of artificial data sets and includes a comparison with CLARA – another approach to *k*-medoid clustering of large data sets, introduced recently. Results indicate that GCA accomplishes a better sampling of the combinatorial search space.

Keywords: Data reduction; *k*-Medoid clustering; Genetic algorithms; Subset selection

Cluster analysis comprises a widely applied science [1–3] within the rapidly growing area known as exploratory data analysis – a denominator for methods which explore the structure of data that does not require the assumptions common to many statistical methods. Numerous applications reported in the literature concern analytical chemical problems [4–10].

In brief, a cluster analysis is concerned with the problem of finding k groups – or partitions, or similarity classes, or indeed clusters – of objects in a metric data matrix according to some plausible (dis)similarity criterion, thereby revealing hidden, a priori unknown, structure. The objects, or patterns, are the rows in the data matrix; each pattern among the K patterns ($k \leq K$), lists L numerical values for a given set of variables that describe some system. A particular partitioning must fulfil the condition that each partition contains at least one object, and that each object belongs to exactly one partition.

Exploratory data analysis methods fit in the broader class of data reduction methods – methods which aim to explicit hidden structure in a $K \times L$ data matrix. Data reduction in cluster analysis is effectuated when a pattern is selected from each of the k clusters and considered as a representative of that cluster. From this viewpoint, a clustering problem can also be seen as a subset selection problem: the selection of a subset of k representative patterns from the source set of K patterns. It should be realized that

Correspondence to: C.B. Lucasius, Laboratory for Analytical Chemistry, Faculty of Science, Katholieke Universiteit Nijmegen, Toernooiveld 1, 6525 ED Nijmegen (Netherlands). After Nov. 1: Dept. of Chemistry, Dalhousie University, Halifax, Nova Scotia B3H 4J3 (Canada).

pattern selection is but one way to accomplish data reduction. In other approaches to data reduction, one reduces the L variables to l variables (dimensionality reduction), using some criterion in order to minimize the loss of information. Variable reduction can be accomplished either by the selection of a subset of l variables from the source set of L variables, or by the creation of l new (ad hoc, or latent) variables such as in principal components analysis (linear, Karhunen–Loeve projection) or in non-linear mapping [9] in generalized form. Genetic algorithms appear to be competitive in both variable reduction [11–16] and pattern reduction [17].

Method validation criteria

In this paper, generally important criteria for the validation of computational methods are assumed to be:

The quality of the end solution found by the method;

The amount of computation time required by the method; here, "computation time" is defined as the time the method uses in order to terminate according to some criterion other than an imposed maximum time that the user is prepared to wait in practice, e.g., according to a convergence criterion or a criterion based on a predefined acceptable quality of the estimated solution; in contrast, "running time" is defined as the time that the method is allowed to run in practice, never exceeding a predetermined maximum waiting time;

The amount of computer memory required by the method;

The ease of developing and implementing the method;

The ease of using the method.

In the course of this paper, these criteria are regularly addressed in order to validate the methods of interest. For the moment, it is important to realize that these criteria can be mutually conflicting in practice. For instance, it may be difficult to maximize the quality of the end solution and at the same time minimize the amount of computation time. Indeed, it turns out in practice that simultaneous optimization of the criteria often forces one to make compromises.

COMBINATORIAL OPTIMIZATION APPROACH TO CLUSTERING

In this section, we examine clustering as a combinatorial optimization problem and motivate the choice for a so-called partitional clustering strategy when large data sets are concerned. A genetic algorithm is proposed as a strategy that can be brought to bear competitively on partitional clustering.

Measures of dissimilarity for optimality criteria

The collection of all legal clusterings, or partitionings, for a particular clustering problem is hereafter called the search space. In searching for the best partitioning in this space, an optimality criterion – or evaluation criterion, or objective function – is applied in order to rate any candidate partitioning according to a plausible figure of merit (utility, quality). Here, "plausible" indicates the intuition that a particular clustering is better when the average dissimilarity between intra-cluster objects is smaller, while the average dissimilarity between inter-cluster objects is larger. Many ways seem acceptable to formalize this notion into an optimality criterion. An example is an optimality criterion based on the so-called k-medoid model, which comes up in several sections below.

Pairwise inter-object dissimilarities, or distances, are denoted as d_{ij}, where i and j are unique indices attached to the objects ($1 \leq \{i, j\} \leq K$). The distances can be calculated according to different measures, e.g. [2] the Minkowski distance, Mahalanobis distance, and $1 - |r_{ij}|$ (where r_{ij} denotes the correlation coefficient). The distances are elements in a square, $K \times K$, distance matrix, **D**, which is mathematically derived from the $K \times L$ data matrix (i.e., the data set), **X**. Owing to the properties $d_{ij} = d_{ji}$ (symmetry) and $d_{ii} = 0$, only the $K(K-1)/2$ d_{ij} values for $i < j$, comprising the upper triangle of **D** (diagonal exclusive), need to be stored in computer memory or calculated in run-time as they are needed. Incidentally, for larger L values it becomes more attractive to store the d_{ij} values in memory,

because the time of their calculation is proportional to L.

The second order Minkowski distance, also known as the Euclidean distance, is popular and therefore adopted in our study. Moreover, it is hereafter implicitly assumed that **D** is calculated from an autoscaled (that is, z-transformed) **X**; in this way, equal importance is given to the L variables.

Sampling the search space

Clustering techniques which have apparently enjoyed most widespread application up to now, fall within the categories *hierarchical clustering* and *partitional clustering* [2,3,6,9].

In order to motivate our choice for partitional clustering, we briefly pass in review the sampling properties of hierarchical clustering first. The main shortcoming of hierarchical clustering is shown to be related to a "greedy" way in which the search space is sampled. General consensus exists that partitional clustering methods amount to a much better sampling scheme, in general. That this optimism is not entirely justified follows in due course when we discuss a recently developed, highly praised partitional clustering method and show that it too is in fact based on a greedy sampling scheme which, although certainly quite different from an hierarchical sampling scheme, features some striking parallels with the hierarchical scheme in a more subtle sense.

Properties of hierarchical clustering

Hierarchical clustering is traditionally most applied, for its speed and its ease of implementation and use. A sequence of nested partitionings is generated incrementally, such that at the bottom level each object forms a separate cluster, or singleton ($k = K$), and at the top level all objects form one single cluster ($k = 1$); hence, all values of k are dealt with in the same run. One of the $K - 2$ intermediate levels represents the solution of the problem, and is chosen at the discretion of the user (through visual inspection of a graphical representation of the sequence, called a dendrogram). The procedure is either started at the bottom level, merging one object with a cluster at a time (agglomerative strategy), or at the top level, splitting one object from a cluster at a time (divisive strategy). In either case, each step is performed in a greedy way in that the merging/splitting object is selected deterministically (i.e., not probabilistically) according to the greatest relative gain in overall similarity, and the choice is irreversible (i.e., can not be canceled at a later stage if that would then increase overall similarity).

The most important shortcoming of hierarchical clustering is the poor sampling of the search space: due to greedy nature of the search heuristic, only a tiny fraction of the search space is sampled. Adding to that the presence of sub-optimal partitionings, it turns out that this fraction does not necessarily contain the best partitioning or even an acceptable partitioning. More quantitatively, the number of partitions that are evaluated is:

$$(K-1) + (K-2) + \cdots + 2 = (K+1)(K-2)/2$$

For $K = 19$, this is 170. Indeed, the search space is much larger, considering that the number of legal partitionings for given K and k is:

$$P_k^K = \frac{1}{k!} \sum_{i=1}^{k} (-1)^{k-i} \frac{k!}{i!(k-i)!} i^K \approx \frac{k^K}{k!} \qquad (1)$$

For $K = 19$ and $k = 4$, say, this is 11 259 666 000 – merely the size of a subspace in the entire search space defined by a fixed K. (The size of the entire search space is obtained by summing for $k = 1, \cdots, K$.) When k is kept fixed, the size of the search space grows exponentially with K (reaching astronomical proportions quickly), whereas the portion sampled during the search grows only as a quadratic function of K; we say that hierarchical clustering has a *time complexity* of $O(K^2)$, or order 2 in K. Thus, with increasing K, the disparity between the size of the search space and that of the portion sampled grows rapidly. It follows from practice that for large data sets – more precisely, typically for $K > 100$ – the solutions found by hierarchical clustering are no longer acceptable, as a rule; the comparatively

short convergence time is then meaningless, of course.

Properties of partitional clustering

There is a general consensus among practitioners that when it comes to clustering of large data sets, a non-hierarchical, or partitional, clustering method is imperative. By definition, such a method employs a search heuristic which performs steps in the search space that are not confined to irreversible merges/splits of objects with/from clusters, thus allowing a better sampling of the search space.

Partitional clustering problems – or rather partitioning problems in general – are provably $\mathcal{NP}$-complete [18]. Formally, this means that it is impossible, or at least extremely difficult, to obtain a search heuristic that can find the true solution of the problem in polynomial time [19]. Intuitively, a practically appropriate search heuristic must be "intelligent", i.e., neither too "weak" (e.g., not exhaustively scanning the search space) nor too "strong" (i.e., not too greedy); such search heuristics are also called "moderate" [19]; reasonably efficient and reasonably reliable (robust).

Countless partitional clustering methods are conceivable. Approaches which guarantee that the best partitioning will be found, e.g., enumerative search, are not practically feasible, as the entire search space must be scanned exhaustively; this is an astronomical enterprise for problems of interest ($K > 100$). On the other hand, for practically feasible approaches, among which some are briefly passed in review in the next section, it is not guaranteed that the best partitioning will be found, albeit near-optimal or acceptable partitionings can be obtained, in general.

At this juncture, we emphasize that in the remainder of this paper it is implicitly assumed that $K > 100$ and $k \ll K$ (typically $k < K/10$), unless explicitly stated otherwise.

Approaches to partitional clustering

Among putatively intelligent methods for partitional clustering are the following.

The branch and bound method [20] has been applied to partitional clustering by Koontz et al. [21] and later by Massart et al. [22]. However, the method has been criticized as computationally too expensive for the large data sets frequently encountered in practice. Moreover, the method is based on assumptions which are often not realistic in practice, viz.: the optimality criterion must satisfy monotonicity (a subset should not be better than any larger set that contains it) and a lowerbound on the optimum (maximum) must be known. Also, the development and implementation of the method is sometimes criticized as being error-prone due to the complex bookkeeping explicitly needed.

Simulated annealing [23–25] has been applied to partitional clustering by Klein and Dubes [26]. This method is based on probabilistic (i.e., nondeterministic) search heuristics that are relatively easy to develop and implement. An advantage of probabilistic search heuristics, in general, is that end solutions do not depend strongly on the initial estimate. Good results have been obtained in various applications. However, the space of "cooling" schedules is huge and complex, i.e., to find an acceptable configuration of the method is normally troublesome.

Recently, artificial neural networks have also found promising application to partitional clustering [27–29]. In this methodology too, the configuration space is huge and complex, and finding an acceptable configuration is normally troublesome.

Tabu search [30–32] has been proposed for large-scale combinatorial problem solving, inter alia, and can thus be brought to bear on partitional clustering. (An application of tabu search involving hierarchical clustering is described in [33].)

A method apparently tailored to partitional clustering – CLARA, from Clustering LARge Applications – was recently introduced by Kaufman and Rousseeuw, and later also applied by Hopke and co-workers [3,34–37]. Based on these pilot studies, CLARA has been praised for its efficiency and robustness attributed to a reportedly unique, intelligent statistical resampling heuristic. CLARA is founded upon the aforementioned k-medoid model, and is used for the comparative part of our study.

Motivation for a genetic algorithm

Genetic algorithms [19,38–45] have been applied competitively to various complex, large-scale optimization problems of practical importance [39,40,46–49] (including several problems in analytical chemistry, referenced in [19,50]), and therefore naturally seem a profitable choice to tackle partitional clustering problems. Genetic algorithms for partitioning problems in general, have only recently attracted the attention of some scientists [51–55]. (Historically, genetic algorithms were first predominantly applied to numerical parameter estimation problems, later also substantially to sequencing problems, e.g., scheduling problems. At this point in time, one can only speculate on the impact that genetic algorithms are going to have on partitioning problems.)

One of the, up to now few, studies involving genetic algorithms for partitional clustering specifically, is due to Bhuyan et al. [51]. They conducted a comparison with a greedy partitional clustering technique, and showed that the genetic algorithm performs better. However, they did not use large data sets ($K < 60$). Our study is different in that we challenge large data sets ($K = 1000$) and perform a comparison with another partitional clustering technique (CLARA).

The power (efficiency and robustness) of genetic algorithms can be intuitively appreciated by considering one of their distinguishing characteristics, namely: not one candidate solution, but rather a collection of candidate solutions, in encoded form, is iteratively modified by the search heuristics. In this way, the search is multi-directional; that is, multiple searches are carried out in a single run. Importantly, as these searches interact, i.e., exchange information to enhance mutual guidance, the overall search can become very efficient. The collection, or *population*, of encoded candidate solutions undergoes a simulated evolution process reminiscent of natural evolution according to Darwin; that is, at each time step, or *generation*, in which the population is updated, the relatively well ranking solutions reproduce and create offspring, while the relatively low ranking solutions are repelled from the population. More light on the mechanics of genetic algorithms is shed below.

THEORY

Here we give a summary of CLARA as it has been described in the literature, and introduce a genetic algorithm for partitional clustering, named GCA, from genetic clustering algorithm. CLARA and GCA employ the same objective function, based on the k-medoid model.

The k-medoid framework

A clustering heuristic that is based on the k-medoid model [3,22,34–37] evaluates a set of k selected objects considered representative for the k clusters to be found within the source set of K objects. Given the set of representative objects, the remaining objects are assigned to the nearest representative object (Fig. 1), using the chosen distance measure (Euclidean distance in our case). The underlying philosophy of this deterministic *object assignment* procedure is that a better set of clusters is obtained when the k representative objects are more centrally located in the cluster they define. For this reason, the (supposedly) optimal representative objects are called medoids, and a suitable objective function to be minimized is the sum, D_k, of the distances of the respective

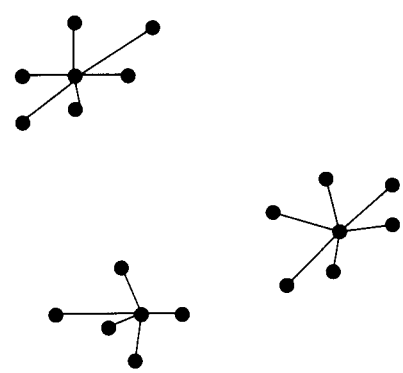

Fig. 1. Illustration of the k-medoid model: object assignments to medoids.

medoids to all the other objects of the same cluster:

$$D_k = \sum_{\kappa=1}^{k} \sum_{\substack{i \text{ assigned} \\ \text{to medoid } \kappa}} d_{\kappa i} \qquad (2)$$

where the $d_{\kappa i}$ values are retrieved from the distance matrix **D**. Alternatively, the average distance, $\delta_k = D_k/(K-k)$, can be minimized, but the calculations are then numerically less accurate [3].

Importantly, due to the object assignment implied by the k-medoid model, the target k-ary (k-way) partitioning problem is, in essence, reduced to a binary (2-way) partitioning problem, or subset selection problem; from *this* perspective, the first partition is the subset of the k medoids to be selected, and the second partition is the thereby implied complementary subset of the $K-k$ non-medoid objects. Accordingly, the number of possible k-medoid subsets comprising the search space is given by:

$$S_k^K = \frac{K!}{k!(K-k)!} \qquad (3)$$

which, although sizably smaller than P_k^K (Eqn. 1), is in practice still beyond exhaustive search when large data sets are concerned. For $k \ll K$, S_k^K grows explosively with k. (By "explosive" we mean "faster than quadratically, in many cases even faster than a higher-order polynomial".)

Other important characteristics of the k-medoid model are: (1) the implicit assumption of hyperspherical clusters in the L-dimensional data space; (2) the objective function (D_k) exhibits bias for large k values, as can be readily appreciated by considering the extreme case of singleton clusters ($k = K$, resulting in $D_k = 0$).

Due to the bias in the objective function, a clustering method based on the k-medoid model is normally configured such that k remains constant during the search; in that case, therefore, we speak of a fixed-size subset selection problem [45,50]. (Ideally, one would prefer to approach k-medoid clustering as an unknown-size subset selection problem, as that would allow one to implicitly obtain the best k in a single run.) In practice, runs are often repeated for different values of k, and the best k is found according to an off-line cluster validation criterion applied to the results; one such a criterion is based on the recently introduced silhouette analysis [3,36, 37,56], which however lies outside the scope of this paper.

Any clustering method based on the k-medoid model is said to belong to the class of k-medoid clustering methods, although the most popular method therein is often referred to as "the" k-medoid method. Recently, the name PAM (partitioning around medoids) was coined for the k-medoid method. Incidentally, relative to the so-called k-means method [3], developed earlier, PAM is often praised for its: (1) robustness; (2) good characterization of all clusters that are not too elongated; (3) good detection of outliers.

PAM consists of two procedures: a *building* procedure followed by a *swapping* procedure, each based on a different incremental stepping heuristic. In general, incremental stepping heuristics (including the abovementioned hierarchical clustering methods) have a time complexity that is quadratic in the dimensionality of the system under consideration. Indeed, both procedures in PAM can be estimated to have approximately time complexity $O(K^2)$ for fixed k; also, the time complexity is approximately $O(k^2)$ for fixed K. (In making these estimates, it is assumed that the computation time of PAM is predominantly determined by the summation of distances to calculate D_k; this is reasonable, because the burden of other computations, mostly distance retrievals from **D** stored in memory, and object assignments, is, in comparison, negligible.)

For a detailed description of PAM, the reader is referred to [3]; here, we suffice with the following concise outline.

In the building procedure, the first step concerns the selection of the object that represents the best medoid if $k = 1$; that is, D_1 is minimized, all objects are considered to belong to the same cluster. In each consecutive step, a new medoid is added to the set of medoids, namely the object which maximizes some predefined contribution (relative gain); the stepping goes on until all k medoids are selected. Although the contributions evaluated in each step may be regarded as the

values delivered by an objective function other than D_k, the overall procedure is supposed to minimize D_k; that is, the building procedure aims to minimize D_k indirectly.

Using the set of k medoids thus obtained, the swapping procedure attempts to further improve this set by successively considering all pairs of objects for which one object is a medoid and the other is not. In each pair, the roles of medoid and non-medoid are interchanged as part of a strategy to calculate some predefined contribution, and in each time-step the exchange which yields the largest contribution is accepted. The procedure terminates when there are no more pairs for which an exchange leads to improvement. Note that the swapping procedure too aims to minimize D_k indirectly by maximizing contributions in the respective steps performed.

It is to be ascribed to PAMs quadratic time complexity in K that computation times become unacceptably long in practice when large data sets are used. One way to potentially circumvent this problem is to estimate the best clustering of all objects from *samples* of objects passed to PAM. Such an approach (statistical resampling) is embodied in CLARA, discussed next.

CLARA

In CLARA [3], PAM is called M times by an embedding, or major, iteration cycle, where M is a control parameter; in this vein, PAM may be considered the embedded, or minor, iteration cycle of CLARA. In each major iteration, PAM performs a clustering of K' objects selected from the K objects in the entire data set. The value of $K'(<K)$ is chosen according to the equation $K' = Ak + B$, where A and B are control parameters; the standard values for M, A and B are listed below.

In the first major iteration, the sample of K' objects for PAM is selected randomly from the K objects. After PAM has completed clustering this sample, the remaining $K-K'$ objects are quickly assigned to the respective nearest k medoids; next, D_k (Eqn. 2) is calculated directly for all objects thus clustered. Subsequent major iterations follow a similar scheme, except that the sample of K' objects for PAM is now required to include the set of k medoids most recently found and accepted. Only if the new set of medoids found turns out to be better (i.e., features a lower D_k) than the most recently accepted set, it will be accepted for use in the next major iteration; otherwise it is rejected and the most recently accepted set is reused in the next major iteration.

Computation time

As a consequence of CLARA's quadratic time complexity in k (assuming $K' = Ak + B$), any reasonable maximum allocated running time is reached quickly as k increases. This is probably an important reason why, to our knowledge, the few hitherto reported applications of CLARA typically feature $k < 10$. However, a more important reason why small k values are used, probably lies in the fact that the size of the search space grows explosively with increasing k (Eqn. 3); that is, with increasing k, the disparity between the size of the search space and that of the portion sampled grows rapidly. Ironically, a similar drawback was diagnosed above for hierarchical clustering. These arguments should warn us that CLARA is actually a greedy partitional clustering method, even though this has hitherto not been mentioned so explicitly in the literature. Therefore, it seems reasonable to suspect, at this juncture, that with increasing k, the search is increasingly likely to converge into sub-optima, especially when complex data sets are concerned. Whether this is indeed the case, can only be assessed empirically; this issue is addressed in the experimental part of our study.

GCA

In this section, we discuss a general flowchart of genetic algorithms, and indicate how it applies to GCA in particular. The flowchart comprises modules concerned with the exploration of the search space, as well as modules concerned with the exploitation of useful information collected along the way. The need for a balance between exploration and exploitation, and other general conditions for optimal performance, are emphasized. In general, the optimal choice of the explo-

ration operators in a genetic algorithm depends on the type of domain under consideration, as will become evident in the course of the discussion.

As opposed to CLARA (or embedded PAM, actually), GCA calculates D_k directly in order to evaluate each candidate solution. This allows a better sampling of the search space.

Flowchart

Genetic algorithms comprise a family of probabilistic optimization methods based loosely upon principles of natural evolution. That is to say, they fulfil a widely accepted but not very strickt description, or generic flowchart [45,50] (negative-indexed steps represent preliminary actions):

– 3. Parameterize the objective function (module 0). The domain parameters incorporated in the objective function are set, using domain-dependent input data. In the objective function of GCA, this input is the distance matrix **D** (initially derived from the data matrix **X**).

– 2. Parameterize the genetic routines (modules –1, 1, 2, 3, a, b, 4). Control parameters are set, using domain-independent input data. Examples of such parameters are the probabilities for recombination and mutation (see modules a and b below); other important control parameters, e.g., the population size, are elucidated in the course of the further discussion.

– 1. Initiate strings. The initial population is created. Each string in the population uniquely encodes a candidate solution of the target problem; many encodings are possible for a particular problem, and the one chosen reflects an educated guess of the implementor. Normally, the strings are of a fixed length. Without prior knowledge available, the initial population usually comprises strings that represent random candidate solutions. The population size is specified by the user (in module –2 above).

0. Evaluate strings. Each string in the population is decoded to obtain its actual meaning. This is then passed on to the objective function, ϕ, or D_k in GCA, in order to calculate and store a numerical value indicating performance, called the raw fitness, $f_0 = \phi$. It is hereby assumed, without loss of generality, that ϕ is a maxization criterion; if this is not the case, as in GCA, then f_0 is calculated by applying some inverting transformation to ϕ, e.g., sign inversion ($f_0 = -\phi$) or reciprocation ($f_0 = 1/\phi$). In this way, any genetic algorithm always explicitly maximizes f_0. (This measure is called "raw" to emphasize how close it stands to the problem domain, having undergone minimal numerical transformation.)

Next, a termination criterion is applied, based on either the observed performance or on a maximum generation. If it succeeds, the algorithm terminates; otherwise it continues. In GCA, the termination criterion is based on a predetermined maximum generation, i.e., based on the allocated running time.

1. Scale fitnesses. Raw fitnesses are scaled in a number of (possibly 0) transformation steps when they are not suitable as such for the selective reproduction or -replacement procedure (modules 2 and 4 below). Linear scaling is widely employed; it is an option in GCA besides another scaling mode mentioned in due course.

2. Selectively reproduce strings. A selection criterion that shows bias for strings with comparatively high (scaled) fitness values is iteratively applied to the strings in the population; each selected string is copied to a temporary (new) population, subject to a size not larger than the current population. Due to the ensuing selection "pressure", the temporary population may be expected to perform better than the current population. In many implementations, the strings are reproduced according to roulette selection; that is, probabilistically with expected rates proportional to their (scaled) fitness; roulette selection is an option in GCA besides another selection mode mentioned in due course.

3. Pair strings. In preparation for recombination (module a below), pair the strings in the temporary population to obtain parent pairs. The pairing is either random (as is the case in many implementations, including GCA) or according to a more sophisticated criterion.

a. Recombine strings. The recombination operator is iteratively applied to the pairs of parent strings in the temporary population with probability p_r (the recombination probability). Upon success for a particular pair, equally sized string

fractions ("partial candidate solutions") are selected and swapped so that new strings (child strings) are formed in the temporary population; the fractions are selected probabilistically, ideally according to the so-called building block principle discussed below. Upon failure, the child strings normally simply become copies of the parent strings.

b. Mutate strings. The mutation operator is iteratively applied to strings in the temporary population. In a particular string, random local changes are imposed, each with probability p_m (the mutation probability). Mutation too introduces diversity into the temporary population, but merely with the aim to enhance the productivity of recombination.

4. Selectively replace strings. The strings in the temporary population replace an equal number of strings in the current population; the latter are selected according to some criterion, e.g. one with bias for the worst performing strings. In many implementations, including GCA, the size of the temporary population equals that of the current population, leaving complete replacement – or replacement without "generation gap", or generational population handling – as the only possibility.

Return to 0.

At any stage of a run of a genetic algorithm, the best candidate solution so far encountered is normally kept track of, and upon termination the best candidate solution ever encountered is shown to the user.

The modules 1, 2, 3 and 4 are called exploitation modules, as they affect the survival rates of the strings in the population, hence are concerned with the *exploitation* of important information currently stored in the population as indicated by (raw or scaled) fitness. These modules can be chosen quite independently of the type of target problem [45,57]. Incidentally, fitness scaling is only needed if the chosen reproduction- or replacement module uses fitness values instead of fitness ranks [57]. The modules a and b, on the other hand, are concerned with the *exploration* of the search space. The choice of these modules depends considerably on the type of target problem and, related to that, on the encoding chosen to represent the candidate solutions.

Structurally simple as a genetic algorithm may seem and intuitively appealing its underlying evolutionary principles, the overall evolution process is mechanically very complex due to the large amount of procedural interactions that take place through the population, the central medium of all procedural actions. This mechanical complexity, in combination with the huge configuration space, spanned by all possible procedural components and their possible parameterizations, can make the search for a configuration that leads to an acceptable performance a troublesome enterprise for which, not surprisingly, no standard methodology is available.

Principal conditions for optimal performance

Two important conditions for efficient and efficacious search are [19,45,50]: (1) the exploration and exploitation are balanced; (2) the exploration is intelligent.

The first condition can be accomplished by parameterizing the selected modules appropriately. That this task is not easy may be ascribed to the mechanical complexity of genetic algorithms, as pointed out above; it demands some field experience, albeit general guidelines can be obtained from the mainstream literature on the subject.

The second condition can be fulfilled by using exploration operators which strive after maximum modification of strings (hence maximum exploration) at minimal loss of relevant implicit information, or properties, stored in the strings. This can be accomplished with the recombination operator. As this operator takes as input a pair of parent strings, cuts them into fractions, and exchanges some of these fractions between the strings to produce two new, equally sized strings (child strings), it preserves, as opposed to the mutation operator, all constituent elements of the original string pair – intuitively an important minimal condition to preserve relevant properties from both parent strings. In this way, recombination exhibits assembly behavior and thus can accomplish, more so than mutation, comparatively

large leaps in progress, even when the operation does not show bias for any particular property. With bias for the good properties, the recombination operator is even more intelligent; this notion is commonly called the *building block principle* [19,38,39,45]. Of course, this principle requires that the designer of the recombination operator knows what the good properties for the given type of search task are. It is important to realize that if such knowledge is based on false assumptions, the search can be frustrated (i.e., deceived) and performance can thus be seriously degraded.

The exploration operators

For the comparison of GCA with CLARA to be meaningful, the modification operators (recombination and mutation) in GCA are based on the k-medoid model; that is, the operators modify strings in such a way that each new string still represents a legal set of k medoids selected from the source set of K objects.

Recombination. Initially, it was our intention to use the recombination operators that have recently become available for k-way partitioning problems in general [51–55]; for $k = 2$, then, our purpose would in principle be served, considering the two partitions in this case as, respectively, the subset of medoids and the thereby implied complementary subset of non-medoid objects. However, upon closer inspection these operators turn out to fall short seriously, since they regard finding k, as well as finding the sizes of the k partitions, a part of the search task. In this way, these operators have an unacceptable amount of overhead (redundancy) associated with them for our purposes. This provided us with the incentive to design home-made recombination operators dedicated to fixed-size subset selection problems.

Our recombination operators for fixed-size subset selection problems are [45,57,58] **D_SX** (general-purpose subset recombination) and **D_MX** (mix subset recombination); the prepended "D" in the names serves to remind of the fact that direct (rather than binary) subset encoding is used [45,50,57], i.e., the strings that represent candidate subset are simply a concatenation of indices that directly and uniquely denote the selected elements. Unlike **D_MX**, **D_SX** can be used in additional modes, wherein it is aimed to preserve, respectively, the order and position of elements in the parent strings [57–60]. These additional modes are, however, meaningless for k-medoid selection; that is, if **D_SX** is used, then only its regular mode (wherein the placement of elements is immaterial) would make sense for our purposes. Empirically, we established that **D_SX** in regular mode results in performance similar to **D_MX**. The latter is more memory efficient, and was therefore implemented in GCA.

In general, many recombination operators, including **D_MX**, when applied to two parent strings (P_1, P_2), produce two child strings (C_1, C_2):

$$P_1, P_2 \xrightarrow{\text{D\_MX}} C_1, C_2$$

The procedure for the swapping of string fractions that is part of any recombination operator, is applied with probability p_r, the recombination probability; otherwise, C_1 and C_2 simply become copies of P_1 or P_2, respectively. **D_MX** takes into account the constraints related to direct subset encoding, namely: any element that represents an object in the source set of objects, should occur at most once in the string of elements that represents a candidate subset. **D_MX** works as follows, using $P_1 = 237$ and $P_2 = 482$ (hence $k = 3$) for illustration purposes:

(1) Mix P_1 and P_2:

(a) Append copies of P_1 and P_2 to obtain, say, Q:

$$Q = 2_1 3_1 7_1 4_2 8_2 2_2$$

The subscripts are not actually part of the elements, but merely serve to remind of the original parent.

(b) Randomly scramble the elements, e.g.:

$$Q = 4_2 2_2 2_1 8_2 7_1 3_1$$

(2) Add new material; that is, apply the following built-in mix mutation: With a predetermined probability $p_{m,\text{mix}}$, replace each of the first k consecutive elements in Q by a copy of an element indicated randomly, but never more than once, in the source set, e.g.:

$$Q = 5\,2_2 7\,8_2 7_1 3_1$$

Note that in this example, 2 of the k trials succeeded (at the first and third position).

(3) Randomly scramble the elements again, e.g.:

$Q = 2_2 7_1 7 3_1 5 8_2$

(4) Build C_1 by copying k elements from Q, starting at the leftmost element and going elementwise to the right, subject to the condition that elements that are already in C_1 are skipped:

$C_1 = 2\,7\,3$

(5) Build C_2 by copying k elements from Q, starting at the rightmost element and going elementwise to the left, subject to the condition that elements that are already in C_2 are skipped:

$C_2 = 8\,5\,3$

Mutation. Besides the built-in mutation, a point mutation operator, **D_PM**, is independently applied to all strings in the population: one element in a child string C is selected randomly with a predetermined probability, $p_{m,\text{point}}$, and, upon success, replaced by a copy of an element indicated randomly in the complementary subset to produce C':

$C \xrightarrow{\text{D\_PM}} C'$

where, for instance, $C = 3\,6\,8$ and $C' = 3\,4\,8$. (Incidentally, **D_PM** is the equivalent of one iteration in **D_TM**, trade mutation, described in [57,58].)

Computation time

In any genetic algorithm run, a population comprising N strings evolves for G generations. In many implementations, including GCA, by far most of the computational effort resides in the NG string evaluations. In GCA, the time of one such evaluation is proportional to the $K - k$ distances summed to obtain D_k. Thus, the computation time of GCA is proportional to $NG(K - k)$.

Optimal values for N and G depend on how one chooses to define "optimal", e.g., as minimal D_k (i.e., maximal quality of the end solution); or as some compromise between minimal NG (i.e., minimal computation time) and minimal D_k. Irrespective of the criterion used, however, it is not straightforward how to theoretically derive optimal values for N and G. This may be ascribed to the mechanical complexity of genetic algorithms, in general, which obstructs reliable theoretical modeling of the search, thus making an empirical approach imperative. Intuitively, it is reasonable to expect that optimal values for N and G are such that their product, NG, increases with increasing problem dimensionality (defined by K and k).

For all practical purposes, the computation time of a particular, not necessarily optimally configured genetic algorithm may be taken equal to the convergence time, i.e., to the time after which D_k no longer decreases noticeably. This definition is convenient because convergence can easily be detected empirically (using some predefined convergence criterion).

Although the theoretical relation between the convergence time and the problem dimensionality is generally unknown, there exist theoretical arguments in favor of the statement that genetic algorithms can reach time complexities that are a small, possibly even fractional, power of the problem dimensionality – while (near-)optimal or acceptable solutions are still found. This attractive property stems from the so-called *schema theorem*: the mathematical framework of genetic algorithms. It predicts that the search space is sampled exponentially in time if the principal conditions for optimal performance (as discussed above) apply [19]. More precisely, as population members – points in the search space – are explicitly evaluated, an exponentially growing portion of the search space is implicitly sampled; the implicit sampling is a consequence of the fact that schemata, or, basically, similarities between points in the search space, are taken advantage of during the search. Implicit exponential sampling of the search space distinguishes genetic algorithms from other search methods. It is widely believed that this property is responsible for the empirically established fact that a linear increase in the problem dimensionality, which normally leads to an exponential increase in the size of the search space, usually does not cause an exponential increase in the computation time; instead, a low-order polynomial increase is observed in most studied cases. (In the experimental part of our study, we aim at making a similar observation.)

EXPERIMENTAL

Here the computer programs used in this study are described, the comparison strategy followed is outlined and the configuration of GCA is discussed in detail.

Computer programs

All computer programs were developed in the computer language C for portability and speed of execution. They were run on a SUN Sparc Station 2 (under UNIX). Using this hardware, for GCA the maximum allocated running time of a few hours was empirically found to correspond approximately with $NG < 100\,000$ (the number of string evaluations). This constraint was taken into account in empirically deriving optimal values for N and G, as described below.

CLARA. The computer program for CLARA was created from scratch, as described in [3]. For small values of k, it can be empirically established that the convergence time (computation time) of CLARA is well within a reasonable maximum allocated running time, e.g., within a few hours, say, employing abovementioned type of computer; this convergence does not automatically imply that the best or even an acceptable solution is found. The statement that a few hours is a reasonable running time, is based on the assumption that other analytical activities can be carried out independently while computation is performed, or computation can be performed overnight; moreover, computation is nowadays fast and relatively inexpensive.

GCA. The computer program for GCA was created using a so-called genetic algorithm prototype in GATES (genetic algorithm toolbox for evolutionary search) – a library of domain-independent routines [50,57]; by "domain-independent" routines are meant routines that can be used for other application domains as well. Among the prototypes available in GATES, the one dedicated to regular, fixed-size subset selection problems was chosen. Simply phrased, a prototype is a prefabricated, template genetic algorithm without an objective function. Accordingly, GCA was basically obtained by merely programming the objective function and linking it to the prototype.

In practice, the convergence time of a genetic algorithm often turns out to be larger than that of a more locally (greedily) searching method applied to the same problem. While this seems to contradict the theoretical claims of efficiency, it should be realized that, as evidenced by many practical applications, genetic algorithms tend to find solutions of considerably better quality. Empirically, we established that the computation time of GCA, as applied to the data sets used in this study, approximates a reasonable maximum running time (a few hours) employing abovementioned type of computer.

In both CLARA and GCA, **D**'s upper triangle, or hereafter simply **D** for short, is calculated from **X** and then stored in memory in a reduced form. The motivation for the reduction is that otherwise **D** occupies an unacceptable amount of memory for large K values of interest, as the amount needed grows quadratically with K.

In CLARA, the reduction in **D** is accomplished by taking advantage of the fact that in each of the M major iterations, PAM considers only a sample of $(K' < K)$ objects. More precisely, in each major iteration, **D** is calculated only for the objects in the sample, and stored in memory for quick access by PAM as the latter executes. A modification to CLARA that we believe is worth considering in the future, is the following. Before CLARA starts its major iterations, **D** is calculated from all K objects and then stored in memory in a compressed format, as elucidated shortly. In each iteration, **D** (compressed) is passed to PAM, along with a vector of K' integers that serve to index the objects in a particular sample. Using this vector of indices, compressed distances are quickly retrieved from **D** in PAM as they are needed.

Reduction in **D** through compression is implemented in GCA. The compression comes down to encoding real values as integers. In order to store a real number, e.g., a distance $d_{ij}(i < j)$, at least 64 bits are needed on many computers. We accomplish the compression of d_{ij} into a bitfield (bit row) of $\ell < 64$ bits by calculating the integer compressed distance, d_{ij}^*, for d_{ij} according to:

$$d_{ij}^* = \text{integral part of } (2^\ell - 1)\frac{d_{ij}}{d_{\max}} \qquad (4)$$

where d_{max} is the maximum d_{ij} in (uncompressed) **D** and ℓ is the chosen digitization resolution (in bits); in order to avoid an unacceptable truncation error, ℓ must not be too small. The bitfields of the respective d_{ij}^*'s are concatenated contiguously to form a so-called compact bitstring, i.e., a bitstring in which all bits are actual computer bits (instead of, say, bytes confined to the values 0 and 1); d_{ij}^* is accessed as the hth bitfield on the compact bitstring, where $h = j + (i - 1)K - i(i + 1)/2$ $(i < j)$; the technicalities of bitfield access on compact bitstrings are elucidated in [57,65]. In our study, we used $\ell = 10$ for all d_{ij}^*'s; this amounts to a compression of nearly 85% relative to 64-bit real numbers.

Upon decompression, a digital real value, the decoded distance, is obtained:

$$d_{ij} = \frac{d_{ij}^*}{2^\ell - 1} d_{max} \quad (5)$$

The summation of d_{ij}'s, then, yields D_k. However, since optimizing D_k^* (the sum of d_{ij}^*'s, hereafter oftentimes referred to as "response") is equivalent with optimizing D_k, run-time decompression is not necessary and has therefore been omitted from GCA. (The equivalence applies since the same ℓ is used for all d_{ij}^*'s, thus conserving mutual importance among the L variables.)

GENERATE. The computer program GENERATE was developed for the creation of artificial data sets. The rationale for using artificial data sets is that the structure is a priori known, thus enabling a better validation of the methods used [2,61]; this is important at the present stage wherein still little is known about the relative viability of genetic algorithms as applied to clustering problems. GENERATE complies with the k-medoid model in that it creates hyperspherical clusters according to a method described in [2]; furthermore, the clusters created by this method feature Gaussian distributed object densities, and we purposefully avoided overlap between the clusters.

Three data sets were created for our study, each comprising $K = 1000$ objects (in a two-dimensional data space ($L = 2$) to allow graphical display) but different amounts of clusters: $k = 15$, $k = 25$ and $k = 50$; these (autoscaled) data sets are contained in files named `dat15.x`, `dat25.x`, and `dat50.x`, respectively, and are illustrated in Fig. 2a–c (The extension `.x` reminds of the formal notation of the data matrix, **X**.)

Comparison strategy

A comparison between two methods is meaningful if both are optimally configured; when only one method is optimally configured and the other turns out to perform better nonetheless, then too a comparison is meaningful, although this can only be concluded afterwards, of course. Unfortunately, however, for many optimization methods used in practice, including CLARA and GCA, there is no standard methodology available to find an optimal working point in their configuration space. Therefore, in practice, one needs to accept the best configuration found for each method after evaluating a fair but limited amount of configurations, using the best available means. Since the comparison can not be made more reliable in practice, due reserve in drawing conclusions is in place.

Configuration of CLARA

The configuration of CLARA has been optimized earlier by its creators and the result was presented in the literature [3]. Since further optimization is beyond the purposes of this pilot study, we adopted this standard configuration: $M = 5$ (the number of major iterations), $A = 2$ and $B = 40$ in $K' = Ak + B$ (the number of objects in the sample of objects passed to PAM).

Configuration of GCA

In general, the most successful strategy to optimize the configuration of a genetic algorithm turns out to be making educated estimates based on rules of thumb obtained through practice, i.e., on expert intuition [19,45,50]. The disadvantage of this approach, however, is that the expert involved can often not rationally explain the choices made.

Another approach that might be considered is a fractional factorial design, e.g., a Plackett-Burman design [62]. (A full factorial design, or grid

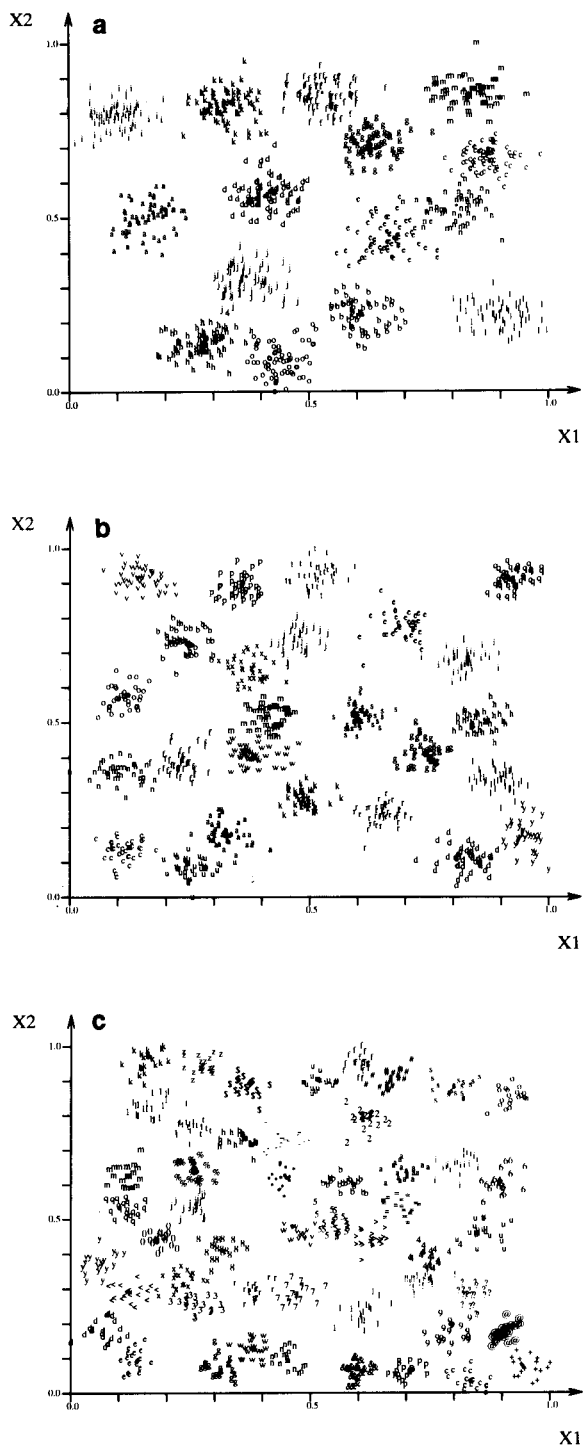

Fig. 2. Artificial data sets for (a) $k = 15$, (b) $k = 25$ and (c) $k = 50$ ($K = 1000$, $L = 2$). (Cluster membership is denoted by arbitrarily chosen characters.)

search, would provide a guaranteed means to find the optimal configuration, but is not feasible within practically reasonable time due to the large amount of factors involved.) The disadvantage of fractional factorial designs is that they are based on strong assumptions, e.g., on the assumption that the factors involved are not correlated. Since such assumptions are not acceptable for a complex matter such as genetic configuration (where the factors are genetic control parameters, among which many are strongly correlated), it is important to practise great restraint in drawing conclusions from the results.

Our approach to the configuration of GCA is a combination of the abovementioned two approaches, as follows. Using the experience we have with the application of genetic algorithms, we selected a number of supposedly influential factors (control parameters) and made educated guesses at two more or less realistic levels for these; in this way, it is not likely that the space of configurations considered contains very bad configurations. These levels were used in a Plackett-Burman design to study the factor effects; the response measured to calculate these effects was the D_k^* of the best string in the population of the generation of interest. The properties of a Plackett-Burman design can be summarized as follows:

By conducting n experiments (where n is a multiple of 4), $n - 1$ variables are screened, assuming first-order factor effects only (hence, assuming the lack of factor correlations);

In most Plackett-Burman designs (including those considered for our study) the factors are tested at $l = 2$ levels, indicated in a binary way as "+" and "−"; for numerical factors, these levels indicate "high" and "low" values, respectively;

In the experiments, each factor is set $n/2$ times to "+" and $n/2$ times to "−";

In order to enable statistical calculations, one or more so-called dummy variables are taken into account;

Results are evaluated using a Student's t-test.

We adopted a ($n = 12$, $l = 2$) Plackett-Burman design, in which the binary levels are as listed in Table 1.

TABLE 1

Binary levels for the ($n = 12$, $l = 2$) Plackett-Burman design

		x_i										
		x_1	x_2	x_3	x_a	x_4	x_5	x_6	x_b	x_7	x_8	x_9
Experiment	1	+	+	−	+	+	+	−	−	−	+	−
	2	−	+	+	−	+	+	+	−	−	−	+
	3	+	−	+	+	−	+	+	+	−	−	−
	4	−	+	−	+	+	−	+	+	+	−	−
	5	−	−	+	−	+	+	−	+	+	+	−
	6	−	−	−	+	−	+	+	−	+	+	+
	7	+	−	−	−	+	−	+	+	−	+	+
	8	+	+	−	−	−	+	−	+	+	−	+
	9	+	+	+	−	−	−	+	−	+	+	−
	10	−	+	+	+	−	−	−	+	−	+	+
	11	+	−	+	+	+	−	−	−	+	−	+
	12	−	−	−	−	−	−	−	−	−	−	−

The definition of the factors and their levels are listed in Table 2; roulette selection was used (see module 2 in the flowchart). The following factors require some further explanation (see [45,57] for more details): x_3 (fitness offset) is a control parameter used in fitness translation, the first fitness scaling step usually applied to the raw fitness (see modules 0 and 1 in the flowchart); after fitness translation, the fitness of the worst-performing string equals the fitness offset; x_4 (fitness scaling factor) is another handle to affect fitness ratios; this factor is either the sensitivity in static linear fitness scaling mode or the segregation degree in sigmoid fitness scaling mode, whichever applies; both modes basically stabilize the competition between strings in roulette selection; x_6 (fraction elitism) is the fraction of strings which enjoy the privilege of guaranteed survival (reproduction); in GCA, these strings are additionally "immunized" (protected) against modification by recombination and mutation.

TABLE 2

Levels considered in the ($n = 12$, $l = 2$) Plackett-Burman design

x_i	Control parameter	−	+
x_1	Number of generations	100	200
x_2	Population size	100	200
x_3	Fitness offset	0.0	0.02
x_a	dummy	Irrelevant	Irrelevant
x_4	Fitness scaling factor	1.5	2.5
x_5	Fitness scaling mode	Static linear	Sigmoid
x_6	Fraction elitism	0.0	0.01
x_b	dummy	Irrelevant	Irrelevant
x_7	Mix recombination probability	0.5	0.9
x_8	Point mutation probability	0.2	0.4
x_9	Mix mutation probability	0.0	0.125

The experiments for the design were carried out using data set `dat15.x`. Due to the probabilistic nature of genetic algorithms, the response is distributed. Therefore, in order to get a rough impression about the reliability of the results, each experiment was carried out in duplo. A summary of the results is given in the next section; details of the calculations involved are beyond the purposes of this paper, as they can be derived from the theory in the cited literature on Plackett-Burman designs.

The configuration thus obtained was not only used in runs for data set `dat15.x`, but also in runs for data sets `dat25.x` and `dat50.x`, assuming that optimal configuration does not depend dramatically on the choice of the data set; this assumption seems reasonable in view of the widespread consensus among practitioners that genetic algorithms are configurationally robust [19,45]. (The chosen data set is considered a legitimate part of the configuration, because it determines the parameterization of the objective function, module 0 in the flowchart.)

In a section below, the configuration found is corroborated in three ways. One of these is the

use of an additional, ($n = 8$, $l = 2$) Plackett-Burman design involving x_2, x_4, x_5, x_7, x_8, x_9 (and a dummy factor), the factors that were observed to have the most indeterminate impact in the first Plackett-Burman design.

At first glance, a legitimate point of objection against the pursued comparison between CLARA and GCA is that the running time of CLARA (used in standard configuration) is much smaller than the running time of GCA. In principle, one way to make the comparison more fair, would be to configure GCA for less string evaluations. However, this approach is not practically feasible since genetic algorithms are "heavy duty" optimizers; that is, at least in the order of 1000 to 10 000 string evaluations must typically take place in many cases before genetic search acquires enough "momentum" to commence searching efficiently. For this reason, we decided to ignore the disparity between the running times in the first instance; this makes sense in view of the pilot nature of our study and of the fact that it can not be a priori ruled out that CLARA finds better solutions despite the shorter running time. In the second instance, if these investigations would reveal that GCA finds better solutions, then, in order to make the comparison more fair, we would decide to conduct additional runs with CLARA configured for running times closer to those of GCA.

RESULTS AND DISCUSSION

Configuration

The results of the experiments according to the ($n = 12$, $l = 2$) Plackett-Burman design lead to the configuration listed in Table 3; the result $x_1 = 200$ has been omitted from this table.

The spread we observed in the response warned us that this configuration needs further corroboration. This was done in the following three different ways. First, the abovementioned smaller ($n = 8$, $l = 2$) Plackett-Burman design was conducted. This did not lead to new results. However, since recombination is normally the most important genetic exploration operator, we considered it worthwhile to examine four finer levels about 0.5, namely 0.3, 0.4, 0.6, and 0.7; from this fine-tuning it became apparent that level 0.4 is the best, and we switched to it. Second, we conducted some additional experiments for arbitrary combinations of binary levels other than those listed in Table 1. Again, no improvement was observed. Finally, we verified the levels for the recombination and mutation operators by way of a so-called empirical complexity analysis [19,57]. In such an analysis, a particular search heuristic of interest, the recombination or mutation operator in our case, is allowed to perform an explorative walk in the search space. From the time-series of fitness values thereby obtained, one can derive (auto)correlation information indicating the ruggedness of the fitness landscape. This ruggedness is also called the apparent problem complexity; "apparent", as it is merely "perceived" by the search heuristic used. A lower apparent problem complexity is an indication of a better configuration of the search heuristic used. All combinations of binary levels for the recombination and mutation probabilities were tried, and the levels listed in Table 3 were again found to be the best.

TABLE 3

Levels obtained for the ($n = 12$, $l = 2$) Plackett-Burman design

Control parameter	Level
Population size	200
Fitness offset	0.02
Fitness scaling factor	2.5
Fitness scaling mode	Static linear
Fraction elitism	0.01
Mix recombination probability	0.5
Point mutation probability	0.2
Mix mutation probability	0.125

Global sampling behavior

An impression of the global sampling behavior of a particular search method, as applied to a particular problem, can be obtained by measuring the frequency distribution of responses (or fitnesses) for the points sampled in the search space during a fixed-length run. Figure 3 depicts typical response frequency distributions obtained for random search (through a random walk) and

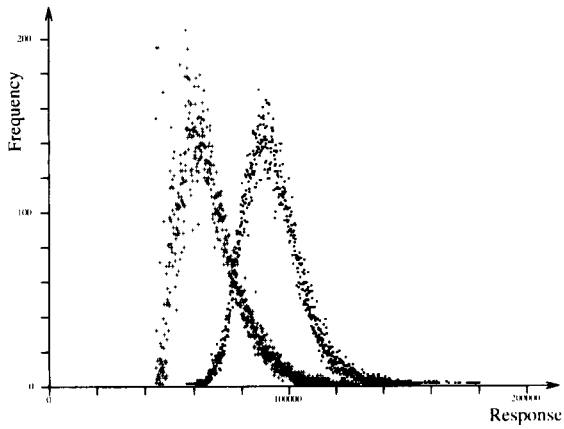

Fig. 3. Response frequency distributions after 40000 string evaluations by GCA and random search, respectively, using `dat15.x`; the width chosen for the consecutive response intervals is 100 response units. ■ = Random search; + = GCA.

GCA, respectively. The procedure is as follows. A range of feasible responses is subdivided into a number of small, equally sized intervals. The method of interest is then run for a fixed amount of string evaluations, and the occurences of responses falling within the respective intervals are counted in run-time; the count for each interval corresponds with a point in the response frequency distribution concerned. Useful information can be derived from response frequency distributions; for instance, from the response frequency distribution for random search in Fig. 3 one may conclude that there are many non-optimal regions on the response landscape.

Response frequency distributions owe their appeal to being universal; that is, any pair of methods can be qualitatively compared through visual inspection of their respective response frequency distributions. A larger separation between the distributions indicates a larger difference in sampling efficiency, i.e., a larger difference in the ability to catch and exploit promising leads in the search space. Such a comparison is only meaningful, of course, if the number of string evaluations is chosen large enough. The 40000 evaluations used in order to obtain Fig. 3 are considered enough, because for a sequence of increasing numbers of evaluations performed by either random search or GCA, we empirically established that the response frequency ratios converge at a number of evaluations well below 40000. (Convergence of this kind reflects a state of "dynamic equilibrium". The reason why a genetic algorithm too reaches such a dynamic equilibrium, is that it constantly escapes optima in searching for better optima, not "knowing" when the global optimum is reached.)

Comparisons between a genetic algorithm and random search are often described in the literature on genetic algorithms. The rationale for this is that a genetic algorithm, being probabilistic, can degrade to random search in the worst case; among plausible reasons why such may occur are a bad configuration or an inappropriate target problem. Hence, a plausible minimal condition for using a genetic algorithm is that it should perform better than random search. In this respect, response frequency distributions provide a useful prescreening tool to test whether mentioned minimal condition is fulfilled. It appears from Fig. 3 that GCA passes such a test successfully.

Evolution of the population variance

In any genetic algorithm, sufficient population variance (diversity) must be maintained during the search for recombination to be productive [45]. Figure 4 illustrates the evolution of the population variance measured as the variance in

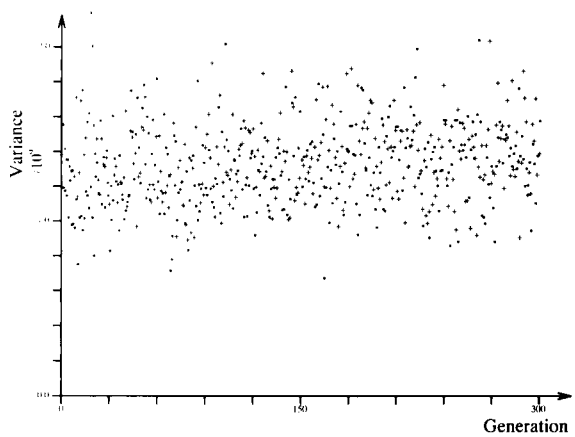

Fig. 4. Evolution of the population variance (duplo runs). ■ = Run 1; + = run 2.

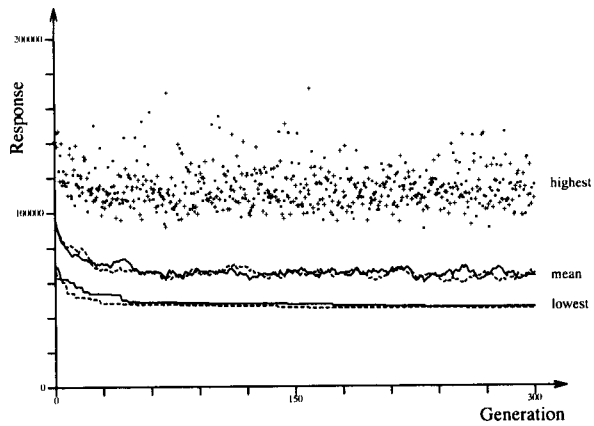

Fig. 5. Evolution of the lowest, highest and mean response (duplo runs). ———, lowest/mean response (run 1); ------, lowest/mean response (run 2); ■ = highest response (run 1); + = highest response (run 2).

string responses for a population at a particular generation. (This approach is simple, yet provides a useful rough estimate since strings must be different if their responses are different; note that the opposite is not necessarily true: different strings may have the same response). Similar results were obtained for `dat25.x` and `dat50.x`. Added to the fact that the search converges (see next section), these results confirm that the configuration employed is acceptable. For instance, despite the strong selection pressure (exploitation) arising from elitism, a proper balance between exploration and exploitation is apparently maintained (since the average variance appears to remain constant).

Evolution of the response

It is informative to keep track of the lowest- (best-), highest- (worst-) and mean response in the population as it evolves (Fig. 5). In this figure, it can be seen that the highest response evolves in a near-random way; this indicates that the genetic algorithm samples remote "corners" of the search space, which is desirable in order that local optima can be escaped. Nonetheless, as may be inferred from the way in which the mean response evolves and as is indeed to be generally expected, by far more search effort arises from the better strings in the population. The evolution of the lowest response exhibits the lowest noise level, which is also generally to be expected; moreover, note that the lowest response never rises, which is to be attributed to elitism.

Figures 6a–c show in detail the evolution of the lowest response for the three data sets of interest. In these figures, the impact of a second genetic optimization step, using a modified configuration, is also shown; incidentally, such strategies wherein it is aimed to improve the result of a genetic algorithm by a second, differently configured genetic algorithm have been called sequential self-hybridization [45]. The configuration was modified as follows. Starting from the knowledge that, in general, recombination becomes less productive upon convergence and mutation then becomes a comparatively more important exploration operator accordingly, the mix recombination probability was changed from 0.4 to 0.0 (rendering the built-in mix mutation probability meaningless, of course); the point mutation probability was changed from 0.2 to 1.0; since this amounts to a stronger exploration, the level of exploitation was also enhanced (in order to maintain a proper balance between exploration and exploitation) by changing the fraction elitism from 0.01 to 0.02, and by switching from roulette selection to rank-based threshold selection [45,57]; in this selection mode, strings with a fitness rank below some predefined threshold stand no chance of survival, i.e., are deterministically purged from the population, rendering the fitness scaling factor (x_4) and fitness scaling mode (x_5) meaningless.

Upon visually inspecting Fig. 6a–c altogether, one may draw the following important conclusions. First, it is evident that a second optimization step can lead to a significant improvement; incidentally, this underscores the general intuition that if genetic configuration is to stay optimal during genetic search, then, ideally, it should evolve dynamically in response to the evolving population; nonetheless, only few applications of dynamically evolving genetic configurations have been reported up to now (see e.g., [13,63]), as it is apparently difficult to find generally successful strategies in practice. Second, convergence is reasonably approached within 300 generations, i.e., within the maximum allocated running time. Re-

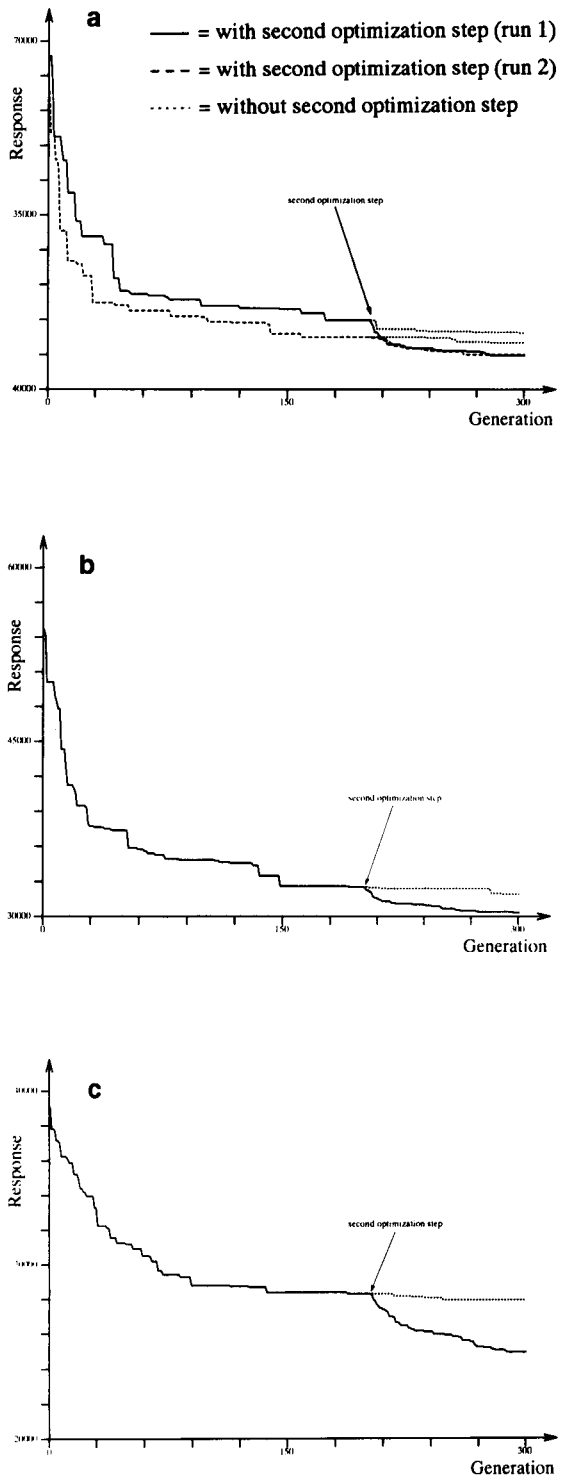

Fig. 6. Evolution of the lowest response for: (a) `dat15.x` (duplo runs); (b) `dat25.x`; (c) `dat50.x`.

lated to that, third, from the evolution of the lowest response it appears that the time constant of the convergence process is approximately 30 generations for all data sets, i.e., not strongly dependent on k. This suggests that GCA's time complexity in k is small, which is a valuable result since the end solutions are acceptable (as follows from the next section). In other words, the schema theorem (see above) seems to apply in the cases studied, indicating that GCA recognizes implicit structure in data spaces quickly. However, it should be borne in mind that the used data sets are ideal (with hyperspherical, non-overlapping clusters).

In contrast, for CLARA the time constant of convergence, estimated from similar response evolution plots, was found to grow considerably faster with increasing k. (These results are not shown since the solutions found by CLARA are inferior to those found by GCA, as follows from the next section.)

Comparison of CLARA and GCA

In this section, we compare CLARA and GCA by the validation criteria outlined in the introductory part.

Quality of the end solution. For the best solutions found in two runs with GCA (with the second optimization step) and two runs with CLARA, the values of D_k (decoded from D_k^*, in case of GCA, using Eqn. 5 after the runs) are listed in Table 4.

These results indicate that GCA finds significantly better clusterings, on average. Also, GCA seems more robust (reliable) as the spread in its results is smaller, although this may also be a consequence of the larger running time.

TABLE 4

Sum of distances for end solutions (duplo runs)

D_k (sum of distances)				
Data set	GCA		CLARA	
`dat15.x`	48.6959	48.769	59.208	67.9976
`dat25.x`	36.5417	36.7439	45.0311	49.3854
`dat50.x`	30.8936	31.0254	40.2195	39.0047

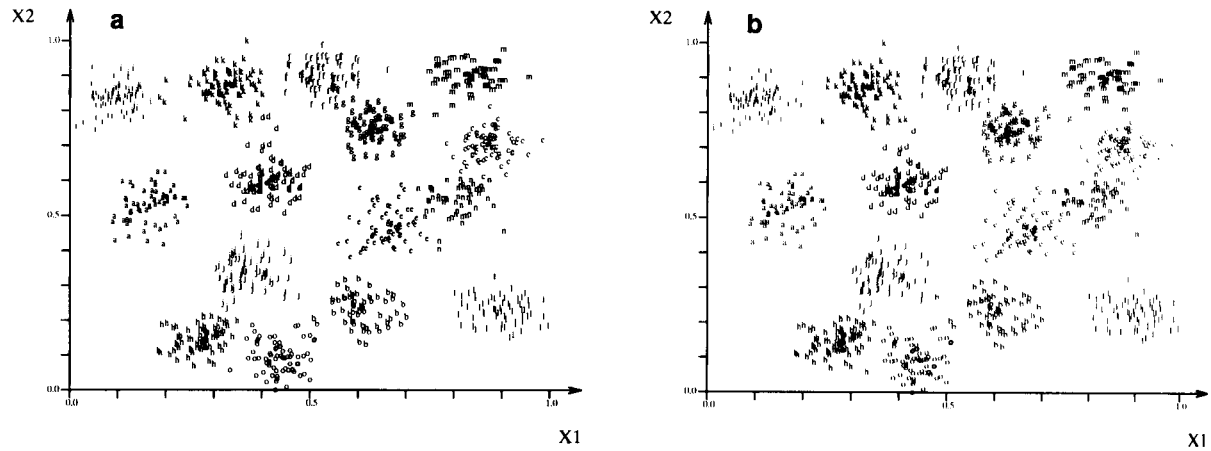

Fig. 7. Clustering found for data set `dat15.x` using: (a) CLARA; (b) GCA (cf. Fig. 2a).

It makes sense to extend the above comparison with a visual inspection of graphical plots of the clusters found, as it can not be generally ruled out that two different sets of medoids with different D_k result in the same clustering; this is especially likely the case when clusters are well separated. Such plots are shown in Fig. 7a and b and Fig. 8a and b for `dat15.x` and `dat50.x`, respectively.

From Fig. 7a and b it follows that both CLARA and GCA generally manage to find all clusters in `dat15.x`. CLARA seems to have somewhat more difficulty with objects that lie between clusters, but since the computation time is much shorter, this is a price many practitioners would probably be willing to pay.

From Fig. 8a and b it follows that CLARA does not succeed in finding all clusters in `dat50.x`, as some are joined together while others are split up; such performance is likely to be deemed unsatisfactory by many practitioners. GCA, on the other hand, still finds all clusters, although now it too seems to have some difficulty with objects that lie between clusters.

Computation time. From our experiments it follows that GCA requires considerably more running time in order to attain convergence. In order to make the comparison more fair, we

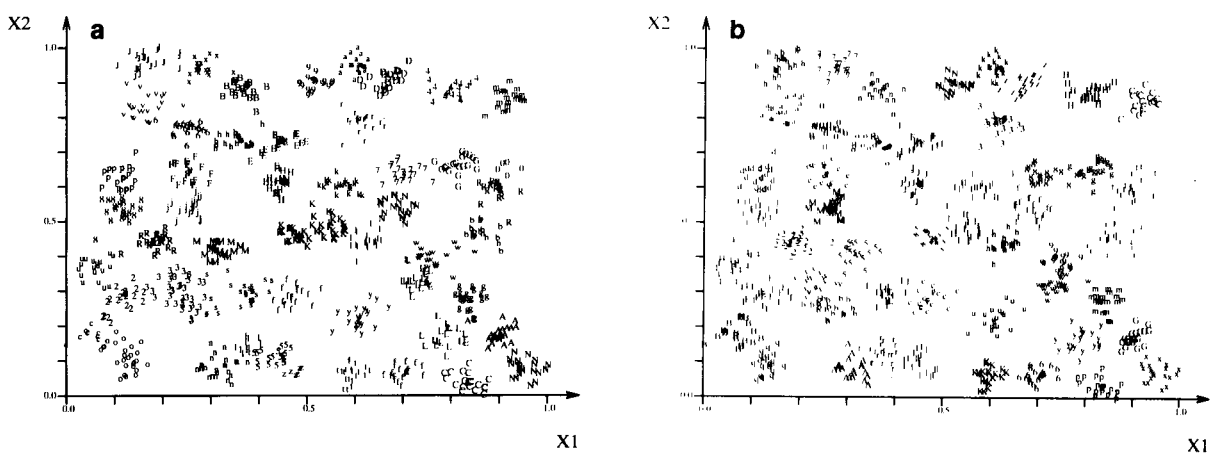

Fig. 8. Clustering found for data set `dat50.x` using: (a) CLARA; (b) GCA (cf. Fig. 2c).

examined whether CLARA would perform better when it is configured differently such that its computation time is larger (but still within the maximum allocated running time). This can be done in several ways. Recall that CLARA performs M major iterations, in each of which PAM performs a clustering of $K' = Ak + B < K$ objects, with 5, 2 and 40 as standard values for M, A and B, respectively. Hence, the present aim would be served by increasing M or K'. Both approaches were pursued, using the three artificial data sets available. We suffice with the following summary of the results.

Larger M values (leading to a linear increase in the computation time) generally did not improve the results significantly. Indeed, for M values that correspond with computation times approximately equal to the running time of GCA, the latter still performed considerably better for all data sets.

On the other hand, larger K' values (leading to a quadratic increase in the computation time) generally improved the results markedly, which is in agreement with results reported by Hopke and Kaufman [36]. For K' values that correspond with computation times approximately equal to the running time of GCA, CLARA performed virtually as good as GCA for `dat15.x` and almost as good for `dat25.x`, but by far worse for `dat50.x`. It is therefore concluded that for larger k values (i.e., for larger, more complex clustering problems), CLARA is increasingly prone to run into a sub-optimal solution from which it can not escape. We ascribe this shortcoming to the apparently greedy search heuristics used in both the minor cycle (PAM) and major cycle, in either cycle each step starting deterministically from the best that was found in the preceding step.

Memory usage. For both CLARA and GCA, memory usage is well within the memory specifications of the hardware used. Both programs save considerably on computer memory usage, as they store **D** in reduced form. GCA uses approximately 50 to 100 kB more computer memory, accounting for a somewhat larger program code and a population.

Ease of development and implementation. If developed from scratch, the programming and debugging of CLARA and GCA consumes approximately equal effort. In our specific case, GCA was obtained with minimal effort since we borrowed a genetic algorithm prototype from a genetic software library (abovementioned GATES) that was available. On the other hand, however, the optimization of GCA is considerably more laborious due to the larger amount of (correlated) control parameters.

Ease of use. Once implemented and optimized, CLARA and GCA feature comparable ease of use. If wider distribution among routine users is intended, a more advanced user interface is desirable in both programs.

CONCLUSIONS AND OUTLOOK

A pilot study has been presented that treats the background, feasibility and competitiveness of GCA, a genetic algorithm for k-medoid partitional clustering of large data sets. In general, GCA turns out to be practically feasibe for problems of this kind, as it finds acceptable solutions in reasonable time.

The competitiveness of GCA was rated with respect to CLARA, an earlier approach to k-medoid clustering of large datasets. This comparison has been carried out using artificial data sets with a known, ideal structure (hence with known k) for verification purposes.

For small values of k, both CLARA and GCA find acceptable solutions. Those found by GCA are only slightly better at the expense of a considerably larger amount of computation time. However, with increasing values of k, the picture changes drastically: the computation time of CLARA increases quadratically; in addition, the quality of the solutions found drops rapidly below acceptable. The computation time of GCA, on the other hand, increases much slower and acceptable solutions are still found. These results indicate that GCA is a better choice when many clusters are present in the target data set. Whether this conclusion still applies when non-ideal, real-world data sets are used, is an important subject for future investigation.

A fruitful avenue for further research seems to lie in the sequential hybridization [45] of GCA with another method to enhance performance. We demonstrated that self-hybridization (in our case, a second optimization step to GCA by GCA itself) comprises a viable approach. In a similar way, GCA can be combined with CLARA to obtain a hybrid searching system with better performance. For instance, GCA can be post-hybridized with CLARA by passing the solution found by GCA to CLARA for further improvement; this demands that CLARA is customized such that in the first major iteration the sample of objects passed to PAM contains the set of medoids found by GCA. Also, GCA can be pre-hybridized with CLARA by seeding the (otherwise normally random) initial population of GCA with a few solutions found by CLARA. Preliminary results that we have obtained with such post- and pre-hybridization strategies are encouraging and underscore the viability of hybrid searching systems in general.

In principle, GCA lends itself excellently for parallelization [64], as each string in the population can be evaluated independently from the other strings. When parallelized, the computation is distributed across a host processor and several slave processors; most of the code for GCA is loaded on the host processor (except for the objective function), while each slave processor accommodates a small sub-population, possibly as small as one string, and the code for the objective function to evaluate the strings therein. In contrast, CLARA is more difficult to parallelize because the successive major iterations are not mutually independent [35,37]; moreover, memory demands are higher, as PAM needs to be loaded on each of the slave processors. Importantly, the parallelization of GCA can be accomplished without specialized parallel hardware such as transputer systems that make memory access and host-slave communication fast, because the overall speed of execution is mostly determined by string evaluations. An example of a parallel system of processors that would suffice, is a local area network of workstations; the software required for the communication is comparatively simple and cheap.

REFERENCES

1 R. Dubes and A.K. Jain, in M.C. Yovits (Ed.), Clustering methodologies in exploratory data analysis, Advances in Computers, Vol. 19, Academic Press, New York, 1980, pp. 113–215.
2 A.K. Jain and R.C. Dubes, Algorithms for Clustering Data, Prentice-Hall, Englewood Cliffs, NJ, 1988.
3 L. Kaufman and P.J. Rousseeuw, Finding Groups in Data, An Introduction to Cluster Analysis, Wiley, Chichester, 1990.
4 P.C. Jurs and T.L. Isenhour, Chemical Applications of Pattern Recognition, Wiley, New York, 1975.
5 K. Varmuza, Pattern Recognition in Chemistry, Lectures Notes in Chemistry, Vol. 21, Springer-Verlag, New York, 1980.
6 D.L. Massart and L. Kaufman, The Interpretation of Analytical Chemical Data by the Use of Cluster Analysis, Chemical Analysis, Vol. 65, Wiley, New York, 1983.
7 P.C. Jurs, Computer Software Applications in Chemistry, Wiley, New York, 1986.
8 M.A. Sharaf, D.L. Illman and B.R. Kowalski, Chemometrics, Chemical Analysis, Vol. 82, Wiley, New York, 1986.
9 D.L. Massart, B.G.M. Vandeginste, S.N. Deming, Y. Michotte and L. Kaufman, Chemometrics: A Textbook, Elsevier, Amsterdam, 1988.
10 J. Zupan, Algorithms for Chemists, Wiley, New York, 1989.
11 W. Siedlecki and J. Sklansky, Pattern Recognition Lett., 10 (1989) 335.
12 C.B. Lucasius and G. Kateman, Trends Anal. Chem., 10 (1991) 254.
13 T.-H. Li, C.B. Lucasius and G. Kateman, Anal. Chim. Acta, 268 (1992) 123.
14 R. Leardi, R. Boggia, and M. Terrile, J. Chemom., 6 (1992) 267.
15 C.B. Lucasius, M.L.M. Beckers and G. Kateman, Anal. Chim. Acta, (1993) submitted for publication.
16 C.B. Lucasius, A.H.C. van Kampen, L.M.C. Buydens and G. Kateman, Chemom. Intell. Lab. Syst., (1993) in preparation.
17 C.B. Lucasius, A.D. Dane and G. Kateman, Anal. Chim. Acta, 282 (1993) 647.
18 F. Maffioli, in N. Christofides, A. Mingozzi, P. Toth and C. Sandi (Eds.), Combinatorial Optimization, Wiley, New York, 1979, Chap. 5.
19 C.B. Lucasius and G. Kateman, Chemom. Intell. Lab. Syst., 19 (1993) 1.
20 A.H. Land and A.G. Doig, Econometrica, 28 (1960) 497.
21 W.L.G. Koontz, P.M. Narendra and K. Fukunaga, IEEE Trans. Comp., C-23 (1975) 908.
22 D.L. Massart, F. Plastria and L. Kaufman, Pattern Recognition, 16 (1983) 507.
23 S. Kirkpatrick, C.D. Gelatt, Jr., and M.P. Vecchi, Science, 220 (1983) 671.
24 P.J.M. van Laarhoven and E.H.L. Aarts, Simulated Annealing: Theory and Applications, Mathematics and its

Applications (East European Series), Reidel, Dordrecht 1987.
25 E.H.L. Aarts and J.H.M. Korst, Simulated Annealing and Boltzmann Machines. A Stochastic Approach to Combinatorial Optimization and Neural Computing, Wiley, Chichester, 1989.
26 R.W. Klein and R. Dubes, Pattern Recognition, 22 (1989) 213.
27 B. Kamgar-Parsi, J.A. Gualtieri, J.E. Devaney and B. Kamgar-Parsi, Biol. Cybernetics, 63 (1990) 201.
28 W.J. Melssen, J.R.M. Smits, G.H. Rolf and G. Kateman, Chemom. Intell. Lab. Syst., 18 (1993) 195.
29 J.R.M. Smits, W.J. Melssen, L.M.C. Buydens and G. Kateman, Chemom. Intell. Lab. Syst., (1993) in press.
30 F. Glover, ORSA J. Comput., 1 (1989) 190.
31 F. Glover, ORSA J. Comput., 2 (1990) 4.
32 C.R. Reeves, (Ed.), Modern Heuristic Techniques for Combinatorial Problems, Advanced Topics in Computer Science, Blackwell, Oxford, 1993.
33 P. Hansen, B. Jaumard and S. Da Silva, J. Classification, (1993) in press.
34 L. Kaufman and P. Rousseeuw, in E. Gelsema and L. Kanal (Eds.), Pattern Recognition in Practice II, Elsevier, Amsterdam, 1986, pp. 425–437.
35 L. Kaufman, P.K. Hopke and P.J. Rousseeuw, Computational Statistics Quarterly, 2 (1988) 129.
36 P.K. Hopke and L. Kaufman, Chemom. Intell. Lab. Syst., 8 (1990) 195.
37 P.K. Hopke, in E.J. Karjalainen (Ed.), Scientific Computing and Automation (Europe) 1990, Elsevier, Amsterdam, 1990, pp. 9–19.
38 J.H. Holland, Adaptation in Natural and Artificial System, University of Michigan Press, Ann Arbor, MI, 1975, Revised edition, MIT Press, Cambridge, MA, 1992.
39 D.E. Goldberg, Genetic Algorithms in Search, Optimization, and Machine Learning, Addison-Wesley, Reading, MA, 1989.
40 L. Davis (Ed.), Handbook of Genetic Algorithms, Van Nostrand Reinhold, New York, 1991.
41 Y. Davidor, Genetic Algorithms and Robotics: A Heuristic Strategy for Optimization, World Scientific, Singapore, 1991.
42 Z. Michalewicz, Genetic Algorithms + Data Structures = Evolution Programs, Artificial Intelligence Series, Springer Verlag, Berlin, 1992.
43 J.H. Holland, Sci. Am., 267 (1992) 44.
44 J.R. Koza, Genetic Programming: On the Programming of Computers by Means of Natural Selection, MIT Press, Cambridge, MA, 1992.
45 C.B. Lucasius and G. Kateman, Chemom. Intell. Lab. Syst. (1993) in press.
46 J.J. Grefenstette (Ed.), Proceedings of the First International Conference on Genetic Algorithms, Lawrence Erlbaum, Hillsdale, NJ, 1985.
47 J.J. Grefenstette (Ed.), Proceedings of the Second International Conference on Genetic Algorithms, Lawrence Erlbaum Associates Hillsdale, NJ, 1987.
48 J.D. Schaffer (Ed.), Proceedings of the Third International Conference on Genetic Algorithms, Morgan Kaufmann, San Mateo, CA, 1989.
49 R.K. Belew and L.B. Booker (Eds.), Proceedings of the Fourth International Conference on Genetic Algorithms, Morgan Kaufmann, San Mateo, CA, 1991.
50 C.B. Lucasius and G. Kateman, Comput. Chem. (1993) submitted for publication.
51 J.N. Bhuyan, V.V. Raghavan and V.K. Elayavalli, in R.K. Belew and L.B. Booker (Eds.), Proceedings of the Fourth International Conference on Genetic Algorithms, Morgan Kaufmann, San Mateo, CA, 1991, pp. 408–415.
52 G. von Laszewski, in R.K. Belew and L.B. Booker (Eds.), Proceedings of the Fourth International Conference on Genetic Algorithms, Morgan Kaufmann, San Mateo, CA, 1991, pp. 45–52.
53 D.R. Jones and M.A. Beltramo, in R.K. Belew and L.B. Booker (Eds.), Proceedings of the Fourth International Conference on Genetic Algorithms, Morgan Kaufmann, San Mateo, CA, 1991, pp. 442–449.
54 E. Falkenauer, in R. Gutiérrez and M.J. Valderrama (Eds.), Proceedings of the Fifth International Symposium on Applied Stochastic Models and Data Analysis, World Scientific, Singapore, 1991, pp. 198–206.
55 E. Falkenauer, A Genetic Algorithm for Conceptual Clustering, Technical Report Report FMS39, CRIF Industrial Automation, Brussels, December 1991.
56 P.J. Rousseeuw, J. Comput. Appl. Mathematics, 20 (1987) 53–65.
57 C.B. Lucasius and G. Kateman, Comput. Chem. (1993) submitted for publication.
58 C.B. Lucasius and G. Kateman, in R. Männer and B. Manderick (Eds.), Proceedings of the Second Workshop on Parallel Problem Solving from Nature, Elsevier, Amsterdam, 1992, 239–247.
59 R. Wehrens, C.B. Lucasius, L. Buydens and G. Kateman, Anal. Chim. Acta, 277 (1993) 313.
60 R. Wehrens, C.B. Lucasius, L. Buydens and G. Kateman, J. Chem. Inf. Comput. Sci., 33 (1993) 245.
61 G.W. Milligan, Psychometrika, 50 (1985) 123.
62 K. Jones, Int. Lab., November (1986) 32.
63 L. Davis, in J.D. Schaffer (Ed.), Proceedings of the Third International Conference on Genetic Algorithms, Morgan Kaufmann, San Mateo, CA, 1989, p. 61.
64 J. Stender (Ed.), Parallel Genetic Algorithms: Theory and Applications, Frontiers in Artificial Intelligence and Applications, IOS Press, Amsterdam, 1993.
65 C.B. Lucasius, PhD Thesis, Katholieke Universiteit Nijmegen, 1993.

Analytica Chimica Acta, 282 (1993) 671–677
Elsevier Science Publishers B.V., Amsterdam

Apparent content curves: a method to resolve spectral interferences in samples with *n* components

M. Llobat-Estelles, A.R. Maurí-Aucejo, R. Marín-Saez, M.D. San Martín-Ciges and A. Cerdán Vidal

Departamento de Química Analítica, Universitat de Valencia, Dr. Moliner 50, E-46100 Burjassot, Valencia (Spain)

(Received 2nd April 1993; revised manuscript received 7th June 1993)

Abstract

A mathematical method that permits the determination of an analyte in the presence of *n* interferents was developed. In order to apply the method it is not necessary to know the nature and/or the number of interferents. The proposed procedure is based on obtaining the apparent content curves for the samples and the determination of the analyte may be carried out in the same way as for binary mixtures. The procedure was applied to the determination of theophylline in anti-asthmathic pharmaceutical products and good results were obtained in all instances.

Keywords: UV–Visible spectrophotometry; Apparent content curves; Interferences; Pharmaceuticals; Theophylline

The development of mathematical methods aimed at the resolution of overlapped response curves constitutes a field of great analytical interest. Most of the proposed procedures imply the separation of each of the component responses although, in many instances, this operation is impractical or impossible. However, some methods allow to the resolution of overlapped response curves without the need for independent measurements of the responses. These methods are mainly based on derivative spectroscopic techniques [1,2], iterative procedures (Kalman filter, simplex) [3,4] or transformation of the data, e.g., Fourier transformation [5].

Apparent content curves are the basis of a mathematical method that permits the identification of an interferent present in a binary mixture and the subsequent determination of the analyte, without the need to use standard solutions of the interferent [6]. Ternary mixtures containing variable (interferent A)/(interferent B) ratios can be resolved in a similar way [7]. These methods have been applied to the analysis of binary and ternary mixtures by UV spectrophotometry and spectrofluorimetry [8,9], although they can be used in any analytical technique that provides pseudo-Gaussian recordings.

The aim of this work was to adapt this approach to the analysis of multi-component samples when the number and nature of the interferents in the sample are not known. In order to do this it is only necessary to use a simulated spectrum that reproduces the behaviour of the total interferents present in the sample.

Correspondence to: M. Llobat-Estelles, Departamento de Química Analítica, Universitat de Valencia, Dr. Moliner 50, E-46100 Burjassot, Valencia (Spain).

THEORETICAL

For analytical techniques that provide $S_{\lambda_i} = f(\lambda_i)$ (S_{λ_i} being the value of the analytical signal considered), the apparent content curves were obtained by plotting F_{λ_i} values against λ_i, where

F_{λ_i} is defined as

$$F_{\lambda_i} = \frac{(S_T)_{\lambda_i}}{(\alpha_A)_{\lambda_i}}$$

$(S_T)_{\lambda_i}$ being the analytical signal for the sample and $(\alpha_A)_{\lambda_i}$ the coefficient of response of the analyte at the wavelength considered.

Assuming that $(S_T)_{\lambda_i} = (\Sigma S_k)_i$ (k = each of the constituents), F_{λ_i} is given by

$$F_{\lambda_i} = C_A + \left(\frac{\sum \alpha_k C_k}{\alpha_A}\right)_{\lambda_i} \quad (1)$$

and the corresponding Q value at the three working wavelengths is

$$Q = \frac{\left(\frac{\sum \alpha_k C_k}{\alpha_A}\right)_{\lambda_1} - \left(\frac{\sum \alpha_k C_k}{\alpha_A}\right)_{\lambda_2}}{\left(\frac{\sum \alpha_k C_k}{\alpha_A}\right)_{\lambda_1} - \left(\frac{\sum \alpha_k C_k}{\alpha_A}\right)_{\lambda_3}} \quad (2)$$

Analogously to binary mixtures, the parameter Q represents a measure of the variation of the interferent effect introduced by the components of the sample at the three working wavelengths. However, unlike in binary mixtures, this parameter depends on the concentration of each of the components and therefore it cannot be used for the identification of the interferents.

On the other hand, the sample can be considered as a binary interference–analyte mixture in such a manner that we can write

$$\left(\sum \alpha_k C_k\right)_{\lambda_i} = (\alpha_{ap})_{\lambda_i} C_{ap} \quad (3)$$

In this way, the determination of the analyte in the sample would be carried out following the procedure proposed for binary mixtures.

Logically, prior to the determination of the analyte, it is necessary to know which is the appropriate interference in each instance. To do this, a simple computational program was developed that, by modifying the amplitude and/or the position of a pseudo-Gaussian curve, allows a simulated spectrum to be obtained that reproduces the features of the total interferents present in each instance.

Choosing the simulated spectrum

Obviously, the simulated spectrum must provide a Q value identical with that obtained for the sample and therefore we can write

$$\frac{\left(\frac{\sum \alpha_k C_k}{\alpha_A}\right)_{\lambda_1} - \left(\frac{\sum \alpha_k C_k}{\alpha_A}\right)_{\lambda_2}}{\left(\frac{\sum \alpha_k C_k}{\alpha_A}\right)_{\lambda_1} - \left(\frac{\sum \alpha_k C_k}{\alpha_A}\right)_{\lambda_3}} = \frac{\left(\frac{\alpha_p}{\alpha_A}\right)_{\lambda_1} - \left(\frac{\alpha_p}{\alpha_A}\right)_{\lambda_2}}{\left(\frac{\alpha_p}{\alpha_A}\right)_{\lambda_1} - \left(\frac{\alpha_p}{\alpha_A}\right)_{\lambda_3}} \quad (4)$$

$(\alpha_p)_{\lambda_i}$ being the coefficients of response of the simulated spectrum at the working wavelengths. In this way, the program looks for $(\alpha_p)_{\lambda_i}$ values which agree with the above expression.

However, several mathematical solutions are possible and, obviously, only one is the correct one. With the aim of finding the correct solution, some limitations were introduced into the program. First, obtaining values of C_A (analyte concentration) lower than the minimum apparent content curve must, logically, be rejected. Second, it can be stated that the behaviour of both the simulated interferent and the interferent in the sample are identical only if

$$\left(\frac{\alpha_{ap} C_{ap}}{\alpha_p}\right)_{\lambda_1} = \left(\frac{\alpha_{ap} C_{ap}}{\alpha_p}\right)_{\lambda_2} = \left(\frac{\alpha_{ap} C_{ap}}{\alpha_p}\right)_{\lambda_3} = C_p \quad (5)$$

For this reason, it is necessary look for $(\alpha_p)_{\lambda_i}$ values which, in addition to providing identical Q values, offer proportional signals at the three working wavelengths.

P parameter. With the purpose of finding the conditions that meet the previous assumption, the parameter P is defined as

$$P = \frac{\left(\frac{F_x}{F_p}\right)_{\lambda_1} - \left(\frac{F_x}{F_p}\right)_{\lambda_2}}{\left(\frac{F_x}{F_p}\right)_{\lambda_1} - \left(\frac{F_x}{F_p}\right)_{\lambda_3}} \quad (6)$$

Taking into account that

$$\left(\frac{F_x}{F_p}\right)_{\lambda_i} = \frac{C_A + \left(\frac{\sum \alpha_k C_k}{\alpha_A}\right)_{\lambda_i}}{\left(\frac{\alpha_p}{\alpha_A}\right)_{\lambda_i}}$$

$$= \left(\frac{\alpha_A}{\alpha_p}\right)_{\lambda_i} C_A + \left(\frac{\sum \alpha_k C_k}{\alpha_p}\right)_{\lambda_i} \quad (7)$$

we can write

$$P = \frac{C_A\left(\frac{\alpha_A}{\alpha_p}\right)_{\lambda_1} - C_A\left(\frac{\alpha_A}{\alpha_p}\right)_{\lambda_2} + \left(\frac{\sum \alpha_k C_k}{\alpha_p}\right)_{\lambda_1} - \left(\frac{\sum \alpha_k C_k}{\alpha_p}\right)_{\lambda_2}}{C_A\left(\frac{\alpha_A}{\alpha_p}\right)_{\lambda_1} - C_A\left(\frac{\alpha_A}{\alpha_p}\right)_{\lambda_3} + \left(\frac{\sum \alpha_k C_k}{\alpha_p}\right)_{\lambda_1} - \left(\frac{\sum \alpha_k C_k}{\alpha_p}\right)_{\lambda_3}} \quad (8)$$

According to Eqns. 3 and 5, the expression for P becomes

$$P = \frac{\left(\frac{\alpha_A}{\alpha_p}\right)_{\lambda_1} - \left(\frac{\alpha_A}{\alpha_p}\right)_{\lambda_2}}{\left(\frac{\alpha_A}{\alpha_p}\right)_{\lambda_1} - \left(\frac{\alpha_A}{\alpha_p}\right)_{\lambda_3}} \quad (9)$$

and, as can be seen, under these conditions

$$P = \frac{\left(\frac{1}{F_p}\right)_{\lambda_1} - \left(\frac{1}{F_p}\right)_{\lambda_2}}{\left(\frac{1}{F_p}\right)_{\lambda_1} - \left(\frac{1}{F_p}\right)_{\lambda_3}} \quad (10)$$

Therefore, if the values of P obtained using Eqns. 6 and 10 coincide, we can state that the behaviour of both simulated and real interferences are identical at the working wavelengths. Therefore, the program verifies the accomplishment of this condition.

On the other hand,

$$C_p = \left(\frac{\alpha_{ap} C_{ap}}{\alpha_p}\right)_{\lambda_i} = \frac{\left(\frac{\alpha_{ap} C_{ap}}{\alpha_A}\right)_{\lambda_i}}{\left(\frac{\alpha_p}{\alpha_A}\right)_{\lambda_i}} \quad (11)$$

and considering Eqns. 1 and 3:

$$C_p = \frac{(F_x)_{\lambda_i} - C_A}{(F_p)_{\lambda_i}} \quad (12)$$

Taking into account Eqn. 12, the expression for P becomes

$$P = \frac{\frac{1}{(F_x)_{\lambda_1} - C_A} - \frac{1}{(F_x)_{\lambda_2} - C_A}}{\frac{1}{(F_x)_{\lambda_1} - C_A} - \frac{1}{(F_x)_{\lambda_3} - C_A}} \quad (13)$$

Logically, the value of P obtained using this expression must agree with the value obtained by means of Eqns. 6 and 10. The verification of this condition is also tested by the program.

Finally, a last limitation imposed to the program is based on the relationship existing between Q and P values.

Relationship between Q and P. The expression for P given in Eqn. 13 can be written as follows:

$$P = \frac{(F_x)_{\lambda_2} - (F_x)_{\lambda_1}}{(F_x)_{\lambda_3} - (F_x)_{\lambda_1}} \frac{(F_x)_{\lambda_3} - C_A}{(F_x)_{\lambda_2} - C_A} \quad (14)$$

and as

$$Q = \frac{(F_x)_{\lambda_2} - (F_x)_{\lambda_1}}{(F_x)_{\lambda_3} - (F_x)_{\lambda_1}} \quad (15)$$

the value of P becomes

$$P = Q\left[\frac{(F_x)_{\lambda_3} - C_A}{(F_x)_{\lambda_2} - C_A}\right] \quad (16)$$

In this way, the value of C_A can be obtained through the following expression:

$$C_A = \frac{Q(F_x)_{\lambda_3} - P(F_x)_{\lambda_2}}{Q - P} \quad (17)$$

The accomplishment of this condition constitutes the last restriction imposed on the solutions found by the program.

Choosing the working wavelengths

It is obvious that the selection of the working wavelengths affects the Q value obtained for the sample. As the Q value is necessary for finding

the correct simulated spectrum, it is evident that this value must be as accurate as possible.

With the aim of establishing the wavelengths that provide a Q value with the maximum precision, the following expression of the random error for Q is obtained.

$$Q = \frac{(F_x)_{\lambda_1} - (F_x)_{\lambda_2}}{(F_x)_{\lambda_1} - (F_x)_{\lambda_3}}$$

$$S_Q^2 = \left[\frac{\delta Q}{\delta (F_x)_{\lambda_1}}\right]^2 S^2_{(F_x)_{\lambda_1}} + \left[\frac{\delta Q}{\delta (F_x)_{\lambda_2}}\right]^2 S^2_{(F_x)_{\lambda_2}} + \left[\frac{\delta Q}{\delta (F_x)_{\lambda_3}}\right]^2 S^2_{(F_x)_{\lambda_3}}$$

The random error of F_{λ_i} is, evidently, a function of the random error of absorbance measurements. As we can consider that, under the working conditions (close working wavelengths and similar absorbance values), the influence of the different sources of instrumental imprecision are similar for all values of F_{λ_i} obtained, and so we can write

$$S^2_{(F_x)_{\lambda_1}} = S^2_{(F_x)_{\lambda_2}} = S^2_{(F_x)_{\lambda_3}} = S^2$$

and we obtain

$$S_Q^2 = \left\{\frac{2Q(Q-1)+2}{\left[(F_x)_{\lambda_1} - (F_x)_{\lambda_3}\right]^2}\right\} S^2 \qquad (18)$$

As the above expression shows, the selection of the wavelengths must be done in such a manner that the Q value is as small as possible and $(F_x)_{\lambda_1} - (F_x)_{\lambda_3}$ is, obviously, as large as possible.

EXPERIMENTAL

Apparatus

A Perkin-Elmer Lambda 16 UV–visible spectrophotometer was used for absorbance measurements.

Reagents

All reagents were of analytical-reagent grade.

Stock solutions of Methyl Red, Methyl Orange, Cresol Red, Alizarin and Tropaeolin OO in water were prepared. Dilute solutions of these compounds buffered with KH_2PO_4–NaOH buffer (pH 7) were also prepared. A stock solution of theophylline in water was used.

Procedure

The spectrophotometric determination of an compound in the presence of n interferents is carried out as follows. First, spectra of samples and standard solutions of an analyte of various concentrations are obtained. Apparent content curves for each sample are then plotted and, following the criteria indicated above, working wavelengths are chosen. Finally, using the computer program, the concentration of the analyte in each sample is calculated.

RESULTS AND DISCUSSION

Determination of Cresol Red in multi-component mixtures

Spectra of several acid–base indicators are shown in Fig. 1. As can be seen, the presence of

TABLE 1

Composition of samples

Sample No.	Cresol Red (mol l^{-1})	Methyl Red (mol l^{-1})	Methyl Orange (mol l^{-1})	Alizarin (mol l^{-1})	Tropaeolin OO (mol l^{-1})
1	1.05×10^{-5}	7.43×10^{-6}	6.11×10^{-6}	–	8.33×10^{-6}
2	2.09×10^{-5}	7.43×10^{-6}	3.05×10^{-6}	–	8.33×10^{-6}
3	1.57×10^{-5}	3.71×10^{-6}	6.11×10^{-6}	–	8.33×10^{-6}
4	5.23×10^{-6}	7.43×10^{-6}	6.11×10^{-6}	–	4.16×10^{-6}
5	1.31×10^{-5}	–	6.11×10^{-6}	–	2.54×10^{-6}
6	1.83×10^{-5}	7.43×10^{-6}	6.11×10^{-6}	1.62×10^{-5}	8.33×10^{-6}
7	2.35×10^{-5}	7.43×10^{-6}	3.05×10^{-6}	2.46×10^{-5}	8.33×10^{-6}

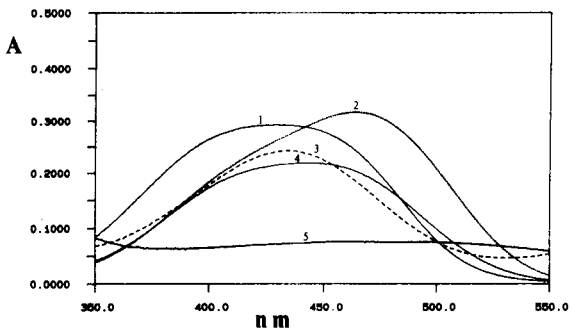

Fig. 1. Spectra obtained for (1) 1.5×10^{-5} mol l^{-1} Methyl Red, (2) 1.2×10^{-5} mol l^{-1} Methyl Orange, (3) 1.05×10^{-5} mol l^{-1} Cresol Red, (4) 1.67×10^{-5} mol l^{-1} Tropaeolin OO and (5) 1.02×10^{-5} mol l^{-1} Alizarin.

Methyl Red, Methyl Orange, Alizarin and Tropaeolin OO produces a strong spectral interference with the determination of Cresol Red at pH 7. For this reason, the determination of Cresol Red in presence of these compounds cannot be carry out directly.

Samples containing various amounts of each compound were prepared (Table 1). Also, a calibration graph for Cresol Red was prepared by dilution of a stock solution of this compound. Spectra of samples and calibration graphs were then obtained and, following the described procedure, apparent content curves for each sample were constructed (Fig. 2). As can be seen, in all instances substantial interference exists. From the values of F_{λ_i} working wavelengths were chosen following the criteria indicated earlier.

Finally, the analyte concentration was calculated for each sample using the computer program. The results obtained are given in Table 2 and, as can be seen, are in agreement with the theoretical contents in all instances.

Determination of theophylline in pharmaceuticals

The analysis of pharmaceuticals was carried out following the same procedure. The qualitative compositions of the tested pharmaceuticals are given in Table 3. The compounds present in these pharmaceuticals have absorption spectra that produces spectral interferences in the determination of theophylline. This requires the use of a strategy that allows to the elimination of the interferents.

Some samples are in the form of tablets or capsules and others as syrups. Tablets or capsules are dissolved in water or in 0.1 M NaOH when

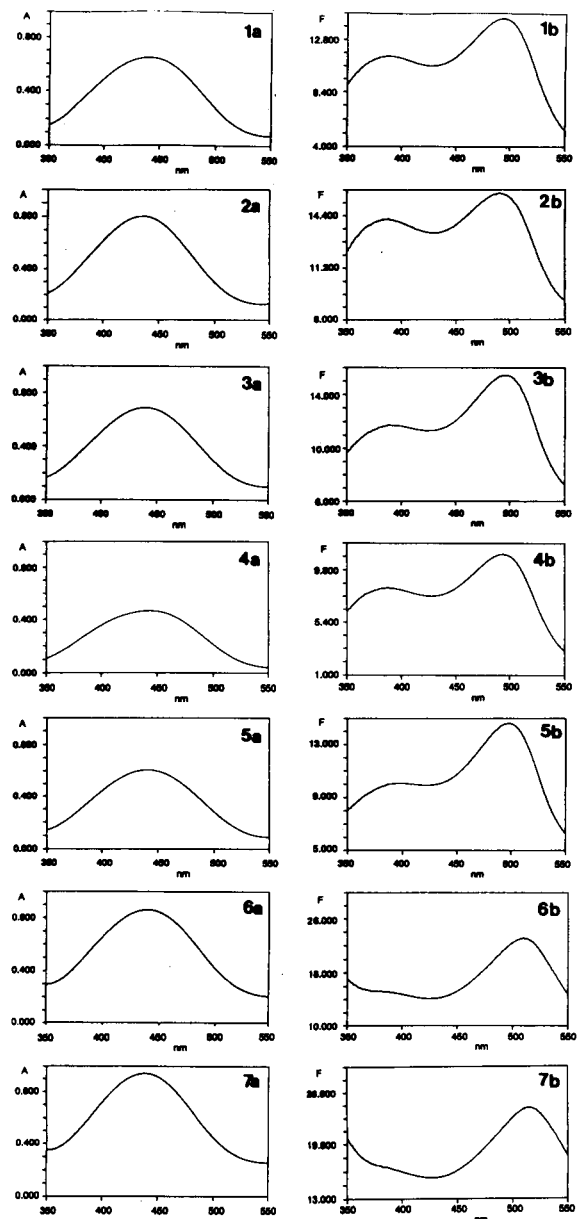

Fig. 2. (a) Spectra and (b) apparent content curves obtained for several mixtures of acid–base indicators. Compositions of samples 1–7 are given in Table 1.

TABLE 2

Results obtained for Cresol Red contents

Sample No.	Cresol Red content (mol l^{-1})		Relative error (%)
	Theoretical	Found	
1	1.05×10^{-5}	1.0×10^{-5}	−4.8
2	2.09×10^{-5}	2.0×10^{-5}	−4.3
3	1.57×10^{-5}	1.52×10^{-5}	−3.2
4	5.23×10^{-6}	5.1×10^{-6}	−2.5
5	1.31×10^{-5}	1.36×10^{-5}	+3.8
6	1.83×10^{-5}	1.93×10^{-5}	+5.5
7	2.35×10^{-5}	2.38×10^{-5}	+1.3

phenobarbital is present, and the excipient is removed by filtration. Syrops simply require dilution.

Spectra of samples and calibration graphs for theophylline, in a suitable medium for each sample, were obtained and apparent content curves of the samples were plotted (Fig. 3). Working wavelengths were then chosen and the analyte concentrations calculated for each sample. The analysis of each pharmaceutical was carried out with three replicates of three independent samples.

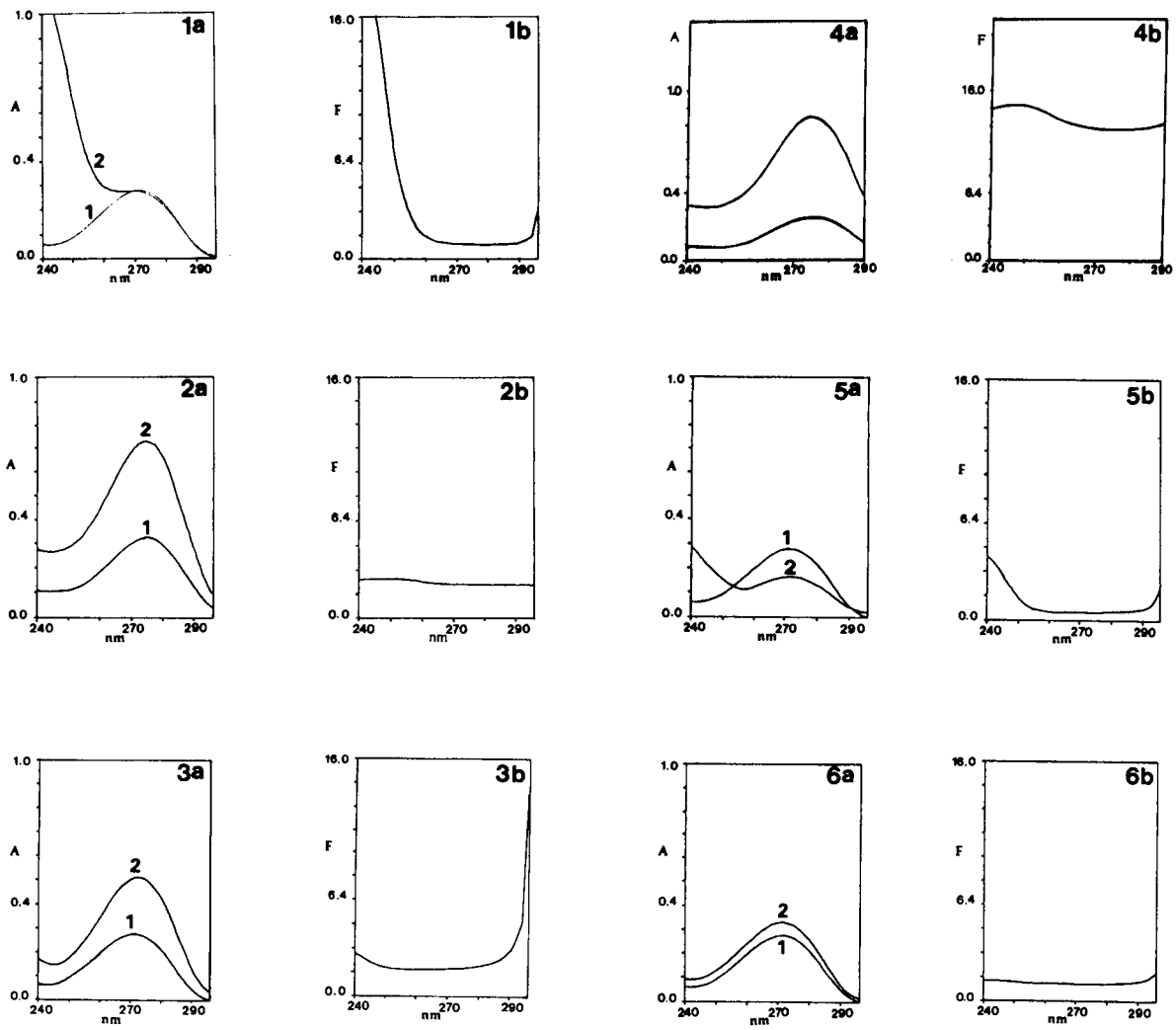

Fig. 3. (a) Spectra of samples (2) and standard solution of theophylline (1). (b) Apparent content curves obtained for pharmaceuticals. Descriptions of samples 1–6 are given in Table 3.

TABLE 3

Qualitative composition of pharmaceuticals

Sample No.	Composition	Dosage form
1	*N*-Acetyl-DL-homocysteine thiolactone + theophylline	Capsule
2	Ephedrine hydrochloride + phenobarbital + theophylline	Tablet
3	Proxyphylline + diprophylline + theophylline	Tablet
4	Ephedrine sulphate + phenobarbital + theophylline	Tablet
5	Thonzylamine hydrochloride + theophylline sodium glycinate + ephedrine + potassium iodide + menthol	Syrup
6	Ephedrine hydrochloride + theophylline + diphenhydramine hydrochloride + dexamethasone + calcium lactate	Tablet

The results obtained are given in Table 4. As can be seen, the determination of theophylline in pharmaceuticals using the proposed procedure gave good results in all instances. The relative errors are $< 10\%$.

TABLE 4

Results obtained for theophylline content in pharmaceuticals

Sample No.	Theophylline content (mg) [a]		Relative error (%)
	Theoretical	Found	
1	0.042	0.042 ±0.002	–
		0.041 ±0.002	−2.4
		0.042 ±0.004	–
2	0.173	0.165 ±0.009	−4.6
		0.16 ±0.01	−7.5
		0.166 ±0.005	−4
3	0.082	0.09 ±0.03	9.7
		0.085 ±0.006	3.6
		0.09 ±0.02	9.7
4	0.131	0.131 ±0.001	–
		0.128 ±0.001	−2.3
		0.129 ±0.003	−1.5
5	0.092	0.095 ±0.009	3.3
		0.09 ±0.01	−2.2
		0.092 ±0.004	−0.3
6	0.050	0.055 ±0.003	10
		0.054 ±0.001	8
		0.0053 ±0.002	6

[a] Amount of theophylline found per tablet or capsule or 15 ml of syrup.

Conclusions

The principal advantage of the proposed procedure is the possibility of determining one analyte in the presence of n interferents without knowing the number or nature of each of the components of the sample. Also, the method provides satisfactory results in an simple and rapid manner. The best results are obtained when the noise in determining Q, and therefore the instrumental noise, are as low as possible.

The application of the method requires a previous estimation of the shape of the spectrum of the total interferents at the working wavelengths. Hence, it is necessary to know if the total interferents provide increasing or decreasing signals in the interval of wavelengths considered. Once this fact has been established, the computational program looks for the appropriate spectrum. To establish this general behaviour of the total interferents it is only necessary, generally to make a comparison between the spectrum of the sample and that of the analyte. Hence the above condition is not a limitation for the application of the proposed procedure.

REFERENCES

1 P. Gonzalez-Hierro, M.M. Velazquez, J.M. Cachaza and L.J. Rodriguez, J. Pharm. Biomed. Anal., 5 (1987) 395.
2 J.J. Aaron and M.D. Gaye, Talanta, 35 (1988) 513.
3 L. Yiming and R. Yu, Analyst, 112 (1987) 1135.
4 H.R. Wilk and S.D. Brown, Anal. Chim. Acta, 225 (1989) 37.
5 D.G. Cameron and D.J. Moffatt, Appl. Spectrosc., 41 (1987) 539.
6 M. Llobat Estellés, R. Marin Saez and M.D. San Martín Ciges, Fresenius' J. Anal. Chem., 342 (1992) 538.
7 A.R. Maurí Aucejo, M. Llobat Estelles, R. Marín Saez, M.D. San Martín Ciges and C. Alvarez Alonso, Fresenius' J. Anal. Chem., (1993) in press.
8 R. Marín Saez, M. Llobat Estellés, M.D. San Martín Ciges and A.R. Maurí Aucejo, Anal. Lett., 26 (1992) 641.
9 M. Llobat Estellés, C. Alvarez Alonso and A.R. Maurí Aucejo, Analusis, 21 (1993) 35.

Analytica Chimica Acta, 282 (1993) 679–685
Elsevier Science Publishers B.V., Amsterdam

Discrete event simulation of an analytical laboratory

Kirk L. Shanahan

Westinghouse Savannah River Company, Savannah River Technology Center 773-41A, Aiken, SC 29808 (USA)

Roy E. Beck, Charles E. Taylor and Ronie B. Spencer

Westinghouse Savannah River Company, Defense Waste Processing Facility 704-28S, Aiken, SC 29808 (USA)

(Received 18th December 1992; revised manuscript received 24th May 1993)

Abstract

A general purpose simulation system (GPSS) discrete event simulation of the Savannah River Site Defense Waste Processing Facility Analytical Facility has been constructed. It was used to estimate laboratory analysis times at process analytical hold points and to study the effect of sample numbers on those times. Typical results are presented for three different simulations representing increasing levels of complexity, and for different sampling schemes. Example equipment utilization time plots are included. Laboratory personnel found the simulations very useful for resource and schedule planning.

Keywords: Discrete event simulation; Simulation system

The Savannah River Site (SRS) Defense Waste Processing Facility (DWPF) has been constructed to encapsulate high level radioactive waste generated during the thirty-eight years of SRS operations in canistered, highly durable glass. The canisters will eventually be shipped to a permanent waste repository for final storage. The actual glass preparation processing strategies are still under development, but the overall plan calls for a batch process with hold points at several places. Each hold point will necessitate the collection of analytical data.

Current operational plans dictate the use of statistical process control, which requires periodic characterization of variance components. The original plan required analysis of 32 samples in duplicate to determine variance components as part of the normal process operations. However, the current analytical methods were complex and contained long sample preparation steps. This led the DWPF Analytical Laboratory management to request a study of turnaround times and resource utilization, so that the laboratory's effect on overall batch cycle times could be estimated.

In a manufacturing organization, this type of study would be a typical application of the industrial engineering technique of discrete event simulation (DES). However, most chemists are never exposed to this type of computer modeling and as such are unaware of the benefits that can be obtained by the application of industrial engineering technology to the chemical laboratory. One group that has applied this technology to the analytical laboratory is that of Klaessen et al. [1]. This paper describes the application of the DES language GPSS (general purpose simulation system) [2,3] in building a model of the DWPF Analytical Laboratory Facility.

Correspondence to: K.L. Shanahan, Westinghouse Savannah River Company, Savannah River Technology Center 773-41A, Aiken, SC 29808 (USA).

BACKGROUND

Process

The DWPF process has four major subprocesses [4]. They are: caesium precipitation with tetraphenylborate, waste slurry receipt with composition/property adjustment, slurry mix preparation, and melter feeding. These subprocesses will be referred to as the PR, SRAT, SME, and MF processes, respectively.

The DWPF was not designed to allow materials to be returned to a tank once they have been transferred. Therefore, several process control hold points have been defined to avoid such situations. The PR process has four analytical hold points, the SRAT has two, the SME one, and the MF has no hold points. However the MF process does require a parallel analysis of vessel contents. In addition, many of the process steps involve evaporation and condensation, and all condensate collection tanks must be analyzed before their contents can be transferred elsewhere.

The DWPF has plans to run for about 1 1/2 years with nonradioactive feeds before beginning processing of radioactive waste. These cold runs will allow process operations to be fine tuned and any problems to be identified. Once radioactive material is introduced into the system, the facility must be operated remotely.

Analytical facility

The process chemical analyses will be performed in a small analytical facility located in the main process building. Because of the (eventual) highly radioactive nature of the samples, most of the sample collection and preparation will be done remotely, using master–slave manipulators mounted in shielded cells. The analytical facility has three sample cells where samples from various process vessels are collected. In a typical operation one vessel can be sampled from only one point in a single cell. Samples are then passed to the first of a set of three chemical cells where sample preparation and some analyses are conducted. As the samples are sequentially diluted and aliquoted to reduce the total radioactivity in the actual analysis sample, they are moved into the second and then third cells for further preparation and analysis. In many cases, the samples are diluted enough that they can be removed from the cells via a glovebox for analysis on contained instruments mounted in hoods.

The process samples are usually slurries of radioactive waste and glass-forming materials, but some samples from water condensation equipment are also submitted. The samples are usually filtered and dried, sometimes vitrified, and dissolved with sodium peroxide or acid matrices. Multiple dissolution techniques using microwave and conventional furnaces are employed.

A wide range of analytical techniques are employed, which include: inductively coupled plasma emission spectroscopy, atomic absorption spectrometry, ion chromatography, gas chromatography, liquid chromatography, ultraviolet–visible spectrophotometry, total inorganic and organic carbon analysis, pH measurement, weight percent solids and density measurement. The laboratory is equipped with one of each type of instrument.

Problem

The laboratory was requested to collect and analyze 32 samples in duplicate to establish the process' statistical characteristics for composition and weight percent solids analyses. Other analytical information needed was derived from single samples analyzed in duplicate. Each major feed composition change was to require an equivalent set of analytical results. The possibility of having to repeat the 32 samples on one additional batch per feed type was also recognized. This formed the basis of the first simulation scenario.

Simulation of the first scenario, abbreviated as the "32×2 case", showed an unacceptable batch cycle time extension due to slow laboratory turnaround times. Therefore a second scenario was investigated where only four samples were collected and each analyzed in duplicate, the "4×2 case". This scenario was found to be the maximum process load the laboratory could have without significantly impacting batch cycle times.

Model construction consisted of defining the various operational steps associated with each particular analytical method into a chain of events. The chains were then appropriately combined into blocks with multiple parallel paths

representing a major analytical set. Sampling operations were added to simulate sample collection and distribution. The analytical sets were then combined with simple time delay blocks representing the process steps into the full process model.

The initial model had many simplifying assumptions embedded in it. For example, condensate analyses were not initially considered, and technicians were considered to be fully interchangeable. Other known simplifications included: no breaks, vacations, etc. for technicians; no waste removal operations included; no equipment down-time. The effect of most of these simplifications was estimated by flat-rate increases in calculated turnaround times.

Simulations were run at two levels. Small models representing each analytical set were used to study equipment and/or technician loading during the analyses and to obtain turnaround time values. The full process model was then run to simulate the interactions produced when all major subprocesses were in operation. Comparisons of analytical set turnaround times were then made to assess any potential slowdown.

EXPERIMENTAL

The software used in this project was GPSS/PC (trademark of Minuteman software, Stow, MA) for IBM compatible computers under the DOS operating system. A 640K and an expanded memory version are supplied. Both versions have several interactive graphics windows which were useful in debugging the program and understanding what was happening during the simulation.

The full DWPF model required the use of expanded memory to run while using DOS 4.0, but a system using only DOS 5.0 had enough standard memory to run the model if it was stripped down by excluding programming statements aimed at studying queuing. The model is approximately 2000 lines long.

Resource utilization data were printed to a flat file, transferred to a MicroVAX computer, and incorporated into the RS/1 software package for analysis and presentation. The GPSS software also produces some statistical information on resource utilization which was examined.

The model was constructed before the DWPF laboratory was fully functional. Sequence diagrams showing each method's individual steps with time estimates were constructed and used as programming guides. Time estimates for operational steps requiring the use of manipulators were obtained by observing similar operations in other site laboratories conducting remote sample preparation. Instrumental analysis times were estimated from operating experience based on nonradioactive sample analysis on the same or similar equipment installed in other site laboratories. The full model used simple time delays for simulated chemical process operations. Times for these steps were obtained as best estimates from the cognizant process engineers.

RESULTS

Table 1 lists the DWPF process' sequential steps. The chemical processing step times as supplied by the process engineers are included. Times shown for the analytical steps are simulation re-

TABLE 1

DWPF process steps for the "4×2" case

Description (acronym)	Time
PR Process Step 1	90
Analytical Set 1 (PRL1)	239 (0)
PR Process Step 2	180
Analytical Set 2 (PRL2)	231 (0)
PR Process Step 3	270
Analytical Set 3 (PRL3)	111 (0)
PR Process Step 4	840
Analytical Set 4 (PRL4)	496 (19)
PR Process Step 5	60
SRAT Process Step 1	60
Analytical Set 6 (SRAT1)	846 (15)
SRAT Process Step 2	2058
Analytical Set 7 (SRAT2)	858 (11)
SRAT Process Step 3	60
SME Process Step 1	2880
Analytical Set 8 (SME)	1485 (17)
SME Process Step 2	60
MF Process Step	5160
Analytical Set 8 (MFT)	1504 (35)

TABLE 2

Simulated analytical processing times for the "4×2" case

Process	Partial - 1 Batch	Partial - 10 Batches	Full - 10 Batches
PR	1097 (12)	1242 (6)	1415 (16)
SRAT	1711 (30)	1773 (3)	1992 (16)
SME	1469 (11)	1634 (7)	1794 (31)
MF	1597 (5)	1782 (15)	1882 (23)

sults for the simple analysis set, without any other activities occurring. In the more complex analytical sets, the sample arrival to the different analytical method/preparation chains is randomized, so differing times can be obtained. The numbers presented are an average of five simulations. The standard deviations are shown in parentheses.

Table 2 presents results for three simulation cases. The "Partial - 1 Batch" case represents one batch processing through the core DWPF processes only. The "Partial - 10 Batches" case represents ten batches processing through the core processes. Thus each subprocess of the DWPF process could potentially be running at the same time. The "Full - 10 Batches" case represents the addition of some independent instrument quality control samples on periodic bases and four short analytical sets arising from overheads condensation processes. Numbers shown are time in minutes for the analytical sections of the subprocesses. A minimum of three and a maximum of five runs were used to derive this data. The standard deviation is shown in parentheses.

Figure 1 is a sequence plot spanning the full, 10 batch simulation for the "32 × 2" case. Plotted sequentially is the time each RCT subprocess analytical set required to be processed. The minimum time was 110 min, which is also the fastest allowable time. The maximum time observed was 2471 min, representing more than a twenty fold increase in processing time.

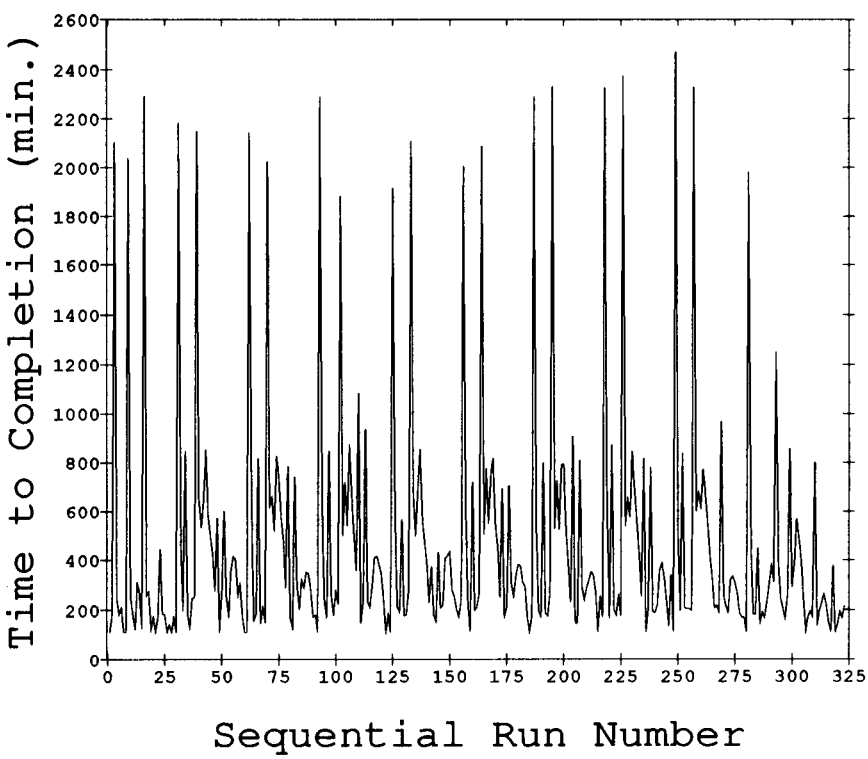

Fig. 1. Time required to complete RCT sample analyses during the "32 × 2" full (10 batch) simulation.

Resource utilization was examined for each analytical subset as well as for the overall simulation. For unique resources a line plot showing when the resource was in use was prepared and combined into one graph. Fig. 2 shows one such graph of this data for a center cut of the full 10-batch simulation. (The center cut was triggered by the beginning of the fifth batch's processing.) For multiple resources (such as technicians), a multi-valued graph was constructed, showing how many were in use at a given time. Figure 3 shows that plot for the technicians (TECHS) and laboratory information management system terminals (LIMS).

Discussion

The primary purpose of modeling the DWPF Analytical facility was to aid the facility managers in planning resource and manpower requirements. Therefore during construction of the model, weekly review meetings were held with all concerned laboratory personnel to validate any modeling assumptions. Approximately two man-weeks of time were spent in developing the original simulation. Subsequent revision for the second scenario was accomplished more quickly, but an equal time investment was spent in evaluating the impact of sample numbers.

Table 2 illustrates the effects of sample competition for the limited facility resources. When multiple batches are processed, each subprocess can be running at the same time. Thus, multiple sets of samples arrive at the same time. Quality control and condensate process operations samples further complicate the situation. Each additional sample set causes the overall process times to extend due to conflicting requests for the same resources. In some situations, extensive delays can be experienced. It is identifying these delays that most aids facility personnel in their planning activities.

For the example presented in Fig. 1, the maximum time observed to process the RCT samples was unacceptably long. Major delays are indica-

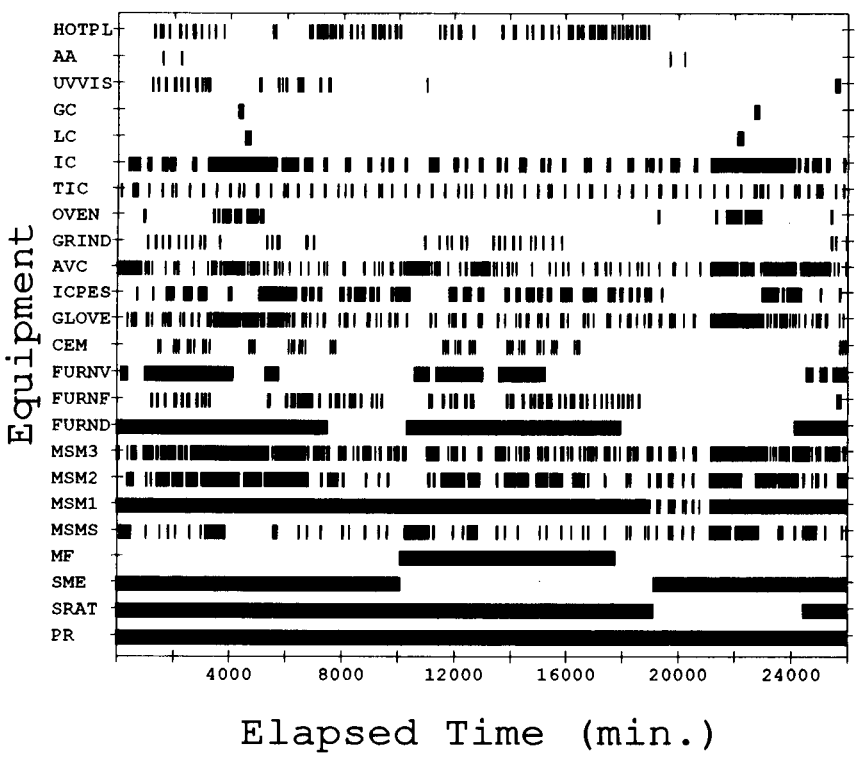

Fig. 2. Equipment utilization for a center cut of the "32 × 2" full simulation [$t(0) = 76187$ min, see Glossary for abbreviations].

tive of where the major process loads were occurring in the laboratory. A prioritization scheme could be constructed that would allow these samples to be analyzed first, thereby reducing the turnaround time to acceptable levels. This scheme could be built into the simulation to explore the effect on other sample's turnaround times.

Conclusions

Facility personnel examined utilization plots and GPSS/PC resource utility numbers to determine if enough time was available for waste removal and other omitted activities. Additional time for those activities was then included on a flat percentage basis. Between the standard and custom utility numbers and plots, facility managers were able to get a relatively clear picture of where bottlenecks were occurring. The adjusted estimates were used to estimate the laboratory's impact on the overall DWPF process schedule.

Based on these results and analysis, facility operations were slightly restructured. In some cases, alternate analysis schemes were indicated, and resources to conduct these schemes are now being developed.

Model refinement continues with limitations being addressed and alternate operating scenarios postulated. Timings are being verified by actual experience as the Laboratory comes on-line. Incorporation of random error noted in these studies will occur in a major model revision. Because of the ease with which a model can be changed, it will serve as the basis for future off-line "what-if" testing. This will serve as a guide to future equipment and procedure changes.

In conclusion, discrete event simulation has shown itself to be a valuable tool. It allows reasonable technical estimates of facility performance to be made. It simplifies the task of performance improvement by showing synergistic ef-

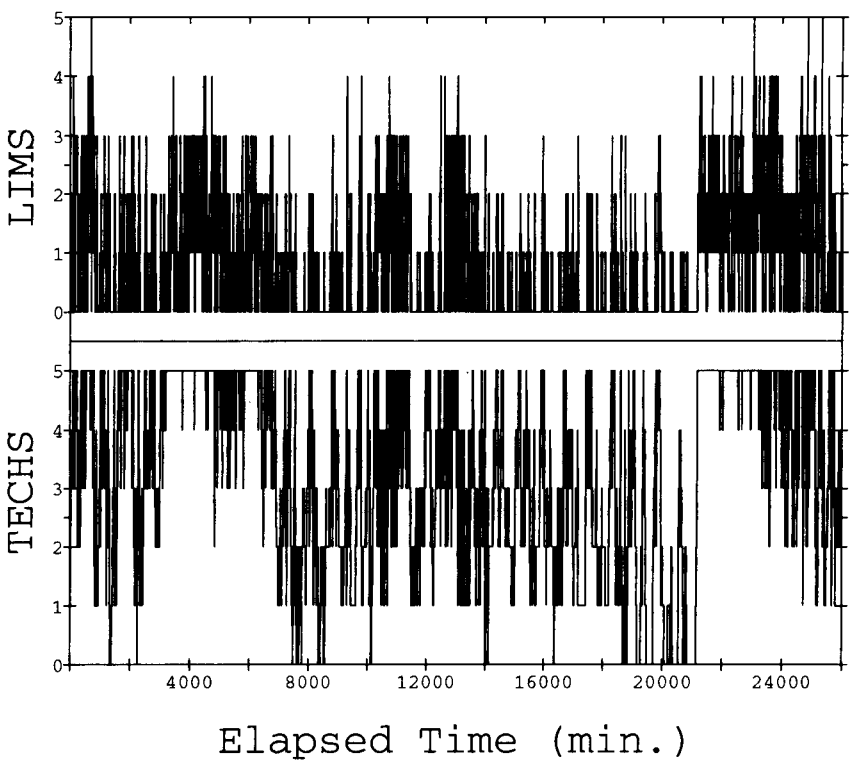

Fig. 3. Technician (lower) and LIMS (upper) utilization for a center cut of the "32 × 2" full simulation [$t(0) = 76187$ min].

fects on the computer, before equipment is purchased or replaced and/or procedures are altered. A refined, current laboratory model represents a cost-effective planning tool.

This paper was prepared in connection with work done under Contract No. DE-AC09-89SR18035 with the U.S. Department of Energy.

GLOSSARY

Acronym	*Definition*
AA	atomic absorption (spectophotometer)
AVC	automated volatility computer
CEM	microwave furnace
FURND	muffle furnace for drying
FURNF	muffle furnace for fusion
FURNV	muffle furnace for vitrification
GC	gas chromatograph
GLOVE	glovebox
GRIND	sample grinder
HOTPL	hot plate
IC	ion chromatograph
ICPES	inductively coupled plasma emission spectrometer
LC	liquid chromatograph
LIMS	laboratory information management system terminals
MF	melter feed (process)
MSMS	master–slave manipulator in sample cell
MSM1	master–slave manipulator in cell 1
MSM2	master–slave manipulator in cell 2
MSM3	master–slave manipulator in cell 3
OVEN	sample drying oven
PR	precipitate reactor
RCT	recycle condensate tank
SME	slurry mix evaporator
SRAT	slurry receipt and adjustment tank
TIC	total inorganic carbon/total organic carbon (analyzer)
UVVIS	ultraviolet–visible (absorption spectophotometer)

REFERENCES

1 J. Klaessens, B. Vandeginste and G. Kateman, Anal. Chim. Acta, 223 (1989) 205; and references therein.
2 T.J. Schriber, Simulation Using GPSS, Wiley, New York, 1974.
3 K.A. Dunning, Getting Started in GPSS, Engineering Press, San Jose, CA, 1985.
4 A.S. Choi, J.R. Fowler, R.E. Edwards and C.T. Randall, in Proceedings of the 1991 Joint International Waste Management Conference, Seoul, Vol. 2, Korean Nuclear Society, Seoul, 1991, p. 33.

Analytica Chimica Acta, 282 (1993) 687–693
Elsevier Science Publishers B.V., Amsterdam

Pulsed-laser fluorescence detection in capillary zone electrophoresis of some banned substances in sport

E. Gonzalez, R. Montes and J.J. Laserna

Department of Analytical Chemistry, Faculty of Sciences, University of Malaga, 29071-Malaga (Spain)

(Received 9th March 1993; revised manuscript received 24th May 1993)

Abstract

A system of capillary zone electrophoresis with pulsed-laser fluorescence detection is presented. A pulsed nitrogen laser delivering 2.5 mJ per pulse at 337.1 nm is proposed as a light source. Parameters that influence the detector performance were studied. Three drugs (triamterene, acebutolol and bendroflumethiazide) were determined to evaluate the laboratory-constructed capillary electrophoresis system. The technique was applied to human urine.

Keywords: Electrophoresis; Fluorimetry; Pharmaceuticals; Pulsed-laser detection

Capillary zone electrophoresis (CZE) is an important technique that provides a high separation efficiency with a short time of analysis. Compared with liquid chromatography, CZE is a much simpler instrumental approach, allowing extremely high separation efficiencies from simple atomic ions [1] to large DNA fragments [2–8]. A challenging issue in CZE is the detection and monitoring of the analytes after they have been separated, as sub-nanolitre volumes are involved in the detection process. Conventional absorbance detectors are not sensitive enough for such small sampling volumes owing to the short optical path length. The detection limits of typical UV–visible absorbance detectors equipped with commercial CZE instruments are about 10^{-3} absorbance [9].

The laser has been demonstrated to be an ideal light source for CZE, as its high irradiance and spatial coherence facilitate the delivery of large photon fluxes on small volume samples. So far, laser-based detectors for CZE have used continuous-wave (CW) laser sources, including the He–Cd laser (lines at 325 and 442 nm) and the argon ion laser (lines at 488 and 514.5 nm) [9–14]. A significant drawback to CW visible lasers is that only a limited number of molecular species absorb in the spectral region covered. An interesting alternative is offered by the pulsed nitrogen laser, as its output at 337.1 nm is able to excite a range of organic molecules. It is a long-lasting device requiring only occasional cleaning of the optics. In addition, enormous laser energy can be concentrated into a small sample volume. For instance, a modest 2.5 mJ, 10 ns pulse focused to a 75-μm diameter spot (the typical diameter of a capillary) results in an irradiance at the focal area of 5.6×10^9 W cm^{-2}. Such a great photon flux is capable of providing detection of a single molecule in the focal region. Pulsed lasers require gated detection devices for signal recovery and accurate timing for synchronization of the excitation–detection cycles. Boxcar averagers are state-of-the-art instruments for this purpose.

In this paper, a laboratory-constructed CZE system is presented. A pulsed nitrogen laser (337.1 nm) was used as an excitation source. The use of

Correspondence to: J.J. Laserna, Department of Analytical Chemistry, Faculty of Sciences, University of Malaga, 29071-Malaga (Spain).

pulsed lasers for detection in CZE has not been reported previously. Fluorescence was detected with a fast silicon photodiode and processed with a boxcar averager. The performance of the system was evaluated by using Rhodamine 6G as a model compound. The system was also evaluated for the separation and detection of fluorescent drugs banned in sport (triamterene, acebutolol and bendroflumethiazide). The analytical figures of merit and the analysis of urine samples are discussed.

EXPERIMENTAL

Apparatus

A schematic diagram of the capillary electrophoresis apparatus is illustrated in Fig. 1. A Laser Photonics Model UV 12 pulsed nitrogen laser (337.1 nm, 2.5 mJ, pulse width 10 ns) was used as an excitation source. The central part of the laser beam was isolated with an iris diaphragm (8 mm diameter aperture) and focused on to the capillary with a Suprasil $f/1.5$, 20-mm diameter lens. Fluorescence was collected perpendicular to the capillary and the exciting beam (ortho configuration) with a 3-cm focal length microscope objective. Fluorescence was spectrally filtered to reject the laser scattered light with a 10-mm path length piece of Plexiglas. This proved more effective for UV light rejection than, for instance, carbon disulphide or 1×10^{-3} M potassium dichromate solution at a similar path length. Fluorescence was detected with a fast silicon pin photodiode. The photoactive area was ca. 1 mm^2. A laboratory-constructed voltage-mode preamplifier was used to convert the photocurrent to voltage. The gain of the preamplifier was 10^7 V A^{-1}. The preamplifier output was acquired with a Stanford Research Systems SR250 boxcar averager. A Tektronix 2245A 100-MHz oscilloscope was used to monitor the waveform magnitude. The oscilloscope was also used to monitor the setting of the gate width and delay of the boxcar system. The aperture delay was 8 μs and the aperture duration was 600 ns, which gave the best signal-to-noise ratio. The oscilloscope and the boxcar were optically triggered with a beam deflected from the exciting laser and a fast photodiode. The analogue signal from the boxcar was

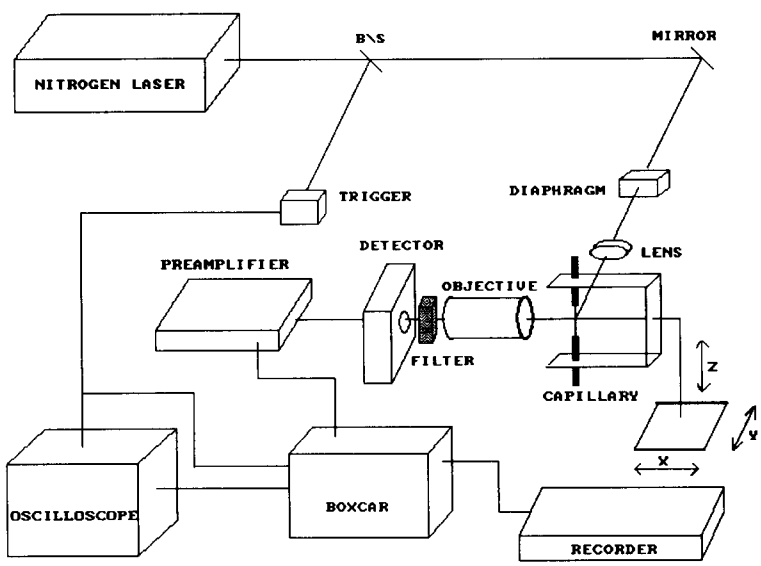

Fig. 1. Schematic diagram of the CZE apparatus. B/S = beam splitter.

recorded with a Perkin-Elmer Model 023 chart recorder.

Electrophoresis was driven by a 30 000-V high-voltage power supply [Spellman High Voltage Electronics (Plainview, NY) Model CZE 1000 R; current range 0–300 μA; voltage range 0–30 kV] and performed in a 100 cm $\times$ 75μm i.d. polyamide-coated fused-silica capillary tube (Polymicro Technologies, Phoenix, AZ). Electrical connection at both ends of the capillary was effected with platinum electrodes immersed in small-volume reservoirs. The sample was introduced via electromigration of the sample solution on to the capillary with a 10-kV injection applied for 10 s.

Chemicals and procedure

All chemicals used were of analytical-reagent or research grade. The drugs employed as reference compounds were from Sigma. Water was demineralized (Millipore) and all samples were dissolved in the zone buffer solution [Titrisol (pH 8), Merck]. Standard solutions of drugs were prepared at different pH [buffer systems contained 20% (v/v) methanol to help to dissolve the drugs]. Human urine samples from volunteers not receiving any kind of pharmaceutical therapy were analysed. The urine from a patient receiving a daily dose of triamterene was also analysed. Prior to use, the capillary was vacuum-cleaned successively with 0.1 M sodium hydroxide (3 min), distilled water (3 min) and buffer solution (5 min).

RESULTS AND DISCUSSION

Fluorescence detection

Boxcar averagers provide the potential to increase the signal-to-noise ratio (S/N) in a pulsed-laser experiment by averaging a number of data points before the output signal is sent to the recording device. As one averages many noisy samples of a signal, the average will converge to the mean value of the signal, and the noise will average to zero. However, averaging a large number of points in high-efficiency CZE may result in a decrease in peak height, as large signal gradients occur close to the peak concentration maximum. This effect is illustrated in Fig. 2a for the injection of 1×10^{-6} M Rhodamine 6G (R6G),

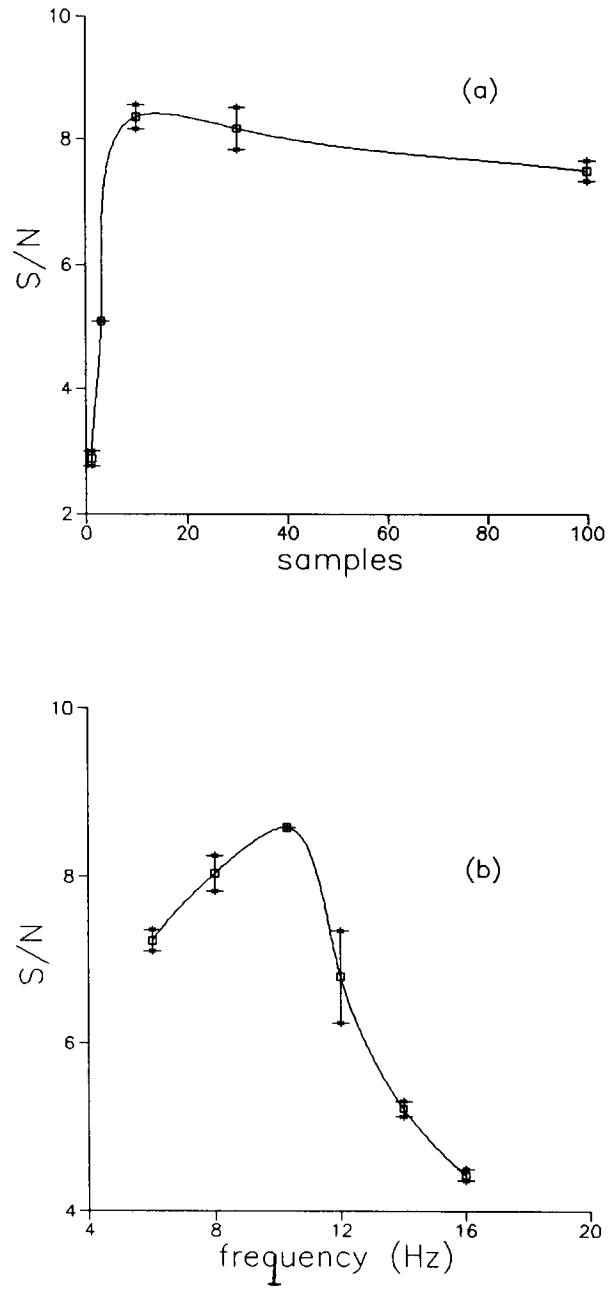

Fig. 2. Variation of S/N with (a) the number of samples in the boxcar and (b) the laser frequency. Error bars represent the standard deviations for three replicate measurements.

used as a model compound. As expected, S/N increases increasing number of data samples. However, averaging more than ten samples results in decreased S/N values as the points defining the peak maximum are averaged with points of fewer intensity. The time to acquire a given number of data points can be reduced by increasing the excitation frequency, i.e., by increasing the laser repetition rate. Figure 2b shows the effect of the laser frequency on S/N. The optimum laser frequency is 10 Hz. At higher repetition rates S/N degrades owing to laser flicker noise. The combination of ten averaged points and 10 Hz results in one point being sent to the output device each second. This value is adequate for most experiments on high-efficiency CZE.

Figure 3 shows the dependence of the R6G peak height on injection voltage, migration voltage and injection time. With increasing injection voltage and injection time the peak height increased whereas it decreased with increasing migration voltage. The reason for this is that as the migration voltage increases, the residence time of the sample segment on the detector decreases. Consequently, for a given laser repetition rate, the number of data points defining the peak profile decreases, resulting in a smaller average signal. Unfortunately, the parameters that enhanced detection also caused a decrease in efficiency. For instance, the peak width at half maximum increased linearly with increasing injection time, whereas it decreased with increasing migration voltage in the range 5–30 kV. Hence some compromise between detection power and separation efficiency has to be reached.

Effect of pH on separation of drugs in CZE

Three drugs (triamterene, bendroflumethiazide and acebutolol) were determined to evaluate the laboratory-constructed capillary electrophoresis system. The effect of pH on the separation (migration time), efficiency (peak width) and detection (peak height) of the three drugs was evaluated. The results are illustrated in Fig. 4. It is apparent that for triamterene the migration time and the peak height are favourable at basic pH values, whereas maximum efficiency is achieved

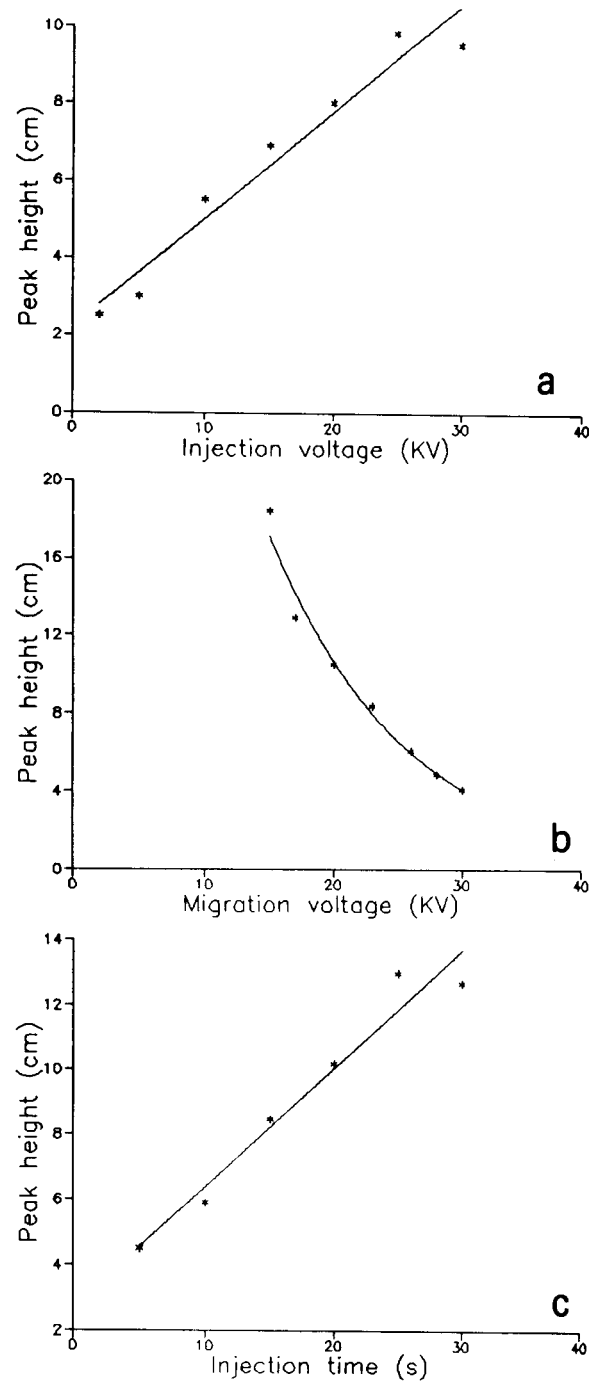

Fig. 3. Variation of peak height with injection voltage (top), migration voltage (centre) and injection time (bottom). Rhodamine 6G concentration 1×10^{-6} M.

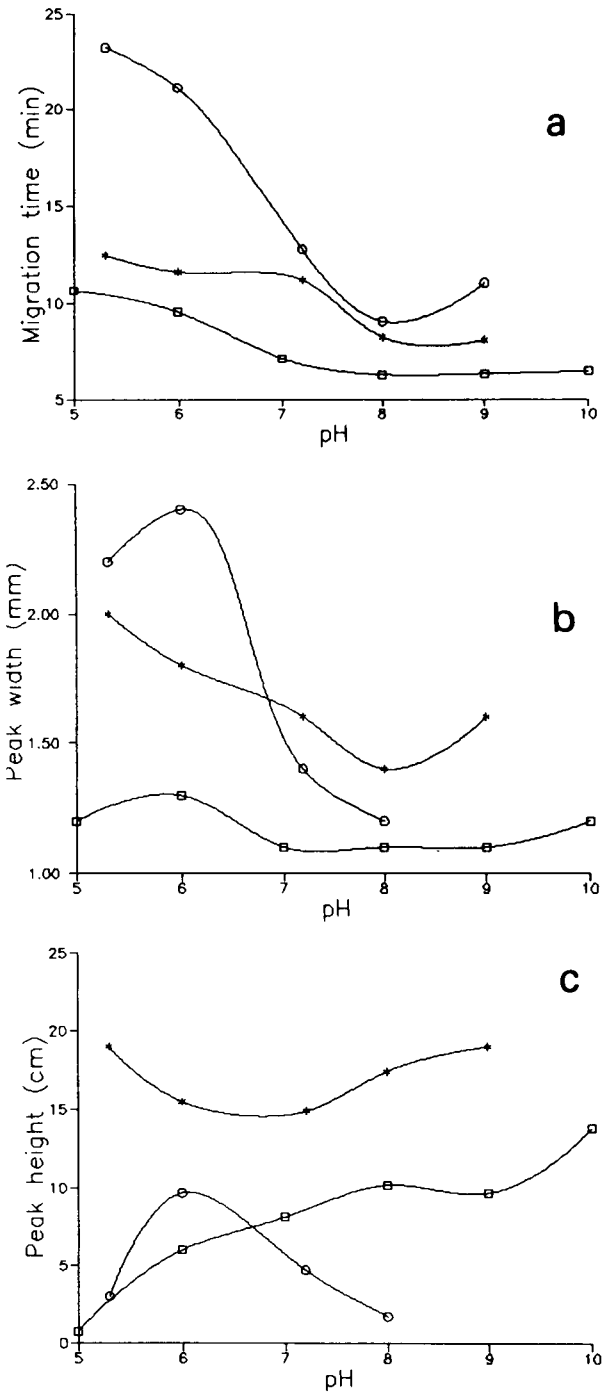

Fig. 4. Variation of migration time (top), peak width (centre) and peak height (bottom) with pH for (*) 1×6^{-6} M triamterene, (○) 3×10^{-5} M bendroflumethiazide and (□) 1×10^{-4} M acebutolol.

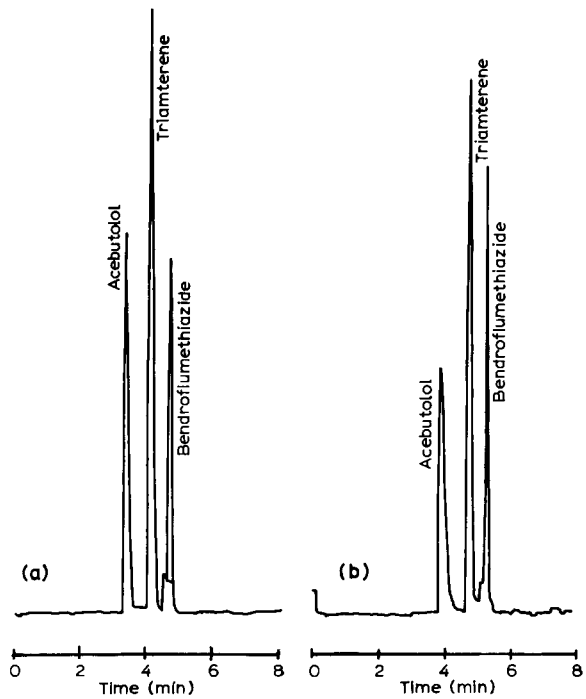

Fig. 5. Direct fluorescence detection by CZE. (a) Electropherogram of a standard containing acebutolol (1×10^{-4} M), triamterene (1×10^{-6} M) and bendroflumethiazide (3×10^{-5} M); (b) electropherogram of spiked urine.

at pH 8. For bendroflumethiazide, the migration time and peak width are minimum at pH 6. The best separation and efficiency parameters for acebutolol occur at pH 10. As a compromise between detectability and speed of analysis, further studies were conducted at pH 8. Figure 4 shows that a greater separation of the three drugs would occur, for instance, at pH 9. However, the high efficiency provided by CZE allows a fairly good separation at pH 8 (see Fig. 5) in a shorter analysis time.

Analytical figures of merit

Table 1 summarizes the limits of detection (LOD) and reproducibilities for three migration parameters (peak height, migration time and peak width) of the CZE method for the drugs studied. The LOD for triamterene (0.31 fmol) is about two orders of magnitude lower than that for acebutolol (88 fmol) and bendroflumethiazide (18

TABLE 1

Analytical figures of merit of the CZE determination of some drugs

Drug	LOD (mol) [a]	R.S.D. (%) [b]		
		Peak height	Migration time	Peak width
Triamterene	3.1×10^{-16}	5.8	1.5	10.2
Acebutolol	8.8×10^{-14}	5.6	2.1	12.1
Bendroflu-methiazide	1.8×10^{-14}	4.1	2.4	14.1

[a] Limit of detection for $S/N = 2$. [b] Relative standard deviation for $n = 5$

fmol). In addition to variations in the fluorescence quantum yields, the reason for this difference is the lack of tunability of the nitrogen laser, which prevents effective excitation of the last two drugs at 337.1 nm. The relative standard deviation of the measurements is about 5%, and is limited by flicker noise in the laser source. The reproducibility of the migration times is satisfactory. The precision of the peak width measurements is poorer and is related to the use of a graphical procedure for width calculation. Analogue-to-digital conversion of the boxcar output would allow data processing using a standard computer program and a improvement in peak width evaluation.

Separation and urine analysis

The recorder output for the analysis of mixtures of the three drugs is illustrated in Fig. 5. Human urine samples were spiked with three drugs of interest and analysed by CZE as proposed here. Figure 5a shows the separation of acebutolol, triamterene and bendroflumethiazide in a standard solution at pH 8. The three drugs were separated in 5 min. It should be noted that the baseline was restored after each component had passed through the detector. Figure 5b shows the electropherogram corresponding to a urine sample spiked with the three drugs. No sample conditioning was necessary, urine being injected directly into the capillary by electromigration. For acebutolol and, to a lesser extent, triamterene, the efficiency was lower than that obtained for drug standards. However, the separation was still satisfactory. Figures 5a and b also show that a small drift in migration time occurs when the drugs are injected in urine. The drift to longer migration time was reproducible from run to run. No laser-induced fluorescence peaks were observed for a blank urine, which indicates the suitability of the detector for direct urine analysis.

The electropherogram of a urine sample from a patient receiving triamterene medication is presented in Fig. 6a. The peak at 4.8 min corresponds to triamterene, whereas that at 6.1 min is due to a fluorescent drug or metabolite present in this sample. The triamterene concentration was ca. 3×10^{-6} M (0.76 μg ml^{-1}) as compared with the peak height of a triamterene standard in urine (Fig. 6b).

CZE is concluded to be a viable separation method for the direct analysis of urine samples. The absence of the column filling required in LC and the peak-free baseline provided by urine when fluorescence detection is used make sample preconditioning unnecessary in CZE. In spite of the complexity of the instrumental set-up, pulsed-laser fluorimetry is a feasible detection scheme. LOD values in the femtomole range seem to be readily achievable by this approach.

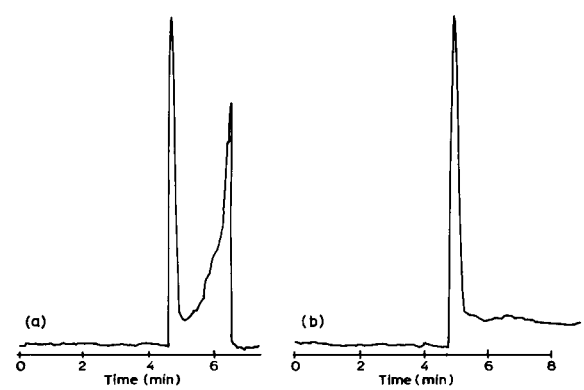

Fig. 6. Electropherogram of a urine sample from a patient receiving triamterene medication (left) compared with the peak height of a triamterene standard (3×10^{-6} M) in urine (right).

REFERENCES

1 L. Gross and E.S. Yeung, J. Chromatogr., 480 (1989) 169.
2 A.S. Cohen, D.R. Najarian, J.A. Smith and B.L. Karger, J. Chromatogr., 458 (1989) 323.
3 M. Zhu, D.L. Hansen, S. Burd and F. Gannon, J. Chromatogr., 480 (1989) 311.
4 D.N. Heiger, A.S. Cohen and B.L. Karger, J. Chromatogr., 516 (1990) 33.
5 H.E. Schwartz, K. Ulferder, F.J. Sunzeri, M.P. Busch and R.G. Brownlee, J. Chromatogr., 559 (1991) 267.
6 K.J. Ulferder, H.E. Schwartz, J.M. Hall and F.J. Sunzeri, Anal. Biochem., 200 (1992) 260.
7 A. Guttman and N. Cooke, Anal. Chem., 63 (1991) 2038.
8 M. Strege and A. Lagu, Anal. Chem., 63 (1991) 1233.
9 T. Odake, T. Kitawori, and T. Samada, Anal. Chem., 64 (1992) 2870.
10 H. Swerdlow, J.Z. Zhang, D.Y. Chen, H.R. Harke, R. Grey, S. Wu and N.J. Dovichi, Anal. Chem., 63 (1991) 2835.
11 J.A. Taylor and E.S. Yeung, Anal. Chem., 64 (1992) 1741.
12 F. Maystre and A.E. Bruno, Anal. Chem., 64 (1992) 2885.
13 G.A. Marsch, R. Jankowiak, J.H. Farhat and G.J. Small, Anal. Chem., 64 (1992) 3038.
14 T.T. Lee and E.S. Yeung, Anal. Chem., 64 (1992) 3045.

Analytica Chimica Acta, 282 (1993) 695–701
Elsevier Science Publishers B.V., Amsterdam

Chemiluminescence investigation of the interaction of metalloporphyrins with nucleic acids

Yun-Xiang Ci, Yuan-Gang Zheng, Jian-Ke Tie and Wen-Bao Chang

Department of Chemistry, Peking University, Beijing 100871 (China)

(Received 13th January 1993; revised manuscript received 21st May 1993)

Abstract

The interaction of water-soluble cationic porphyrin *meso*-tetrakis(4-*N*-methylpyridinyl)porphyrin (TMPyP) manganese derivatives with DNA was demonstrated by their catalytic activity on the luminol–H_2O_2 chemiluminescence (CL) system. The catalytic activity of Mn-TMPyP on the CL reaction was markedly enhanced when the complex was bound to DNA. The native form of DNA and thermally denatured DNA show the same degrees of enhancement. Different degrees of enhancement were obtained when Mn-TMPyP interacted with RNA and polynucleotides, whereas the interaction of nucleotides and bases with Mn-TMPyP had no effect on its catalytic activity. To examine the effect of the peripheral group of the porphyrin on its bonding properties, the interaction of manganese tetrakis(4-aminophenyl)porphyrin (Mn-$TPPA_4$), manganese tetrakis(carboxylphenyl)porphyrin (Mn-$TPPC_4$), manganese tetrakis(sulphophenyl)porphyrin (Mn-$TPPS_4$) and manganese tetrakis(4-trimethylaminophenyl)porphyrin (Mn-TAPP) with DNA was tested. Only the Mn-$TPPA_4$-catalysed CL reaction was significantly enhanced. The effects of the native form of DNA and thermally denatured DNA on the Mn-$TPPA_4$-catalysed CL reaction were very different to that on the Mn-TMPyP-catalysed CL reaction. With a fixed concentration of Mn-TMPyP there was a saturated concentration of DNA with respect to the metalloporphyrin (M-P). The binding number of M-P to DNA was estimated. Optimum conditions of the M-P–DNA complex-catalysed luminol CL reaction were evaluated by using a flow-injection system. The use of the analytical parameters of the phenomenon as a means of determining DNA was examined. The detection limit (signal-to noise ratio > 3) of DNA was 0.20 ng ml^{-1}. The relative standard deviation ($n = 11$) of the determination of 10 ng ml^{-1} DNA was 2.6%.

Keywords: Chemiluminescence; Flow injection; Metalloporphyrins; Nucleic acids

Because of their interesting chemical properties and biological importance, porphyrins (P) and metalloporphyrins (M-Ps) are among the most interesting natural products. Examples include their vital functions in haemoproteins, cytochromes, catalases, peroxidases and reductases as the prosthetic groups for a host of naturally occurring enzymes and proteins [1]. Chemists and biologists have often attempted to mimic the biological properties of such natural systems [2]. M-Ps have been widely used in the chemical modelling of cytochrome P-450 [3], peroxidase [4] and catalase [5]. The successful association of various oxygen atom donors (hydrogen peroxide, sodium hypochlorite, alkyl hydroperoxides or potassium peroxodisulphate) with synthetic M-Ps led to a better understanding of the chemistry of metal–oxo species and their implications in those enzymes. Regarding applications in analytical chemistry, M-Ps have been used successfully as mimetic peroxidase in calorimetric [6], fluorimetric [7] and chemiluminescent [8] analyses.

In addition to the use of M-P complexes as biomimetic catalysts in the oxygenation of hydrocarbons, interactions of M-Ps with nucleic acids have also been the subject of a number of investi-

Correspondence to: Yun-Xiang Ci, Department of Chemistry, Peking University, Beijing 100871 (China).

gations. The DNA affinity of these flat tetrapyrrolic macrocycles is very high. The mode of M-P binding to DNA depends on many factors, e.g., ionic strength, porphyrin to base-pair ratio and mainly the porphyrin geometry. The size and charge of peripheral groups attached at the *meso* position of tetraarylporphyrins and the presence or absence of axial ligands on the inserted metals determine the interaction site on the polynucleotide. The most actively studied DNA-binding M-Ps are metal complexes of the tetracationic water-soluble compound *meso*-tetrakis(4-*N*-methylpyridinyl)porphyrin (TMPyP) [9]. Several exhaustive reviews in this field are available [10,11]. Regarding the binding mode of TMPyP derivatives, TMPyP itself is an intercalating agent, as are its metallated derivatives, such as Cu(II), Ni(II) and Pd(II) derivatives, whereas Mn(II), Fe(II), Co(III) and Zn(II) complexes of TMPyP bind to the outside of DNA with a significant preference for A–T sequences compared with G–C sequences [9].

In this work, the interaction of metallated TmPyP derivatives with DNA were studied by examining the catalytic activity of Mn-TMPyP on the luminol–H_2O_2 CL reaction. The presence of DNA can significantly enhance the Mn-TMPyP-catalysed CL reaction. The use of this phenomenon as a means of determining DNA was examined.

EXPERIMENTAL

Reagents

Calf thymus DNA (CT DNA) and yeast RNA were purchased from Hua-Mei Biochemical, poly[A], -[G], -[U], -[C], -[AG], and -[AGU] and luminol from Sigma Chemical and nucleotides and bases from Shanghai Biochemicals. All other reagents were of analytical-reagent grade from Beijing Chemical Works. All aqueous solutions were prepared with doubly distilled water.

Stock standard solutions of CT DNA (400 μg ml^{-1}, 1.3×10^{-3} M base concentration), polynucleotides (100 μg ml^{-1}), nucleotides (1 mg ml^{-1}) and bases (200 μg ml^{-1}) were prepared by dissolving the samples in water and stored at 4°C. A working standard solution of luminol was prepared by diluting the stock standard solution (2.5×10^{-2} M in 0.10 M NaOH) with 0.10 M Na_2CO_3–$NaHCO_3$ buffer (pH 10.50). Metalloporphyrins used in the study were prepared as reported previously [12,13].

Apparatus

The flow system used for flow-injection analysis was identical with the system used previously [12]. Luminol and H_2O_2 reagent solutions were pumped (4.0 ml min^{-1} for each solution) and mixed through a mixing coil (150×1 mm i.d.) by one peristaltic pump of an intelligent flow-injection sampler (Xi'an Spring Institute) and delivered directly to the flow cell. The catalyst solutions were pumped by another pump and a certain amount of the solution (150 μl) was injected into the luminol–H_2O_2 stream by the solenoid valve automatically. The CL produced was monitored by a GD-1 luminometer (Northwest Research Institute of Geology) and the peak height of the signal was recorded with a Type 3056 pen recorder.

Ultrasonic denaturation of DNA was performed in a Model CQ250 bath-type cleaning sonicator (Shanghai Ultrasonic Instrument Factory).

Procedures

Interactions of M-Ps with DNA, polynucleotides, nucleotides and bases were performed in distilled water. Solutions of 2×10^{-8} M Mn-TMPyP and 1 μg ml^{-1} DNA were reacted as the final concentrations in a 5-ml volumetric flask and the mixture was used as the catalyst solution to optimize the CL reaction conditions. The optimum pH was obtained by varying the pH of the luminol–H_2O_2 stream with 0.10 M carbonate buffer.

RESULTS AND DISCUSSION

Optimization of the enhanced CL reaction conditions

The optimum pH of the DNA-enhanced luminol–H_2O_2–Mn-TMPyP CL reaction was ob-

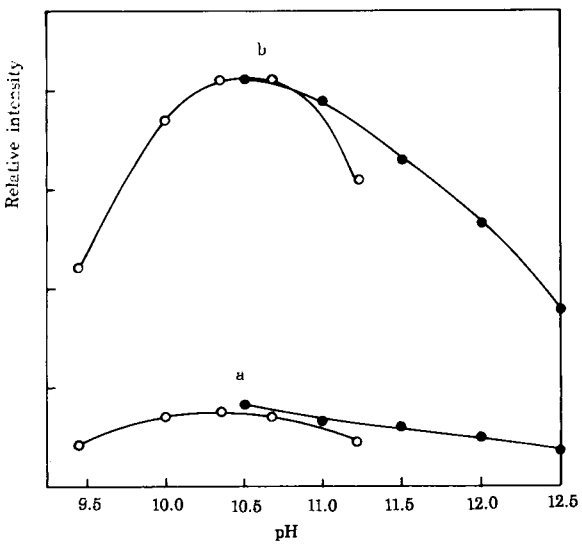

Fig. 1. Effect of pH on (a) Mn-TMPyP-catalysed and (b) DNA-enhanced luminol–H_2O_2 CL reactions. ○ = Na_2CO_3–$NaHCO_3$ buffer; ● = $NaHCO_3$–NaOH buffer. Luminol, 2.5×10^{-4} M; H_2O_2, 0.01 M; Mn-TMPyP, 2×10^{-8} M; DNA, 1 μg ml^{-1}.

tained by varying the pH of the luminol–H_2O_2 stream. For buffer control, 0.10 M Na_2CO_3–$NaHCO_3$ (pH 9.46–11.22) and $NaHCO_3$–NaOH (pH 10.50–12.50) buffers were used. Figure 1 shows the effect of pH on the relative CL intensity in the presence and absence of DNA. At pH 10.50 there is a relatively high enhanced CL signal whereas the unenhanced CL intensity is relatively low. Therefore, a buffer of pH 10.50 (0.10 M Na_2CO_3–$NaHCO_3$) was selected for use in subsequent studies.

In an attempt to establish the optimum pH for the interaction of M-Ps with DNA, 0.05 M barbital–HCl buffer (pH 6.50–8.20) was used for buffer control in DNA and Mn-TMPyP solution. No enhancement was found which was considered as the effect of ionic strength. Pasternack et al. [14] have reported that the binding constant of M-P to nucleic acids decreases with increasing ionic strength. Therefore, the interaction of DNA was performed in distilled water.

The effect of luminol concentration on the CL reaction in the presence and absence of DNA was examined by fixing the concentration of H_2O_2, Mn-TMPyP and DNA at 0.01 M, 2×10^{-8} M and 1 μg ml^{-1}, respectively. The pH of the luminol solution was fixed at 10.50. The luminol concentration was varied from 2.5×10^{-6} to 5×10^{-4} M. As the luminol concentration increased, the relative intensity increased rapidly. At luminol concentrations $> 7.5 \times 10^{-5}$ M, the ratio of the relative CL intensity in the presence and absence of DNA remained the same. In order to obtain an easily detectable CL signal, 2.5×10^{-4} M luminol was chosen as the optimum concentration.

Using the optimum conditions established, the effects of H_2O_2 concentration on the Mn-TMPyP-catalysed and DNA-enhanced CL reaction were examined. The results are shown in Fig. 2. An H_2O_2 concentration of 0.03 M was selected as the optimum concentration in further studies.

Interaction of metalloporphyrin with nucleic acid

The M-Ps extensively used for the DNA interaction study were metallated TMPyP derivatives. As the complexes are devoid of hydrogen bond donor and acceptor possibilities, it was proposed

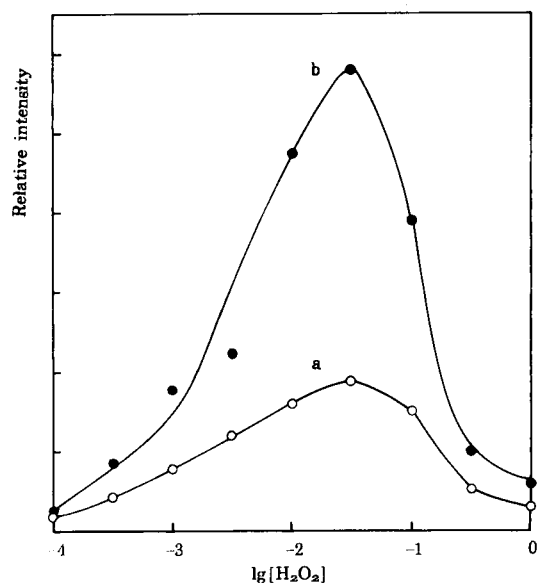

Fig. 2. Effect of H_2O_2 concentration on (a) Mn-TMPyP-catalysed and (b) DNA-enhanced CL reactions. Luminol, 2.5×10^{-4} M; Mn-TMPyP, 2×10^{-8} M; DNA, 1 μg ml^{-1}; pH, 10.50.

TABLE 1

Enhancement effects of DNA, polynucleotides, nucleotides and bases on M-P-catalysed luminol CL reaction, expressed as relative DL intensities (arbitrary units) [a]

Parameter [b]	Blank	RNA	DNA	Poly	[A]	[G]	[U]	[C]	[AG]	[AGU]
I_{CL1}	10.0	48.0	49.0		60.0	65.0	60.0	35.0	51.0	51.0
I_{CL2}	8.00	45.0	45.5		40.0	43.0	45.0	46.0	38.5	38.5
	Nucleotides				Bases					
I_{CL1}	10.5				9.5					
I_{CL2}	8.00				8.5					

[a] Concentrations of DNA, RNA, polynucleotides, nucleotides and bases are 1 μg ml^{-1}. Nucleotides include AMP, GMP, UMP, TMP, dAMP, dCMP, GTP and ATP. Bases include A, G, U, C and T. Mn-TMPyP, 2×10^{-8} M. [b] I_{CL1} = Mn-TMPyP-catalysed CL system; I_{CL2} = Mn-TPPA$_4$-catalysed CL system.

that electrostatic and steric effects associated with the minor groove, one of the two grooves of B-form DNA, are the factors controlling specificity. For the metallated TMPyP derivatives three modes of binding between DNA and M-P complexes have been recognized: intercalated when M-P do not have axial ligands; outside DNA binding for complexes with axial ligands; and minor groove binding in the case of Mn-TMPyP [2].

As Mn-TMPyP has a high affinity for nucleic acids and a high catalytic activity in the luminol–H_2O_2 CL reaction, it was used in the CL study of the interaction of M-P with DNA. Under the optimum conditions obtained, interactions of Mn-TMPyP with CT DNA and yeast RNA were examined by using the Mn-TMPyP-catalysed CL reaction. Both of them enhanced the Mn-TMPyP-catalysed CL significantly. In order to obtain additional information on the enhancement mechanism, the effects of polynucleotides, nucleotides and bases on the Mn-TMPyP-catalysed CL reaction were examined. The results are summarized in Table 1. No enhancement occurred for nucleotides and bases and polynucleotides showed different degrees of enhancement.

As mentioned above, the size and charge of peripheral groups attached at the *meso* position of the M-P are also of importance for DNA interaction. Therefore, the interaction of DNA with Mn-TPPS$_4$, Mn-TPPC$_4$, Mn-TPPA$_4$ and Mn-TAPP was examined under the same conditions as for Mn-TMPyP. Only the Mn-TPPA$_4$-catalysed CL reaction was enhanced by DNA.

Denaturation experiment

In order to compare the interactions between M-Ps and natural and denatured DNA, the native form of DNA was denatured either by incubating it at 100°C for 20 min followed by cooling in ice–water or by sonication in a bath-type sonicator for 10 min. The interactions of the denatured DNA with Mn-TMPyP and Mn-TPPA$_4$ differ considerably. The denatured DNA can enhance the Mn-TMPyP-catalysed CL reaction to

TABLE 2

Results of denaturation experiment, expressed as relative CL intensities (arbitrary units).

Parameter [a]	Before denaturation		Thermal denaturation		Sonic denaturation	
	Blank	Sample	A	B	A	B
DNA (μg ml^{-1})	0.0	0.1	0.1	0.1	0.1	0.1
I_{CL1}	10.0	48.0	49.0	48.0	22.0	20.0
I_{CL2}	8.00	46.0	9.00	8.50	6.00	7.00

[a] I_{CL1} = Mn-TMPyP-catalysed CL system; I_{CL2} = Mn-TPPA$_4$ catalysed CL system. Mn-TMPyP, 2×10^{-8} M. [b] A = DNA denaturation before interaction with M-P; B = DNA denaturation after interaction with M-P.

almost at the same extent as the native DNA, whereas for the Mn-TPPA$_4$-catalysed CL reaction no enhancement was found for the denatured DNA. In addition, the enhancement effect of sonically denatured DNA on the MnTMPyP-catalysed CL reaction was less than that of thermally denatured DNA. The possible reason for this is that DNA was partially interrupted under the sonication conditions and the enhancement effect of long-chain single-stranded DNA on the M-P-catalysed CL reaction is greater than that of the short-chain type. The results are presented in Table 2.

Nature of the enhancement effect

The microenvironment and the axial coordinate conditions of M-Ps are critical for their catalytic activities. Characteristic structural features for peroxidase, cytochrome P-450 and catalase include the following: all of these enzymes have an M-P as their prosthetic group; (2) one side of the M-P molecule binds both the oxygen and the substrate and this cofactor is deeply buried in the protein [15]; and no additional catalytically active groups have been found at this active site. As ideal chemical models for these enzymes, a fifth ligand for M-P (such as the phenolic hydroxyl of tyrosine for catalase, the imidazole of histidine for peroxidase and a sulphydryl of cystine for cytochrome P-450) that characterizes these enzymes is often necessary, which occupies one side of the porphyrin plane such that the substrate can be located on the opposite face of the M-P. Recently we have found that when an M-P was bound to serum albumin, the peroxidic activity of the M-P was dramatically enhanced, which is explained by hydrophobic and coordinate interactions of M-Ps with protein [13].

The most reasonable mode of binding of Mn-TMPyP with DNA is end-on within the minor groove. Raner et al. [16] have shown that the Mn-TMPyP complex, which possesses bulky substituents in the P plane, exhibits a cleavage specificity that is identical with that of the parent compound. This observation, along with recent linear dichroism studies on the P–DNA interaction [17], strongly suggests that the P is not only bound end-on to DNA, but that the Watson and Crick hydrogen bonding between A and T is disrupted at the site of binding. The angle of orientation of the M-P relative to the DNA helix axis is 62–67°.

Based on the above observations, the enhancement effect of DNA on the Mn-TMPyP-catalysed luminol CL reaction was explained as follows. When Mn-TMPyP was bound to DNA via outside binding, the binding leads to melting or partial melting of the DNA, and the coordination effect of A or T to Mn in Mn-TMPyP makes the M-P–DNA complexes behave in the same way as iron P in natural peroxidase, in which the Fe of the M-P is coordinated with histidine, the interaction of which is responsible for the effective decomposition of H_2O_2.

Interestingly, both the natural and denatured DNA have almost the same enhancement effect on the Mn-TMPyP-catalysed CL reaction. The possible binding of these axially ligated cationic M-Ps to single-stranded polynucleotides has not been demonstrated. A recent study of the degradation of DNA, RNA and polynucleotides of defined structure by Mn-TMPyP–$KHSO_5$ showed that Mn-TMPyP-mediated polynucleotide degradation involves binding of the M-P to its substrates prior to degradation [18]. In the present enhanced CL system, the enhancement effect of denatured DNA was explained as the binding of M-P to single-stranded DNA through electrostatic and coordinate interactions just as for the interaction of M-Ps with polymers [19] in which the catalytic activity of the M-P was enhanced. Also consistent with this view was the finding that the polynucleotides demonstrated an enhancement effect on the Mn-TMPyP-catalysed CL reaction whereas no enhancement was found for nucleotides and bases, as Table 1 shows.

As indicated above, the native form of DNA can enhance the Mn-TPPA$_4$-catalysed CL reaction whereas denatured DNA has no such effect. The enhancement effect of the native form of DNA on the Mn-TPPA$_4$-catalysed CL reaction was explained by outside bonding of Mn-TPPA$_4$ to DNA, which provides a favourable microenvironment for the catalytic activity of the M-P. With denatured DNA, the NH_2 groups of Mn-TPPA$_4$ take part in the hydrogen bond formation

with bases on the single-stranded DNA in which Mn-TMPyP was completely enclosed in the single-stranded DNA polymer. Therefore, both of the axial coordinate sites may be occupied by bases and lower catalytic activity was obtained [12].

Analytical parameters of DNA-enhanced CL reaction

After establishing the effect of DNA on the M-P-catalysed CL reaction, the use of the analytical parameters of the enhancement the CL reaction as a means of determining DNA were examined by using a flow-injection system. A calibration graph for DNA was obtained by varying the concentration of DNA from 20 to 200 ng ml^{-1} with a fixed concentration of Mn-TMPyP of 2×10^{-8} M. A typical plot of DNA concentration versus relative CL intensity is presented in Fig. 3. The relative CL intensity increases rapidly as the concentration of DNA increases. At concentrations of DNA > 100 ng ml^{-1}, the CL intensity levelled off. This indicates that Mn-TMPyP is saturated by DNA. The concentration of DNA corresponding to the turning point of the curve represents the saturation concentration of DNA

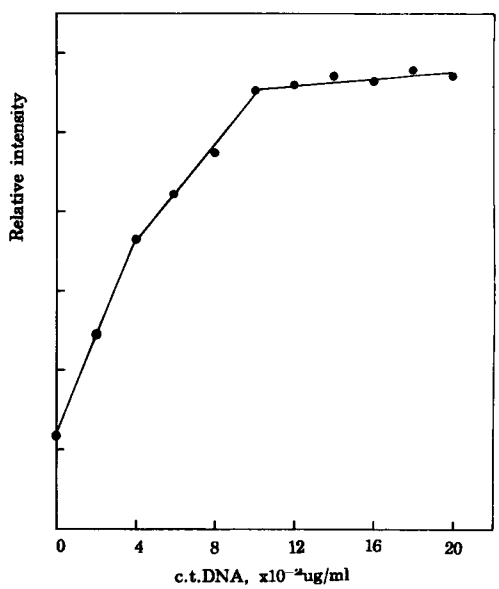

Fig. 3. Typical calibration graph for DNA. Mn-TMPyP, 2×10^{-8} M.

TABLE 3

Analytical parameters of DNA-enhanced CL reaction

Parameter [a]	Mn-TMPyP (M)			
	4×10^{-9}	2×10^{-8}	1×10^{-7}	5×10^{-7}
Working range DNA (ng ml^{-1})	1–18	20–100	50–500	200–2000
R	0.9951	0.9887	0.9894	0.9949
N	11.3	9.1	9.7	8.0

[a] R = correlation coefficient of line of best fit (six points); N = mole ratio of DNA to M-P.

with respect to the M-P. The mole ratio of DNA (base concentration) to M-P means the base number per binding of M-P molecule. It is expected that when the concentration of the M-P is increased, the method can be extended to the measurement of high DNA concentration. Table 3 summarizes the working ranges of DNA at different concentrations of Mn-TMPyP and other analytical parameters. It was found that when the Mn-TMPyP concentration was $< 2 \times 10^{-8}$ M, the Mn-TMPyP-catalysed CL signal decreased rapidly. The possible reason for this is the ab-

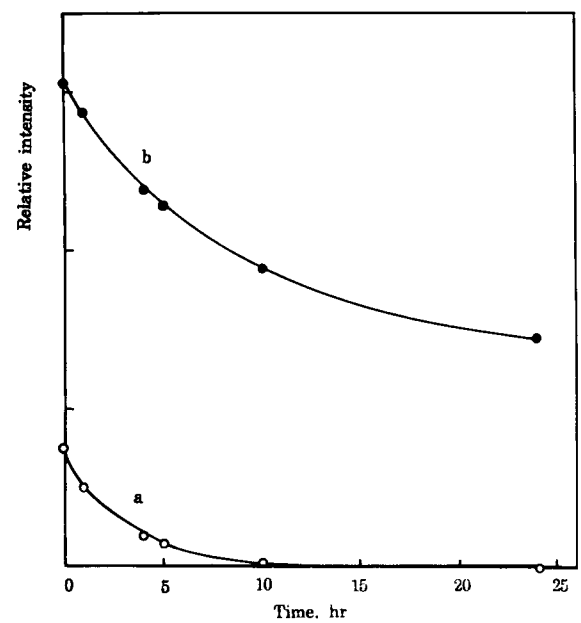

Fig. 4. Time curves of (a) Mn-TMPyP-catalysed and (b) DNA-enhanced CL reactions Mn-TMPyP, 4×10^{-9} M; DNA, 10 ng ml^{-1}.

sorption of the M-P on the flask surface. The interaction of the M-P with DNA will protect the M-P from such absorption and the CL intensity decreased slowly. Figure 4 shows the Mn-TMPyP (4×10^{-9} M)-catalysed and DNA-enhanced CL signals as a function of time.

Under the optimum conditions obtained, the detection limit (signal-to-noise ratio > 3) of DNA was 0.20 ng ml^{-1} and the relative standard deviation ($n = 11$) was 2.6% for the determination of 10 ng ml^{-1} DNA.

REFERENCES

1 K.M. Smith (Ed.), Porphyrins and Metalloporphyrins, Elsevier, Amsterdam, 1975.
2 B. Meunier, Chem. Rev., 92 (1992) 1411, and references cited therein.
3 T.J. McMurry and J.T. Grooves, in P. Ortize de Montellano (Ed.), Cytochrome P-450: Structure, Mechanism and Biochemistry, Plenum, New York, 1986, Chap. 1.
4 T.G. Traylor and P.J. Ciccone, J. Am. Chem. Soc., 111 (1989) 8413, and references cited therein.
5 P.N. Balasubramanian, E.S. Schmidt and T.C. Bruice, J. Am. Chem. Soc., 109 (1987) 7865.
6 T. Satio, M. Mifune, S. Nakashima, Y. Tanaka, M. Chikuma and H. Tanaka, Chem. Pharm. Bull., 34 (1986) 5016.
7 G.F. Zhang and P.K. Dasgupta, Anal. Chem., 64 (1992) 517.
8 T. Hara, M. Toriyama and K. Tsukagoshi, Bull. Chem. Soc. Jpn., 56 (1983) 2267.
9 B. Ward, A. Skorobogaty and J.C. Dabrowiak, Biochemistry, 25 (1986) 7827.
10 R.J. Fiel, J. Biomol. Struct. Dyn., 6 (1989) 1259.
11 L.G. Marzilli, New J. Chem., 14 (1990) 409.
12 Y.X. Ci, J.K. Tie, Q.W. Wang and W.B. Chang, Anal. Chim. Acta, 269 (1992) 109.
13 J.K. Tie, W.B. Chang and Y.X. Ci, Anal. Chem., in press.
14 R.F. Pasternack, E.J. Gibbs and J.J. Villafranca, Biochemistry, 22 (1983) 2406.
15 R. Raag, and T.L. Poulos, Biochemistry, 28 (1989) 917.
16 G. Raner, B. Ward and J.C. Dabrowiak, J. Coord. Chem., 19 (1988) 17.
17 N.E. Geacintov, V. Ibanez, M. Rougee and R.V. Bensasson, Biochemistry, 26 (1987) 3087.
18 R.B. Van Atta, J. Bernadou, B. Meunier and S.M. Hecht, Biochemistry, 29 (1990) 4783.
19 G. Labat and B. Meunier, J. Chem. Soc., Chem. Commun., (1990) 1414.

Analytica Chimica Acta, 282 (1993) 703–709
Elsevier Science Publishers B.V., Amsterdam

Design of a flue gas probe for ammonia measurement

K. Hjuler and K. Dam-Johansen

Department of Chemical Engineering, Technical University of Denmark, Building 229, 2800 Lyngby (Denmark)

(Received 22nd March 1993; revised manuscript received 8th June 1993)

Abstract

The emission of nitrogen oxides from combustion can be limited by selective catalytic reduction (SCR) and selective non-catalytic reduction (SNR) by ammonia. In order to control the ammonia slip in these processes it is desirable to measure the ammonia outlet concentration continuously. The problems in doing this are discussed, among which are homogeneous and heterogeneous reactions of ammonia with nitric oxide in the sampling system. The design and test of a diluting flue gas probe is presented, where ammonia is converted to and detected as nitric oxide. The efficiency of various converter designs for the probe was studied in the laboratory.

Keywords: Catalytic methods; Ammonia; Flue gas probe

During the last years much effort has been put into the development and test of analysis methods for the detection of ammonia in flue gas. Basically, two problems have to be considered when extractive ammonia analysis is carried out: the sampling technique, and the detection principle of the analyzer.

The design of a sampling technique is not a trivial problem as ammonia may adsorp on surfaces in the sample gas lines or on fly ash [1], and it may react with oxygen, nitric oxides, sulphur dioxide, and sulphur trioxide present in the flue gas. Moreover, the ammonia may be unevenly distributed in the flue gas channel or reactor where the sample is taken. Unwanted side reactions take place homogeneously at high temperatures (above about 800°C) [2] and heterogeneously above about 250°C due to catalytic effects of fly ash [3] or steel [4–7]. Below this temperature in a wet flue gas, sulphur trioxide is converted to gaseous sulphuric acid which may condense as ammonium sulphate in the presence of ammonia. At still lower temperatures (below about 70°C) sulphur dioxide, water, and ammonia forms ammonium sulphite on surfaces, which subsequently is oxidized to ammonium sulphate by oxygen and nitrogen dioxide. This problem has been extensively studied in a recent work [8]. The potential problem of salt formation has, in a particular design, been solved by removing sulphur dioxide selectively in the flue gas probe [5].

Gaseous ammonia may be detected directly and continously in a number of ways, including mass spectrometry, IR and UV spectrometry, laser spectrometry [9,10], gas sensing electrodes, and automized wet chemical methods [11]. Typically, the manufacturers may test their analyzers by measuring ammonia in nitrogen or other relatively simple mixtures. By testing in this way most commercially available ammonia analyzers are generally suitable, i.e., they are linear and have reasonable response times. However, tests per-

Correspondence to: K. Dam-Johansen, Department of Chemical Engineering, Technical University of Denmark, Building 229, 2800 Lyngby (Denmark).

formed with simulated flue gas may show significant cross sensivities for other flue gas components. For example, tests of an UV and an IR anayzer in our laboratory have shown severe cross sensivities for SO_2 and NO in the UV range and for water in the IR range. Janssen et al. [3] found that mass spectrometry was unsuitable for detection of ammonia in presence of flue gas contents of water and oxygen. In general, technically sophisticated methods of detection may not be suitable for a process environment with vibrations, dust, heat, etc.

Ammonia may also be detected indirectly by chemiluminescence or UV spectrometry if it is converted to nitric oxide. The NH_3 to NO converter used in commercial equipment is typically a tube reactor made of steel, which acts as a catalyst due to the presence of metal oxides on the surface. The use of platinum as a catalyst has also been reported [12,13]. As nitric oxide is also present in the unconverted flue gas this is a differential technique, with the drawback that the accuracy is lowered when the nitric oxide concentration is high compared to the ammonia concentration. However, on $DeNO_x$ plants the NH_3 and NO concentrations are normally of the same order of magnitude and calculations show that the deterministic uncertainty of the method should be lower than 3 ppm. Other nitrogen species such as HCN, CH_3NH_2, etc., are oxidized as well as NH_3 and may be detected as such, if present. Reduced sulphur species are also oxidized, and about 1% of any SO_2 present may be oxidized to SO_3. The formation of SO_3 may cause problems with salt formation and corrosion downstream of the converter if the measurement system is not designed to take this into account.

On the basis of our experiences with ammonia measurements on flue gas we find that the differential technique is reliable, reasonably accurate, and moderate in cost. A measurement system based on this technique has been designed. In the following the design and laboratory test of the ammonia to nitric oxide converter is discussed, and the final measurement system is presented. The measurement system was tested both on a pilot scale SCR plant and on a full scale SNR plant.

EXPERIMENTAL

To determine the optimal design and operating conditions of an NH_3 to NO converter (reactor), laboratory test were performed at temperatures in the 640–1000°C range, gas residence times from 0.02 to 0.5 s, and various ammonia inlet concentrations with and without NO present. The outlet concentration of NO was determined by chemiluminiscence.

Two reactors were operated at atmospheric pressure: an 1.8 mm i.d. stainless (316) steel tube, and a 5.3 mm i.d. quartz glass U tube (10 cm in length) containing 2.33 g platinum/rhodium net (90:10, 80 mesh) as a catalyst. This catalyst is well known from the production of nitric acid for its high selectivity and stability. The oxygen partial pressure was constant at about 4.3 vol.-%. A third reactor could be operated at pressures down to 0.1 atm: a 10 mm i.d. quartz glass tube (10.4 cm in length), also containing 2.33 g Pt/Rh net. In this reactor the oxygen partial pressure was constant at about 6.1 vol.-%. All tubes were heated electrically in a tubular furnace and the temperature was controlled within ± 5°C.

RESULTS AND DISCUSSION

Converter efficiency

By varying the length (5–40 cm) of steel tube inserted into the furnace, the results shown in Fig. 1 were obtained. The temperature and the inlet partial pressure of NH_3 were 640°C and 200 ppm respectively (1 atm total pressure). At a gas flow-rate of 75 ml min^{-1} (at 298 K and 1 atm), the observed conversion of NH_3 to NO was apparently lower than at 520 ml min^{-1} (*Re* about 1200), indicating that the reaction is limited by mass transfer to the tube wall. The observed conversion is calculated as $([NO]_o - [NO]_i)/[NH_3]_i$, where i and o denotes inlet and outlet concentrations respectively.

The steel converter efficiency increased significantly when the temperature was increased from 640 to 900°C, Fig. 2. According to the kinetics discussed below, homogeneous reactions between NH_3 and NO have increasing importance above

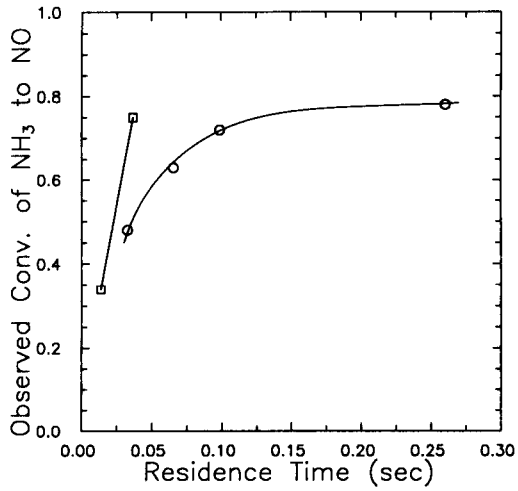

Fig. 1. Observed conversion of NH_3 versus the residence time using the type 316, 1.8 mm i.d., steel tube reactor. The length of reactor was varied. Reaction conditions: 200 ppm NH_3, 640°C, 4.3 vol.-% O_2, (○) flow-rate 75 ml min^{-1}, (□) flow-rate 520 ml min^{-1}.

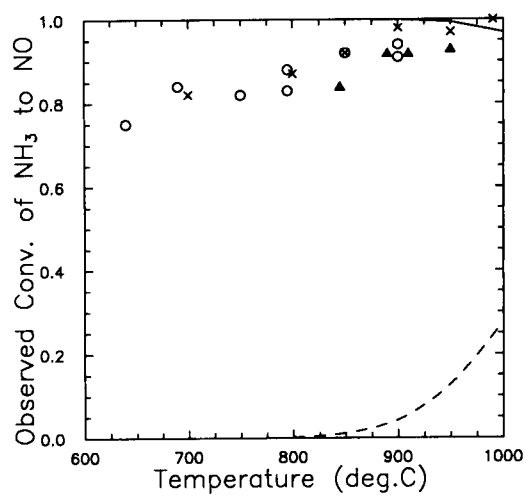

Fig. 2. Observed conversion of NH_3 versus the reactor temperature for the three reactors studied. The calculated conversions for the steel (considering only homogeneous reactions, dashed line) and the atmospheric pressure Pt/Rh (solid line) converters are shown for comparison. Reaction conditions: steel (○): 200 ppm NH_3, residence time $32/T$ s (T in Kelvin), flow rate 520 N ml min^{-1}, 4.3 vol.-% O_2. Pt/Rh, 1 atm. (▲): 200 ppm NH_3, residence time $73/T$ s, flow-rate 520 ml min^{-1}, 4.3 vol.-% O_2. Pt/Rh, reduced pressure (×): 20 ppm NH_3, 75 ppm NO, residence time 0.09–0.12 s, flow-rate 1260 ml min^{-1}, 6.1 vol.-% O_2.

800°C (solid line) and some NH_3 is converted to N_2, thereby lowering the observed conversion. The high temperature caused carbon particles to be released from the 316 steel reactor tube, and it was damaged irreversibly. On this basis the steel converter was found unsuitable for practical application, and the work continued with the platinum converters.

The results obtained with the platinum converter operated at atmospheric pressure are compared with a mathematical model including both homogenous and heterogeneous kinetics. The homogeneous reactions involved in selective non-catalytic reduction of nitric oxide (SNR) at atmospheric pressure was studied by Duo et al. [2], who found that the kinetics of the overall reaction could be simplified as:

$$r_{NO} = k_{ox} \cdot [NH_3] - k_r \cdot [NH_3][NO] \quad (1)$$

$$r_{NH_3} = -k_{ox} \cdot [NH_3] - k_r \cdot [NH_3][NO] \quad (2)$$

where $k_{ox} = 2.212 \cdot 10^{14} \cdot \exp(-38160/T)\ s^{-1}$ and $k_r = 2.450 \cdot 10^{14} \cdot \exp(-29400/T)\ m^3\ mol^{-1}\ s^{-1}$ at about 4 vol.-% of oxygen. r_i is the rate of formation of component i in mol $m^{-3}\ s^{-1}$. Plug flow was assumed for the gas. The heterogeneous rate of reaction was assumed to be mass transfer limited and the empirical correlations for mass transfer coefficients in nets developed by Shah and Roberts [14] were used:

$$-r_{NH_3} = k_g a W [NH_3]\ (\text{mol}\ s^{-1}) \quad (3)$$

where $k_g = j_d G/\delta Sc^{-2/3}$ (cm s^{-1}), $j_d = 0.865/\epsilon(Re/\epsilon)^{-0.648}$ for $0.4 < Re < 9$ and $j_d = 0.644/\gamma(Re/\gamma)^{-0.57}$ for $5 < Re < 245$. a is the specific surface area of the net ($cm^2\ g^{-1}$), W the weight of catalyst, G the mass velocity (g $cm^{-2}\ s^{-1}$), δ the gas density, and Sc the Schmidt number. The characteristic dimension of the Reynold number (Re) is the wire diameter (cm), ϵ is the porosity of a single net, and γ the projected plane porosity of a single net.

The temperature dependency of the conversion obtained using the Pt/Rh catalyst reactor operated at atmospheric pressure is shown in Fig. 2. The corresponding calculated NH_3 to NO conversion is shown for comparison (solid line). According to the calculations, the mass of catalyst

present is more than 100 times higher than needed, i.e., complete conversion would be obtained if no homogeneous reactions took place. Due to homogeneous reactions upstream of the catalyst, the calculated observed conversion is not complete above about 900°C. However, the experimental observed conversion is even lower and shows the opposite trend, which is probably due to the catalysis of side reactions.

The effect of homogeneous reactions is more clearly seen when NO is present in the inlet gas, Fig. 3. In this case the observed conversion increases with the NH_3/NO inlet ratio, approaching the conversion without NO present. This problem may be analyzed by dividing Eqn. 1 with Eqn. 2:

$$d[NO]/d[NH_3] = -(k_{ox} - k_r \cdot [NO]) / (k_{ox} + k_r \cdot [NO]) = 0 \quad (4)$$

therefore

$$[NO] = k_{ox}/k_r = 0.903 \cdot \exp(-8760/T) \text{ mol m}^{-3} \quad (5)$$

The "critical" NO concentration, calculated by Eqn. 5, is shown in Table 1 versus the temperature. It is shown that if the NO inlet concentration is higher than the critical value, then NO tends to be removed by homogeneous reactions and vice versa. In Fig. 3, the NO inlet concentration is 230 ppm, which is above the critical value of about 50 ppm (at 910°C). In this case NO is removed by homogeneous reactions and the observed conversion becomes relatively low.

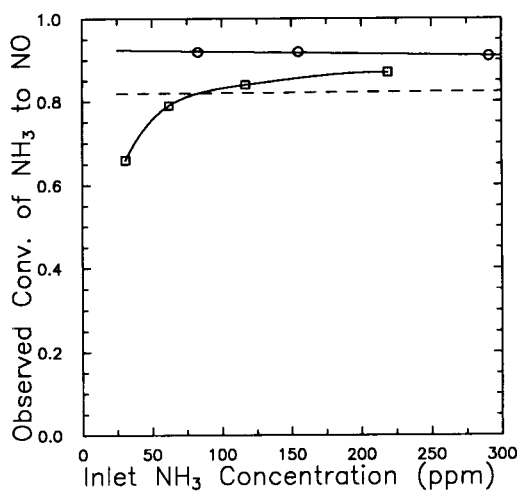

Fig. 3. Observed conversion of NH_3 versus the inlet NH_3 partial pressure for the atmospheric pressure Pt/Rh reactor. The calculated conversion with 230 ppm NO present is also shown (dashed line). Reaction conditions: (○) 0 ppm NO, (□) 230 ppm NO, 910°C, residence time 0.077–0.101 s, flow-rate 375 N ml min^{-1}, 4.3 vol.-% O_2.

TABLE 1

"Critical" NO concentration, calculated by Eqn. 5, versus temperature

Temperature (°C)	[NO] (ppm)
700	8.9
800	22.7
900	49.7
1000	97.0

It has been reported that almost complete conversion in presence of NO is possible at reduced pressure (0.1 atm) using a Pt catalyst at 760°C [12]. In addition, the catalyst should be less susceptible to poisoning. The effect of pressure reduction was also investigated in this work. A vaccuum pump was connected to the 10 mm i.d. quarts glass tube with catalyst (Pt/Rh 2.33 g), and the flow and pressure was adjusted by means of needle valves. The homogeneous kinetics discussed above has not been verified at reduced pressure, and are therefore not modelled as the second order terms (NH_3–NO reactions) are influenced more than the first order terms.

The effect of the temperature on the observed conversion at about 0.23 atm pressure was shown in Fig. 2. The data show practically the same temperature dependence as the atmospheric pressure converters tested. In Fig. 4 is seen that the observed conversion increases when the pressure is decreased in the 0.9–0.1 atm range. With 175 ppm of NO present and 0.1 atm pressure the observed conversion was nearly constant at about 0.90 independent of the NH_3 inlet partial pressure. It was found that any NO_2 present was reduced to NO at temperatures above 900°C. Therefore NO_2 also has to be reduced in the converter by pass stream in order to obtain a correct difference signal. A molybdenum oxide

catalyst is typically employed for this purpose, but, as also reported by Janssen et al. [3], we have observed that NO and NO_2 are reduced to N_2 in the presence of NH_3, and it is therefore recommended that NH_3 is removed selectively from the converter by pass stream.

Measurement system

A measurement system with gas diluting was designed on the basis of the laboratory tests in cooperation with the instrument manufacturer (Instrumatic, Denmark). It comprises a stainless steel flue gas probe and a chemiluminescence NO_x analyzer, Fig. 5. The probe contains a diluter, a catalytic platinum/rhodium converter operated at low pressure, and a selective NH_3 absorber in the converter by-pass stream. A filter cartridge with quartz wool and a 2.7-μm membrane filter is mounted at the probe inlet. The gas is diluted with silica gel dryed air to a dew point of about 0°C by means of heated critical orifices. A converter pressure of 0.3 atm is achieved by placing the converter down-stream of the diluter, i.e. the sample stream of about 200 ml min^{-1} is diluted before converting. A part of the diluted and converted sample stream (about 3 l min^{-1}) is fed to a 2-channel chemiluminescence

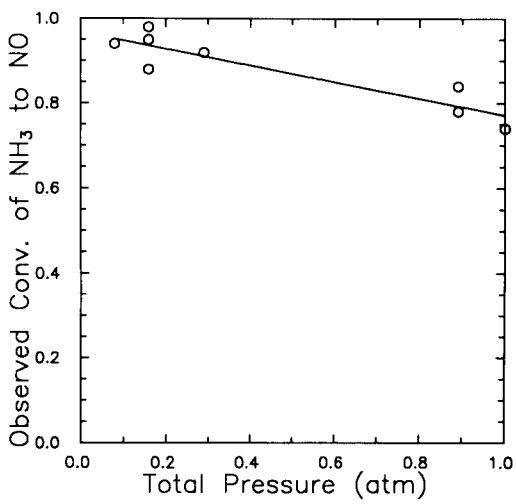

Fig. 4. Conversion of NH_3 versus the total pressure for the reduced pressure Pt/Rh reactor. Reaction conditions: 130 ppm NH_3, 170 ppm NO, 950°C, residence time 0.50 s, flow rate 240 ml min^{-1}, 6.1 vol.-% O_2.

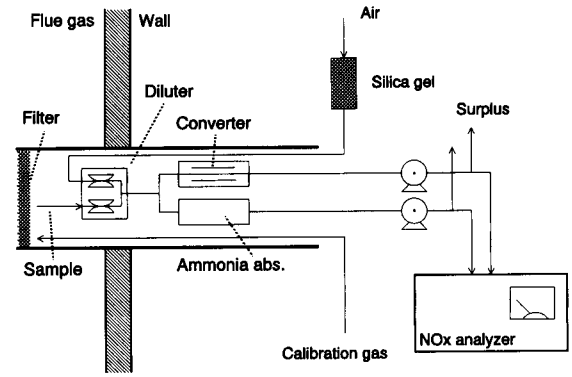

Fig. 5. Outline of the ammonia measurement system with flue gas filter, heated critical orifices for dilution, high temperature converter, selective ammonia scrubber, and two channel chemiluminescence NO_x analyzer.

NO_x immision analyzer (Monitor Labs.) through unheated PTFE lines. A relatively low converter temperature of 900°C was chosen due to an otherwise significant shortened lifetime of the converter thermocouple and heating element.

As shown in Fig. 5, calibration gas is injected at the probe inlet. Twice a week the measurement system was zero point calibrated with nitrogen gas, and end point calibrated with certified standard NO calibration gas (200 ppm ± 2%). The converter efficiency was tested with certified standard NH_3 calibration gas (42 ppm + 2%). The concentration of the NH_3 calibration gas was checked by flow injection analysis (FIA) as described below.

Field tests

SCR pilot plant. The ammonia measurement system was tested at a low dust SCR pilot plant at a coal fired facility. The flue gas probe was installed at the outlet of the SCR reactor at a temperature of about 385°C. Wet chemical ammonia measurements were made for comparison using an ion selective electrode (ISE). The gas was sampled for about 1 h by means of a glass probe to two bubble flasks in series containing 0.1 M sulfuric acid. During the sampling period the reactor NH_3/NO_x inlet ratio was kept constant. The NO_x level was typically 10–20 ppm. The gas was dryed using silica gel, and the total quantity sampled was measured using a gas meter. After

sampling, the glass probe and gas lines were flushed with distilled water. The liquid samples were combined and made up to a known volume.

In Fig. 6, the probe measurements are compared with the results obtained using ISE (both wet gas basis, 7.5 vol.-% H_2O). The probe measurements were evaluated graphically as 1 h averages to be comparable. Using the wet chemical method as a reference, the agreement is reasonable although a zero point error of about 1 ppm is found. This zero point error may be due to nitrogen oxidation using air as a diluent. In the laboratory test a zero point error of about 0.2 ppm was typically found. Unfortunately, both the heating element and the thermocouple of the converter failed several times during the test period due to heat impaction. Afterwards the system was modified in the way that the converter was heated separately and placed downstream of the probe and diluting unit, but still operating at reduced pressure.

SNR full scale plant. The flue gas probe with separately heated converter was tested during full scale experiments with selective non-catalytic reduction (SNR) of nitric oxide by ammonia [15]. The probe was mounted in the stack at about 120°C. Wet chemical ammonia measurements by FIA were made for comparison. The gas sampling method for FIA was the same as for ISE. The determination of ammonia nitrogen by FIA was carried out as described in Tecator Application Notes [16], except that a 1.0 M sodium hydroxide solution was used to ensure a pH value above 11 after mixing with the sample stream.

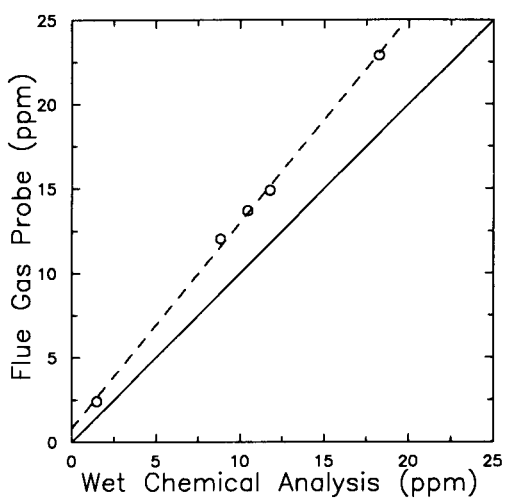

Fig. 6. Comparison of measurements obtained by the flue gas probe and by wet chemical measurements (ISE). The results were obtained at an SCR pilot plant.

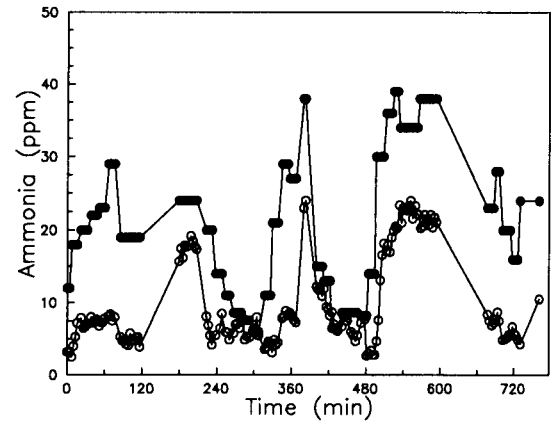

Fig. 7. Stack NO_x concentration and NH_3 slip during full scale SNR experiments. The NH_3 slip was measured using the probe (○) and by wet chemical measurements (FIA) (●) for comparison.

In Fig. 7, the NO_x concentration in the stack and the NH_3 slip, measured using the probe and FIA respectively, are shown for a period of time where SNR experiments were carried out. The NH_3 slip increased from below 10 ppm to about 25 ppm when NH_3 was injected, and the NO_x level (not shown) was simultaneously reduced from about 450 ppm to about 225 ppm. The variation with time of the probe measurements agrees well with the FIA measurements, but the probe measurements are consistently too low. Any explanation to this has not been found. It is apparently not due to homogeneous reactions as the sample gas is diluted about 20 times upstream of the converter, i.e., the NO concentration at the converter inlet was lower than the critical value of about 50 ppm.

REFERENCES

1 W. Bujak and H. Gutberlet, VGB Kraftwerkstechnik, 68 (1988) 1294.

2 W. Duo, K. Dam-Johansen and K. Østergaard, Can. J. Chem. Eng., 70 (1992) 1014.
3 F. Janssen, F. van den Kerkhof, J. Lefers, P. Lodder and L. Luierweert, Anal. Chim. Acta, 190 (1986) 245.
4 W. Gajewski, M. Schott and J. Sprehe, VDI Berichte, 608 (1987) 301.
5 W. Gajewski, VGB Kraftwerkstechnik, 68 (1988) 632.
6 A.M. Erken, VGB Kraftwerkstechnik, 68 (1988) 1286.
7 G.L Bauerle, S.C. Wu and K. Nobe, Ind. Eng. Chem. Prod. Res. Dev., 17 (1978) 123.
8 K. Hjuler and K. Dam-Johansen, I&EC Research, 31 (1992) 2110.
9 A. Olafsson, M. Hammerich, J. Bülow and J. Henningsen, Appl. Phys. B, 49 (1989) 91.
10 H. Neckel, Chem. Ing. Tech. 63 (1991) 844.
11 P. Lodder and J.B. Lefers, VGB Kraftwerkstechnik, 68 (1988) 1301.
12 J.E. Hardy and J.J. Knarr, J. Air Pollut. Control Ass., 32 (1982) 376.
13 S. Takashi and I. Yamashita, JSME Int. J., 32 (1989) 449.
14 M.A. Shah and D. Roberts, in H.M. Hulburt (Ed.), Chemical Reaction Engineering – II, Adv. Chem. Ser. Vol. 133, ACS, Washington, DC, 1974, p. 259.
15 M. Jødal, T.L. Lauridsen and K. Dam-Johansen, Env. Prog., 11 (1992) 296.
16 Tecator Application Notes AN 50/84 and ASN 5001/84 (1984).

Analytica Chimica Acta, 282 (1993) 711–719
Elsevier Science Publishers B.V., Amsterdam

Thermal diffusivity of skin measured by two photothermal techniques

S.M. Brown, M.L. Baesso, Jun Shen and R.D. Snook

Department of Instrumentation and Analytical Science, University of Manchester Institute of Science and Technology, P.O. Box 88, Manchester M60 1QD (UK)

(Received 15th March 1993; revised manuscript received 23rd June 1993)

Abstract

The thermal diffusivity of pig abdomen *stratum corneum* has been determined using photothermal beam deflection measurements and time-resolved mode mismatched thermal lens spectrometry. The most precise determination ($2.9 \pm 0.5 \times 10^{-4}$ cm^2 s^{-1}) was obtained using the thermal lens technique. The practical utility of both techniques is discussed.

Keywords: Photothermal beam deflection; Skin; Thermal diffusivity; Thermal lens spectrometry

There have been recent reports on the use of photoacoustic spectrometry in skin research with an emphasis upon measuring the depth of penetration of topically applied substances [1,2]. In principle this technique is simple. The thermal diffusion length, i.e. the depth from which a measurable thermal wave and hence photoacoustic signal can be observed is given by the following simple expression:

$$\mu = (D/\pi f)^{1/2} \quad (1)$$

where μ is the thermal diffusion length (cm), D is the thermal diffusivity (cm^2 s^{-1}) and f is the modulation frequency (Hz) of the beam of monochromatic light which illuminates the sample.

By changing the frequency of modulation, therefore the diffusion length can be changed such that a depth profile of the sample can be determined. For accurate depth resolution an accurate and precise value of the thermal diffusivity of the sample under investigation must be known. Whilst such accurate and precise values are known for many materials such as metals there is no universally accepted value for skin. The thermal diffusivity of skin will depend upon its physical nature, e.g. degree of hydration and the species from which the skin is taken as well as the area of the body from which it is taken. In addition there have been no systematic comparisons of values for a standard skin sample obtained by different techniques. However, Warner et al. [3] have reported a value of $2.8 \pm 0.9 \times 10^{-4}$ cm^2 s^{-1} for dry epidermis using a photothermal technique.

In this paper two different photothermal techniques are used to determine thermal diffusivity of pig abdomen *stratum corneum*. The techniques used were photothermal beam deflection spectrometry using a laser source and laser induced thermal lens spectrometry. The principles, experi-

Correspondence to: R.D. Snook, Department of Instrumentation and Analytical Science, University of Manchester, Institute of Science and Technology, P.O. Box 88, Manchester M60 1QD (UK).

mental details, results and discussion appertaining to each of these techniques are presented separately for clarity.

PHOTOTHERMAL BEAM DEFLECTION SPECTROMETRY

Principles

The principles of photothermal beam deflection have been completely described by Aamodt and Murphy [4] and proved experimentally in this laboratory [5]. A modulated laser is used as a source to illuminate the sample. Provided that the sample has a finite absorption coefficient some of the radiation will be absorbed. In solids, deactivation of excited states normally takes place via non-radiative mechanisms giving rise to a modulated heat source. This heat diffuses back to the surface of the sample where it is transferred to the contacting medium (in this case air). This results in a modulated refractive index gradient in the air which can be probed using a low-power laser beam which passes through the heat field orthogonal to the pump laser beam. The refractive index gradient deflects the probe beam orthogonally to its direction of propagation. The deflection can be resolved into two components using a quadrant position sensor in the far field of the probe beam as illustrated in Fig. 1. The

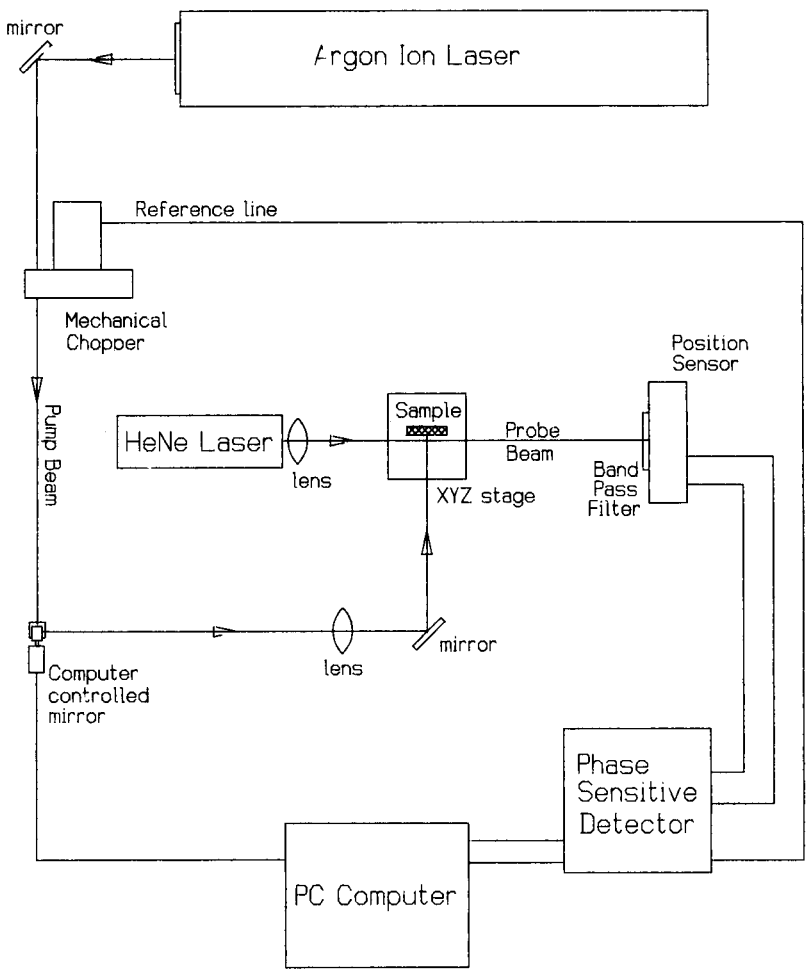

Fig. 1. Experimental arrangement for photothermal beam deflection measurements.

normal component represents a deflection normal to the surface of the sample and the second component, the transverse signal represents the deflection parallel to the surface. To record these signals experimentally the pump beam is scanned across the surface using a suitable scan and stop mechanism. At each position the normal and transverse signal are measured.

The bipolar nature of the transverse signal reflects the direction of deflection, i.e. left or right as the beam propagates. Kuo et al. [6] have shown that the distance x_0 shown on the transverse signal in Fig. 2 varies with modulation frequency, x_0 becoming smaller as the pump modulation frequency is increased. Furthermore, Kuo et al. showed that if x_0 is plotted against $1/f^{1/2}$ then a straight line will be derived for which the gradient, g, is given by

$$g = (1.4\pi D)^{1/2} \quad (2)$$

from which the thermal diffusivity, D, can be calculated.

Experimental

The photothermal beam deflection measurements were performed on samples of pig abdomen isolated *stratum corneum*. The samples were mounted on glass microscope slides and held in place by applying a cyanoacrylate adhesive around their edges. Isolated *stratum corneum* samples were used, rather than samples of epidermis, as the latter proved difficult to mount satisfactorily, leading to insufficient signal levels for accurate measurements.

The front face of the sample was illuminated by the beam from a Coherent Ltd. Innova-90 argon ion laser. The laser was used in multi-line mode (principal wavelengths 514.5 and 488.0 nm), providing a power of 6 W. As shown in Fig. 1, this laser beam, the "pump beam", passed through a mechanical chopper (Ortec-Brookdeal 9479) and was reflected off a computer-controlled rotational mirror (General Scanning Inc. G100 PD) before being focused down onto the sample surface by a 40-cm focal length biconvex lens.

The temperature gradient created in the air adjacent to the sample surface by this was probed by a second laser beam, the "probe beam", from a Siemens LGK7632 He–Ne laser. This beam passed through a 20-cm focal length biconvex lens, and skimmed the sample surface, reaching a focus where it intersected the pump beam. The probe beam then continued over the sample, through a He–Ne bandpass filter, to remove ambient light, and onto a quadrant photodiode (RS 652-027) position sensor used to measure the deflection of the probe beam. The normal and transverse signal outputs of the sensor were fed

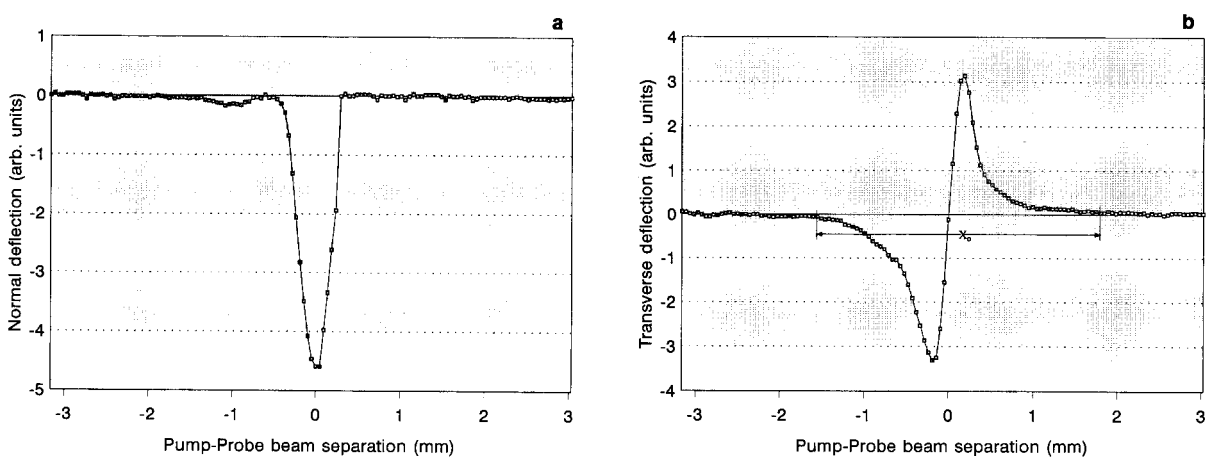

Fig. 2. (a) Normal deflection signal. (b) Transverse deflection signal showing base line width, X_0.

to an EG & G Brookdeal 5206 sensitive detector and from these were captured by a personal computer.

The computer-controlled mirror allowed the pump beam to be scanned down the sample, in a direction perpendicular to the probe beam. As the path length between the mirror and the sample surface was long, the pump beam remained approximately perpendicular to the sample surface throughout each scan. This set-up permitted the magnitude of the probe beam deflection signals to be captured at varying pump/probe beam separations. Experiments were carried out in air at room temperature and humidity (typically 50% relative humidity at 22°C).

Results and discussion

Using the experimental set-up described above, photothermal beam deflection signals were obtained from pig abdomen isolated *stratum corneum* at various pump beam chopping frequencies. Typical normal and transverse deflection signals are shown in Fig. 2. The top signal (Fig. 2a) is of a "normal" deflection, that is deflection of the probe beam away from the sample surface by the refractive index of gradient set up by the heating action of the pump beam. The lower signal (Fig. 2b) is of the corresponding "transverse" deflection, that is deflection of the probe beam across the sample surface. The spatial profiles of these signals are shown and are in good agreement with the accepted theory for the technique [4].

With increasing pump beam chopping frequency (f) both normal and transverse signals decreased in height and width as expected. The transverse signal is somewhat noisy in the wings so it is difficult to take an accurate measurement of x_0, therefore to improve the accuracy each signal width was measured at half height to avoid the baseline noise. Full baseline widths were then calculated by assuming that the transverse signals were differentiated Gaussian in shape, an assumption which is compatible with theory. The values of x_0 were then plotted against $1/f^{1/2}$ for frequencies between 5 and 32.5 Hz as shown in Fig. 3a.

Such a plot, obtained from a 30 μm thick sample of pig abdomen isolated *stratum corneum* is shown in Fig. 3. Each point on the graph is an average of three signal widths. The frequency range on the graph is from 2 to 20 Hz, corresponding to signals from depths of approximately 44 to 17 μm in the sample, respectively, using an assumed value of $D = 3 \times 10^{-4}$ cm^2 s^{-1} and Eqn. 1. The valid region of this plot is between 10 and 20 Hz; below 10 Hz ($\mu = \sim 31$ μm) a contribution from the backing layer and interface with the *stratum corneum* and interface can be expected. Above 20 Hz the thermal diffusion length in air

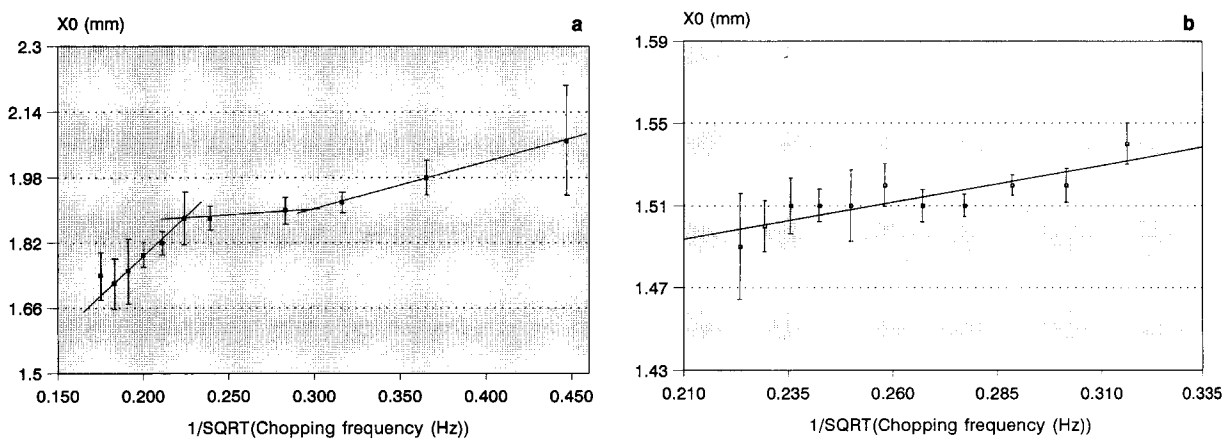

Fig. 3. (a) Transverse signal width X_0 versus $1/f^{1/2}$ between $f = 5$ and 32.5 Hz. (b) Transverse signal width X_0 versus $1/f^{1/2}$ between $f = 10$ and 20 Hz.

became less than the diameter of the probe beam. This caused the probe beam to be affected by the thermal properties of the surrounding air, not just those of the sample, again leading to anomalous results. The experiment was repeated in the range 10–20 Hz (Fig. 3b) to obtain a gradient of 0.36 mm $s^{-1/2}$ which gave a thermal diffusivity of $2.9 \pm 1.2 \times 10^{-4}$ cm^2 s^{-1} which is in good agreement with other values reported in this paper and by Warner et al. [3] for dry human epidermis. The high level of uncertainty associated with the measurement is because the optical absorptivity of *stratum corneum* at visible wavelengths is low, leading to weak signals, even with high pump beam powers. Additionally the final value is the square of a very small gradient, amplifying any uncertainties in the initial measurements. Triplicate determination on the same sample gave an average thermal diffusivity of $3.0 \pm 0.9 \times 10^{-4}$ cm^2 s^{-1}. The low optical absorptivity of *stratum corneum* in the visible band will actually be a benefit in future work, in which we intend to monitor the diffusion of chemical species through *stratum corneum* samples.

THERMAL LENS MEASUREMENTS

Principles

Thermal lens spectrometry (TLS) has enjoyed great success since first reported by Gordon et al. [7]. TLS has been applied mainly to ultra-weak optical absorption measurements of transparent samples because of its high sensitivity [8–10]. The time-resolved method permits the measurement of the development of the thermal lens in a short time, and the optical absorption coefficient and thermal diffusivity of a sample can be absolutely measured [11–13]. Furthermore, it has been proved that the dual-beam thermal lens measurement is independent of light scattering [14]. TLS, therefore, is suitable for thermal diffusivity measurements of skin. Finally, TLS requires only apparatus commonly available in modern laser research, and no unusual detection apparatus is required.

In the dual-beam thermal lens measurement a sample is placed in a TEM_{00} Gaussian laser beam (excitation beam), and a temperature rise is produced by non-radiative decay processes following the optical energy absorption. Since the refractive index of the sample is changed with temperature, a refractive index gradient is produced, creating a lens-like optical element, the so-called thermal lens. A weak TEM_{00} Gaussian laser beam (probe beam), which is co-linear with the excitation beam, passing through the thermal lens, will be affected, resulting in a variation in its spot size and hence intensity at the beam centre. By measuring these changes, information of the thermal and optical properties of the sample can be obtained. A theoretical model for a continuous-wave (CW) laser-induced mode-mismatched dual-beam TLS has been developed [11] and the variation of the intensity in the centre of the probe beam caused by the thermal lens can be expressed as:

$$I(t) = I(0)\left(1 - \frac{\theta}{2}\tan^{-1}\left\{\frac{2mv}{\left[(1+2m)^2 + v^2\right]\frac{t_c}{2t} + 1 + 2m + v^2}\right\}\right)^2 \quad (3)$$

where

$$\theta = -\frac{P_e A l}{k\lambda_p}\frac{dn}{dT} \quad (4)$$

$$m = \left(\frac{\omega_{1p}}{\omega_e}\right)^2 \quad (5)$$

$$v \approx \frac{Z_1}{Z_c}(Z_2 > Z_c) \quad (6)$$

and

$$t_c = \frac{\omega_e^2}{4D} \quad (7)$$

Here $I(0)$ is the initial intensity when t or θ is zero, P_e is the excitation beam power (W), A is the absorption coefficient (cm^{-1}), λ_p is the probe

beam wavelength (cm), dn/dT is the refractive index change of the sample with temperature (K^{-1}), $Z_c = \pi\omega_{0p}^2/\lambda_p$ is the confocal distance (cm), $D = k/(\rho c)$ is the thermal diffusivity of the sample ($cm^2\ s^{-1}$), k is the thermal conductivity (J s^{-1} cm^{-1} K^{-1}), ρ is the density of the sample (g cm^{-3}), c is the specific heat of the sample (J g^{-1} K^{-1}) and t_c is the characteristic thermal time constant (s). θ and t_c can be determined by measuring the time-resolved intensity signal, $I(t)$, and fitting Eqn. 1; ω_e, Z_c and ω_{0p} can be obtained from the spot size measurements [11]. The thermal diffusivity, D, can be determined from t_c in Eqn. 7. The mathematical expression Eqn. 3 is simple and is convenient to use. However, this model assumes the sample is an infinite medium both in the radial and axial directions (in cylindrical coordinates in the sample). Recent studies have shown that when the sample thickness (axial direction) is still assumed to be infinite, the radial-infinite treatment is valid if the sample radius is larger than 2.5 times both the excitation and probe beam radii in the sample, which is easily satisfied in the thermal lens experiment. To measure the thin-film sample, a thin-film model of TLS has also been developed [15]. It shows that when the sample thickness is larger than 0.2 cm, the infinite model, Eqn. 3, describes the behaviour well from $t = 0$ to $t \to \infty$, while the relative difference between the thin film and the infinite models is less than 3% within $t = 5t_c$ for a sample of thickness 20 μm. This means that the infinite model can be used to study a thin-film sample, such as skin, by measuring the time-resolved thermal lens signals with short t to obtain optical and thermal parameters of the sample.

Experimental

The experimental apparatus for time-resolved measurement of the skin sample is shown in Fig. 4. The excitation laser is a Kr^+ laser at 647.1 nm, which was focused by three converging lenses (lens 1–3), and the sample was put at the focal plane of lens 3. Exposure of the sample to the excitation beam was controlled by means of a shutter, which was put at the focal plane of lens 1. The excitation beam was divided by a neutral density filter (absorbance = 3), filter 3. One beam was attenuated to 5 mW and was incident on the sample, while the other was reflected onto a photodiode to trigger a digital oscilloscope. The He–Ne probe beam was attenuated to 0.8 mW by a neutral density filter (absorbance = 1), filter 1. After focusing by lens 4, the probe beam was

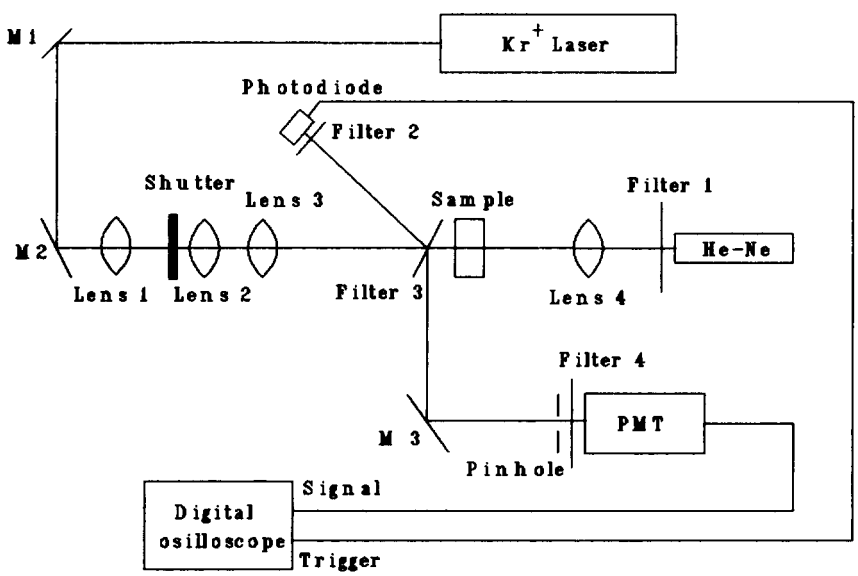

Fig. 4. Experimental arrangement for thermal lens measurements.

TABLE 1

Experimental parameters

Excitation laser power in the sample	5 mW
Excitation laser spot size (ω_e) in the sample	6.13×10^{-3} cm
Probe laser power in the sample	0.8 mW
Probe laser spot size (ω_{1p})	1.07×10^{-2} cm
m	3.06
v	1.01
Z_c of the probe beam	2.82 cm
Z_2	~100 cm

incident on the sample and carefully centred to pass through the thermal lens to maximise the thermal lens signal. After passing through the sample the probe beam was reflected by filter 3 and mirror 3 to a pinhole mounted before a photomultiplier tube (PMT). A band-pass filter, filter 4, at the He–Ne laser wavelength was placed over the PMT to prevent stray light entering the PMT. The spot size of the probe beam at the pinhole was about 10 cm because of scattering by the sample, and the radius of the pinhole used here was 0.5 cm. The output of the PMT was coupled to the digital oscilloscope. The parameters of the experimental set-up such as ω_{0p}, ω_e, ω_{1p} and Z_c were measured as described in [11], and are summarised in Table 1.

The sample used was 30 μm thick pig *stratum corneum*. In the experiment, the digital oscilloscope was set at the fifteen times average mode, and the transient trace of the thermal lens build-up signal as a fifteen-measurement average was recorded. The magnitude of the signal with time was recorded by moving the cursor along the trace. In the experiment, the shutter opening time was 1/15 s and the shutter was left open for 1 min.

Results and discussion

Figure 5 shows the normalised time-resolved thermal lens signal of the sample with its best fit curve. The correlation coefficient to the fit was found to be $R > 0.9999$. The values of $\theta = 0.25 \pm 0.03$ and $t_c = 32 \pm 5$ ms corresponding to the thermal diffusivity, $D = 2.9 \pm 0.5 \times 10^{-4}$ cm^2 s^{-1}, were found. In the experiment the position of the laser beams at the sample was changed three times, and time-resolved thermal lens measurements were carried out. The average of these three determinations was $2.9 \pm 0.5 \times 10^{-4}$ cm^2 s^{-1}. Thus the same results of the thermal diffusivity of the sample were obtained, which are in good agreement with the thermal diffusivity value of the same sample measured by the photothermal beam deflection method.

TLS is suitable then for studying transparent samples. Fortunately, the main optical absorption band of *stratum corneum* and epidermis is located in the UV region, and there is an optical window between 600 and 1300 nm [16], which offers the possibility of measuring the thermal diffusivity of thin-film skin samples using TLS with a long wavelength laser such as Kr^+ at 647.1 nm and He–Ne at 632.8 nm.

Optical scattering is usually a problem for optical measurement of skin samples. However, in a dual-beam thermal lens experiment, light scattering affects thermal lens signal magnitudes by decreasing the excitation beam power available to form the thermal lens, rather than by attenuating

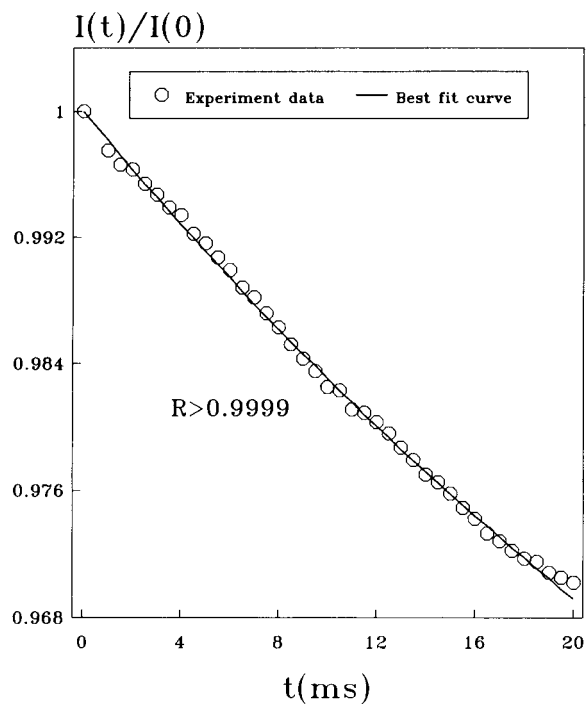

Fig. 5. Time-resolved thermal lens data and best fit curve.

the probe beam, which is affected to an equal extent before and after the thermal lens forms. Scattered light produces no direct interference in a thermal lens experiment because the light which is not absorbed makes no contribution to the induced temperature rise and refractive index gradient. Small to moderate losses in sensitivity occur, which are proportional to the attenuation of the excitation power when scattering occurs. Reasonable scattering losses therefore are easily compensated in the thermal lens experiments [13] and do not effect t_c and therefore thermal diffusivity measurements. Thin-film skin samples can therefore be studied by using TLS.

COMPARISON OF TECHNIQUES

The results for thermal diffusivity obtained by photothermal beam deflection and TLS are in excellent agreement. However, the errors for the determination by TLS are somewhat smaller, being ± 0.5 cm^2 s^{-1} compared to ± 0.9 cm^2 s^{-1} for the beam deflection measurement. The error is larger in the latter case owing to the susceptibility of the measurement to refractive index changes in the air just above the sample caused by turbulence. Also the measurement is being carried out where the optical absorbance of skin is extremely low. Even at the high powers used in this study the overall signal-to-noise level is low. To make a better measurement in terms of signal-to-noise level would require a UV laser to exploit the higher absorbance of skin in that spectral region. Surface roughness of the sample also plays a part in degrading the signal-to-noise level in the beam deflection measurement by causing scatter which alters the amount of energy absorbed. In contrast the time-resolved thermal lens technique relies upon the measurement of the critical time t_c which is independent of the illumination level and therefore is less susceptible to scattering of the pump beam. Any scattering of the probe beam during thermal lens measurement in its passage through the sample remains essentially constant during the lensing process.

The poor signal-to-noise ratio in the beam deflection measurements for skin in the spectral region chosen will actually be advantageous when studying topically applied substances with strong absorbances in that region as the background contribution will be negligible.

The probe beam deflection measurement may also have the advantage over the thermal lens technique for thicker samples than the *stratum corneum* studied here. Preliminary studies in this laboratory have shown that for skin thicknesses of ca. 100 μm the probe He–Ne beam of the thermal lens technique is completely attenuated. Thus no thermal lens signal can be observed. There is also no possibility of carrying out in situ measurements with the thermal lens spectrometer whereas this can be envisaged with the beam deflection measurements provided the subject can be immobilised and a suitable absorber is applied such that low pump laser powers can be employed to avoid burning.

Further work will use the value of $2.9 \pm 0.5 \times 10^{-4}$ cm^2 s^{-1} for thermal diffusivity to obtain depth-related information of absorbed chemicals and preparations. These techniques will also be applied to epidermis.

We acknowledge the support of S.M. Brown and the project by Unilever Research, Port Sunlight Laboratory. We also acknowledge the support of M.L. Baesso by the Universidade Estadual de Maringa, and CNPq, Brazil, and the Hartstone Foundation for the support of J. Shen.

REFERENCES

1 B. Sennhenn, M. Rohr, K. Giese and K. Kolmel, in P. Hess and J. Pelzl (Eds.), Photoacoustic and Photothermal Phenomena, Springer Verlag, Heidelberg, 1988, p. 548.
2 K. Giese, A. Nicolaus, B. Sennhenn and K. Kölmel, Can. J. Phys., 64 (1986) 1139.
3 V. Warner, K. Giese, B. Sennhenn, K. Plamann and K. Kölmer, Phys. Med. Biol., 37 (1992) 21.
4 L.C. Aamodt and J.C. Murphy, J. Appl. Phys., 52 (1981) 4903.
5 S. Culshaw, PhD Thesis, University of Manchester, 1993.
6 P.K. Kuo, L.D. Favro and R.L. Thomas, in J.A. Sell (Ed.), Photothermal Investigations of Solids and Fluids, Academic Press, London, 1989, Chap. 6, 198–212.
7 J.P. Gordon, R.C.C. Leite, R.C. Morre, S.P.S. Porto and J.R. Whinnery, J. Appl. Phys., 36 (1965) 3.

8 J. Shen and R.D. Snook, Anal. Proc., 26 (1989) 403.
9 K.L. Jansen and J.M. Harris, Anal. Chem., 57 (1985) 1698.
10 R.L. Swofford, M.S. Burberry, R.L. Long and A.C. Albercht, J. Chem. Phys. 66 (1977) 664.
11 J. Shen, R.D. Lowe and R.D. Snook, Chem. Phys., 165 (1992) 385.
12 M.L. Baesso, J. Shen and R.D. Snook, Chem. Phys. Lett., 197 (1992) 255.
13 J.F. Power and H. Langford, Anal. Chem., 60 (1989) 842.
14 J. Shen and R.D. Snook, J. Appl. Phys., 73 (1993) 5286.
15 J. Shen, M.L. Baesso and R.D. Snook, Phys. Rev. B, (1993) submitted for publication.
16 R.R. Anderson and J.A. Parrish, J. Invest. Dermatol., 77 (1981) 13.

ANALYTICA CHIMICA ACTA, VOL. 282 (1993)

AUTHOR INDEX

Calendar of forthcoming meetings

★ *indicates new or amended entry*

November 1–4, 1993
Oslo, Norway
LAB '93, Laboratory Exhibition. *Contact:* Norges Varemesse, P.O. Box 130, Skoyen, 0212 Oslo 2, Norway. Tel.: +47 2-43 90100; Fax: +47 2-43 1914.

★ ***November 1–4, 1993***
Amsterdam, The Netherlands
Laboratory Information Management Systems (LIMS). A Four-Day Practical Course with Vendor Demonstrations. *Contact:* The Center for Professional Advancement, Oudezijds Voorburgwal 316A, 1012 GM Amsterdam, The Netherlands. Fax: +31 20-6202136.

November 2–4 1993
Helsinki, Finland
KEMIA 93. Finnish Chemical Congress and Exhibition. *Contact:* Ms. Anita Haatainen, tel.: +358 0 150-9207, or Mr. Seppo Niiranen, tel.: +358 0 150-9215.

★ ***November 2–5, 1994***
Amsterdam, The Netherlands
Fourier Transform Infrared (FTIR) Spectroscopy: Principles, Techniques and Applications; Sampling and Sample Preparation; Selecting an Instrument; Hyphenated Systems. A Four-Day Intensive Course. *Contact:* The Center for Professional Advancement, Oudezijds Voorburgwal 316A, 1012 GM Amsterdam, The Netherlands. Fax: +31 20-6202136.

★ ***November 4–5, 1993***
Munich, Germany
1st Journal of Organometallic Chemistry Conference on Applied Organometallic Chemistry. *Contact:* COMST, P.O. Box 415, 1001 Lausanne 1, Switzerland. Tel.: +41 21-234886; Fax: +41 21-234972.

★ ***November 7–10, 1993***
Charleston, SC, USA
Electrophoresis '93. *Contact:* Mrs. Janet Cunningham, Electrophoresis Society, P.O. Box 279, Walkersville, MD 21793, USA. Tel.: +1 301 898-3772.

December 6–8, 1993
Stockholm, Sweden
Symposium on Purity Determination of Drugs. *Contact:* Swedish Academy of Pharmaceutical Sciences, P.O. Box 1136, S-111 81 Stockholm, Sweden. Tel.: +46 8 245085; Fax: +46 8 205511.

★ ***January 5–7, 1994***
San Diego, CA, USA
WCFIA 94. 6th Winter Conference on Flow Injection Analysis. *Contact:* WCFIA 94, Gary Christian, Department of Chemistry, BG-10, University of Washington, Seattle, WA 98195. Tel.: +1 206 543-1635; Fax: +1 206 685-3478; E-mail: christia@chem.washington.edu.

January 10–15, 1994
San Diego, CA, USA
1994 Winter Conference on Plasma Spectrochemistry. *Contact:* Dr. R. Barnes, ICP Information Newsletter, Department of Chemistry, GRC Towers, University of Massachusetts, Amherst, MA 01003-0035, USA. Tel.: +1 413-545-2294; Fax: +1 413-545-4490. *(Further details published in Vol. 272, No. 2).*

★ ***January 11–14, 1994***
Baltimore, MD, USA
5th International Symposium on Supercritical Fluid Chromatography and Extraction. *Contact:* Prof. Larry T. Taylor, Department of Chemistry, Virginia Polytechnic and State University, Blacksburg, VA 24061, USA. Tel.: +1 703 231-6680; Fax: +1 703 231-8517.

★ ***January 25–28, 1994***
San Diego, CA, USA
3rd International Symposium on Automation, Robotics and Artificial Intelligence applied to Analytical Chemistry and Laboratory Medicine. *Contact:* SCITEC, av. de Provence 20, 1000 Lausanne 20, Switzerland. Tel.: +41 21 624 1533; Fax: +41 21 624 1549.

★ ***January 31–February 3, 1994***
San Diego, CA, USA
HPCE '94. 6th International Symposium on High Performance Capillary Electrophoresis. *Contact:* Shirley Schlessinger, HPCE '94 Symposium Manager, 400 East Randolph Street, Suite 1015, Chicago, IL 60601, USA. Tel.: +1 312 527-2011.

★ ***February 13–16, 1994***
San Francisco, CA, USA
2nd International Glycobiology Symposium: Current Analytical Methods. *Contact:* Paddy Batchelder, P.O. Box 370, Pleasanton, CA, USA. Tel.: +1 510 426-9601; Fax: +1 510 846-2242.

★ ***February 21–25, 1994***
Prague, Czech Republic
International Symposium and Exhibition on Fibre Optic Sensors and Environmental Monitoring. *Contact:* Direct Communications GmbH, Att. Ms. Karin Burger, Xantener Strasse 22, D-1000 Berlin 15, Germany. Tel.: +49 30-8815047; Fax: +49 30-8822028; Telex: 181 479 speco d.

February 22–25, 1994
Antwerp, Belgium
HTC 3. Third International Symposium on Hyphenated Techniques in Chromatography. *Contact:* Royal Flemish Chemical Society (KVCV), Working Party on Chromatography, c/o Dr. R. Smits, BASF Anstwerpen N.V., Central Laboratory, Scheldelaan, B-2040 Antwerp, Belgium. Tel.: +32 3 568 2831; Fax: +32 3 568 3250; Telex: 31047 basant b. *(Further details published in Vol. 268, No. 2).*

★ ***February 23–25, 1994***
Workshops and short courses to precede HTC 3, Third International Symposium on Hyphenated Techniques in Chromatography. *Contact:* Royal Flemish Chemical Society (KVCV), Working

Party on Chromatography, c/o Dr. R. Smits, BASF Anstwerpen N.V., Central Laboratory, Scheldelaan, B-2040 Antwerp, Belgium. Tel.: +32 3 568 2831; Fax: +32 3 568 3250; Telex: 31047 basant b.

February 28–March 4, 1994
Chicago, IL, USA
PITTCON '94. Pittsburgh Conference on Analytical Chemistry and Applied Spectroscopy. *Contact:* Pittsburgh Conference, Suite 332, 300 Penn Center Blvd., Pittsburgh, PA 15235-9962, USA.

March 27–30, 1994
Galveston, TX, USA
International Federation of Automatic Control (IFAC) Symposium on Modeling and Control in Biomedical Systems. *Contact:* IFAC Biomedical Symposium, University of Texas Medical Branch, Box 55176, Galveston, TX 77555-5176, USA. Tel.: +1 409 770-6628 or 770-6605; Fax: +1 409 770-6825.

★ ***April 10–13, 1994***
Mandelieu La Napoule, France
ANATECH 94. 4th International Symposium on Analytical Techniques for Industrial Process Control. *Contact:* ANATECH 94 Secretariat, Elsevier Advanced Technology, Mayfield House, 256 Banbury Road, Oxford OX2 7DH, UK. Tel.: +44 865 512242; Fax: +44 865 310981.

April 19–22, 1994
Munich, Germany
ANALYTICA 94. 14th International Trade Fair for Biochemical and Instrumental Analysis with International Conference. *Contact:* Bernhard Schauder, ANALYTICA Press Office, Münchener Messe- und Ausstellungs-Gesellschaft mbh, Messegelénde, Postfach 12 10 09, D-8000 Munich 12, Germany. Tel.: +49 89-51070; Fax: +49 89-5107506; Telex: 5212086 ameg d.

★ ***April 19–21, 1994***
Manchester, UK
CHEMSPEC EUROPE 94. Exhibition (April 20–21) and Symposium (April 19–20). *Contact:* Jane Malcolm-Coe, PR & Publicity Manager, FMJ International Publications Ltd., Queensway House, 2 Queensway, Redhill, Surrey RH1 1QS, UK. Tel.: +44 737 768611; Fax: +44 737 761685.

May 8-13, 1994
Minneapolis, MN, USA
HPLC '94. 18th International Symposium on High Performance Liquid Chromatography. *Contact:* Janet E. Cunningham, Barr Enterprises, P.O. Box 279, Walkersville, MD 21793, USA. Tel.: (301) 898-3772; Fax: (301) 898-5596.

★ ***May 22–26, 1994***
Venice, Italy
ESEAC '94. 5th European Conference of Electroanalysis. *Contact:* Prof. Salvatore Daniele, Department of Physical Chemistry, The University of Venice, Calle Larga S. Marta 2137, I-30123 Venice, Italy. Tel. +39 41 5298503; Fax: +39 41 5298594.

★ ***May 24–27, 1994***
Toronto, Ont., Canada
International Symposium on Metals and Genetics. *Contact:* Prof. B. Sarkar, Dept. of Biochemistry, The Hospital for Sick Children, 555 University Avenue, Toronto, Ont., Canada M5G 1X8.

★ ***May 30–June 1, 1994***
Bergen, Norway
SSIR 94. Scandinavian Symposium on Infrared and Raman Spectroscopy. *Contact:* Dr. Alfred A. Christy, Department of Chemistry, Allegt. 41, University of Bergen, N-5007 Norway. Tel.: +47 55 213363; Fax: +47 55 329058); or Laila Kyrkjebø, Department of Chemistry, University of Bergen. Tel.: +47 55 213342).

★ ***May 30–June 3, 1994***
Nagoya, Japan
Pyrolysis 94. 11th International Symposium on Analytical and Applied Pyrolysis. *Contact:* Dr. H. Ohtani, Department of Applied Chemistry, Nagoya University, Nagoya 464-01, Japan. Tel.: +81 52-7815111, ext. 4664/3560; Fax: +81 52-7814895.

★ ***June 1–3, 1994***
New Orleans, LA, USA
Biosensors '94. 3rd World Congress on Biosensors. *Contact:* Kay Russell, Elsevier Advanced Technology, Mayfield House, 256 Banbury Road, Oxford OX2 7DH, UK. Tel.: +44 865 512242; Fax: +44 865 310981.

★ ***June 5–7, 1994***
Bruges, Belgium
VIth International Symposium on Luminescence Spectrometry in Biomedical Analysis — Detection Techniques and Applications in Chromatography and Capillary Electrophoresis. *Contact:* Prof. Dr. Willy R.G. Baeyens, Symposium Chairman, University of Ghent, Pharmaceutical Institute, Dept. of Pharmaceutical Analysis, Lab. of Drug Quality Control, Harelbekestraat 72, B-9000 Ghent, Belgium. Tel.: +32 9-2214175; Fax: +32 9-2218951.

★ ***June 8–11, 1994***
Toledo, Spain
Flow Analysis VI. 6th International Conference on Flow Analysis. *Contact:* M. Valcarcel or M.D. Luque de Castro, Flow Analysis VI, Departmento de Química Analítica, Facultad de Ciencias, E-14004 Córdoba, Spain. Tel.: +34 57 218616; Fax: +34 57 218606.

★ ***June 13–15, 1994***
Lund, Sweden
FFF'94. 4th International Symposium on Field-Flow Fractionation. *Contact:* The Swedish Chemical Society, The Analytical Section, Wallingatan 24, 3tr, S-11124 Stockholm, Sweden. Fax: +46 46104525.

June 19–24, 1994
Bournemouth, UK
20th International Symposium on Chromatography. *Contact:* The Executive Secretary, Chromatographic Society, Suite 4, Clarendon Chambers, 32 Clarendon Street, Nottingham NG1 5JD, UK. Tel.: +44 603-500596; Fax: +44 602-500614.

★ ***June 20–22, 1994***
Valladolid, Spain
ESOPS-11. 11th European Symposium on Polymer Spectroscopy. *Contact:* J.M. Pastor, ESOPS-11, Física de la Materia Condensada, Facultad de Ciencias, Universidad de Valladolid, 47005 Valladolid, Spain. Tel.: +34 83 423194; Fax: +34 83 423192 or 423013.

★ ***June 28–29, 1994***
Singapore
CHEMSPEC ASIA 94. Exhibition and Conference. *Contact:* Jane Malcolm-Coe, PR & Publicity Manager, FMJ International Publications Ltd., Queensway

House, 2 Queensway, Redhill, Surrey RH1 1QS, UK. Tel.: +44 737 768611; Fax: +44 737 761685.

★ ***July 11–14, 1994***
Norwich, UK
Spectroscopy Across the Spectrum IV: Techniques and Applications of Analytical Spectroscopy. *Contact:* Dr. D.L. Andrews, Hon. Secretary, Spectroscopy Across the Spectrum IV, School of Chemical Sciences, University of East Anglia, Norwich NR4 7TJ, UK.

★ ***July 20–22, 1994***
Hull, UK
7th Biennial National Atomic Spectroscopy Symposium. *Contact:* Dr. Steve Haswell, School of Chemistry, University of Hull, Hull HU6 7RX, UK. Tel: +44 482-465469.

★ ***July 31–August 5, 1994***
Ottawa, Ont., Canada
8th International Symposium on Molecular Recognition and Inclusion. *Contact:* Mrs. Hguette Morin-Dumais, 8th ISMRI, Steacie Institute for Molecular Sciences, National Research Council Canada, Room 1157, 100 Sussex Drive, Ottawa, Ont., Canada K1A 0R6. Tel.: +1 613 990-0936; Fax: +1 613 954-5242; E-mail: ismri@ned1.sims.nrc.ca.

July 1994
Maastricht, The Netherlands
International Chemometrics Research Meeting. *Contact:* Laboratory for Analytical Chemistry, Faculty of Science, Catholic University of Nijmegen, Toernooiveld 1, 6525 ED Nijmegen, The Netherlands.

★ ***August 2–6, 1994***
Changchun, P.R. China
The Second Changchun International Symposium on Analytical Chemistry (CISAC). *Contact:* Prof. Qinhan Jin, Department of Chemistry, Jilin University, Changchun 130023, P.R. China. Tel.: 0431-822331, ext. 2433; Fax: 0431-823907.

★ ***August 22–26, 1994***
Hong Kong
ICORS '94. XIV International Conference on Raman Spectroscopy. *Contact:* Prof. Nai-Teng Yu, ICORS '94, c/o Department of Chemistry, The Hong Kong University of Science and Technology, Clear Water Bay, Kowloon, Hong Kong.

★ ***August 23–26, 1994***
Guildford, UK
QSA-8. International Conference on Quantitative Suface Analysis: Techniques and Applications. *Contact:* Doreen Tilbrook, Division of Materials Metrology, National Physical Laboratory, Teddington, Middlesex TW11 0LW, UK.

September 11–16, 1994
Essen, Germany
EUCMOS XXII. XXII European Congress on Molecular Spectroscopy. *Contact:* Congress Secretariat, Gesellschaft Deutscher Chemiker, Abt. Tagungen, P.O. Box 900440, W-6000 Frankfurt 90, Germany. Tel.: +49 69 7917-366; Fax +49 69 7917-475; Telex 4 170 497 gdch d. *(Further details published in Vol. 272, No. 2).*

★ ***September 18–22, 1994***
Chambéry, Savoy, France
14th International CODATA Conference. Data and Knowledge in a Changing World: The Quest for a Healthier Environment. *Contact:* Prof. J.-E. Dubois, ITODYS, Université Paris 7, 1 rue Guy de la Brosse, 75005 Paris, France. Fax: +33 1 42881466. E-mail: codata@paris7.jussieu.fr (Internet).

September 21–23, 1994
Stockholm, Sweden
5th International Symposium on Pharmaceutical and Biomedical Analysis: *Contact:* Swedish Academy of Pharmaceutical Sciences, P.O. Box 1136, S-111 81 Stockholm, Sweden. Tel.: +46 8 245085; Fax: +46 8 205511.

September 22–24, 1994
Constanta, Romania
12th Conference on Analytical Chemistry. *Contact:* Dr. Gabirel-Lucian Radu, Romanian Society of Analytical Chemistry, 13 Blvd. Carol I, Sector 3, 70346 Bucharest, Romania.

★ ***October 3–7, 1994***
St. Petersburg, Russia
ISCMS '94. International Symposium: Chromatography and Mass Spectrometry in Environmental Analysis. *Contact:* ISCMS '94, Dr. Alexander Rodin, State Institute of Applied Chemistry, Dobrolubov Ave. 14, 197198, St. Petersburg, Russia. Tel.: +7 812 2389786; Fax: +7 812 2338989; Telex: 121345 ptb sigma.

★ ***October 17–19, 1994***
Strasbourg, France
3rd International Symposium on Supercritical Fluids: Thermodynamics, Physico-chemical Properties, Technology and Applications. *Contact:* ISASF, Mle. Brionne, ENSIC, P.O. Box 451, F-54001 Nancy Cedex, France. Tel.: +33 83175003; Fax: +33 83350811.

★ ***November 9–11, 1994***
Montreux, Switzerland
11th Montreux Symposium on Liquid Chromatography–Mass Spectrometry (LC/MS; SFC/MS; CE/MS; MS/MS). *Contact:* M. Frei-Häusler, Postfach 46, CH-4123 Allschwil 2, Switzerland. Tel.: +41 61-4812789; Fax: +41 61-4820805.

March 6–10, 1995
PITTCON '95. Pittsburgh Conference on Analytical Chemistry and Applied Spectroscopy. *Contact:* Pittsburgh Conference, Suite 332, 300 Penn Center Blvd., Pittsburgh, PA 15235-9962, USA.

★ ***May 9–12, 1995***
Jülich, Germany
6th International Hans Wolfgang Nürnberg Memorial Symposium on Metal Compounds in Environment and Life, 6: Analysis, Speciation and Specimen Banking. *Contact:* Dr. H.W. Dürbeck, Institute of Applied Physical Chemistry, Research Center, Jülich (KFA), P.O. Box 1913, D-5170 Jülich, Germany.

July 9–15, 1995
Hull, UK
SAC 95. *Contact:* Analytical Division, The Royal Society of Chemistry, Burlington House, Piccadilly, London W1V 0BN, UK. Tel.: +44 71 437-8656; Fax: +44 71 734-1227.

★ ***August 27–September 1, 1995***
Leipzig, Germany
CSI XXIX. Colloquium Spectroscopicum Internationale XXIX. *Contact:* Gesellschaft Deutscher Chemiker, Abt. Tagungen, P.O. Box 90 04 40, D-60444 Frankfurt/ Main, Germany.

★ ***August 27–September 1, 1995***
Budapest, Hungary
10th International Conference on Fourier Transform Spectroscopy. *Contact:* Mrs. Klára Láng/Mr. Attila Varga, Conference Office, Roland Eötvös Physical Society, P.O. Box 433, H-1371 Budapest, Hungary. Tel./Fax: +36 1 201-8682.

★ ***September 12–15, 1995***
Leuven, Belgium
5th International Symposium on Drug Analysis. *Contact:* Prof. J. Hoogmartens, Drug Analysis '95, Institute of Pharmaceutical Sciences, Van Evenstraat 4, B-3000 Leuven, Belgium. Tel.: +32 16 283440; Fax: +32 16 283448.

711\414\140\079\03

BIOAFFINITY CHROMATOGRAPHY

By **J. Turková,** Czechoslovak Academy of Sciences, Institute of Organic Chemistry and Biochemistry, Prague, Czech Republic

Journal of Chromatography Library Volume 55

Bioaffinity chromatography is now the preferred choice for the purification, determination or removal of many biologically active substances. The book includes information on biologically active substances with their affinants, solid supports and methods of coupling, summarized in tables covering classical, high-performance liquid and large-scale bioaffinity chromatography.

Optimization of the preparation and the use of highly active and stable biospecific adsorbents is discussed in several chapters. Following a chapter dealing with the choice of affinity ligands, affinity-sorbent bonding is described in detail. Other chapters give information on solid supports, the most common coupling procedures and a general discussion of sorption and elution. Several applications of bioaffinity chromatography are described, e.g. quantitative evaluation of biospecific complexes and many applications in medicine and in the biotechnology industry.

Contents:

© 1993 819 pages Hardbound
Price: Dfl. 495.00 / US $ 282.75
ISBN 0-444-89030-0

ELSEVIER
SCIENCE PUBLISHERS

ORDER INFORMATION

For USA and Canada
ELSEVIER SCIENCE PUBLISHERS
Judy Weislogel, P.O. Box 945
Madison Square Station
New York, NY 10160-0757
Fax: (212) 633 3880

In all other countries
ELSEVIER SCIENCE PUBLISHERS
P.O. Box 330
1000 AH Amsterdam
The Netherlands
Fax: (+31-20) 5862 845

US$ prices are valid only for the USA & Canada and are subject to exchange rate fluctuations; in all other countries the Dutch guilder price (Dfl.) is definitive. Customers in the European Community should add the appropriate VAT rate applicable in their country to the price(s). Books are sent postfree if prepaid.

Experimental Design: A Chemometric Approach

Second, Revised and Expanded Edition

by **S.N. Deming** *and* **S.L. Morgan**

Data Handling in Science and Technology Volume 11

Now available is the second edition of a book which has been described as *"...an exceptionally lucid, easy-to-read presentation... would be an excellent addition to the collection of every analytical chemist. I recommend it with great enthusiasm."* (Analytical Chemistry).

N.R. Draper reviewed the first edition in Publication of the International Statistical Institute *"...discussion is careful, sensible, amicable, and modern and can be recommended for the intended readership."*

The scope of the first edition has been revised, enlarged and expanded. Approximately 30% of the text is new. The book first introduces the reader to the fundamentals of experimental design. Systems theory, response surface concepts, and basic statistics serve as a basis for the further development of matrix least squares and hypothesis testing. The effects of different experimental designs and different models on the variance-covariance matrix and on the analysis of variance (ANOVA) are extensively discussed. Applications and advanced topics (such as confidence bands, rotatability, and confounding) complete the text. Numerous worked examples are presented.

The clear and practical approach adopted by the authors makes the book applicable to a wide audience. It will appeal particularly to those who still need to know efficient ways of carrying out experiments. It will also be an ideal text for advanced undergraduate and graduate students following courses in chemometrics, data acquisition and treatment, and design of experiments.

Contents:

1993 416 pages
Price: US $ 177.25 / Dfl. 310.00
ISBN 0-444-89111-0

ORDER INFORMATION

For USA and Canada
ELSEVIER SCIENCE PUBLISHERS
Judy Weislogel
P.O. Box 945
Madison Square Station,
New York, NY 10160-0757
Tel: (212) 989 5800
Fax: (212) 633 3880

In all other countries
ELSEVIER SCIENCE PUBLISHERS
P.O. Box 211
1000 AE Amsterdam
The Netherlands
Tel: (+31-20) 5803 753
Fax: (+31-20) 5803 705

US$ prices are valid only for the USA & Canada and are subject to exchange rate fluctuations; in all other countries the Dutch guilder price (Dfl.) is definitive. Customers in the European Community should add the appropriate VAT rate applicable in their country to the price(s). Books are sent post-free if prepaid.

ELSEVIER
SCIENCE PUBLISHERS

PUBLICATION SCHEDULE FOR 1994

	S'93	O'93	N'93	D'93	J	F						
Analytica Chimica Acta	281/1 281/2 281/3	282/1 282/2 282/3	283/1 283/2	283/3 284/1 284/2	284/3 285/1 285/2	285/3 286/1 286/2						
Vibrational Spectroscopy		6/1			6/2							

INFORMATION FOR AUTHORS

Detailed "Instructions to Authors" for *Analytica Chimica Acta* was published in Volume 256, No. 2, pp. 373–376. Free reprints of the "Instructions to Authors" of *Analytica Chimica Acta* and *Vibrational Spectroscopy* are available from the Editors or from: Elsevier Science Publishers B.V., P.O. Box 330, 1000 AH Amsterdam, The Netherlands. Telefax: (+31-20) 5862845.

Manuscripts. The language of the journal is English. English linguistic improvement is provided as part of the normal editorial processing. Authors should submit three copies of the manuscript in clear double-spaced typing on one side of the paper only. *Vibrational Spectroscopy* also accepts papers in English only.

Abstract. All papers and reviews begin with an Abstract (50–250 words) which should comprise a factual account of the contents of the paper, with emphasis on new information.

Figures. Figures should be prepared in black waterproof drawing ink on drawing or tracing paper of the same size as that on which the manuscript is typed. One original (or sharp glossy print) and two photostat (or other) copies are required. Attention should be given to line thickness, lettering (which should be kept to a minimum) and spacing on axes of graphs, to ensure suitability for reduction in size on printing. Axes of a graph should be clearly labelled, along the axes, outside the graph itself. All figures should be numbered with Arabic numerals, and require descriptive legends which should be typed on a separate sheet of paper. Simple straight-line graphs are not acceptable, because they can readily be described in the text by means of an equation or a sentence. Claims of linearity should be supported by regression data that include slope, intercept, standard deviations of the slope and intercept, standard error and the number of data points; correlation coefficients are optional.

Photographs should be glossy prints and be as rich in contrast as possible; colour photographs cannot be accepted. Line diagrams are generally preferred to photographs of equipment.

Computer outputs for reproduction as figures must be good quality on blank paper, and should preferably be submitted as glossy prints.

Nomenclature, abbreviations and symbols. In general, the recommendations of the International Union of Pure and Applied Chemistry (IUPAC) should be followed, and attention should be given to the recommendations of the Analytical Chemistry Division in the journal *Pure and Applied Chemistry* (see also *IUPAC Compendium of Analytical Nomenclature, Definitive Rules*, 1987).

References. The references should be collected at the end of the paper, numbered in the order of their appearance in the text (*not* alphabetically) and typed on a separate sheet.

Reprints. Fifty reprints will be supplied free of charge. Additional reprints (minimum 100) can be ordered. An order form containing price quotations will be sent to the authors together with the proofs of their article.

Papers dealing with vibrational spectroscopy should be sent to: Dr J.G. Grasselli, 150 Greentree Road, Chagrin Falls, OH 44022, U.S.A. Telefax: (+1-216) 2473360 (Americas, Canada, Australia and New Zealand) or Dr J.H. van der Maas, Department of Analytical Molecule Spectrometry, Faculty of Chemistry, University of Utrecht, P.O. Box 80083, 3508 TB Utrecht, The Netherlands. Telefax: (+31-30) 518219 (all other countries).

0003-2670/93/$06.00

This issue is printed on acid-free paper.

PRINTED IN THE NETHERLANDS

Intelligent Software for Chemical Analysis

Edited by **L.M.C. Buydens** and **P.J. Schoenmakers**

Data Handling in Science and Technology Volume 13

Various emerging techniques for automating intelligent functions in the laboratory are described in this book. Explanations on how systems work are given and possible application areas are suggested. The main part of the book is devoted to providing data which will enable the reader to develop and test his own systems. The emphasis is on expert systems; however, promising developments such as self-adaptive systems, neural networks and genetic algorithms are also described.

The book has been written by chemists with a great deal of practical experience in developing and testing intelligent software, and therefore offers first-hand knowledge. Laboratory staff and managers confronted with commercial intelligent software will find information on the functioning, possibilities and limitations thereof, enabling them to select and use modern software in an optimum fashion. Finally, computer scientists and information scientists will find a wealth of data on the application of contemporary artificial intelligence techniques.

Contents:

1. Introduction. Automation and intelligent software. Expert systems. Neural networks and genetic algorithms. Reader's guide. Concepts. Conclusions.

2. Knowledge-based Systems in Chemical Analysis (P. Schoenmakers). Computers in analytical chemistry. Sample preparation. Method selection. Method development. Instrument control and error diagnosis. Data handling and calibration. Data interpretation. Validation. Laboratory management. Concluding remarks. Concepts. Conclusions. Bibliography.

3. Developing Expert Systems (H. van Leeuwen). Introduction. Prerequisites. Knowledge acquisition. Knowledge engineering. Inferencing. Explanation facilities. The integration of separate systems. Expert-system testing validation and evaluation. Concepts. Conclusions. Bibliography.

4. Expert-System-Development Tools (L. Buydens, H. van Leeuwen, R. Wehrens). Tools for implementing expert systems. Tool selection. Knowledge-acquisition tools. Concepts. Conclusions. Bibliography. **5. Validation and Evaluation of Expert Systems for HPLC Method Development - Case Studies** (F. Maris, R. Hindriks). Introduction. Case study I: Expert systems for method selection and selectivity optimization. Case study II: System-optimization expert system. Case study III: Expert system for repeatability testing, applied for trouble-shooting in HPLC. Case study IV: Ruggedness-testing expert system. General comments on the evaluations. Concepts. Conclusions. Bibliography.

6. Self-adaptive Expert Systems (R. Wehrens). Introduction - maintaining expert systems. Self-adaptive expert systems: Methods and approaches. The refinement approach of SEEK. Examples from analytical chemistry. Concluding remarks. Concepts. Conclusions. Bibliography.

7. Inductive Expert Systems (R. Wehrens, L. Buydens). Introduction. Inductive classification by ID3. Applications of ID3 in analytical chemistry. Concluding remarks. Concepts. Conclusions. Bibliography. **8. Genetic Algorithms and Neural Networks** (G. Kateman). Introduction. Genetic algorithms. Artificial neural networks. Concepts. Conclusions. Bibliography. **9. Perspectives.** Limitations of Intelligent Software. Dealing with intelligent software. Potential of intelligent software. **Index.**

© 1993 366 pages Hardbound
Price: Dfl. 350.00 (US $ 200.00)
ISBN 0-444-89207-9

ELSEVIER
SCIENCE PUBLISHERS

ORDER INFORMATION

For USA and Canada
ELSEVIER SCIENCE PUBLISHERS
Judy Weislogel, P.O. Box 945
Madison Square Station
New York, NY 10160-0757
Fax: (212) 633 3880

In all other countries
ELSEVIER SCIENCE PUBLISHERS
P.O. Box 330
1000 AH Amsterdam
The Netherlands
Fax: (+31-20) 5862 845

US$ prices are valid only for the USA & Canada and are subject to exchange rate fluctuations; in all other countries the Dutch guilder price (Dfl.) is definitive. Customers in the European Community should add the appropriate VAT rate applicable in their country to the price(s). Books are sent postfree if prepaid.

0003-2670(19931029)282:3;1-5